From WIMPs to FIMPs: Advanced Methods and Phenomenological Studies

Dissertation submitted for the award of the title
"Doctor of Natural Sciences"
to the Faculty of Physics, Mathematics and Computer Science of
Johannes Gutenberg University Mainz

Emanuele Copello
born in Varese, Italy

Mainz, March 25, 2026

JOHANNES GUTENBERG UNIVERSITÄT MAINZ

From WIMPs to FIMPs: Advanced Methods and Phenomenological Studies,

Author: Emanuele Copello

Date of First Submission: August 30, 2024
Date of Second submission: March 25, 2026
Date of defense: May 27, 2026

Dedicated to my beloved wife
and to our families.

"perché tutte le immagini portano scritto:
≪più in là≫"
Eugenio Montale, *Maestrale*, Ossi di Seppia

"There are more things in Heaven and Earth, Horatio,
than are dreamt of in your philosophy."
William Shakspeare, *Hamlet* (1, 5, 167-8)

"A few observations and much reasoning lead to error;
many observations and a little reasoning to truth."
Alexis Carrel

Abstract

The elusive nature of dark matter (DM) has prompted a variety of theoretical models and experimental searches aimed at uncovering its properties. This thesis explores three approaches to advance the understanding of DM production within simplified t-channel models, where DM interacts with a Standard Model (SM) fermion through a heavier gauge-charged mediator.

First, we highlight the importance of non-perturbative effects from long-range interactions like the Sommerfeld effect and bound state formation in colored co-annihilations. We implement such effects in `micrOMEGAs`, a popular code to compute the DM relic abundance, and we find that previous exclusions of parameter space by direct detection and LHC searches may still be viable, emphasizing the potential of long-lived particle (LLP) and bound-state searches at the LHC.

Second, we analyze thermal corrections to freeze-in production of feebly interacting DM using the Closed-Time-Path formalism. We perform a detailed analysis of the DM rate equation and we compute its relic abundance by using 1PI-resummed propagators derived from a 2PI effective action that includes the full dependence on relevant mass scales. Our results show significant deviations from the semiclassical Boltzmann approach and the Hard-Thermal-Loop approximation, demonstrating the role of theoretical uncertainties in determining DM properties. We also address the issue of negative spectral sums in models featuring gauge-charged scalar fields.

Lastly, we study freeze-in production during non-instantaneous reheating after inflation, showing that low reheating temperatures and different inflationary potentials can alter DM production. We highlight the impact of inflationary dynamics on DM freeze-in and LLP searches, stressing the importance of accurately defining the reheating temperature.

Zusammenfassung

Die schwer fassbare Natur der Dunklen Materie (DM) hat eine Vielzahl theoretischer Modelle und experimenteller Suchmethoden hervorgebracht, um ihre Eigenschaften zu entschlüsseln. Diese Dissertation untersucht drei Ansätze zum Verständnis der DM-Produktion innerhalb vereinfachter t-Kanal-Modelle, bei denen DM mit einem Fermion des Standardmodells (SM) durch ein schwereres gaugeladenes Vermittlerteilchen interagiert.

Zunächst untersuchen wir, wie farbige Koannihilationskanäle die Vorhersagen über die Massen der Teilchen im dunklen Sektor beeinflussen und betonen dabei die Bedeutung nicht-perturbativer Effekte wie den Sommerfeld-Effekt und die Bildung von gebundenen Zuständen. Wir implementieren solche Effekte in einem weit verbreiteten Code zur Berechnung der DM-Reliktdichte und stellen fest, dass zuvor durch direkte Detektion und LHC-Suchen ausgeschlossene Parameterbereiche möglicherweise doch noch relevant sind. Wir unterstreichen das Potenzial von Suchen nach langlebigen Teilchen (*Long-lived Particles* oder *LLP*) und gebundenen Zuständen am LHC.

Zweitens analysieren wir thermische Korrekturen zur Freeze-in-Produktion von schwach interagierender DM unter Verwendung des Closed-Time-Path-Formalismus. Wir führen eine detaillierte Analyse der DM-Rategleichung durch und berechnen ihre Reliktdichte mithilfe 1PI-resummierter Propagatoren, die aus einer 2PI-Effektiven-Wirkung abgeleitet sind und die volle Abhängigkeit von relevanten Massen berücksichtigen. Unsere Ergebnisse zeigen signifikante Abweichungen vom semiklassischen Boltzmann-Ansatz und der Hard-Thermal-Loop-Näherung, was die Rolle theoretischer Unsicherheiten bei der Bestimmung von DM-Eigenschaften verdeutlicht. Wir behandeln auch das Problem negativer Spektralsummen in Modellen mit gaugeladenen Skalarfeldern.

Abschließend untersuchen wir die Freeze-in-Produktion während der nicht-instantanen Reheating-phase nach der Inflation und zeigen, dass niedrige Reheating-temperaturen und unterschiedliche Inflationspotentiale die DM-Produktion verändern können. Wir heben die Auswirkungen der Inflationsdynamik auf die DM-Freeze-in-Produktion und LLP-Suchen hervor und betonen die Bedeutung einer genauen Definition der Reheating-temperatur.

List of Publications

This thesis is based on the publications and preprints [1–5] listed below. The results of [1] have been presented at the international conference "NuDM-2022", resulting in the publication in the special issue of the journal Letters of High Energy Physics [2]. Parts of the results of [1] and some follow-up ideas took part in the collaborative white paper [3] as a contribution to the Snowmass 2021 process. Here, we highlight the contributions made by the thesis author. Other authors are referred to with their corresponding initials.

[1] M. Becker, E. Copello, J. Harz, K. Mohan and D. Sengupta, *Impact of Sommerfeld Effect and Bound State Formation in Simplified t-Channel Dark Matter Models*, JHEP **08** (2022) 145 [2203.04326].
The idea for the project originated with JH, who also played a central role in supervising and providing guidance throughout its development and shaping the structure of the manuscript. The thesis author contributed to the preliminary feasibility study and performed analytical calculations as well as numerical simulations, including the development of new `C++` code routines and the creation of plots using `Mathematica`. The analysis of experimental limits was done by KM and DS–the thesis author has contributed to the derivation of constraints for resonance searches at colliders– but incorporated into the simulation results by MB and EC. The manuscript was mainly written by the thesis author and MB, with contributions and corrections from JH, KM, and DS. All authors supervised the project's development and discussed the results. All authors revised the manuscript. This work constitutes the topic in Chapters IV and V.

[2] M. Becker, E. Copello, J. Harz, K. Mohan and D. Sengupta, *Implications of Non-perturbative Effects for Colored Dark Sectors*, LHEP 2023 (2023) 363.
Results of [1] are published in the proceedings of the "NuDM-2022" conference.

[3] J. L. Feng et al. *The Forward Physics Facility at the High-Luminosity LHC*, J.Phys.G **50** (2023) 3, 030501 [2203.05090].
Invited contribution for the white paper on "The Forward Physics Facility at the High-Luminosity LHC" within the Snowmass 2021 process following the work in [1]. The thesis author proposed and discussed with the co-authors of [1] the potential to leverage existing works on detecting quirks with the FASER experiment at the LHC to identify signatures of different types of bound states and detect long-lived, heavy-colored particles. A preliminary analysis was written by the thesis author in collaboration with MB and DS.

[4] M. Becker, E. Copello, J. Harz, J. Lang, Y. Xu, *Confronting Dark Matter Freeze-in during Reheating with Constraints from Inflation*, JCAP **01** (2024) 053 [2306.17238].
The thesis author and JH contributed to the initial ideas leading to the paper. JH played a central role in supervising and providing guidance throughout its development and shaping the structure of the manuscript, while the thesis author, in particular, conducted the literature research and explored various types of reheating potentials and inflaton decay mechanisms, expanding an initial effort done together

with MB, JH, and JL. The thesis author participated in the cross-checking of every calculation and the discussion of the results. All authors supervised the project's development and discussed the results. The manuscript was primarily written by the thesis author, M. Becker, and Y. X and revised and corrected by all authors. The publication is part of Chapter X.

[5] M. Becker, E. Copello, J. Harz, C. Tamarit, *Dark Matter Freeze-in from Non-equilibrium QFT: towards a Consistent Treatment of Thermal Effects*, JCAP **03** (2025) 071 [2312.17246].
The project originated from an idea of JH, who also played a central role in supervising and providing guidance throughout its development and shaping the structure of the manuscript. The thesis author and MB conducted the literature research to investigate the study's feasibility. They derived all analytical results and performed the numerical analysis, with active technical support provided by CT. The thesis author and MB also implemented and simulated the code on the NHR-MOGON HPC cluster of the University of Mainz. The manuscript was mainly written by the thesis author and MB, with contributions from JH and CT, and revised by all authors. All authors supervised the project's development and discussed the results. This work is part of Chapters VI to VIII.
During the feasibility study, the thesis author obtained some analytical results for modeling featuring Majorana DM candidates that have been expanded and collected in Chapter IX. These findings are original and not included in [5].

[6] C. Arina et al., *t-channel dark matter at the LHC*, CERN-LPCC-2025-001, IRMP-CP3-25-07, TTK-25-07 Eur.Phys.J.C **85** (2025) 9, 975 [2504.10597].
The thesis author participated in discussions regarding the cosmology section of the white paper, contributing to paragraphs on non-perturbative effects and freeze-in with low reheating temperatures.

Furthermore, the development of the code necessary for [1] led to the following publications, which are not part of this thesis's work:

[7] M. Becker, E. Copello, J. Harz, M. Napetschnig, *Manual for SE+BSF4DM - A micrOMEGAs package for Sommerfeld Effect and Bound State Formation in colored Dark Sectors.*

[8] M. Becker, E. Copello, J. Harz, M. Napetschnig, *Sommerfeld Effect and Bound State Formation for Dark Matter Models with Colored Mediators with SE+BSF4DM.*

Finally, the author of this thesis has contributed to the preliminary stages of several works recently published. Developments in Chapters VI and VII, along with Ref. [5], laid the foundation for the research later published in [9] and [10]. The thesis author participated in the initial discussions and calculations, drawing on the expertise and results from [5], but was not directly involved in the core development of the publications themselves.

At the beginning of the chapters detailing the author's research in relation to published works, a declaration of contribution is provided. Additionally, each main section within these chapters includes a reiterated statement clarifying the author's specific contributions presented in that section.

If not stated otherwise, the figures presented in this thesis were created by the author himself, or the author has contributed to designing them. Figures that collaborators created for a paper in which the thesis author was involved, as well as figures reproduced from published works that do not feature the thesis author as a contributor, are given the corresponding credit.

Contents

Prologue

CHAPTER I

Introduction

Over the last century, two groundbreaking theories have emerged as the cornerstones of high-energy physics: the Standard Model (SM) of Particle Physics and the Lambda Cold Dark Matter (ΛCDM) model of Cosmology.

The SM of Particle Physics is one of the most significant achievements in modern physics. It provides a comprehensive framework for understanding elementary particles and their fundamental interactions, except for gravity. Developed throughout the latter half of the 20th century, it describes all known elementary particles, with the discovery of the Higgs boson at the Large Hadron Collider (LHC) in 2012 as the final monumental confirmation of the theory. Despite its successes, the SM has limitations. It does not account for a quantum description of gravity or explain certain observations, most notably neutrino oscillations, which imply that neutrinos have mass, a property not included in the SM.[1]

In parallel, cosmology has been revolutionized by the ΛCDM model, based on General Relativity (GR), together with the theory of cosmic inflation. The model assumes a Universe that is homogeneous and isotropic on large scales (the *cosmological principle*), containing dark energy (Λ) that drives its accelerated expansion and Cold Dark Matter (CDM) that explains gravitational effects not attributable to visible matter alone, including the Large-Scale Structure (LSS) of the Universe. Supported by observations of the cosmic microwave background (CMB) and of the matter power spectrum, inflation justifies the cosmological principle and provides an origin for the formation of structure. The ΛCDM model presents challenges to the SM, as no known particle, field, or interaction within the SM can fully explain dark matter (DM), dark energy, or cosmic inflation. The inability of the SM to account for the baryon asymmetry of the Universe, namely the observed excess of matter over antimatter, also suggests the need for physics Beyond the Standard Model (BSM).

This thesis focuses on the DM problem. Since the 1920s, observations of stellar motion in galaxy clusters and rotation curves of spiral galaxies have indicated the presence of "invisible" mass—DM—that cannot be explained by luminous baryonic matter. DM is thought to make up about 85% of the Universe's matter content and about 26% of its energy density, yet its nature remains one of the most profound mysteries in physics. In the SM, only neutrinos could potentially be DM, but the way structures are formed in the Universe precludes them from fulfilling this role. Other explanations, such as primordial

[1]There are many more issues and curiosities about the SM as a theory that have received substantial attention in recent years, most notably the hierarchy problem, the strong CP problem, quantum triviality, the flavour puzzle, the inability to unify the EW and strong interactions at a higher scale, the particle desert, not to mention the lack of a consistent and mathematically complete gauged QFT in four-dimensional spacetimes (mass gap problem).

black holes or modified gravity theories like MOdified Newtonian Dynamics (MOND), will be reviewed in Chapter II. The most widely explored hypothesis is that DM is a BSM particle, perhaps part of a dark sector, interacting weakly with visible matter or consisting of particles much heavier than the TeV scale. This might explain why such a particle has not been detected at colliders, by telescopes, or in underground experiments.

In recent years, *simplified models* of DM have sparked the interest of the theoretical and experimental communities. These are theoretical frameworks designed to capture the essential physics of DM interactions within a minimalistic setup, particularly relevant for collider experiments. These models introduce a DM particle and a mediator that couples DM to SM particles through renormalizable operators. They are constructed to include just enough complexity to describe key physical processes at collider energies while limiting the number of new particles and parameters, making them practical for experimental searches. Moreover, they serve as a bridge between broader effective predictions and more detailed, parameter-rich predictions of complete models (e.g., supersymmetry).

In this work, we focus on the class of simplified models going under the name of t-channel models. These involve charged or colored mediators that are exchanged off-shell when interacting with DM plus a SM fermion. Both the mediators and the DM share the same stabilizing symmetry.[2] This leads to different experimental signatures. Unlike their s-channel counterpart, t-channel interactions do not feature resonant enhancement, and their constraints come from searches targeting final states with missing energy plus jets or leptons. Some t-channel models also resemble scenarios in the Minimal Supersymmetric Standard Model (MSSM), such as the squark-neutralino system. Therefore, they allow researchers to study key physical processes that could originate from MSSM physics but in a less complex and less constrained framework.

The study of simplified DM models is particularly timely due to the high energies accessible at the LHC, which challenge the validity of effective descriptions and necessitate models that can probe DM interactions within these energy scales. As the LHC continues to gather data, there is a growing need for models that can accurately describe potential DM signals while remaining computationally feasible and experimentally testable. Additionally, the growing sensitivity and scope of direct and indirect detection searches demand a comprehensive analysis of DM phenomenology that remains efficient and effective, without being hindered by model complexity. Simplified DM models meet this need, making them a powerful and highly testable tool for ongoing and future DM searches.

How can we be sure that a certain experiment is targeting a parameter space region compatible with DM? Specifically, how do we compare experimental results with cosmological and astrophysical observations? The most precise quantity related to DM measured to date is its cosmic relic abundance, known with an accuracy at the sub-percent level of error. By understanding if a given combination of parameters (e.g., masses and couplings) provides the correct abundance, we can correctly interpret experimental bounds and, with some luck, signals. The way this abundance was established in the early Universe is crucially dependent on the specific process through which DM particles were produced and left as a cosmic relic.

As we will review in Chapter III, the cosmological evolution of the DM number density is commonly obtained by solving its Boltzmann equation, which depicts the competition

[2]Simplified DM models are divided into two categories: s-channel and t-channel models. They differ primarily in the nature of their mediators, the interaction topologies, and the resulting experimental signatures. In s-channel models, DM is charged under a stabilizing symmetry, while the mediator is not necessarily. The mediator is typically a neutral particle that can be produced on-shell, leading to experimental searches focusing on resonance phenomena.

between the rate of expansion of the Universe, diluting the number density, and the DM interaction rate, which determines the rate of change in the number of DM particles. In the literature, it is historically assumed that the DM relic abundance was set during *radiation domination* (RD), when the energy density of the Universe was dominated by the radiation bath of relativistic particles, expanding adiabatically at a well-defined rate. At the same time, the interaction rate is typically derived with standard QFT techniques by calculating the cross-sections of the creation and destruction processes happening in-vacuum with states that are assumed to be asymptotically free and interact instantaneously. In this 'empirical' approach, the only way to account for the statistical properties of the thermal bath is by manually incorporating the distribution functions of particles involved in the reactions. Solving the Boltzmann equation provides a simple and effective way to relate the properties of the Universe, model parameters, and associated DM phenomenology, making it a successful approach.

These assumptions and simplifications warrant scrutiny. Examining them is crucial because the process by which DM is produced directly influences predictions for model parameters, such as the correlation between particle masses and interaction couplings. These parameters are what experiments aim to constrain, and accurately interpreting these constraints is vital. Misinterpretations could lead to the premature exclusion of a model or, conversely, the failure to recognize a viable parameter region. Thus, a deeper understanding of DM production processes and the underlying cosmological conditions is essential for making correct inferences about the viability of DM models based on experimental data.

This thesis aims to dissect and examine three ways of advancing the accuracy of DM production calculations in simplified t-channel models. First, by incorporating *long-range effects* arising from colored mediators in co-annihilation scenarios, notably the Sommerfeld effect and the formation of mediators' bound states. Second, by accounting for *thermal corrections* arising from the interactions of the mediators with the primordial finite-density thermal bath. Third, by considering the possibility of a *prolonged reheating phase* after cosmic inflation. As we will see, all these investigations reveal the crucial necessity of accurately accounting for non-trivial effects to guarantee a higher level of precision in the calculation and reduce the theoretical uncertainty when confronting a model with experimental bounds. Moreover, the methods developed here have broader applicability beyond simplified DM models and DM physics, extending to the wider realm of particle production in the early Universe.

The thesis is structured as follows:

In Chapter II, we review the evidence supporting DM from various astrophysical and cosmological observations, while also addressing related tensions and controversies. We outline the historically significant DM candidates, with a particular focus on simplified t-channel DM models, and we highlight key detection strategies. Alternative theories to particle DM are also discussed.

In Chapter III, we present the theoretical framework for describing the Universe's expansion within the ΛCDM model and demonstrate how to compute the evolution of DM particle number density from a given particle physics model. Our focus will be on two main paradigms: the freeze-out and freeze-in mechanisms.

Chapter IV reviews DM production in co-annihilation scenarios, emphasizing the impact of non-perturbative effects from long-range forces, notably the Sommerfeld effect and

Bound State Formation. We collect and present key results necessary for incorporating these effects into the DM Boltzmann equation.

In Chapter V, we demonstrate the influence of such long-range effects on the phenomenology of simplified t-channel DM models, highlighting their interplay with collider constraints and direct detection experiments.

In Chapter VI, we discuss the relevance of thermal corrections to freeze-in production and justify the necessity of a fully-fledged thermal QFT approach, specifically the CTP formalism. We review this formalism and show how to derive the rate equation for the DM number density.

Chapter VII presents a calculation of the DM interaction rate for a simplified t-channel model with a singlet scalar DM candidate, using the CTP formalism. We compute the 1PI-resummed propagators in the interaction rate while retaining all mass scales. The analytical derivations, along with their implementation in a numerical routine, are presented in detail.

Chapter VIII discusses the result of the numerical Monte Carlo integration of the DM interaction rate in the CTP formalism and with various approximated approaches, such as the HTL approximation and the Boltzmann equation approach. The resulting DM abundance across a broad parameter range and the different methods are compared to show how more precise calculations can lead to discrepancies in the prediction of the DM abundance.

In Chapter IX, we analyze a similar scenario involving Majorana DM and a gauge-charged scalar mediator. We focus on the issue of a negative spectral sum in the 1PI-resummed scalar spectral density within the Feynman gauge and propose alternative resolutions.

Finally, in Chapter X, we explore freeze-in production during an extended reheating phase post-inflation and demonstrate the phenomenological implications at colliders arising from different reheating potentials and inflaton decay modes.

CHAPTER II

Dark Matter

The investigation into the origin of Dark Matter (DM), the missing luminous matter in astrophysical objects and cosmological structures, has now extended beyond a century. The historical trajectory of DM research has paralleled the major revolutions in modern particle physics and cosmology since the 1920s, as comprehensively documented in Ref. [11]. This narrative continues to evolve, penned by tens of thousands of scientists globally, as the nature of this elusive phenomenon remains one of the most significant (if not the preeminent) challenges in astrophysics and, to some extent, particle physics.

In this chapter, we provide a concise literature-based review of the observations indicating the existence of DM and discuss the evidence supporting and opposing the hypothesis that DM constitutes a novel form of matter. We will examine various particle candidates that have been extensively studied over the past four decades, with particular attention to how perspectives have shifted following the advent of the Large Hadron Collider (LHC) and the era of precision cosmology. We will highlight the principal experimental efforts aimed at detecting or producing DM particles, and how these efforts constrain or invalidate different particle physics models. Finally, we will also mention alternative explanations for DM, focusing on modifications to the theory of gravity, and evaluate their respective successes and shortcomings.

For more comprehensive reviews on the subject, readers can refer to the extensive recent review in Ref. [12] and other notable reviews [13–18]. More specialized reviews will be cited in the following sections.

II.1 Observational Evidences

The first hints pointing to the need for *extra* matter content in galaxies date back to the works of Kapteyn [19], Jeans [20], and Oort [21] who already mentioned the possible existence of some *dark bodies* to account for the motion of stars in the local Milky Way, perhaps in the form of faint stars.

It is however with the pioneering works of Zwicky [22, 23] and of Smith [24] on the apparent velocity of galaxies inside the Coma and Virgo clusters that the problem of DM started to be taken seriously, while observations on the rotational curves of spiral galaxies in the 1970s [25] finally persuaded the community to embrace the "missing matter problem" in astrophysical environments at multiple scales.

In the following, we give an overview of the most important pieces of evidence, starting from local measurements of galaxies and galaxy clusters up to observations of the large-scale structure of the Universe and of the Cosmic Microwave Background.

II.1.1 Galaxy Dynamics

Spiral galaxies. In the 1970s, a series of works exploited the advent of 21-cm radioastronomy to measure velocities of gas and stars of spiral galaxies and compare them with optical observations [25–30]. Assume an axisymmetric galaxy of radius R, and take the circular velocity v_c of a gas particle, say, neutral hydrogen, at a distance r from the center of the galaxy. The galaxy has a mass that grows with distance as $M(r) = 4\pi\rho r^3/3$, ρ being its volume density, up to $r = R$. Outside, the galaxy can be viewed as a pointlike source of gravitation with total mass $M = 4\pi\rho R^3/3$. Thus, the velocity of the gas particle follows from energy conservation as

$$v_c = \begin{cases} \sqrt{\dfrac{4\pi G_N \rho}{3}}\, r & r \leq R \\ \sqrt{\dfrac{G_N M}{r}} & r > R \end{cases} . \tag{II.1}$$

Hence, the expected behavior is that the velocity increases linearly inside the galaxy and has a so-called Keplerian fall-off $v_c \sim r^{-1/2}$ outside. Remarkably, while the measured *rotation curves* of the observed galaxies agreed well inside the galactic disks, they exhibited a flat or very slow decrease in radius at large distances! An obvious solution immediately seemed to imply the existence of non-luminous matter in the outer regions of the galaxies. This hypothesis of a spherical massive population of invisible objects–what today we call the *dark matter halo*–embedding the galactic luminous matter, became more and more accepted by the community [31, 32], further corroborated by studies on the stability of galactic disks [33], on the dispersion velocities in elliptical galaxies [34], and by further confirmation of the rotation curves profile in the optical band [29]. Fig. II.1 shows the rotation curves measured by Rubin and Ford for the Andromeda galaxy (left panel) [25], and for several more galaxies (right panel) [29]. Last year, the Milky Way Keplerian fall-off might have been finally detected [35].

Elliptical galaxies To estimate the mass of an elliptical galaxy one can rely on a variety of methods [36], comprising determining the stellar velocity dispersion using the Virial theorem, measuring the velocities of neutral hydrogen rings around the galaxy with rotation curves similar to those in spiral galaxies, observing the X-ray emissions from hot gas in hydrostatic equilibrium around ellipticals, studying ionized gas, globular clusters, gravitational lensing, and others. Overall, until the late 1990s, there was no clear, conclusive statement about the presence of DM in elliptic galaxy environments [37–39]. More recent studies have indicated that their evolution and structure are compatible with models involving a DM halo [40–42].

Local density. Efforts to determine the local DM density, crucial for both galactic dynamics and DM detection, have evolved significantly over time. From the earlier works [19–21] to the improved methods in the 1980s [43,44], up to more recent refinements thanks to data from surveys like Hipparcos, SDSS, and RAVE [45], the need for invisible matter nearby the solar system in roughly the same amount of the visible one appeared with more and more evidence. The results, though, varied depending on various assumptions, especially on the shape of the DM halo. Based on measurements from the SDSS, the Milky Way is consistent with having a spherical DM halo with radius $\sim 8\,\mathrm{kpc}$. There are also indications of a mean local DM density around $0.4 - 0.6\,\mathrm{GeV/cm^3}$. At the same time, the need for a more precise measurement has underscored the need for more sophisticated

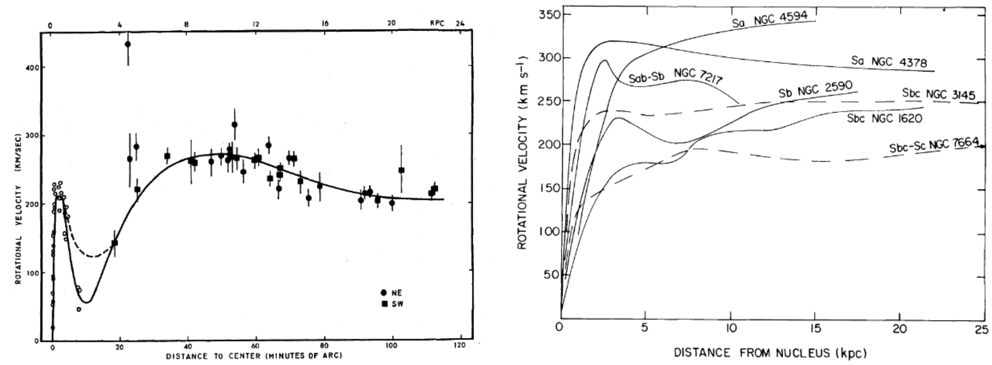

Figure II.1: *Left:* Rotation curve of M31 (Andromeda galaxy) as measured by Rubin and Ford in 1970 [25]. *Right:* Rotation curves of several galaxies from Rubin and Ford (1978) [29].

models and assessment of uncertainties [46]. Future date releases from the Gaia satellite (the most recent one is [47]) promise more precise three-dimensional models, crucial for understanding the distribution of DM in our galaxy.

Small-scale anomalies. At the galactic scale, there are a few issues with the standard Cold Dark Matter (CDM) model, assuming that galaxies are embedded in a virialized halo of dark massive particles. The predictions of the CDM model are, in fact, often inconsistent with observations on small scales, particularly below hundreds of kpc [48–50]. Three main problems include: *i*) the *core-cusp problem*, which refers to a discrepancy between the predicted steep density profiles of DM halos (cusp profiles) in N-body simulations [51] and the flatter profiles (core profiles) observed in low-mass galaxies [52]; *ii*) the *missing satellites* or *dwarf galaxy problem*, concerning the overabundance of predicted satellite galaxies in simulations (~ 1000) compared to the observed number in the Local Group (~ 50), though recent analyses re-affirm the consistency of models [53]; *iii*) the *Too Big To Fail problem*, which arises from the inconsistency between the predicted large masses of DM subhalos and the observed central masses of the brightest satellite galaxies in the Local Group. Solutions to these problems have been proposed, ranging from baryonic feedback coming from the explosion of supernovae, to Warm DM, self-interacting DM, and ultralight particles (cf. Section II.2).

II.1.2 Galaxy Cluster Dynamics

In the 1930s, assuming Newtonian gravity and applying the virial theorem, Zwicky estimated the mass of the Coma cluster from the average velocities of roughly 800 individual galaxies, measured via the Doppler shift of galactic spectra [22, 23]. He found that $M_{\text{cluster}} \simeq 4.5 \times 10^{13}\ M_\odot$, where $M_\odot$ is one solar mass. Previous observations assumed that a typical galaxy had a luminosity 8.5×10^7 times that of the Sun, leading Zwicky to conclude that the *mass-to-light ratio* of the Coma cluster was around 500. Despite potentially large uncertainties in various parameters, his method paved the way for studying the velocity and density profiles of DM in astrophysical systems [45]. Correcting for these uncertainties, Coma's velocity dispersion still points to the existence of DM (*dunkle Materie*, as Zwicky called it in [22]). Similarly, Smith's work on the Virgo cluster [24] concluded that luminous matter alone cannot explain the motion of galaxies within the cluster.

Modern methods combine X-ray observations of hot intra-cluster gas and *gravitational*

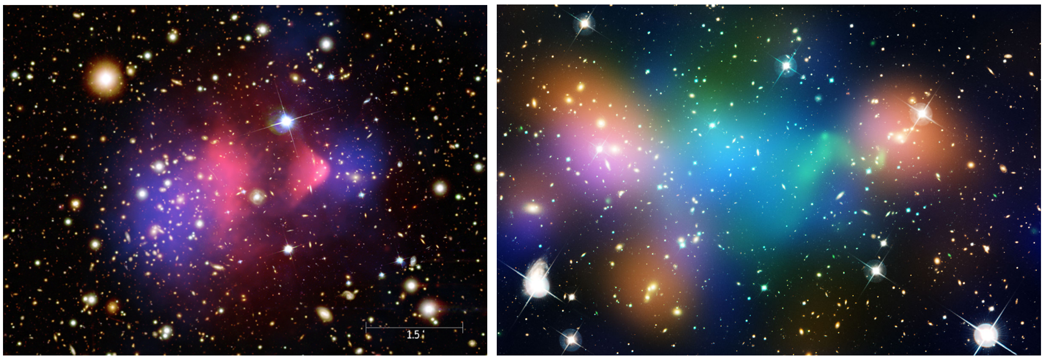

Figure II.2: The Bullet Cluster (left) and Abell 520 (right), where the optical images are combined with the inferred DM distribution (on the left in blue, on the right in cyan) and the observed hot gas and starlight distribution (on the left in pink, on the right in orange). *Credits left image:* X-ray: NASA/CXC/CfA/M.Markevitch et al.; Optical: NASA/STScI; Magellan/U.Arizona/D.Clowe et al.; Lensing Map: NASA/STScI; ESO WFI; Magellan/U.Arizona/D.Clowe et al.. *Credits right image:* NASA, ESA, CFHT, CXO, M.J. Jee (University of California, Davis), and A. Mahdavi (San Francisco State University).

lensing to determine the density and temperature of baryonic content and gravitational effects. Of particular importance is the study of colliding clusters, notably 1E0657-558, known as the *Bullet Cluster* [54] (see also [55]). The Bullet Cluster, depicted in the left panel of Fig. II.2, shows a composite of optical images (luminous matter), X-rays (hot gas in pink), and gravitational lensing (total mass in blue). The pink and blue distributions do not overlap, which would be unexpected if only normal matter were present. In contrast, if the clusters have a DM halo, the luminous component could be slowed down during the collision due to interactions, friction, and shock waves, while the majority of the gravitational mass, primarily from the non-luminous DM component, would pass through unimpeded. This discrepancy highlights evidence for the non-collisional nature of DM [56]. The spatial offset between total mass and baryonic mass centers, with 8σ significance, suggests these clusters are predominantly composed of weakly interacting DM. Analyzing 72 cluster collisions, Ref. [57] claimed 7.6σ evidence for DM.

Controversies and tensions. Despite the common opinion on colliding clusters such as the Bullet, there are some controversies about how rare events of this type in the Universe are and how to correctly interpret their existence. The two colliding sub-clusters have exceptionally high velocities ($\sim 3000\,\mathrm{km/s}$) for their age in a ΛCDM Universe. While early analyses claimed that there is no real issue with ΛCDM [58], subsequent studies [59] claimed that there is only a 10% probability of finding a similar system as the Bullet cluster in the entire sky (up to redshift $z = 0.3$), which, combined with the fact that [54] used only $\sim 5\%$ of the sky coverage, would reduce these odds to $\sim 0.5\%$. At the same time, the existence of objects such as Abell 520, nicknamed the "Train Wreck Cluster", show the exact opposite behavior, with the estimated DM density via gravitational lensing concentrated in the central part of the collision. This poses significant challenges to the (almost) collisionless nature of DM, as suggested by the Bullet cluster [60]. The tension worsens significantly when inexplicably massive clusters are taken into account. For instance, ACT-CL J0102-4915, commonly known as El Gordo is the most massive cluster at redshift $z > 0.8$ (it is located at $z = 0.87$), with a monster mass of $\sim 2\times10^{15} M_\odot$ [61], which is extremely unexpected in the ΛCDM theory at such a distance [62]. Its dimensions and peculiar shape seem to require that two very massive sub-clusters had to collide with high relative velocity, which would be in a 5.4σ tension with the ΛCDM model (5.7σ when combined with the Bullet cluster) [63].

II.1.3 Large Scale Structure

If DM dominates the Universe's matter budget, its particles' properties shape the formation and evolution of the Universe's structure. Thus, the DM problem is linked to the large-scale structure (LSS) of the Universe, as first realized and computed by various pioneering works between the 1970s and the 1980s [67–70]. This has been by now observed with great detail thanks to experiments such as the Sloan Digital Sky Survey (SDSS) [64], whose detected *cosmic web* of structures (filaments, superclusters, voids, etc.) is depicted in the upper panel in Fig. II.3 (see also [71] for the most recent results extending up to 11 Gyr in distance).

The role of a CDM component is crucial in amplifying tiny local over- and underdensities in the matter field, enhancing the aggregation of baryonic matter into potential wells in the early Universe, thereby driving the formation of galaxies, clusters, superclusters, and filaments in a hierarchical evolution [72, 73]. Standard cosmological models predict that primordial inhomogeneities were extremely small, around ten parts per million, as indicated by the smoothness of the CMB radiation (see next section). Relativistic baryons and photons could not cluster effectively due to oscillations from pressure waves and electromagnetic interactions, and damping by the Universe's expansion, whereas a collisionless, non-relativistic DM component has a density profile that grows over time. Thus, primordial DM inhomogeneities grew, starting with shorter perturbation length scales followed by larger ones. After the first atoms formed, baryons decoupled from radiation and fell into the gravitational wells created by DM. This agrees with the smooth power-law behavior observed in the *matter power spectrum* (upper right panel of Fig. II.3), quantifying the variance in local inhomogeneities for each mode k, the inverse of the perturbation length scale.

Moreover, N-body simulations have now reached a remarkable level of precision and sophistication, emulating the motion and dynamics of up to $N \sim 10^{12}$ massive particles, covering time intervals almost as long as the age of the Universe ($\sim 10^{10}$ years) and volumes of $\sim (10\ \text{Gpc})^3$ with kpc resolution—a significant improvement compared to efforts from 40 years ago [73]. These simulations consistently highlight DM as the cornerstone ingredient in explaining the structure we observe [66, 74]. Higher precision is achieved with more realistic simulations that include the magneto-hydrodynamics of baryons, despite their computational complexity. Recent results are encouraging, confirming that the ΛCDM model with baryons accurately describes the evolution of structures from cosmic to galactic scales.

II.1.4 Cosmic Microwave Background

The Cosmic Microwave Background (CMB) is the residual thermal radiation from the Big Bang, which fills the universe almost uniformly in every direction at an average black-body temperature about 2.725 K, with relative fluctuations of order 10^{-5}. It was first detected serendipitously by Penzias and Wilson in 1965 [76] with immediate repercussions in the study of cosmology [77–79]. This radiation is a crucial observational tool in cosmology, providing a snapshot of the universe when it was just about 380,000 years old, a period known as the *recombination* era. At this time, the universe had cooled enough for protons and electrons to combine and form neutral hydrogen atoms, allowing photons to travel freely without constant scattering by charged particles.

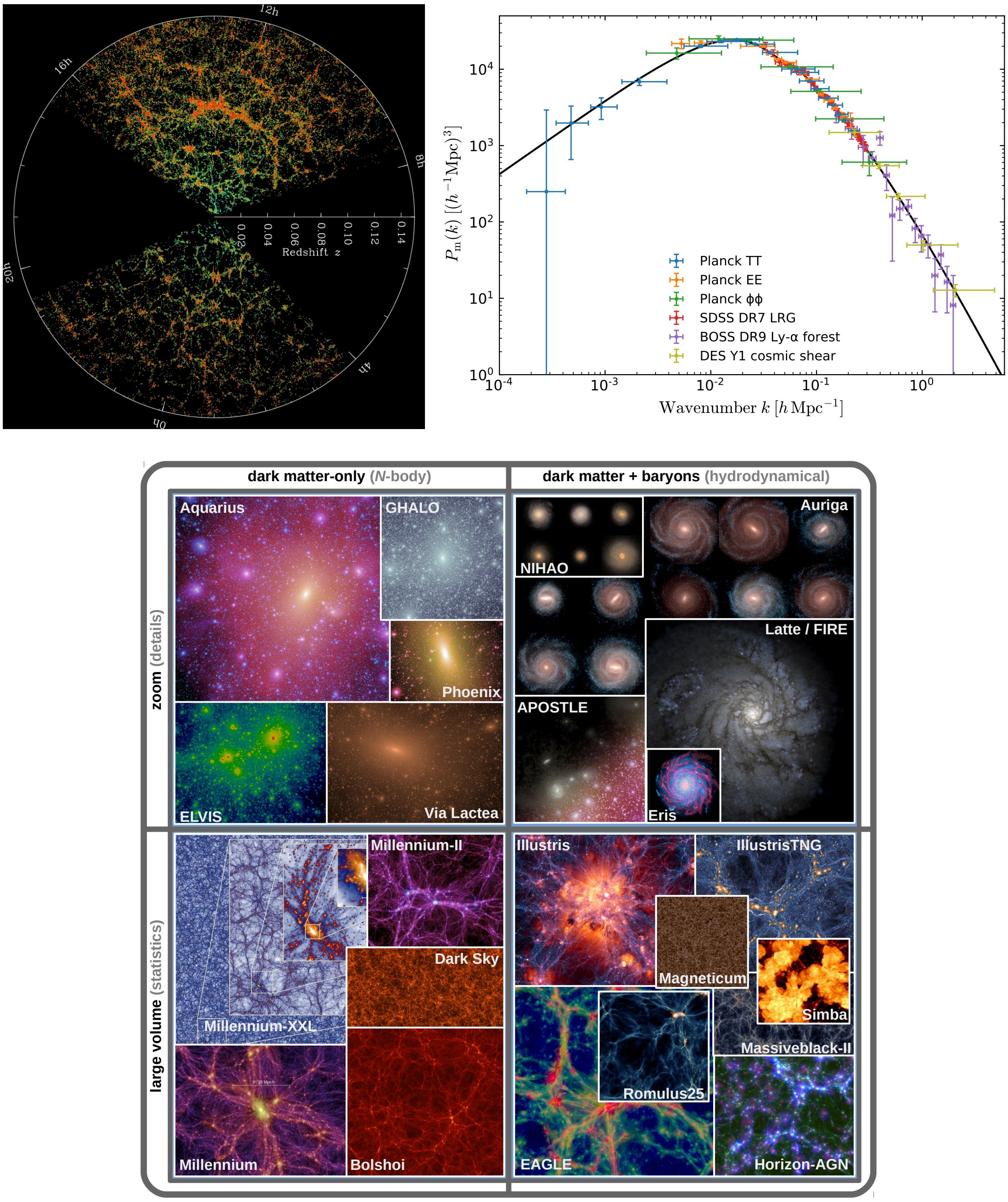

Figure II.3: *Upper panel:* The cosmic web as observed by the SDSS [64]. *Credits:* M. Blanton and SDSS. *Middle panel:* The growth and dumping of the matter power spectrum with the wavenumber (inverse wavelength) as determined by different cosmological observations [65]. *Credits:* ESA and the Planck Collaboration. *Lower panel:* Collection of several numerical N-body simulations with and without baryons from [66] from which references to the simulation works can be found.

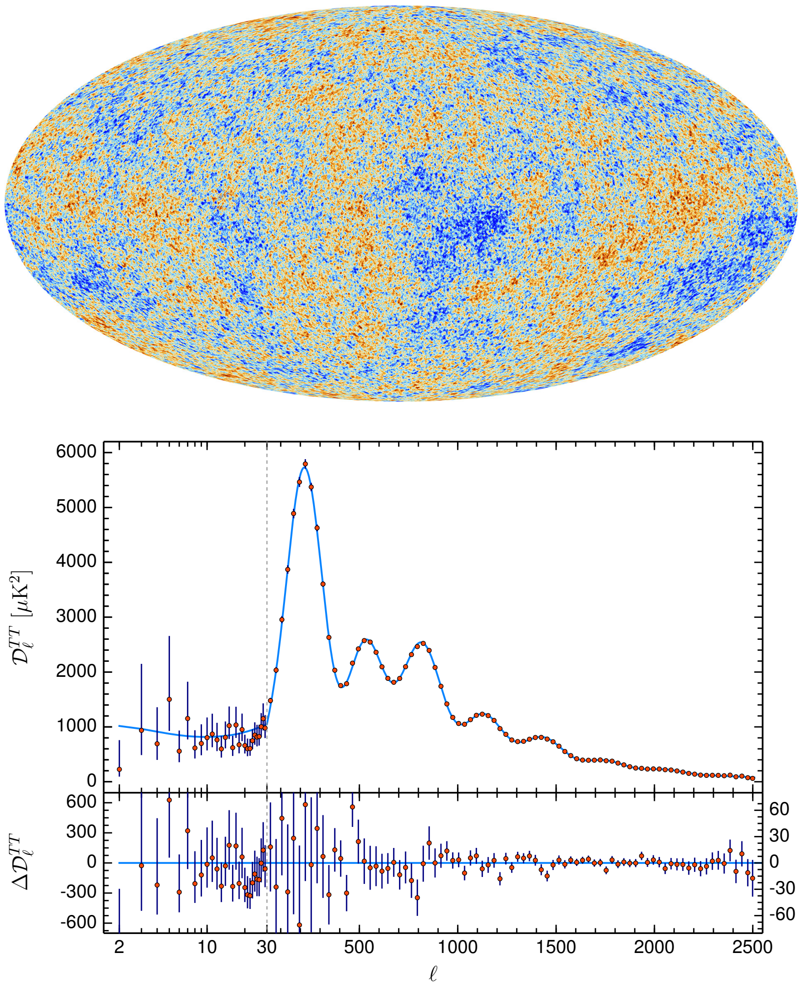

Figure II.4: Results from the Planck 2018 release [65, 75]. *Upper panel:* All-sky map of the CMB temperature fluctuations, spanning a range from -300μ K (bluer shades) to $+300\mu$ K (redder shades) about the average of ~ 2.7 K. *Lower panel:* Angular power spectrum of the TT-modes of the CMB as a function of the multipole moment ℓ, the angular frequency (inverse angular separation).

The observed temperature fluctuations have been measured at various wavelengths using different instruments, such as the Planck satellite [65, 75], whose all-sky map is displayed in the upper panel of Fig. II.4. The *angular power spectrum* (see lower panel) quantifies the correlation between inhomogeneities at different angular separations, θ, in the sky. This can also be expressed as a function of the multipole moment (or angular frequency), $\ell \sim \pi/\theta$.

The impressive uniformity of the CMB has led cosmologists to adopt the theory of *cosmic inflation*, which proposes a period of exponential expansion during the universe's earliest moments, before the formation of the radiation bath (see Section X.2 for a brief review). If inflation was driven by a quantum field, its primordial quantum fluctuations could have been imprinted on the spacetime metric, seeding the initial matter density oscillations that eventually evolved into the LSS we observe today (cf. Section II.1.3). These features would have influenced the distribution of baryons and photons just before recombination, a process that would be significantly affected by the presence of DM.

The peaks in the CMB power spectrum are caused by acoustic oscillations in the baryon-photon fluid. The positions of these peaks depend on the density of DM, as less DM results in a later radiation-matter equality. The amplitude of the peaks is influenced by the relative amounts of DM and normal matter, with only normal matter participating in acoustic oscillations. Comprehensive fits to the data show that the Standard Model of cosmology (ΛCDM + Gaussian primordial inflationary perturbations) accurately reproduces the observed CMB power spectrum and allows for the most precise determination of the DM relic abundance today $\Omega_c h^2$. This corresponds to the CDM energy-matter density relative to the critical density of the Universe today $\rho_c = 3H_0^2/8\pi G$, with G being Newton's constant and $H_0 = h \times 100\,\mathrm{km/s\,Mpc^{-1}}$ the Hubble expansion parameter today (cf. Section III.1 for more details on cosmological parameters). The current measurement is [75]

$$\Omega_c h^2 = 0.1200 \pm 0.0012 \qquad 68\%\,\text{C.L. TT,TE,EE+lowE+lensing}\,, \tag{II.2}$$

which roughly translates into a $\sim$ 26% amount of CDM in the energy budget of the Universe.

A more detailed analysis of the CMB power spectrum reveals that the relative heights of the second and third peaks provide key information about the amounts of baryonic matter (coupled to photons) and DM (providing gravitational influence). The third peak's height is significantly higher than it would be if only baryonic matter were present, which provides what is probably the strongest evidence for the existence of (and the need for) DM. If the Universe contained only baryonic matter, the third peak would be notably suppressed, contradicting observational data. Moreover, the overall shape and the position of the peaks are strongly influenced by the amount of dark energy in the Universe. Assuming a cosmological constant Λ with negative pressure, it is found that $\Omega_\Lambda \simeq 0.7$.[1]

II.1.5 Tensions in the ΛCDM model

Cosmology is currently facing what some authors have described as a genuine crisis. Increasing tensions and controversies exist over the interpretation of data and simulations, particularly regarding the scales at which the ΛCDM concordance model of cosmology and, more broadly, the cosmological principle of spatial homogeneity and isotropy, can be reliably applied.

Without any doubt, the most alarming issue today relates to the *Hubble tension*. This refers to the discrepancy between measurements of the Hubble constant H_0, which represents the current expansion rate of the universe. Local measurements using methods such as Cepheid variable stars and Type Ia supernovae as standard candles yield values between $71-73\,\mathrm{km/s/Mpc}$ [82,83], while observations of the early universe, particularly the CMB, combined with assuming the ΛCDM model, yield a lower value around 67 km/s/Mpc [75]. This discrepancy has grown over time with measurements reaching a higher and higher precision so that the tension is now way above the 5σ level, triggering the community to try to get to the bottom of it [84].[2]

A vast amount of explanations to understand the Hubble tensions are currently considered, such as New Physics responsible for the change in the expansion rate of the early Universe (e.g., Early Dark Energy and its variations), to the variation of some of the

[1] A very useful tutorial explaining these and other features can be found on Wayne Hu's web page [80], while, for an in-depth understanding, we refer to Dodelson's book [81].

[2] Improved measurements using the James Webb Space Telescope (JWST) could help resolve the issue, as suggested by the Chicago Carnegie Hubble Program (CCHP) [85]. Recent claims from April 2024 by CCHP members (not yet publicly available or peer-reviewed) indicate that the tension might have significantly decreased below 3σ, with new blinded (re-)analyses suggesting $H_0 \simeq 69$ km/s/Mpc [86], compatible with Planck results and the newest DESI measurements [87] of $H_0 \simeq 68$km/s/Mpc.

parameters of fundamental interactions over cosmological times, or involving late Universe dark energy solutions or DM in the form of dark radiation. These and many other possibilities are comprehensively reviewed in Refs. [88, 89].

Here, we only mention that, apart from New Physics explanations, none of which is currently even close to being satisfactory, a solution could also lie in problems with the *cosmological distance ladder*. This is a sequence of methods used to measure distances in the universe, ranging from radar in the solar system to redshift-distance relations for distant galaxies. Each step, including parallax, Cepheid variables, and Type-Ia supernovae, builds its calibration on the previous ones, enabling astronomers to map cosmic distances with increasing precision. This hierarchical approach ensures accurate distance measurements across vast scales, but it is currently a subject of inquiry due to inconsistencies and systematic uncertainties. However, as reviewed in Ref. [90], there are indications that not even a better-calibrated ladder would resolve the Hubble tension.

Finally, several anomalies and oddities are resiliently emerging within the ΛCDM concordance model, including the S_8 anomaly [91], the CMB dipole anomaly [92], the high-redshift 21cm anomaly [93], and various small-scale anomalies, among others [50, 89, 94]. These issues suggest that it might be time to reconsider the cosmological principle, the foundational assumption of modern cosmology. Additionally, mounting evidence indicates that the existence of giant voids near the Local Group, such as the KBC void [95], is incompatible with both the evolution of cosmic structures in ΛCDM and the cosmological principle at Gpc scales. The presence of this significant matter density deficit nearby could potentially explain the Hubble tension (if it is indeed real) and other anomalies [96, 97].

II.2 Dark Matter Candidates

Given what we have discussed in the previous section, there are essentially two possibilities to explain observations. Either all the discrepancies are solved by the existence of DM in the form of particles or macroscopic objects with the right characteristics, or the laws of physics need to be modified in certain conditions and no DM is needed. The second option will be briefly explored in Section II.4, while we dedicate the majority of this section to the DM hypothesis, especially in its elementary particle form.

We briefly review some of the historically famous DM candidates as well as the most modern vision on this research area, while we refer to Refs. [12, 13, 98–102] for a complete overview. As a matter of fact, the number of possible explanations for DM is difficult to track as newer and newer ideas are brought forward. In general, DM could be made of very massive macroscopic objects, as well as by elementary or composite particles with masses ranging from a few eV up to the Planck scale $M_{\rm Pl} \sim 10^{19}\,\mathrm{GeV}$, down to wavelike scalars as light as 10^{-21} eV behaving like classical fields on astrophysical distances. The viable range of DM masses can, in principle, span more than 90 orders of magnitude[3]

$$10^{-21}\,\mathrm{eV} < M < 10^{75}\,\mathrm{eV}\,, \tag{II.3}$$

as shown in Fig. II.5 from [12]. The lower bound stems from requiring that the de Broglie wavelength associated to the DM particles is not too large to disrupt the formation of structures on the largest scales, while the upper bound comes from observations pointing to the existence of DM in dwarf galaxies of masses around $10^5\,M_\odot \sim 10^{35}\,\mathrm{kg}$.

Before we list some of the possible explanations lying on this vast landscape, we need to make sure that we know what a decent DM candidate should look like, that is to say,

[3] Using $1\,\mathrm{eV} \simeq 1.8 \times 10^{-36}$ kg, this is equivalent to $10^{-57}\,\mathrm{kg} < M < 10^{37}\,\mathrm{kg}$.

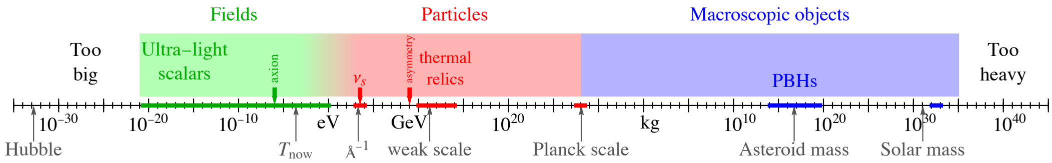

Figure II.5: Theoretically viable mass range for DM candidates. Figure taken from [12].

what the requirements or properties are that it needs to have.

II.2.1 Requirements

If we assume the validity of the ΛCDM model, there are several requirements a good DM candidate needs to have to match experimental observations and constraints.

- ***Cold***. DM must be non-relativistic at the time of matter-radiation equality when the Universe was roughly 50,000 years old. When the universe became matter-dominated, those density fluctuations primordially imprinted started to grow, eventually creating the LSS we observe today, as explained in the previous section. A relativistic *hot* DM (HDM) candidate ($M <$ keV) would have had a too long *free-streaming length*, incompatible with the existence of structures on small scales. A *warm* DM (WDM) particle candidate, something in between CDM and HDM, is a viable possibility, and it is currently constrained in different ways, especially by observations of the Lyman-α forest and the 21-cm line. A recent analysis combining Lyman-α observations and N-body simulations puts the WDM mass lower bound to $M \gtrsim 5.7\,\text{keV}$ [103].
- ***Dark***... of course! Which translates into having null or very tiny electric charge q: smaller than 10^{-10} for DM particles with $M \lesssim$ TeV, not more than $q \simeq 0.3$ for macroscopic objects. Moreover, it is unlikely that it can have a colour charge and, in general, is not a singlet under the gauge group of the Standard Model (SM) of particle physics. These conclusions come from the non-observation of any cosmic ray or photon signals and from the requirements of being consistent with Big Bang Nucleosynthesis (BBN), being as collisionless as possible, not disrupting structures, to explain clusters' shapes, and stabilizing galaxy disks [12, 104].
- ***Stable***. DM needs to have a lifetime at least of the order of the age of the Universe ~ 13.8 Gyr $\sim 10^{17}$ s so that its (possible) decays have no cosmological effect. Lower bounds depend on the type of candidate and at present date can vary between $10^{17}\,\text{s} - 10^{28}\,\text{s}$.
- ***(Almost) Collisionless***. Direct and indirect detection experiments constrain the interaction cross-section of DM particle candidates on visible matter (cf. Section II.3), which needs to be much smaller than typical weak interaction cross-sections. Self-interactions are constrained by observations at every cosmological scale, implying that DM particles can interact with themselves only for cross-sections smaller than those typical of strong interactions.
- ***Non-baryonic***. In order not to disrupt the observed primordial abundance of light elements from BBN, and the features of the CMB power spectrum, DM cannot be SM baryonic as this would imply a much larger overall abundance of baryonic matter in the Universe, which is ruled out.

II.2.2 Pre-LHC ideas

Standard Model DM. Since DM needs to be neutral, stable, weakly interacting, and with a gravitational mass, SM **neutrinos** might appear as the ideal candidates. However, the cosmological density of neutrinos implies that the sum of their masses over the three flavour generations must be $\sum_\nu m_\nu \lesssim 0.1\,\mathrm{eV}$ [105]. In contrast, the DM density is reproduced if their masses amount to 11 eV, also ruled out by laboratory experiments currently setting an upper bound on the heaviest neutrino mass eigenstate at $\lesssim$ eV. Moreover, such a light thermal relic would wash out any structure formation.

Other possibilities brought forward in the 1980s regarded neutral bound states of quarks also known as **quark nuggets** or **strangelets**, or also of **Q-balls** [106, 107] whose existence is questioned both by issues with their stability and because in the SM they would require a primordial QCD phase transition of the first order, while lattice simulations indicate that the transition is rather a smooth crossover. Things could be different if Beyond the Standard Model (BSM) degrees of freedom were involved.

Another interesting possibility is that of **hexaquarks**, a neutral spin-0 di-baryon bound state of six valence quarks whose existence is hypothesized by QCD but never confirmed [108]. Whether hexaquarks can be a DM candidate is a matter of debate as they are strongly constrained by various experiments, but their properties are still largely unknown and need better lattice simulations to be understood [109, 110]. For other solutions involving electroweak and gravitational bound states, see [12].

In the early days of DM research, a considered hypothesis was that of Massive Astrophysical Compact Halo Objects (**MACHOs**), extended celestial bodies made of ordinary baryonic matter such as faint stars, planets, etc. The problem with MACHOs is the last requirement in Section II.2.1: they are baryonic and thus ruled out by cosmological observations for any possible mass.

Primordial Black Holes. Primordial black holes (PBH) are black holes formed *before* BBN out of ordinary (SM) matter when large homogeneities with wavenumber k re-enter the horizon after inflation and gravitationally collapse to form a black hole [111–114]. Planck-scale PBH would almost immediately evaporate away due to Hawking radiation [115], while PBH formed at temperatures before BBN could have a mass ranging from that of an asteroid to that of a supermassive black hole. In general, the later the horizon re-entry, the larger the primordial density length $\lambda \propto 1/k$ and hence the more massive the PBH. Other PBH formation mechanisms involve the gravitational collapse triggered by inflationary perturbations or by bubble collision during first-order phase transitions in theories beyond the SM. In principle, PBHs could reproduce the observed DM if just a tiny fraction of all the primordial matter densities collapsed. In practice, several experimental constraints limit the viable mass range of PBH to constitute the whole DM in the window $10^{-16} M_\odot < M < 10^{-12} M_\odot$ [116–118]. However, several caveats can relax these bounds, such as assuming a non-monochromatic mass function, how PBH would move and cluster inside galaxies, whether they constitute only a fraction of the DM, etc. The recent rise of Gravitational Wave (GW) astronomy is expected to boost the search of PBH and unravel their role as a potential DM candidate [119–121].

Sterile Neutrinos. The SM neutrinos exist solely in a left-handed doublet representation of $SU(2)$, paired with their lepton counterparts and possessing weak isospin $\pm 1/2$. No evidence of right-handed neutrinos (RHNs) has been found. If RHNs do exist, they must be *inert* under the SM gauge group, lacking color charge, being electroweak singlets, and having no weak hypercharge. Hence, they are also referred to as *sterile neutrinos.* The existence of RHNs could naturally explain why (at least two out of three) SM neutrinos have such small masses, potentially via the *seesaw mechanism*, which was especially popular in the context of Grand Unification Theories. This mechanism would require RHNs to be very heavy ($\gg$ TeV), earning them the name Heavy Neutral Leptons (HNLs). For sterile neutrinos to be viable DM candidates, they must be sufficiently massive to avoid disrupting cosmic structures, as dictated by the Gunn-Tremaine bound of $M \gtrsim$ keV [122, 123]. Several production mechanisms for sterile neutrino DM have been proposed, including non-resonant oscillations [124], resonant oscillations due to in-medium effects [125], and the freeze-in mechanism (cf. Section III.5.2). However, current experimental limits heavily constrain the parameter space for sterile neutrinos, reducing their attractiveness as DM candidates over time [4].

(QCD) Axions. An axion is a hypothetical elementary particle proposed to resolve the strong CP problem in quantum chromodynamics (QCD) by ensuring the CP symmetry is conserved in strong interactions in a dynamical and not fine-tuned way [130, 131]. It is a light, neutral particle that emerges as the pseudo-Nambu-Goldstone boson from the spontaneous breaking of a new $U(1)$ symmetry at high energies, a concept introduced by Peccei and Quinn in 1977 [132, 133]. Of the several QCD axion models, the most famous are the KSVZ axion model [134, 135] and the DFSZ axion model [136, 137], while string theory predicts a whole "axiverse" [138]. Axions have immediately been considered an ideal DM candidate [139] as they cosmologically behave as pressureless non-relativistic matter, they interact very weekly with SM particles such that they avoid several experimental constraints, they are stable on cosmological timescales, and various theories such as the misalignment mechanism (cold axions), thermal production (hot axions) or topological defects from cosmic strings make sure that axions can yield the correct DM relic abundance [139, 140]. Recent theoretical advancements, however, suggest that the strong CP problem may not exist, potentially eliminating the need for a QCD axion [141, 142].

Supersymmetric particles. Supersymmetry (SUSY) [143] has arguably been one of the most remarkable ventures in theoretical modeling and experimental exploration in high-energy physics over the past five decades. It is a theoretical framework that extends the SM by proposing a symmetry between fermions and bosons. In SUSY, every particle has a corresponding superpartner with opposite spin-statistic properties (fermions have bosonic partners while bosons have fermionic partners). SUSY was invoked to solve several issues in particle physics, such as the hierarchy problem and the smallness of the Higgs mass, while providing the unification of forces, and, in principle, ideal DM particle candidates. Moreover, if SUSY is seen as a gauge (local) symmetry, it gives rise to *supergravity*, a quantum gravity framework that finds its natural realization in superstring theories. Despite its theoretical appeal, SUSY has not yet been experimentally confirmed, and the LHC results have dampened the enthusiasm for a theory that captivated researchers for half a century. Even if SUSY were realized in nature, it would not address several naturalness problems that initially motivated its study.

[4] Besides DM physics, RHNs can play an important role in the generation of a primordial baryon asymmetry, the seed for the present-day observed overabundance of matter over antimatter, which the Standard Models of particle physics and of cosmology alone cannot explain [126]. Mechanisms of these type go under the name of **baryogenesis** (when the asymmetry is directly generated in the baryonic sector) or **leptogenesis** (when the asymmetry is generated in the leptonic sector and then transferred onto the baryonic one via non-perturbative 'sphaleron' processes) [127–129].

Among the many supersymmetric particles, several potential DM candidates exist in the Minimal Supersymmetric Standard Model (MSSM) [144]. **Neutralinos** are mass eigenstates given by the mixing of the neutral components of the superpartners of the B (*binos*) and W (*winos*) vector bosons and of the Higgs scalar doublets (*higgsinos*). Depending on the value of the mixing parameters, neutralinos can come in an (almost) pure eigenstate of one of the mixing superpartners. They have often been regarded as the paradigmatic example of a DM particle [145, 146] in that they are neutral and the lightest state is stable thanks to R-parity, the leftover of SUSY-breaking, although LHC results have already exploited their realization at the weak scale. If at all, neutralinos could be found in the multi-TeV regime. Other MSSM-motivated candidates (or from extensions of the MSSM) include *gravitinos* [147] (the spin-3/2 superpartners of gravitons), *axinos* and *saxions* [148] (fermionic and scalar superpartners of the QCD axions), and *sneutrinos* [149] (scalar superpartner or neutrinos) [150–154].

WIMPs. Weakly Interacting Massive Particles (WIMPs) have long been considered the DM candidates *par excellence* [15, 146]. What a WIMP is can be a matter of debate. In its original form, WIMPs are neutral particles with masses at the electroweak scales that interact with interaction cross-sections with a magnitude typical of weak interactions. Remarkably, these few requirements are sufficient to yield a thermal relic whose abundance would exactly match that of DM. Moreover, WIMPs would be naturally realized by particles in the MSSM [146], such as neutralinos, or by minimal extensions to the SM [155, 156], and could be easily produced at colliders or detected in underground laboratories. This is the famous *WIMP miracle.* Unfortunately, no WIMP has ever been found and current limits on their interaction cross-sections, paired with null results at the LHC, have essentially ruled out their existence in their vanilla form. Nonetheless, the term WIMP is now being used as a synonym for a particle in thermal equilibrium in the early Universe with masses between $\mathcal{O}(100)$ GeV up to $\mathcal{O}(10)$ TeV whose relic abundance is set by the *freeze-out mechanism* (cf. Section III.5.1) and whose dynamics might be much more convoluted than previously considered [100, 102]. For instance, in this thesis, we will explore the case for thermal DM particles as part of a dark sector in so-called simplified t-channel models (cf. Section II.2.4 and Chapter V).

For other ideas that have held sway for several decades, such as extra dimensions and Kaluza-Klein modes, composite Higgs models, split SUSY, and others, we again refer to reviews such as Refs. [12, 13].

II.2.3 Recent Ideas

The absence of experimental evidence for any new particles, aside from the discovery of the Higgs boson at the LHC in 2012, has caused a significant paradigm shift in addressing fundamental questions in physics. Previously, research was often driven by a top-down approach based on first principles and "aesthetic" preferences. However, the current trend is more conservative and bottom-up: starting from empirical data, researchers test numerous models with minimal assumptions and parameters, allowing observations to guide the direction of inquiry. This approach remains largely agnostic about whether a more fundamental principle underlies the simple assumptions made. Advances in computing power, along with more precise measurements of SM parameters and improved resolution in astrophysical and cosmological surveys, are expected to provide greater clarity in the quest for DM and other unresolved issues in physics [99].

(Ultra)Light Particles. An emerging area of interest in DM research is the possibility of DM particles in the sub-GeV mass range [157–159]. Particles with masses above a few meV still behave like discrete particles at atomic and molecular scales, while those below this threshold exhibit wavelike properties for any detector. These ideas have spurred the development of numerous models and search strategies, leveraging innovative materials and techniques for direct detection. Examples include superconductors, Dirac materials, noble liquids, and superfluid helium, to name a few. In the sub-eV regime, a wide array of DM candidates becomes viable, including Weakly Interacting Slim Particles (**WISPs**) such as QCD axions, axion-like particles (**ALPs**), and hidden photons [160]. At the extreme lower end of the spectrum, ultralight scalar particles (or **ULAs** for ultralight ALPs) can have masses as low as $\sim 10^{-21}$ eV, and they are also known as **Fuzzy DM** [161, 162]. These particles have such small masses that their de Broglie wavelength can extend to macroscopic scales, potentially spanning the diameter of a galaxy. Consequently, the DM field behaves classically, with its phenomenology better described by fluid dynamics and collective phenomena rather than particle physics. Theoretical motivations for ALPs and ULAs extend beyond addressing the strong CP problem, while they have recently gained significant attention as potential DM candidates [140, 163].

Feebly Interacting Particles. Feebly Interacting (Massive) Particles (**FIPs** or **FIMPs**) are a challenging and active area of research [164]. The concept is that DM consists of particles that interact with the visible sector only through very small couplings, typically via a portal interaction mediated by another BSM state, such as a *dark photon* (dark photons themselves can also be candidates for DM) or the interaction could be mediated by other heavy dark states potentially charged under the SM gauge group. This latter scenario will be extensively explored in this thesis (cf. Section II.2.4 and Chapters VII and X). A robust theoretical framework for FIPs is provided by *hidden valley sectors* [165]. Many light DM candidates, such as sterile neutrinos and ALPs can be classified as FIPs due to their typically very suppressed couplings to SM particles. At the opposite end of the mass spectrum, superheavy particles with masses $M > 100$ TeV, also known as *WIMPzillas* [166,167], can also serve as DM candidates. These particles must be non-thermally produced and exhibit feeble interactions with SM particles. Examples of such production mechanisms include sourcing by inflation [168] and gravitational production [169].

Confining Dark Sectors. DM may reside within a diverse and intricate dark sector, potentially as complex as the visible sector of the SM. For instance, it is plausible that DM is not a fundamental particle but rather a composite entity. Recent attention has focused on theories incorporating a confining force within the dark sector. This force could be the SM's strong force, as seen in scenarios like colored DM [170]. Alternatively, novel dark forces akin to dark QCD or dark SU(N) theories [171, 172], encompassing concepts like gluequark DM, dark glueballs, dark baryons and mesons, and even dark atoms, have garnered attention. The allure of dark sectors has intensified in recent years due to the possibility that they underwent phase transitions in the early Universe, potentially giving rise to cosmic strings and the nucleation of false vacuum bubbles. Collisions between these cosmic defects could generate a stochastic gravitational wave background (SGWB), yielding distinct signatures. This interest has been further fueled by compelling evidence supporting the existence of an SGWB from various Pulsar Timing Arrays [173].

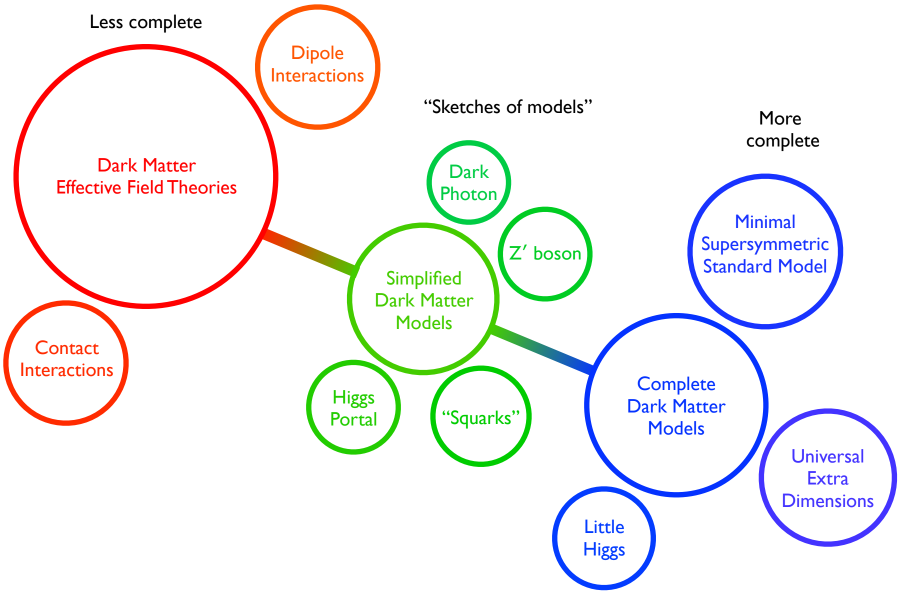

Figure II.6: Schematic view of simplified DM models viewed as an intermediate level of complexity between effective descriptions and more complete models. *Credits:* T. Tait [174].

EFTs and Simplified Models.

A bottom-up approach to the search for DM has had the effect of letting theoreticians experiment with simplified versions of more structured theories to the point that several fields gained their own independence and self-existence. An example is **Effective field theories** (EFTs). EFTs simplify complex problems by focusing on relevant phenomena at a specific energy scale, with the concept that dynamics at different scales can be decoupled when the scale separation is sufficiently large. High-energy effects are suppressed in low-energy processes; thus, EFTs allow for systematic approximations while encapsulating the influence of high-energy physics through expansion in effective parameters and interactions. DM EFTs have been especially exploited in the context of collider searches [175] and direct detection searches [176], but also used to investigate alternative production mechanisms of DM particles in the early Universe [177].

While very useful for low-energy laboratories such as direct detection experiments, the challenge with using effective operators lies in their inability to accurately reflect the physical processes occurring at colliders. Instead of merely observing 'DM + something' events, the critical events involve the direct production of new particles that mediate interactions between DM and the SM particles. By focusing solely on effective operators, we would miss the production of mediators (integrated out in the EFT approach), which are essential for capturing the primary interaction channels at colliders. Therefore, effective operators fall short in representing the full spectrum of the most important interaction channels.

This is why in the last decade **Simplified Models** of DM became so popular [174, 178–189]. They are theoretical frameworks for exploring the properties and interactions of DM particles in a phenomenological and versatile way. These models aim to capture the essential features of DM from so-called "UV complete models" (e.g., SUSY) while minimizing complexity and, at the same time, not necessarily relying on an EFT (see however [190, 191]). In this sense, they lie in between effective and complete descriptions as shown in Fig. II.6 from [174]. They are particularly useful as benchmark scenarios for comparing the capabilities of different experimental and observational probes, systematically exploring the parameter space and comparing predictions with experimental data. Moreover, they can accommodate a wide range of DM candidates and interaction mechanisms.

Broadly speaking, simplified models consist of at least two BSM fields: a DM candidate and a (heavy) mediator. DM can only communicate with other particles through the interaction with the mediator (modulo self-interactions). Therefore, we can classify simplified models into two macro-categories:

- **s-channel models**: DM has interaction vertices *exclusively* with the mediator. The mediator is a color singlet and can couple to pairs of DM states and pairs of SM fields. DM can thus annihilate into SM particles via 2-to-2 processes with one mediator exchanged in the s-channel, featuring potential resonant enhancements. The mediators and the SM fields have to be even under the symmetry that stabilizes DM, say $\mathbb{Z}_2$, but DM has to be odd. This implies that s-channel mediators can only couple to both pairs of SM particles and pairs of DM particles. Mediators in these models could be heavy vector bosons such as dark photons, scalars such as Higgs-like particles, pseudo-scalars, or tensor fields. At the same time, DM is generally considered to be fermionic, but it can also have spin 0.

- **t-channel models**: DM has an interaction vertex with one mediator *and* one SM particle, typically a SM fermion. Due to gauge invariance, the mediator has to share the same SM gauge quantum numbers as the SM partner. DM can thus annihilate into SM particles via 2-to-2 processes with one mediator exchanged in the t-channel. The mediators and DM have to be odd under the stabilizing symmetry, while the SM fields have to be even. Typical mediators in these models feature colored charged scalars (squark-like), electroweak-charged scalars (slepton-like), and vectorlike fermions, while DM can be any type of field with spin from 0 to 1. Another feature here is that mediators can directly decay into DM particles (+ a SM particle). One of the first motivations to study t-channel models is that some of them resemble systems in the MSSM.

The dark matter (DM) models explored in this thesis build on recent efforts to classify and thoroughly investigate simplified t-channel models [6, 187–189], integrating comprehensive collider analyses with constraints from direct and indirect detection searches.

t-channel mediators, being charged under the Standard Model (SM), exhibit a rich phenomenology. They can potentially be produced and detected at colliders, either directly or through the observation of missing energy signatures associated with their decay products, possibly including the DM itself. Additionally, if DM exhibits strong coupling, its interactions with nuclei in underground detectors could induce nuclear recoils, providing detectable signals. Furthermore, DM annihilations in dense galactic regions could result in distinctive photon and cosmic ray emissions, typical signatures of WIMP-like particles.

Conversely, if DM couples very weakly, making it FIMP-like, detection becomes more challenging. In such scenarios, the only feasible detection method might involve observing long-lived mediators decaying at displaced vertices within detectors or even outside them. This possibility is explored in Chapter X, where we examine the impact of FIMP DM production from mediator decays during extended reheating phases following inflation, an interplay absent in s-channel models where mediators do not decay into DM directly.

As we will explore in the following chapters, SM-charged mediators open up a broad spectrum of possibilities for understanding their role in the early Universe, particularly by examining the influence of their gauge interactions. For example, long-range potentials can non-perturbatively alter interactions between mediators (see Chapters IV and V), while their close coupling with the primordial thermal plasma can significantly modify their spectral properties (see Chapters VI, VII and IX), thereby strongly influencing DM genesis.

In the following section, we review the framework for studying t-channel models of DM developed in Refs. [187–189].

II.2.4 Simplified t-Channel Models

In the t-channel framework, the SM is augmented with a DM field X, which is a singlet under the SM gauge group $SU(3)_c \otimes SU(2)_L \otimes U(1)_Y$, and a mediator Y, which is charged under the SM gauge group. The classification of these models is determined by the spin statistics of the dark sector particles and the gauge quantum numbers of the mediator. Using the notation of [188], the most general Lagrangian comprising all the possibilities is

$$\mathcal{L} = \mathcal{L}_{\rm SM} + \mathcal{L}_{\rm kin} + \mathcal{L}_F(\chi) + \mathcal{L}_F(\tilde{\chi}) + \mathcal{L}_S(S) + \mathcal{L}_S(\tilde{S}) + \mathcal{L}_V(V) + \mathcal{L}_V(\tilde{V})\,, \tag{II.4}$$

where $\mathcal{L}_{\rm SM}$ is the SM Lagrangian and $\mathcal{L}_{\rm kin}$ contains gauge-invariant kinetic and mass terms for all the new fields. These are six possible DM candidates that we denote as follows: $\tilde{S}$ (real scalar), S (complex scalar), $\tilde{\chi}$ (Majorana fermion), χ (Dirac fermion), $\tilde{V}_\mu$ (real vector), V_μ (complex vector).

The Lagrangians for these scalar, fermionic, and vector DM candidates are given by

$$\mathcal{L}_S(X) = \left(\lambda_L \bar{\psi}_L L X + \lambda_u \bar{\psi}_u u X + \lambda_d \bar{\psi}_d d X + \text{h.c.}\right)\,, \tag{II.5}$$

$$\mathcal{L}_F(X) = \left(\lambda_L \bar{X} L \phi_L^\dagger + \lambda_u \bar{X} u \phi_u^\dagger + \lambda_d \bar{X} d \phi_d^\dagger + \text{h.c.}\right)\,, \tag{II.6}$$

$$\mathcal{L}_V(X) = \left(\lambda_L \bar{\psi}_L \not{X} L + \lambda_u \bar{\psi}_u \not{X} u + \lambda_d \bar{\psi}_d \not{X} d + \text{h.c.}\right)\,. \tag{II.7}$$

Here, L is a SM $SU(2)_L$ fermion doublet in the left-handed representation and it can represent either a quark doublet or a lepton doublet.[5] In this context, u stands for the right-handed up-type quark u_R (as no right-handed neutrinos are present in the SM), while d can denote either a right-handed lepton e_R or a down-type quark d_R. The scalar mediators are denoted by ϕ, and their gauge quantum numbers are determined by the gauge group representations of the SM fermion they interact with. For example, ϕ_Q is a left-handed doublet. Similarly, the fermionic mediators are represented by ψ. The Feynman slashed notation $\not{X} = \gamma_\mu X^\mu$ indicates that X^μ is a vector DM field. The DM couplings λ span the entire flavor space and are thus understood as 3×3 complex matrices. Note that the most generic case involves one 3×3 complex matrix of couplings for each $SU(2)_L$ model type, 12 mediators (each with its own mass parameter), and one DM mass. For colored models, this amounts to an additional 40 parameters, while for colorless models, the number only reduces to 30. Such a situation would deviate significantly from the simplification intended by the "simplified model" philosophy. Thus, we will always assume that coupling matrices are flavor diagonal and degenerate, meaning that only *one* coupling parameter needs to be considered for each $SU(2)_L$ representation. Similarly, all

[5]The framework presented in [187] focuses exclusively on color-charged mediators and quarks, as these particles can be produced at colliders and exhibit a broader range of phenomenological signatures compared to color-neutral states.

mediator masses are assumed equal. The parameter space dramatically shrinks to only three parameters for each model type:

$$\{M_X,\, M_Y,\, \lambda\}\,. \tag{II.8}$$

In [187], models are assigned specific names to facilitate their classification. For instance, the `S3M`-type and `S3D`-type models comprise a scalar mediator (`S`) ϕ (or $\tilde{\phi}$) and a DM field with mass M_χ that is either Majorana (`M`) or Dirac (`D`). The `3` indicates that the scalar mediator is a color triplet. For colorless models, we refer to them as `S1M`-type and `S1D`-type. For models with a universal coupling to all flavors, we have

$$\mathcal{L}_{\text{uni},1} = \sum_{F=L,u,d} \sum_{\alpha=1}^{3} \left(\lambda_\phi \bar{X} F_\alpha \phi^\dagger_{F_\alpha} + \text{h.c.}\right)\,, \tag{II.9}$$

where $X = \chi$ (Dirac) or $\tilde{\chi}$ (Majorana), and α is a generation index. One can further restrict the Lagrangian to a single generation and flavor to simplify the analysis. For example, the `S3MuR` model corresponds to a Majorana DM coupling only to the up-type right-handed quarks, resembling a system with a bino-like neutralino DM and a squark mediator in the MSSM. The parameters of the models are:

$$\{M_\chi,\, M_\phi,\, \lambda_\phi\}\,, \tag{II.10}$$

In an analogous way, we have the `F3S`-type and `F3C`-type models where the mediators are vector-like fermions (`F`) ψ all degenerate in mass and DM is a real (`S`) or complex (`C`) scalar with mass M_S. The mediators live in the triplet representation of $SU(3)_c$. For color singlets, we could use `F1S` and `F1C`. All couplings are taken to be universal and flavor-diagonal, resulting in the following Lagrangian:

$$\mathcal{L}_{\text{uni},2} = \sum_{F=L,u,d} \sum_{\alpha=1}^{3} \left(\lambda_\psi \bar{\psi}_{F_\alpha} F_\alpha X + \text{h.c.}\right)\,, \tag{II.11}$$

where $X = \tilde{S}$ (real scalar) or S (complex scalar). The model parameters are

$$\{M_S,\, M_\psi,\, \lambda_\psi\}\,. \tag{II.12}$$

Finally, vector DM models are also a possibility. In this framework, they are called `F3V` and `F3W` for real and complex vectors, respectively, of mass M_V. All fermion mediators are color triplets and degenerate with mass M_ψ. For colorless mediators, we may use the names `F1V` and `F1W`. In this thesis work, however, we will not discuss such scenarios.

Relevance to this thesis work

The primary objective of this framework is to comprehensively address the phenomenology of various models in a systematic and automated manner. This workflow leverages multiple codes that utilize the UFO library [192], a standardized language for encoding model properties such as fields, quantum numbers, parameters, and interaction vertices. These files are read by various tools for diverse purposes, including generating Feynman diagrams, simulating next-to-leading order corrections, parton showers, and jets, and calculating cosmological evolution variables such as the DM number density and expected signatures in direct and indirect detection experiments.

The typical "phenomenological flow" of codes begins with the `FeynRules` package [193] to implement the model Lagrangian, field content, and parameters, and to generate the UFO library. In Chapter V, we utilize the generated files for certain `S3M` models featuring Majorana fermion DM candidates and colored scalar mediators to compute the DM relic abundance using `micrOMEGAs` [194]. This software package utilizes the UFO library to solve the DM Boltzmann equation (cf. Chapter III) considering all relevant tree-level processes.

Specifically, we will extend `micrOMEGAs` for the `S3MuR`, `S3MdR`, and `S3MqL` models to include non-perturbative effects arising from the long-range interaction of gluonic Coulomb forces exchanged by colored mediators, namely the Sommerfeld Effect (SE) and Bound State Formation (BSF). As detailed in Chapter IV, these effects become significant corrections to the DM interaction rate in scenarios where mediators and DM differ in mass by less than 20%, thereby crucially impacting the phenomenology of the simplified t-channel models under consideration.

Although these effects have only recently begun to be incorporated in DM studies, their systematic inclusion in the "phenomenological flow" such as in `micrOMEGAs`, has not been previously attempted. In our work, we have addressed this gap by providing a functional patch to `micrOMEGAs`, utilized in [1] and described in Chapter V. The completion of this patch has been recently made public in [7, 8].

Simplified t-channel models will also serve as the framework in Chapter VII and Chapter X where we investigate the freeze-in production mechanism of DM (cf. Section III.5.2). In the former, we demonstrate the systematic inclusion of in-medium finite-temperature effects on the evolution of DM number density, comparing our results with existing literature. The latter section highlights how modifications to the thermal history of the Universe, specifically scenarios with low reheating temperatures, impact DM production and the expected signatures at colliders.

As a final remark, we would like to stress once more the significance of understanding the intricacies of simplified t-channel models. We believe the answer is multifaceted. First, if DM manifests as a new particle detectable at colliders, it must have some portal connection with the SM, as suggested by various theoretical frameworks such as SUSY. Simplified models offer a versatile framework to analyze different phenomena with fewer theoretical constraints, allowing nature and experiments to guide the direction of research. Ultimately, the outcome is often beyond the control of theorists, as history has demonstrated over the last four decades.

Secondly, if a new signature compatible with BSM physics is observed, how can we ascertain that it originates from DM? While multiple signatures and confirmations from various perspectives are essential, a critical aspect of interpretation lies in relating terrestrial signals to specific DM models and their cosmological evolution. Neglecting relevant effects and subtleties in this evolution could lead to discrepancies between predictions and discoveries, potentially indicating a

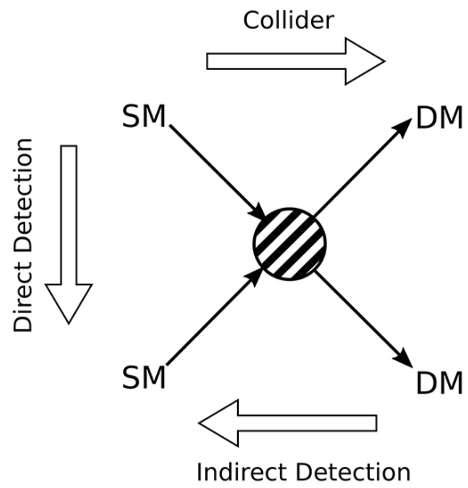

Figure II.7: A scheme of the three main types of searches for DM particles. The interaction between DM and SM particles follows the direction of the arrows. Figure from [195].

misinterpretation of experimental results that could have been resolved with better theoretical calculations and reduced uncertainty.

Furthermore, as we already mentioned, ongoing initiatives are aiming to provide the experimental community with meaningful benchmark points and parameter ranges to search for signals of simplified t-channel models. [6, 189] Therefore, comprehending the full spectrum of theoretical possibilities and uncertainties is timely and crucially important.

In the next section, we will review some of the most important types of experimental searches aiming at detecting signals to be correlated with DM. In particular, we will highlight their importance in relation to the simplified models here described.

II.3 Experimental Searches

The existence of DM is primarily inferred through its gravitational effects, providing insights into its total mass, distribution, and interactions across different astrophysical scales. To further elucidate its nature, investigations focus on three main approaches, which are schematically shown in Fig. II.7: **Direct Detection**, which aims to capture the recoil of DM particles interacting with nuclei or electrons in sensitive underground detectors; **Indirect Detection,** which seeks signatures of DM annihilation or decay products in cosmic rays, photons, or neutrinos; and **Accelerator-based Detection**, where DM particles are produced and studied in controlled environments like particle colliders, aiming to observe missing energy or exotic decay channels that could indicate the presence of DM. Each approach plays a crucial role in complementing gravitational evidence to unravel the mystery of DM's composition and interactions with ordinary matter.

II.3.1 Direct Detection

Direct detection (DD) experiments search for signatures left by DM particles in the galactic halo interacting with detector materials, typically manifesting as energy deposits with distinct kinematics. These experiments are conducted deep underground to shield ultra-pure detector materials from cosmic radiation, minimizing background noise. Given the expected extremely low interaction rates and energy yields, even minimal interference can lead to false positives.

The primary categories of DD searches involve DM scattering on nuclei and electrons. Other non-standard techniques include scattering on phonons, the Migdal effect, and inelastic scatterings, which are currently under investigation [12, 196]. Historically, scattering on nuclei has been the dominant method due to the largest momentum transfer in elastic scattering occurring when the projectile and target masses are comparable. This approach has led the field for many years, especially as early expectations placed DM in the electroweak-scale regime, aligning with the masses of nuclei like Xe and Ar and their isotopes, which are approximately $\mathcal{O}(100)$ GeV. Conversely, in the sub-GeV regime, which has only recently garnered attention, scattering on electrons ($m_e = 511\,\mathrm{keV}$) is proving to be the most efficient choice. The low energy deposit means that a range of quantum-mechanical effects becomes relevant, as DM interactions become sensitive not only to individual scattering sites but also to the material structure of the detector.

The event rate R for DM elastic scattering on a single nucleus with mass number A is the number of events per nuclear recoil energy E_R and its differential form is given by [12]

$$\frac{\mathrm{d}R}{\mathrm{d}E_R} = \frac{N_T}{m_T}\int_{v>v_{\min}}^{\infty} \frac{\mathrm{d}\sigma_A}{\mathrm{d}E_R} v \, \frac{\rho_\oplus}{M} f_\oplus(\mathbf{v})\, \mathrm{d}^3\mathbf{v}\,. \tag{II.13}$$

Here, N_T represents the number of target nuclei in the detector's target material of mass m_T, and σ_A denotes the DM-nucleus interaction cross-section, which is determined by the particle physics model of DM. The integral is performed over the DM velocity v in the Earth's frame, typically ranging from 200 to 500 km/s. The integral includes factors such as the local DM density $\rho_\oplus \approx \rho_\odot \approx 0.4\,\mathrm{GeV/cm^3}$, and assumes a Maxwellian distribution for the local DM velocity distribution. The lower integration bound, $v_{\min}$, signifies the minimum velocity required for a DM particle to transfer a kinetic energy E_R to the nucleus, and is defined as $v_{\min} = \sqrt{\frac{m_A E_R}{2\mu_A^2}}$, where $\mu_A = \frac{m_A M}{m_A + M}$ denotes the reduced mass of the DM-nucleus system. Here, $m_A \approx A m_N$, with m_N representing the mass of a single nucleon, typically 939 MeV in the isospin limit where $m_p = m_n = m_N$.

The interaction cross-section can be **spin-independent** (SI) or **spin-dependent** (SD). In the first case, the nucleus can be resolved coeherently and the differential cross-section is directly proportional to the cross-section for DM scattering on nucleons (protons and neutrons) σ_{SI} and to the nuclear form factor.

In the regime of small momentum exchange, where DM interacts with the entire nucleus coherently as a point particle, the SI cross-section can be expressed as [12]:

$$\sigma_{\mathrm{SI}}^A\Big|_{q\to 0} = A^2\sigma_{\mathrm{SI}} \approx \sigma_{\mathrm{SI}} \begin{cases} A^2 & \text{for } M \ll m_N, \\ A^4/(1 + A m_N/M)^2 & \text{for } m_N \ll M < m_A, \\ A^4 & \text{for } M \gg m_A. \end{cases} \tag{II.14}$$

Notice how the coherent interaction enhances the cross-section by factors of A.

SD searches aim to detect interactions between the spin of DM and the spin of nucleons. The theory underlying this interaction is more complex. The SD differential cross-section for DM scattering off a nucleon σ_{SD} grows with the spin-spin interaction strength and hence with the total DM spin, while it decreases with the maximal recoil energy. For a heavy nucleus of mass number A the formula is more complicated due to the incoherent resolution of each nucleon. In the zero momentum exchange limit, one can obtain an approximated formula which reads as [12]

$$\sigma_{\mathrm{SD}}^{A} \approx \sigma_{\mathrm{SD}} S(0) \times \begin{cases} 1 & \text{for } M \ll m_{N,A}, \\ A^2 & \text{for } M \gg m_{N,A}. \end{cases} \tag{II.15}$$

Here, $S(0)$ is the zero momentum limit of the nuclear response function, which takes into account the form of the nuclear wavefunctions.

Detection techniques and detector materials vary depending on the experimental goals. Some of the most employed techniques include detectors based on noble liquid scintillators (e.g., XENON [197], LUX-ZEPLIN (LZ) [198], DarkSide [199], PandaX [200]), scintillating crystals (e.g., DAMA/LIBRA [201], SABRE [202], COSINE [203]), cryogenic detectors (e.g., CDMS [204], EDELWEISS [205], CRESST [206]), and superheated liquids (e.g., PICO [207]). Fig. II.8 illustrates the state-of-the-art in DM detection. The left panel shows experimental constraints on the SI cross-section as a function of DM mass, while the right panel displays constraints on the SD cross-section. Current bounds are approaching the so-called "neutrino floor", which is an irreducible background predicted from coherent neutrino-nucleus scattering for neutrinos with energies $\lesssim$ GeV. This background could obscure a potential DM signal, hence the name "neutrino fog". Solar neutrinos dominate this background for DM masses below tens of GeV, while atmospheric neutrinos are more relevant for heavier DM. One potential approach to overcome these irreducible obstacles is through directional detectors. These detectors aim to trace the recoil track of nuclei when a DM particle passes through the detector, leveraging the Earth's relative motion with respect to the DM halo and revolutionizing DM detection in the Galaxy.

Relevance to this thesis work

Limits from the XENON1T and PICO-60 DD experiments, as well as future projections from the DARWIN project, will be key ingredients in the analysis of the constrained parameter space in the simplified t-channel models analyzed in Chapter V (cf. Sections V.A and VIII.2), where we will demonstrate how accounting for non-perturbative effects from long-range interactions (cf. Chapter IV for an overview) sensibly morph the constrained and allowed parameter regions (cf. also the corresponding paper [1]).

II.3.2 Indirect Detection

Indirect Detection (ID) encompasses methods and experiments seeking signals of DM interactions in astrophysical environments, manifesting as excesses in photon, cosmic ray, and neutrino fluxes. Typically focusing on heavier DM candidates, often in the GeV mass range and above, ID experiments aim to detect annihilation or decay products of DM particles. While in this thesis we will focus on DD and collider limits due to their relevance to the models and parameter space studied, we provide a concise overview of ID directions. For further details, comprehensive reviews such as [12, 208] are recommended.

If our Galaxy resides within a DM halo where DM particles interact beyond gravitational effects, annihilation or decay processes may produce observable signals. These include high-energy gamma-ray photons observed by satellites like FERMI-LAT [209] and AMS-02 [210], and by ground-based Cerenkov telescopes such as HESS [211], VERITAS [212], and MAGIC [213]. Alternatively, low-energy X-ray photons can be produced as secondary photons from electron-positron annihilations following DM interactions or as

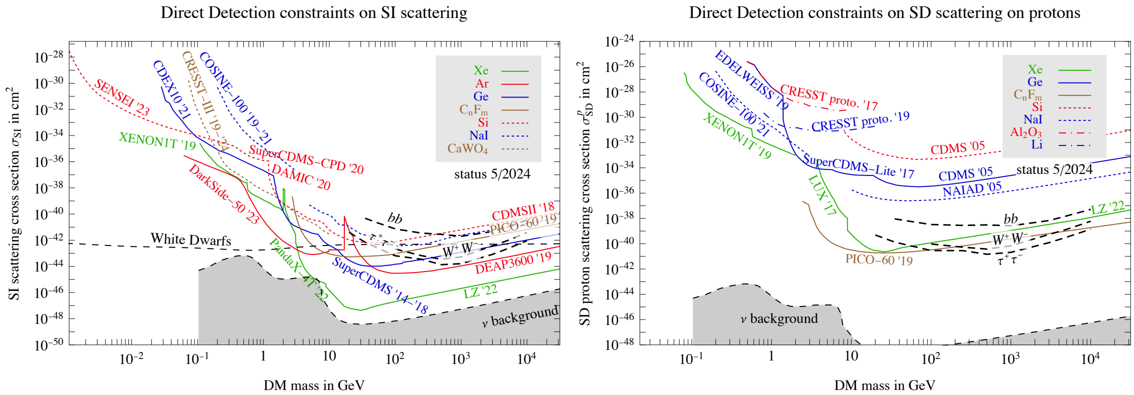

Figure II.8: Current bounds on the DM cross-section on nucleons as a function of the DM mass. *Left panel:* limits on the SI cross-section. *Right panel:* limits on the SD cross-section on protons (neutrons give similar results). Figures from [12].

primary photons in light DM models (e.g., sterile neutrinos), detectable by telescopes like CHANDRA [214] and INTEGRAL [215].

Cosmic rays are electrically charged particles arriving on Earth from practically any possible astrophysical object. They primarily consist of particles like positrons, electrons, anti-protons, and anti-deuterons, and can also originate from DM annihilation or decay. The challenge here is the complex background, which hides a potential DM signal since all these cosmic rays are copiously produced by the sun, stellar activity in the Galaxy, and supernova explosions. Their propagation is affected by diffusive effects, energy losses, and other interactions with the interstellar medium. Two major issues associated with ID are the accurate modeling of the source environment (the galactic center, a supernova remnant, a neutron star, etc), which is usually very complex, and the propagation of the astroparticle messengers through the galaxy until they reach a detector such as a telescope. Significant experiments in this domain include the already cited AMS-02, PAMELA [216], the Pierre Auger Observatory [217], and various Cerenkov telescopes sensitive to cosmic ray fluxes (e.g., the future CTA [218]).

Neutrinos, being electrically neutral and weakly interacting, serve as ideal messengers for DM signals as they propagate through the Galaxy unaffected by magnetic fields or dense environments. Detecting neutrinos, however, poses challenges due to their elusive nature and indirect energy reconstruction methods. The largest neutrino detector on Earth is the IceCube Neutrino Observatory [219] at the Earth's South Pole, while other important experiments are ANTARES [220] and SuperKamiokande [221].

II.3.3 Collider Searches

DM may manifest itself in collider experiments, which are sophisticated machines that accelerate particles along circular or linear paths, causing them to collide either with each other or with a fixed target. Typically, DM would appear as *missing energy* in reconstructed events due to its weak interactions with ordinary matter. However, gauge-charged mediators could be produced directly due to their interactions with SM particles in scenarios involving a richer dark sector, such as in SUSY or simplified models. These mediators could subsequently decay into DM states, yielding distinctive signals that vary depending on the specific model. Reviews on collider searches for DM can be found in, for instance, [12, 222].

Collider experiments encompass various types, with the most prominent being the

LHC [223], a proton-proton (pp) circular collider with a circumference of approximately 27 km and current center-of-mass energy of $\sqrt{s} = 13.6$ TeV, expected to reach 14 TeV. Its upcoming High-Luminosity LHC (HL-LHC) upgrade aims for an integrated luminosity of ~ 3000/fb [224]. The LHC's discoveries include the Higgs boson in 2012 and the verification of many SM predictions with enhanced precision. Despite these achievements, no significant deviations from the SM have been observed so far, suggesting several possibilities: DM could be heavier than the LHC's reach (beyond the TeV regime), have extremely feeble interactions that make it challenging to detect at colliders, or it might not be a new particle altogether.

Due to substantial QCD background issues in pp colliders, an alternative approach involves constructing more powerful lepton colliders, following the success of the Large Electron-Positron (LEP) collider, which reached energies up to 200 GeV. [225] Although lepton colliders operate at lower energies compared to pp colliders, they offer a clean experimental environment suitable for precision measurements. If DM induces minute deviations in SM observables, precision collider physics could prove indispensable.

Particles produced in colliders are detected through various means: calorimeters measure the energy deposited by electrons and photons, the detector's outer layers track muons escaping the inner layers, QCD jets generated by hadronization processes immediately following the emission of a quark or a gluon are reconstructed with sophisticated triggers and algorithms, and the missing energy carried away by neutrinos, invisible to colliders, is inferred by the event kinematics. DM may leave traces through one or a combination of these detection signatures.

Mono-X searches

Typical signatures of DM in collider experiments include *mono-X* searches, where a single visible particle (X), such as a photon, jet, or W/Z boson, recoils against Missing Transverse Energy (MET). This indicates the production of DM particles. Mono-X searches are relatively model-independent and highly sensitive to New Physics. However, their signal-to-noise ratio can be challenging to optimize due to the significant presence of neutrinos produced from weak processes following the collision (besides the QCD background, of course).

High-mass resonances

Other possibilities involve searching for excesses of events in the form of resonances at specific values of the invariant mass, which might signal the existence of a new BSM state. Prime examples are diphoton resonances, where new particles decay in pairs of photons, which famously rose to the headlines when the 750 GeV diphoton excess was found at the LHC in 2015. However, later data did not confirm it. These types of searches (together with multi-jet, multi-lepton, and other signatures) are called *prompt* because they assume that BSM states are produced close to the interaction vertex.

Searches of these types are mainly carried out by the ATLAS [226] and CMS [227] experiments at the LHC. Dedicated analyses are heavily model-dependent due to the abundance of parameters in (realistic) DM particle models that have to be fixed to derive bounds on observables such as cross-sections, decay widths, branching ratios, etc. For example, Ref. [228] has recently provided a thorough analysis constraining DM s-channel models featuring a spin-0 (Higgs) or a spin-1 (dark photon) portal.

Long-Lived Particle (LLP) Signatures.

Due to the absence of statistically significant prompt signals and increasingly stringent constraints, recent years have seen growing interest in alternative signatures from *long-lived particles* (LLPs). If BSM particles possess suppressed couplings, small mass splittings, or limited phase space for decay, they may travel macroscopic distances before decaying, giving rise to striking displaced or non-pointing signatures.

LLP searches exploit the unique capability of modern detectors to reconstruct such unconventional topologies. Below we summarize the main experimental categories, following Refs. [229–234]:

- **Heavy Stable Charged Particles (HSCPs):** LLPs that are charged and long-lived enough to exit the detector ($c\tau \gtrsim 1$ m) are reconstructed as slow, highly ionizing tracks in the inner tracker and muon system. Time-of-flight and dE/dx measurements are used to discriminate them from SM muons. Current CMS and ATLAS analyses exclude sleptons or vectorlike leptons with $c\tau \gtrsim 0.1-100$ m for $m \lesssim 600$ GeV [229, 235]. If the LLP also carries QCD color, it hadronizes into *R-hadrons*, forming the basis of so-called "R-hadron" searches.
- **Disappearing or Kinked Tracks (DT/KT):** For intermediate lifetimes ($10^{-2} \lesssim c\tau/\mathrm{m} \lesssim 10$), charged LLPs may decay inside the inner tracker. If decay products are soft or neutral, the track appears to "disappear"; if they are visible, the track abruptly changes direction (a "kinked" track). ATLAS and CMS searches target such signatures by identifying tracks with missing outer hits and minimal calorimeter energy deposition [230, 233, 234, 236]. These searches are particularly sensitive to electroweak multiplets (e.g., Higgsino or wino-like states).
- **Displaced Vertices and Displaced Leptons (DV/DL):** When an LLP decays within the tracker volume, its displaced decay products can form a secondary vertex several millimeters to tens of centimeters from the primary interaction point. Dedicated DV and DL searches relax standard impact-parameter constraints and use triggers designed for displaced leptons or large MET. ATLAS analyses consider opposite- and same-flavor lepton pairs [231], while CMS focuses primarily on displaced $e\mu$ pairs [232, 237]. ATLAS is most sensitive around $c\tau \sim 10^{-2}$ m, whereas CMS extends to shorter lifetimes of order 10^{-3} m.

Together, HSCP, DT, and DL searches probe a broad range of lifetimes and decay modes, covering $10^{-4}\ \mathrm{m} \lesssim c\tau \lesssim 10^{3}$ m. Their complementarity allows collider experiments to explore vast regions of parameter space that would otherwise remain unconstrained in prompt analyses.

In the context of DM models with feebly coupled mediators—such as the simplified t-channel scenarios studied in this thesis—LLP searches are particularly powerful. There, mediators charged under the SM gauge group can be produced at colliders and decay into DM plus a visible SM fermion:

$$P \longrightarrow \mathrm{DM} + f_{\mathrm{SM}}\,,$$

where P is either a scalar or vectorlike fermion and f_{SM} a charged lepton or quark. Depending on the mediator mass and coupling strength, these decays may occur with macroscopic lifetimes, producing any of the LLP signatures listed above.

II.3.4 Synergy of Experimental Probes in this Thesis

The diverse array of experimental strategies reviewed above—spanning direct detection, prompt collider signals, and long-lived particle signatures—forms the empirical foundation against which the theoretical predictions of this thesis are tested. In the subsequent chapters, we will demonstrate that the interpretation of these constraints is intrinsically dependent on the rigorous treatment of particle production mechanisms.

Specifically, in Chapter V, we integrate limits from Direct Detection (XENON1T, PICO-60) and prompt collider searches (mono-jet, multi-jet) to constrain the parameter space of simplified t-channel models. Crucially, we will show that including non-perturbative effects such as **Sommerfeld enhancement** and **bound state formation** (cf. Chapter IV) fundamentally alters the exclusion boundaries defined by these experiments, opening up parameter regions that standard perturbative calculations would deem excluded [1]. A key aspect of this analysis involves the use of **high-mass resonance searches** (e.g., diphoton final states), which we demonstrate provide a robust, coupling-independent probe of the mediator mass, complementing the coupling-dependent missing-energy searches.

Furthermore, the sensitivity to **Long-Lived Particles** plays a pivotal role in the analysis of non-thermal production scenarios. In Chapter X, we employ constraints from HSCP, disappearing track, and displaced vertex searches to bound the properties of feebly interacting mediators. We will establish a direct link between the cosmological history of the Universe—specifically the *reheating epoch*—and the macroscopic lifetime of these mediators. Consequently, we argue that the interpretation of collider exclusions is not purely a particle physics exercise but is inextricably linked to the underlying cosmological assumptions.

II.4 Alternatives to Dark Matter

The non-discovery of particles associated with DM (or, in fact, any BSM particles) and the increasing number of tensions and inconsistencies within the Standard Model of Cosmology prompt the question of whether DM exists at all. While this may seem like a bold assertion, there are reasons to consider alternative explanations. One possibility is that the answer to the overwhelming evidence that General Relativity combined with ordinary matter cannot account for most astrophysical phenomena and cosmological observations may lie in a modification of the laws of gravitation. The most important theory of this kind is MOdified Newtonian Dynamics (MOND), proposed by M. Milgrom in 1983 [238–241] as an alternative to the CDM paradigm to explain the puzzling flattening of the rotation curve of galaxies at large radii.[6] What MOND essentially does is modify Newton's law of motion $F = ma$ in the regime of small accelerations. In this theory, below a certain critical acceleration a_0, the law becomes

$$F = m\mu\left(\frac{a}{a_0}\right)a\,, \tag{II.16}$$

where μ is an interpolating function that reproduces Newtonian dynamics for $a \gg a_0$ and leads to the *Milgrom's law* $F = ma^2/a_0$ in the deep-MOND regime $a \ll a_0$. The quadratic dependence below a_0 allows for the flattening of the rotation curve without a CDM component. This is a consequence of $a^2 \propto 1/r^2$ being invariant under space and time dilation. In fact, repeating the exercise of Eq. (II.1), we can equate Newton's universal

[6]For reviews on MOND theories, their predictions, and their confirmation/falsification, we refer to, e.g., Refs. [242–244].

law of gravitation to the modified Newton's law of motion to obtain [12]

$$\frac{GmM_b(r)}{r^2} = F \simeq \begin{cases} ma & \text{if } a > a_0, \\ ma^2/a_0 & \text{if } a < a_0, \end{cases} \implies v(r) \simeq \begin{cases} (GM_b(r)/r)^{1/2} & \text{Newton}, \\ (GM_b(r)/a_0)^{1/4} & \text{MOND}, \end{cases} \tag{II.17}$$

where $M_b(r)$ is the baryonic mass within a radius r. We observe that, in addition to predicting a flat rotation curve, MOND predicts a precise proportionality $v_\infty \propto M_b^{1/4}$ between the rotational velocity at large radii v_∞ and the baryonic mass M_b of an astrophysical object. This relationship is known as the *baryonic Tully-Fisher relation* [245], one of MOND's most significant predictions and arguably its greatest success.

Observations of hundreds of galactic rotation curves consistently align with this MOND prediction over at least four orders of magnitude, encompassing both faint dwarf galaxies and star-rich massive galaxies. In contrast, the standard CDM model does not naturally predict this correlation unless structure formation with DM dynamically generates this common behavior across various scales, possibly by considering complex baryonic dynamics in galaxy formation—a process that remains unclear to date. By fitting the MONDian law of gravitation, the critical acceleration value can be determined, yielding [12]

$$a_0 \simeq 1.2 \times 10^{-10}\,\mathrm{m/s^2}\,. \tag{II.18}$$

Notice that MOND predicts this value to be *universal*, i.e., applicable to every astrophysical system. However, it has been claimed that there is no possibility for the existence of such a universal critical acceleration a_0, effectively ruling out MOND at more than 10σ [246]. This claim has sparked a series of rebuttals and replies among different researchers [247–249]. The bottom line is that the purported falsification of MOND may have resulted from analysis errors and misinterpretation of the results.

Another feature that CDM models struggle to explain is the observed correlation between the radial gravitational acceleration and the acceleration based on baryons alone at a generic radius. This indicates that "For any feature in the luminosity profile there is a corresponding feature in the rotation curve and vice versa," also known as *Renzo's rule* [250]. The CDM model predicts that the rotation curves of galaxies should be primarily determined by the distribution of DM, typically assumed to be a smooth and spherically symmetric halo. Therefore, the detailed features in the rotation curve should not directly correlate with the distribution of visible matter alone. The CDM model would require a specifically and finely tuned distribution of DM to match the features seen in the visible matter. In contrast, MOND can link the observed dynamics to the visible matter distribution, providing a straightforward explanation for the direct correlation observed in Renzo's rule, without invoking unseen DM.

As discussed in Section II.1.2, cluster collisions have often been regarded as strong evidence in favor of collisionless CDM and a significant challenge for MOND theories since MOND predicts the "phantom" mass distribution to follow the distribution of baryonic matter, which is not observed in such collisions [54, 251]. An ad-hoc solution to this problem involves postulating MOND *plus* some amount of DM in the form of light neutrinos [244]. Similarly, the existence of the El Gordo cluster, the KBC void, and other tensions in the ΛCDM model could be explained with MONDian dynamics [62, 63, 252].

The main challenges with MOND theories arise when considering the largest scales[7], where, in contrast, the ΛCDM concordance model finds its greatest success, displaying a

[7]Some issues with MOND theories were claimed to be found in globular clusters [253] but were later refuted [254].

remarkable consistency within many observations of the LSS and the CMB. Here, MOND in its non-relativistic form struggles to reproduce the CMB anisotropies and the formation of structures [255], and it faces significant difficulties in explaining gravitational lensing effects. For one, non-relativistic MONDian dynamics is an empirical paradigm that probes very low acceleration regimes and cannot be a universal law at every scale, as it violates momentum conservation and does not align with predictions from General Relativity. Several non-relativistic theories embedding the vanilla MOND and attempting to address some of its issues have been proposed over the years, including AQUAdratic Lagrangian (AQUAL) [241] as modified Poisson gravity, Quasilinear MOND (QUMOND) [256], and other generalizations [257]. For the other, MOND theories require embedding in a more fundamental theory of modified gravity consistent with relativity.

In 2004, Bekenstein formulated the first Tensor-Vector-Scalar (TeVeS) relativistic theory of MOND [258]. One of its key predictions is that ordinary matter must couple to a modified metric tensor, leading to a discrepancy between the speeds of light and gravitational waves. This was essentially ruled out by the simultaneous detection of the gravitational wave event GW170817 from a neutron star binary merger and its electromagnetic counterpart, demonstrating that gravity propagates at the speed of light up to at least 40 Mpc [259, 260]. Nevertheless, some of these issues can be reconciled in recent attempts involving Einstein-Aether theories, entropic (or emergent) gravity, and bimetric gravity [261–267].

We conclude by mentioning two recent observations that have been claimed to challenge or even rule out MOND theories. Recent analyses suggest that some galaxies are surprisingly deficient in DM [268–270]. One possibility is that gravitational interactions stripped the DM, while another is that it was driven out during the galaxy's formation by merging protogalactic fragments. Interestingly, these results could be interpreted as evidence *in favor* of the particle nature of DM, as opposed to universal modifications of gravitational laws. However, it is crucial to ensure that the considered data effectively probe the regime where MOND theories would apply (the low acceleration regime). For instance, in the case of [270], the authors themselves state that no definitive conclusions can be drawn. In fact, Ref. [271] argues that MOND is perfectly consistent with DM-deficient dwarf galaxies in the Fornax cluster.

Another recent puzzling tension arises from the analysis of the stellar motion of wide binaries in the Milky Way conducted by two different groups using the GAIA satellite. While Ref. [272] claimed that MOND should be excluded on small scales with a 16σ confidence, Ref. [273] concluded the exact opposite, showing a 10σ deviation from Newtonian gravity. Thus, we can conclude that the dispute between the two views is far from being settled and further investigations are needed.

In conclusion, while MOND theories have garnered scientific interest due to their successes, they remain a subject of controversy and skepticism. One major challenge is their difficulty in being integrated into a more fundamental theory of nature. Additionally, they are not linked to other unresolved issues in the SM of particle physics, and their successes are often limited, requiring significant revisions, as we have outlined.

This is not necessarily a critical flaw, as similar challenges have been faced and continue to be faced by any theory in particle physics. However, the advantages of a particle-based explanation for DM are considerable. These include the potential for a deeper connection to a fundamental theory of nature, addressing other issues within the SM, its detectability, and the highly advanced level of global collaboration in this research field.

While the development of MOND theories would benefit from improved scientific practices and a reduction in bias, the current strengths and potential of particle-based DM explanations still surpass those of MOND, making the latter a less favored approach at present.

Concluding Remarks

For over a century, the physics community has accumulated evidence suggesting that ordinary matter, combined with General Relativity, cannot fully explain the properties of astrophysical objects across nearly every scale. In contrast, the inclusion of a cold dark matter (DM) component within galaxies, clusters, and the entire Universe offers a unified explanation for these discrepancies.

If DM is indeed a new particle, its discovery would mark the presence of physics beyond the Standard Model (BSM), which is eagerly sought to address various unresolved issues in the Standard Model of particle physics. Despite the recent limitations exposed in the otherwise successful ΛCDM concordance model during what is known as the "precision era of cosmology", the particle hypothesis remains the most compelling option. It accounts for a vast array of observations across all cosmological scales and holds the crucial potential of being linked to one or more fundamental problems within the SM.

Numerous theories propose DM as a thermal relic, such as WIMP-like particles or FIMPs. An example is the simplified t-channel models discussed in Section II.2.4, where the key distinction between these possibilities lies in the strength of the DM coupling. While these models are conceptually simple, they pose significant computational challenges and exhibit a rich phenomenology. Whether they represent the best model of DM is ultimately up to experimental validation. However, they serve as a comprehensive framework for testing the impact of state-of-the-art methods in computing DM properties. These methods are crucial not only for accurately interpreting the models and their experimental constraints but also for advancing theoretical and computational techniques applicable to other areas, such as alternative DM models, leptogenesis, and gravitational wave studies.

In this thesis, we will focus on computing the most critical property of DM: its relic abundance, as defined in Eq. (II.2). This measurement is the most precise indicator of the amount of DM in the Universe today and plays a pivotal role in distinguishing between different particle types, production mechanisms, and parameter values in the models under consideration. The next chapter will explore the methods for calculating this essential quantity.

CHAPTER III

Particle Production in the Early Universe

After reviewing the observational evidence underpinning the Dark Matter (DM) problem, the most extensively studied DM candidates and theoretical frameworks, and the principal experimental search strategies, we now turn to a set of more fundamental questions: how did DM originate in our Universe? At which stage of cosmic history was it produced? And through which mechanisms did it evolve toward its present-day relic abundance, $\Omega_{\rm DM}h^2 = 0.120$?

Addressing these questions requires an understanding of *particle production in the early Universe*, where the thermal history and expansion of the Universe are studied in conjunction with the microscopic processes governing particle interactions in a hot and dense environment. In the earliest stages following the Big Bang, the extreme temperatures and densities provided favorable conditions for the creation of a wide variety of particle species, including viable DM candidates. As the Universe expanded and cooled, the competition between particle interaction rates and the cosmic expansion rate determined whether these species remained in equilibrium, decoupled from the thermal bath, or were produced out of equilibrium, ultimately shaping their relic abundances observed today.

This chapter is devoted to explaining how such processes can be consistently described and to establishing the theoretical framework used to derive the evolution equations governing particle abundances in an expanding Universe.

We begin by briefly reviewing the key ingredients of the ΛCDM concordance model of cosmology and summarizing the thermal history of the Universe, which together provide the cosmological backdrop for the particle-production mechanisms discussed in the remainder of the chapter.

III.1 Cosmology of the Expanding Universe

III.1.1 ΛCDM Cosmology

The standard theory for describing the cosmos is the Hot Big Bang model, which is based on a few simple assumptions [81, 274]. The Universe at very large scales (at least 260 Mpc [275]) is spatially homogeneous and isotropic on average and is described by the Friedmann-Lemâitre-Robertson-Walker metric (FLRW) [276–279],

$$\mathrm{d}s^2 = -\mathrm{d}t^2 + a^2(t)\left[\frac{\mathrm{d}r^2}{1-kr^2} + r^2\mathrm{d}\theta^2 + r^2\sin^2\theta\mathrm{d}\phi^2\right] \overset{k\equiv 0}{=} \mathrm{d}t^2 - a^2(t)\,(\mathrm{d}x^2+\mathrm{d}y^2+\mathrm{d}z^2), \tag{III.1}$$

where $a(t)$ is the scale factor, responsible for the evolution of the spatial hypersurfaces, $k = \{0, 1, -1\}$ is a constant characterizing the global geometry of the FLRW manifold, which can be spatially flat ($k = 0$), closed as a sphere ($k = 1$), or open as a hyperbolic surface ($k = -1$). Notice that we used the mostly negative signature for the metric and natural units ($c = 1$). The normalization for $a(t)$ implies $a(t_0) = 1$ at the present time t_0.

Second, the matter-energy content in the Universe can be modeled by a perfect fluid with stress-energy tensor given by $T^\mu_\nu = \mathrm{diag}(\rho, -P, -P, -P)$, where ρ and P are respectively the energy density and the isotropic pressure of the fluid. Einstein's field equations [280] applied to such a Universe translate into the Friedmann equations regulating the evolution of the expansion of the Universe as a function of its matter-energy content, yielding

$$\left(\frac{\dot{a}}{a}\right)^2 \equiv H^2 = \frac{\rho}{3M_{\mathrm{Pl}}^2} - \frac{k}{a^2}, \tag{III.2}$$

$$\frac{\ddot{a}}{a} = -\frac{1}{6M_{\mathrm{Pl}}^2}(\rho + 3P). \tag{III.3}$$

Here, $H = \dot{a}/a$ is the Hubble rate, with dots representing derivatives with respect to cosmic time t, whereas $M_{\mathrm{Pl}} = 2.4 \times 10^{18}\,\mathrm{GeV}$ is the reduced Planck Mass and k is the spatial curvature. Experimental data are pointing with very high precision to a flat Universe so that we can safely neglect the curvature term in our equations and set $k = 0$ [75].

To solve the Friedmann equations, one has to close the system with the additional *equation of state* for the barotropic fluids

$$P = w\rho, \tag{III.4}$$

where w is a constant that discriminates the different types of fluids:

$$\begin{cases} w = 0 & \text{pressureless non-relativistic matter,} \\ w = 1/3 & \text{relativistic particles (radiation),} \\ w = -1 & \text{vacuum energy.} \end{cases} \tag{III.5}$$

Vacuum energy can be described by a cosmological constant Λ that can be added to Einstein's field equations as $\Lambda g_{\mu\nu}$ term. By using the first law of thermodynamics $\mathrm{d}(\rho V) = -P\mathrm{d}V$, where $V = a^3$ is the volume of a comoving cube, we obtain the following continuity equation

$$\dot{\rho} + 3H(\rho + P) = 0 \qquad \Longrightarrow \qquad \dot{\rho} + 3H\rho(1 + w) = 0. \tag{III.6}$$

From solving this equation, we find the scaling behavior of the energy densities as a function of the scale factor, yielding

$$\rho \propto a^{-3(1+w)}, \tag{III.7}$$

so that we have different scaling for the various types of matter-energy:

$$\rho = \begin{cases} a^{-3} & \text{pressureless non-relativistic matter,} \\ a^{-4} & \text{relativistic particles (radiation),} \\ const & \text{vacuum energy.} \end{cases} \tag{III.8}$$

Consequently, in a single-component universe, the time dependence of the scale factor differs case by case, since Eq. (III.2) reduces to

$$\frac{\dot{a}}{a} \propto a^{-\frac{3}{2}(1+w)}, \tag{III.9}$$

whose solutions scale as $a(t) \propto t^{\frac{2}{3(1+w)}}$ such that we end up with a variety of expansion behaviors, depending on the specific value of w. In particular,

$$a(t) \propto \begin{cases} t^{2/3}, \\ t^{1/2}, \\ e^{Ht}, \end{cases} \qquad \Longrightarrow \qquad H(t) \propto \begin{cases} 1/2\, t^{-1} & \text{pressureless matter,} \\ 2/3\, t^{-1} & \text{radiation,} \\ \text{const} & \text{vacuum energy.} \end{cases} \tag{III.10}$$

Notice that, from Eq. (III.3), if the dominant fluid has $w < -1/3$, the Universe undergoes a period of accelerated expansion. However, in a multi-component universe, things become more complicated, since we have to take into account the sum of all contributions

$$\rho_{TOT} = \rho_r + \rho_m + \rho_\Lambda,$$

with ρ_r, ρ_m, and $\rho_\Lambda = 3M_{\rm Pl}^2\Lambda$ the energy densities of radiation, pressureless matter, and Λ, respectively. Analytical solutions are not so straightforward to obtain. However, thanks to the different scaling, we can infer in which period of cosmic history the various components dominated the universe's energy budget. At early times, the energy density is completely dominated by the thermalized primordial bath, which behaves like radiation. As time flows, pressureless matter overcomes until it gets completely subdued by the constant contribution of the vacuum energy, which does not feel the red-shifting of the scale factor.

If we put $k = 0$, we can define the *critical density* ρ_c as

$$\rho_c = 3M_{\rm Pl}^2 H^2, \tag{III.11}$$

which is the energy density the Universe should have to be spatially flat. Today its value is $\rho_{c0} = 1.05371(5) \times 10^{-5} h^2\, ({\rm GeV}/c^2)\, {\rm cm}^{-3}$. To compare present day energy densities with ρ_{c0}, we define the *critical density parameter* as

$$\Omega_i = \frac{\rho_{i0}}{\rho_{c0}} = \frac{\rho_{i0}}{3M_{\rm Pl}^2 H_0^2}, \tag{III.12}$$

where the subscript '0' indicates a value today, at $a = a_0 = 1$. Dividing Eq. (III.2) by H^2, one finds

$$1 = \frac{\sum_i \rho_i}{\rho_c} - \frac{k}{a^2H^2} = \sum_i \Omega_i - \frac{k}{a^2H^2}.$$

Observing how $\Omega_{\rm TOT} = \sum_i \Omega_i$ differs from 1 tells us what is the spatial curvature of the Universe. The latter term is usually rewritten as $\Omega_k = -k/a^2H^2$ and Planck 2018 data suggest this to be consistent with zero, hence a spatially flat Universe [75]. According to the same analysis, the Universe's energy density consists of

$$\Omega_\Lambda \simeq 68.5\%, \quad \Omega_m \simeq 26.4\% + 4.9\%, \quad \Omega_r \simeq 0.0054\% + 0.0037\%, \tag{III.13}$$

where Ω_Λ is the Dark Energy (DE) component, consistent with a cosmological constant Λ, Ω_m is the matter component divided in a dominant Cold Dark Matter (CDM) component ($\Omega_c \simeq 26.4\%$) and a subdominant baryonic component, made of atoms ($\Omega_b \simeq 4.9\%$). Radiation accounts for less than 10^{-4} with slightly more photons than neutrinos (considered massless). These findings justify the name 'ΛCDM' for the cosmological model of the Universe.

III.1.2 Thermal History

As the Universe expands, particles get more and more diluted and the temperature of the Universe decreases. But, what do we mean by the word "temperature" in Cosmology? This term holds significance solely within a system at thermal equilibrium, a state attainable when particles within it interact closely, sharing identical thermodynamic properties. To quantify these properties, we need some proper definitions within basic equilibrium thermodynamics in an expanding universe. Here, we summarize the more complete treatment found in classical references such as Refs. [274, 281].

The phase space distribution of particles in the early Universe is $f(\mathbf{x}, \mathbf{p}, t) = f(p, T, \mu)$, where we used the homogeneity and isotropy assumption to rewrite f solely as a function of $p = |\mathbf{p}|$, the temperature T and the chemical potential μ. Moreover, an implicit average over spatial coordinates is understood. The *number density*, *energy density* and *isotropic pressure* of particles are defined from f as

$$n(T,\mu) = \frac{g}{(2\pi)^3} \int \mathrm{d}^3\mathbf{p}\, f(p,T,\mu)\,, \tag{III.14}$$

$$\rho(T,\mu) = \frac{g}{(2\pi)^3} \int \mathrm{d}^3\mathbf{p}\, E(p) f(p,T,\mu)\,, \tag{III.15}$$

$$P(T,\mu) = \frac{g}{(2\pi)^3} \int \mathrm{d}^3\mathbf{p}\, \frac{p^2}{3E(p)} f(p,T,\mu)\,, \tag{III.16}$$

where $E^2 = p^2 + m^2$ and where the factor 3 accounts for isotropy in all three spatial directions.

If we assume particles to be in *kinetic equilibrium*, their phase-space distributions follow Bose-Einstein (BE) or Fermi-Dirac (FD) statistics,

$$f(p,T,\mu) = \left[\exp\left(\frac{E-\mu}{T}\right) + c\right]^{-1}\,, \tag{III.17}$$

where the $c = -1$ holds for bosons, $c = +1$ for fermions, and $c = 0$ is their non-relativistic approximation, namely a Maxwell-Boltzmann distribution.

Neglecting the chemical potentials in the early universe[1], our thermodynamic variables can be rewritten in the relativistic regime ($T \gg m$) as

$$n_{\mathrm{eq}}(T) = \frac{g}{\pi^2} T^3 \times \begin{cases} 3\zeta(3)/4 & c = +1, \\ 1 & c = 0, \\ \zeta(3) & c = -1, \end{cases} \tag{III.18}$$

$$\rho_{\mathrm{eq}}(T) = \frac{g}{\pi^2} T^4 \times \begin{cases} 7\pi^4/240 & c = +1, \\ 3 & c = 0, \\ \pi^4/30 & c = -1, \end{cases} \tag{III.19}$$

where ζ is the Riemann's zeta function and $\zeta(3) \approx 1.2$. In the non-relativistic regime ($T \ll M$), all distribution functions reduce to the Maxwell-Boltzmann one, yielding

$$n(T) = g \left(\frac{mT}{2\pi}\right)^{3/2} e^{-m/T} \tag{III.20}$$

[1]For an explanation, refer to Section 6 of Chapter 15 in Weinberg's book [282]. This can be justified because the Universe is electrically neutral, with the baryon density estimated to be less than a billionth of the photon density and the lepton density also negligible, of similar magnitude as the baryon number. While precise calculations would consider non-zero chemical potentials, such details are beyond the scope of this thesis.

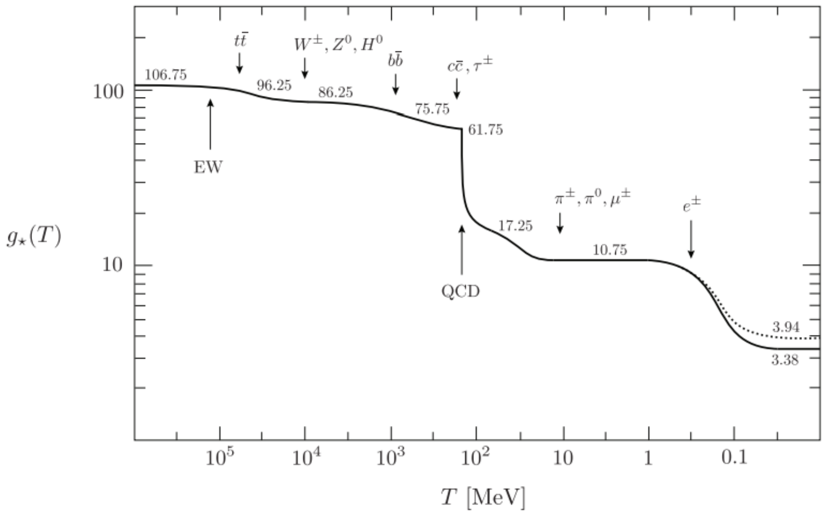

Figure III.1: Evolution of the effective number of relativistic degrees of freedom g_* (solid line) and the effective number of entropy degrees of freedom $g_{*,s}$ (dashed line) as a function of the temperature of the Universe assuming only the particle content of the SM. Notice the QCD phase transition at $T \sim 100\,\text{MeV}$, and the e^+e^- annihilation at $T \sim 1\,\text{MeV}$. Figure from [283].

and

$$\rho(T) = mn(T)\,. \tag{III.21}$$

If some process occurs at thermal equilibrium, then the particles involved share the same temperature. On the contrary, there are cases in which some species i are not in equilibrium with the others and possess their own T_i. In that case, the total energy density of relativistic particles can be written as

$$\rho(T) = \frac{\pi^2}{30} g_*(T) T^4\,, \tag{III.22}$$

where

$$g_*(T) = \sum_{i=BE} g_i \left(\frac{T_i}{T}\right)^4 + \frac{7}{8} \sum_{i=FD} g_i \left(\frac{T_i}{T}\right)^4 \tag{III.23}$$

is the (energy) *effective number of relativistic degrees of freedom*, which takes into account the fact that with the diminishing of T, the contribution of particles that are no longer relativistic disappears. The evolution of $g_*(T)$ assuming only SM particle content is illustrated in Fig. III.1. It runs from 106.75, when all SM particles are relativistic and part of the thermal bath, down to 3.38, the present-day value. Notice the sudden jumps in correspondence of the QCD phase transition $T \sim 100\,\text{MeV}$ and after the decoupling of weak interactions at $T \sim \text{MeV}$. The last ingredient we need for tracking the thermal history is the *entropy of a comoving volume*,

$$S(a,T) = a^3\, \frac{\rho(T) + P(T)}{T}\,, \tag{III.24}$$

which is a conserved quantity in the expanding universe as long as the particle species are in thermal equilibrium. If we consider relativistic particles, $P = \rho/3$, this quantity can be rewritten as

$$S(a,T) = \frac{2\pi^2}{45} g T^3 a^3 \tag{III.25}$$

for a single species. If there were many species with different equilibrium temperatures (a typical situation when describing the early Universe), the total entropy reads

$$S(a,T) = \frac{2\pi^2}{45} g_{*,s}(T)\, T^3 a^3\,, \tag{III.26}$$

where

$$g_{*,s}(T) = \sum_{i=\mathrm{BE}} g_i \left(\frac{T_i}{T}\right)^3 + \frac{7}{8}\sum_{i=\mathrm{FD}} g_i \left(\frac{T_i}{T}\right)^3 \tag{III.27}$$

is the *entropy effective number of relativistic degrees of freedom.* Its evolution in time is depicted with dashed lines in Fig. III.1 tracking the same behavior and values of $g_*(T)$ for $T > 1\mathrm{MeV}$. After neutrino decoupling, electron-positron annihilations re-heat the photon plasma leading to a slight increase in the photon entropy, explaining the deviation from g_* and the final value of $g_{*,s} = 3.94$.

Another very commonly used quantity is the entropy density, namely the entropy per comoving volume, which is

$$s(T) = S(T)/a^3 = \frac{2\pi^2}{45} g_{*,s}(T)\, T^3. \tag{III.28}$$

If we assume that all along the expansion history of the Universe entropy is conserved, then one has $g_{*,s}^{1/3}\, Ta = const$, anytime thermal equilibrium is assured. This also implies the validity of Tolman law [284], namely $T \propto a^{-1}$. Thus, one can write an equation for the evolution of the temperature with cosmic time which reads as follows

$$\mathrm{d}\left(g_{*,s}^{1/3} Ta\right) = 0 \implies \frac{1}{T}\frac{\mathrm{d}T}{\mathrm{d}t} = -H\left(1 + \frac{1}{3}\frac{\mathrm{d}\ln g_{*,s}}{\mathrm{d}\ln T}\right)^{-1}\,, \tag{III.29}$$

or, by employing the conformal time $\tau = \ln(a/a_0)$, as

$$\frac{1}{T}\frac{\mathrm{d}T}{\mathrm{d}\tau} = -\left(1 + \frac{1}{3}\frac{\mathrm{d}\ln g_{*,s}}{\mathrm{d}\ln T}\right)^{-1}\,. \tag{III.30}$$

Note that, in case entropy is *not* conserved, we cannot use Eq. (III.29) to derive a relation between temperature and time/scale-factor. This case will be treated in Section X.3, where we will analyze non-adiabatic cosmic expansions, namely with phases where entropy increases over time. For the standard case of a Universe in a radiation-dominated era and followed by a matter-dominated era, entropy is almost always conserved so that these formulae can be safely used.[2]

III.2 From Liouville to Boltzmann

Let us consider a physical process where particles are created and destroyed. We want to compute the evolution of the total number of one of the species, which is given by the integral of its distribution function $f(\mathbf{x},\mathbf{p},t)$ over the entire phase space,

$$N = \int f(\mathbf{x},\mathbf{p},t)\, \mathrm{d}^3\mathbf{x}\, \mathrm{d}^3\mathbf{p}\,. \tag{III.31}$$

[2]Some exceptions are during the QCD cross-over around $T \sim 100$ MeV and after neutrino decouple and $e^+e^- \to \gamma\gamma$ annihilations reheat the photon plasma around $T \sim 1$ MeV.

Let us also assume that an instantaneous force $\mathbf{F}$ acts on an infinitesimal phase space volume. Exploiting Liouville's theorem [285], which affirms that in the absence of collisions, the phase space distribution is constant, we have [286]

$$f\left(\mathbf{x}+\frac{\mathbf{p}}{m}\Delta t, \mathbf{p}+\mathbf{F}\Delta t, t+\Delta t\right)\,\mathrm{d}^3\mathbf{x}\,\mathrm{d}^3\mathbf{p} = f(\mathbf{x},\mathbf{p},t)\,\mathrm{d}^3\mathbf{x}\,\mathrm{d}^3\mathbf{p}\,. \tag{III.32}$$

Since we are mainly interested in collisional systems, the change in the number of particles in an infinitesimal volume reads

$$\begin{aligned}\mathrm{d}N_{\mathrm{coll}} &= \left\{f\left(\mathbf{x}+\frac{\mathbf{p}}{m}\Delta t, \mathbf{p}+\mathbf{F}\Delta t, t+\Delta t\right) - f(\mathbf{x},\mathbf{p},t)\right\}\,\mathrm{d}^3\mathbf{x}\,\mathrm{d}^3\mathbf{p} \\ &= \left(\frac{\partial f}{\partial t}\right)_{\mathrm{coll}}\mathrm{d}t\,\mathrm{d}^3\mathbf{x}\,\mathrm{d}^3\mathbf{p}. \end{aligned} \tag{III.33}$$

Differentiating this expression with respect to $\mathrm{d}^3\mathbf{x}\,\mathrm{d}^3\mathbf{p}\,\mathrm{d}t$, we obtain

$$\frac{\mathrm{d}N_{\mathrm{coll}}}{\mathrm{d}^3\mathbf{x}\,\mathrm{d}^3\mathbf{p}\,\mathrm{d}t} = \left(\frac{\partial f}{\partial t}\right)_{\mathrm{coll}} = \frac{\mathrm{d}f}{\mathrm{d}t}, \tag{III.34}$$

highlighting how the total derivative of f rules the net change of particles per unit time and unit phase space volume. The total derivative of f reads

$$\begin{aligned}\frac{\mathrm{d}f}{\mathrm{d}t} &= \frac{\partial f}{\partial t} + \nabla_{\mathbf{x}} f\cdot\frac{\mathrm{d}\mathbf{x}}{\mathrm{d}t} + \nabla_{\mathbf{p}} f\cdot\frac{\mathrm{d}\mathbf{p}}{\mathrm{d}t} \\ &= \frac{\partial f}{\partial t} + \frac{\mathbf{p}}{m}\cdot\nabla_{\mathbf{x}} f + \mathbf{F}\cdot\nabla_{\mathbf{p}} f \\ &\overset{!}{=} \left(\frac{\partial f}{\partial t}\right)_{\mathrm{coll}}. \end{aligned} \tag{III.35}$$

This is the *classical Boltzmann equation.* If we introduce the classical Liouville kinetic operator [274],

$$\hat{\mathbb{L}}[\cdot] = \partial_t + \frac{\mathbf{p}}{m}\cdot\nabla_{\mathbf{x}} + \mathbf{F}\cdot\nabla_{\mathbf{p}}\,, \tag{III.36}$$

where $\mathbf{p} = \mathrm{d}\mathbf{v}/\mathrm{d}t$ and $\mathbf{F} = \mathrm{d}\mathbf{p}/\mathrm{d}t$, Eq. (III.35) can be rewritten as

$$\hat{\mathbb{L}}[f] = \hat{\mathbb{C}}[f]\,, \tag{III.37}$$

where $\hat{\mathbb{C}}[f]$ is the collision operator, to be specified case by case, according to which reactions are considered.

The whole argument works well in a flat spacetime. However, in a generic metric, we cannot neglect spacetime curvature and the fact that particle dynamics is governed by the covariant generalization of classical mechanics laws, General Relativity [280]. One can generalize the Liouville operator into a covariant form as [281]

$$\hat{\mathbb{L}}[\cdot] = P^\mu\frac{\partial}{\partial P_\mu} - \Gamma^\mu_{\nu\sigma}P^\nu P^\sigma\frac{\partial}{\partial P_\mu}, \tag{III.38}$$

where P^μ is the particle four-momentum and $\Gamma^\mu_{\nu\sigma}$ a Christoffel symbol [287]. To compute the covariant Liouville operator, we need to specify the spacetime manifold on which the dynamics occur. According to the Cosmological Principle, this is given by the Friedmann-Leamâitre-Robertson-Walker metric tensor which we have reviewed in Section III.1.1.

III.3 Boltzmann Equation in FLRW Cosmology

To compute the Liouville operator, we need the Christoffel symbols in the FLRW metric. Exploiting the homogeneity and isotropy, the distribution function can only depend on energy and time so that $\nabla_{\mathbf{x}} f = 0$. This simplifies the Liouville operator since we only need the following Christoffel symbols

$$\Gamma^0{}_{00} = 0, \qquad \Gamma^0{}_{ij} = \frac{\dot{a}}{a} g_{ij}\,,$$

and the term in Eq. (III.38) is simply

$$\Gamma^0{}_{ij} P^i P^j = \frac{\dot{a}}{a} g_{ij} p^i p^j = \frac{\dot{a}}{a} |\mathbf{p}|^2\,.$$

Hence,

$$\hat{\mathbb{L}}[f] = E\frac{\partial f}{\partial t} - \frac{a}{\dot{a}}|\mathbf{p}|^2 \frac{\partial f}{\partial E}. \tag{III.39}$$

We can easily rearrange the Boltzmann equation, multiplying by the number of internal degrees of freedom g, dividing by the energy E and integrating on the Lorentz-invariant phase space measure (LIPS),

$$d\Pi = \frac{d^3\mathbf{p}}{(2\pi)^3\, 2E}, \tag{III.40}$$

obtaining

$$\frac{g}{(2\pi)^3 E} \int \mathrm{d}^3\mathbf{p}\, \hat{\mathbb{L}}[f] = \frac{g}{(2\pi)^3} \int \frac{\mathrm{d}^3\mathbf{p}}{E}\, \hat{\mathbb{C}}[f]. \tag{III.41}$$

Simplifying the l.h.s of this equation gives

$$\begin{aligned}
\frac{g}{(2\pi)^3 E} \int \mathrm{d}^3\mathbf{p}\, \hat{\mathbb{L}}[f] &= \frac{g}{(2\pi)^3 E} \int d^3\mathbf{p} \left[E\frac{\partial f}{\partial t} - \frac{\dot{a}}{a}|\mathbf{p}|^2 \frac{\partial f}{\partial E}\right] = \\
&= \dot{n} - \frac{\dot{a}}{a}\frac{g}{2\pi^2} \int_0^\infty \mathrm{d}p\, p^4 \frac{\partial f}{\partial E} = \dot{n} - \frac{\dot{a}}{a}\frac{g}{2\pi^2} \int_0^\infty \mathrm{d}p\, p^3 \frac{\partial f}{\partial p} = \\
&= \dot{n} - \frac{\dot{a}}{a}\frac{g}{2\pi^2} \left[f p^3 |_0^\infty - 3\int_0^\infty \mathrm{d}p\, p^2 f \right] = \\
&= \dot{n} + 3\frac{\dot{a}}{a} n.
\end{aligned} \tag{III.42}$$

In the second step, we used the definition of *number density*, given by the integral of the distribution function over the phase space, which reads from Eq. (III.14) with $\mu = 0$ as

$$n(t) = \frac{g}{(2\pi)^3} \int \mathrm{d}^3\mathbf{p}\, f(E,t)\,. \tag{III.43}$$

In the third step, we used the fact that thanks to $E^2 = p^2 + m^2$, we have $\frac{1}{E}\frac{\partial}{\partial E} = \frac{1}{p}\frac{\partial}{\partial p}$, in the fourth we integrated by parts and in the last one we used the assumption that at the boundary we do expect the distribution function to vanish very rapidly.

To summarize, our final Boltzmann equation is

$$\dot{n}(t) + 3Hn(t) = \frac{g}{(2\pi)^3} \int \frac{\mathrm{d}^3\mathbf{p}}{E}\, \hat{\mathbb{C}}[f] \equiv \sum_\alpha \gamma_\alpha\,, \tag{III.44}$$

where the last term is the sum of all decays, scattering, and annihilation processes that contribute to the reduction or the increase of the number density. We call γ_α the DM **interaction rate density** of the process α. Notice also the behavior of a non-collisional system, i.e., one where $\hat{\mathbb{C}}[f] = 0$. In this case, the number density scales as $n(t) \propto a(t)^{-3}$, meaning that the number of particles in a comoving volume is conserved.

III.3.1 Comoving Yield and Relic Abundance

It is common practice to absorb the dependence on the expanding Universe by using comoving variables. To this aim, we introduce the *comoving number density* $Y = n/s$, with $s = 2\pi^2/45\, g_{*,s} T^3$ the entropy density (cf. Eq. (III.28)) and the time variable $z = m_\chi/T$, trading the time coordinate for the inverse temperature (a growing quantity as the Universe cools down while expanding). One can also choose a mass scale different than m_χ in the definition of z, depending on the relevant mass scale one is interested in. For instance, if decays are the dominant DM production process, it is useful to employ the mass of the decaying particle. The transformed Boltzmann equation is given by

$$zHs\frac{\mathrm{d}Y_\chi}{dz} = \gamma_\chi \,. \tag{III.45}$$

After solving for Y_χ, one can find the DM relic abundance at the present date from the density parameter (cf. Eq. (III.12)) as follows:

$$\Omega_{\mathrm{DM}} h^2 = \frac{\rho_{\mathrm{DM}}}{\rho_c/h^2} = \frac{s_0}{\rho_c/h^2} m_{\mathrm{DM}} Y_{\mathrm{DM}}^\infty = 0.12 \left(\frac{m_{\mathrm{DM}}}{\mathrm{TeV}}\right) \left(\frac{Y_{\mathrm{DM}}^\infty}{10^{-12}}\right) , \tag{III.46}$$

where $\rho_c \simeq 10^{-5} h^2\,\mathrm{GeV\,cm^{-3}}$ is the critical density of the Universe, $s_0 \simeq 2891\,\mathrm{cm^{-3}}$ the entropy density today, $h = H_0/(100\,\mathrm{km\,s^{-1}\,Mpc^{-1}})$ with H_0 the Hubble parameter today [105], and $Y_{\mathrm{DM}}^\infty = Y_{\mathrm{DM}}(z = \infty)$ the comoving DM yield today. Here, we used the fact that DM is a non-relativistic fluid and hence its energy density scales as

$$\rho_{\mathrm{DM}} = n_{DM} m_{\mathrm{DM}} = s\, Y_{\mathrm{DM}}\, m_{\mathrm{DM}} \,.$$

Due to the Hubble tension (cf. Section II.1.5), it is preferable to express observables independently of the value of the Hubble constant today, hence the use of $h \approx 0.7$ above.

III.4 Collision Operators

We want to understand how to actually calculate the Boltzmann equation. To do this, we need to specify the form of the collision operators on the r.h.s of Eq. (III.44) (or equivalently of Eq. (III.45)). These encapsulate the information regarding the interactions that create and deplete the DM particles and, thus, their number density.

Consider a theory involving Standard Model (SM) particles $B_1, B_2, \ldots$ in thermal equilibrium, alongside a dark sector containing an inert DM state χ and a mediator particle X that interacts with both the visible and dark sectors. This setup is exemplified by simplified t-channel models discussed in Section II.2.4, which are central to this thesis. DM can annihilate or be produced through processes such as mediator decays and inverse decays, for instance, $X \leftrightarrow \chi + B_1$, as well as through pair and single annihilation processes like $\chi + \chi \leftrightarrow B_1 + B_1$, $\chi + X \leftrightarrow B_1 + B_2$, and others.

For three-body decays such as $1 \to \chi + 2$, the interaction density is given by:

$$\begin{aligned}\gamma_{1\leftrightarrow\chi+2} = &\int \mathrm{d}\Pi_1\, \mathrm{d}\Pi_2\, \mathrm{d}\Pi_\chi\, (2\pi)^4\, \delta^{(4)}(p_1 - p_\chi - p_2)\\ &\times \{|\mathcal{M}_{\chi+2\to 1}|^2\, f_\chi f_2[1\pm f_1] - |\mathcal{M}_{1\to\chi+2}|^2\, f_1[1\pm f_\chi][1\pm f_2]\}\\ &= \int \mathrm{d}\Pi_1\, \mathrm{d}\Pi_2\, \mathrm{d}\Pi_\chi\, (2\pi)^4\, \delta^{(4)}(p_1 - p_\chi - p_2)\\ &\times |\mathcal{M}_{1\to\chi+2}|^2 \{f_\chi f_2[1\pm f_1] - f_1[1\pm f_\chi][1\pm f_2]\}\ ,\end{aligned} \tag{III.47}$$

where the probability of a process to happen, encoded in the matrix elements $\mathcal{M}$ summed over the initial and final polarization states, is integrated over all the phase space configurations $\mathrm{d}\Pi_j$ (cf. Eq. (III.40)) the jth species can assume, weighted by their statistical distribution functions f_j and in such a way that momentum is conserved, which is guaranteed by the Dirac delta function.[3]

In the second step, we also assumed that the decay processes are CP-conserving so that, using the CPT theorem, the matrix elements of the direct and inverse reactions are the same, namely $|\mathcal{M}_{1\to\chi+2}|^2 = |\mathcal{M}_{2+\chi\to 1}|^2$. The first addend in the parentheses accounts for the *depletion* of DM particles via inverse decays, whereas the second term represents the *creation* of DM via decays. The $-$ $(+)$ indicates the presence of a Pauli blocking (Bose enhancement) effect in the final states according to the quantum statistics the involved particles obey. In the early Universe, the typical energies are high enough to let us omit these quantum contributions.

Following the same logic, for a 2-to-2 process of the type $1+2\leftrightarrow 3+4$, the interaction density is given by

$$\begin{aligned}\gamma_{1+2\leftrightarrow 3+4} = &\int \mathrm{d}\Pi_1\, \mathrm{d}\Pi_2\, \mathrm{d}\Pi_3\, \mathrm{d}\Pi_4\, (2\pi)^4\, \delta^{(4)}(p_1 + p_2 - p_3 - p_4)\\ &\times \left\{|\mathcal{M}_{3+4\to 1+2}|^2\, f_3 f_4[1\pm f_1][1\pm f_2] - |\mathcal{M}_{1+2\to 3+4}|^2\, f_1 f_2[1\pm f_3][1\pm f_4]\right\}\\ = &\int \mathrm{d}\Pi_1\, \mathrm{d}\Pi_2\, \mathrm{d}\Pi_3\, \mathrm{d}\Pi_4\, (2\pi)^4\, \delta^{(4)}(p_1 + p_2 - p_3 - p_4)\\ &\times |\mathcal{M}|^2\, \{f_3 f_4[1\pm f_1][1\pm f_2] - f_1 f_2[1\pm f_3][1\pm f_4]\}\ ,\end{aligned} \tag{III.48}$$

where we considered again the case for CP-conserving matrix elements. The Boltzmann equation for the DM number density n_χ follows from summing all the collision terms of the types in Eqs. (III.47) and (III.48) allowed by the theory. For instance, by considering $1\leftrightarrow 2$ and $2\leftrightarrow 2$ processes, usually the dominant ones if allowed by symmetries and kinematics, we obtain

$$\dot{n}_\chi + 3Hn_\chi = \sum_{ij} \gamma_{i\leftrightarrow\chi+j} + \sum_{ijk} \gamma_{i+j\leftrightarrow\chi+k}\ , \tag{III.49}$$

Notice that the scattering term automatically includes single and pair annihilations.

Suppose now that the system is in kinetic equilibrium so that we can assume that all particles have equilibrium distribution functions. If we approximate them with Maxwell-Boltzmann statistics, we obtain for the ith species

$$f_i = \frac{1}{e^{(E_i-\mu_i)/T}\pm 1} \approx e^{-(E_i-\mu_i)/T}\ ,$$

[3]One may wonder why we are integrating only over three-momenta and not over energies. Technically, we would have $\int d^3\mathbf{p}\, dE$, but since $E^2 = \mathbf{p}^2 + m^2$, we are forced to insert a Dirac delta, $\int d^3\mathbf{p}\, dE\, \delta(E^2 - \mathbf{p}^2 - m^2)$. Using the property $\delta(f(x)) = \sum_i \delta(x-x_i)/|f'(x_i)|$, with $f(x_i)=0$, we end up with $\int d^3\mathbf{p} \int_0^\infty dE\, \delta(E - \sqrt{\mathbf{p}^2 - m^2})/2E = \int d^3\mathbf{p}/2E\,|_{E=\sqrt{\mathbf{p}^2+m^2}}$.

$$\Downarrow$$
$$1 \pm f_i \approx 1\,.$$

Substituting these approximations into Eqs. (III.47) and (III.48) and using energy conservation, Eq. (III.49) becomes

$$\begin{aligned}
\dot{n}_\chi + 3Hn_\chi = &-\sum_{ij} \int d\Pi_\chi\, d\Pi_i\, d\Pi_j\, (2\pi)^4\, \delta^{(4)}(p_i - p_\chi - p_j) \\
&\qquad \times |\mathcal{M}_{i\to\chi+j}|^2\, e^{-\frac{E_i}{T}} \left(e^{\frac{\mu_\chi+\mu_j}{T}} - e^{\frac{\mu_i}{T}}\right) \\
&-\sum_{ijk} \int d\Pi_\chi\, d\Pi_i\, d\Pi_j\, d\Pi_k\, (2\pi)^4\, \delta^{(4)}(p_i + p_j - p_\chi - p_k) \\
&\qquad \times |\mathcal{M}_{i+j\to\chi+k}|^2\, e^{-\frac{E_i+E_j}{T}} \left(e^{\frac{\mu_\chi+\mu_k}{T}} - e^{\frac{\mu_i+\mu_j}{T}}\right).
\end{aligned}$$

Defining the *equilibrium* number density as

$$n_i^{\text{eq}}(t) = \frac{g_i}{(2\pi)^3} \int d^3\mathbf{p_i}\, e^{-E_i/T}, \tag{III.50}$$

with g_i the number of internal degrees of freedom of the ith species, we have $f_i \simeq f_i^{\text{eq}}\, e^{\mu_i/T} = e^{-E_i/T} n_i/n_i^{\text{eq}}$ so that the Boltzmann equation becomes

$$\begin{aligned}
\dot{n}_\chi + 3Hn_\chi = &-\sum_{ij} \int d\Pi_\chi\, d\Pi_i\, d\Pi_j\, (2\pi)^4\, \delta^{(4)}(p_i - p_\chi - p_j) \\
&\qquad \times |\mathcal{M}_{i\to\chi+j}|^2\, e^{-\frac{E_i}{T}} \left(\frac{n_\chi n_j}{n_\chi^{\text{eq}} n_j^{\text{eq}}} - \frac{n_i}{n_i^{\text{eq}}}\right) \\
&-\sum_{ijk} \int d\Pi_1\, d\Pi_i\, d\Pi_j\, d\Pi_k\, (2\pi)^4\, \delta^{(4)}(p_1 + p_i - p_j - p_k) \\
&\qquad \times |\mathcal{M}_{i+j\to\chi+k}|^2\, e^{-\frac{E_i+E_j}{T}} \left(\frac{n_\chi n_k}{n_\chi^{\text{eq}} n_k^{\text{eq}}} - \frac{n_i n_j}{n_i^{\text{eq}} n_j^{\text{eq}}}\right).
\end{aligned} \tag{III.51}$$

III.4.1 Interaction Rates

We now introduce the *thermally averaged decay rate* as

$$\langle \Gamma_{ij} \rangle = \frac{1}{n_i^{\text{eq}}} \int \mathrm{d}\Pi_\chi\, \mathrm{d}\Pi_i\, \mathrm{d}\Pi_j\, (2\pi)^4 \delta^{(4)}(p_i - p_\chi - p_j) |\mathcal{M}|^2\, e^{-\frac{E_i}{T}}\,, \tag{III.52}$$

and the *thermally averaged cross section* (times the relative velocity),

$$\langle \sigma v_{ijk} \rangle = \frac{1}{n_i^{\text{eq}}} \frac{1}{n_j^{\text{eq}}} \int \mathrm{d}\Pi_\chi\, \mathrm{d}\Pi_i\, \mathrm{d}\Pi_j\, \mathrm{d}\Pi_k\, (2\pi)^4 \delta^{(4)}(p_i + p_j - p_\chi - p_k) |\mathcal{M}|^2\, e^{-\frac{E_i+E_j}{T}}\,, \tag{III.53}$$

by weighting the average over the equilibrium number densities of the initial state particles. Substituting Eqs. (III.52) and (III.53) into Eq. (III.51), we obtain

$$\dot{n}_\chi + 3Hn_\chi = -\sum_{ij} n_i^{\text{eq}} \langle \Gamma_{ij} \rangle \left[\frac{n_\chi n_j}{n_\chi^{\text{eq}} n_j^{\text{eq}}} - \frac{n_i}{n_i^{\text{eq}}}\right] - \sum_{ijk} n_i^{\text{eq}} n_j^{\text{eq}} \langle \sigma v_{ijk} \rangle \left[\frac{n_\chi n_k}{n_\chi^{\text{eq}} n_k^{\text{eq}}} - \frac{n_i n_j}{n_i^{\text{eq}} n_j^{\text{eq}}}\right]. \tag{III.54}$$

More generically, one can write the Boltzmann equation as

$$\dot{n}_\chi + 3Hn_\chi = \sum_{\text{processes}} \gamma_\chi^{\text{eq}}\left(\mathcal{I} \to \mathcal{F}\right) \left(\prod_{i\in\mathcal{I}} \frac{n_i}{n_i^{\text{eq}}} - \prod_{f\in\mathcal{F}} \frac{n_f}{n_f^{\text{eq}}} \right) \equiv \gamma_\chi \,, \tag{III.55}$$

with $\mathcal{I} \to \mathcal{F}$ describes a process with an initial state $\mathcal{I}$ and a final state $\mathcal{F}$ that contains at least one DM particle and with

$$\gamma_\chi^{\text{eq}}\left(\mathcal{I} \to \mathcal{F}\right) = \int \left(\prod_{i\in\mathcal{F}\cup\mathcal{I}} \frac{d^3\vec{p}_i}{(2\pi)^3\, E_i} \right) \left|\mathcal{M}\left(\mathcal{I} \to F\right)\right|^2 (2\pi)^4 \delta \left(\sum_{i\in\mathcal{I}} p_i - \sum_{j\in\mathcal{F}} p_j \right) \prod_{i\in\mathcal{I}} f_i^{\text{eq}} \,. \tag{III.56}$$

Notice that, in this definition, γ^{eq} absorbs the equilibrium number density factors appearing in front of the sum signs in Eq. (III.54). Explicitly, for decay processes of the type $i \to \chi + j$, the interaction rate density is given by

$$\left(\gamma_{ij}\right)_{\text{dec}} = \frac{y_{\text{DM}}^2 m_i}{16\pi^3} \left(1 + \frac{m_j^2}{m_i^2} - \frac{m_\chi^2}{m_i^2} \right) \sqrt{\lambda\left(m_i^2, m_j^2, m_\chi^2\right)}\; T\, K_1(m_i/T) \,, \tag{III.57}$$

where y_{DM} is the coupling between DM and particles i and j, with masses m_χ, m_i, and m_j, respectively, and where

$$\lambda(a, b, c) = a^2 + b^2 + c^2 - 4bc \tag{III.58}$$

is the Källen triangular function [288], while K_1 a modified Bessel function of the second kind [289].

Similarly, the interaction rate density for scattering processes $i + j \to \chi + k$ can be expressed as

$$\gamma_{ijk} = \frac{T}{64\pi^4} \int_{s_{\max}}^{\infty} \mathrm{d}s\, \hat{\sigma}_{ijk}(s)\, \sqrt{s}\, K_1(\sqrt{s}/T) \,, \tag{III.59}$$

with $s_{\max} = \max\{(m_i + m_j)^2, (m_\chi + m_k)^2\}$ the minimum center-of-mass energy by kinematic constraints. Here, $\hat{\sigma}_{ijk}(s)$ is the reduced cross-section for the considered scattering process, defined as

$$\hat{\sigma}_{ijk}(s) = 2s\, \lambda \left(1, \frac{m_i^2}{s}, \frac{m_j^2}{s} \right) \sigma_{ijk}(s) \,, \tag{III.60}$$

with $\sigma_{ijk}(s)$ being the cross-section of the scattering process.

Now that we have the fundamental ingredients to calculate the DM rate equation and the evolution of its number density, what remains to do is to specify the conditions under which this dynamics takes place, for instance, by setting the initial conditions and by specifying the **mechanism** of DM production.

III.5 Production Mechanisms

Two of the most studied production mechanisms are the **freeze-out** and the **freeze-in** of the DM number density. In the first, DM is in equilibrium with the thermal radiation bath of SM particles, and its relic abundance is determined by the moment the Universe has sufficiently expanded that it becomes increasingly difficult for two DM particles to find each other and annihilate away, effectively shutting off their interactions. Oppositely, the freeze-in mechanism features DM particles which only have a very feeble coupling to the SM bath. Their initial abundance is negligible and their number density increases from zero thanks to decay and scattering processes that have DM in the final state and some other particles in the radiation bath as initial states. As soon as these "parent" particles are torn apart by the expanded Universe, their interactions are no longer efficient to further produce DM particles, and, therefore, a relic abundance of DM is set. As will become clear soon, the differences and complementarities of these two mechanisms are imprinted in how the Boltzmann equation is solved and how the yield depends on the microphysics of the particular DM model considered.

III.5.1 Freeze-out

Let us assume that the DM particles χ annihilate into lighter states ℓ as $\chi+\overline{\chi} \leftrightarrow \ell+\bar{\ell}$, where the bar indicates antiparticles (if some charge is involved such as the case for WIMPs, cf. Section II.2). Light states are tightly coupled to the thermal bath, maintaining their equilibrium densities, implying $n_\ell = n_\ell^{\rm eq}$. We also assume that the dark sector features no CP-violating interactions and that, initially, the same amount of χ and $\bar{\chi}$ populated the Universe, $n_\chi = n_{\overline{\chi}}$. From energy conservation implying $E_\chi + E_{\overline{\chi}} = E_\ell + E_{\bar{\ell}}$, we can write $n_\ell n_{\bar{\ell}} = n_\chi^{\rm eq} n_{\overline{\chi}}^{\rm eq} = (n_\chi^{\rm eq})^2$.

Thus, the Boltzmann equation in Eq. (III.54) reduces to

$$\dot{n}_\chi + 3Hn_\chi = -\langle\sigma v\rangle \left[n_\chi^2 - (n_\chi^{\rm eq})^2\right] . \tag{III.61}$$

We now transform this equation by using comoving variables (cf. Eq. (III.45)) and by assuming a radiation-dominated Universe, for which the Hubble rate reads from Eq. (III.2) and Eq. (III.22) as

$$H = \frac{\pi}{3\sqrt{10}} g_*^{1/2} \frac{T^2}{M_{\rm Pl}} . \tag{III.62}$$

The Boltzmann equation for the DM comoving yield with $z = m_\chi/T$ reads

$$\frac{{\rm d}Y_\chi}{{\rm d}z} = -c\, g_{*,{\rm eff}}^{1/2} \frac{\langle\sigma v\rangle}{z^2} \left[Y_\chi^2 - (Y_\chi^{\rm eq})^2\right] , \tag{III.63}$$

where

$$c = \sqrt{\pi/45}\, M_{\rm Pl}\, m_\chi , \tag{III.64}$$

$$g_{*,{\rm eff}}^{1/2} = \frac{g_{*,s}}{\sqrt{g_*}} \left(1 - \frac{z}{3g_{*,s}} \frac{{\rm d}g_{*,s}}{{\rm d}z}\right) \simeq \frac{g_{*,s}}{\sqrt{g_*}} . \tag{III.65}$$

Notice that the derivative appearing in the second line and coming from Eq. (III.30) is totally irrelevant for our purposes since in this work we will focus on epochs in the early Universe where the relativistic degrees of freedom can only mildly change. Moreover, the variation in the derivative is logarithmic and therefore negligible.

Since DM is a cold relic, its evolution can be described in terms of non-relativistic dynamics. In particular, its cross-section is expected to have some proportionality to the relative velocity between interacting particles: $\sigma v \propto v^n$, with $n \geq 0$. Also, since from kinetic theory arguments, one has $\langle v\rangle \sim T^{1/2}$, we can parameterize the cross section times the relative velocity as [290]

$$\langle\sigma v\rangle = \sigma_0 (T/m_\chi)^n = \sigma_0 z^{-n} , \tag{III.66}$$

where σ_0 is a constant and m_χ has been introduced for dimensional reasons. Here, $n = 0$ represents the case of s-wave cross sections, $n = 1$ for p-wave cross sections, etc. The reason behind this naming is found when expanding the interaction amplitude in terms of partial-waves such as Bessel functions and Legendre polynomials which provide the matching between powers of momentum (or velocity) and values of the total orbital angular momentum. More about partial-wave expansions will be discussed in Section IV.2. This parameterization is of particular help when multiple partial-wave contributions are involved. For example, both an s-wave and a p-wave term contribute to annihilations, we could write $\sigma_{tot} = \sigma_s + \sigma_p z^{-1}$.

Let us follow [274] and focus on the simple single partial-wave situation. The Boltzmann equation becomes

$$\frac{dY_\chi}{dz} = -\frac{\lambda}{z^{n+2}}\left[Y_\chi^2 - (Y_\chi^{\mathrm{eq}})^2\right] , \tag{III.67}$$

with $\lambda = \sigma_0 s(z = 1)/H(z = 1) \simeq 0.2 M_{\mathrm{Pl}}\, m_\chi (g_{*,s}/g_*^{1/2})\, \sigma_0$. At very high temperatures before freeze-out ($z \lesssim z_{f.o.}$), the comoving number density follows its equilibrium value, $Y_\chi \simeq Y_\chi^{\mathrm{eq}} \simeq 1$, while at lower temperatures and after freeze-out ($z \gtrsim z_{f.o.}$) the equilibrium abundance is exponentially suppressed, $Y_X^{eq} \sim e^{-x}$, and can be neglected. Thus, we can approximate Eq. (III.67) with

$$\frac{dY_\chi}{dz} \simeq -\frac{\lambda}{z^{n+2}} Y_\chi^2 \,.$$

Solving this differential equation with a separation of variables yields

$$Y_\chi^\infty \simeq \frac{n+1}{\lambda} z_{f.o.}^{n+1} \simeq \frac{3.79(n+1) z_{f.o.}^{n+1}}{(g_{*,s}/g_*^{1/2}) M_{\mathrm{Pl}} m_\chi \sigma_0} \,, \tag{III.68}$$

from which we see that the relic density strongly depends on the freeze-out temperature, the mass of the frozen-out particle, the type of non-relativistic scattering, and especially the cross section σ_0. Numerical results show that the exact moment (or temperature) at which freeze-out occurs is not very sensitive to the precise microphysics involved. In fact, one finds $z_{f.o} \sim \ln\lambda \sim \ln(M_P m_\chi \sigma_0)$, and typical values lie around $z_{f.o.} \simeq 20 - 30$.

III.5.2 Freeze-in

Let us now assume that the DM particles χ are not in thermal equilibrium with the SM bath with which they do not share any coupling. Instead, they only interact with a parent particle X which is itself in thermal contact with SM particles, which we collectively call B (for "bath" particles). The initial χ abundance is zero and the DM coupling is assumed to be very small. Thus, assuming a Z_2 or similar stabilizing symmetry shared in the dark sector, the only way DM can be produced is by direct decays $X \to \chi B$ or single and pair annihilations like $X\, B_1 \to \chi B_2$ and $X\, X \to \chi\chi$ of parent particles into DM states. Backward reactions are suppressed until a sufficient number of DM particles are created. If the production reactions keep being efficient to the point that DM reaches equilibrium, backreactions switch on and we end up in the freeze-out case. Otherwise, as soon as DM production stops, no other process can further create or deplete the χ number density, which remains frozen, only redshifting with the expansion of the Universe.

For simplicity, let us assume that the parent particle decay is the dominant process and that $m_X \gg m_\chi$ and $m_B = 0$. We can write the Boltzmann equation for the DM comoving yield Y_χ as a function of the time variable $z = m_X/T$, where we choose the mass of the

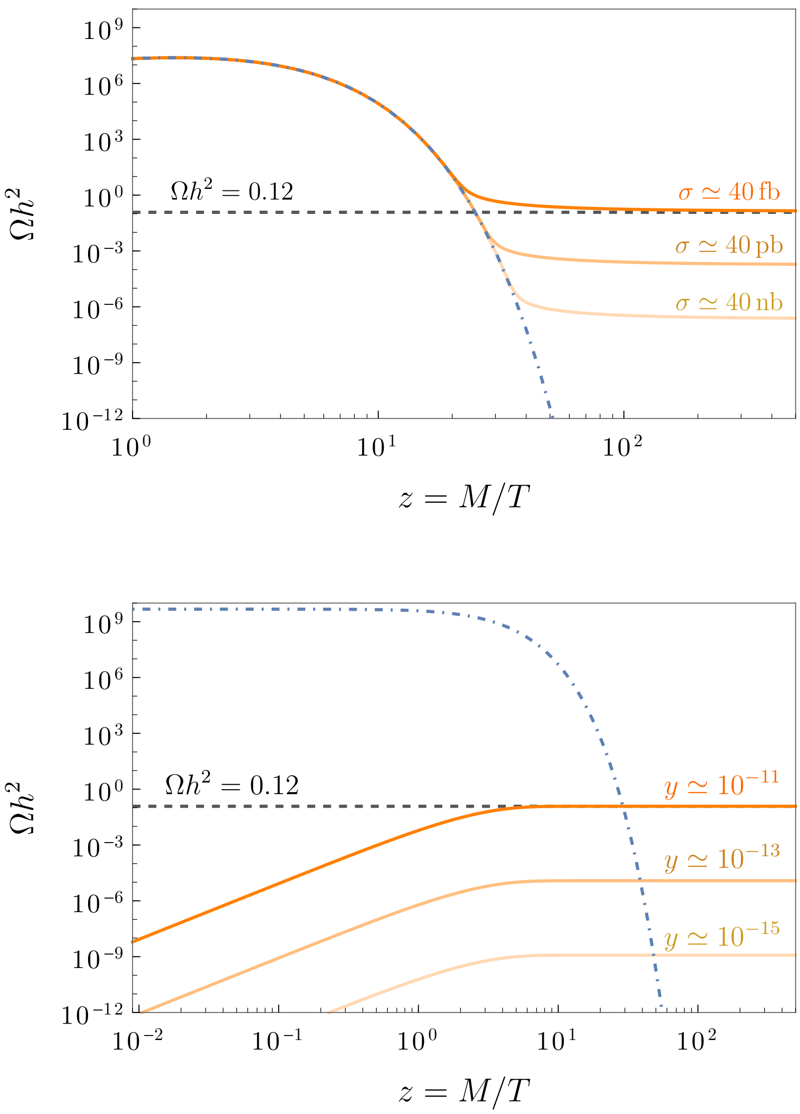

Figure III.2: The evolution of the relic density as a function of the time variable $z = M/T$ for a 1 TeV DM candidate. *Upper panel:* Thermal freeze-out. The larger the DM annihilation cross-section, the smaller the final yield. *Lower panel:* Freeze-in. The higher the DM coupling the stronger the decay rate (of a much heavier parent particle) and the larger the relic abundance. The dashed gray line marks the observed DM abundance [75]. The dot-dashed blue line indicates the equilibrium abundance of DM particles with its characteristic Boltzmann suppression.

parent particle as our reference scale:

$$\begin{aligned} zsH\frac{\mathrm{d}Y_\chi}{\mathrm{d}z} &\simeq \gamma_{X\to\chi B} = 2g_X \int \mathrm{d}\Pi_X\, \Gamma_X m_X f_X^{\mathrm{eq}} \\ &= \frac{g_X}{2\pi^2}\frac{m_X^2\Gamma_X}{z}K_1(z)\,, \end{aligned} \tag{III.69}$$

where we have neglected the inverse reaction (inverse decays in this case) and where Γ_X is the decay width of the parent particle. Performing algebraic manipulation and integrating over z, one obtains [291]

$$Y_\chi(z) \simeq \frac{45}{0.334\pi^4}\frac{g_X M_{\mathrm{Pl}}\Gamma_X}{m_X^2 g_{\star s}\sqrt{g_\star}} \int_{z_{\min}}^{z} \mathrm{d}z'\, K_1(z')\,(z')^3\,, \tag{III.70}$$

where the integration extremes have to be specified. The integrand is an increasing function of time until roughly $z \simeq 1$ after which the Bessel function picks up an exponential suppression, signaling the Boltzmann tail of the (non-relativistic) parent particle distribution function. Therefore, the yield increases until $z \simeq 1$, after which it freezes to a constant value. The exact point in time is called the *freeze-in temperature* and, numerically, it is usually found to lie between $z = z_{\rm fi} \simeq 2 - 5$. This behavior is shown in Fig. III.2.

If we want to obtain the yield *today*, Y_χ^0, we evaluate the function at the present temperature, namely, we set the upper integration boundary to $z = m_X/T_0 \simeq \infty$, which in practice is a very good approximation given that after $z_{\rm fi}$ the comoving yield does not change (in this vanilla scenario). The lower bound corresponds to the maximum temperature (equivalently, the earliest time) in which DM production is considered. Given the sensitivity of freeze-in to initial conditions, it is important to correctly assess in which temperature interval DM is produced. We will discuss at length this issue in the final chapter of this thesis (cf. Chapter X). Here, we can perform the approximation in which the bulk of the production happens well inside Radiation Domination, where the Universe evolves adiabatically, $H \sim T^2$, and nothing exotic happens. In this case, we can assume the maximum temperature to be the reheating temperature after inflation, which given our assumptions, is much larger than the freeze-in temperature (i.e., the parent particle mass) and can be considered infinitely large. Thus, $z_{\rm min} \simeq 0$, and the integral can be solved analytically, yielding

$$Y_\chi^0 \simeq \frac{135 g_X}{8\pi^3\, 0.33\, g_{\star s}\sqrt{g_\star}} \left(\frac{M_{\rm Pl}\,\Gamma_X}{m_X^2}\right) , \tag{III.71}$$

where the number of energy and entropy relativistic degrees of freedom are evaluated at the freeze-in temperature. Assuming $\Gamma_X \sim y_{\rm DM}^2 m_X/(8\pi)$, one recovers the correct DM relic abundance whenever

$$\Omega_{\rm DM} h^2 \simeq 0.12 \left(\frac{y}{2\cdot 10^{-12}}\right)^2 \frac{m_\chi}{m_X} . \tag{III.72}$$

We see that the required DM couplings have to be extremely small, in conformity with our initial assumptions. We will come back to the freeze-in mechanism in the second part of this thesis, where we will dive deep into two key aspects affecting how particles interact in the primordial plasma: incorporating in-medium effects from statistical field theory, cf. Chapters VI and VII, and non-standard expansions the Universe might have undergone in the earliest epochs (cf. Chapter X).

III.5.3 Other Mechanisms

There are many other production mechanisms explored in the literature besides freeze-out and freeze-in, each of which originated from different motivations, such as satisfying certain experimental constraints, giving rise to new phenomenology and potential signatures, and pairing with specific models of DM or cosmology. Three famous exceptions to freeze-out were for instance formulated in 1990 by Ref. [292], regarding *resonantly-enhanced* DM production due to s-channel annihilations, *threshold* effects responsible for the production of *forbidden DM* particles, namely when DM annihilates into heavier states, and *co-annihilations*, which occur when DM is close in mass with other dark sector particles. The latter case will be extensively discussed in the following chapters.

Another "exception" occurs when the interconversion rate between dark sector particles is suppressed. This occurs when processes such as $\chi + \ldots \leftrightarrow X + \ldots$, χ being the

DM, and X a dark sector particle, which keeps the dark sector in chemical equilibrium, are proportional to small couplings. In this case, dubbed **conversion-driven freeze-out** [293] (CDFO) or **co-scattering** [294], the DM abundance is not set by dark sector particle annihilations, but is *driven* by the freezing-out of the interconversion processes. Such a mechanism lies between the freeze-out and the freeze-in regimes.

For couplings even tinier than those typical of freeze-in, heavy parent particles in thermal equilibrium could be so long-lived that they could undergo freeze-out before they have time to decay into DM particles. Eventually, they decay into DM, and their abundance is entirely converted into the DM relic abundance. This mechanism is called **superWIMP** [148, 295].

One could drop the assumption that DM was always in kinetic equilibrium, which is typically the case since elastic processes of the type $\chi + \ldots \leftrightarrow \chi + \ldots$ are very efficient if relativistic particles are involved in '. . . ' (they are not Boltzmann-suppressed). However, at some point after chemical decoupling, DM particles go out of kinetic equilibrium with consequences on their matter spectrum at small scales [296]. Note, however, that kinetic decoupling can also occur much earlier and interfere with chemical decoupling and the freeze-out process, as pointed out in [297].

Other possibilities involve self-interacting DM (**SIDM**) [298, 299], invoked to explain features of structures at small scales and of cluster collisions (cf. Sections II.1.2 and II.1.3); strongly-interacting massive particles (**SIMPs**), which can interact with couplings of the order of the QCD strong interaction and yield the correct relic abundance via $3 \to 2$ processes [300]; ELastically DEcoupling Relics (**ELDERs**) are in kinetic equilibrium with themselves and in chemical equilibrium with the SM plasma. After kinetic decoupling, the "cannibalization" phase driven by $3 \to 2$ processes occurs, eventually freezing the remaining DM comoving number density [301]; DM can also undergo processes of the type $\chi_i\chi_j \to \chi_k + \ldots$ when part of a dark sector including several dark components χ. These **semi-annihilations** can account for the correct abundance [302]. DM could be produced non-thermally and not be self-conjugate due to some asymmetry in the dark sector. Mechanisms addressing this possibility go under the name of asymmetric DM (**ADM**) [303–305]. Thermal **squeeze-out**, as discussed in [306], explores confinement phase transitions within dark sectors characterized by non-Abelian dark gauge groups (such as dark QCD), highlighting how contracting pockets in the deconfined phase enhance dark matter annihilation rates until the phase transition halts, thereby establishing a relic abundance.

Many more possibilities have been proposed in recent years that are not listed here.

III.6 Scope and Limitations of the Standard Particle-production Framework

The freeze-out and freeze-in paradigms reviewed in this chapter constitute the standard theoretical framework for describing the cosmological production of dark matter. Despite their conceptual differences, both mechanisms rely on a common set of theoretical ingredients: a Boltzmann equation governing the evolution of number densities, interaction rates computed from microscopic particle physics, and a background cosmology fixing the expansion history of the Universe. Together, these elements provide a remarkably efficient bridge between fundamental model parameters and observable phenomenology, which largely explains their widespread adoption in the literature.

At the same time, this efficiency rests on a number of assumptions that are rarely questioned once the framework is in place. First, the collision terms entering the Boltzmann equation are typically constructed from short-distance, point-like interactions, implicitly assuming that non-perturbative or long-range effects are either absent or negligible. Second, interaction rates are usually obtained from in-vacuum quantum field theory amplitudes and only subsequently embedded into a thermal environment through a manual thermal averaging procedure. Third, the dilution term in the Boltzmann equation is almost universally fixed by the standard ΛCDM expansion history, assuming radiation domination throughout the relevant epochs of dark matter production.

While these assumptions are internally consistent and often well justified, they are not guaranteed to hold across the full range of particle models and cosmological histories currently under consideration. Crucially, departures from any one of them can modify the relation between particle properties, cosmological evolution, and the predicted relic abundance, thereby reshaping the phenomenological interpretation of experimental constraints. This is particularly relevant in regimes where dark matter production is sensitive to threshold effects, collective phenomena in the thermal bath, or non-standard expansion histories.

The remainder of this thesis is devoted to a systematic examination of these underlying assumptions and to the development of more refined theoretical tools where they break down. In the first part of this thesis (Part I), we examine the impact of long-range interactions in thermal dark matter scenarios (WIMPs), where non-perturbative effects such as Sommerfeld enhancement and bound-state formation require a modification of the standard freeze-out treatment (Chapters IV and V). The second part (Part II) focuses on feebly interacting dark matter (FIMPs) and addresses the limitations of semi-classical rate calculations by deriving the evolution of the dark matter abundance from non-equilibrium thermal quantum field theory (Chapters VI to IX). Finally, we explore how departures from the standard radiation-dominated expansion history alter freeze-in production and its phenomenological implications (Chapter X).

With this perspective, the discussion of freeze-out and freeze-in presented in this chapter should be viewed not as an endpoint, but as a reference framework. It establishes the baseline against which the subsequent chapters quantify, in concrete and phenomenologically relevant settings, how refined treatments of particle interactions and cosmology reshape our understanding of dark matter production in the early Universe.

Part I

WIMPs

CHAPTER IV

Co-annihilations and Long-Range Non-Perturbative Effects

This chapter presents a detailed literature-based review of WIMP-like particle production in a thermalized dark sector, with a particular focus on the co-annihilation regime. Here, DM is close in mass with one or several mediators, whose annihilations into SM particles drive the freeze-out of the DM number density. We explore how this regime is influenced by long-range forces mediated by massless SM vector bosons, which interact with the mediators according to their SM quantum numbers. Specifically, we discuss the Sommerfeld effect and the formation and decay of bound states composed of mediator pairs, illustrating how these phenomena modify the Boltzmann equation governing DM.

The concepts and equations presented in this chapter lay the groundwork for the primary investigations in Chapter V of this thesis, where we delve into these effects in greater depth. There, we will apply the knowledge here presented in a simplified t-channel DM model featuring color-charged mediators and assess the impact of gluon-mediated long-range forces on the parameter space of the model, with particular attention to the co-annihilating regime.

We begin this chapter by reviewing co-annihilation scenarios.

IV.1 Co-annihilation Scenarios

Assume that there exist particles in the dark sector that interact with each other and that are nearly degenerate in mass. For instance, let us assume that there exists a tower of states χ_n and that for $n \geq 2$ they have a mass slightly larger than the state χ_1. If the *mass splitting* $\Delta m_n = m_{\chi_n} - m_{\chi_1}$ is much larger than the freeze-out temperature $T_{\rm fo}$ of χ_1, by the time the interactions of χ_1 go out of equilibrium, all the heavier particles are already Boltzmann suppressed. On the contrary, if Δm_n is comparable to $T_{\rm fo}$, the heavier partners remain thermally accessible:

$$\Delta m_n \gg T_{\rm fo} \;\longrightarrow\; n_n \propto e^{-\Delta m_n/T_{\rm fo}} \ll 1, \tag{IV.1}$$

$$\Delta m_n \sim T_{\rm fo} \;\longrightarrow\; n_n \propto e^{-\Delta m_n/T_{\rm fo}} \sim 1. \tag{IV.2}$$

This means that reactions that involve particles almost degenerate in mass with χ_1 will play a role in setting the abundance of the χ_1 relic. Let us assume that the dark sector particles enjoy a symmetry that guarantees their stability against decaying. This could be, for instance, a $\mathbb{Z}_2$ symmetry or the supersymmetric R-parity under which dark sector particles are odd but SM particles are even. The reactions involving the depletion of the state χ_i allowed by such a symmetry are summarized by

$$\chi_i\,\chi_j \leftrightarrow X\,Y, \tag{IV.3}$$
$$\chi_i\,X \leftrightarrow \chi_j\,Y, \tag{IV.4}$$
$$\chi_i \leftrightarrow \chi_j\,X + \ldots, \tag{IV.5}$$

where X and Y are some SM particles in the thermal bath. The first reactions are called *annihilations* when $i = j$, ***co-annihilations*** when $i \neq j$, while the second line refers to *elastic scattering* when $i = j$ or *conversion processes/inelastic scattering* when $i \neq j$. The last line corresponds to decays which can be of 2-body or higher particle multiplicity type.

The Boltzmann equation for n_i reads as [292, 307]

$$\begin{aligned}\frac{\mathrm{d}n_i}{\mathrm{d}t} + 3Hn_i = &- \sum_{j,X} \langle \sigma_{ij} v_{ij} \rangle \left(n_i n_j - n_i^{\text{eq}} n_j^{\text{eq}} \right) \\ &- \sum_{j\neq i} \left[\langle \sigma'_{Xij} v_{ij} \rangle \left(n_i n_X - n_i^{\text{eq}} n_X^{\text{eq}} \right) - \langle \sigma'_{Xji} v_{ij} \rangle \left(n_j n_X - n_j^{\text{eq}} n_X^{\text{eq}} \right) \right] \\ &- \sum_{j\neq i} \left[\Gamma_{ij} \left(n_i - n_i^{\text{eq}} \right) - \Gamma_{ji} \left(n_j - n_j^{\text{eq}} \right) \right] ,\end{aligned} \tag{IV.6}$$

where the $\chi_i \chi_j$ annihilation cross-section is

$$\sigma_{ij} = \sum_X \sigma(\chi_i \chi_j \to X)\,, \tag{IV.7}$$

the interconversion $\chi \to \chi_j$ cross-section reads as

$$\sigma'_{Xij} = \sum_Y \sigma(\chi_i X \to \chi_j Y)\,, \tag{IV.8}$$

and the decay rates are given by

$$\Gamma ij = \sum_X \Gamma(\chi_i \to \chi_j X)\,. \tag{IV.9}$$

v_{ij} is the relative velocity between the species i and j. The equilibrium abundances and the thermal averages are defined in Eqs. (III.50) and (III.53).

We assume that the lightest stable particle (LSP) in the dark sector has a lifetime much larger than the age of the Universe (a necessary condition for being a DM candidate and a common one in certain supersymmetric scenarios like the MSSM), while all the other species have a decay rate much faster than the Hubble rate. This means that, given the imposed $\mathbb{Z}_2$ symmetry (which in the MSSM is the R-parity), all of these particles but the LSP will eventually decay into the LSP itself and into other SM particles. Thus, the evolution of the LSP can be described by the *sum* of the number densities of all dark sector species, namely

$$n = \sum_{i=1}^{N} n_i\,. \tag{IV.10}$$

A close look to Eq. (IV.6) reveals that, when summing over i, the contributions from interconversion and decay processes, namely the second and third lines, cancel out. Thus, we remain with the following Boltzmann equation

$$\frac{\mathrm{d}n}{\mathrm{d}t} + 3Hn = - \sum_{i,j=1}^{N} \langle \sigma_{ij} v_{ij} \rangle \left(n_i n_j - n_i^{\text{eq}} n_j^{\text{eq}} \right)\,. \tag{IV.11}$$

We can further simplify this equation by observing that, provided that chemical equilibrium between different species is maintained, meaning that interconversion rates are high enough, the distribution functions of the χ_i particles follow the equilibrium ones. In particular, we can use

$$\frac{n_i}{n} \simeq \frac{n_i^{\rm eq}}{n^{\rm eq}}\,. \tag{IV.12}$$

Let us see if this is indeed the case. We compare the rates of the annihilation reactions, yielding

$$n_i n_j \sigma_{ij} \sim T^3 m_i^{3/2} m_j^{3/2} e^{-\frac{m_i+m_j}{T}}\,, \tag{IV.13}$$

$$n_i n_X \sigma'_{ij} \sim T^{9/2} m_i^{3/2} e^{-\frac{m_j}{T}} \sigma'_{ij}. \tag{IV.14}$$

Computing the ratio of the second rate to the first one and assuming that the cross-sections are of the same order, $\sigma'_{ij} \simeq \sigma_{ij}$, we obtain

$$\frac{\text{(IV.14)}}{\text{(IV.13)}} \sim \frac{n_X}{n_j} \sim \left(\frac{T}{m_j}\right)^{3/2} e^{m_i/T} \frac{\sigma'_{ij}}{\sigma_{ij}} \sim 6\times 10^8, \tag{IV.15}$$

where we have also taken $m_j \simeq m_i$, and $m_i/T \sim x_{\rm fo} \simeq 25$. These simple estimates show that around the freeze-out temperature, interconversion rates are way stronger than annihilation rates. This is due to the much larger number density of (massless) SM particles in the thermal background which receives no Boltzmann suppression. Importantly, even if the cross-sections are separated by a few orders of magnitude, our conclusion does not change. The magnitude of these rates guarantees the validity of Eq. (IV.12). A situation where chemical equilibrium is not guaranteed may occur when the DM coupling that regulates DM interactions is too small. In this case, one is not allowed to perform the approximation in Eq. (IV.12) and one needs to consider the full set of coupled Boltzmann equations. In this regime, the DM-production mechanism is called *conversion-driven freeze-out* [293,308] or *co-scattering* [294] (as anticipated in Section III.5.3).

By substituting Eq. (IV.12) into Eq. (IV.11), we find that the evolution of the total number density and hence of the DM abundance is regulated by a single Boltzmann equation,

$$\frac{{\rm d}n}{{\rm d}t} + 3Hn = -\left\langle \sigma_{\rm eff} v\right\rangle \left(n^2 - n_{\rm eq}^2\right)\,, \tag{IV.16}$$

where the effective thermally averaged cross-section times relative velocity reads

$$\left\langle \sigma_{\rm eff} v\right\rangle = \sum_{ij} \left\langle \sigma_{ij} v_{ij}\right\rangle \frac{n_i^{\rm eq}}{n^{\rm eq}} \frac{n_j^{\rm eq}}{n^{\rm eq}}\,. \tag{IV.17}$$

IV.1.1 Co-annihilations in Simplified t-Channel Models

Let us consider the case of a simplified t-channel DM model as the ones presented in Section II.2.4. For convenience with the notation of Chapter V, we call the DM candidate with χ and the co-annihilation partners with X_i, with $i = 1, 2, \ldots$.

The evolution of the dark sector is determined by the coupled Boltzmann equations for the Majorana fermion χ and its coloured scalar partners X_i. Assuming that elastic scatterings and conversion processes such as $X_i \leftrightarrow \chi q_i$ occur much faster than the Hubble expansion, chemical equilibrium is maintained among all $\mathbb{Z}_2$-odd states until freeze-out. Under this approximation, the total comoving number density can be written as

$$\tilde{Y} \equiv \frac{\tilde{n}}{s} = Y_\chi + 2 \sum_{i=u,c,t} Y_{X_i} \,, \tag{IV.18}$$

where the factor of two accounts for particles and antiparticles of the scalar fields. The corresponding Boltzmann equation, in terms of the dimensionless variable $z = m_\chi/T$, takes the form:

$$\frac{\mathrm{d}\tilde{Y}}{\mathrm{d}z} = -c\, g_{*,\mathrm{eff}}^{1/2} \frac{\langle \sigma_{\mathrm{eff}} v_{\mathrm{rel}} \rangle}{z^2} \left(\tilde{Y}^2 - \tilde{Y}_{\mathrm{eq}}^2 \right) \,, \tag{IV.19}$$

with

$$Y_\chi^{\mathrm{eq}} \simeq \frac{90}{(2\pi)^{7/2}} \frac{g_\chi}{g_{*S}} z^{3/2}\, e^{-z} \,, \tag{IV.20}$$

$$Y_X^{\mathrm{eq}} = Y_{X^\dagger}^{\mathrm{eq}} \simeq \frac{90}{(2\pi)^{7/2}} \frac{g_X}{g_{*S}} [(1+\delta)z]^{3/2}\, e^{-(1+\delta)z} \,, \tag{IV.21}$$

and with $g_\chi = 2$ and $g_X = 3$ being the internal degrees of freedom of the Majorana particle χ and the coloured scalars X. Moreover, we have defined the total and the relative mass splitting as

$$\Delta m \equiv m_X - m_\chi, \quad \delta \equiv \frac{m_X - m_\chi}{m_\chi} \equiv \frac{\Delta m}{m_\chi} \,. \tag{IV.22}$$

The effective annihilation cross-section in Eq. (IV.19) is given by

$$\langle \sigma_{\mathrm{eff}} v_{\mathrm{rel}} \rangle = \sum_{ij} \langle \sigma_{ij} v_{ij} \rangle \frac{Y_i^{\mathrm{eq}}}{\tilde{Y}^{\mathrm{eq}}} \frac{Y_j^{\mathrm{eq}}}{\tilde{Y}^{\mathrm{eq}}} , \tag{IV.23}$$

where $\langle \sigma_{ij} v_{ij} \rangle$ comprises of all the annihilation cross-sections of two co-annihilating species i and j. In the regime where the colored scalars are considerably heavier than χ, their abundance becomes exponentially suppressed by the Boltzmann factor, leaving direct $\chi\chi$ annihilation as the dominant process determining the relic density. Conversely, when the mass splitting is small, co-annihilations remain significant during freeze-out and can substantially modify the predicted relic abundance.

IV.1.2 Considerations on Co-annihilations

Two important assumptions underlie this analysis. First, we require that elastic scatterings between dark sector particles and the SM bath occur rapidly compared to annihilation processes, such that the phase-space distributions of the dark sector states track those of the thermal bath. Second, we assume that processes converting one dark sector particle into another are sufficiently rapid to maintain chemical equilibrium throughout the freeze-out epoch. These approximations allow for a simplified and tractable description of the coupled Boltzmann equations governing the number densities.

In the context of co-annihilation, the direct DM annihilation process does not need to dominate. The annihilations involving multiple particles within a dark sector can encompass various other aspects. For instance, when the DM state interacts primarily through gravity and the annihilations predominantly involve a next-to-lightest state with weak interactions. Co-annihilating dark sectors have been investigated for years because they allow to evade the vanilla WIMP scenario, where DM has a sizable coupling to the

SM and masses within the ~ 100 GeV scale, a paradigm that has by now been cornered by multiple experimental endeavors [100, 196, 208, 222] (cf. also Section II.3).

On the contrary, as we will show in Chapter V, a small mass splitting between the lightest stable state and the co-annihilating partners allows for much larger DM masses, up to the multi-TeV regime, while making prompt searches less sensitive due to the small energy deposited in hadron jets, as well as allowing for more stable next-to-lightest states due to the reduced phase space. These are attractive features that could explain why no BSM particle has yet been detected at the LHC.

In fact, starting from the '90s and up to twenty years later, the most studied co-annihilation models took place within the MSSM or one of its variations (the "complete" variant of simplified DM models), where a neutralino, the lightest supersymmetric particle, serves as the DM candidate, while scalar fermions (squarks or sleptons), or gluinos have nearly degenerate masses and co-annihilate with it [292, 307, 309–318]. More recently, the case for co-annihilations in the stop-neutralino system has been revisited in [319–323] by a more in-depth analysis including loop corrections, renormalization scheme uncertainties, and non-perturbative effects from long-range forces. Also, high-scale SUSY scenarios have been re-considered in light of no significant signals beyond the SM at the LHC, including gaugino co-annihilations [324], such as the bino-wino system [325–330]

As a matter of fact, most models that feature a multi-particle dark sector include co-annihilation scenarios among the possible ways of providing the correct DM abundance and evading experimental constraints. For instance, these comprise models such as the Little Higgs [331], the Inert Doublet [332], Minimal Dark Matter [156], and simplified models in general [333], including the t-channel models described in Section II.2.4. In particular, in simplified t-channel models, DM can either pair annihilate via its Yukawa interaction or have interconversion co-annihilations with its mediator and a SM particle. Therefore, in the co-annihilation regime, the evolution of its number density and the freeze-out of its relic abundance are mainly driven by those processes that involve the mediators alone. These could be single or pair annihilations of mediators into SM states, as well as multi-body decays, which are usually of lesser importance.

In these models, the mediators share the same gauge quantum numbers of the SM state they interact with and thus interact with at least one SM gauge boson. In the unbroken phase of the electroweak symmetry, all the SM bosons are massless and thus can mediate a long-range interaction of Coulomb type, whereas, as soon as the symmetry is broken, roughly at $T_{\mathrm{EW}} \sim 150\,\mathrm{GeV}$, the W and Z bosons masses make the interaction short-ranged and of Yukawa type.

As we will see in the following section, a mediator is influenced by the long-range features as long as its dynamics are non-relativistic, meaning that it moves sufficiently slowly and "has the time" to resolve the non-instantaneous interaction. This is the case for a co-annihilation-driven freeze-out, which is non-relativistic by definition. Moreover, for multi-TeV mediator masses, even the W and Z bosons can be perceived as massless, either because all the relevant processes that yield the DM abundance happen before EWSB, or because, effectively, the W and Z masses are negligible. In the co-annihilating regime, including such effects turns out to be crucial for a precise description of DM production and a sensible interpretation of experimental exclusion limits.

IV.2 Sommerfeld Effect (SE)

IV.2.1 Quantum-mechanical Derivation

Consider two electrically charged particles with mass m approaching each other from infinity with relative velocity $v \ll 1$. Before they can feel each other, their behavior is fully described by a plane wave wavefunction,

$$\psi_k^{(0)}(z) = e^{ikz}, \tag{IV.24}$$

where we took the z-axis as the axis along which the movement occurs and where k is the particle momentum along the z-axis. If the two particles did not carry any charge, the plane wave description would always hold. However, they can interact due to their electric charge, and, to a first "hard" approximation, their interaction is simply described by a "bare" point-like cross-section times relative velocity

$$\sigma_0 \equiv (\sigma v)_0 \simeq \pi \frac{\alpha^2}{m^2}\,. \tag{IV.25}$$

Moreover, they source a central Coulomb potential

$$V(r) = \pm \frac{\alpha}{r}\,, \tag{IV.26}$$

where $\alpha = e^2/(4\pi)$ is the fine structure constant, e the electric charge and $\pm$ indicates if the potential is repulsive $(+)$ or attractive $(-)$. Before the particles meet, they start feeling the long-range Coulomb force which can repel or attract them, prompting a deceleration or an acceleration towards each other. Quantum-mechanically, this means that the wavefunctions get distorted in a well-known manner: the quantum-mechanical scattering in the presence of a central potential has the effect that the outgoing wavefunction is made of a plane wave component and a spherical wave [334]

$$\psi_k(z, r, \theta) \sim e^{ikz} + f(\theta)\frac{e^{ikr}}{r} \quad \text{as}\, r \to \infty\,. \tag{IV.27}$$

The cross-section is now given by

$$\sigma v = \sigma_0\, S(v)\,, \tag{IV.28}$$

where the $S(v)$ factor can *enhance* or *reduce* the interaction probability, depending on the sign of the potential. The factor is defined as the ratio between the long-range influenced cross-section and the bare (or "hard") one:

$$S(v) = \frac{\sigma v}{\sigma_0}\,. \tag{IV.29}$$

Equivalently, it can be characterized as the ratio between the probability of finding a particle at the origin of the two-particle system (the interaction point) when the long-range potential is considered and when not:

$$S(v) = \frac{|\psi_k(0)|^2}{|\psi_k^{(0)}(0)|^2}\,. \tag{IV.30}$$

This factor is called the **Sommerfeld factor** after Arnold Sommerfeld who first theorized the effect in 1931 while studying the scattering of slowly moving electrons and positrons

[335]. To determine what $S(v)$ looks like, we need to study the full quantum system and find an expression for the wavefunction at the origin.

The Schrödinger equation with a central potential in the center-of-momentum (CoM) frame reduces to

$$-\frac{\nabla^2_{\rm rel}}{2\mu}\psi_k = \left(\frac{k^2}{2\mu} - V(r)\right)\psi_k\,, \tag{IV.31}$$

where $\mu = m/2$ is the reduced mass and $k^2/(2\mu)$ the kinetic energy of the CoM. Thanks to the spherical symmetry, we can expand ψ into radial wavefunctions and Legendre polynomials

$$\psi_k = \sum_\ell A_\ell R_{k\ell}(r)\, P_\ell(\cos\theta)\,, \tag{IV.32}$$

where A_ℓ is a coefficient that depends on the angular momentum ℓ. By further defining the reduced radial wavefunction $u_{k\ell}(r) \equiv rR_{k\ell}(r)$, the Schrödinger equation becomes

$$\frac{\mathrm{d}^2}{\mathrm{d}r^2}u_{k\ell}(r) = \left[m\,V(r) + \frac{\ell(\ell+1)}{r^2} - k^2\right]u_{k\ell}(r)\,. \tag{IV.33}$$

Since the solutions in the absence of a potential are spherical Bessel functions that behave near the origin as $(kr)^\ell$, only the $\ell = 0$ term is relevant in this limit. This needs not to be the case if other symmetries impose that the interaction in the s-wave limit is null (see later). For now, let us assume for simplicity that $\ell = 0$. To solve the second order ODE in Eq. (IV.33), we need two boundary conditions. One is found at the origin, where $u_k(0) = 0$. The other is at infinity, where the system is asymptotically free and thus

$$u_k(\infty) = \sin\left(kr + \delta_V\right)\,, \tag{IV.34}$$

where δ_V is a phase that depends on the properties of the potential. Following [336–339], the solution to Eq. (IV.33) is given by

$$u_k(x) = C_1\sqrt{x}J_1(2\sqrt{x})\,, \tag{IV.35}$$

where C_1 is an integration constant, $x = \alpha m r$ and $J_1(x)$ is a Bessel function of the first kind. After some steps, one finds that the boundary conditions impose C_1 to take the form of

$$C_1 = \frac{\varepsilon\,\Gamma\left(1 - \frac{i}{2\varepsilon}\right)}{e^{-\frac{\pi}{4\varepsilon}}\,e^{i\eta}}\,, \tag{IV.36}$$

with $\varepsilon = k/(\alpha m)$ and η being a phase that plays no role once taking the absolute value squared to calculate the probability of finding the reduced system at the origin. This yields

$$|\psi_k(0)|^2 = \frac{|\Gamma(1+\frac{i}{2\varepsilon})|^2}{e^{-\frac{\pi}{2\varepsilon}}}|k|^2\,. \tag{IV.37}$$

This also implies that the bare probability when the potential vanishes, namely when $\alpha \to 0$ and $\varepsilon \to \infty$, is simply $|\psi_k^{(0)}(0)|^2 = |k|^2$. Computing the ratio of the two probabilities, one arrives at an expression for the $\ell = 0$ Sommerfeld factor of a Coulomb potential:

$$S_{\ell=0}(v) = \frac{|\psi_k(0)|^2}{|\psi_k^{(0)}(0)|^2} = \frac{\pi/\varepsilon}{1-e^{-\pi/\varepsilon}} = \frac{2\pi\zeta}{1-e^{-2\pi\zeta}}\,, \tag{IV.38}$$

where one defines

$$\zeta \equiv \frac{\alpha}{v} = \alpha\frac{\mu}{k} = \frac{1}{2\varepsilon}\,. \tag{IV.39}$$

Notice that ζ can be either positive or negative, depending on the sign of the Coulomb potential. When $\zeta > 0$, $S_{\ell=0} \geq 1$, and we can have the following limits:

$$S_{\ell=0} = \frac{2\pi\zeta}{1-e^{-2\pi\zeta}} \longrightarrow \begin{cases} \dfrac{2\pi\alpha}{v} & \text{if } \alpha \gg v \\ 1 & \text{if } \alpha \ll v \end{cases}, \tag{IV.40}$$

which have a clear physical interpretation. When the gauge coupling strength α is much larger than the relative velocity, the Coulomb force further attracts the interacting particle *enhancing* the cross-section. On the contrary, if this interaction is negligible in comparison to their kinetic energy, the cross-section is left unaltered. Analogously, when $\zeta < 0$, we have a mirror behavior,

$$S_{\ell=0} = \frac{-2\pi|\zeta|}{1-e^{2\pi|\zeta|}} \longrightarrow \begin{cases} \exp\left(-2\pi\dfrac{|\alpha|}{v}\right) & \text{if } |\alpha| \gg v \\ 1 & \text{if } |\alpha| \ll v \end{cases}, \tag{IV.41}$$

where now the repulsive nature of the potential *suppresses* the cross-section by an exponential factor any time the long-range force dominates, while it leaves it unaltered when negligible. We show these behaviors in Fig. IV.1. Notice that, the reason why the long-range behavior starts being important in correspondence of $\alpha \sim v$ is traceable in the following argument. The typical interaction distance is given by the inverse of the average relative momentum $k = \mu v_{\rm rel}$ exchanged between two scattering particles. When the interaction distance approaches the Bohr radius $(\mu\alpha)^{-1}$ of the system, equating the two lengths gives $\alpha \sim v_{\rm rel}$. Therefore:

long-range effects arise when the interaction length $(\mu v_{\rm rel})^{-1}$ is about the Bohr radius $(\mu\alpha)^{-1}$ of the system.

Notice that, a self-consistent calculation of the Sommerfeld effect is needed when applying a factorized Sommerfeld factor to the tree-level s-wave cross-section, which can lead to violation of partial-wave unitarity due to the appearance of zero-energy bound-states. This has been done in Ref. [339] where the interference of short-range interactions is taken into account leading to a variation of the Sommerfeld factor that does not lead unitarity violation.

IV.2.2 Field-theoretical Viewpoint

A QFT approach to the Sommerfeld effect helps us understand the source of its non-perturbative nature. Let us consider two incoming particles X with mass m and relative velocity v that scatter off one another via the exchange of a massless gauge boson with coupling strength α. The Feynman diagram describing the process is depicted in Fig. IV.2.

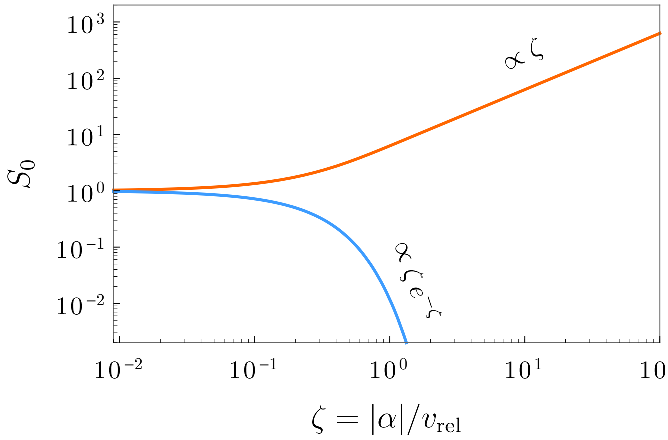

Figure IV.1: Sommerfeld factor S_0 in Eq. (IV.38) for a Coulomb potential for s-wave scatterings as a function of $\zeta = |\alpha|/v_{\rm rel}$. The orange (cyan) line shows the case for an attractive (repulsive) force with $\alpha > 0$ ($\alpha < 0$), asymptotically going to a linear enhancement (exponential suppression) at small velocities. At large velocities $S_0 \to 1$ in both scenarios.

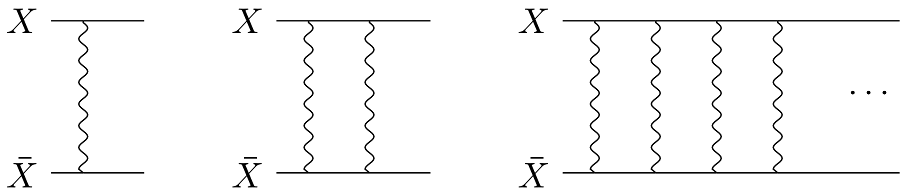

Figure IV.2: *Left:* Scattering of two charged particles X via exchange of a gauge boson (wavy line). *Middle:* Diagram with two insertions of gauge boson exchanges. *Right:* Ladder diagram with an infinite number of gauge boson insertions.

Each interaction vertex brings a factor of $\sqrt{\alpha}$, the gauge coupling. The gauge boson propagator is in a t-channel configuration and therefore the matrix element of the interaction can be approximated as

$$(\sqrt{\alpha})^2 \frac{1}{t} \sim \frac{\alpha}{q^2} \propto \frac{\alpha}{v^2} \,, \tag{IV.42}$$

where we have only taken track of the powers in α and v. If we insert another gauge boson exchange, as in the middle of Fig. IV.2, each propagator brings a factor $\sim 1/v^2$, while each interaction vertex a power $\sim \sqrt{\alpha}$. However, we also have to consider the loop integration. Let us name q the loop momentum. The zero component scales as the kinetic energy, $q_0 \sim v^2$, while the spatial components are simply $|\vec{q}| \sim v$. Thus, the loop integration measure scales as $\mathrm{d}^4 q = \mathrm{d}q_0 \mathrm{d}q^3 \sim v^5$. Combining all the factors, the two-gauge boson exchange diagram scales as

$$v^5 \frac{\alpha}{v^2} \alpha \left(\frac{1}{v^2}\right)^3 = \frac{\alpha^2}{v^3} \,. \tag{IV.43}$$

If the dynamics of the interaction occurs in a regime where $\alpha \sim v$, *both* Eq. (IV.42) and Eq. (IV.43) scale as $1/v \sim 1/\alpha$, which means that even if we continue to add new gauge boson exchanges, the order in α never changes. This signals a clear breakdown of perturbation theory and the need for a resummation of the entire **ladder diagram** (right diagram in Fig. IV.2), made of infinite rung insertions.

If $\alpha \sim v$, each rung insertion contributes as $1/v \sim 1/\alpha$.

The fact that for $\alpha \sim v$ we obtain a non-perturbative behavior and that the Sommerfeld effect introduced in the previous section is relevant is a first hint that the two phenomena are somewhat intertwined.

In fact, as shown in [340], the non-perturbative nature of the ladder diagram arising in the non-relativistic regime is the consequence of the solution of the following Bethe-Salpeter equation [341] defining the non-perturbative 4-point vertex

$$i\Gamma(p_1, p_2; p_3, p_4) = i\tilde{\Gamma}(p_1, p_2; p_3, p_4) + \int \frac{\mathrm{d}^4 q}{(2\pi)^4} \, \tilde{\Gamma} \, G(q) \, G(p_1 + p_2 - q) \, \Gamma \,, \tag{IV.44}$$

where p_1 and p_2 are the incoming momenta, while p_3 and p_4 are the outgoing ones. Here $\tilde{\Gamma}$ are two-particle irreducible diagrams and G is the non-perturbative propagator. In the non-relativistic limit, this 4-point function can be simplified by defining

$$\chi(p_1, p_2; p_3, p_4) = G(p_1) G(p_2) \Gamma(p_1, p_2; p_3, p_4) \tag{IV.45}$$

which, after some steps reduces the Bethe-Salpeter to a Schrödinger equation in integral form given by

$$\left(\frac{\mathbf{p}^2}{m} - E \right) \psi_{\mathrm{BS}}(\mathbf{p}) + \int \frac{\mathrm{d}^3 q}{(2\pi)^3} \, V(\mathbf{p} - \mathbf{q}) \, \psi_{\mathrm{BS}}(\mathbf{q}) \,, \tag{IV.46}$$

where one defines the Bethe-Salpeter wavefunction as

$$\psi_{\mathrm{BS}}(\mathbf{p}) = \int \frac{\mathrm{d}p_0}{2\pi} \, \chi\left(P, p\right) \,. \tag{IV.47}$$

In these steps, we have also introduced the change of variables $p = (p_1 - p_2)/2$ and $P = (p_1 + p_2)/2$. The Bethe-Salpeter wavefunction is nothing but the solution to the Schrödinger equation with a potential V accounting for the interactions included in the vertex function $\tilde{\Gamma}$. More specifically, the matrix element of the non-perturbative interaction can be written as follows [340]

$$\mathcal{M}_{\mathrm{ladder}}(p_1, p_2; \{p_f\}) \approx \int \frac{\mathrm{d}^3 \mathbf{k}}{(2\pi)^3} \mathcal{M}_{\mathrm{inst}}(\mathbf{k} - \mathbf{k}, \{\mathbf{p}_f\}) \, \psi_{\mathrm{BS}}(\mathbf{k}) \,, \tag{IV.48}$$

where $\mathcal{M}_{\mathrm{inst}}$ refers to the matrix element in the instantaneous approximation, without the ladder. The ratio between the cross-section with and without the ladder diagram is precisely the Sommerfeld factor, in complete analogy with the more intuitive method illustrated in the previous section.

IV.2.3 Higher Partial Waves

If we include higher angular momentum values, the solution of the Schrödinger equation determining the wavefunction components follows similarly and yields the following result for the ℓ-wave Sommerfeld factor [337, 340]

$$S_\ell = \left| \frac{(2\ell + 1)!}{(\ell!\,)^2} \frac{\partial^\ell R_\ell(z)}{\partial z^\ell} \bigg|_{z=0} \right|^2 \,, \tag{IV.49}$$

where $z = 2mrv$ is a dimensionless variable. The radial wavefunction in this case reads as

$$R_\ell(z) = \frac{z^\ell e^{-iz/2}}{\Gamma(2\ell+2)} e^{\pi\zeta/2}\, \Gamma\left(1+\ell+i\zeta\right)\, {}_1F_1\left(1+\ell+i\zeta; 2\ell+2; iz\right) \tag{IV.50}$$

where ${}_1F_1$ is the confluent hypergeometric function of the first kind [289]. By inserting this expression in the Sommerfeld factor in Eq. (IV.49), one obtains

$$S_\ell = \left|\Gamma\left(1+\ell+i\zeta\right)\right|^2 \frac{e^{\pi\zeta}}{(\ell!\,)^2} = S_0 \prod_{b=1}^{\ell} \left(1+\frac{\zeta^2}{b^2}\right) , \tag{IV.51}$$

with S_0 given by Eq. (IV.38). This shows how the ℓ-th partial wave correction factorizes into the s-wave contribution times products of terms that are progressively less relevant due to the presence of $\zeta^2 \sim \alpha^2 \ll 1$. However, there is an important caveat to this result, that is, when deriving the Sommerfeld factor, it is assumed that each partial wave ℓ in the transition amplitude can be expanded as p^ℓ (or v^ℓ) for low momenta. This allows matching each partial-wave contribution to σv with its Sommerfeld factor S_ℓ. Namely, if we expand

$$(\sigma v)^{(0)} = \sigma_0 + \sigma_1\, v^2 + \sigma_2\, v^4 + \dots , \tag{IV.52}$$

where each coefficient corresponds to the $\ell = 0$ (or s-wave) term, $\ell = 1$ (or p-wave) term, $\ell = 2$ (or d-wave) term, and so on, the Sommerfeld-corrected cross-section reads as

$$\sigma v = \sigma_0\, S_0 + \sigma_1\, S_1 + \sigma_2\, S_2 + \dots , \tag{IV.53}$$

with each S_ℓ correction multiplying a single partial-wave term. This recipe only works if the amplitude is dominated by a single partial-wave process so that the Sommerfeld correction is just a multiplicative factor to the tree-level cross-section.

However, this needs not be the case if one takes a full expansion of the amplitude in powers of p, as shown in [342], where the ℓ-th amplitude reads as

$$\mathcal{M}_\ell \propto \sum_{n\geq 0} p^{\ell+2n} , \tag{IV.54}$$

with $n \geq 0$ being an integer number. Consequently, one finds

$$(\sigma v_{\rm rel})^{(0)} \sim |\mathcal{M}^{(0)}|^2 = \sum_\ell |\mathcal{M}_\ell^{(0)}|^2 \propto \sum_{\ell,n,n'} p^{2(\ell+n+n')} . \tag{IV.55}$$

This implies that terms proportional to p^2 are not purely "p-wave" and receive contributions from states with $\ell = 0$ (e.g., when $n = 1$ and $n' = 0$). For the successive terms in the momentum expansion scaling with p^{2m}, the contribution emerges from $m+1$ different partial-waves so that utilizing the partial-wave terminology fails for $m \neq 0$. Up to which n one can expand depends on the process one is analyzing, but it becomes clear that the ℓ-th Sommerfeld factor can be attached to different powers of p in $\mathcal{M}_\ell$, not only to p^ℓ. Re-deriving the Sommerfeld-corrected squared matrix element, one finds [342]

$$\sigma v_{\rm rel} \sim |\mathcal{M}^{(S)}|^2 = \sum_\ell |\mathcal{M}_\ell^S|^2 \propto \sum_\ell S_\ell \sum_{n,n'} p^{2(\ell+n+n')} . \tag{IV.56}$$

In this form, the Sommerfeld factors can no longer be factored out due to the inclusion of higher orders in the momentum expansions at a specified order in ℓ. Consequently, one must decide the extent to which the cross-section expansion of the process under correction is to be expanded and then multiply each term in the expansion by the respective Sommerfeld factor. However, in this and the subsequent chapters, we will not delve into this refinement. For the processes of interest, the $\ell = 0$ Sommerfeld correction will adequately account for the relevant corrections in dark matter phenomenology. Nevertheless, we will avoid referring to terms in σv proportional to v^0, v^2, etc., as s-wave, p-wave, etc.

IV.3 Bound State Formation (BSF)

So far, we have focused on the distortion produced by the long-range potential to the *scattering* wavefunction, a solution to Schrödinger equation with positive energy eigenvalues. However, as it is well known, there exists another class of solutions involving *negative* energy levels: bound states. Non-relativistic quantum mechanics tells us that the discrete spectrum of solutions to the Schrödinger equation given by [334]

$$\left[-\frac{\nabla^2_{\rm rel}}{2\mu} + V(r)\right] \psi_{n\ell m}(\mathbf{r}) = \mathcal{E}_n \psi_{n\ell m}(\mathbf{r})\,, \tag{IV.57}$$

with an attractive Coulomb potential (repulsive potentials do not admit discrete solutions) reads as [334, 343]

$$\psi_{n\ell m}(\mathbf{r}) = R_{n\ell}(r) Y_{\ell m}(\Omega)\,, \tag{IV.58}$$

$$R_{n\ell(r)} = (2\kappa/n)^{3/2} \left[\frac{(n-\ell-1)!}{2n(n+\ell)!}\right]^{1/2} e^{-\kappa r/n} \,(2\kappa r/n)^\ell \, L^{2\ell+1}_{n-\ell-1}(2\kappa r/n)\,, \tag{IV.59}$$

where $Y_{\ell m}(\Omega)$ are the spherical harmonics and $L_{n-\ell-1}$ are generalized Laguerre polynomials. The wavefunctions are normalized according to

$$\int \mathrm{d}^3\mathbf{r}\, \psi^*_{n\ell m}(\mathbf{r})\, \psi_{n'\ell' m'}(\mathbf{r}) = \delta_{nn'}\delta_{\ell\ell'}\delta_{mm'}\,. \tag{IV.60}$$

The energy eigenvalues are degenerate in ℓ and m, respectively, the total and orbital angular momentum quantum numbers, and only depend on n as

$$\mathcal{E}_n = -\frac{\mu(\alpha^B)^2}{2n^2} = -\frac{\kappa^2}{2\mu n^2}\,, \tag{IV.61}$$

with $\kappa = \mu\alpha^B$ being the Bohr momentum. This is a peculiar feature of hydrogen-like systems. The coupling strength for bound states α^B is evaluated at the momentum of the interaction when its RGE evolution is accounted for. In this case, it is the Bohr momentum itself. This differs from the coupling strength of the scattering interaction that gives rise to the Sommerfeld effect, where the typical average momentum exchange is the relative momentum $k = \mu v_{\rm rel}$. We will refer to the scattering coupling strength as α^S. The coupling strength can also depend on group factors in non-Abelian theories (see later in Section IV.4.3). Here, however, we will remain agnostic on the particular gauge group the force carrier belongs to and derive general results for Coulomb potentials.

The ground state is characterized by the quantum numbers $\{n\ell m\} = \{100\}$ with the corresponding spherically symmetric wavefunction reading as [343]

$$\psi_{100}(r) = \frac{\kappa^{3/2}}{\sqrt{\pi}}\, e^{-\kappa r}\,. \tag{IV.62}$$

We shall now ask ourselves: what is the probability for a pair of particles with mass m to meet and form a bound state? One might be tempted to answer this question by identifying this probability with the modulus squared of the bound state wavefunction at the origin of the system. However, this only corresponds to the probability of finding the bound state at the origin and does not provide information about the transition from the initial state, where the two particles are at an infinite distance and start to interact under the influence of the Coulomb potential, to the final state where the two particles are effectively bound.

Therefore, what we need to compute is the *transition amplitude* between an initial *scattering state* wavefunction with momentum $\mathbf{k}$ and positive energy eigenvalue, $\psi_{\mathbf{k}}$, which is a solution to the Schrödinger equation belonging to the continuum spectrum, and the final bound state wavefunction $\psi_{n\ell m}$, which is a solution to the same equation but belongs to the discrete spectrum and has a negative energy eigenvalue.

In particular, the transition has to remove energy from the interacting system. The missing energy is carried away by the radiation emitted during the transition in the form of quanta of the force carrier, the same that generates the Coulomb potential. For vector bosons, as the case here examined, this is a *dipole transition* with interaction Hamiltonian of the form $\sqrt{4\pi\alpha^{\rm BSF}}\omega\mathbf{r}\cdot\mathbf{E}$, $\alpha^{\rm BSF}$ refers to the coupling strength at the radiative vertex and it is evaluated at the typical average momentum transfer for the interaction, namely $\omega = \mu/2\left((\alpha^B)^2 + v_{\rm rel}^2\right)$ that is the difference between the final and initial state energies. $\mathbf{E}$ is the classical electric field.

From standard Quantum Mechanics, the probability of forming a bound state is proportional to the matrix element squared, given by

$$
\begin{aligned}
|\mathcal{M}_{\mathbf{k}\to\{n\ell m\}}|^2 &= \frac{2}{3}(4\pi\alpha^{\rm BSF})Q^2\omega^2|\langle\psi_{n\ell m}(\mathbf{r})|\mathbf{r}|\psi_{\mathbf{k}}(\mathbf{r})\rangle|^2 \\
&= \frac{2}{3}(4\pi\alpha^{\rm BSF})Q^2\omega^2\frac{1}{2\ell+1}\sum_m\int {\rm d}^3\mathbf{r}{\rm d}^3\mathbf{r}'\left(\mathbf{r}\cdot\mathbf{r}'\right)\psi_{n\ell m}(\mathbf{r})\psi^*_{n\ell m}(\mathbf{r}')\psi^*_{\mathbf{k}}(\mathbf{r})\psi_{\mathbf{k}}(\mathbf{r}')\,,
\end{aligned}
\tag{IV.63}
$$

where Q is the charge of the interacting particles. In the non-Abelian case, where a gluon mediates the Coulomb potential, one has to substitute $Q^2 \to C_2^{[\mathbf{R}]}$, the quadratic Casimir of $SU(N_c)$ in the representation $[\mathbf{R}]$. The matrix element can be computed by employing the solutions to the Schrödinger equation in Eq. (IV.58) and in Eq. (IV.50). We refer the reader for the details of the calculation in the general case with arbitrary values of n and ℓ to, e.g., Refs. [344–347], where formulae for Abelian and Non-Abelian Coulomb potentials are treated.

Here, we want to highlight the case that will be of greatest interest to us, namely the capture into the ground state $\{100\}$. The differential cross-section for this process to happen is defined by [345]

$$
v_{\rm rel}\frac{{\rm d}\sigma_{\mathbf{k}\to\{100\}}}{{\rm d}\Omega} = \frac{\omega}{1024\pi^2\mu^3}|\mathcal{M}_{\mathbf{k}\to\{100\}}|^2\sin^2\theta\,,
\tag{IV.64}
$$

where θ is the angle between the momenta of the outgoing radiated vector boson and the incoming scattering state in the CoM frame. Since the capture into the ground state is spherically symmetric, we can directly integrate over the solid angle to obtain the BSF cross-section times relative velocity [345],

$$
\sigma_{\rm BSF}v_{\rm rel} = \frac{(\alpha^B)^2 + v_{\rm rel}^2}{768\,\pi\mu^2}|\mathcal{M}_{\mathbf{k}\to\{100\}}|^2\,.
\tag{IV.65}
$$

The calculation of the matrix element squared can be performed with standard quantum mechanics [344, 348], and it has been recently revisited in several works in the DM literature. For example, one can adopt:

- a Feynman diagrammatic approach, by analyzing the Bethe-Salpeter equations, the relativistic extension of the Schrödinger equation including the continuum and the discrete spectrum, and the 5-point Green's function that gives rise to the transition amplitude between scattering and bound states with radiation emission [345, 349–355]. This is a powerful method because it allows for a generic and controlled calculation from *first-principles* of QFT of any possible transition including BSF via emission of scalar mediators and massive mediators of any gauge group, as well as transitions between different bound states.
- an effective field theory (EFT) approach that borrows the methods of potential non-relativistic EFTs for quarkonium and "darkonium" studies (e.g., pNRQCD and pNRQED [327, 328, 356–362]) to calculate observables such as the BSF cross-section and capture rate [363–367].
- more "traditional" methods relying on quantum mechanical arguments [368–373].

We refer the reader to this literature and the references therein for details about the calculation. Here, we want to show the results of interest to our discussion in preparation for the next chapter. Specifically, the BSF cross-section for the capture into the ground state with the emission of an (Abelian or non-Abelian) vector boson reads as

$$\sigma_{\rm BSF} v_{\rm rel} = \sigma_0 \, S_{\rm BSF}(\zeta_S, \zeta_B)\,, \tag{IV.66}$$

where $\sigma_0 = \pi(\alpha^B)^2/(4\mu^2)$, and, in analogy with the Sommerfeld effect, one defines the BSF factor [351]

$$S_{\rm BSF}(\zeta_S, \zeta_B) = \frac{2^9}{3}\left(\frac{2\pi\zeta_S}{1-e^{-2\pi\zeta_S}}\right)(1+\zeta_S^2)\frac{\zeta_B^4}{(1+\zeta_B^2)^3} e^{-4\zeta_S \,\mathrm{arccot}(\zeta_B)} \tag{IV.67}$$

as a function of

$$\zeta_S = \alpha^S/v_{\rm rel}\,, \qquad \zeta_B = \alpha^B/v_{\rm rel}\,. \tag{IV.68}$$

In $S_{\rm BSF}$, the factor in the first parenthesis is identical to the s-wave Coulomb Sommerfeld factor (cf. Eq. (IV.38)). This is not a coincidence since the overlap integral involves the convolution of a scattering wavefunction, which is influenced by the Sommerfeld effect, as explained in the previous section. The Sommerfeld factor lies in the normalization of the scattering wavefunction. The second term accounts for the p-wave correction to S_0 (cf. Eq. (IV.51)). The presence of this second factor comes from the fact that the radiative capture is, at leading order, a dipole transition between the initial scattering state and the final bound state. These transitions impose a selection rule $\Delta\ell = \pm 1$ on the orbital angular momentum, such that for the final bound state to be in the ground state (100), the initial scattering state must be in a $\ell = 1$ state, hence the p-wave correction. The last factor accounts for the convolution of the bound state wavefunction with the radiative vertex.

In Fig. IV.3 we show the rate between the BSF and the perturbative annihilation cross-sections, namely $S_{\rm BSF}$, as a function of ζ (we take $\zeta_S = \zeta_B$ for simplicity). At large velocities, when $\zeta_S, \zeta_B \ll 1$, the BSF cross-section is suppressed by $S_{\rm BSF} \simeq \zeta_B^4 \sim (\alpha^B/v_{\rm rel})^4 \ll 1$. On the other hand, at low velocities, we obtain the characteristic scaling $S_{\rm BSF} \sim \alpha^S/v_{\rm rel}$

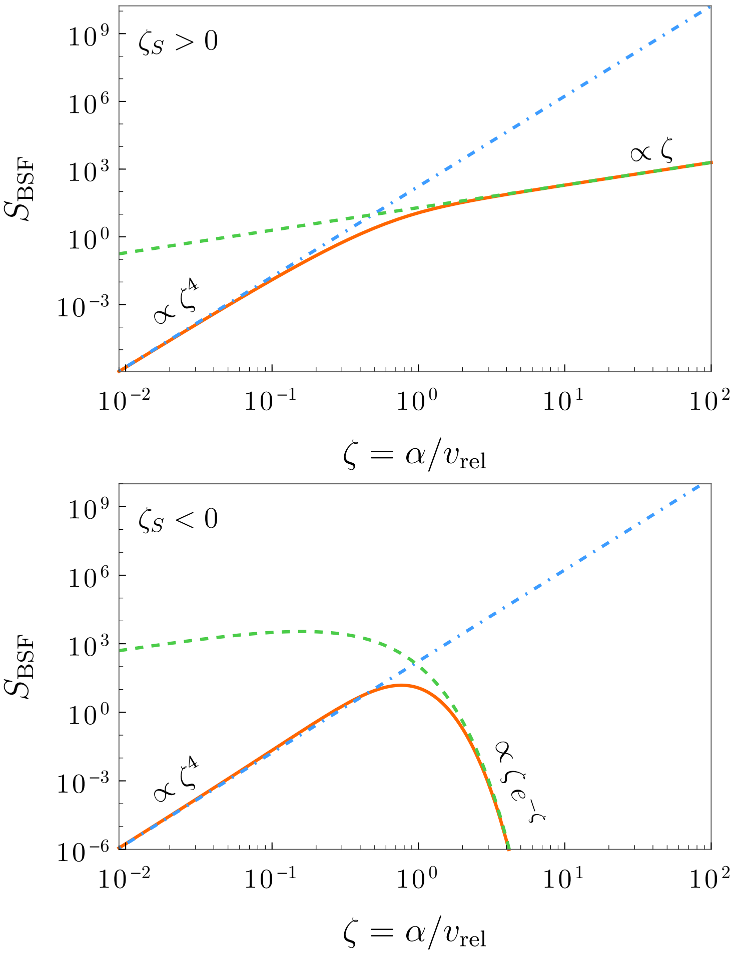

Figure IV.3: BSF factor $S_{\rm BSF}$ of Eq. (IV.67) as a function of the parameter $\zeta = \alpha/v_{\rm rel}$ in the case with $|\zeta_S| = \zeta_B \equiv \zeta$. The upper panel shows the case for an attractive force in the initial scattering state ($\zeta_S > 0$), while the lower panel applies to a repulsive force ($\zeta_S < 0$). The asymptotic behavior at large velocities (small ζ) is the same $\propto \zeta^4$ in both cases and it is shown with the dashed light cyan line, while, at small velocities (large ζ), BSF is linearly enhanced (exponentially suppressed) if the initial states attract (repel) each other, shown in dot-dashed light green.

when the interaction between the scattering state is attractive, hence if $\zeta_S \gtrsim 1$ and $\zeta_B \gtrsim 1$. The BSF cross-section in this case is enhanced. Moreover, the BSF factor and cross-section are maximized when $\alpha^S/\alpha^B = 0.5$ (and for $\alpha^S, \alpha^B \sim v_{\rm rel}$) signaling that the radiative transition is most probable to happen when the potentials governing the interactions between the free and the bound states are very similar. Finally, when the interaction is repulsive ($\zeta_S < 0$) and at low velocities, $\zeta_S \gtrsim -1$ and $\zeta_B > 1$, the BSF probability becomes exponentially suppressed, $S_{\rm BSF} \sim\propto \exp(-2\pi|\zeta_S|)$, as it becomes harder to form bound states when two incoming particles experience a strong repulsive force. These qualitative behaviors agree with what we show in Fig. IV.3.

Similarly to the case for perturbative and Sommerfeld-affected cross-sections, we can define a thermally-averaged BSF cross-section by weighting $\sigma_{\rm BSF} v_{\rm rel}$ with the Maxwellian distribution of bound states traveling at speed $v_{\rm rel}$ as follows [351]:

$$\langle \sigma_{\rm BSF} v_{\rm rel} \rangle = \left(\frac{\mu}{2\pi T}\right)^{3/2} \int \mathrm{d}^3 v_{\rm rel} \exp\left(-\mu v_{\rm rel}^2/2T\right) \left[1 + f_A(\omega)\right] \sigma_{\rm BSF} v_{\rm rel} \,. \tag{IV.69}$$

Here, $\omega = \mu/2\left[(\alpha)^2 + v_{\rm rel}^2\right]$ is the energy emitted by the radiated gauge boson, which equals its kinetic energy minus the (negative) binding energy $\mathcal{E}_{100} = -\mu(\alpha)^2/2$ of the newly formed bound state, and $f_A(\omega) = (\exp(\omega/T) - 1)^{-1}$ is its distribution function, accounting for the final-state Bose-enhancement factor $1 + f_A(\omega)$. This term is necessary to ensure the detailed balance between bound state formation and ionization reactions (the inverse process), i.e. *ionization equilibrium.*

IV.3.1 Bound-state Ionization and Decays

If bound states are successfully formed via a capture process in the early Universe, such as

$$X_1 + X_2 \to \mathcal{B}_{n\ell} + A\,, \tag{IV.70}$$

with A being the emitted radiation in the form of vector boson quanta, they can be ionized by the same vector bosons that are part of the thermal plasma and dissociate back into their constituents,

$$\mathcal{B}_{n\ell} + A \to X_1 + X_2\,. \tag{IV.71}$$

These two processes are the inverse of each other. Alternatively, they can directly decay into radiation or other particles,

$$\mathcal{B}_{n\ell} \to A + A + \dots\,. \tag{IV.72}$$

Ionization usually dominates at temperatures larger than the binding energy, when particles in the thermal plasma are sufficiently energetic to disrupt the bound state. We can derive the ionization probability from detailed balance arguments. Suppose the amplitude squared to form and dissociate a bound state are the same due to CP-invariance,

$$|\mathcal{M}_{X_1+X_2\to\mathcal{B}+A}|^2 = |\mathcal{M}_{\mathcal{B}+A\to X_1+X_2}|^2\,. \tag{IV.73}$$

The cross-section of the two processes is related by [351]

$$\frac{\sigma_{\rm ion}}{\sigma_{\rm BSF}} = \frac{g_1 g_2}{g_\mathcal{B} g_A}\left[\frac{(s-m_1^2-m_2^2)^2-4m_1^2m_2^2}{(s-m_A^2-m_\mathcal{B}^2)^2-4m_A^2m_\mathcal{B}^2}\right]^{1/2}\frac{|\mathbf{P}_1|}{|\mathbf{P}_A|}\,, \tag{IV.74}$$

where the g's are the internal degrees of freedom, s is the CoM energy squared, and $\mathbf{P}$ refers to the momentum of the particle in the CoM frame. In the non-relativistic regime, we can set

$$s \simeq (m_1 + m_2 + \mathcal{E}_\mathbf{k})^2 \simeq (m_1 + m_2 + \mathcal{E}_{n\ell} + \omega)^2, \tag{IV.75}$$

where $\mathcal{E}_\mathbf{k} = \mu v_{\rm rel}/2$ is the kinetic energy of the initial scattering state in the CoM frame. In this frame we can also set $|\mathbf{P}_1| = |\mathbf{P}_2| = \mu v_{\rm rel}$ and $|\mathbf{P}_A| = |\mathbf{P}_\mathcal{B}| = \omega$, to obtain

$$\sigma_{\rm ion} = \frac{g_1 g_2}{g_A g_\mathcal{B}}\left(\frac{\mu^2 v_{\rm rel}^2}{\omega^2}\right)\sigma_{\rm BSF}\,. \tag{IV.76}$$

This is the so-called *Milne relation* [348, 374]. The ionization rate follows from [351]

$$\Gamma_{\rm ion} = \frac{g_A}{2\pi^2}\int_{\omega_{\rm min}}^\infty {\rm d}\omega \frac{\omega^2}{e^{\omega/T}-1}\,\sigma_{\rm ion}\,. \tag{IV.77}$$

Notice how at large temperatures the Bose-Einstein distribution of radiation enhances the rate, while at low temperatures it makes it exponentially suppressed, in agreement with our physical intuition.

The decay of a bound state is proportional to the perturbative annihilation cross-section of the scattering states times the probability density of finding a bound state at the origin of the CoM system [345, 346, 351]. For the decay of the $\{100\}$ ground state, we only need the s-wave component of the cross-section, namely

$$\Gamma_{\text{dec}} = \left(\sigma_{\text{ann}}^{s-\text{wave}} v_{\text{rel}}\right) \, |\psi_{100}(0)|^2 \, . \tag{IV.78}$$

By employing Eq. (IV.62), we obtain $|\psi_{100}(0)|^2 = (\mu\alpha^B)^3/\pi$, and, together with assuming $(\sigma_{\text{ann}}^{s-\text{wave}} v_{\text{rel}}) \simeq g_1 g_2 \pi (\alpha^S)^2/\mu^2$, leads to [351]

$$\Gamma_{\text{dec}} \simeq 16 g_1 g_2 \mu (\alpha^S)^2 (\alpha^B)^3 \, . \tag{IV.79}$$

In Section IV.4.3 we will consider the non-Abelian case of the capture of coloured triplet massive states into the ground state by emission of a gluon. The BSF cross-section, the ionization rate (caused by energetic gluons in the plasma), and the decay rate into pairs of gluons will also depend on the colour decomposition of the considered interactions.

IV.3.2 Effective DM Boltzmann Equation with BSF

The formation and subsequent decay of bound states involving dark sector particles can affect the DM relic abundance by effectively opening up a new annihilation channel, whether it is the DM particles themselves that form the bound states or whether the dark sector mediators bind together and drive the depletion of the DM number density in the co-annihilation regime. These effects must be incorporated as additional terms into the system of coupled Boltzmann equations that control the evolution of the number densities of bound and unbound particles.

In principle, one would need to account for the evolution of the number densities of each bound state that is formed, including excited states, and also consider all the transitions allowed by kinematics and selection rules. Here, we make two simplifications. First, we only focus on bound states formed by mediator particles; second, we take into account only their ground state.

IV.3.2.1 Boltzmann Equation for Simplified t-channel Models

Let us consider the case of simplified t-channel DM models (cf. Sections II.2.4 and IV.1.1). Here, the DM candidate χ interacts with heavier mediators X that are charged under the SM gauge group and can form bound states via emission of the vector boson they interact with. This case will be treated in greater detail in the next chapter. The coupled Boltzmann equations for the yields of DM, Y_χ, of the mediators $Y_X + Y_{X^\dagger}$ (particle and anti-particle), and of the mediator bound states $Y_{\mathcal{B}}$ take the following form (see also [349, 372, 375]):

$$\frac{\mathrm{d}Y_\chi}{\mathrm{d}z} = \gamma_{\text{DM}}, \tag{IV.80}$$

$$\frac{\mathrm{d}\left(Y_X + Y_{X^\dagger}\right)}{\mathrm{d}z} = 2\left(\frac{\mathrm{d}Y_X}{\mathrm{d}z}\right)_{\text{w/oBSF}} - 2\frac{c\sqrt{g_{*,\text{eff}}}}{z^2}\left\langle\sigma_{\text{BSF}} v_{\text{rel}}\right\rangle \left(Y_X^2 - \left(Y_X^{\text{eq}}\right)^2 \frac{Y_{\mathcal{B}}}{Y_{\mathcal{B}}^{\text{eq}}}\right), \tag{IV.81}$$

$$\frac{\mathrm{d}Y_{\mathcal{B}}}{\mathrm{d}z} = -\frac{c\sqrt{g_{*,\text{eff}}}}{z^2 s}\Gamma_{\text{dec}}\left(Y_{\mathcal{B}} - Y_{\mathcal{B}}^{\text{eq}}\right) + \frac{c\sqrt{g_{*,\text{eff}}}}{z^2}\left\langle\sigma_{\text{BSF}} v_{\text{rel}}\right\rangle \left(Y_X^2 - \left(Y_X^{\text{eq}}\right)^2 \frac{Y_{\mathcal{B}}}{Y_{\mathcal{B}}^{\text{eq}}}\right). \tag{IV.82}$$

The DM interaction rate density is simply determined by the decay and scattering processes it is subject to (cf. Section III.4.1) and it is not influenced by the bound state dynamics. The first term in the collisional part of the mediators' equation refers to any number-changing interaction that does not involve bound states (decay into DM states, scatterings with SM particles, etc.), while the second term is a gain/loss term due to BSF. This same term appears with the opposite sign in the bound state Boltzmann equation, where we have also added the loss term attributed to the decay of the bound states into radiation. Notice that, due to the Milne relation in Eq. (IV.76), we can swap the BSF cross-section with the ionization rate as follows

$$\Gamma_{\mathrm{ion}} = \langle \sigma_{\mathrm{BSF}} v_{\mathrm{rel}} \rangle \, s \frac{Y_X^{\mathrm{eq}\,2}}{Y_{\mathcal{B}}^{\mathrm{eq}}} \, . \tag{IV.83}$$

Second, by assuming that the bound states are meta-stable and close-to-equilibrium, we can approximate their number density $Y_{\mathcal{B}}$ as being almost constant, $\mathrm{d}Y_{\mathcal{B}}/\mathrm{d}z \approx 0$. This assumption is reasonable as long as chemical equilibrium between free particles is assured (a premise that holds within the co-annihilation regime) and that the processes involving the bound states (formation, ionization, rapid decays, level transitions, etc.) are fast enough to exceed the Hubble expansion, which is indeed the case for temperatures larger than their binding energies (see also Ref. [375] for a recent, more detailed argumentation). By setting the l.h.s of Eq. (IV.82) to zero, we can algebraically solve the r.h.s. for $Y_{\mathcal{B}}$ to find [372]

$$\frac{Y_{\mathcal{B}}}{Y_{\mathcal{B}}^{\mathrm{eq}}} = \frac{\Gamma_{\mathrm{dec}} + \Gamma_{\mathrm{ion}} \left(\frac{Y_X}{Y_X^{\mathrm{eq}}} \right)^2}{\Gamma_{\mathrm{tot}}} \, , \tag{IV.84}$$

where $\Gamma_{\mathrm{tot}} = \Gamma_{\mathrm{dec}} + \Gamma_{\mathrm{ion}}$. By inserting Eq. (IV.84) back into Eqs. (IV.81) and (IV.82) and by further summing Eq. (IV.80) with Eq. (IV.82), we can now turn the convoluted system of Boltzmann equations into a much simpler form where we only have to consider a single Boltzmann equation for the total number density of the dark sector particles, in a very similar fashion as for the bare co-annihilation scenario,

$$\begin{aligned} \frac{\mathrm{d}\left(Y_\chi + 2Y_X\right)}{\mathrm{d}z} &= \left(\frac{\mathrm{d}\left(Y_\chi + 2Y_X\right)}{\mathrm{d}z} \right)_{\mathrm{w/oBSF}} - \frac{2c\sqrt{g_{*,\mathrm{eff}}}}{z^2 s} \frac{\Gamma_{\mathrm{dec}}}{\Gamma_{\mathrm{tot}}} \left[\frac{Y_{\mathcal{B}}^{\mathrm{eq}}}{\left(Y_X^{\mathrm{eq}}\right)^2} \Gamma_{\mathrm{ion}} \left(Y_X^2 - \left(Y_X^{\mathrm{eq}}\right)^2 \right) \right] \\ &= \left(\frac{\mathrm{d}\left(Y_\chi + 2Y_X\right)}{\mathrm{d}z} \right)_{\mathrm{w/oBSF}} - 2\frac{c\sqrt{g_{*,\mathrm{eff}}}}{z^2} \frac{\Gamma_{\mathrm{dec}}}{\Gamma_{\mathrm{tot}}} \langle \sigma_{\mathrm{BSF}} v_{\mathrm{rel}} \rangle \left(Y_X^2 - \left(Y_X^{\mathrm{eq}}\right)^2 \right) \\ &= \left(\frac{\mathrm{d}\left(Y_\chi + 2Y_X\right)}{\mathrm{d}z} \right)_{\mathrm{w/oBSF}} - \frac{c\sqrt{g_{*,\mathrm{eff}}}}{z^2} 2 \langle \sigma_{\mathrm{BSF}} v_{\mathrm{rel}} \rangle_{\mathrm{eff}} \left(Y_X^2 - \left(Y_X^{\mathrm{eq}}\right)^2 \right) \, , \end{aligned} \tag{IV.85}$$

The effects introduced by BSF have been reabsorbed into an effective thermally-averaged BSF cross-section, affecting the evolution of the constituents' number density (and the total yield), which reads as [349, 351]

$$\langle \sigma_{\mathrm{BSF}} v_{\mathrm{rel}} \rangle_{\mathrm{eff}} \equiv \langle \sigma_{\mathrm{BSF}} v_{\mathrm{rel}} \rangle \frac{\Gamma_{\mathrm{dec}}}{\Gamma_{\mathrm{dec}} + \Gamma_{\mathrm{ion}}} \, , \tag{IV.86}$$

weighting the BSF cross-section by the fraction of bound states that decay into radiation and change the number density of dark sector particles. At large temperatures, since the ionization processes are much more efficient than bound state decays, the effective contribution of bound states in the dark sector evolution is negligible, so the relic density calculation is independent of the BSF cross-section. As the universe cools down, the ionization rate becomes exponentially suppressed and, eventually, all bound states decay, efficiently depleting the dark sector scalars.

This means that the effect of BSF on the Boltzmann equation can be relevant even at temperatures close to the binding energy ($T \gtrsim \mathcal{E}_{\mathcal{B}}$), way lower than typical freeze-out temperatures. For instance, assuming $\alpha \sim 0.1$, $\mathcal{E}_{\mathcal{B}} \sim \kappa^2/(2\mu) \sim \mu\alpha^2 \sim m_X/400$ is way smaller than $T_{\text{fo}} \sim m_X/25$. In fact, BSF is typically efficient at times of the order of $z = m_X/T \sim 10^3$, as one can find by solving the complete Boltzmann equation for the total yield $\tilde{Y} = Y_\chi + 2Y_X$ (following from Eq. (IV.85)):

$$\frac{\mathrm{d}\tilde{Y}}{\mathrm{d}z} = -\frac{c g_{*,\text{eff}}^{1/2}}{z^2} \langle \sigma_{\text{eff}} v_{\text{rel}} \rangle \left(\tilde{Y}^2 - \left(\tilde{Y}^{\text{eq}} \right)^2 \right) - 2 \frac{c g_{*,\text{eff}}^{1/2}}{z^2} \langle \sigma_{\text{BSF}} v_{\text{rel}} \rangle_{\text{eff}} \left(Y_X^2 - \left(Y_X^{\text{eq}} \right)^2 \right). \tag{IV.87}$$

Here, the first term in the collisional part corresponds to the standard co-annihilation term without BSF, but including the SE for those processes that are affected by long-range forces. The second term accounts for the DM depletion via BSF. Obviously, for each BSF, one needs a corresponding term to add to the BSF contribution in Eq. (IV.87). This is the case treated in the next Chapter V, where we consider a model featuring bound states formed by more types of mediator pairs appearing in multiple flavour family copies.

IV.4 Sommerfeld Effect and Bound State Formation in Coloured Models

The general framework discussed in the previous sections becomes particularly rich when applied to non-Abelian gauge theories like QCD. Colored mediators X interacting via gluon exchange exhibit a complex structure of long-range interactions that depends on their color representations. This section provides the theoretical foundation for understanding these effects, which will be crucial for the simplified t-channel models analyzed in the following chapter.

IV.4.1 Color Decomposition and Non-Abelian Potentials

When two colored mediator particles interact, their combined color state can be decomposed into irreducible representations of $SU(3)_C$. For particles in representations $\mathbf{R}_1$ and $\mathbf{R}_2$, the tensor product decomposes as:

$$\mathbf{R}_1 \otimes \mathbf{R}_2 = \bigoplus_{\hat{\mathbf{R}}} \hat{\mathbf{R}}\,. \tag{IV.88}$$

If the dynamics of the mediators' interaction is non-relativistic (as the case of interest for DM freeze-out), each irreducible representation $\hat{\mathbf{R}}$ experiences a different Coulomb-like potential:

$$V_{[\hat{\mathbf{R}}]}(r) = -\frac{\alpha_g^{[\hat{\mathbf{R}}]}(Q)}{r}, \tag{IV.89}$$

The effective coupling constant in each representation is related to the strong coupling $\alpha_s(Q)$ by:

$$\alpha_g^{[\hat{\mathbf{R}}]}(Q) = \alpha_s(Q) \times \frac{1}{2}\left[C_2(\hat{\mathbf{R}}) - C_2(\mathbf{R_1}) - C_2(\mathbf{R_2})\right] \equiv \alpha_s(Q) \times k_{[\hat{\mathbf{R}}]}, \tag{IV.90}$$

where $C_2(\mathbf{R})$ is the quadratic Casimir invariant. The factor $k_{[\hat{\mathbf{R}}]}$ determines whether the potential is attractive ($k_{[\hat{\mathbf{R}}]} > 0$) or repulsive ($k_{[\hat{\mathbf{R}}]} < 0$).

We demonstrate the relation in Eq. (IV.90). Consider the generators of the representations R_1 and R_2 and denote them with $T^a_{R_1}$ and $T^a_{R_2}$. Their tensor product for the irreducible representation R_J reads as

$$\begin{aligned}
\left[T^a_{R_1} \otimes T^a_{R_2}\right]_J = & \qquad\qquad\qquad\qquad\qquad\qquad\qquad\qquad\qquad\qquad\qquad\qquad\text{(IV.91)}\\
&= \frac{1}{2}\left[\left(T^a_{R_1} + T^a_{R_2}\right)^2_J - \left(T^a_{R_1}\right)^2 - \left(T^a_{R_2}\right)^2\right] &\text{(IV.92)}\\
&= \frac{1}{2}\left[T^a_{R_J}T^a_{R_J} - \left(C_2(R_1) + C_2(R_2)\right)\mathbb{1}_{R_1} \otimes \mathbb{1}_{R_2}\right] &\text{(IV.93)}\\
&= \frac{1}{2}\left[C_2(R_J) - C_2(R_\mathbf{1}) - C_2(R_\mathbf{2})\right], &\text{(IV.94)}
\end{aligned}$$

where we used

$$C_2(R)\mathbb{1}_R = T^a_R T^a_R$$

.

For the lowest dimensional representations of $SU(3)$, the quadratic Casimirs read as:

$$C_2(\mathbf{1}) = 0, \tag{IV.95}$$
$$C_2(\mathbf{3}) = C_2(\bar{\mathbf{3}}) = 4/3, \tag{IV.96}$$
$$C_2(\mathbf{6}) = C_2(\bar{\mathbf{6}}) = 10/3, \tag{IV.97}$$
$$C_2(\mathbf{8}) = 3, \tag{IV.98}$$

If the incoming interacting particles are in the fundamental ($\mathbf{3}$) or anti-fundamental ($\bar{\mathbf{3}}$) representation, as in the case relevant for the simplified t-channel models discussed in Chapter V, we have the following irreducible decompositions and corresponding colour factors:

$$\mathbf{3} \otimes \bar{\mathbf{3}} = \mathbf{1} \oplus \mathbf{8} \implies k_\mathbf{1} = -\frac{4}{3}, \quad k_\mathbf{8} = +\frac{1}{6}, \tag{IV.99}$$
$$\mathbf{3} \otimes \mathbf{3} = \bar{\mathbf{3}} \oplus \mathbf{6} \implies k_{\bar{\mathbf{3}}} = -\frac{2}{3}, \quad k_\mathbf{6} = +\frac{1}{3}. \tag{IV.100}$$

Inserting them in Eq. (IV.90) and then in Eq. (IV.89), we obtain the decomposed potentials as follows:

$$V_\mathbf{1} = -\frac{4}{3}\frac{\alpha_s}{r}, \tag{IV.101}$$
$$V_\mathbf{8} = +\frac{1}{6}\frac{\alpha_s}{r}, \tag{IV.102}$$
$$V_{\bar{\mathbf{3}}} = -\frac{2}{3}\frac{\alpha_s}{r}, \tag{IV.103}$$
$$V_\mathbf{6} = +\frac{1}{3}\frac{\alpha_s}{r}. \tag{IV.104}$$

IV.4.2 Sommerfeld Enhancement in Non-Abelian Theories

The color-dependent long-range Coulomb potentials of the strong force lead to modified annihilation cross-sections due to the Sommerfeld effect as given in Eq. (IV.38). According to the irreducible representation of the interaction, the Sommerfeld enhancement factor for each interaction channel depends on the color factor $k_{[\mathbf{R}]}$:

$$S_{0,[\mathbf{R}]} = S_0\left(k_{[\mathbf{R}]}\frac{\alpha_s}{v_{\rm rel}}\right), \tag{IV.105}$$

As already discussed, depending on the structure of the interaction (cf. Section IV.2.3), the non-perturbative correction to the cross-section can actually be more complicated than a simple multiplicative factor. Notice that, for a representation leading to an attractive potential, the Sommerfeld factor will *enhance* the perturbative cross-section, while in the case of a repulsive gluon potential, the cross-section will be suppressed.

The specific form and combination of these corrections depends on the detailed model implementation, which will be discussed in the following chapter for concrete t-channel models (cf. Chapter V). There, we will show how for incoming colored states in the fundamental representation of $SU(3)$, the total cross-section can be written as a sum of contributions from different color channels.

IV.4.3 Bound State Formation in Non-Abelian Theories

Bound state formation in non-Abelian theories is particularly rich due to the multiple color channels available. The formation process:

$$X_1 + X_2 \;\rightarrow\; \mathcal{B}(X_1X_2) + g, \tag{IV.106}$$

can occur in different color representations, each with its own binding energy and formation cross-section.

The binding energies follow the hydrogen-like spectrum:

$$\mathcal{E}_n^{[\hat{\mathbf{R}}]} = -\frac{\kappa^2_{[\hat{\mathbf{R}}]}}{2\mu n^2}, \tag{IV.107}$$

where the Bohr momentum depends on the color representation:

$$\kappa_{[\hat{\mathbf{R}}]} \equiv \mu\,\alpha_{g,[\hat{\mathbf{R}}]} = \mu\,k_{[\hat{\mathbf{R}}]}\,\alpha_s. \tag{IV.108}$$

For colored mediators transforming in the fundamental representation, the most important bound states are usually those in the attractive color singlet channel ($\mathbf{3}\otimes\bar{\mathbf{3}}\rightarrow\mathbf{1}$), which have the deepest binding energy and whose BSF cross-section and formation rate are the highest. The color octet states are, on the other hand, repulsive and do not form bound states, unless additional attractive potentials play a role in the interaction of the colored state, such as in the case of BS formed due to the emission of a massless Higgs field at high energies [352, 376].

In Fig. IV.4, we illustrate a representative five-point Feynman diagram for bound-state formation, in which a free gluon is emitted while multiple gluon exchanges mediate the long-range interaction between the incoming particles and the constituents of the emerging bound state. This diagram captures both the perturbative radiative transition and the non-perturbative dynamics associated with the attractive QCD potential [1, 345, 351].

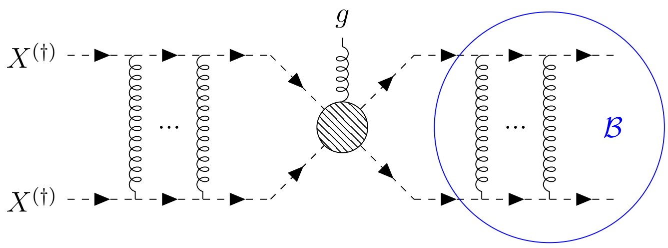

Figure IV.4: The Feynman diagram illustrating the radiative capture of a scalar triplet pair into a bound state depicts several components. The initial state involves a pair of scalar triplets, which could be $XX^\dagger$, XX, or $X^\dagger X^\dagger$, with non-perturbative wavefunctions for the scalar triplet pair. The diagram includes a perturbative 5-point function that features the radiative vertex, represented by a gray dashed blob. In the final state, the diagram shows the bound state $\mathcal{B}$ and an on-shell radiated gluon g. *Figure created by the thesis author and also published in [1].*

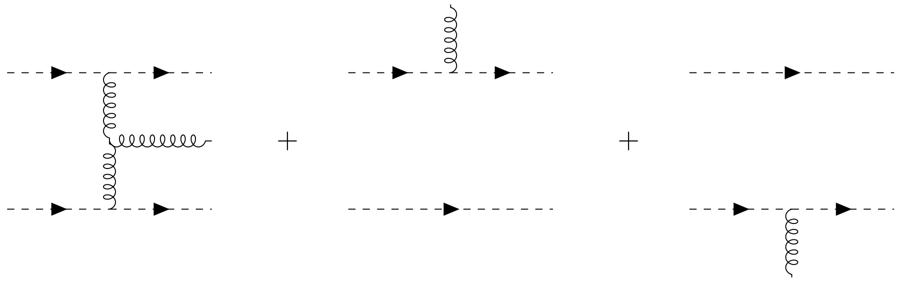

Figure IV.5: Tree-level contributions to the radiative vertex depicted in Fig. IV.4. The leftmost diagram represents radiation from the gluon propagator. The remaining two diagrams illustrate contributions arising directly from emission off external legs. *Figure created by the thesis author and also published in [1].*

The non-Abelian structure of the radiative vertex is emphasized in Fig. IV.5. The leftmost diagram is specific to non-Abelian gauge theories and arises from gauge-boson self-interactions, whereas the remaining two diagrams correspond to gluon emission from external legs. These latter contributions are also present in Abelian theories, highlighting the qualitative difference between Abelian and non-Abelian bound-state formation mechanisms [1, 345, 351].

IV.4.4 Ionization and Decay of Bound States

The impact of bound states on dark sector evolution is controlled by the competition between their destruction through ionization and their decay into lighter states. This competition determines when bound states can effectively contribute to number-changing processes.

IV.4.4.1 Ionization Processes

Bound states formed via gluon emission can be dissociated by energetic gluons from the thermal plasma. For color-singlet bound states, the ionization rate follows from the Milne relation and can be written as [351]:

$$\Gamma_{\text{ion},[\mathbf{1}]} = g_g \int_{\omega_{\min}}^{\infty} \mathrm{d}\omega \frac{\omega^2}{2\pi^2} \frac{1}{e^{\omega/T} - 1} \sigma_{\text{ion}}, \tag{IV.109}$$

$$\sigma_{\text{ion}} = \frac{g_1\, g_2}{g_g g_{\mathcal{B}}} \left(\frac{\mu^2 v_{\text{rel}}^2}{\omega^2}\right) \sigma_{\text{BSF}}, \tag{IV.110}$$

where $g_g = 8$ denotes the internal degrees of freedom of gluons, respectively. For capture into the singlet ground state, $g_{\mathcal{B}} = 1$.

The Bose-Einstein distribution enhances ionization at early times, while at $T \ll \omega$ the rate becomes exponentially suppressed. This temperature dependence is crucial: at temperatures above the binding energy, ionization dominates and bound states do not contribute appreciably to number-changing processes.

IV.4.4.2 Bound State Decay

Once ionization ceases to be effective, bound states decay predominantly through the annihilation of their constituents. For $\ell = 0$ states, the decay rate can be expressed in terms of the s-wave annihilation cross-section and the bound state wavefunction at the origin. For a color-singlet ground state decaying into gluons [351]:

$$\Gamma_{\text{dec},[\mathbf{1}]} = \frac{64}{81} \mu\, (\alpha_s^{\text{ann}})^2 (\alpha_{s,[\mathbf{1}]}^B)^3, \tag{IV.111}$$

where the couplings are evaluated at the appropriate annihilation and binding scales.

IV.4.4.3 Effective BSF Cross-Section

Assuming bound states remain close to equilibrium and evolve adiabatically, the effects of formation, ionization, and decay can be consistently absorbed into an effective thermally-averaged BSF cross-section:

$$\langle \sigma_{\text{BSF}} v_{\text{rel}} \rangle_{\text{eff}} \equiv \left\langle \sigma_{\text{BSF}}^{[\mathbf{8}]\to[\mathbf{1}]} v_{\text{rel}} \right\rangle \frac{\Gamma_{\text{dec}[\mathbf{1}]}}{\Gamma_{\text{dec}[\mathbf{1}]} + \Gamma_{\text{ion},[\mathbf{1}]}}. \tag{IV.112}$$

At early times, the ratio $\Gamma_{\text{dec}}/(\Gamma_{\text{dec}} + \Gamma_{\text{ion}})$ suppresses the contribution of bound states. In contrast, at later times, it approaches unity, allowing BSF to efficiently reduce the number density of colored mediators. This transition typically occurs at temperatures far below the standard freeze-out scale, implying that BSF can remain relevant at $z \sim 10^3$.

The total effective annihilation cross-section entering the Boltzmann equation is obtained by summing the perturbative annihilation channels and the BSF contribution for each flavor:

$$\langle \sigma_{XX^\dagger} v_{\text{rel}} \rangle_{\text{eff}} = \sum_i \left(\left\langle \sigma_{X_i X_i^\dagger} v_{\text{rel}} \right\rangle + \left\langle \sigma_{\text{BSF}}^{[\mathbf{8}]\to[\mathbf{1}]} v_{\text{rel}} \right\rangle \frac{\Gamma_{\text{dec}[\mathbf{1}]}}{\Gamma_{\text{dec}[\mathbf{1}]} + \Gamma_{\text{ion},[\mathbf{1}]}} \right), \tag{IV.113}$$

which replaces the purely perturbative annihilation term in the effective cross-section.

Concluding Remarks

In the co-annihilation regime, the presence of heavy gauge-charged particles in the thermal bath mediates interactions between dark matter (DM) and the visible sector, giving rise to long-range forces. These interactions induce non-perturbative effects that cannot be captured by fixed-order perturbation theory.

In the non-relativistic limit, we have shown how the Sommerfeld effect of each partial wave enters the S-matrix amplitude of annihilation processes. In the simplest situation, where a single partial wave dominates, the SE factorizes from the short-distance dynamics and acts as a multiplicative correction to the perturbative cross section. This *Sommerfeld factor* can either enhance or suppress the annihilation rate, depending on whether the effective potential is attractive or repulsive.

Moreover, the formation of bound states of the mediators provides an additional annihilation channel. When efficient, bound-state formation BSF invariably reduces the DM abundance. In the co-annihilation regime, as we will demonstrate in the next chapter, the effective cross section in Eq. (IV.86) remains sizable even beyond the standard freeze-out epoch, typically occurring at $z_{\text{fo}} \equiv m_{\text{DM}}/T \sim 25$–$30$. Consequently, BSF can significantly alter the thermal history of DM and its phenomenology. In particular, BSF becomes most relevant at temperatures comparable to the binding energy of the bound state, which depends on the underlying interaction. In non-Abelian theories, the structure of SE and BSF is further enriched by the color decomposition of the initial and final states into irreducible representations.

In co-annihilation scenarios involving coloured mediators, typical values of the strong coupling, $\alpha_s \sim 0.1$, imply $z_{\text{BSF}} \sim 2m_{\text{DM}}/\mu\alpha_s^2 \sim 400$, so that the DM number density continues to be depleted through BSF and subsequent bound-state decay at relatively late times. This effect can lead to substantial modifications of the relic abundance and to important phenomenological consequences.

In the next chapter, we present an efficient numerical implementation of these non-perturbative effects for coloured simplified t-channel models featuring a Majorana DM particle and coloured scalar triplet mediators. We show that QCD-induced long-range interactions have a pronounced impact on the viable parameter space. We further provide a detailed phenomenological analysis illustrating how the parameter space is progressively reshaped when Sommerfeld enhancement and bound-state formation are included, and we discuss the sensitivity of current and future experimental searches to these effects.

CHAPTER V

Impact of Sommerfeld Effect and Bound State Formation on Simplified t-Channel DM Models

In the previous chapter, we have understood that in certain scenarios, accounting for the effects generated by the long-range behavior of attractive and repulsive forces modifies the calculation of fundamental properties and observables related to the production of Dark Matter (DM) particles in the Early Universe. The Sommerfeld Effect (SE) is responsible for non-perturbatively affecting the interaction cross-sections that enter the collision operators in the Boltzmann equation, whereas the formation and decay of metastable bound states can efficiently contribute to the depletion of dark sector particles. In the co-annihilation regime, such effects can sensibly change the prediction of the DM relic density, demanding their precise implementation in any phenomenological study where dark sector particles are sensitive to long-range distortions.

In this chapter, we will analyze such an impact in the framework of the simplified t-channel DM models that we have described in Section II.2.4, demonstrating how the parameter space is modified when accounting for SE and Bound State Formation (BSF). These modifications affect the way current experimental facilities are probing the model in such a way that i) portions of parameter space thought to be excluded open up again and ii) a complementary approach to experimental searches is needed.

This work is one of the first to address the phenomenological impact of non-perturbative effects in simplified DM models from an all-around perspective, implementing theory developments into a widely-used computational framework (`micrOMEGAs`) to perform parameter scans and combining them with experimental limits, as we are going to show.

To systematically investigate these phenomena, we must first establish the theoretical framework by defining the specific models under consideration and identifying all relevant (co-)annihilation channels. This foundation enables us to understand where and how long-range effects will manifest, setting the stage for their detailed implementation and subsequent phenomenological analysis.

Statement of Personal Contribution for this Chapter

The research presented in this chapter is derived from a collaborative project originating from an idea of JH that resulted in Ref. [1], from which this chapter takes the conducted analysis, presented results, and derived conclusions. The principal contributions to this publication of the thesis author include:

- The technical implementation into `micrOMEGAs` of the cross-sections for the Sommerfeld effect and bound-state formation, as well as the necessary modification of how the Boltzmann equation is calculated (together with MB, following an initial suggestion of JH).
- The execution of the numerical scans required to generate the data presented in the parameter space plots throughout this chapter (together with MB).
- The drawing of all diagrams and tables.
- The creation of Figs. V.2 and V.11.
- With the collaborators: analysis and interpretation of the results, derivation of the conclusions, and writing of the paper.
  At the beginning of the relevant sections, we will emphasize which parts have been directly done by the thesis author alone, which resulted from a combined effort with the papers' co-authors, and which are taken from the literature.

V.1 S3M Models and Annihilation Channels

Declaration: This section presents the specific implementation details for the DM model and cosmological calculations used in this chapter. The thesis author analyzed the co-annihilation channels and wrote the text in the paper, while all authors reviewed the results and corrected the text. The text presented here is a restructured version of the publication.

Model Lagrangian

We consider the class of models denoted as `S3M` (cf. Section II.2.4). Here, the DM candidate is a Majorana fermion singlet χ with mass m_{DM}, interacting with a Yukawa coupling g_{DM} with a SM fermion (a quark q in our case) and a coloured charged scalar mediator X with mass $m_X \geq m_{\mathrm{DM}}$.

The scalar mediators transform in the fundamental representation of $SU(3)$ and are thus color triplets. Depending on the mediator quantum numbers, we distinguish three scenarios — referred to as the u_R, d_R, and q_L models — corresponding to right-handed up-type quarks, right-handed down-type quarks, and left-handed quark doublets, respectively [174,186–188,377]. The scalar mediators carry specific SM gauge quantum numbers under $SU(3)_c \times SU(2)_L \times U(1)_Y$: $(3,1)_{2/3}$ for the u_R model, $(3,1)_{-1/3}$ for the d_R model, and $(3,2)_{-1/6}$ for the q_L model.

The interaction Lagrangian of the dark sector reads as:

$$\mathcal{L} \supset \sum_i (D_\mu X_i)^\dagger (D^\mu X_i) + \sum_{i,j} \left(g_{\mathrm{DM},ij} X_i^\dagger \bar{\chi} P_R q_j + g^*_{\mathrm{DM},ij} X_i \bar{q}_j P_L \chi \right) \,, \tag{V.1}$$

where D_μ is the usual covariant derivative incorporating the interactions of the mediators with the SM. For simplicity, we take the couplings to be real, flavor-diagonal, and universal ($g_{ij} = g\,\delta_{ij}$), thereby avoiding flavor-mixing effects that would complicate the analysis through flavor-violating processes.

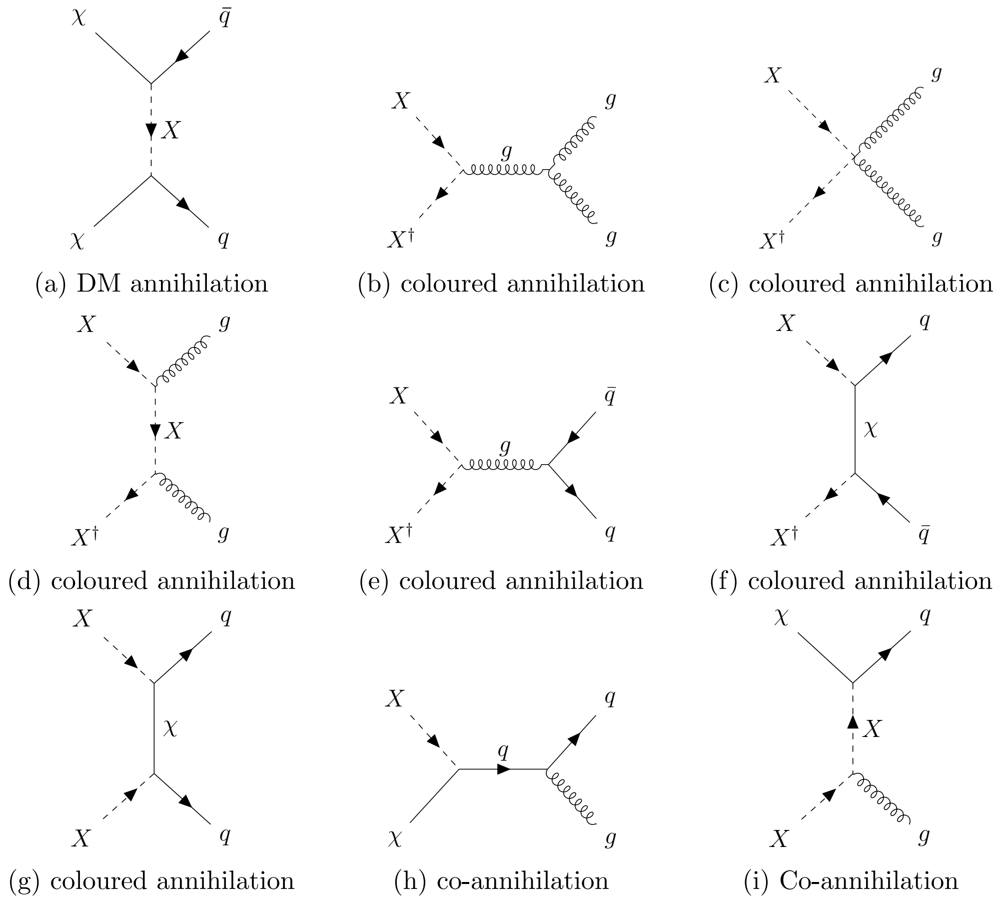

(a) DM annihilation (b) coloured annihilation (c) coloured annihilation
(d) coloured annihilation (e) coloured annihilation (f) coloured annihilation
(g) coloured annihilation (h) co-annihilation (i) Co-annihilation

Figure V.1: Representative Feynman diagrams corresponding to the main subset of processes contributing to (co-)annihilations described in Table V.1. *Figure created by the thesis author and also published in [1].*

Annihilation Channels

The relic abundance of χ is established by solving the Boltzmann equation as outlined in the previous chapters (cf. Eq. (IV.19)). The processes that govern the DM number density evolution are not only dominated by DM pair-annihilations, $\chi\chi \to$ SM SM, but also by co-annihilation channels involving the colored scalars. As we saw in Section IV.1, these channels are active when DM and the mediators are nearly degenerate in mass. In the model here considered, these processes include $\chi X \to$ SM, $\chi X^\dagger \to$ SM, and $XX^\dagger$ annihilations into SM particles. Representative Feynman diagrams illustrating these interactions are provided in Fig. V.1.[1]

The annihilation and co-annihilation dynamics in the t-channel scenarios considered are shaped by the mass splitting between the dark matter candidate χ and the colored scalar mediators X_i, as well as the relative sizes of the Yukawa and gauge couplings. Table V.1 summarizes the dominant annihilation channels (the same as Fig. V.1), highlighting their parametric dependence on the mass splitting $\Delta m = m_X - m_\chi$ (second column) and the leading velocity dependence in the non-relativistic limit (third column). These processes can be read off from Eq. (IV.23) by expanding it and accounting for the (co)-annihilation

[1]For clarity, only gluon-mediated interactions are explicitly shown, since the strong coupling dominates; however, in the u_R and d_R scenarios, photon and Z exchange and production can also contribute, while in the q_L case, $W^\pm$ exchange and production are additionally relevant.

processes as follows

$$\begin{aligned}\langle\sigma_{\rm eff}v_{\rm rel}\rangle &= \frac{2Y_X^{\rm eq}Y_{X^\dagger}^{\rm eq}\langle\sigma_{XX^\dagger}v_{\rm rel}\rangle}{\tilde{Y}_{\rm eq}^2} + \frac{2Y_X^{\rm eq}Y_X^{\rm eq}\langle\sigma_{X^{(\dagger)}X^{(\dagger)}}v_{\rm rel}\rangle}{\tilde{Y}_{\rm eq}^2} \\ &+ \frac{4Y_\chi^{\rm eq}Y_X^{\rm eq}\langle\sigma_{\chi X^{(\dagger)}}v_{\rm rel}\rangle}{\tilde{Y}_{\rm eq}^2} + \frac{Y_\chi^{\rm eq}Y_\chi^{\rm eq}\langle\sigma_{\chi\chi}v_{\rm rel}\rangle}{\tilde{Y}_{\rm eq}^2} \\ &= \frac{2}{\left[g_\chi + 2\sum_i g_{X_i}(1+\delta)^{3/2}e^{-\delta z}\right]^2}\Bigg[\Big(\langle\sigma_{XX^\dagger}v_{\rm rel}\rangle + \langle\sigma_{X^{(\dagger)}X^{(\dagger)}}v_{\rm rel}\rangle\Big)g_X^2(1+\delta)^3\,e^{-2z\delta} \\ &\quad + 2\langle\sigma_{\chi X^{(\dagger)}}v_{\rm rel}\rangle g_X g_\chi(1+\delta)^{3/2}e^{-\delta z} + \langle\sigma_{\chi\chi}v_{\rm rel}\rangle g_\chi^2\Bigg]. \end{aligned} \tag{V.2}$$

where we have taken into account the multiplicities originating from the summation in Eq. (IV.23).

Notice how, for large mass splittings ($\delta \gg 1$), the co-annihilation contributions from the cross-sections $\langle\sigma_{XX^\dagger}v_{\rm rel}\rangle$, $\langle\sigma_{X^{(\dagger)}X^{(\dagger)}}v_{\rm rel}\rangle$, and $\langle\sigma_{\chi X^{(\dagger)}}v_{\rm rel}\rangle$ become completely negligible, while only direct DM annihilations, $\langle\sigma_{\chi\chi}v_{\rm rel}\rangle$, can produce DM particles, as expected.

In the degenerate limit ($\delta = 0$), all coannihilation processes contribute to the effective production rate. Their relative weights are given by

$$\frac{2g_X^2}{(g_\chi + 2\sum_i g_{X_i})^2},\quad \frac{2g_X^2}{(g_\chi + 2\sum_i g_{X_i})^2},\quad \frac{4g_X g_\chi}{(g_\chi + 2\sum_i g_{X_i})^2},\quad \frac{g_\chi^2}{(g_\chi + 2\sum_i g_{X_i})^2}, \tag{V.3}$$

corresponding to the channels XX^*, X^*X, $X\chi$, and $\chi\chi$, respectively.

For the u_R and d_R models, we consider three copies of $SU(2)$-singlet colored scalars. Each scalar carries only color degrees of freedom, yielding $g_X = 3$, while the Majorana singlet dark matter particle has $g_\chi = 2$. Since there are three mediator fields, we obtain $\sum_i g_{X_i} = 9$, and therefore

$$g_\chi + 2\sum_i g_{X_i} = 20. \tag{V.4}$$

Substituting these values into Eq. (V.3), the relative contributions of the four channels are

$$(XX^*,\ X^*X,\ X\chi,\ \chi\chi) = (0.045,\ 0.045,\ 0.06,\ 0.01), \tag{V.5}$$

In contrast, the q_L model involves $SU(2)$-doublet mediators, leading to six copies of color-triplet scalars. In this case, $\sum_i g_{X_i} = 18$, and thus

$$g_\chi + 2\sum_i g_{X_i} = 38. \tag{V.6}$$

The corresponding relative contributions become

$$(XX^*,\ X^*X,\ X\chi,\ \chi\chi) = (0.0125,\ 0.0125,\ 0.0166,\ 0.0028), \tag{V.7}$$

The larger multiplicity of mediators in the q_L model therefore enlarges the denominator in Eq. (V.3), suppressing the effective annihilation rate relative to the u_R and d_R cases. This difference constitutes the main qualitative distinction among the three models in the computation of the relic abundance (cf. Section V.3), although the absolute magnitudes of the individual annihilation cross-sections may differ substantially.

In the co-annihilating parameter region, we observe that t-channel direct annihilations of DM into quarks, as well as pair annihilations of the scalar-antiscalar triplets into quark-antiquark pairs, are velocity-suppressed in the massless quark limit and are therefore

Process	Contribution to $\langle\sigma v\rangle$	$v_{\rm rel}$	Colour structure	BSF
$\chi\chi \to q_i\bar{q}_i$	$g_{\rm DM}^4$	$v_{\rm rel}^2$ $(m_q = 0)$ $v_{\rm rel}^0$ $(m_q \neq 0)$	none	✗
$X_i X_j^\dagger \to gg$	$g_s^4 e^{-2z\delta}$	$v_{\rm rel}^0$	$\vert\mathcal{M}\vert^2\sim \frac{2}{7}[\mathbf{1}] + \frac{5}{7}[\mathbf{8}]$	✓
$X_i X_j^\dagger \to q_i\bar{q}_j$	$(\alpha g_{\rm DM}^2 + \beta g_s^2)^2 e^{-2z\delta}$	$v_{\rm rel}^2$ $(m_q = 0)$ $v_{\rm rel}^0$ $(m_q \neq 0)$	$\vert\mathcal{M}\vert^2\sim f_1(g_{\rm DM}, g_s)[\mathbf{1}]$ $+f_8(g_{\rm DM}, g_s)[\mathbf{8}]$	
$X_i X_j \to q_i q_j$	$g_{\rm DM}^4 e^{-2z\delta}$	$v_{\rm rel}^0$	$\vert\mathcal{M}\vert^2\sim \frac{1}{3}[\bar{\mathbf{3}}] + \frac{2}{3}[\mathbf{6}]$	✓
$X_i X_i \to q_i q_i$	$g_{\rm DM}^4 e^{-2z\delta}$	$v_{\rm rel}^0$	$\vert\mathcal{M}\vert^2\sim [\mathbf{6}]$	
$X_i\chi \to q_i A$	$g_{\rm DM}^2 g_{\rm gauge}^2 e^{-z\delta}$	$v_{\rm rel}^0$	none	✗

Table V.1: Summary of the key processes contributing to DM (co-)annihilation (see corresponding Feynman diagrams in Fig. V.1). The second column details the coupling structure and the suppression factor associated with the mass splitting δ. Here, $g_{\rm gauge}$ represents the gauge coupling at the $q\bar{q}A$ vertex, where A denotes the relevant gauge boson (such as g, γ, Z, and $W^\pm$, with $W^\pm$ applying exclusively to the q_L model). In the $XX^\dagger \to q\bar{q}$ process, α and β generically represent contributions from Yukawa- and gluon-mediated interactions. The third column provides the dominant velocity dependence of $\sigma v_{\rm rel}$ in the low-velocity limit, distinguishing between massive and massless quarks, with the latter being most pertinent to our analysis. The fourth column breaks down the squared matrix element into contributions from different color configurations $[\hat{\mathbf{R}}]$, where f_1 and f_8 are functions of the coupling constants. The fifth column indicates whether the initial-state particles can (✓) or cannot (✗) form a bound state, with a ✓ symbol denoting suppressed BSF when particles are not in conjugate representations. *Table created by the thesis author for [1].*

subdominant across nearly all relevant parameter space. The top quark mass, however, would not be negligible for light DM and small mass splittings. Yet, as shown in Section V.3, typical Yukawa couplings in this parameter space are $g_{\rm DM} \lesssim 10^{-1}$, and these processes are further suppressed by $g_{\rm DM}^4$.

Generally, when the Yukawa coupling $g_{\rm DM}$ is smaller than the strong coupling g_s, processes that lack gluon vertices are negligible, even if they are not velocity-suppressed (e.g., $XX \to qq$).

V.1.1 Long-Range Effects for Coloured Annihilations

As detailed in Section IV.4, coloured (annihilation) processes are affected in the non-relativistic regime by the long-range Coulomb gluon potential of the interacting mediators via the non-perturbative SE. Moreover, the formation and subsequent decay and ionization of Bound States (BS) of the dark sector mediators act effectively as an additional annihilation channel for the DM particles in the co-annihilation regime (small mass splittings).

V.1.1.1 Sommerfeld Effect

Given that the mediators are color triplets, their interaction is decomposed as $\mathbf{3}\otimes\bar{\mathbf{3}} = \mathbf{1}\oplus\mathbf{8}$ and $\mathbf{3}\otimes\mathbf{3} = \bar{\mathbf{3}}\oplus\mathbf{6}$, leading to the potentials given in Eqs. (IV.101) to (IV.104).

This means that the Sommerfeld-corrected cross-sections can be written as (see also [342])

$$\sigma_{\mathbf{3}\otimes\bar{\mathbf{3}}\to gg} v_{\rm rel} = \sigma_{\mathbf{3}\otimes\bar{\mathbf{3}}\to gg,0}\left(\frac{2}{7}S_{0,[\mathbf{1}]} + \frac{5}{7}S_{0,[\mathbf{8}]}\right), \tag{V.8}$$

$$\sigma_{\mathbf{3}\otimes\bar{\mathbf{3}}\to q\bar{q}} v_{\rm rel} = \sigma_{\mathbf{3}\otimes\bar{\mathbf{3}},0}\left(f_{[\mathbf{1}]}(g_s, g_{\rm DM})S_{0,[\mathbf{1}]} + f_{[\mathbf{8}]}(g_s, g_{\rm DM})S_{0,[\mathbf{8}]}\right), \tag{V.9}$$

$$\sigma_{\mathbf{3}\otimes\mathbf{3}\to qq} v_{\rm rel} = \sigma_{\mathbf{3}\otimes\mathbf{3}\to qq,0}\, S_{0,[\mathbf{6}]}\,, \tag{V.10}$$

$$\sigma_{\mathbf{3}_i\otimes\mathbf{3}_j\to q_i q_j} v_{\rm rel} = \sigma_{\mathbf{3}_i\otimes\mathbf{3}_j\to q_i q_j,0}\left(\frac{1}{3}S_{0,[\bar{\mathbf{3}}]} + \frac{2}{3}S_{0,[\mathbf{6}]}\right). \tag{V.11}$$

Here, we used the s-wave Sommerfeld factors in Eq. (IV.105)

$$S_{0,[\mathbf{R}]} = S_0\left(k_{[\mathbf{R}]}\frac{\alpha_s}{v_{\rm rel}}\right) \tag{V.12}$$

As anticipated, when $v_{\rm rel} \lesssim k_{[\mathbf{R}]}\alpha_s$, the SE can significantly impact the perturbative cross-sections, by either substantially amplifying (attractive potential) or reducing (repulsive potential) it, thereby affecting the annihilation processes discussed in Section V.1. Making use of the four values of $k_{[\mathbf{R}]}$ from the potentials in Eqs. (IV.101) to (IV.104), the four necessary SE factors are [342]:

$$S_{0,[\mathbf{1}]} = S_0\left(\frac{4\alpha_s^S}{3v_{\rm rel}}\right),\ S_{0,[\mathbf{8}]} = S_0\left(\frac{-\alpha_s^S}{6v_{\rm rel}}\right),\ S_{0,[\bar{\mathbf{3}}]} = S_0\left(\frac{2\alpha_s^S}{3v_{\rm rel}}\right),\ S_{0,[\mathbf{6}]} = S_0\left(\frac{-\alpha_s^S}{3v_{\rm rel}}\right). \tag{V.13}$$

We notice that the annihilation into a quark-antiquark pair is the most intricate case. In fact, decomposing the color structure of the amplitude is nontrivial due to the interference between QCD- and Yukawa-dominated diagrams [342]. Generally, each term in the squared matrix element must be evaluated for its individual color contribution, and the resulting color weight factors—here represented as functions $f_{[\mathbf{1}]}$ and $f_{[\mathbf{8}]}$ of the couplings g_s and $g_{\rm DM}$—must then be determined. However, since these processes are velocity-suppressed in our model, we will neglect the SE for them.

Finally, in the last process in Eq. (V.11), we consider the case of distinguishable particles in both the initial and final states. This situation arises, for instance, in reactions like $X_i + X_j \to q_i + q_j$, where i and j refer to distinct flavors.

Notice that, for annihilation processes dominated by velocity-dependent terms (see Table V.1), it is important to consider SE corrections across different partial-wave contributions. However, in the following, we focus exclusively on the dominant s-wave SE corrections, disregarding higher partial-wave contributions. The latter introduces corrections proportional to $\zeta_s^2 \propto \alpha_s^2$, which are of order $\mathcal{O}(10^{-2})$ and do not significantly alter the results.

V.1.1.2 Bound State Formation

The colored scalars can form bound states, as demonstrated in the previous chapter and the possible BSF channels are constrained by color algebra. For scalars transforming as triplets and anti-triplets under $SU(3)$, the decomposition of tensor products determines which capture processes are allowed. In the case of particle–antiparticle scattering, gauge invariance permits the transitions

$$(X + X^\dagger)_{[\mathbf{8}]} \to \{\mathcal{B}(XX^\dagger)_{[\mathbf{1}]} + g\}_{[\mathbf{8}]}, \tag{V.14a}$$

$$(X + X^\dagger)_{[\mathbf{1}]} \to \{\mathcal{B}(XX^\dagger)_{[\mathbf{8}]} + g\}_{[\mathbf{1}_S]}, \tag{V.14b}$$

$$(X + X^\dagger)_{[\mathbf{8}]} \to \{\mathcal{B}(XX^\dagger)_{[\mathbf{8}]} + g\}_{[\mathbf{8}_{S,A}]}. \tag{V.14c}$$

However, only the color-singlet potential is attractive. As a result, capture into singlet bound states from an octet initial configuration dominates the phenomenology and is the only process retained in the following. Possible exceptions may arise in the presence of additional attractive long-range forces, such as Higgs exchange, which are not considered here (see instead Refs. [352, 376]).

Analogous considerations apply to particle–particle scattering. While several color channels are in principle allowed, capture into $[\bar{\mathbf{3}}]$ bound states suffers from destructive interference at the level of the squared matrix element [1, 345]. Consequently, these contributions are parametrically suppressed, and the dominant BSF effect again originates from the formation of the color-singlet ground state $(n\ell m) = (100)$.

Excited bound states can, in general, participate indirectly through radiative transitions or direct decays, thereby modifying the annihilation history. Recent studies have systematically incorporated these effects [346, 347, 375]. In the co-annihilation regime relevant for this thesis, however, their quantitative impact remains subleading, and restricting the analysis to the ground state provides an accurate description. Updated treatments, including excited-state dynamics, can be found in [7, 8].

V.1.1.3 Model-Specific BSF Considerations

For the simplified t-channel models considered in this work, several specific aspects of bound state dynamics are relevant:

Constituent instabilities

The colored scalars themselves can decay via Yukawa interactions into a DM particle and a quark. Including such effects consistently through detailed balance necessarily increases the effective BSF contribution. We adopt the conservative approach of neglecting constituent decays, which provides a lower bound on the impact of bound states.

Flavor considerations

Bound states formed from different-flavor scalar pairs have suppressed contributions. Their decay into gluons is forbidden by the flavor-diagonal structure of the Lagrangian, and decays into quark-antiquark pairs are both coupling- and velocity-suppressed. These channels can be safely neglected in the co-annihilation regime.

V.1.1.4 Neglecting Electroweak Potentials

In our analysis, we neglect the Yukawa-type potentials induced by electroweak gauge boson exchange (see, e.g., [330, 355, 378–380] for dedicated studies). At long distances, these interactions are exponentially suppressed, making their impact negligible for light dark matter. A sizeable correction would require the Bohr radius of the two-body state to be smaller than the mediator's Compton wavelength, i.e.

$$(\alpha\, m_X/2)^{-1} \lesssim m_A^{-1} \Longleftrightarrow \mu\alpha < m_A \tag{V.15}$$

For electroweak-strength couplings ($\alpha \simeq 0.02$), this condition is only fulfilled if the coloured partner mass satisfies $m_X \gtrsim 8$ TeV. On the other hand, freeze-out typically occurs at $T \sim m_\chi/30 \simeq m_X/30$ in the co-annihilation regime. Since electroweak symmetry breaking takes place at $T_{\rm EWSB} \sim 150$ GeV, the W and Z bosons are massive during freeze-out only if $m_X \lesssim 4.5$ TeV. Consequently, for the mass range of interest in this study, the electroweak contribution to the potential can safely be ignored.

We demonstrate the statement above with a simple estimate. Consider a mediator mass $m_X \simeq 2$TeV, so that its reduced mass is $\mu \simeq 1$TeV. Taking typical values of the gauge coupling constants at the TeV scale, we have [381]:

$$g_3 \simeq 1.1 \implies \alpha_3 = \frac{g_3^2}{4\pi} \simeq 0.096\,, \tag{V.16}$$

$$g_2 \simeq 0.65 \implies \alpha_2 = \frac{g_2^2}{4\pi} \simeq 0.033\,, \tag{V.17}$$

$$g_1 \simeq 0.45 \implies \alpha_1 = \frac{g_1^2}{4\pi} \simeq 0.016\,. \tag{V.18}$$

This implies

$$\mu\alpha_3 \simeq 96\text{GeV} > m_g = 0\,, \tag{V.19}$$

$$\mu\alpha_2 \simeq 33\text{GeV} < m_W \simeq 80\text{GeV}\,, \tag{V.20}$$

$$\mu\alpha_1 \simeq 16\text{GeV} < m_Z \simeq 91\text{GeV}\,. \tag{V.21}$$

$$\tag{V.22}$$

Thus, the condition in Eq. (V.15) is fulfilled only for the α_3 coupling, making it the only relevant long-range interaction at such energy scales. Equivalently, if we write the potential of a mediator charged under all the SM gauge groups, and we take the singlet representations of the two-particle interaction forming the bound states in $SU(3)_c$ and $SU(2)_L$, and with weak hypercharge equal to 1/2, we obtain:

$$V(r) = -\frac{4}{3}\frac{\alpha_3}{r} - \frac{3}{4}\frac{\alpha_2}{r}e^{-m_W r} - \frac{1}{4}\frac{\alpha_1}{r}e^{-m_Z r}\,. \tag{V.23}$$

Plugging the values of the coupling strengths and evaluating the potential at the shortest Bohr radius for $\mu = 1$TeV, the strong coupling one,

$$(\mu\alpha_3)^{-1} = 1.04 \times 10^{-2}\text{GeV}^{-1}\,,$$

one obtains

$$V(r = (\mu\alpha_3)^{-1}) \simeq \underbrace{-12.307}_{g} - \underbrace{1.002}_{W} - \underbrace{0.149}_{Z}\,. \tag{V.24}$$

This confirms the dominance of the strong coupling at the TeV energy scale at the strong coupling Bohr radius. For larger Bohr radii, such as the ones of the α_2 and α_1 couplings, the effect is even more pronounced.

The relic density calculation presented in the following sections incorporates bound state effects through the effective annihilation cross-section Eq. (IV.112), which captures late-time mediator depletion while remaining conservative with respect to constituent instabilities and flavor-off-diagonal bound states. The corresponding cosmological evolution is governed by the modified Boltzmann equation discussed in Chapter IV (cf. Eq. (IV.87)).

V.2 Numerical Implementation of SE and BSF for Coloured Model

Declaration: The theoretical framework outlined in Section IV.4 provides the basis for the present section, where we concentrate on the numerical implementation of SE and BSF effects in simplified t-channel models. The derivation of the results, as well as their mathematical formulation and numerical realization for the models considered, was carried out by the thesis author and MB in [1]. This work was performed in close and continuous collaboration with JH, who originally proposed the underlying idea and provided guidance on its numerical implementation. The implementation presented here establishes the foundational framework for this approach and predates the more advanced developments later published in Refs. [7, 8]. The text has been substantially revised from the original publication and supplemented with additional material.

Building upon the theoretical framework developed in Section IV.4, we now turn to the practical implementation of SE and BSF effects in simplified t-channel models. To compute the DM relic abundance, we employ the numerical package `micrOMEGAs` [315,382], a widely used tool for precision calculations in particle dark matter phenomenology.

`micrOMEGAs` is a `C`-based framework designed to compute the relic density of DM in generic particle physics models, together with a broad range of related observables, including direct and indirect detection cross sections, collider signatures, and other phenomenological quantities. It supports thermal freeze-out scenarios with up to two DM components, freeze-in production including relativistic and quantum-statistical effects, and, in its most recent versions [383], multi-component dark sectors and conversion-driven freeze-out. The program is interfaced with `CalcHEP` [384], which automatically generates Feynman diagrams and evaluates matrix elements and phase-space integrals once the particle model is specified. Model information can be provided in the Universal FeynRules Output (UFO) format [192], enabling the automated construction of all relevant amplitudes and cross sections. This integrates perfectly with the universal t-channel framework described in Section II.2.4 (see [6]).

Thanks to this infrastructure, `micrOMEGAs` efficiently computes all annihilation and co-annihilation processes contributing to the evolution of the DM number density and numerically solves the Boltzmann equation to obtain the final relic abundance.

However, the public version of `micrOMEGAs` does not provide an automated treatment of non-perturbative effects such as Sommerfeld enhancement, which are crucial in models with long-range interactions like those considered here. Moreover, bound-state formation and the subsequent decay and ionization processes, which can significantly alter the relic abundance in the co-annihilation regime, are not implemented by default.

To incorporate these effects while preserving the numerical efficiency and flexibility of `micrOMEGAs`, we extended the code by modifying existing routines and implementing new modules tailored to the computation of SE and BSF contributions.

V.2.1 Strong Coupling Constants

The implementation of the SE and BSF in `micrOMEGAs` requires the evaluation of the strong coupling constant at the characteristic momentum scales of the underlying non-relativistic processes. Since these scales differ significantly between scattering, bound-state dynamics, and radiative transitions, a consistent treatment of the running coupling $\alpha_s(Q)$ is essential.

The momentum dependence of α_s is already implemented in `micrOMEGAs` through the function `alphaQCD(Q)`, which solves the renormalization group equation for the QCD coupling. More precisely, the scale evolution of $\alpha_s(Q)$ is governed by the QCD β-function,

$$Q^2 \frac{\mathrm{d}\alpha_s}{\mathrm{d}Q^2} = -\left(b_0\alpha_s^2 + b_1\alpha_s^3 + \dots\right) , \tag{V.25}$$

$$b_0 = \frac{11C_A - 4n_f T_R}{12\pi} = \frac{33 - 2n_f}{12\pi} , \tag{V.26}$$

$$b_1 = \frac{17C_A^2 - n_f T_R(10C_A + 6C_F)}{24\pi^2} = \frac{153 - 19n_f}{24\pi^2} , \tag{V.27}$$

where n_f denotes the number of active quark flavours at the scale Q, and C_A, C_F, and T_R are the usual $SU(3)$ colour factors. In `micrOMEGAs`, the running of $\alpha_s(Q)$ is implemented up to next-to-next-to-leading order (NNLO).

However, in the presence of long-range interactions and bound states, the relevant momentum transfer is process-dependent and must be determined self-consistently.

Relevant momentum scales.

For scattering states entering the Sommerfeld effect, the typical momentum transfer is set by the relative momentum of the incoming particles,

$$Q_{\mathrm{SE}} \sim \mu v_{\mathrm{rel}}, \tag{V.28}$$

where $\mu = m_X/2$ is the reduced mass of the interacting pair. For bound states in a colour representation $\hat{\mathbf{R}}$, the characteristic scale is instead the Bohr momentum,

$$\kappa_{[\hat{\mathbf{R}}]} \equiv \mu\, \alpha^B_{g,[\hat{\mathbf{R}}]}, \tag{V.29}$$

which controls the bound-state wavefunction and the potential entering the Schrödinger equation.

Radiative bound-state formation involves an additional momentum scale associated with the emitted gluon. In the non-relativistic limit, energy conservation implies

$$Q^{\mathrm{BSF}} \equiv \omega \simeq \mathcal{E}_{\mathbf{k}} - \mathcal{E}_{n\ell m} = \frac{\mu}{2}\left[v_{\mathrm{rel}}^2 + (\alpha^B_{g,[\hat{\mathbf{R}}]})^2\right] , \tag{V.30}$$

while gluon emission from the exchanged mediator in non-Abelian diagrams is characterized by

$$Q^{\mathrm{NA}} \simeq |\mathbf{p} - \mathbf{q}| \simeq \mu\sqrt{v_{\mathrm{rel}}^2 + (\alpha^B_{g,[\hat{\mathbf{R}}]})^2}. \tag{V.31}$$

In the regime where BSF is most efficient, $v_{\mathrm{rel}} \ll \alpha^B_g$, one finds $Q^{\mathrm{NA}} \simeq \mu\, \alpha^B_{g,[\hat{\mathbf{R}}]} = \kappa_{[\hat{\mathbf{R}}]}$, such that the strong coupling entering the non-Abelian vertex coincides with that governing the bound-state potential.

Vertices	α_s	α_g	**Average momentum transfer Q**
Wavefunction (ladder diagram) of *scattering* rate in colour rep. $\hat{\mathbf{R}}$	α_s^S	$\alpha^S_{g,[\mathbf{R}]} = (\alpha_s^S/2)\times$ $\times[C_2(\mathbf{R_1}) + C_2(\mathbf{R_2}) - C_2(\hat{\mathbf{R}})]$	$k = \mu v_{\mathrm{rel}}$
Wavefunction (ladder diagram) of *scattering* rate in colour rep. $\hat{\mathbf{R}}$	$\alpha^B_{s,[\hat{\mathbf{R}}]}$	$\alpha^B_{g,[\mathbf{R}]} = (\alpha_s^S/2)\times$ $\times[C_2(\mathbf{R_1}) + C_2(\mathbf{R_2}) - C_2(\hat{\mathbf{R}})]$	$\kappa_{\hat{\mathbf{R}}} = \mu\alpha^B_{g,[\mathbf{R}]}$
Formation of bound states of colour rep. $\hat{\mathbf{R}}$: gluon emission	$\alpha^{\mathrm{BSF}}_{s,[\hat{\mathbf{R}}]}$		$\mathcal{E}_{\mathbf{k}} - \mathcal{E}_{n\ell} =$ $\frac{\mu}{2}\left[v_{\mathrm{rel}}^2 + (\alpha^B_{g,[\mathbf{R}]}/n)^2\right]$
Radiative vertex in non-Abelian diagram for capture in colour rep. $\hat{\mathbf{R}}$	$\alpha^{\mathrm{NA}}_{s,[\hat{\mathbf{R}}]}$		$\mu\sqrt{v_{\mathrm{rel}}^2 + (\alpha^B_{g,[\mathbf{R}]})^2}$

Table V.2: The definition of the strong coupling constants $\alpha_s(Q)$ used in this work and their dependence on the colour representation $\hat{\mathbf{R}}$ of the interaction and on the average momentum transfer Q at which they are evaluated. Taken from Tab. 1 in [351].

Definition of effective couplings.

For each process, we introduce three scale-dependent strong couplings,

$$\alpha_s^{\mathrm{B}}(Q), \qquad \alpha_s^{\mathrm{BSF}}(Q), \qquad \alpha_s^{\mathrm{NA}}(Q), \tag{V.32}$$

which are evaluated at the corresponding momentum scales and combined with colour factors to define the effective interaction strength $\alpha_g^{[\hat{\mathbf{R}}]}(Q) = k_{[\hat{\mathbf{R}}]}\alpha_s(Q)$. The colour decomposition of the relevant two-particle states is given by

$$\mathbf{3}\otimes\bar{\mathbf{3}} = \mathbf{1}\oplus\mathbf{8}, \qquad \mathbf{3}\otimes\mathbf{3} = \bar{\mathbf{3}}\oplus\mathbf{6}, \qquad \bar{\mathbf{3}}\otimes\bar{\mathbf{3}} = \mathbf{3}\oplus\bar{\mathbf{6}}\,. \tag{V.33}$$

All relevant momentum scales and coupling definitions are summarized in Table V.2.

Numerical implementation.

To efficiently evaluate these couplings during the relic-density computation, we precompute α_s^{B}, α_s^{BSF}, and α_s^{NA} for a grid of reduced masses μ and relative velocities v_{rel}. The resulting values are stored in lookup tables (`alpha_table_331`, `alpha_table_333`, `alpha_table_336`, `alpha_table_338`) corresponding to the different colour channels. They are accessed through dedicated routines such as `read_table_alpha331(void)`, while the function `alphaS_type(type,mX,vrel,*table)` returns the appropriate coupling constant for a given process, mass, and velocity.

This allows for a systematic and representation-independent construction of the effective QCD potentials entering the SE and BSF calculations.

V.2.2 Sommerfeld Effect Implementation

The SE modifies the annihilation and co-annihilation cross sections of non-relativistic particles by resumming long-range interactions in the initial state. In general, SE depends on the partial-wave decomposition of the scattering amplitude and on the colour structure of the interacting particles, as discussed in Sections IV.2.3 and IV.4.1.

In this work, we restrict ourselves to the dominant contributions relevant for coloured co-annihilation in simplified t-channel models:

- s-wave dominated processes,
- gluon-mediated long-range interactions,
- initial states in the $\mathbf{3}$ and $\bar{\mathbf{3}}$ representations of $SU(3)$.

This approximation captures the leading non-perturbative effects in the parameter region of interest while keeping the numerical implementation tractable.

Coulomb Sommerfeld factor.

For a Coulomb-like potential, the s-wave Sommerfeld factor is given by

$$S_0(\zeta) = \frac{2\pi\zeta}{1 - e^{-2\pi\zeta}}, \qquad \zeta = \frac{\alpha}{v_{\rm rel}}. \tag{V.34}$$

We implement this expression in `C++` as follows:

```cpp
double SommerfeldCoulomb(double zeta)
{
    if (std::abs(zeta) < 1e-12) return 1.0;
    return 2.0 * M_PI * zeta / (1.0 - std::exp(-2.0 * M_PI * zeta));
}
```

This function returns the Coulomb enhancement factor and is numerically stable in the limit $v_{\rm rel} \to 0$.

Colour-decomposed Sommerfeld factors.

For coloured particles, the Sommerfeld factor must be projected onto the irreducible colour representations of the initial state. For the relevant $SU(3)$ decompositions, we implement the factors as described in Sections IV.4.2 and V.1.1.1 and following the rules for identical initial particles, as described in [342]:

$$S_0^{\mathbf{3}\otimes\bar{\mathbf{3}}} = \frac{2}{7} S_0\left(\frac{4}{3}\frac{\alpha_s}{v}\right) + \frac{5}{7} S_0\left(-\frac{1}{6}\frac{\alpha_s}{v}\right), \tag{V.35}$$

$$S_0^{\mathbf{3}\otimes\mathbf{3}} = \begin{cases} \dfrac{1}{3} S_0\left(\dfrac{2}{3}\dfrac{\alpha_s}{v}\right), & X_1 \neq X_2, \\ S_0\left(-\dfrac{1}{3}\dfrac{\alpha_s}{v}\right), & X_1 = X_2 \ (s\text{-wave}), \\ S_0\left(\dfrac{2}{3}\dfrac{\alpha_s}{v}\right), & X_1 = X_2 \ (p\text{-wave}). \end{cases} \tag{V.36}$$

The corresponding implementation automatically selects the appropriate colour coefficients:

```cpp
double SommerfeldFactor(double alphaS, double vrel,
                        int c1, int c2, long n1, long n2, int partialWave)
{
    if (c1 == 1 || c2 == 1) return 1.0; // singlet states

    struct Channel { double cfac, weight; };
    std::vector<Channel> channels;

    // 3 x 3bar -> 1 + 8
    if ((c1 == 3 && c2 == -3) || (c1 == -3 && c2 == 3)) {
        channels.push_back({ 4.0/3.0, 2.0/7.0 });   // singlet
        channels.push_back({-1.0/6.0, 5.0/7.0 });   // octet
    }

    // 3 x 3 or 3bar x 3bar -> 3bar + 6
    if ((c1 == 3 && c2 == 3) || (c1 == -3 && c2 == -3)) {
        if (n1 != n2) {
            channels.push_back({ 2.0/3.0, 1.0/3.0 });
        } else {
            if (partialWave == 0)  // s-wave
                channels.push_back({-1.0/3.0, 1.0});
            else                    // p-wave
                channels.push_back({ 2.0/3.0, 1.0});
        }
    }

    double SE = 0.0;
    for (const auto& ch : channels) {
        double zeta = ch.cfac * alphaS / vrel;
        SE += ch.weight * SommerfeldCoulomb(zeta);
    }
    return SE;
}
```

Sommerfeld-corrected cross sections in `micrOMEGAs`.

To incorporate SE into the relic-density computation without recomputing matrix elements from scratch, we exploit the `micrOMEGAs` hook function

`void improveCrossSection(...).`

This function is automatically called by `micrOMEGAs` during the thermal averaging procedure when computing the DM interaction rate and allows us to modify the cross-sections of the relevant annihilation processes on the fly.

Our strategy is to:

1. identify coloured initial states,
2. extract the s-wave coefficient of the annihilation cross section,
3. evaluate the running strong coupling at the scale $Q = \mu v_{\rm rel}$,
4. compute the colour-decomposed Sommerfeld factor,
5. rescale the cross section accordingly.

The implementation reads:

```cpp
void improveCrossSection(long n1,long n2,long n3,long n4,double Pcm,double *cs)
{
    // Convert PDG codes to particle names
```

```
    char* name1 = pdg2name(n1);
    char* name2 = pdg2name(n2);
    char* name3 = pdg2name(n3);
    char* name4 = pdg2name(n4);

    // Extract quantum numbers (spin, charge, colour)
    int s1,q1,c1, s2,q2,c2;
    qNumbers(name1,&s1,&q1,&c1);
    qNumbers(name2,&s2,&q2,&c2);

    // Apply Sommerfeld effect only to coloured initial states
    if (c1 == 1 || c2 == 1) return;

    // Particle masses
    double mp1 = pMass(name1);
    double mp2 = pMass(name2);
    double mp3 = pMass(name3);
    double mp4 = pMass(name4);

    // Reduced mass of the initial state
    double mu = mp1 * mp2 / (mp1 + mp2);

    // Centre-of-mass energy
    double sqrts = sqrt(mp1*mp1 + Pcm*Pcm) + sqrt(mp2*mp2 + Pcm*Pcm);

    // Relative velocity (relativistic definition)
    double vrel = vRel(Pcm, mp1, mp2);

    // Regulator to avoid divergence at v -> 0
    const double vcut = 1e-5;
    if (vrel < vcut) vrel = vcut;

    // Momentum corresponding to vcut
    double pcut = plowv(vcut, mp1, mp2);

    // Interaction scale for Sommerfeld effect
    double QSE = mu * vrel;

    // Running strong coupling at scale QSE
    double alphaSE = alphaQCD(QSE);

    // Build process name: "X1,X2->X3,X4"
    std::string procString =
        std::string(name1) + "," + name2 + "->" + name3 + "," + name4;

    char* procName = new char[procString.length() + 1];
    strcpy(procName, procString.c_str());

    // Initialize process in micrOMEGAs
    numout* channel = newProcess(procName);
    procInfo1(channel, &nsub, &nin, &nout);

    // Backup current matrix element configuration
    int nsub22mem = nsub22;
    double (*sqme22mem)() = sqme22;

    // Extract s-wave contribution in the low-velocity limit
    int err = 0;
    double swave =
        cs22(channel, 0, pcut, -1.0, +1.0, &err) / (3.89379E8) * vcut;
```

```

    // Compute Sommerfeld factor (s-wave, partialWave = 0)
    double SE = SommerfeldFactor(alphaSE, vrel, c1, c2, n1, n2, 0);

    // Sommerfeld-corrected cross section
    double sigmaV = swave * SE;
    *cs = sigmaV / vrel;

    // Restore matrix element configuration
    nsub22 = nsub22mem;
    sqme22 = sqme22mem;

    delete[] procName;
}
```

Several internal `micrOMEGAs` routines are used in this implementation.

The function `pdg2name` converts a particle identifier into its corresponding model name. It relies on the Particle Data Group (PDG) numbering scheme, which assigns unique integer codes to elementary particles for use in Monte Carlo generators, with positive numbers for particles and negative numbers for antiparticles.

The function `plowv` returns the center-of-mass momentum corresponding to a given relative velocity and particle masses, and is used to consistently extract the low-velocity limit of the annihilation cross section.

Finally, the function `cs22` computes the total $2 \to 2$ scattering cross section for a given process previously initialized by `newProcess`, performing the phase-space integration over the squared matrix element generated by `CalcHEP`.

In this way, Sommerfeld corrections are applied exclusively to processes with coloured initial states, while the automated matrix-element generation of `CalcHEP` is fully preserved. This modular implementation ensures numerical stability, correct colour treatment, and consistent inclusion of velocity-dependent non-perturbative effects in the relic-density computation.

V.2.3 Bound-State Formation Channels Implementation

While the Sommerfeld enhancement modifies the amplitudes of already existing annihilation processes, bound-state formation (BSF) introduces genuinely new reactions that deplete the dark-sector number density in the co-annihilation regime. Therefore, BSF effects cannot be incorporated through the same procedure used for Sommerfeld-corrected scattering cross sections (cf. `improveCrossSection`), but must instead be implemented directly at the level of the Boltzmann equation.

Concretely, the thermally averaged annihilation cross section entering the interaction rate must be promoted to the effective quantity in Eq. (IV.113), which reads as

$$\langle \sigma_{XX^\dagger} v_{\rm rel} \rangle_{\rm eff} = \sum_i \left(\left\langle \sigma_{X_i X_i^\dagger} v_{\rm rel} \right\rangle + \left\langle \sigma_{\rm BSF}^{[\mathbf{8}]\to[\mathbf{1}]} v_{\rm rel} \right\rangle \frac{\Gamma_{{\rm dec}[\mathbf{1}]}}{\Gamma_{{\rm dec}[\mathbf{1}]} + \Gamma_{{\rm ion},[\mathbf{1}]}} \right) . \tag{V.37}$$

This requires a direct modification of the interaction rate appearing on the right-hand side of the Boltzmann equation as implemented in `micrOMEGAs`.

V.2.3.1 Modification of the Boltzmann Solver

In micrOMEGAs, the interaction rate is defined in the source file omega.c. To consistently include BSF effects, three modifications are necessary.

1) Extended integration range.

Bound-state effects typically become relevant at temperatures much lower than the freeze-out temperature, corresponding to $z = m_X/T \sim \mathcal{O}(10^3)$. Therefore, we employ the routines darkOmega2 or darkOmega2TR, which allow manual control of the final integration temperature. We set

$$T_{\text{end}} = 10^{-3}\,\text{GeV}, \tag{V.38}$$

ensuring that the Boltzmann equation is integrated well into the epoch where BSF processes dominate. Given that the mediator masses in the simulation considered range from $\mathcal{O}(100\,\text{GeV})$ to $\mathcal{O}(10\,\text{TeV})$, this choice is conservative and numerically stable.

2) Access to interaction rates.

The dark-sector particle content is initialized via fillCDMmem(), while the interaction rates are constructed through TabDmEq. Within this routine, the function aRate4(T, vs1100, vs2200, ...) computes the thermally averaged annihilation rates of dark-sector particles. Since BSF contributes only once to the annihilation of a given particle pair, it suffices to modify the term vs1100, corresponding to the dominant co-annihilation channel.

3) Insertion of the BSF contribution.

For a model with a single mediator with assigned PDG code 2000002[2] and a dark matter particle with assigned PDG code 52, the BSF contribution to the interaction rate can be added as follows inside the aRate4 function in omega.c:

```
int gDM = 2;
double xJH = pMass(pdg2name(52)) / T;
double deltaJH =
    (pMass(pdg2name(2000002)) - pMass(pdg2name(52)))
    / pMass(pdg2name(52));

vs1100 += improveAveragedCrossSection(2000002, -2000002,
                                      pMass(pdg2name(52)), T)
          * g1 * g1 * 2.0 * pow(3.0, 2) * pow(1.0 + deltaJH, 3)
          / pow(gDM * exp(xJH * deltaJH)
                + 2.0 * 3.0 * pow(1.0 + deltaJH, 3.0 / 2.0), 2);
```

Here, deltaJH denotes the relative mass splitting between the mediator and the dark matter particle. The function improveAveragedCrossSection computes the effective BSF contribution to $\langle \sigma v \rangle$, including ionization and decay effects.

V.2.3.2 Structure of the BSF Implementation

The function improveAveragedCrossSection constitutes the core of the BSF implementation. It evaluates the effective bound-state formation cross section derived in Eq. (IV.112) by combining three ingredients:

- the BSF cross-section via integrating bsf_cs_integrand,

[2]In the actual three S3M models, we obviously account for all the present flavour families.

- the bound-state ionization rate via integrating `vsf_ion_integrand`
- the bound-state decay width defined with `GammaDecay`

These quantities are implemented through the following routines:

BSF Cross-section Integrand

This routine computes the integrand of the thermal average of the BSF cross-section (cf. Eq. (IV.69)):

$$\langle \sigma_{\rm BSF} v_{\rm rel} \rangle = \left(\frac{\mu}{2\pi T}\right)^{3/2} \int \mathrm{d}^3 v_{\rm rel} \exp\!\left(-\mu v_{\rm rel}^2/2T\right) \left[1 + f_g(\omega)\right] \sigma_{\rm BSF} v_{\rm rel} \,.$$

For a given relative velocity $v_{\rm rel}$ and set of model parameters, it evaluates the BSF cross section, including the appropriate color factors and gauge couplings (evaluated at the correct momentum), and multiplies it by the phase-space measure and thermal distribution functions. Special care is taken in the $v_{\rm rel} \to 0$ limit, where an analytic expression is used to avoid numerical instabilities arising from the $1/v_{\rm rel}$ behaviour of the BSF factor. The resulting quantity is later integrated over the relative velocity for thermal averaging.

```
double bsf_cs_integrand(double vrel, const Parameters& pars)
{
    const int c1 = pars.color1;
    const int c2 = pars.color2;
    const double mu = pars.m;
    const double T  = pars.T;

    double result = 0.0;

    // Couplings
    double alpha_s_BSF = 0.0;
    double alpha_s_B   = 0.0;
    const double alpha_s_S = alphaQCD(mu * vrel);
    double alpha_g_B   = 0.0;
    double alpha_g_S   = 0.0;

    // Only color triplet-antitriplet case
    if ((c1 == 3 && c2 == -3) || (c1 == -3 && c2 == 3)) {
        alpha_s_B   = alphaS_type(1, mu, vrel, alpha_table_331);
        alpha_s_BSF = alphaS_type(2, mu, vrel, alpha_table_331);
        alpha_g_B   = 4.0 / 3.0 * alpha_s_B;
        alpha_g_S   = -1.0 / 6.0 * alpha_s_S;
    }

    if (c1 == -c2) {
        const double cas2  = casimir2(c1);
        const double cas2G = casimir2(8);
        const double dR    = static_cast<double>(c1);
        const double fc    = std::pow(1.0 + cas2G / (2.0 * cas2), 2.0);

        const double omega = mu / 2.0 * (std::pow(alpha_g_B, 2) + std::pow(vrel, 2));

        const double bose =
            1.0 + 1.0 / (std::exp(omega / T) - 1.0);

        const double boltzmann =
            std::pow(mu / (2.0 * M_PI * T), 1.5) *
            std::exp(-mu * vrel * vrel / (2.0 * T));

```

```
        double S_BSF = 0.0;

        if (vrel > 1e-5) {
            const double zeta_s = alpha_g_S / vrel;
            const double zeta_b = alpha_g_B / vrel;

            S_BSF =
                2.0 * M_PI * zeta_s / (1.0 - std::exp(-2.0 * M_PI * zeta_s)) *
                (1.0 + zeta_s * zeta_s) *
                std::pow(zeta_b, 4) *
                std::exp(-4.0 * zeta_s * acot(zeta_b)) /
                std::pow(1.0 + zeta_b * zeta_b, 3);
        } else {
            // v -> 0 limit
            S_BSF =
                2.0 * std::exp(-4.0 * alpha_g_S / alpha_g_B) *
                M_PI * std::pow(alpha_g_S, 3) / std::pow(alpha_g_B, 2);
        }

        const double sigma_v =
            M_PI * alpha_s_BSF * alpha_g_B / (mu * mu) *
            std::pow(2.0, 7) / 3.0 * cas2 / (dR * dR) * fc * S_BSF;

        const double measure =
            4.0 * M_PI * (vrel > 1e-5 ? vrel * vrel : vrel);

        result = sigma_v * measure * bose * boltzmann;
    }

    return result;
}
```

Ionization Rate Integrand

This routine computes the integrand of the thermal average of the bound-state dissociation cross section, as given in Eqs. (IV.109) and (IV.110):

$$\Gamma_{\text{ion},[\mathbf{1}]} = g_g \int_{\omega_{\min}}^{\infty} \mathrm{d}\omega \frac{\omega^2}{2\pi^2} \frac{1}{e^{\omega/T}-1} \sigma_{\text{ion}},$$
$$\sigma_{\text{ion}} = \frac{g_X^2}{g_g g_{\mathcal{B}}} \left(\frac{\mu^2 v_{\text{rel}}^2}{\omega^2}\right) \sigma_{\text{BSF}}.$$

It evaluates the BS ionization cross-section for a given relative velocity v_{rel}, including color factors, gauge couplings, and statistical factors associated with gluon absorption. The integrand is weighted by the appropriate phase-space measure and thermal occupation number (following the Boltzmann distribution). As in the BSF case, the $v_{\text{rel}} \to 0$ limit is treated analytically to ensure numerical stability. The result determines the rate of bound-state destruction in the thermal plasma.

```
double bsf_diss_integrand(double vrel, const Parameters& pars)
{
    const int c1 = pars.color1;
    const int c2 = pars.color2;
    const int s1 = pars.spin;
    const double mu = pars.m;
    const double T  = pars.T;
```

```

    double result = 0.0;

    double alpha_s_BSF = 0.0;
    double alpha_s_B   = 0.0;
    const double alpha_s_S = alphaQCD(mu * vrel);
    double alpha_g_B   = 0.0;
    double alpha_g_S   = 0.0;

    if ((c1 == 3 && c2 == -3) || (c1 == -3 && c2 == 3)) {
        alpha_s_B   = alphaS_type(1, mu, vrel, alpha_table_331);
        alpha_s_BSF = alphaS_type(2, mu, vrel, alpha_table_331);
        alpha_g_B   = 4.0 / 3.0 * alpha_s_B;
        alpha_g_S   = -1.0 / 6.0 * alpha_s_S;
    }

    if (c1 == -c2) {
        const double cas2  = casimir2(c1);
        const double cas2G = casimir2(8);
        const double fc    = std::pow(1.0 + cas2G / (2.0 * cas2), 2.0);
        const double gX    = g_i(s1, c1);
        const double gB    = 1.0;

        const double omega = mu / 2.0 * (std::pow(alpha_g_B, 2) + std::pow(vrel, 2));
        const double statistic = 1.0 / (std::exp(omega / T) - 1.0);

        double S_BSF = 0.0;

        if (vrel > 1e-5) {
            const double zeta_s = alpha_g_S / vrel;
            const double zeta_b = alpha_g_B / vrel;

            S_BSF =
                2.0 * M_PI * zeta_s / (1.0 - std::exp(-2.0 * M_PI * zeta_s)) *
                (1.0 + zeta_s * zeta_s) *
                std::pow(zeta_b, 4) *
                std::exp(-4.0 * zeta_s * acot(zeta_b)) /
                std::pow(1.0 + zeta_b * zeta_b, 3);
        } else {
            S_BSF =
                2.0 * std::exp(-4.0 * alpha_g_S / alpha_g_B) *
                M_PI * std::pow(alpha_g_S, 3) / std::pow(alpha_g_B, 2);
        }

        const double sigma_v =
            M_PI * alpha_s_BSF * alpha_g_B / (mu * mu) *
            std::pow(2.0, 7) / 3.0 * cas2 / (c1 * c1) * fc * S_BSF;

        const double prefac =
            std::pow(gX, 2) * std::pow(mu, 3) / (2.0 * std::pow(M_PI, 2) * gB);

        const double measure = (vrel > 1e-5 ? vrel * vrel : vrel);

        result = sigma_v * measure * statistic * prefac;
    }

    return result;
}
```

Decay Rate function

This routine computes the decay width of a bound state formed by two colored particles, which is given by Eq. (IV.78)

$$\Gamma_{\text{dec}} = \left(\sigma_{\text{ann}}^{s\text{-wave}} v_{\text{rel}}\right) |\psi_{100}(0)|^2 .$$

It first determines the relevant quantum numbers and reduced mass of the system, then evaluates the bound-state wave function at the origin in the Coulomb approximation. The decay width is obtained by summing over all allowed annihilation channels through the corresponding s-wave coefficients, with a conservative estimate based on gluonic final states in our simplified treatment. For singlet BS, it reduces to Eq. (IV.111).

```
double GammaDecay(long n1, long n2)
{
    double Gamma = 0.0;
    double swavecoeff = 0.0;
    double WaveFctSq = 0.0;

    const char* name1 = pdg2name(n1);
    const char* name2 = pdg2name(n2);

    int s1, s2, q1, q2, c1, c2;
    qNumbers(name1, &s1, &q1, &c1);
    qNumbers(name2, &s2, &q2, &c2);

    const double m1 = pMass(name1);
    const double m2 = pMass(name2);
    const double mu = m1 * m2 / (m1 + m2);

    double alpha_s_B = 0.0;
    if ((c1 == 3 && c2 == -3) || (c1 == -3 && c2 == 3)) {
        alpha_s_B = alphaS_type(1, mu, 0.1, alpha_table_331);
    }

    // Conservative estimate: gluon final state only
    if (bsfmethod == -1) {
        const long ng = 21; // gluon PDG code

        swavecoeff =
            2.0 / 7.0 *
            coefficient_swave(n1, n2, ng, ng) *
            std::fabs(g_i(s1, c1)) * std::fabs(g_i(s2, c2));

        if (c1 == -c2) {
            WaveFctSq =
                std::pow(2.0, 6) * std::pow(mu, 3) /
                (std::pow(3.0, 3) * M_PI) *
                std::pow(alpha_s_B, 3);

            Gamma = WaveFctSq * swavecoeff;
        }
    }

    for (int i = 0; i < nModelParticles; ++i) {
        for (int j = 0; j < nModelParticles; ++j) {

            const bool ok =
                ModelPrtcls[i].name[0]  != '~' &&
```

```
                ModelPrtcls[i].aname[0] != '~' &&
                ModelPrtcls[j].name[0]  != '~' &&
                ModelPrtcls[j].aname[0] != '~';

            if (!ok) continue;

            const int n3 = ModelPrtcls[i].NPDG;
            const int n4 = ModelPrtcls[j].NPDG;

            if (n3 != 25 && n4 != 25) {
                swavecoeff += coefficient_swave(n1, n2, n3, n4);
            }
        }
    }

    Gamma = WaveFctSq * swavecoeff;
    return Gamma;
}
```

V.2.3.3 Effective BSF Cross Section

The function `improveAveragedCrossSection` performs the following steps:

1. identification of the colour and spin quantum numbers of the initial-state particles;
2. computation of the bound-state decay rate via `GammaDecay`;
3. evaluation of the thermally averaged BSF cross section and ionization rate via numerical integration of `bsf_cs_integrand` and `bsf_ion_integrand` using the native integration methods;
4. construction of the effective BSF contribution,

$$\langle \sigma v \rangle_{\text{BSF,eff}} = \frac{\Gamma_{\text{dec}}}{\Gamma_{\text{dec}} + \Gamma_{\text{ion}}} \langle \sigma v \rangle_{\text{BSF}}. \tag{V.39}$$

A representative implementation is given below:

```
double improveAveragedCrossSection(long n1, long n2,
                                   double mdm, double T)
{
    double Decay_rate = 0.0, Ion_rate = 0.0, bsf_eff = 0.0;

    int s1, s2, q1, q2, c1, c2;
    char* name1 = pdg2name(n1);
    char* name2 = pdg2name(n2);
    qNumbers(name1, &s1, &q1, &c1);
    qNumbers(name2, &s2, &q2, &c2);

    bool o1 = (name1[0] == '~');
    bool o2 = (name2[0] == '~');

    if (o1 && o2 && c1 != 1 && c2 != 1) {

        Decay_rate = GammaDecay(n1, n2);

        if (c1 == -c2) {
            double mu = pMass(name1) * pMass(name2)
                        / (pMass(name1) + pMass(name2));

            Parameters pars = {s1, c1, c2, mu, T};
```

```

            double bsfaverage =
                simpsonArg(bsf_cs_integrand, pars, 0.0, 1.0, 1e-5);

            Ion_rate =
                simpsonArg(bsf_ion_integrand, pars, 0.0, 1.0, 1e-5);

            double decayWeight =
                Decay_rate / (Decay_rate + Ion_rate);

            bsf_eff = decayWeight * bsfaverage;
        }
    }

    return bsf_eff;
}
```

This implementation mirrors the theoretical structure developed in Section IV.4. Bound-state formation acts as an additional depletion channel whose efficiency is controlled by the competition between formation, ionization, and decay. By embedding these effects directly into the interaction rate of the Boltzmann equation, we obtain a consistent and numerically stable treatment of BSF within the `micrOMEGAs` framework.

Having established the complete numerical implementation of Sommerfeld enhancement and bound-state formation effects, we now turn to the phenomenological analysis. The robust computational framework developed above enables systematic parameter scans that reveal how these non-perturbative effects reshape the viable parameter space of simplified t-channel dark matter models. The following sections present the results of these scans and their implications for dark matter phenomenology.

V.3 Impact of SE and BSF on the Model Parameters

Declaration: The results presented in this section are based on a joint analysis by the thesis author and MB, as reported in Ref. [1]. The thesis author contributed in particular to the parameter scans and the preparation of the figures. The interpretation of the results was developed through discussions with MB and JH. The text constitutes a revised version of the original publication, which was co-authored by the thesis author and MB and reviewed by all co-authors.

In this section, we run the modified version of `micrOMEGAs` outlined in Section V.2 for the u_R, d_R, and q_L models, and we assess how long-range effects alter their parameter space. Afterwards, we quantify their influence on the relic density and the corresponding experimental constraints on the parameters of the dark sector.

V.3.1 Mass Splitting vs. Dark Matter Mass

Fig. V.2 illustrates the impact of non-perturbative effects on the viable parameter space in the $(m_{\rm DM}, \Delta m)$ plane for the u_R, d_R, and q_L models introduced in Section V.1. For a fixed Yukawa coupling $g_{\rm DM}$, each band denotes the combinations of $m_{\rm DM}$ and $\Delta m = m_X - m_{\rm DM}$ that reproduce the observed relic abundance within 5σ, $\Omega_{\rm DM}h^2 = 0.120 \pm 0.005$ [75]. Results are shown for two representative values of the coupling: $g_{\rm DM} = 10^{-2}$ (orange) and $g_{\rm DM} = 1$ (blue) and for $m_{\rm DM}$ ranging between 100GeV and 3000GeV, while the mass splitting is varied between 0 and 100GeV. Dotted, dashed, and solid lines correspond to

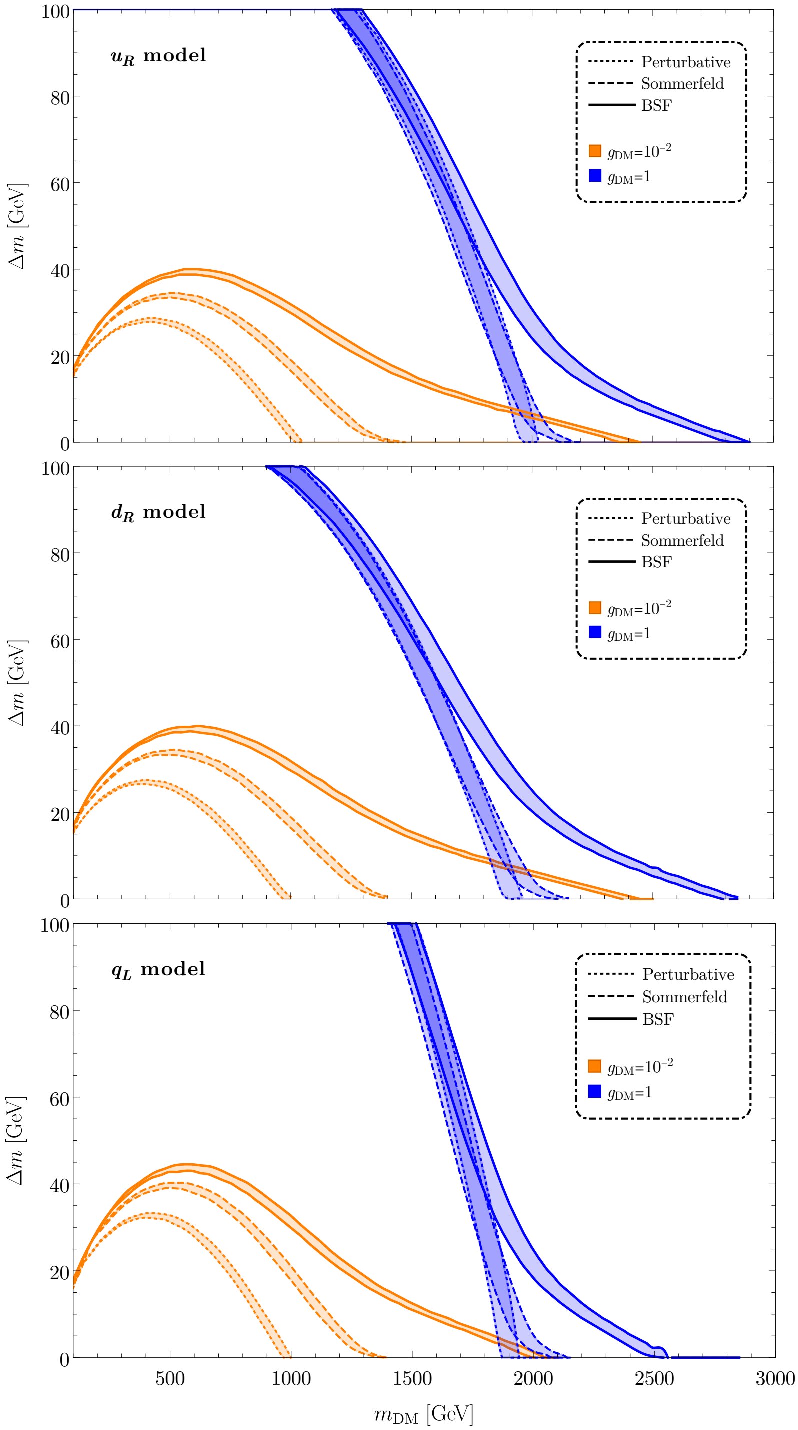

Figure V.2: Figure showing the mass splitting $\Delta m = m_X - m_{\rm DM}$ versus the DM mass $m_{\rm DM}$ for the three models considered: u_R (top), d_R (middle), and q_L (bottom). The shaded bands represent the observed DM relic density within a 5σ uncertainty, as reported by [75]. The results are presented by sequentially including different contributions: perturbative effects alone (dotted lines), with the Sommerfeld effect (dashed lines), and with the additional impact of BSF (solid lines). The two-color scheme distinguishes between two benchmark values of the Yukawa coupling: $g_{\rm DM} = 1$ (blue) and $g_{\rm DM} = 10^{-2}$ (orange). *Figure created by the thesis's author and also published in [1].*

perturbative calculations only, including Sommerfeld effect, and including both SE and bound-state formation (BSF), respectively.

General behavior. As anticipated, non-perturbative effects become increasingly relevant for smaller mass splittings and smaller values of $g_{\rm DM}$. For $\delta \equiv \Delta m/m_{\rm DM} \ll 1$, processes involving two colored scalars are no longer Boltzmann suppressed (cf. Table V.1), and multiple gluon exchange enhances annihilation rates through SE, while BSF provides an additional depletion channel. Since BSF is governed predominantly by the strong coupling, its relative importance increases when g_s becomes comparable to or larger than $g_{\rm DM}$. In the parameter region of interest, g_s varies between ~ 1.0 and 1.6, depending on the typical momentum transfer, such that for $g_{\rm DM} = 1$ interactions mediated by g_s are of comparable strength to those controlled by $g_{\rm DM}$.

Key observations:

- **Dependence on Δm:** For fixed $g_{\rm DM}$, the effective annihilation cross-section increases as $\Delta m \to 0$, where co-annihilation and colored annihilation processes become most efficient. Consequently, the DM mass compatible with the relic density reaches its maximum in the degenerate limit (recall that $m_{\rm DM}$ and the DM cross-section are anti-correlated once the relic abundance is fixed).
- **Role of non-perturbative effects:** Including SE and BSF systematically shifts the allowed parameter space toward larger $m_{\rm DM}$, reflecting a more efficient depletion of the DM number density.
- **Coupling dependence:** The relative impact of SE and BSF is largest for small $g_{\rm DM}$, while for $g_{\rm DM} \sim 1$ the enhancement remains significant due to the comparable strength of g_s.

Model-by-model comparison.

- u_R **model:** For $g_{\rm DM} = 10^{-2}$, the maximal DM mass increases from ~ 1.0 TeV in the perturbative treatment to ~ 2.4 TeV once SE and BSF are included. For $g_{\rm DM} = 1$, the corresponding shift is from ~ 2.0 TeV to ~ 2.9 TeV.
- d_R **model:** A similar behavior is observed, with the upper bound on $m_{\rm DM}$ increasing from ~ 1.2 TeV to ~ 2.4 TeV for small $g_{\rm DM}$, and from ~ 1.9 TeV to ~ 2.8 TeV for $g_{\rm DM} = 1$.
- q_L **model:** The impact of BSF is comparatively weaker, in agreement with Eq. (V.3). Here, the maximal DM mass increases from ~ 1.0 TeV to ~ 2.0 TeV for $g_{\rm DM} = 10^{-2}$, and from ~ 1.8 TeV to ~ 2.5 TeV for $g_{\rm DM} = 1$. This reduced sensitivity arises from the dilution of the effective co-annihilation cross-section among a larger number of co-annihilating states.

Key Takeaway:

- SE and BSF dominate the relic-density calculation in the near-degenerate regime $\Delta m/m_{\rm DM} \ll 1$.
- Their impact is strongest when $g_{\rm DM} \lesssim g_s$, where gluon-mediated interactions efficiently enhance annihilation rates.
- The combined non-perturbative effects can increase the maximal DM mass compatible with the observed relic abundance by up to a factor of two.

In the following, we therefore focus on the u_R model, as it captures the essential features observed across all three scenarios, while the qualitative behavior of the d_R and q_L models

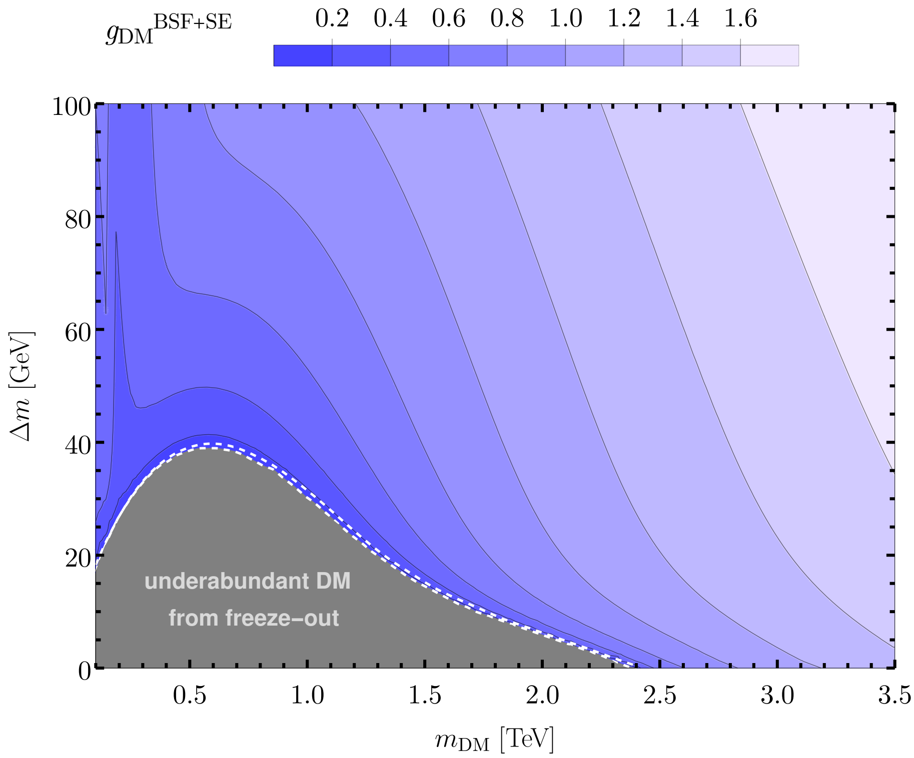

Figure V.3: Values of the Yukawa coupling required to achieve the measured DM relic density $\Omega_{\rm DM}$ for various combinations of mass splitting $\Delta m = m_X - m_{\rm DM}$ and DM mass $m_{\rm DM}$. This plot incorporates SE and BSF effects, which become increasingly significant as the mass splitting approaches smaller values, corresponding to the co-annihilation region. The dashed white lines indicate the range where $10^{-7} \lesssim g_{\rm DM} \lesssim 10^{-2}$. Below this range, maintaining chemical equilibrium between the unbound particles in the dark sector becomes challenging, and the assumption of co-annihilation freeze-out may no longer hold. *Figure created by MB and also published in [1].*

remains largely analogous.

V.3.2 Parameter Space Scan and Lower Bound on the Yukawa Coupling

Fig. V.3 displays the values of the Yukawa coupling $g_{\rm DM}$ required to reproduce the observed dark matter relic abundance in the u_R model, $\Omega_{\rm DM}h^2 \leq 0.125$ (corresponding to $+5\sigma$), in the $(m_{\rm DM}, \Delta m)$ plane. The results include both SE and BSF. The displayed coupling values therefore represent a *lower bound* on $g_{\rm DM}$, as smaller couplings would lead to an overabundance of dark matter.

General trends. The lower bound on $g_{\rm DM}$ becomes increasingly stringent with growing $m_{\rm DM}$. This behavior reflects the decrease of the relic abundance with increasing DM mass, which must be compensated by a larger effective annihilation cross-section. In contrast, for sufficiently large mass splittings, $\Delta m \gtrsim 0.2\, m_{\rm DM}$, annihilation channels involving colored mediators are Boltzmann suppressed, and the relic density approaches the standard freeze-out regime.

Key observations from Fig. V.3:

- **Transition between regimes:** For $\Delta m/m_{\rm DM} \gtrsim 0.2$, co-annihilation processes become inefficient, leading to an abrupt change in the required coupling, visible as a sharp transition in the low-mass region.

- **Near-degenerate regime:** Decreasing the mass splitting reduces the required g_{DM}, as annihilations mediated by lighter propagators are less suppressed and colored annihilation channels become exponentially unsuppressed.
- **Role of non-perturbative effects:** In the co-annihilation region, SE enhances colored annihilations, while colored mediators also participate in BSF, further increasing the effective annihilation rate.

For sufficiently small mass splittings, annihilation processes mediated solely by the strong coupling g_s become nearly sufficient to deplete the dark matter density. This region is indicated by the white dashed contours in Fig. V.3, corresponding to $10^{-7} \lesssim g_{\mathrm{DM}} \lesssim 10^{-2}$. Below this band (gray-shaded region), the Yukawa interaction is too weak to maintain chemical equilibrium within the dark sector, and the standard co-annihilation freeze-out assumption breaks down.

Chemical equilibrium constraint. To estimate the minimal coupling $\tilde{g}_{\mathrm{DM}}$ required to maintain chemical equilibrium between χ and X, we impose

$$\Gamma_X \frac{Y_X^{\mathrm{eq}}}{Y_\chi^{\mathrm{eq}}} > H \tag{V.40}$$

at $T \simeq m_\chi/30$, where Γ_X denotes the interaction rate for the (inverse) decay $X \leftrightarrow \chi q$. Assuming radiation domination, a small mass splitting, and neglecting the quark mass, this condition yields [1]

$$\tilde{g}_{\mathrm{DM}} \gtrsim \sqrt{\frac{m_{\mathrm{DM}}}{\mathrm{GeV}}} \left(1 \times 10^{-9} + 6.8 \times 10^{-11} \frac{m_{\mathrm{DM}}}{\Delta m}\right). \tag{V.41}$$

For $g_{\mathrm{DM}} < \tilde{g}_{\mathrm{DM}}$, thermal freeze-out cannot account for the observed relic abundance. In this region, alternative production mechanisms such as conversion-driven freeze-out or freeze-in become necessary [293, 294, 385]. We emphasize that Eq. (V.41) applies only for $m_{\mathrm{DM}} \gg \Delta m \gg m_q$ and does not capture next-to-leading-order effects relevant for top-associated processes.

V.3.3 Impact of Non-Perturbative Effects

To isolate the role of SE and BSF, Fig. V.4 shows the ratio between the lower bound on g_{DM} obtained with SE+BSF, $g_{\mathrm{DM}}^{\mathrm{SE+BSF}}$, and that derived from perturbative annihilations alone, $g_{\mathrm{DM}}^{\mathrm{Pert}}$.

Interpretation of Fig. V.4:

- **Blue-shaded regions:** SE and BSF enhance the effective annihilation cross-section, reducing the minimal coupling required to reproduce the observed relic abundance.
- **Orange-shaded regions:** The required coupling increases due to Sommerfeld suppression from repulsive color potentials, typically occurring when $g_{\mathrm{DM}} \gtrsim g_s$.

SE affects all processes involving two colored particles in the initial state, independent of whether they are mediated by g_s or g_{DM}. In contrast, BSF proceeds exclusively through gluon exchange and becomes subdominant when $g_{\mathrm{DM}} \gg g_s$. Comparing Figs. V.3 and V.4, the orange regions are seen to coincide with $g_{\mathrm{DM}} \gtrsim g_s \simeq 1$, where direct DM annihilations and colored XX initial states dominate and the gluon potential is repulsive.

Blue regions correspond to small $\Delta m/m_{\mathrm{DM}}$ and $g_{\mathrm{DM}} \lesssim g_s$, where Sommerfeld-enhanced $XX^\dagger$ annihilations and efficient BSF dominate the effective annihilation cross-section. In

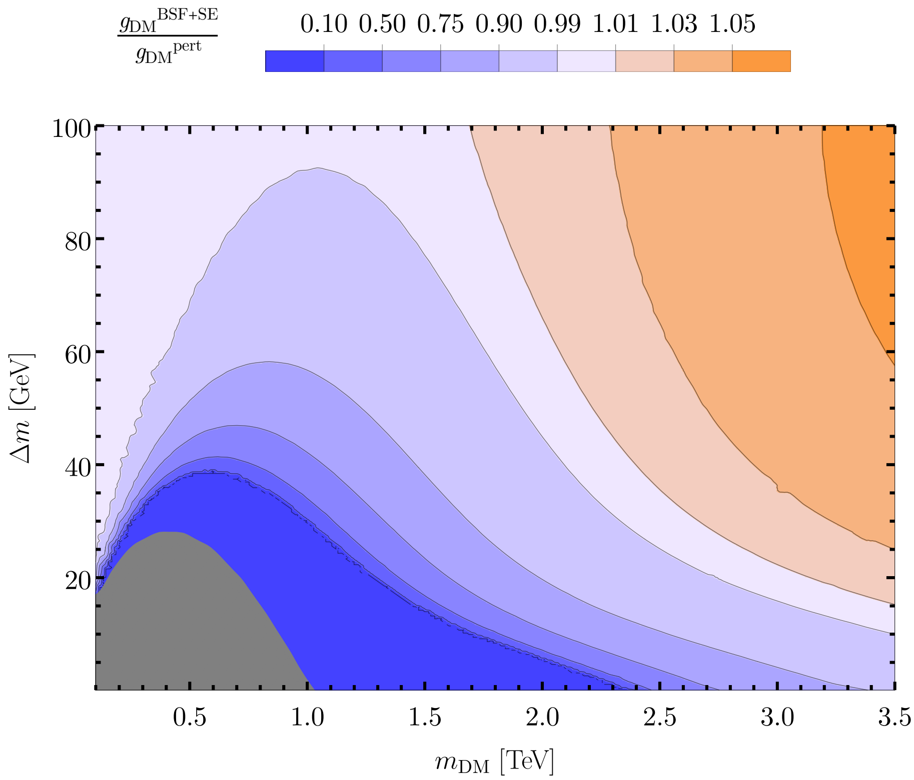

Figure V.4: Comparison of Yukawa coupling values needed to achieve the observed DM relic density $\Omega_{\rm DM}h^2$ in the $(m_{\rm DM}, \Delta m)$ plane. The plot contrasts scenarios that include the SE and BSF with those that consider only perturbative annihilations. Blue-toned regions highlight areas where non-perturbative effects require a lower Yukawa coupling compared to the perturbative case, whereas orange-toned regions indicate where a higher coupling is necessary. *Figure created by MB and also published in [1].*

these regions, attractive potentials and additional bound-state channels produce the most pronounced deviations from the perturbative prediction.

Key Takeaway:

- The lower bound on $g_{\rm DM}$ is strongly shaped by SE and BSF in the co-annihilation regime.
- For $\Delta m/m_{\rm DM} \ll 1$ and $g_{\rm DM} \lesssim g_s$, non-perturbative effects substantially reduce the coupling required to reproduce the observed relic density.
- Below the critical coupling $\tilde{g}_{\rm DM}$, chemical equilibrium fails, and non-thermal production mechanisms become necessary.

Overall, the intricate interplay between mass splittings, Yukawa interactions, and strong dynamics highlights the necessity of including both SE and BSF for a reliable determination of the viable parameter space.

The analysis presented above demonstrates how non-perturbative effects reshape the theoretical predictions for the relic density through their modification of the effective annihilation cross-section Eq. (IV.23). Specifically, we have shown that:

- Sommerfeld enhancement and bound-state formation substantially alter the coupling

$g_{\rm DM}$ required to reproduce the observed relic abundance, particularly in the co-annihilation regime where $\Delta m/m_{\rm DM} \ll 1$

- For $g_{\rm DM} \lesssim g_s$, attractive color potentials lead to enhanced depletion rates, reducing the minimal coupling needed
- For $g_{\rm DM} \gtrsim g_s$, repulsive potentials can suppress annihilation rates, requiring larger couplings
- Below a critical coupling $\tilde{g}_{\rm DM}$, chemical equilibrium in the dark sector breaks down, necessitating non-thermal production mechanisms

These theoretical modifications have direct implications for experimental searches, as the altered coupling requirements change the exclusion boundaries from direct detection, collider, and other searches. The interplay between the modified relic density predictions and experimental constraints forms the focus of the following section, where we examine how the inclusion of SE and BSF effects reshapes the experimentally viable parameter space of simplified t-channel models.

V.4 Interplay with Experimental Constraints

Declaration: This section is based on the results presented in [1], arising from a collaboration involving all authors, with MB and the thesis author contributing prominently to the analysis. The work benefited from important initial guidance by JH, who also introduced the idea of employing BSF searches at colliders as an additional probe. The derivation of the experimental limits was led primarily by KM and DS (with a minor contribution from the thesis author; see Section V.A). The thesis author and MB were chiefly responsible for incorporating these limits into the parameter-space analysis and for interpreting the results in collaboration with the full author team. The text presented here is a thoroughly revised and expanded version of the original publication, with improved exposition and additional material.

This section examines how experimental searches constrain the viable parameter space of the u_R simplified model, and how these constraints evolve when non-perturbative long-range effects are incorporated into the relic density calculations. The analysis presented here synthesizes the comprehensive methodology developed in Ref. [1] and the experimental framework detailed in Section V.A.

The experimental landscape encompasses four complementary approaches to probe the model parameter space:

- **Direct Detection Experiments:** We evaluate constraints from both spin-independent (SI) and spin-dependent (SD) nuclear recoil searches. SI limits from Xenon-1T [386] and SD limits from PICO-60 [207] provide complementary coverage of the parameter space. While SI interactions for Majorana DM arise only at loop level, SD interactions occur at tree level, making both channels essential for comprehensive constraints. Future projections from the DARWIN experiment [387] are also incorporated.
- **Prompt Collider Signatures:** We reinterpret LHC searches targeting mediators that decay promptly to final states including missing transverse energy. ATLAS mono-jet analyses constrain compressed mass spectra, while multi-jet searches probe larger mass splittings [388]. We also include projected sensitivities for the High-Luminosity LHC [224].
- **Bound-State Resonance Searches:** The formation of stoponium-like bound

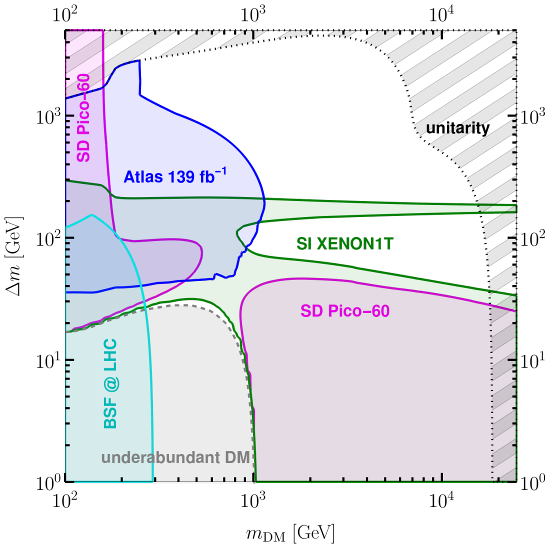

(a) Perturbative Annihilations

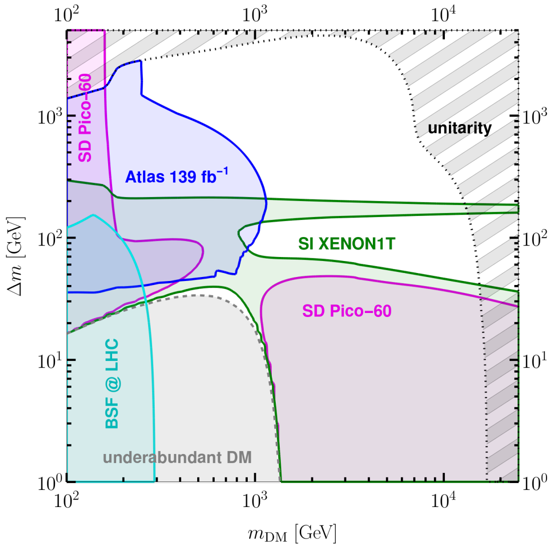

(b) Sommerfeld

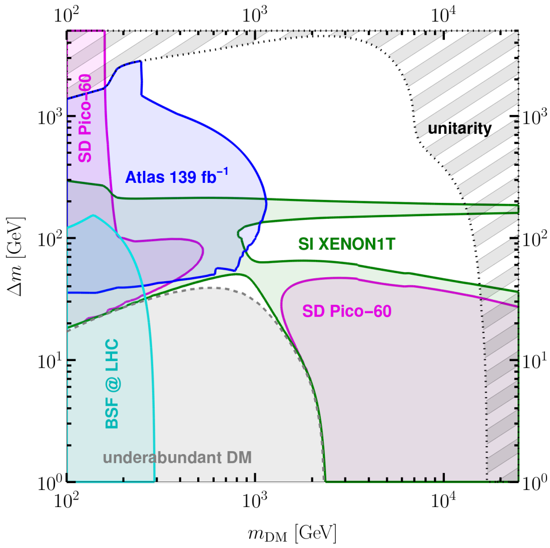

(c) Sommerfeld+BSF

Figure V.5: Experimental exclusion limits on the u_R model in the $(m_{\rm DM}, \Delta m)$-plane. For each point in the plane, we determine the smallest value of $g_{\rm DM}$ such that DM is not overproduced. If this lower bound on $g_{\rm DM}$ contradicts the limits from spin-independent DD (spin-dependent DD, prompt-collider searches, perturbative unitarity, di-photon searches), it is coloured in green (magenta, blue, black, cyan). We show the experimental limits obtained considering perturbative annihilation (a), including the SE (b), and including the SE+BSF (c). The grey dashed line divides the parameter space into two regions. Above, the observed relic density can be generated via thermal freeze-out. Below, thermal freeze-out under-produces DM, and accounting for the complete DM relic density requires other production mechanisms. *Figure created by MB and also published in [1].*

.

states $\mathcal{B}(XX^\dagger)$ at the LHC provides constraints independent of the DM coupling. These strongly-bound states decay primarily to gluons, but the clean diphoton channel yields the most stringent limits. We employ ATLAS high-mass resonance searches [389] to bound mediator masses (cf. Section V.A.2.2).

- **Long-Lived Particle Searches:** In parameter regions characterized by suppressed couplings or small mass splittings, mediators become metastable. We recast CMS Heavy Stable Charged Particle searches [390, 391] to constrain scenarios where R-hadrons produce ionizing tracks or exhibit delayed decays Section V.A.2.3.

Fig. V.5 illustrates the progressive impact of non-perturbative effects on experimental constraints, showing results for three scenarios: perturbative annihilations only (panel (a)), including Sommerfeld enhancement (panel (b)), and incorporating both Sommerfeld enhancement and bound-state formation (panel (c)).

The exclusion methodology proceeds as follows: for each point in the $(m_{\mathrm{DM}}, \Delta m)$ parameter space, we compute the minimal DM coupling $g_{\mathrm{DM},\Omega}$ required to achieve the observed relic abundance. This theoretical requirement is then compared against the most stringent experimental upper bound $g_{\mathrm{DM,exp}}$ from direct detection and collider searches. Parameter points where $g_{\mathrm{DM},\Omega} > g_{\mathrm{DM,exp}}$ are considered excluded. The precise determination of $g_{\mathrm{DM},\Omega}$ employs numerical scans with a customized version of `micrOMEGAs`, as described in Section V.3.

To interpret the qualitative features of these exclusion boundaries, we analyze the parametric dependence of $g_{\mathrm{DM},\Omega}$ on the model parameters. Using the approximate relation $\Omega_{\mathrm{DM}} \sim \langle\sigma v\rangle^{-1}$ for thermal freeze-out, we identify three distinct scaling regimes determined by the relative importance of colored co-annihilation versus direct DM annihilation processes:

1. **Colored-dominated regime:** For DM masses at or below the TeV scale with small mass splittings $\Delta m \ll m_{\mathrm{DM}}$, colored co-annihilation processes dominate the depletion of DM abundance. In this regime, the relic density constraint becomes essentially independent of g_{DM} (provided chemical equilibrium is maintained), allowing $g_{\mathrm{DM},\Omega}$ to approach arbitrarily small values.
2. **Mixed annihilation regime:** For heavier DM masses, $m_{\mathrm{DM}} \gtrsim \mathcal{O}(\mathrm{TeV})$, with continued small mass splittings, colored co-annihilations remain significant but DM-mediated processes become necessary to achieve sufficient depletion. The annihilation rate transitions to being dominated by g_{DM}-dependent channels.
3. **DM-dominated regime:** When mass splittings become large, $\Delta m \gg m_{\mathrm{DM}}$, colored co-annihilations are exponentially suppressed by Boltzmann factors, leaving only direct DM annihilations to set the relic abundance.

These regimes manifest in the parametric scaling

$$g_{\mathrm{DM}}^4 \propto \begin{cases} \to 0 & \text{if } \Delta m \ll m_{\mathrm{DM}} \ \wedge \ m_{\mathrm{DM}} \lesssim \mathcal{O}(\mathrm{TeV}), \\ m_{\mathrm{DM}}^2 & \text{if } \Delta m \ll m_{\mathrm{DM}} \ \wedge \ m_{\mathrm{DM}} \gtrsim \mathcal{O}(\mathrm{TeV}), \\ (\Delta m)^4 m_{\mathrm{DM}}^{-2} & \text{if } \Delta m \gg m_{\mathrm{DM}}, \end{cases} \tag{V.42}$$

which provides a framework for understanding the structure of the experimental exclusion limits presented in the following analysis.

In the following, we examine how these scaling behaviours manifest themselves once current experimental constraints are taken into account, and how they are modified by the

Table V.3: Qualitative behaviour of the DM coupling required to reproduce the relic density in different parametric regimes.

Regime	$m_{\rm DM}$	Δm	Behaviour of $g_{\rm DM,\Omega}$
Coloured-dominated	$\lesssim \mathcal{O}(\text{TeV})$	$\ll m_{\rm DM}$	$g_{\rm DM,\Omega} \to 0$
Mixed annihilation	$\gtrsim \mathcal{O}(\text{TeV})$	$\ll m_{\rm DM}$	$g_{\rm DM,\Omega} \propto m_{\rm DM}^{1/2}$
DM-dominated	any	$\gg m_{\rm DM}$	$g_{\rm DM,\Omega} \propto \Delta m\, m_{\rm DM}^{-1/2}$

inclusion of non-perturbative effects such as Sommerfeld enhancement and bound state formation.

V.4.1 Analysis of Current Experimental Constraints

The combined exclusion boundaries from direct detection searches, collider analyses, and theoretical consistency requirements are displayed in Fig. V.5. The exclusion criterion follows a straightforward comparison: for each parameter point, the minimal DM coupling $g_{\rm DM} \equiv g_{\rm DM,\Omega}$ needed to reproduce the observed relic abundance is computed and contrasted with the most restrictive experimental upper bound $g_{\rm DM,exp}$. Points satisfying $g_{\rm DM,\Omega} > g_{\rm DM,exp}$ are deemed phenomenologically excluded.

The resulting exclusion patterns exhibit characteristic dependencies on the DM mass and mass splitting, which can be analytically understood through the interplay between relic density requirements and detection sensitivities.

Spin-independent direct detection (SI-DD)

The green exclusion regions in Fig. V.5 arise from SI nuclear recoil searches. These constraints achieve maximal strength in the region of large DM masses ($m_{\rm DM} \gtrsim \mathcal{O}(1\text{ TeV})$) combined with small mass splittings ($\Delta m \lesssim 100$ GeV). In this domain, colored co-annihilation processes remain efficient, compelling the relic density requirement to enforce relatively large values of $g_{\rm DM}$.

Conversely, for lighter DM masses ($m_{\rm DM} \lesssim 1$ TeV) with extremely small mass splittings ($\Delta m \lesssim 50$ GeV), SI-DD constraints become considerably weaker. This relaxation occurs because efficient colored annihilations permit the correct relic abundance to be achieved with arbitrarily small $g_{\rm DM}$, effectively evading direct detection sensitivity.

A notable feature is the appearance of an excluded band near $\Delta m \simeq m_t$, which originates from a top-quark resonance enhancement in the one-loop DM-nucleon scattering amplitude [186]. The parametric dependence on mediator masses, SM quark masses, and DM mass enters through Wilson coefficients generated during one-loop renormalization group evolution (see Section V.A Appendix A2 in [186]).

Depending on the mass hierarchy, the SI cross-section in Eq. (V.A.2) exhibits distinct scaling behaviors:

$$\sigma_{\rm SI} \propto \begin{cases} \dfrac{g_{\rm DM}^4}{m_{\rm DM}^2}\dfrac{m_N^4}{(\Delta m)^4}\,, & \text{if } m_q \ll \Delta m \ll m_{\rm DM}, \\[2ex] \dfrac{g_{\rm DM}^4}{m_{\rm DM}^2}\dfrac{m_N^4}{(\Delta m)^4}\dfrac{m_{\rm DM}^6}{(\Delta m)^6}\,, & \text{if } \Delta m \gg m_{\rm DM}, \end{cases} \tag{V.43}$$

When combined with the relic density constraint from Eq. (V.42), this yields the characteristic scaling

$$\sigma_{\mathrm{SI}} \propto \begin{cases} \to 0\,, & \Delta m \ll m_{\mathrm{DM}} \text{ and } m_{\mathrm{DM}} \lesssim \mathcal{O}(\mathrm{TeV}), \\ m_N^4\,(\Delta m)^{-4}\,, & \Delta m \ll m_{\mathrm{DM}} \text{ and } m_{\mathrm{DM}} \gtrsim \mathcal{O}(\mathrm{TeV}), \\ m_N^4 m_{\mathrm{DM}}^2\,(\Delta m)^{-6}\,, & \Delta m \gg m_{\mathrm{DM}}. \end{cases} \tag{V.44}$$

This scaling explains why SI-DD effectively constrains the small-Δm, large-m_{DM} region while remaining largely insensitive to parameter space with large mass splittings due to the strong Δm suppression.

Spin-dependent direct detection (SD-DD)

The magenta exclusion regions in Fig. V.5 represent constraints from SD nuclear recoil searches. Relative to SI-DD, SD constraints exhibit reduced sensitivity for small mass splittings but gain competitive or even dominant strength for $\Delta m \gtrsim 200$ GeV.

This distinctive pattern emerges from the scaling behavior of the SD scattering cross-section presented in Eq. (V.A.1) (detailed derivations can be found in [186]):

$$\sigma_{\mathrm{SD}} \propto \begin{cases} \dfrac{g_{\mathrm{DM}}^4 m_N^2}{(\Delta m)^4} \to 0\,, & \Delta m \ll m_{\mathrm{DM}} \lesssim \mathcal{O}(\mathrm{TeV}), \\ \dfrac{g_{\mathrm{DM}}^4 m_N^2}{(\Delta m)^2\, m_{\mathrm{DM}}^2} \propto \dfrac{m_N^2}{(\Delta m)^2}\,, & \Delta m \ll m_{\mathrm{DM}} \gtrsim \mathcal{O}(\mathrm{TeV}), \\ \dfrac{g_{\mathrm{DM}}^4 m_N^2}{(\Delta m)^4} \propto \dfrac{m_N^2}{m_{\mathrm{DM}}^2}\,, & \Delta m \gg m_{\mathrm{DM}}, \end{cases} \tag{V.45}$$

where the relic density constraint again determines the lower bound on g_{DM}. The weaker Δm suppression in the small mass splitting regime explains the reduced SD-DD sensitivity compared to SI-DD, while the independence from Δm for large mass splittings enables SD-DD to constrain DM masses up to $m_{\mathrm{DM}} \sim 200$ GeV.

Perturbative consistency requirements

The black shaded areas in Fig. V.5 indicate parameter regions where the coupling needed to reproduce the observed relic density violates the conservative perturbative unitarity bound $g_{\mathrm{DM}} < \sqrt{4\pi}$. This theoretical constraint provides an absolute upper limit on the viable parameter space, independent of experimental sensitivities, following the methodology established in [392, 393].

Collider searches and bound-state constraints

Experimental constraints from collider searches are depicted in blue (prompt processes) and cyan (bound-state resonances). Prompt searches achieve optimal sensitivity for $m_{\mathrm{DM}} \lesssim 1.2$ TeV with moderate-to-large mass splittings, where multi-jet+$\not{E}_T$ analyses dominate. In the small mass splitting regime, mono-jet searches become most relevant due to their reliance on initial-state radiation to generate observable signatures.

Bound-state searches exclude mediator masses up to $m_X \lesssim 290$ GeV in regions where the binding energy exceeds the constituent decay width [394]. These searches uniquely probe parameter space inaccessible to both direct detection and prompt collider analyses, playing a vital role in constraining scenarios with small g_{DM}.

V.4.2 Influence of Non-Perturbative Effects on Experimental Constraints

When current experimental constraints from direct detection, collider searches, and theoretical consistency requirements are applied, the surviving parameter space in the $(m_{\mathrm{DM}}, \Delta m)$-plane separates into two qualitatively distinct domains, as illustrated in Fig. V.5. These regions differ not only in the magnitude of the required DM-SM coupling g_{DM} but also in their susceptibility to non-perturbative long-range effects.

Perturbative domain

In the regime characterized by large DM masses and substantial mass splittings, achieving the observed relic abundance necessitates couplings of order $g_{\mathrm{DM}} \gtrsim \mathcal{O}(1)$. Under these conditions, Sommerfeld enhancement and bound-state formation exert minimal influence on the relic density calculation, as DM annihilation processes dominate the depletion mechanisms.

Furthermore, when $g_{\mathrm{DM}} \gtrsim g_s$, the effective potential between colored co-annihilating states becomes repulsive, which suppresses Sommerfeld enhancement of colored annihilation channels. Consequently, the inclusion of SE leads to a modest reduction in the effective annihilation cross-section, requiring slightly larger values of g_{DM} to prevent DM overproduction. This effect marginally strengthens constraints from direct detection, collider searches, and perturbative unitarity, producing only minor shifts in the exclusion contours even for DM masses extending up to $\mathcal{O}(20\text{ TeV})$.

Strongly co-annihilating regime

In contrast, the phenomenology changes substantially in the strongly co-annihilating regime characterised by $m_{\mathrm{DM}} \lesssim 2.5$ TeV and $\Delta m \lesssim 80$ GeV. Here, the relic density can be reproduced with small couplings, $g_{\mathrm{DM}} \sim 10^{-2}$–$10^{-1}$, rendering non-perturbative effects crucial. Sommerfeld enhancement alone increases the annihilation cross-section at the $\sim 10\%$ level and induces only moderate shifts in the exclusion limits. However, when bound state formation is included, the effective annihilation rate is significantly enhanced, allowing substantially smaller values of g_{DM} while still achieving the correct relic abundance.

As a consequence, regions that are excluded at the perturbative level — particularly for 500 GeV $\lesssim m_{\mathrm{DM}} \lesssim 1.5$ TeV — become viable once SE and BSF are taken into account. Quantitatively, the maximum DM mass compatible with current constraints increases from approximately 1 TeV in the perturbative treatment to about 2.4 TeV when BSF is included, while the allowed mass splitting expands from $\Delta m \lesssim 30$ GeV to $\Delta m \lesssim 50$ GeV. In this region, the combined impact of SE and BSF modifies exclusion limits by up to $\mathcal{O}(100\%)$, demonstrating that BSF effects dominate over Sommerfeld enhancement alone.

The gray regions in Fig. V.5 and Fig. V.6 correspond to parameter points where thermal freeze-out underproduces the observed DM relic density. Below the gray dashed line, the couplings required to reproduce the full relic abundance via freeze-out are extremely small, $g_{\mathrm{DM}} \lesssim 10^{-6}$, placing these scenarios beyond the reach of direct detection and prompt collider searches. Nevertheless, such small couplings naturally give rise to long-lived coloured states, opening complementary discovery opportunities via LLP searches.

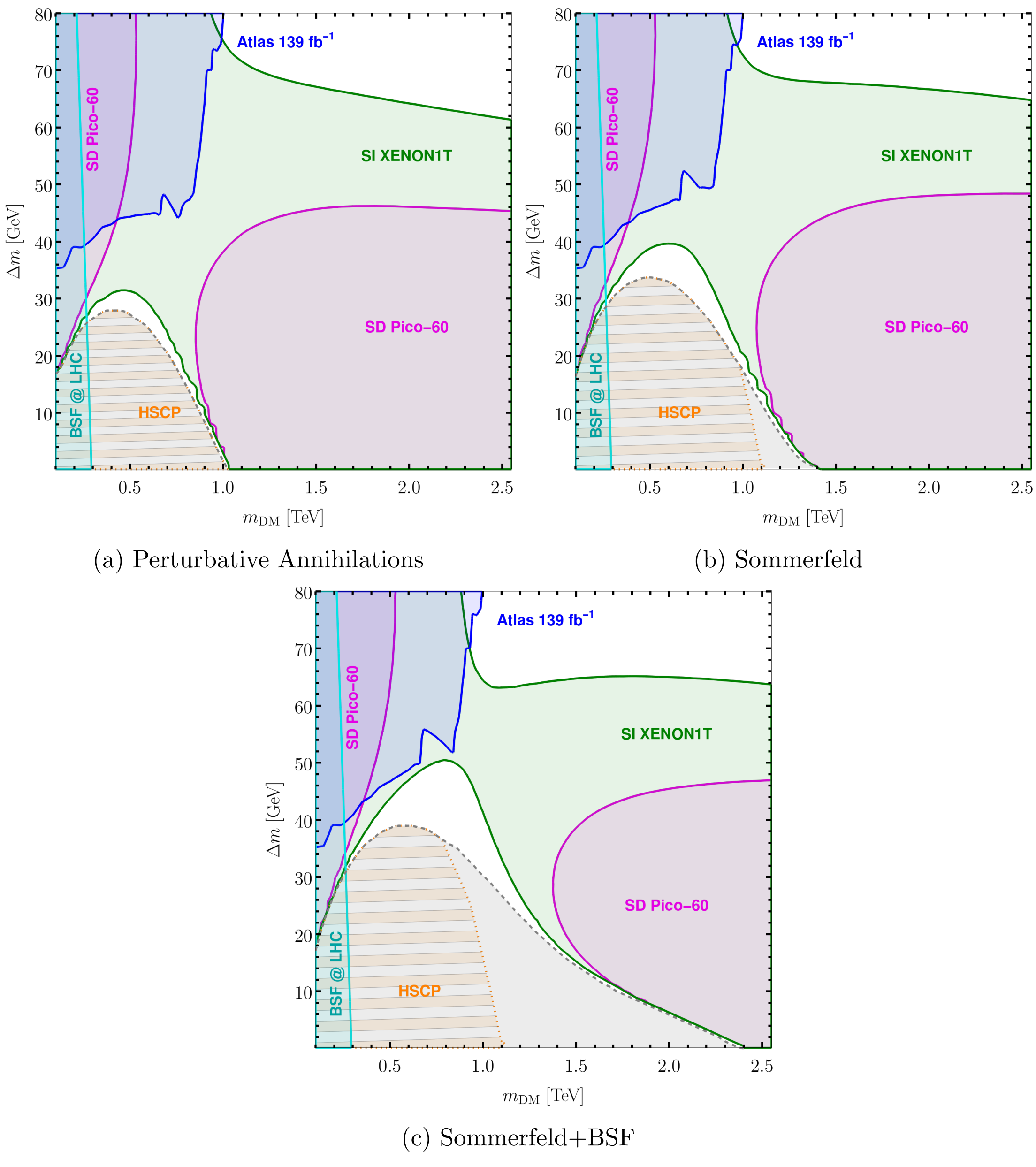

Figure V.6: Experimental constraints in the co-annihilation regime. As previously, exclusions from spin-independent DD (spin-dependent DD, colliders, unitarity, di-photon searches) appear in green (magenta, blue, black, cyan). Additionally, we indicate regions where LLP searches could constrain parameter space requiring non-thermal production mechanisms such as conversion-driven freeze-out or freeze-in, marked in orange. *Figure created by MB and also published in [1].*

Key Takeaway:

Overall, incorporating Sommerfeld enhancement and bound state formation substantially enlarges the phenomenologically viable parameter space, particularly in the strongly co-annihilating regime. Neglecting these effects leads to overly conservative exclusions and an incomplete assessment of experimental sensitivities in simplified t-channel DM models.

V.4.3 Potential of Long-Lived Particle Searches

In regions of parameter space where thermal freeze-out underproduces the observed DM relic density, additional production mechanisms such as conversion-driven freeze-out or freeze-in are required. To characterize this regime, we employ the condition in Eq. (V.40) to estimate a critical coupling $\tilde{g}_{\text{DM}}$, below which (inverse) decays of the coloured mediator fall out of chemical equilibrium during the epoch of DM freeze-out. This threshold provides a useful diagnostic for identifying regions where DM production proceeds out of equilibrium and where long-lived particle (LLP) signatures may arise.

Unlike direct detection and prompt collider searches, which impose upper bounds on the DM–SM coupling g_{DM}, LLP searches constrain g_{DM} from below. Smaller couplings lead to increasingly long-lived coloured scalars X, which can be probed via heavy stable charged particle (HSCP) searches, as discussed in Section V.A.2.3. In Fig. V.6, the parameter regions where $\tilde{g}_{\text{DM}} < g_{\text{DM}}^{\text{LLP}}$ are indicated by orange shading, highlighting the sensitivity of LLP searches to scenarios featuring an out-of-equilibrium dark sector.

Current HSCP searches are sensitive to DM masses up to approximately 1.2 TeV and decay lengths of order $\mathcal{O}(10\text{ cm})$. In the absence of non-perturbative effects, perturbative annihilations alone would exclude essentially the entire parameter space below the gray dashed line in Fig. V.5. However, the inclusion of Sommerfeld enhancement and bound state formation substantially weakens this conclusion by allowing efficient DM annihilation at smaller couplings, thereby extending the viable parameter space to DM masses beyond the present reach of HSCP searches.

As a result, a significant fraction of the non-thermal region remains unconstrained once SE and BSF effects are taken into account. This highlights the importance of LLP searches as a complementary probe of DM scenarios with suppressed couplings, while simultaneously demonstrating that non-perturbative effects must be incorporated to reliably delineate the parameter space accessible to such searches.

V.4.4 Projected Exclusion Limits of Future Experiments

The projected exclusion limits from future experiments are shown in Fig. V.7, where we include the expected sensitivities of the DARWIN direct detection experiment and the High-Luminosity LHC (HL-LHC). Compared to current limits, the increased exposure of next-generation direct detection experiments and the significantly larger data set of the HL-LHC are expected to probe most of the presently unconstrained parameter space shown in Fig. V.5.

In particular, the HL-LHC is expected to improve collider limits by up to two orders of magnitude relative to current searches, while future direct detection experiments will provide the dominant sensitivity across large regions of parameter space. Assuming that DM is a Majorana particle constituting the full relic abundance, the combination of spin-

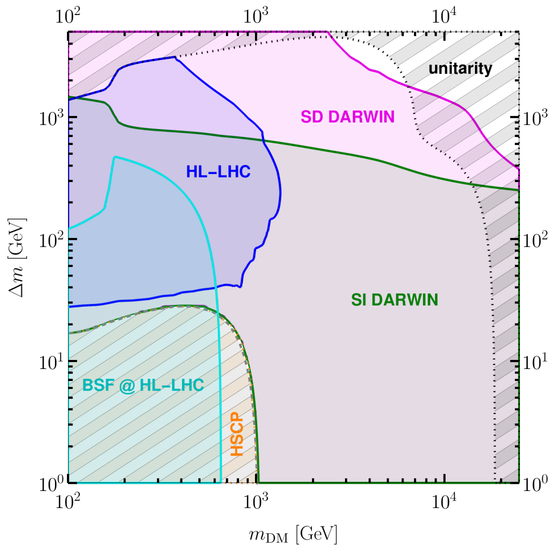

(a) Perturbative Annihilations

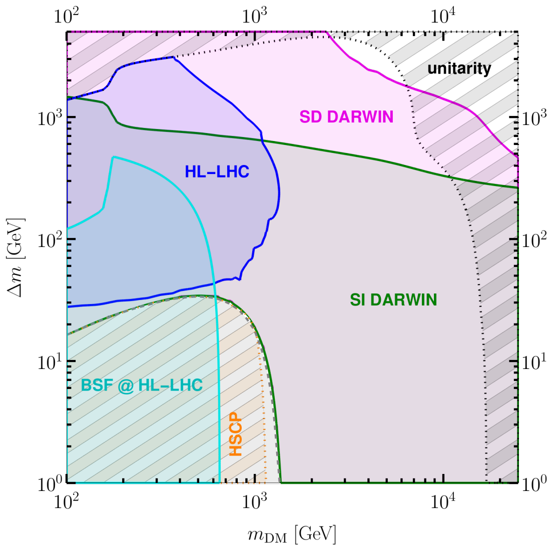

(b) Sommerfeld

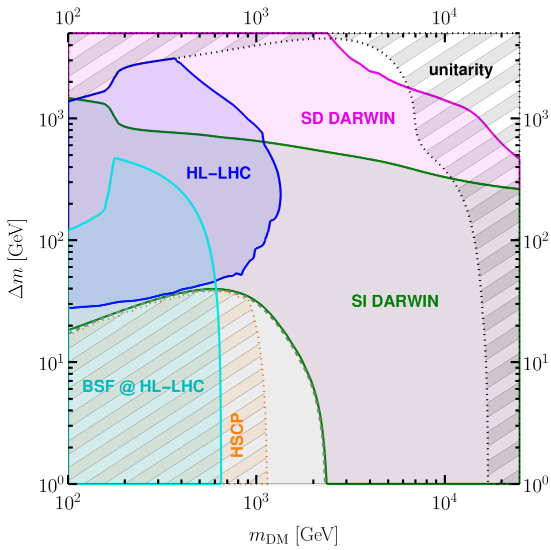

(c) Sommerfeld+BSF

Figure V.7: Same as in Fig. V.5, but employing projected limits from future experiments. *Figure created by MB and also published in [1].*

.

independent and spin-dependent direct detection searches will exclude nearly the entire parameter space above the gray dashed line in Fig. V.7.

Nevertheless, a small but phenomenologically relevant region remains unconstrained. This region corresponds to very small mass splittings, $\Delta m \lesssim \mathcal{O}(\text{GeV})$, and couplings in the range $10^{-6} \lesssim g_{\rm DM} \lesssim 10^{-2}$. Here, direct detection is suppressed, prompt collider searches lose sensitivity due to non-prompt mediator decays, and LLP signatures are not induced. Bound state searches at colliders, discussed in Section V.4.5, are uniquely suited to probe this gap. At the HL-LHC, such searches are expected to extend sensitivity from mediator masses of approximately 290 GeV to roughly 650 GeV.

For larger mass splittings, spin-dependent direct detection constraints become increasingly powerful due to their weaker suppression compared to spin-independent scattering, in accordance with the scaling behaviour discussed in Eq. (V.45).

If no signal is observed in future experiments, three distinct regions will remain viable. First, a region with $g_{\rm DM} \sim \mathcal{O}(1)$ and multi-TeV DM and mediator masses, which could be probed by future high-energy colliders such as the FCC. Second, a narrow band of small couplings near the transition between thermal and non-thermal DM production, where non-perturbative effects play a decisive role. Third, the region below the gray dashed line, where DM is underproduced via freeze-out and must be generated through conversion-driven freeze-out or freeze-in.

In all cases, Sommerfeld enhancement and bound state formation significantly affect the interpretation of experimental sensitivities. Accurately assessing the viability of simplified t-channel DM models, therefore, requires the consistent inclusion of non-perturbative effects in relic density calculations, both for present and future searches.

V.4.5 Potential of Bound State Searches at the LHC

To illustrate the unique role of collider searches for dark-sector bound states, we present in Fig. V.8 the exclusion limits in the $(m_{\rm DM}, g_{\rm DM})$ plane for fixed relative mass splittings $\delta = \Delta m/m_{\rm DM} = 0.01$ (upper panels) and $\delta = 0.05$ (lower panels). The colour coding follows the same convention as in the $(m_{\rm DM}, \Delta m)$ projections shown in Fig. V.5–V.7. Unlike the previous figures, these plots explicitly display regions where the DM relic density is overproduced, as the mass splitting is fixed while the coupling $g_{\rm DM}$ is varied.

The solid black contours in Fig. V.8 delineate the boundary between regions of over-abundant DM and the freeze-out regime. Above this boundary, DM is efficiently depleted during thermal freeze-out, whereas below it, DM is either underproduced or must be generated via non-thermal mechanisms such as conversion-driven freeze-out or freeze-in. While the correct relic density may still be obtained in parts of the non-thermal region, this possibility is not explored further here.

Conventional experimental searches constrain $g_{\rm DM}$ in complementary but limited ways. Direct detection and prompt collider searches impose upper bounds on the coupling, as both DM–nucleon scattering rates and mediator production cross-sections increase with $g_{\rm DM}$. Prompt collider searches further require a minimal coupling to ensure that mediator decays are prompt. Conversely, long-lived particle searches constrain $g_{\rm DM}$ from below but lose sensitivity once mediator decays become too rapid to yield displaced signatures.

Bound state searches occupy a qualitatively different position in this landscape. The production cross-section for an X–$X^\dagger$ bound state at hadron colliders, given by Eq. (V.A.3), is governed primarily by the strong interaction and is largely independent of $g_{\rm DM}$, provided that the decay width of the constituent particles remains smaller than the binding energy of the bound state [394]. If the decay width becomes too large, bound state formation is

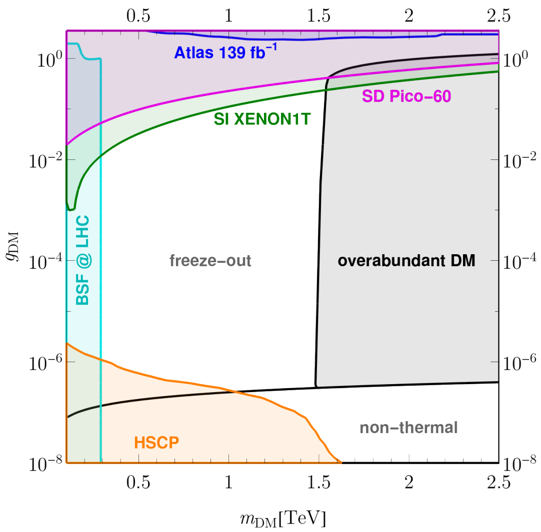

(a) $\delta = 0.01$, current limits

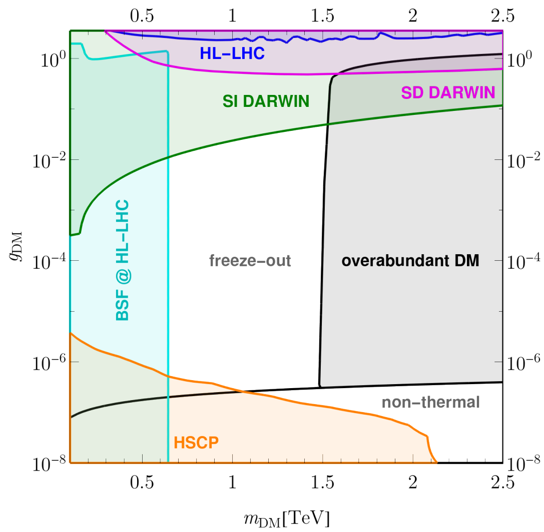

(b) $\delta = 0.01$, projected limits

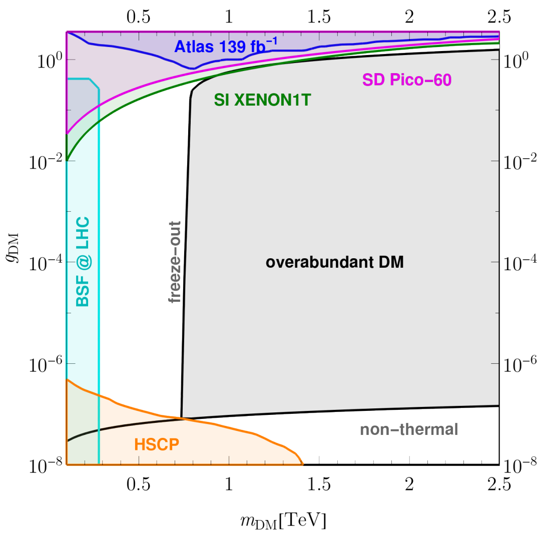

(c) $\delta = 0.05$, current limits

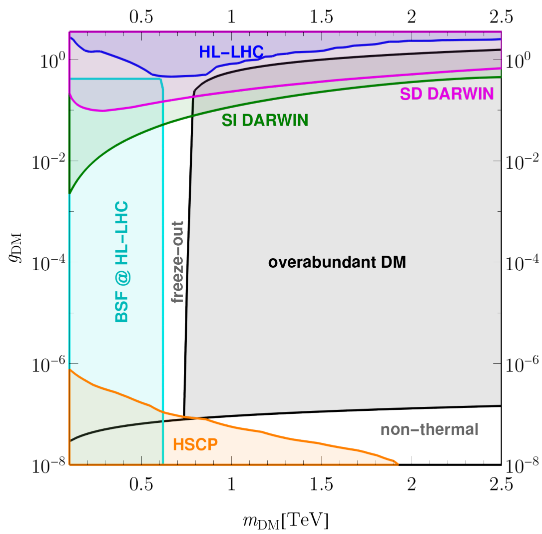

(d) $\delta = 0.05$, projected limits

Figure V.8: Future and current limits are shown in the $(m_{\mathrm{DM}}, g_{\mathrm{DM}})$-plane for a fixed relative mass splitting δ. The limits from spin-independent direct detection (spin-dependent direct detection, prompt collider searches, long-lived particle searches, bound state searches at colliders) are shown in green (magenta, blue, orange, cyan). Additionally, the plane is split into three regions. Firstly a region for small couplings where DM production proceeds non-thermally, secondly, a freeze-out region where DM is either underproduced or matches the observed relic density, which coincides with the boundary of this region to the area of parameter space where DM is overabundant. *Figure created by MB and also published in [1].*

.

suppressed, implying that these searches are effective up to couplings of order $g_{\mathrm{DM}} \lesssim g_s$.

Crucially, once formed, the bound state can decay through gauge-mediated annihilation of its constituents, a channel that does not rely on the DM–SM coupling. As a result, bound state searches remain sensitive to scenarios with extremely small couplings, where direct detection, prompt collider searches, and LLP searches all lose sensitivity. This feature is clearly visible in Fig. V.8, where bound state searches (cyan regions) uniquely probe the coupling range $10^{-6} \lesssim g_{\mathrm{DM}} \lesssim 10^{-2}$.

At the HL-LHC, the reach of bound state searches is expected to improve substantially, extending sensitivity in the strongly co-annihilating regime to DM masses of up to approximately 650 GeV. This makes bound state searches one of the most promising strategies for closing the remaining gaps in the parameter space of coloured co-annihilation scenarios, particularly in regions where non-perturbative effects play a decisive role in determining the DM relic abundance.

In summary, bound state searches at colliders provide a uniquely powerful and complementary probe of simplified t-channel DM models. They are capable of testing regions of parameter space characterized by small mass splittings and suppressed DM–SM couplings, which remain inaccessible to all other current and projected experimental strategies. Their inclusion is therefore essential for achieving a comprehensive and robust exploration of coloured co-annihilation scenarios.

V.5 Conclusions and Outlooks

Across this chapter, we developed a consistent treatment of Sommerfeld enhancement (SE) and bound-state formation (BSF) in simplified t-channel dark-matter models with coloured mediators. By incorporating long-range QCD effects into the relic-density computation and mapping the analytic scaling regimes (cf. Eq. (V.42)), we showed how SE and BSF reshape the effective annihilation rate. For $g_{\mathrm{DM}} \lesssim g_s$, attractive colour potentials enhance depletion; for $g_{\mathrm{DM}} \gtrsim g_s$, repulsive potentials can suppress coloured channels; BSF always increases the rate but becomes irrelevant once $g_{\mathrm{DM}} \gg g_s$. As a consequence, the coupling required to obtain Ω_{DM} is substantially reduced in the co-annihilation regime, reopening parameter space previously excluded at tree level and extending the viable range up to roughly $m_{\mathrm{DM}} \simeq 2.4$ TeV with $\Delta m \lesssim 50$ GeV. Confronting these predictions with spin-independent/spin-dependent direct detection, prompt LHC searches, LLP probes, and bound-state resonances, we demonstrated that including SE+BSF shifts the combined exclusions in a controlled, model-dependent way and explains the persistence of a non-thermal wedge at tiny couplings and compressed spectra, where LLP and bound-state searches provide the leading discovery potential.

Outlook

Looking ahead, it is natural to extend this framework to include the formation and transitions of excited bound states, which have been shown to yield a mild (strong) impact in the co-annihilation (conversion-driven freeze-out) regimes for the same t-channel models [346, 347, 375]. In this direction, a recent preprint [8] builds on the present work and aims to finalise the implementation in `micrOMEGAs` of SE and BSF for coloured mediators, including excited states. It will also be important to study mixed long-range forces in models featuring $SU(2)$ doublets [378, 380], couplings with the Higgs field [352, 376], or even light dark photons [353], with prospects at the future Forward Physics Facility [3]. On the experimental side, improved recasts of HSCP/DT/LLP searches and dedicated

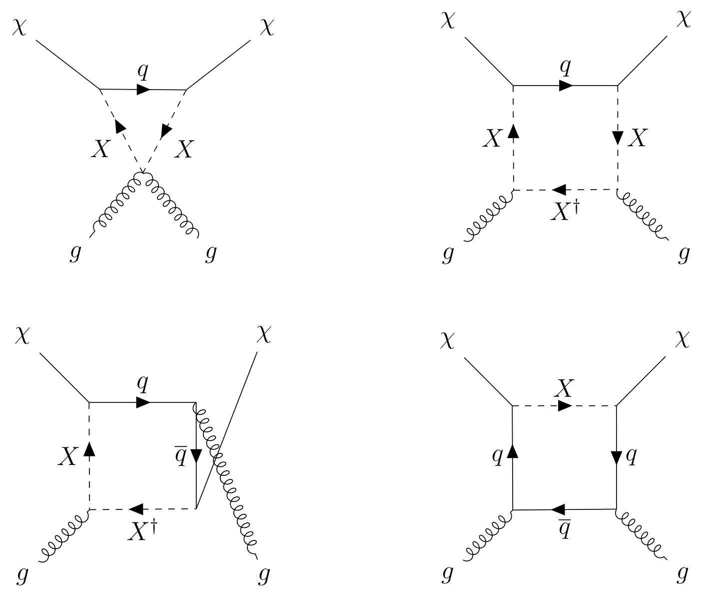

Figure V.9: One-loop diagrams illustrating the elastic scattering between DM and gluons within nucleons, contributing to the spin-independent DM-nucleon cross-section. *Figure created by the thesis author and included in [1].*

diphoton resonance analyses at the HL-LHC, together with next-generation direct detection (e.g. DARWIN) and future colliders, can close the remaining gaps in the parameter space.

V.A Experimental Constraints

Declaration: In this section, we summarize the analysis conducted for [1] using various experimental constraints, necessary to understand the results of this work. Experimental limits have been obtained by DS and KM, who also took care of the text. The thesis author has co-authored the analysis relative to Section V.A.2.2. The text in this section is a shortened version of what was presented in the publication, which was reviewed and corrected by all authors.

In this section, we summarize the experimental searches and analyses employed to constrain the parameter space in Section V.4 as done in Ref. [1]. For a more detailed description, we refer the reader to this publication.

V.A.1 Limits on $g_{\rm DM}$ from Direct Detection

To assess the direct detection (DD) constraints on the parameter space, we adhere to the methodology outlined in Ref. [186]. Direct detection constraints arise from the absence of observed DM-nucleus interactions on Earth. These constraints are categorized into spin-independent (SI) and spin-dependent (SD) interactions (cf. Section II.3.1).

We utilize the SI constraints from the Xenon-1T experiment [386] and SD constraints from the PICO-60 experiment [207]. Additionally, we consider future projections for the planned DARWIN experiment [387].

In our model, the spin-dependent (SD) DM-nucleon scattering is mediated at tree level by the s-channel exchange of a colored mediator X, with the SD DM-nucleon cross-section scaling as $g_{\rm DM}^4$ [186]:

$$\begin{aligned}
\sigma_{\rm SD}^{u_R} &= \frac{3g_{\rm DM}^4}{16\pi}\frac{m_N^2\, m_{\rm DM}^2}{(m_N+m_{\rm DM})^2(m_X^2-m_{\rm DM}^2)}(\Delta u^N)^2,\\
\sigma_{\rm SD}^{d_R} &= \frac{3g_{\rm DM}^4}{16\pi}\frac{m_N^2\, m_{\rm DM}^2}{(m_N+m_{\rm DM})^2(m_X^2-m_{\rm DM}^2)}(\Delta d^N+\Delta_s^N)^2,\\
\sigma_{\rm SD}^{q_L} &= \frac{3g_{\rm DM}^4}{16\pi}\frac{m_N^2\, m_{\rm DM}^2}{(m_N+m_{\rm DM})^2(m_X^2-m_{\rm DM}^2)}(\Delta u^N+\Delta d^N+\Delta s^N)^2,
\end{aligned} \tag{V.A.1}$$

where Δu^N, Δd^N, and Δs^N are matrix elements that are evaluated when taking into account the nuclear axial vector. For spin-independent (SI) scattering, due to the Majorana nature of the DM candidate, there is no velocity-unsuppressed tree-level contribution. Consequently, SI DM-nucleon scattering occurs at the one-loop level, primarily arising from the diagrams depicted in Fig. V.9. Similar to SD scattering, the parametric dependence of the SI DM-nucleon cross-section also scales as $g_{\rm DM}^4$ [186]:

$$\sigma_{\rm SI} = \frac{4g_{\rm DM}^4}{\pi}\left(\frac{m_{\rm DM}\, m_N}{m_{\rm DM}+m_N}\right)^2 |\tilde f_N|^2, \tag{V.A.2}$$

where $\tilde f_N = f_N/g_{\rm DM}^2$ is the matrix element arising from the DM-nucleon interaction, including the Wilson coefficients at one-loop (with the DM coupling factorized out). To determine the SD DM-nucleon scattering cross-section for this simplified model, we perform a comprehensive one-loop matching of the relevant Wilson coefficients, including all possible diagrams and interference effects. We also conduct a renormalization group evolution (RGE) from the mediator mass scale to the low-energy scale (approximately 1 GeV), which is pertinent for DM scattering with heavy nucleons. Detailed procedures for this calculation are provided in Ref. [186]. The inclusion of RGE evolution results in an enhancement of approximately a factor of two at the amplitude level, translating to about a factor of four at the cross-section level.

Given that experimental limits on SI cross-sections are roughly six orders of magnitude stronger than those on SD cross-sections, and that SI cross-sections are enhanced by RGE evolution despite being one-loop suppressed, both SI and SD constraints are crucial for our study.

In Section V.4, we will examine how DD constraints influence the parameter space of the u_R model. The dependence of both SI and SD cross-sections on $g_{\rm DM}^4$ implies that DD experiments provide upper limits on $g_{\rm DM}$ for each data point $(m_{\rm DM}, \Delta m)$. These upper limits, combined with the lower limits on $g_{\rm DM}$ required to avoid DM overproduction, will define the permissible and excluded regions of the parameter space, as discussed in detail in Section V.4.1.

V.A.2 Collider Constraints

Given that both the mediator and DM possess masses on the order of the TeV scale, the models under consideration are also constrained by collider experiments.

Three main types of searches are employed to impose constraints on the parameter space (cf. also Section II.3.3):

1. Prompt Searches: These involve detecting mediators that are produced and decay immediately into DM and jets.

2. Long-Lived Particle (LLP) Searches: The produced mediators are not short-lived and may decay either within or outside the detector.

3. Bound State Formation at the LHC: Pair-produced mediators may form bound states, which then decay into Standard Model (SM) gauge bosons.

V.A.2.1 Prompt Searches

Feynman diagrams illustrating key processes at the LHC are depicted in Fig. V.10. These processes involve the pair production of mediators, associated production of DM with a mediator, and pair production of DM with an Initial State Radiated (ISR) jet. The QCD strong coupling purely mediates the production cross-section of the first of these processes, while the latter processes are controlled by the product of DM coupling $g_{\rm DM}$ and the strong coupling constant. Additionally, processes scaling with $g^4_{\rm DM}$, like pair production of DM and $qq \to XX$, are considered, albeit with subdominant cross-sections for the region of interest. The cross-sections are computed at Next-to-Leading Order (NLO) using the Monte Carlo event generator MG5$_{\rm a}$MC@NLO [395], with the CT14NLO [396] PDF set. The details of the calculation are provided in [186].

Prompt searches at the LHC, particularly mono and multi-jet + $\not{E}_T$ searches, play a crucial role in constraining the parameter space, especially for mass differences $\geq$ 5GeV and sizable couplings. The mono-jet + $\not{E}T$ searches are particularly effective in constraining compressed spectra, relying on a hard ISR jet emission, while the multi-jet + $\not{E}_T$ searches target moderate to high Δm regions due to increased jet activity in the final state.

These searches are reinterpreted using the MadAnalysis5 Public Analysis Database (Ma5-PAD) framework [397] to obtain constraints for the models under consideration. The validation of the reinterpretation process ensures agreement with official documentation within acceptable margins and the details are illustrated in [1] and in [398].

In short, for the mono-jet + $\not{E}_T$ searches, one defines pre-selection criteria and signal regions, with the analysis reproduced and recasted within the Ma5-PAD framework. Signal events are generated at tree-level [395], and then showered and hadronized [399, 400], and the obtained limits in the $(m_\chi, \Delta m)$ plane at the 95% C.L. are determined using a log-likelihood method. Similarly, the multi-jet + $\not{E}_T$ searches target scenarios with significant missing transverse energy, with baseline criteria and signal regions defined accordingly (cf. [1]). The analysis is recast following Ref. [388], with validation confirming agreement with official documentation.

Finally, projections for the forthcoming high-luminosity LHC (HL-LHC) [224] are provided through a naive luminosity-rescaled 95% confidence level exclusion limit. However, more accurate limits depend on proper background estimates from data-driven methods to address high pile-ups at higher luminosities.

V.A.2.2 Bound State Production at LHC

Colored mediators can be produced in pairs at the LHC and can form bound states $\mathcal{B}(XX^\dagger)$. When the coupling of the mediator to DM ($g_{\rm DM}$) is relatively weak, these bound states primarily decay into pairs of gauge bosons. In the scenario under consideration, the dominant decay mode is into pairs of gluons, with a branching ratio of approximately 99%. This is followed by decays into pairs of photons, $Z\gamma$, and then Z-boson pairs.[3]

[3]Decays into W-bosons are relevant for the q_L model but not for the u_R model. Additionally, in the parameter space of interest, the coupling $g_{\rm DM}$ is very small, making decays into quarks or DM negligible. Decays into $Z\gamma$ are suppressed in the u_R model but could be more significant in the q_L model.

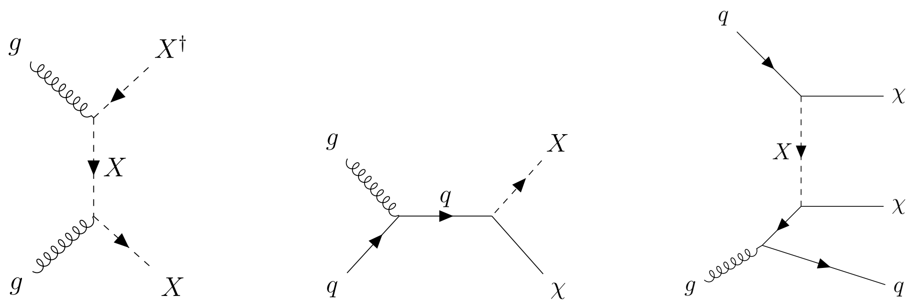

Figure V.10: Feynman diagrams depicting processes at the LHC, following the same notation as in Fig. V.9. The diagrams illustrate the pair production of mediators (left), the associated production of DM with a mediator (center), and the production of a DM pair accompanied by an ISR jet (right). *Figure created by the thesis author also published in [1].*

In this study, we focus on the production of the bound state $\mathcal{B}(XX^\dagger)$ and its subsequent decay into pairs of photons at the LHC. The diphoton decay channel offers the most stringent constraints for the u_R model. These constraints are independent of the DM mass and, for small $g_{\rm DM}$, are not significantly affected by the couplings of the mediator and DM.

To constrain the mass of the mediator, we use results from high-mass ($\gtrsim$ 100 GeV) diphoton searches conducted by the ATLAS experiment [389]. The analysis in Ref. [389] provides limits on the fiducial cross-section (times branching ratio) at 95% C.L., which we adjust using a nearly constant efficiency factor, derived from the detector acceptance and reconstruction efficiency as described in [401], to obtain the total cross-section (times branching ratio).

For calculating the theoretical cross-section, we follow the method outlined in Refs. [402, 403], where the bound-state production cross-section is computed at NLO in QCD, placing constraints on s-wave stoponium production at the LHC.

The leading-order production cross-section for a stoponium-like bound state in the Narrow Width Approximation (NWA) is given by

$$\sigma(pp \to \mathcal{B}(XX^\dagger)) = \frac{\pi^2}{8m_{\mathcal{B}}^3}\Gamma(\mathcal{B}(XX^\dagger) \to gg)\mathcal{P}_{gg}\left(\frac{m_{\mathcal{B}}}{13\text{ TeV}}\right) , \tag{V.A.3}$$

where $\Gamma(\mathcal{B}(XX^\dagger) \to gg)$ represents the decay width of the bound state to gluon pairs, $\mathcal{P}_{gg}$ denotes the gluon luminosity for pp collisions at a 13 TeV center-of-mass energy, and $m_{\mathcal{B}} \simeq 2m_X$ is the mass of the bound state.[4] We utilize the NLO calculation from [402] and evaluate the strong coupling α_s at $\mu = m_{\mathcal{B}}$. This result is then multiplied by the branching ratio of bound state decays into diphoton resonances (around $0.3\% - 0.5\%$). For details on the decay widths of $\mathcal{B}(XX^\dagger)$ to gg, $\gamma\gamma$, $Z\gamma$, and ZZ, see [402, 403].

Considering the three generations of stoponium-like bound states in the u_R model, Fig. V.11 shows the current exclusion limits on the bound state mass by comparing the experimental bound on the production cross-section times the diphoton-resonance branching ratio (black line) with the theoretical prediction (red line) for the u_R model. The exclusion limits on the mediator mass $m_X \simeq m_{\mathcal{B}}/2$ are:

$$100\text{ GeV} \lesssim m_X \lesssim 290\text{ GeV} . \tag{V.A.4}$$

[4]The relation between the masses is not exact due to binding energy, but this difference is negligible compared to the constituent masses.

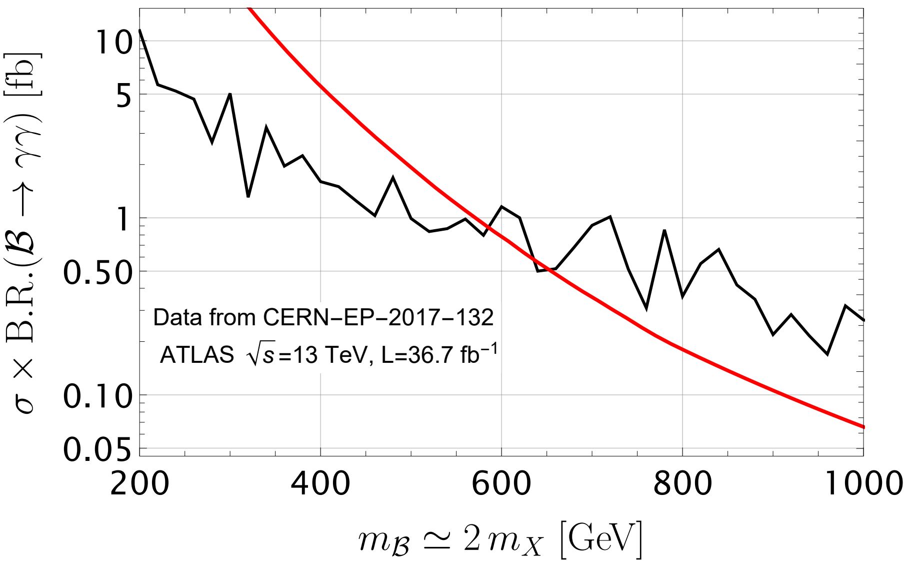

Figure V.11: Exclusion limits on the mass of the $\mathcal{B}(XX^\dagger)$ bound state from collider data. The solid black line represents the total cross-section for $pp \to \mathcal{B}(XX^\dagger) \to \gamma\gamma$ as measured by the ATLAS experiment ($\sqrt{s} = 13$ TeV, $\mathcal{L} = 36.7$ fb^{-1}) [389]. The red line depicts our theoretical prediction for the u_R model. Exclusion occurs where the red line exceeds the experimental limit. *Figure created by the thesis author and also published in [1].*

The lower limit of 100 GeV arises from the experimental analyses used, while small masses could be probed by alternative low-energy experiments.

To estimate the projected exclusion bounds from the HL-LHC, we scale the integrated luminosity relative to the ATLAS data used previously. In particular, we use asymptotic expressions to calculate the significance ($Z = $ signal$/\sqrt{\text{background}}$). Background event numbers are scaled from Fig. 2 of [389] for HL-LHC luminosity. This method is consistent with experimental bounds from full likelihood analyses as noted in [401], and HL-LHC will have a high background event count, making the asymptotic significance a good approximation. The upper bound on the mediator mass is expected to increase significantly for the HL-LHC, with the anticipated limit being

$$m_X \lesssim 650 \text{ GeV} . \tag{V.A.5}$$

It is important to note that these limits are independent of the exact value of $g_{\rm DM}$, the Yukawa coupling between DM and the mediator and SM fermions.

V.A.2.3 Long-Lived Particle Searches

Certain regions of our parameter space feature small mass gaps, resulting in decay widths only detectable by Long-Lived Particle (LLP) searches. For this analysis, we consider searches for heavy stable charged particles (HSCP). Pair-production of mediators can yield charged particles with sufficiently small decay widths to exit the detector before decaying. These charged particles will form R-hadrons governed by QCD dynamics. Charged hadrons with velocities ($\beta = v/c < 1$) traversing the detector leave ionizing tracks, aiding their detection. For R-hadrons decaying outside the detector, time-of-flight (TOF) measurements can distinguish them from Standard Model (SM) particles.

The CMS collaboration has conducted HSCP searches at 8 and 13 TeV LHC energies, primarily within supersymmetric models with long-lived gluinos and squarks [390, 391].

We employ methods similar to those in [184] to reinterpret these CMS searches for HSCP at both energies. CMS focused on long-lived stops, staus, and heavy vectorlike leptons, utilizing tracker-only and tracker+TOF analyses.

We recast the CMS cross-section limits on stops and staus to constraints in our model. The sensitivity regime depends on parent particle lifetimes, with a fraction decaying within the tracker affecting the HSCP signal. We calculate an effective cross-section by multiplying the production cross-section by the efficiency fraction $f_{\mathrm{LLP}}(\tau)$. Tentative projections for the High-Luminosity LHC (HL-LHC) are based on [184], which involves a simple luminosity rescaling of expected signal and observed background events. We normalize the signal events obtained after all cuts to the production cross-section and an integrated luminosity of 3000 fb^{-1}.

For the background, we take the official number of background events from the CMS analysis and normalize it for HL-LHC. However, accurate projections depend on addressing instrumental backgrounds and improving trigger systems and pile-up rate understanding.

Part II

FIMPs

CHAPTER VI

DM Freeze-in from Non-Equilibrium QFT: Motivations and Theoretical Background

In the previous chapter, we examined scenarios where DM relic abundance is set via the freeze-out mechanism, with a particular focus on the co-annihilation regime. A key assumption was that DM remained in thermal contact with the primordial bath until its interactions became too weak to maintain equilibrium, typically occurring when DM and dark sector mediators were in the non-relativistic regime.

In the second part of this thesis, we turn to a complementary paradigm: feebly interacting massive particles (FIMPs) whose abundance is built up through freeze-in. In this regime, the DM population starts essentially from zero and is sourced by rare reactions in the bath, typically decays or annihilations involving a heavier mediator and Standard Model particles (see Section III.5.2). The defining assumption is the smallness of the portal interaction, such that DM never reaches chemical equilibrium and inverse processes remain negligible.

Because production takes place efficiently around temperatures set by the relevant mass scales, freeze-in is intrinsically sensitive to epochs where some of the particles participating in the reactions are still relativistic. If the mediator is itself embedded in the plasma, finite-density effects modify its propagation and kinematics, so that thermal corrections can feed back into the predicted relic abundance. This situation is qualitatively different from freeze-out, whose dynamics are controlled by non-relativistic physics at temperatures well below the particle masses.

The purpose of this chapter is to assemble the theoretical tools needed to treat such finite-temperature effects from first principles. Building on standard results in nonequilibrium thermal QFT, we outline how to obtain the evolution equation for the DM abundance starting from real-time correlation functions. Similar quantum-kinetic equations have long been exploited in other cosmological applications (most notably leptogenesis), but they have not been developed in detail for the phenomenologically motivated freeze-in setups studied in this thesis.

This material prepares the ground for Chapters VII and VIII, where we apply the formalism to simplified t-channel models with scalar DM and gauge-charged vectorlike mediators and then benchmark the resulting predictions against commonly used approximations, including Hard Thermal Loop treatments and semiclassical Boltzmann calculations.

Statement of Personal Contribution for this Chapter
The theoretical concepts and derivations presented in this chapter are mainly based on existing literature and re-elaborated in the context of the published work [5], which originated from an idea of JH. For the most part, the published manuscript was written by the thesis author and MB, while its structure and content evolved through continuous exchange among all authors. The thesis author played a central role in shaping the narrative flow and depth of discussion. As such, the content reproduced here closely follows the form presented in [5], which the author regards as a faithful and effective representation of his contribution to the research and literature review. This chapter serves as a necessary theoretical background to understand its application in Chapter VII. All the references, concepts, and equations were analyzed and discussed in collaboration with the paper's co-authors. In particular, with reference to this chapter, the principal contributions of the thesis author to the associated publication include:

- The literature research and critical review of results and state-of-the-art relevant to the scope of the project, which accounted for more than half of the total project duration.
- The formulation and presentation of the theoretical concepts and equations.

VI.1 State of the Art

Declaration: this section is a reformulation in shorter form of the introduction in [5], written by the thesis author as a result of thorough literature research and review. This was primarily conducted by the thesis author but in continuous discussion with MB, JH and CT. In the paper, all authors reviewed and corrected the text.

Over the last few years, several ingredients that are subleading in vacuum calculations have been recognized as quantitatively relevant for freeze-in at $T \sim M$. A first class of effects concerns the statistics of the bath: using the full Fermi–Dirac/Bose–Einstein distributions in the collision operator, rather than Maxwell–Boltzmann approximations, can shift the final abundance by up to $\mathcal{O}(10\%)$ [382, 404–406].

A second recurring theme is the role of thermal masses, typically of order gT, which are often introduced to render scattering rates finite when t-channel exchanges involve light degrees of freedom. In such cases, the vacuum cross sections exhibit soft/collinear enhancements and a logarithmic sensitivity to the infrared; replacing the exchanged propagators by thermally screened ones regulates these singularities. Depending on the spectrum, thermal masses also reshape decay kinematics and can open or close channels compared to the $T = 0$ case, thereby affecting the freeze-in history (see, e.g., Refs. [383, 405–411]).

While these improvements are widely used, most studies still implement them within a semiclassical Boltzmann framework, where thermal effects enter through modified dispersion relations or regulator masses inserted into vacuum matrix elements (cf. Section III.4.1). This raises the question of how robust such prescriptions are across temperature and coupling regimes, especially when momentum-dependent medium effects become important.

The underlying conceptual issue is that the usual cross sections are computed from *in-out* S-matrix elements between asymptotic, non-interacting states, whereas a hot and dense medium does not admit a clean notion of asymptotic particles. A systematic treatment of finite-density dynamics therefore calls for thermal quantum field theory [412–414]. Depending on the problem, this can be approached either through the imaginary-time (Matsubara) formalism [413, 415, 416] in equilibrium, or through the real-time closed-time-path (Keldysh–Schwinger) formalism [417–429], which is also the standard setting for nonequilibrium physics [430, 431].

A significant advancement in the consistent treatment of DM freeze-in at finite temperatures, moving beyond the semi-empirical Boltzmann approach, has been achieved by Ref. [432]. The authors utilize the imaginary-time formalism to calculate the production rate of Majorana DM fermion particles through three-body and four-body interactions involving a heavier gauge-charged scalar mediator and a Standard Model (SM) fermion in thermal equilibrium (for related freeze-out studies, see [433, 434]). These rates are derived in the ultrarelativistic regime by leveraging the large-momentum limit of Hard Thermal Loop (HTL) resummed propagators for the equilibrated fields [435–437] and incorporating reactions enhanced by multiple soft scatterings with the plasma, which are particularly efficient at high temperatures. Such a quantum phenomenon, known as the Landau-Pomeranchuk-Migdal (LPM) effect [438, 439], is computed for massless particles and is phenomenologically suppressed in the non-relativistic regime ($T \ll M$), where the Born approximation is assumed to prevail. This interpolation enables the characterization of particle production across all temperature regimes, albeit with a high-temperature approximation near the peak of freeze-in production ($T \sim M$). While more refined interpolations are feasible [440], it remains an open question whether accounting for a massive mediator and DM candidate would significantly alter the production rate, given the complexity of the calculations required for a precise and smooth transition between regimes.

VI.1.1 Our Approach

Our strategy is to formulate freeze-in directly at the level of nonequilibrium correlation functions. Concretely, we employ quantum-kinetic Kadanoff–Baym equations [441] derived in the Closed-Time-Path (CTP) formalism, and we connect them to a number-density evolution equation for DM. The central objects are two-point functions defined on a complex time contour; their dynamics follow from Schwinger–Dyson equations that can be obtained as stationarity conditions of a two-particle-irreducible (2PI) effective action [419, 420, 430, 431, 442, 443].[1]

Two aspects make this appealing for freeze-in. First, the CTP is an *initial-value* formalism: it computes time-dependent expectation values in an interacting medium (hence the name *in-in*), rather than scattering probabilities between asymptotic states. Second, once Wightman functions are related to phase-space occupation numbers, the same framework provides a controlled route from microscopic QFT dynamics to macroscopic rate equations.

Historically, these techniques have been developed extensively in baryogenesis and leptogenesis [385, 444–470], whereas explicit applications to dark-matter freeze-in are comparatively scarce [471–475].

In the remainder of this chapter, we summarize the elements of the CTP and the 2PI construction that are needed to set up the kinetic description, and we show how the DM number-density equation emerges. This will serve as the theoretical starting point for

[1] A key advantage of 2PI effective actions is their ability to systematically include quantum and thermal corrections by resumming a significantly wider set of diagrams compared to traditional 1PI methods. This broader resummation capability allows for a more comprehensive exploration of the field configuration space.

Chapter VII, where we apply the formalism to a simplified t-channel model and perform a systematic comparison with approximation schemes commonly used in the freeze-in literature.

VI.2 The Closed-Time-Path Formalism

Declaration: This section presents results from the literature, a large fraction of which were rederived and further developed by the thesis author, MB, and CT in [5]. The use of the CTP formalism was originally proposed by JH. The material presented here extends the discussion in [5] by incorporating a broader range of results from the literature. The original manuscript was written by the thesis author and CT and subsequently reviewed and revised by all authors.

The Closed-Time-Path (CTP) construction (also referred to as the Keldysh–Schwinger or *in-in* formalism) is a standard tool to formulate quantum field theory as an initial-value problem [417, 418, 430, 431, 476–478]. Its central aim is not the computation of transition amplitudes between asymptotic states, but the determination of time-dependent *expectation values* —in particular, n-point correlation functions—in a state that may be far from equilibrium.

This viewpoint is well matched to early-Universe applications. Rather than describing a single scattering event between free particles prepared in the remote past and detected in the remote future, one wants to follow how an interacting medium (the primordial plasma) evolves and sources new excitations. In this situation, the relevant degrees of freedom are encoded in correlators evaluated in the presence of the medium, and the familiar vacuum particle picture underlying the *in-out* S-matrix becomes only an approximation.

VI.2.1 CTP Contour

To make contact with the path-integral formulation used in the CTP approach, it is useful to recall how expectation values are represented in terms of a density operator and time evolution. We follow the line of reasoning in [479], which builds on the original CTP constructions [417,418,480,481] (see also [477]), and we use it here as a pedagogical bridge to the contour-ordered generating functional. In quantum mechanics, given an observable $\hat{\mathcal{O}}$ (Heisenberg picture) and a statistical ensemble described by a density matrix, the expectation value at time t can be written as

$$\langle \mathcal{O} \rangle = \mathrm{Tr}\Big\{\hat{\rho}\hat{O}\Big\} , \tag{VI.1}$$

where $\hat{\rho}$ is the density matrix, which weights the probability of finding the system in a state $|S_n(t)\rangle$ at a given time t. Specifically,

$$\hat{\rho}(t) = \sum_n p_n \, |S_n(t)\rangle \, \langle S_n(t)| \ , \tag{VI.2}$$

with $\sum_n p_n = 1$. In the path-integral formulation of quantum mechanics, the expectation value of an operator is given by

$$\langle \mathcal{O}(t) \rangle = \int \mathcal{D}\phi_{[t,t]} \left\langle \phi(t) \middle| \hat{\rho}(t)\hat{\mathcal{O}}(t) \middle| \phi(t) \right\rangle \ , \tag{VI.3}$$

where $\mathcal{D}$ is the integration measures on the path contour $\mathcal{C}$ which also absorbs an overall normalization constant N. In the Heisenberg picture, we can let the time-dependent state

$|\phi(t)\rangle$ evolve in time under the Hamiltonian $\hat{H}$ as

$$\begin{aligned}|\phi(t)\rangle &= U(t,t_i)\,|\phi(t_i)\rangle = e^{-i\hat{H}(t-t_i-i\varepsilon)}\,|\phi(t_i)\rangle \\ &= \int \mathcal{D}\tilde{\phi}_{[t_i,t]}\left|\tilde{\phi}(t)\right\rangle e^{i\int_{t_i}^{t}\mathrm{d}^4x\,\mathcal{L}\left(\tilde{\phi},\dot{\tilde{\phi}};x\right)}\left\langle\tilde{\phi}(t_i)\middle|\phi(t_i)\right\rangle\,, \end{aligned} \tag{VI.4}$$

where we have inserted the functional representation of the unitary time evolution operator $U(t,t_i)$ involving the Lagrangian density $\mathcal{L}$ which is a functional of the field $\tilde{\phi}$, its time derivative $\dot{\tilde{\phi}}$, and the spacetime coordinates x, where $\tilde{\phi}$ is a dummy integration variable. The infinitesimal positive ε guarantees the convergence of the time evolution and is absorbed into the time arguments. The expectation value can thus be written as

$$\langle\mathcal{O}(t)\rangle = \int \mathcal{D}\phi_{[t_i,t_i]}\left\langle\psi(t_i)\middle|\hat{\rho}(t_i)U(t_i,t)\hat{\mathcal{O}}(t)U(t,t_i)\middle|\psi(t_i)\right\rangle\,. \tag{VI.5}$$

We now use the closure property $U(t_i,t) = U(t_i,t_f)U(t_f,t)$ and insert multiple times the functional representation of U with dummy integration variable $\tilde{\phi}$, ϕ^+, and ϕ^- to further manipulate the expression, yielding

$$\begin{aligned}\langle\mathcal{O}(t)\rangle &= \int \mathcal{D}\phi_{[t_i,t_i]}\left\langle\phi(t_i)\middle|\hat{\rho}(t_i)U(t_f,t_i)U(t_i,t)\hat{\mathcal{O}}(t)U(t,t_i)\middle|\phi(t_i)\right\rangle \\ &= \int \mathcal{D}\phi_{[t_i,t_i]}\mathcal{D}\phi^+_{[t_i,t]}\left\langle\phi(t_i)\middle|\hat{\rho}(t_i)U(t_f,t_i)U(t_i,t)\hat{\mathcal{O}}(t)\middle|\phi^+(t)\right\rangle \\ &\quad\times e^{i\int_{t_i}^{t}\mathrm{d}^4x\,\mathcal{L}\left(\phi^+,\dot{\phi}^+;x\right)}\delta\left(\phi^+(t_f)-\phi(t_i)\right) \end{aligned} \tag{VI.6}$$

$$\begin{aligned} &= \int \mathcal{D}\phi_{[t_i,t_i]}\mathcal{D}\phi^+_{[t_i,t]}\mathcal{D}\tilde{\phi}^+_{[t,t_f]}\mathcal{D}\phi^-_{[t_i,t_f]}\left\langle\phi(t_i)\middle|\hat{\rho}(t_i)\middle|\phi^-(t_i)\right\rangle \\ &\quad\times e^{i\int_{t_f}^{t_i}\mathrm{d}^4x\,\mathcal{L}\left(\phi^-,\dot{\phi}^-;x\right)}\delta\left(\phi^-(t_f)-\tilde{\phi}^+(t_f)\right)\,e^{i\int_{t}^{t_f}\mathrm{d}^4x\,\mathcal{L}\left(\tilde{\phi}^+,\dot{\tilde{\phi}}^+;x\right)}\delta\left(\tilde{\phi}^+(t)-\phi^+(t)\right) \\ &\quad\times \mathcal{O}^+(t)\,e^{i\int_{t}^{t_f}\mathrm{d}^4x\,\mathcal{L}\left(\tilde{\phi}^+,\dot{\tilde{\phi}}^+;x\right)}\delta\left(\phi^+(t_i)-\phi(t_i)\right)\,. \end{aligned} \tag{VI.7}$$

Here, $\mathcal{O}^+(t)$ is the eigenvalue of the $\hat{\mathcal{O}}(t)$ operator on the state $|\phi^+(t)\rangle$, namely $\hat{\mathcal{O}}(t)\,|\phi^+(t)\rangle = \mathcal{O}^+(t)\,|\phi^+(t)\rangle$. We integrate the delta functions to obtain the following expression

$$\begin{aligned}\langle\mathcal{O}(t)\rangle = \int \mathcal{D}^+_{[t_i,t_f]}\mathcal{D}\phi^-_{[t_i,t_f]}&\left\langle\phi^+(t_i)\middle|\hat{\rho}(t_i)\middle|\phi^-(t_i)\right\rangle\,\delta\left(\phi^-(t_f)-\phi^+(t_f)\right)\times \\ &\times\mathcal{O}^+(t)\,e^{i\int_{t_f}^{t_i}\mathrm{d}^4x\,\mathcal{L}\left(\phi^-,\dot{\phi}^-;x\right)}\,e^{i\int_{t_i}^{t_f}\mathrm{d}^4x\,\mathcal{L}\left(\phi^+,\dot{\phi}^+;x\right)}\,. \end{aligned} \tag{VI.8}$$

This is the expectation value of $\hat{\mathcal{O}}(t)$ measured by the state $|\phi^+(t)\rangle$ in a system prepared at the initial time t_i within the statistical ensemble characterized by the density operator $\hat{\rho}$ with ensemble average given by the two integration measures and its matrix element. Recall now the infinitesimal imaginary time $i\varepsilon$ that we introduced in the time evolution operator to guarantee the convergence. Thanks to this prescription we can give an interpretation to the (dummy) integration variable ϕ^+ and ϕ^-. They can be viewed as fields "sitting" at $t \pm i\varepsilon$ so that the expectation value can be expressed as a path integral with a time contour $\mathcal{C}_+$ going from t_i to t_f, where we use $\mathcal{D}^+_{[t_i,t_f]}$, and then a contour $\mathcal{C}_-$ from t_f to t_i, where we use $\mathcal{D}^-_{t_i,t_f}$. The two path integrals can be joined into a single path integral along a combined time-contour $\mathcal{C} = \mathcal{C}_+ \oplus \mathcal{C}_-$, which goes from t_i to itself passing through

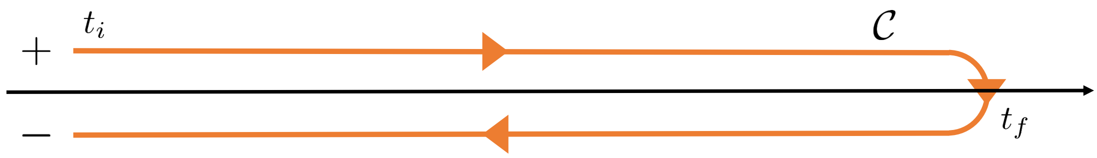

Figure VI.1: The CTP contour in the time variable complex plane. *Figure created by the thesis author.*

t_f, as we illustrate in Fig. VI.1. This Closed-Time Path (CTP) justifies the name of the formalism. From the path integral over the time-path $\mathcal{C}$, and by introducing the sources $J_\pm$ for the fields $\phi^\pm$, one can construct a generating functional $Z_\mathcal{C}[J]$ as

$$Z_\mathcal{C}[J] = Z[J_+, J_-] = \int \mathcal{D}\phi^+ \mathcal{D}\phi^- \, e^{i\int \mathrm{d}^4x \left(\mathcal{L}(\phi^+) - \mathcal{L}(\phi^-) + J_+\phi^+ - J_-\phi^-\right)} \left\langle \phi^+(t_i) \middle| \hat{\rho}(t_i) \middle| \phi^-(t_i) \right\rangle , \tag{VI.9}$$

with which we can construct the correlation functions of the theory through functional differentiation, as shown in the next section. Note that, a crucial simplification that can be made is to stretch the time path to $t_i \to -\infty$ and $t \to +\infty$. This is possible since we are mainly interested in the interactions of fields within a plasma in thermal equilibrium, where the information about initial conditions is lost. An ensemble in thermal equilibrium with temperature $T = 1/\beta$ can be realized by appending a third branch to the time contour, going in the imaginary direction from $t = t_i$ to $t = -i\beta$ [412] and using Gaussian initial conditions. In general, whenever initial correlations between fields can be neglected, initial conditions only enter as a normalization factor for the generating functional and the correlation functions. Otherwise, the choice of the initial state/statistical ensemble can be encoded in the path integral employing appropriate boundary conditions [443, 482].

VI.2.2 CTP Propagators

The Green's functions of the theory can be defined in the usual manner by taking functional derivatives of the generating functional $Z_\mathcal{C}$ with respect to the sources (see, e.g., [443, 467, 477] and references therein). In particular, one can define propagators (two-point functions), which are of special interest because they contain information about the number densities of states in the statistical ensemble, as well as the allowed momentum shells of the states, as we will show later. The CTP propagators of a field ϕ (with conjugate $\bar{\phi}$) are defined as follows [5, 467, 477],

$$iG^{ab}(x,y) = -\frac{\delta^2}{\delta J(x^a)\delta \bar{J}(y^b)} \log Z[J,\bar{J}]|_{J_\pm = 0} = \langle T_\mathcal{C}\phi(x^a)\bar{\phi}(y^b)\rangle \,. \tag{VI.10}$$

The contour $\mathcal{C}$ is parameterized by the coordinates x^a, where $a, b = \pm$ characterizes the respective time branches. The symbol $T_\mathcal{C}$ represents the path ordering of the time contour, and the angular brackets $\langle \dots \rangle$ denote the expectation values of quantum operators $\hat{\mathcal{O}}$ within the statistical ensemble. Specifically, this involves tracing the operators weighted by the density matrix of the theory over every degree of freedom, such that $\langle \hat{\mathcal{O}} \rangle = \mathrm{Tr}\left(\hat{\rho}\,\hat{\mathcal{O}}\right)$.

The notation $\phi(x)$ and $\bar{\phi}(x)$ in Eq. (VI.10) is intended to represent both scalar and fermion fields, with G denoting a generic scalar or fermion two-point function. For a complex scalar field $\varphi(x)$, we have $\phi(x) = \varphi(x)$ and $\bar{\phi}(x) = \varphi^\dagger(x)$. In the case of a Dirac fermion $\Psi(x)$ and its Dirac adjoint $\bar{\Psi}(x)$, we have $\phi(x) = \Psi(x)$ and $\bar{\phi}(x) = \bar{\Psi}(x)$. When it is necessary to distinguish between scalar and fermionic two-point functions, we will use Δ to denote the scalar propagator and S for the fermion propagator.

$$i\Delta^{ab}(x,y) = \langle T_{\mathcal{C}}\, \varphi(x^a)\varphi(y^b)^\dagger \rangle\,, \tag{VI.11}$$

$$i\not{S}^{ab}(x,y) = \langle T_{\mathcal{C}}\, \Psi(x^a)\bar{\Psi}(y^b) \rangle\,. \tag{VI.12}$$

These fields are canonically quantized via their equal-time commutation and anticommutation relations [483]:

$$\Big[\varphi(x), \varphi^\dagger(y)\Big]_{x^0=y^0} = \Big[\dot{\varphi}(x), \dot{\varphi}^\dagger(y)\Big]_{x^0=y^0} = 0, \qquad \Big[\varphi(x), \dot{\varphi}^\dagger(y)\Big]_{x^0=y^0} = i\delta^{(3)}(\vec{x}-\vec{y}), \tag{VI.13}$$

$$\Big\{\Psi(x), \Psi^\dagger(y)\Big\}_{x^0=y^0} = \Big\{\dot{\Psi}(x), \dot{\Psi}^\dagger(y)\Big\}_{x^0=y^0} = 0, \qquad \Big\{\Psi(x), \dot{\Psi}^\dagger(y)\Big\}_{x^0=y^0} = i\delta^{(3)}(\vec{x}-\vec{y})\mathbb{1}. \tag{VI.14}$$

For a given field, there are four possible CTP correlators. These are the time-ordered G^{++} (or G^T) type, the anti-time-ordered G^{--} (or $G^{\bar{T}}$) type, and the two so-called Wightman propagators with G^{+-} (or $G^<$) and G^{-+} (or $G^>$). Specifically, for scalar Green functions, we have [477]

$$i\Delta^{++}(x,y) \equiv i\Delta^T(x,y) = \Big\langle T\, \varphi(x)\varphi(y)^\dagger \Big\rangle\,, \tag{VI.15a}$$

$$i\Delta^{+-}(x,y) \equiv i\Delta^<(x,y) = -\Big\langle \varphi^\dagger(y)\varphi(x) \Big\rangle\,, \tag{VI.15b}$$

$$i\Delta^{-+}(x,y) \equiv i\Delta^>(x,y) = \Big\langle \varphi(x)\varphi(y)^\dagger \Big\rangle\,, \tag{VI.15c}$$

$$i\Delta^{--}(x,y) \equiv i\Delta^{\bar{T}}(x,y) = \Big\langle \bar{T}\varphi(x)\varphi(y)^\dagger \Big\rangle\,, \tag{VI.15d}$$

while, for fermionic Green functions, we have [477]

$$i\not{S}^{++}(x,y) \equiv i\not{S}^T(x,y) = \langle T\, \Psi(x)\bar{\Psi}(y) \rangle\,, \tag{VI.16a}$$

$$i\not{S}^{+-}(x,y) \equiv i\not{S}^<(x,y) = \langle \bar{\Psi}(y)\Psi(x) \rangle\,, \tag{VI.16b}$$

$$i\not{S}^{-+}(x,y) \equiv i\not{S}^>(x,y) = \langle \Psi(x)\bar{\Psi}(y) \rangle\,, \tag{VI.16c}$$

$$i\not{S}^{--}(x,y) \equiv i\not{S}^{\bar{T}}(x,y) = \langle \bar{T}\Psi(x)\bar{\Psi}(y) \rangle\,. \tag{VI.16d}$$

Here, T ($\bar{T}$) denotes time (anti-time) ordering. In the definition of $\not{S}^<$, we added a minus sign due to the anti-commutativity of fermion spinors. Notice that these definitions imply

$$(i\Delta^{<,>}(x,y))^\dagger = i\Delta^{<,>}(y,x)\,, \tag{VI.17}$$

$$(i\gamma^0\not{S}^{<,>}(x,y))^\dagger = i\gamma^0\not{S}^{<,>}(y,x)\,. \tag{VI.18}$$

These two-point functions are not independent. In fact, a closer inspection shows that the time and anti-time ordered Green's functions can be determined directly with the Wightmann functions. Using again G to indicate both scalar and fermion functions, one has

$$G^T(x,y) = \theta(x_0 - y_0)G^>(x,y) + \theta(y_0 - x_0)G^<(x,y)\,, \tag{VI.19}$$

$$G^{\bar{T}}(x,y) = \theta(x_0 - y_0)G^<(x,y) + \theta(y_0 - x_0)G^>(x,y)\,. \tag{VI.20}$$

Moreover, by defining the retarded G^R and advanced G^A propagators as

$$G^R(x,y) = \theta(x_0 - y_0)\left(G^>(x,y) + G^<(x,y)\right)\,, \tag{VI.21}$$

$$G^A(x,y) = \theta(y_0 - x_0)\left(G^>(x,y) + G^<(x,y)\right)\,, \tag{VI.22}$$

it follows that we can relate the propagators also by

$$G^{\mathrm{R}} = G^T - G^< = G^> - G^{\bar{T}}\,, \tag{VI.23}$$

$$G^{\mathrm{A}} = G^T - G^> = G^< - G^{\bar{T}}\,. \tag{VI.24}$$

Notice, in particular, that $G^R(x,y) = G^A(y,x)$.

We decompose the retarded propagators into their Hermitian and anti-Hermitian components as follows [449, 467]:

$$G^{\mathcal{H}} = \frac{1}{2}\left(G^{\mathrm{R}} + G^{\mathrm{A}}\right) = \frac{1}{2}\left(G^T - G^{\bar{T}}\right) = \frac{1}{2}\left(G^{++} - G^{--}\right)\,, \tag{VI.25}$$

$$G^{\mathcal{A}} = \frac{i}{2}\left(G^{\mathrm{R}} - G^{\mathrm{A}}\right) = \frac{i}{2}\left(G^> - G^<\right) = \frac{i}{2}\left(G^{-+} - G^{+-}\right)\,. \tag{VI.26}$$

$G^{\mathcal{A}}$ is particularly important because it represents the spectral density of states. As we will soon demonstrate, this key quantity encapsulates all the information about the spectrum of on-shell single and multi-particle states, as well as their off-shell properties.

$$G^{\mathcal{H}}(x,y) = -i\,\mathrm{sign}(x_0 - y_0)G^{\mathcal{A}}(x,y)\,. \tag{VI.27}$$

Finally, it is worth noting that at thermal equilibrium, where the temperature is $T \equiv 1/\beta$, the propagators effectively reduce to a single independent combination. T his simplification arises because, in thermal equilibrium, the expectation value is given by $\langle \ldots \rangle = \mathrm{Tr}\left(e^{-\beta\hat{H}} \ldots\right)$, and the cyclic property of the trace leads to the Kubo-Martin-Schwinger (KMS) relations [412]:

$$G^>_{\mathrm{eq}}(t) = \pm G^<_{\mathrm{eq}}(t + i\beta)\,, \tag{VI.28}$$

where the $\pm$ sign distinguishes between bosons and fermions. These KMS relations will prove highly valuable, especially when expressed in momentum space.

VI.3 2PI effective action

Declaration: this section presents results from the literature, re-elaborated by the thesis author, MB, and CT for [5]. All authors discussed the results and their interpretation. The text closely follows what was presented in [5], with partial reformulation and integrated with more details on the theoretical background. The text in the paper was written by the thesis author and CT. All authors reviewed and corrected the text.

The statistical properties of an ensemble evolve according to the evolution equations for correlation functions. These equations can be transformed into rate equations for particle number densities. To derive such rate equations, it is advantageous to replace the generating functional $Z_{\mathcal{C}}$ with a functional that depends solely on the one- and two-point functions of the theory and whose equations of motion describe the dynamics of the propagators.

While the one-particle irreducible (1PI) effective action provides a powerful framework for computing scattering amplitudes and vacuum correlation functions, it is not well suited for describing nonequilibrium dynamics beyond linear response. In particular, truncations of the 1PI effective action generally violate conservation laws and fail to resum secular terms that grow with time, rendering them unreliable for long-time evolution problems [443]. This breakdown occurs because the 1PI expansion is essentially an expansion in the number of loops; in a plasma, the presence of a medium requires the resummation of infinite subsets of diagrams (such as "daisy" or "ring" diagrams) to account for Debye screening and thermal masses, which 1PI truncations do not naturally provide without additional manual resummation schemes.

The two-particle irreducible (2PI) effective action [419,420,430,442,443] overcomes these limitations by treating the full propagators as independent dynamical variables. This allows for self-consistent resummations that preserve global symmetries, ensure energy–momentum conservation at any truncation order, and provide a controlled framework for describing the real-time evolution of interacting quantum systems far from equilibrium.

The appropriate functional for this purpose is the two-particle irreducible (2PI) effective action $\Gamma_{\mathcal{C}}^{\rm 2PI}$. The equations of motion derived from this 2PI effective action correspond to the Schwinger–Dyson equations, which govern the dynamics of the propagators.

To construct the 2PI effective action, one begins by extending $Z_{\mathcal{C}}[J]$ to incorporate non-local sources $R(x^a, y^b)$ for two-point functions. The generating functional is defined as [443]:

$$Z[J,R] = \exp(iW[J,R]) = \int \mathcal{D}\phi \exp\left[i\left(S[\phi] + \int_{\mathcal{C}} J\phi + \frac{1}{2}\int_{\mathcal{C}} \phi R \phi\right)\right] \tag{VI.29}$$

By performing Legendre transformations of $-i\log Z_{\mathcal{C}[J,R]}$ with respect to both J and R [419,420,430,442,443], one obtains a functional $\Gamma_{\mathcal{C}}^{\rm 2PI}$ that depends only on the exact one-point functions (averaged fields) and the exact two-point functions, the (full) propagators of the theory.

Conceptually, the 2PI effective action can be viewed as a nonequilibrium generalization of the thermodynamic potential (free energy). Instead of depending only on classical background fields, it depends explicitly on the full two-point functions, which encode both spectral information and statistical occupation numbers. As a result, the equations of motion derived from $\Gamma_{\mathcal{C}}^{\rm 2PI}$ describe, in a unified manner, the coupled evolution of quasiparticle dispersion relations and distribution functions.

This functional can be expressed as [419, 442, 449]:

$$\Gamma_{\mathcal{C}}^{\rm 2PI}[\Delta, S] = i\,\mathrm{tr}\Big[\Delta^{0^{-1}}\Delta\Big] - i\,\mathrm{tr}\Big[S^{0^{-1}}S\Big] + i\,\mathrm{tr}\ln\Delta^{-1} - i\,\mathrm{tr}\ln S^{-1} + \Gamma_2[\Delta, S]\,, \tag{VI.30}$$

where Δ and S are the exact two-point functions for scalar and fermion fields, respectively. Here, Γ_2 represents the sum of all 2PI vacuum graphs constructed using the exact propagators, and Δ^0 and S^0 are the tree-level propagators, which are the inverses of the corresponding kinetic operators in the classical action.[2]

The functional $\Gamma_2[\Delta, S]$ contains all interaction effects beyond the classical action and the Gaussian fluctuations encoded in the logarithmic terms. It is defined as the sum of all closed vacuum diagrams that are two-particle irreducible with respect to cutting two

[2] We will not delve into the treatment of gauge bosons, as their analysis parallels that of scalar fields but involves additional complexities due to their vector nature and the need for gauge fixing (see, for example, Ref. [443]). For our purposes, gauge bosons are considered part of the thermalized SM bath, with which dark sector particles interact. Consequently, we will focus solely on their spectral properties. However, we will revisit the analysis of gauge boson propagators in Chapter IX.

internal propagator lines. Truncating Γ_2 at a given loop order corresponds to a nonperturbative resummation of an infinite class of perturbative diagrams in the resulting equations of motion. Importantly, such truncations preserve global symmetries and conservation laws, provided these symmetries are respected at the level of Γ_2.

By varying the effective action and applying the stationary conditions in the absence of external sources, given by [443, 467]

$$\frac{\delta\Gamma_{\mathcal{C}}^{\mathrm{2PI}}[\Delta, S]}{\delta\Delta^{ba}(y,x)} = 0 \quad \text{and} \quad \frac{\delta\Gamma_{\mathcal{C}}^{\mathrm{2PI}}[\Delta, S]}{\delta \slashed{S}^{ba}(y,x)} = 0\,, \tag{VI.31}$$

we obtain the equations of motion for the propagators [443, 467]:

$$i\Delta^{0\,ab^{-1}}(x,y) = i\Delta^{ab^{-1}}(x,y) + i\Pi^{ab}(x,y)\,, \tag{VI.32}$$

$$i\slashed{S}^{0\,ab^{-1}}(x,y) = i\slashed{S}^{ab^{-1}}(x,y) + i\slashed{\Sigma}^{ab}(x,y)\,. \tag{VI.33}$$

The free propagators are related to the exact propagators through the proper self-energies, which are defined as follows [443, 467]:

$$\Pi^{ab}(x,y) = i\,ab\,\frac{\delta\Gamma_2[\Delta, S]}{i\delta\Delta^{ba}(y,x)}\,, \tag{VI.34}$$

$$\slashed{\Sigma}^{ab}(x,y) = -i\,ab\,\frac{\delta\Gamma_2[\Delta, S]}{i\delta\slashed{S}^{ba}(y,x)}\,. \tag{VI.35}$$

Here, the self-energies are obtained by differentiating the interaction functional $\Gamma_2[\Delta, S]$. Diagrammatically, this operation corresponds to removing a single propagator line from the underlying 2PI vacuum diagrams. Multiplying the self-energy by $-i$ yields the corresponding sum of one-particle irreducible (1PI) diagrams, constructed with full propagators and weighted by the Closed-Time-Path (CTP) branch indices a, b.

In summary, the 2PI effective action furnishes a self-consistent and symmetry-preserving framework for studying nonequilibrium quantum dynamics. By elevating propagators to dynamical variables, it bridges the gap between quantum field theory and kinetic theory and forms the theoretical foundation for deriving rate equations governing particle production and annihilation in the early Universe.

VI.3.1 Schwinger-Dyson and Kadanoff-Baym Equations

Having specified the definitions of the two-point functions, we are now able to derive the Schwinger-Dyson equations for the dressed propagators. This is achieved by applying the convolution of one full propagator with the equations of motion given in Eqs. (VI.32) and (VI.33). The resulting equations are [449, 467]:

$$\left(-\partial^2 - m^2\right) i\Delta^{ab}(x,y) = a\delta_{ab} i\delta^{(4)}(x-y) - i\sum_{c=\pm} c\int \mathrm{d}^4z\, i\Pi^{ac}(x,z)\, i\Delta^{cb}(z,y)\,, \tag{VI.36}$$

$$\left(i\slashed{\partial} - m\right) i\slashed{S}^{ab}(x,y) = a\delta_{ab} i\delta^{(4)}(x-y) - i\sum_{c=\pm} c\int \mathrm{d}^4z\, i\slashed{\Sigma}^{ac}(x,z)\, i\slashed{S}^{cb}(z,y)\,. \tag{VI.37}$$

While these equations describe the dynamics for the four CTP propagators, only two independent combinations of these equations are required (cf. Eq. (VI.23)). Therefore, we can reformulate them into separate sets: one for the retarded and advanced propagators, and another for the Wightman $<, >$ functions.

For scalar propagators, we have [467]

$$(-\partial^2 - m^2)\, i\Delta^{\mathrm{R,A}}(x,y) + i\left(i\Pi^{\mathrm{R,A}} \odot i\Delta^{\mathrm{R,A}}\right)(x,y) = i\delta^{(4)}(x-y)\,, \tag{VI.38}$$

$$(-\partial^2 - m^2) i\Delta^{<,>}(x,y) + i\left(i\Pi^{R} \odot i\Delta^{<,>}\right)(x,y) + i\left(i\Pi^{<,>} \odot i\Delta^{A}\right)(x,y) = 0\,, \tag{VI.39}$$

while for fermion propagators we obtain [467]

$$(i\not{\partial} - m)\, i S\!\!\!/^{\mathrm{R,A}}(x,y) + i\left(i\Sigma\!\!\!/^{\mathrm{R,A}} \odot i S\!\!\!/^{\mathrm{R,A}}\right)(x,y) = i\delta^{(4)}(x-y)\,, \tag{VI.40}$$

$$(i\not{\partial} - m) i S\!\!\!/^{<,>}(x,y) + i\left(i\Sigma\!\!\!/^{R} \odot i S\!\!\!/^{<,>}\right)(x,y) + i\left(i\Sigma\!\!\!/^{<,>} \odot i S\!\!\!/^{A}\right)(x,y) = 0\,. \tag{VI.41}$$

We use the notation $(A \odot B)(x,y) \equiv \int \mathrm{d}^4 z\, A(x,z)\, B(z,y)$ to denote the convolution integrals. Additionally, we have defined the retarded, advanced, and Wightman self-energies in a manner consistent with the definitions provided in Eq. (VI.23).

Equations (VI.38) and (VI.40) describe the retarded and advanced propagators, which are instrumental in characterizing the spectral properties of the fields in the system. These properties become more evident when transitioning from coordinate space to momentum space, as we will soon show. Conversely, Equations (VI.39) and (VI.41) capture the statistical information of the fields, leading to kinetic equations for the distribution functions. This connection becomes clear when substituting the retarded and advanced functions in these equations with spectral and Hermitian components, using the relations in Eq. (VI.26). The result is the Kadanoff-Baym equations [441]:

$$(-\partial^2 - m^2)\Delta^{<,>} - \Pi^{\mathcal{H}} \odot \Delta^{<,>} - \Pi^{<,>} \odot \Delta^{\mathcal{H}} = \frac{1}{2}(\Pi^{>} \odot \Delta^{<} - \Pi^{<} \odot \Delta^{>})\,, \tag{VI.42}$$

$$(i\not{\partial} - m) S\!\!\!/^{<,>} - \Sigma\!\!\!/^{\mathcal{H}} \odot S\!\!\!/^{<,>} - \Sigma\!\!\!/^{<,>} \odot S\!\!\!/^{\mathcal{H}} = \frac{1}{2}(\Sigma\!\!\!/^{>} \odot S\!\!\!/^{<} - \Sigma\!\!\!/^{<} \odot S\!\!\!/^{>})\,. \tag{VI.43}$$

The right-hand side of the equation can be interpreted as the QFT analog of the collision operator found in semi-classical Boltzmann equations, encompassing terms for particle creation and annihilation. Consequently, this term vanishes in thermodynamic equilibrium. This can be directly demonstrated by applying the KMS relations from Eq. (VI.28) to both the Wightman propagators and the self-energies.

The Kadanoff-Baym equations are particularly powerful because they do not assume the quasiparticle approximation a priori. They allow for the study of systems with broad spectral functions where the notion of a well-defined 'particle' might be lost due to strong interactions or high temperatures. Specifically, the convolution structure represents a non-local "memory kernel", meaning the evolution of the system at time t depends on its previous history, a feature that is essential for describing the approach to equilibrium and the emergence of thermal widths.

VI.3.2 Wigner Transform and Gradient Expansion

We now aim to distinguish between microscopic and macroscopic aspects of the physics involved. Specifically, we want to separate statistical fluctuations, which represent the microscopic details, from the macroscopic changes. The latter are less critical for our purposes, as long as the background in which the field dynamics occur evolves slowly. For instance, this is true when the timescales for particle interactions are significantly shorter than those for the expansion of the Universe.

To illustrate this, we first perform a Wigner transformation of the two-point Green's functions. This transformation involves taking a Fourier transform with respect to the relative coordinate r:

$$G(k,x) = \int \mathrm{d}^4 r\, e^{ik\cdot r} G\left(x + \frac{r}{2}, x - \frac{r}{2}\right) , \tag{VI.44}$$

where x represents the mean coordinate. In Wigner space, convolutions take on a simplified form, as demonstrated in Appendix B of [484], yielding

$$\begin{aligned} A \odot B \to (A \odot B)(k,x) &= \int \mathrm{d}^4 r e^{ik\cdot r} \int \mathrm{d}^4 z A\left(x + \frac{r}{2}, z\right) B\left(z, x - \frac{r}{2}\right) \\ &= e^{-i\diamond}\{A(k,x)\}\{B(k,x)\} , \end{aligned} \tag{VI.45}$$

where the diamond operator is defined as

$$\diamond\{A\}\{B\} = \frac{1}{2}\left(\partial_x A \cdot \partial_k B - \partial_k A \cdot \partial_x B\right) , \tag{VI.46}$$

and the exponentiation is interpreted as a series expansion, such as

$$e^{-i\diamond} = \cos\diamond - i\sin\diamond = \sum_{n=0}^{\infty}(-1)^n \frac{(-i\diamond)^{2n}}{(2n)!} + \sum_{n=0}^{\infty}(-1)^n \frac{(-i\diamond)^{2n+1}}{(2n+1)!} . \tag{VI.47}$$

In Wigner space, the Kadanoff-Baym equations are transformed into (see, e.g., [449]),

$$\left(k^2 - \frac{1}{4}\partial^2 + ik\cdot\partial_x - m^2 e^{-\frac{i}{2}\overleftarrow{\partial}_x\cdot\partial_k}\right)\Delta^{<,>} - e^{-i\diamond}\{\Pi^{\mathcal{H}}\}\{\Delta^{<,>}\} - e^{-i\diamond}\{\Pi^{<,>}\}\{\Delta^{\mathcal{H}}\} = \mathcal{C}_\phi , \tag{VI.48}$$

$$\left(\not{k} + \frac{i}{2}\not{\partial}_x - i\gamma^5 m e^{-\frac{i}{2}\overleftarrow{\partial}_x\cdot\partial_k}\right)\not{S}^{<,>} - e^{-i\diamond}\{\not{\Sigma}^{\mathcal{H}}\}\{\not{S}^{<,>}\} - e^{-i\diamond}\{\not{\Sigma}^{<,>}\}\{\not{S}^{\mathcal{H}}\} = \mathcal{C}_\psi , \tag{VI.49}$$

where the collision operators read as

$$\mathcal{C}_\phi = \frac{1}{2}e^{-i\diamond}\left(\{\Pi^>\}\{\Delta^<\} - \{\Pi^<\}\{\Delta^>\}\right) , \tag{VI.50}$$

$$\mathcal{C}_\psi = \frac{1}{2}e^{-i\diamond}\left(\{\not{\Sigma}^>\}\{\not{S}^<\} - \{\not{\Sigma}^<\}\{\not{S}^>\}\right) . \tag{VI.51}$$

Similarly, Eqs. (VI.38) and (VI.40) assume the following forms

$$\left(k^2 - \frac{1}{4}\partial_x^2 + ik\cdot\partial - m^2 e^{-\frac{i}{2}\overleftarrow{\partial}_x\cdot\partial_k}\right) i\Delta^{R/A} - e^{-i\diamond}\{\Pi^{R,A}\}\{\Delta^{R,A}\} = i , \tag{VI.52}$$

$$\left(\not{k} + \frac{i}{2}\not{\partial}_x - i\gamma^5 m e^{-\frac{i}{2}\overleftarrow{\partial}_x\cdot\partial_k}\right) i\not{S}^{R/A} - e^{-i\diamond}\{\not{\Sigma}^{R,A}\}\{\not{S}^{R,A}\} = i . \tag{VI.53}$$

The series expansion of the gradient terms in the exponent of the diamond operator $e^{-i\diamond}$ can be truncated at a certain order if the convoluted operators exhibit only a weak dependence on the mean coordinate x. This truncation effectively simplifies the macroscopic correlation length, which measures how the expanded functions vary with respect to the macroscopic mean coordinate. In situations where the background fields change slowly, such as in thermal equilibrium, their correlation length is much larger than the de Broglie wavelength of the particles in the plasma, which is typically on the order of T^{-1}. This means that the spatial variation of these background fields is negligible compared to the momentum of the particles, namely that $\partial \ll k \sim \lambda_{\rm DB}^{-1} \sim T$. In this case, the gradient expansion is justified.

In Wigner space and up to first order in the gradients, the Kadanoff-Baym equations in Eqs. (VI.48) and (VI.49) become

$$k^0 \partial_t \left(i\Delta^{<,>}\right) = -\frac{1}{2}\left(i\Pi^{>}\, i\Delta^{<} - i\Pi^{<}\, i\Delta^{>}\right) + \mathcal{O}(\partial_t \Pi^{\mathcal{H};<,>}\Delta^{<,>;\mathcal{H}})\,, \tag{VI.54}$$

$$\not{k}\left(iS^{<,>}\right) = -\frac{1}{2}\left(i\not{\Sigma}^{>}\, i\not{S}^{<} - i\not{\Sigma}^{<}\, i\not{S}^{>}\right) + \mathcal{O}\left(\partial_t \not{\Sigma}^{\mathcal{H};<,>}\not{S}^{<,>;\mathcal{H}}\right)\,, \tag{VI.55}$$

These equations are essential because they will eventually yield the fluid rate equations for the DM distribution after integrating over energy, as detailed in Section VI.4. Specifically, the left-hand side is directly related to the time derivative of particle number densities, while the first term on the right-hand side represents the dominant contribution to the particle production rate. The terms involving temporal derivatives, which are discarded, account for gradient corrections to the production rate. In a freeze-in scenario, these gradient corrections are expected to be significantly suppressed due to the tiny coupling involved.

For the retarded and advanced two-point Green's functions, the Schwinger-Dyson equations, given by Eq. (VI.52) and Eq. (VI.53), can be expressed as discussed in [449, 484].[3]

$$\left(k^2 + ik\cdot\partial_x - m^2 - \Pi^{R/A}\right) i\Delta^{R/A} = i\,, \tag{VI.56}$$

$$\left(\not{k} + \frac{1}{2}\not{\partial}_x - m - \not{\Sigma}^{R/A}\right) i\not{S}^{R/A} = i\,. \tag{VI.57}$$

In Wigner space, the KMS relations given in Eq. (VI.28) are expressed as

$$G^{\rm eq,>}(k) = \pm e^{\beta k^0} G^{\rm eq,<}(k)\,, \tag{VI.58}$$

where the positive (negative) sign corresponds to bosons (fermions). Due to translation invariance in equilibrium, the Green's functions $G^{\rm eq}$ depend solely on the spatial relative coordinate. Consequently, their Wigner transform simplifies to a Fourier transform dependent only on momentum. From Eqs. (VI.58) and (VI.26), it is clear that the Wightman propagators are directly related to the spectral density of states $G^{\rm eq,\mathcal{A}}$ as follows:

$$iG^{\rm eq,<}(k) = \pm 2 f_{\mp}(k^0) G^{\rm eq,\mathcal{A}}(k)\,, \tag{VI.59}$$

$$iG^{\rm eq,>}(k) = \mp 2 f_{\mp}(-k^0) G^{\rm eq,\mathcal{A}}(k)\,, \tag{VI.60}$$

where the $\pm$ signs are as previously indicated.

The functions $f_{\mp}$ represent the Bose-Einstein and Fermi-Dirac distribution functions in thermal equilibrium:

$$f_{\mp}(p^0) = \frac{1}{e^{p^0/T} \mp 1}\,, \tag{VI.61}$$

with $T = 1/\beta$.

These relations simplify our calculations by reducing the complexities of the CTP formalism—specifically, the doubling of degrees of freedom—to just evaluating a single function: the spectral density of states.

[3] Alternative approaches addressing quantum kinetic equations without relying on 2PI effective action expansions or approximated Kadanoff-Baym equations have been explored for scalar field dynamics in the early Universe, with applications to dark matter and reheating after inflation [485–495].

VI.3.2.1 Spectral Sum Rules

In Wigner space, the spectral densities have to obey a *spectral sum rule* that is a direct consequence of the equal-time canonical (anti)commutation relations in Eqs. (VI.13) and (VI.14). Let us take the example of scalars. Eq. (VI.13) in Wigner space becomes

$$\Big[\varphi(t,\vec{k}), \dot{\varphi}^\dagger(t',\vec{k})\Big]_{t=t'} = i\,. \tag{VI.62}$$

The spectral function can be rewritten with field operators as

$$\Delta^{\mathcal{A}}(t,\vec{k}) = \frac{1}{2}\left(\Delta^> - \Delta^<\right)(t,\vec{k}) = \frac{1}{2}\left\langle\Big[\phi(t,\vec{k}), \phi^\dagger(0,\vec{k})\Big]\right\rangle. \tag{VI.63}$$

Taking the time derivative of this expression and setting $t=0$ afterward yields

$$\dot{\Delta}^{\mathcal{A}}(0,\vec{k}) = \frac{1}{2}\left\langle\Big[\dot{\phi}(t,\vec{k}), \phi^\dagger(0,\vec{k})\Big]\right\rangle|_{t=0} \tag{VI.64}$$

$$= -\frac{i}{2}\,. \tag{VI.65}$$

Now consider the Fourier transform of $\dot{\Delta}^{\mathcal{A}}$ with respect to t and evaluated at $t=0$

$$\dot{\Delta}^{\mathcal{A}}(t,\vec{k})|_{t=0} = \frac{\mathrm{d}}{\mathrm{d}t}\int\frac{\mathrm{d}k^0}{2\pi}e^{-itk^0}\Delta^{\mathcal{A}}(k^0,\vec{k})\bigg|_{t=0} \tag{VI.66}$$

$$= -\frac{i}{2}\int\frac{\mathrm{d}k^0}{\pi}k^0\Delta^{\mathcal{A}}(k)\,. \tag{VI.67}$$

This implies the following bosonic spectral sum rule

$$\int\frac{\mathrm{d}k^0}{\pi}k^0\Delta^{\mathcal{A}}(k) = 1\,. \tag{VI.68}$$

Similarly, for fermionic fields, we obtain the following fermionic spectral sum rule from the equal-time anticommutation relations in Wigner space:

$$\int\frac{\mathrm{d}k^0}{\pi}\frac{1}{4}\mathrm{Tr}\Big\{\gamma^0\not{S}^{\mathcal{A}}(k)\Big\} = \mathbb{1}\,. \tag{VI.69}$$

In the last equation, we used the identity matrix in the representation of the Clifford algebra generated by the Gamma matrices. These sum rules are critical since they come from the quantization conditions; thus, their validity ensures the consistency of the theory and of the solutions of the Schwinger-Dyson equations.

VI.3.2.2 Tree-level Propagators

When neglecting the interactions with the plasma, Eqs. (VI.56) and (VI.57) are solved by the tree-level propagators, that is to say, by the solutions to the Klein-Gordon and the Dirac equations for scalars and fermions, respectively. In Wigner space and assuming thermal equilibrium, they read for bosonic fields as [431, 467, 477]

$$i\Delta^T_{\mathrm{eq}}(k) = \frac{i}{k^2 - m^2 + i\mathrm{sign}(k_0)\epsilon} + 2\pi\delta(k^2-m^2)\mathrm{sign}(k_0)\,f^{\mathrm{eq}}_-(k_0)\,, \tag{VI.70}$$

$$i\Delta^{\bar{T}}_{\mathrm{eq}}(k) = \frac{-i}{k^2 - m^2 + i\mathrm{sign}(k_0)\epsilon} + 2\pi\delta(k^2-m^2)\mathrm{sign}(k_0)\,\left(1+f^{\mathrm{eq}}_-(k_0)\right)\,, \tag{VI.71}$$

$$i\Delta^<_{\rm eq}(k) = 2\pi\delta(k^2-m^2)\text{sign}(k_0)f_-^{\rm eq}(k_0)\,, \tag{VI.72}$$
$$i\Delta^>_{\rm eq}(k) = 2\pi\delta(k^2-m^2)\text{sign}(k_0)\left(1+f_-^{\rm eq}(k_0)\right)\,, \tag{VI.73}$$

where $f_-(k_0)$ is the Bose-Einstein distribution. For fermionic fields, one has

$$iS^T_{\rm eq}(k) = \frac{i(\not{k}+m)}{k^2-m^2+i\text{sign}(k_0)\epsilon} + (\not{k}+m)2\pi\delta(k^2-m^2)\text{sign}(k_0)\,f_+^{\rm eq}(k_0)\,, \tag{VI.74}$$
$$iS^{\bar{T}}_{\rm eq}(k) = \frac{-i(\not{k}+m)}{k^2-m^2+i\text{sign}(k_0)\epsilon} + (\not{k}+m)2\pi\delta(k^2-m^2)\text{sign}(k_0)\left(1-f_+^{\rm eq}(k_0)\right)\,, \tag{VI.75}$$
$$iS^<_{\rm eq}(k) = -(\not{k}+m)2\pi\delta(k^2-m^2)\text{sign}(k_0)f_+^{\rm eq}(k_0)\,, \tag{VI.76}$$
$$iS^>_{\rm eq}(k) = (\not{k}+m)2\pi\delta(k^2-m^2)\text{sign}(k_0)\left(1-f_+^{\rm eq}(k_0)\right)\,, \tag{VI.77}$$

where $f_+(k_0)$ is the Fermi-Dirac distribution. Notice that, without the assumption of thermal equilibrium, the expressions would be slightly different and we could not use the Bose-Einstein and the Fermi-Dirac distributions (see, e.g., appendix A of [468]). Following the definition in Eq. (VI.26), the anti-Hermitian propagators read as

$$\Delta^{\mathcal{A}}(k) = \pi\,\text{sign}(k^0)\,\delta\left(k^2-m^2\right)\,, \tag{VI.78}$$
$$S^{\mathcal{A}}(k) = \pi\,\text{sign}(k^0)\,(\not{k}+m)\,\delta\left(k^2-m^2\right)\,, \tag{VI.79}$$

which explains why they are also called *spectral densities*: they determine the density and the dispersion relation of states that are *on-shell* at a particular energy shell. The Wightman functions for scalar fields also follow from Eqs. (VI.26) and (VI.78) as

$$i\Delta^<(k) = 2\Delta^{\mathcal{A}}(k)f_-(k)\,, \tag{VI.80}$$
$$i\Delta^>(k) = 2\Delta^{\mathcal{A}}(k)\left(1+f_-(k)\right)\,, \tag{VI.81}$$

while using Eq. (VI.79) yields

$$iS^<(k) = -2S^{\mathcal{A}}(k)f_+(k)\,, \tag{VI.82}$$
$$iS^>(k) = 2S^{\mathcal{A}}(k)\left(1-f_+(k)\right)\,. \tag{VI.83}$$

VI.3.2.3 Resummed Propagators

We will now retain the interaction with the plasma as described in Eq. (VI.56) and Eq. (VI.57), and assume spatial homogeneity and isotropy. This allows us to algebraically solve the equations for the *resummed propagators*. For scalar fields, the resummed propagators are given by [431, 467, 477, 479]

$$i\Delta^{R/A} = \frac{i}{k^2-m^2-\Pi^{R/A}} = \frac{i}{k^2-m^2-\Pi^{\mathcal{H}}\pm i\Pi^{\mathcal{A}}}\,, \tag{VI.84}$$

where $+$ corresponds to the retarded propagator and $-$ to the advanced propagator. Consequently, the anti-Hermitian (spectral density) and Hermitian components of the resummed scalar propagators can be expressed as

$$\Delta^{\mathcal{A}} = -\Im\Delta^R = \frac{\Pi^{\mathcal{A}}}{(k^2-m^2-\Pi^{\mathcal{H}})^2+(\Pi^{\mathcal{A}})^2}\,, \tag{VI.85}$$
$$\Delta^{\mathcal{H}} = \Re\Delta^R = \frac{k^2-m^2-\Pi^{\mathcal{H}}}{(k^2-m^2-\Pi^{\mathcal{H}})^2+(\Pi^{\mathcal{A}})^2}\,. \tag{VI.86}$$

Similarly, the retarded and advanced propagators for fermion fields are given by

$$i\not{S}^{R/A} = \frac{i}{\not{k} - m - \not{\Sigma}^{R/A}} = \frac{i}{\not{k} - m - \not{\Sigma}^{\mathcal{H}} \pm i\not{\Sigma}^{\mathcal{A}}} \,. \tag{VI.87}$$

The resummed anti-Hermitian and Hermitian parts of the propagator can be obtained similarly, though they involve more complexity due to the presence of Dirac matrices. By introducing the notation

$$\not{\Sigma}^{\mathcal{H}/\mathcal{A}} = \gamma^{\mu}\,\Sigma_{\mu}^{\mathcal{H}/\mathcal{A}}, \tag{VI.88}$$

a more compact representation of the resummed propagators reads as

$$\not{S}^{\mathcal{A}} = -\Im \not{S}^{R} = \left(\not{k} + m - \not{\Sigma}^{\mathcal{H}}\right)\frac{\Gamma}{\Omega^2+\Gamma^2} - \not{\Sigma}^{\mathcal{A}}\frac{\Omega}{\Omega^2+\Gamma^2}\,, \tag{VI.89}$$

$$\not{S}^{\mathcal{H}} = \Re \not{S}^{R} = \left(\not{k} + m - \not{\Sigma}^{\mathcal{H}}\right)\frac{\Omega}{\Omega^2+\Gamma^2} + \not{\Sigma}^{\mathcal{A}}\frac{\Gamma}{\Omega^2+\Gamma^2}\,, \tag{VI.90}$$

with Γ and Ω representing the width and the pole of the propagators, reading

$$\Gamma \equiv 2\left(k - \Sigma^{\mathcal{H}}\right)\cdot\Sigma^{\mathcal{A}}, \tag{VI.91}$$

$$\Omega \equiv \left(k - \Sigma^{\mathcal{H}}\right)^2 - (\Sigma^{\mathcal{A}})^2 - m^2\,. \tag{VI.92}$$

These resummed expressions are central to the study of particles in a thermal bath. The spectral density $\Delta^{\mathcal{A}}$ (and similarly $\not{S}^{\mathcal{A}}$) no longer consists of sharp delta functions but rather Breit-Wigner-like peaks. The width $\Pi^{\mathcal{A}}$ (or Γ for fermions) physically represents the interaction rate of the particles with the medium. In the context of dark matter freeze-in, this broadening of the spectral function allows for production processes that would be kinematically forbidden at tree-level, effectively capturing the effects of multiple soft scatterings and off-shell production in the early Universe.

VI.4 Derivation of the Fluid Equation for Freeze-in

Declaration: this section presents results from the literature, re-elaborated by the thesis author for [5]. All authors discussed the results and their interpretation. The text is a substantially reworked version of what was presented in [5] with expanded theoretical information and stylistic adjustments. The text in the paper was written by the thesis author and was reviewed and corrected by all authors.

In this section, we derive an analog of the Boltzmann equation for the number density of a scalar field denoted by s (representing our dark matter candidate). [4] This derivation bridges the gap between the formal Schwinger-Dyson equations of the 2PI framework and the macroscopic fluid equations used in cosmology. The starting point is the kinetic equation for a scalar propagator in Wigner space, as given in Eq. (VI.54).

VI.4.1 The Kadanoff-Baym Ansatz and Quasiparticle Limit

Focusing on the freeze-in production scenario, we assume that the dark matter s interacts very weakly with the Standard Model (SM) bath. This implies that the dark matter

[4] We choose s instead of ϕ, as previously used, because this is how we will refer to the DM candidate in the t-channel model we will analyze in Chapters VII and VIII.

abundance f_s remains much smaller than the equilibrium distribution ($f_s \ll f_{eq}$) and that the self-energy Π_s is dominated by interactions with thermalized bath particles.

While the bath particles are in equilibrium, the s particles are not. To solve the Kadanoff-Baym equations, we require an *ansatz* that relates the spectral properties to the statistical properties. We employ the generalized fluctuation-dissipation relation, or **Kadanoff-Baym ansatz** [431, 442, 484]:

$$i\Delta_s^<(p) = 2\Delta_s^{\mathcal{A}}(p,x) f_s(p^0,\vec{p})\,, \tag{VI.93a}$$

$$i\Delta_s^>(p) = 2\Delta_s^{\mathcal{A}}(p,x)\left(1 + f_s(p^0,\vec{p})\right)\,. \tag{VI.93b}$$

Mathematically, this ansatz assumes that the non-equilibrium information is entirely contained within the distribution function f_s, while the spectral density $\Delta_s^{\mathcal{A}}$ maintains its structure. In the weak-coupling limit, we further assume the **quasiparticle approximation**, where the spectral density is sharply peaked at the on-shell energy $\omega_p = \sqrt{|\vec{p}|^2 + m_s^2}$:

$$\Delta_s^{\mathcal{A}}(p) \simeq \pi\delta(p^2 - m_s^2)\mathrm{sign}(p^0)\,. \tag{VI.94}$$

Physically, this neglects the thermal width of the dark matter itself (since $\Pi_s^{\mathcal{A}}$ is suppressed by small couplings), though we retain the thermal widths of the bath particles that produce it. This distinction is vital: the production rate depends on the spectral broadening of the *source* fields, not the s field itself.

The number density n_s is defined by integrating the distribution function over the available phase space. In the CTP framework, the relationship between the Wightman propagator and the distribution function is given by:

$$f_s(\omega_p) = \int_0^\infty \frac{\mathrm{d}p^0}{\pi}\, p^0 i\Delta_s^<(p)\,. \tag{VI.95}$$

VI.4.2 The Collision Operator and the Rate Equation

To derive the evolution of f_s, we integrate the kinetic equation (VI.54) over the positive energy branch $p^0 > 0$. The right-hand side of the Kadanoff-Baym equation functions as a collision operator $\mathcal{C}[f_s]$:

$$\begin{aligned}
\partial_t f_s(t,\vec{p}) &= \int_0^\infty \frac{\mathrm{d}p^0}{\pi}\frac{1}{2}\left[\left(i\Pi_s^<\right)\left(i\Delta_s^>\right) - \left(i\Pi_s^>\right)\left(i\Delta_s^<\right)\right] \\
&= \int_0^\infty \frac{\mathrm{d}p^0}{\pi}\Delta_s^{\mathcal{A}}\Pi_s^{\mathcal{A}}\left[f_{eq}(p^0)(1+f_s) - (1+f_{eq})f_s\right] \\
&= \frac{\Pi_s^{\mathcal{A}}(\omega_p,|\vec{p}|)}{\omega_p}\left[f_{eq}(\omega_p) - f_s(t,\vec{p})\right]
\end{aligned} \tag{VI.96}$$

where we applied the KMS relations for the thermal self-energies $i\Pi_s^{<,>}$ of the bath (the DM self-energy contains only fields at thermal equilibrium, for which the KMS relations are always valid). The structure contains a **gain term** (proportional to f_{eq}) representing production from the bath, and a **loss term** (proportional to f_s) representing back-reaction. In the freeze-in regime ($f_s \ll f_{eq}$), the loss term is negligible:

$$\partial_t f_s(t,\vec{p}) \simeq \frac{\Pi_s^{\mathcal{A}}(\omega_p,|\vec{p}|)}{\omega_p} f_{eq}(\omega_p)\,. \tag{VI.97}$$

Integrating over momentum $\int \frac{d^3p}{(2\pi)^3}$ gives the rate of change for the number density:

$$\frac{\mathrm{d}}{\mathrm{d}t} n_s(t) = \int \frac{\mathrm{d}^3\vec{p}}{(2\pi)^3}\frac{\Pi_s^{\mathcal{A}}(\omega_p,|\vec{p}|)}{\omega_p} f_{eq}(\omega_p)\,. \tag{VI.98}$$

VI.4.3 Expansion of the Universe and Conformal Mapping

In the early Universe, we account for the FLRW metric $g_{\mu\nu} = \mathrm{diag}(1, -a^2, -a^2, -a^2)$. Following [457, 467], we use a conformal transformation to map the problem to a Minkowski-like form. Defining conformal time η such that $\mathrm{d}t = a\mathrm{d}\eta$, and scaling the fields (e.g., $\phi \to a\phi$), the kinetic terms remain canonical. All masses and momenta are interpreted as comoving quantities ($m_{\mathrm{com}} = am_{\mathrm{ph}}$, $p_{\mathrm{com}} = ap_{\mathrm{ph}}$).

The physical number density n_{ph} and comoving density n_s are related by $n_s = a^3 n_{\mathrm{ph}}$. Transforming Eq. (VI.98) into physical coordinates yields [5]:

$$\frac{\mathrm{d}}{\mathrm{d}t} n_{\mathrm{ph}}(t) + 3Hn_{\mathrm{ph}} = \int \frac{\mathrm{d}^3\vec{p}}{(2\pi)^3} \frac{\Pi_s^{\mathcal{A}}(\omega_p, |\vec{p}|)}{\omega_p} f_{\mathrm{eq}}(\omega_p) \equiv \gamma_s \,. \tag{VI.99}$$

Using the DM Yield $Y_s = n_{\mathrm{ph}}/s$ and $z = m/T$ (m being some reference mass scale, which can be the DM mass or the mass of some other particle):

$$zHs\frac{\mathrm{d}Y_s}{\mathrm{d}z} = \gamma_s \,. \tag{VI.100}$$

This is equivalent in form to the Boltzmann equation we introduced in Eq. (III.45). However, here it has been derived from field-theoretical principles and where the relation between the QFT description of particle interaction and their statistical and thermodynamical properties is made manifest. On the contrary, the steps that brought us to Eq. (III.45) relied on a combination of classical arguments of fluid dynamics and scattering theory, but its form was never justified from a theoretical point view, but rather a semi-empirical one.

In the next chapter, we will solve Eq. (VI.100) to determine the evolution of the DM number density and abundance from the foundational principles of QFT, applied to a specific model: a simplified t-channel scenario involving a singlet scalar DM candidate. The scalar interacts with an SM fermion through a heavier vectorlike fermion mediator possessing gauge charges. A key aspect of our analysis will be the incorporation of thermal effects via the resummed propagators of the SM-charged fermion species, which contribute to the DM self-energy in the r.h.s of Eq. (VI.99). We will employ their 1PI-resummed form across the full temperature range, avoiding any further approximations, and provide a comparison with commonly used approximation schemes.

To clarify the advantages of the CTP derivation, we summarize the conceptual differences between the classical Boltzmann approach and the 2PI/CTP framework in Table VI.1. The CTP approach avoids double-counting and captures multi-particle effects that are typically missed in the classical approach. In the next chapter, we apply this yield equation to a specific t-channel mediator model.

Concluding Remarks

Building on the extensive literature on the topic, in this chapter, we have reviewed the key quantities employed for describing particle production in non-equilibrium QFT and we have derived the evolution equation of the DM number density in the freeze-in mechanism. The discussion has been carried out within the CTP formalism, which is a powerful and versatile method for computing real-time observables in finite-density environments following a rigorous "from-first-principles" recipe.

Table VI.1: Summary of comparison between the Boltzmann and CTP/2PI frameworks.

Feature	**Classical Boltzmann**	**CTP / 2PI Framework**
Starting Point	Dilute gas, asymptotic states	2PI effective action
Interaction Rate	Vacuum cross-sections $\sigma(v)$	Imaginary part of the self-energy
Kinematics	On-shell delta functions	Resummed spectral functions $\Delta^{\mathcal{A}}$
Statistical Factors	Added manually	Naturally from KMS relations
Medium Effects	Often neglected	With thermal masses and widths
Off-shell Effects	Not captured	Included via integration over $\Pi^{\mathcal{A}}$

When combined with the 2PI effective action approach, this formalism enables a systematic derivation of the DM rate equation from the Kadanoff-Baym equations of the CTP two-point functions, encompassing quantum and thermal corrections across all orders, as encoded in the exact Green's functions. These functions, expressed as Wigner-transformed resummed propagators, effectively capture the full spectrum of interactions between fields and the surrounding plasma.

To accurately assess the impact of these quantum and thermal interactions on DM production, we must adopt a specific DM model and calculate the DM self-energy within the DM interaction rate density using these resummed propagators. This critical step will be undertaken in the next two chapters, where we will focus on a simplified t-channel model of scalar DM to explicitly compute these quantities.

What we are going to present not only marks the first comprehensive analytical and numerical study of this kind within the freeze-in literature but also sets the stage for a thorough comparison with alternative methodologies. Specifically, we will contrast our results—obtained using 1PI-resummed propagators including the in-vacuum mass scales—with other prevalent approaches, such as the Hard Thermal Loop resummation technique and the conventional 'S-matrix' Boltzmann equation approach. By doing so, we will highlight the conditions under which these methods converge or diverge, quantify their disagreement, and offer crucial insights into their respective applicability across different parameter regimes.

CHAPTER VII

Scalar DM from Non-Equilibrium QFT: Production Rates, Self-Energies, and Plasma Dynamics

In this chapter, we apply the Closed-Time-Path (CTP) formalism combined with the two-particle-irreducible (2PI) effective action approach, as reviewed in Chapter VI, to compute the evolution of the Dark Matter (DM) number density and to determine its relic abundance in the context of freeze-in production.

We begin by introducing the particle-physics framework in which our analysis is performed: a simplified t-channel model featuring a vectorlike fermionic heavy mediator that acts as a portal between the visible sector and a feebly interacting scalar DM particle through a Yukawa interaction. We then describe how the DM production rate is computed from its self-energy derived from the 2PI effective action, and we show explicitly how this rate depends on resummed propagators appearing in the self-energy loop. The resummed propagators are evaluated at first order in the loop expansion, which requires a technically involved and lengthy computation that we present in full detail.

Each analytical component is implemented in a dedicated numerical routine written in `C++`. While an overall description of the numerical framework is deferred to Chapter VIII, we provide here the explicit implementation of the individual functions alongside their analytical derivation. For comparison, we also present the DM production rate in the Hard Thermal Loop (HTL) approximation and at tree level. Furthermore, we analyze in detail the pole structure of the fermionic spectral density, highlighting the characteristic features of quantum fields at finite temperature and their role in governing the dynamics of DM interactions.

The computations presented in this chapter constitute the core of the results published in Ref. [5]. They are original and, to the best of our knowledge, represent the first study of this kind in the context of dark matter freeze-in based on the CTP and 2PI formalisms.

Statement of Personal Contribution for this Chapter

The theoretical ideas and derivations presented in this chapter have been developed by the thesis author and MB for [5]. The theoretical foundations are mainly based on existing literature, while most of the analytical results and the numerical implementation are original. All the authors contributed to discussing and interpreting the results. Some of the text here is based on what was presented in [5], which was mainly written by the thesis author, with contributions from MB and CT, while reviewed and corrected by all authors. The original text has been largely reworked and integrated with lots of information regarding the derivation and analysis of various quantities central to the calculation, together with their numerical implementation. In particular, in reference to this chapter, the principal contributions of the thesis author to this publication include:

- The literature research and review.
- The derivation of the resummed fermion spectral densities (together with MB and cross-checked by CT).
- The analysis of the structure of the fermion self-energy and resummed spectral density (together with MB).
- The analysis and derivations in the HTL limit (together with MB).
- The numerical implementation necessary to compute the DM self-energy on the CTP (together with MB).
- The derivation of the matrix elements and cross-sections for the interaction rate in the Boltzmann approach (together with MB).
- The creation of Figs. VII.3.

At the beginning of each section, we will emphasize which parts have been directly done by the thesis author alone, which resulted from a combined effort with the papers' co-authors, and which are taken from the literature. Moreover, a statement on the authors of the text of each section will be provided.

VII.1 Vectorlike Portal FIMP Models

Declaration: this section presents the particle DM model that will be used in the coming sections. The following text is taken from [5] with small adjustments in style and content. The text in the paper was written by the thesis author, while all authors contributed to structuring, reviewing, and refining the manuscript.

We consider a model where DM is represented by a real scalar singlet s, which interacts through a weak Yukawa coupling with a vectorlike BSM fermion F (referred to as the "mediator") and an SM fermion f. This model is often termed the *vectorlike portal* and has been previously explored in the contexts of both freeze-out [496–498] and freeze-in [184, 411], though without accounting for thermal effects. It falls within the `F3S` class of simplified t-channel models as discussed in [188] (cf. Section II.2.4).

The Lagrangian density of the model is given by

$$\mathcal{L} = \mathcal{L}_{\rm SM} + \frac{1}{2}(\partial_\mu s)^2 - \frac{1}{2}m_{\rm DM}^2 s^2 - V(s,H) + \bar{F}\left(i\not{D} - m_F\right)F - \left[y_{\rm DM}\bar{F}P_{L/R}fs + \text{h.c.}\right] , \tag{VII.1}$$

where $V(s,H)$ denotes the scalar potential of DM, potentially including interactions with the Higgs field, D_μ is the covariant derivative, $y_{\rm DM}$ represents the portal Yukawa coupling, and $P_{L/R} = (1 \mp \gamma_5)/2$ are the chiral projection operators. Since we focus on the freeze-in regime, this coupling is assumed to be $y_{\rm DM} \ll 1$. The mediator and DM scalar are stabilized by a Z_2 symmetry under which they are odd, while SM fields remain even, ensuring that DM is the lightest stable particle in the dark sector.

	Y	$SU(2)$	$SU(3)$	G	$\mu = M_Z$	10^4 GeV	10^7 GeV	10^{10} GeV
e_L	$-1/2$	**2**	**1**	$\frac{g_1^2}{4} + \frac{3g_2^2}{4}$	0.38	0.4	0.46	0.52
q_L	$+1/6$	**2**	**3**	$\frac{g_1^2}{36} + \frac{3g_2^2}{4} + \frac{4g_3^2}{3}$	2.3	1.6	1.2	1.0
e_R	-1	**1**	**1**	g_1^2	0.21	0.22	0.24	0.26
u_R	$+2/3$	**1**	**3**	$\frac{4g_1^2}{9} + \frac{4g_3^2}{3}$	2.1	1.3	0.9	0.7
d_R	$-1/3$	**1**	**3**	$\frac{g_1^2}{9} + \frac{4g_3^2}{3}$	2.0	1.2	0.8	0.6

Table VII.1: The effective gauge coupling G as defined in Eq. (VII.2) for the five possible models according to the SM fermion gauge representations. We use the 1-loop β-functions of the SM gauge couplings to estimate G at several renormalization scales μ from the Z pole ($\mu = M_Z$) up to 10^{10} GeV, enclosing some of the values of G considered later in this work. *Table created by the thesis author and included in [5].*

In this work, we exclude the effects of DM self-interactions and any interaction terms between DM and the Higgs in the scalar potential. This simplification allows us to focus on a reduced parameter set, specifically the gauge couplings, the Yukawa coupling $y_{\rm DM}$, and the masses $m_{\rm DM}$ and m_F. Notably, we assume the self-coupling and Higgs interaction to be sufficiently weak to prevent the scalar singlet from equilibrating with itself or the SM bath (see, e.g., Refs. [184, 406, 499, 500]).

To maintain gauge invariance, the heavy mediators F must share the same representation under Standard Model (SM) gauge groups as the SM fermion f they interact with, meaning they are also gauge charged. Given that SM fermions belong to five distinct representations, the model can be realized in five different ways, as the first and second columns of Table VII.1 list. We parameterize the gauge interaction of the vectorlike fermion F and the SM fermion f using an effective gauge coupling G, defined as

$$G = Y^2 g_1^2 + C_2\left(\mathbf{R}_2\right) g_2^2 + C_2\left(\mathbf{R}_3\right) g_3^2\,, \tag{VII.2}$$

where g_1, g_2, and g_3 are the SM gauge couplings corresponding to $U(1)_Y$, $SU(2)_L$, and $SU(3)_C$, respectively. Here, Y denotes the weak hypercharge of f/F, while $\mathbf{R}_2$ and $\mathbf{R}_3$ represent their respective representations under $SU(2)_L$ and $SU(3)_C$, with C_2 as the associated Casimir invariants. Typical values for the effective gauge coupling G across the five model realizations are shown in the third and fourth columns in Table VII.1, where we use the one-loop beta functions of the SM gauge couplings.

Notice that the gauge interactions are sufficiently large to safely assume that the mediators, as well as the SM fermions, interact quickly enough with the thermal bath to reach a state of thermal equilibrium. Thus, we do not need to study their kinetic evolution, because their properties are fully encoded in the equilibrium Green's functions, unequivocally determined by the equilibrium distribution and the spectral properties through their interaction with the thermal bath.

VII.2 Production Rate and Self-Energy

Declaration: this section presents results from the literature, re-elaborated by the thesis author, MB, and CT for [5]. The following text is based on what was presented in the publication, with adjustments in style and content and integrated information. The text in the paper was written by the thesis author and CT, while all authors contributed to structuring, reviewing, and refining the manuscript.

To specify the form of the interaction rate density in Eq. (VI.99), we need to compute the DM self-energy. Formally, the 2PI formalism requires the exact self-energy, obtained from the full 2PI effective action. Since this functional is not known in closed form, a controlled approximation is required. In practice, this amounts to specifying the loop order at which the 2PI effective action is truncated, which directly fixes the perturbative order of the resulting self-energy, as well as the type of propagators entering the calculation.

In the present work, we truncate the 2PI effective action at its lowest non-trivial order. Diagrammatically, this corresponds to retaining only the two-loop contribution to Γ_2 and neglecting all higher-loop terms. For the simplified t-channel DM model considered here, the truncated 2PI effective action reads

$\Gamma_2 = -i$ 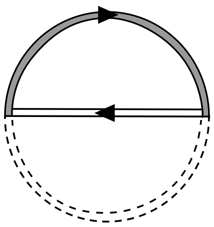 $-\, i$ 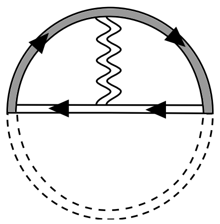 $+\ \dots\,,$ (VII.3)

where double lines denote full propagators. The dashed line represents the scalar DM field, the solid lines correspond to the heavy mediator F (gray) and the SM fermion f (white), and the wavy line denotes a gauge boson. The ellipsis indicates higher-loop contributions and terms involving additional powers of the DM coupling y_{DM}. Throughout this work, only the first term in Eq. (VII.3) is retained.

This truncation implies that the DM self-energy is evaluated at one-loop order, obtained by functional differentiation of the two-loop 2PI effective action. All higher-order contributions to the self-energy are consistently neglected. These include diagrams with additional insertions of DM propagators, which are suppressed by the feeble DM coupling, as well as gauge boson exchanges between fermion lines. The latter correspond to so-called diamond or vertex diagrams and encode quantum interference effects that go beyond the scope of the present approximation.

In particular, gauge boson exchanges between fermion lines can give rise to the Landau–Pomeranchuk–Migdal (LPM) effect [438,439], which becomes relevant in kinematic regimes dominated by lightcone momenta. In hot gauge theories, obtaining the correct leading-order interaction rate in this regime requires the resummation of an infinite series of ladder diagrams [501, 502]. While such effects have been extensively studied in the context of leptogenesis and thermal particle production [503,504], a fully consistent treatment across relativistic and non-relativistic regimes in the presence of multiple in-vacuum mass scales remains an open theoretical challenge. A detailed discussion of the formal origin of these contributions within the 2PI framework can be found in Ref. [5]. Recent developments indicate that LPM effects can have a substantial quantitative impact on DM relic density calculations for small mass splittings between DM and the heavy fermion mediator [10,505].

In the present analysis, however, such effects are not included explicitly. We return to this point when comparing the CTP-based results to those obtained from Boltzmann-like approaches in Section VII.6.1.

The self-energies are obtained by functional differentiation of Γ_2, which corresponds diagrammatically to cutting the diagrams in Eq. (VII.3). As an example, the leading-order contribution to the DM self-energy arises from the first term in Eq. (VII.3) and is obtained by cutting the DM propagator in the corresponding diagram. This yields the one-loop DM self-energy shown in Fig. VII.1. Here, we also consider both orientations of the

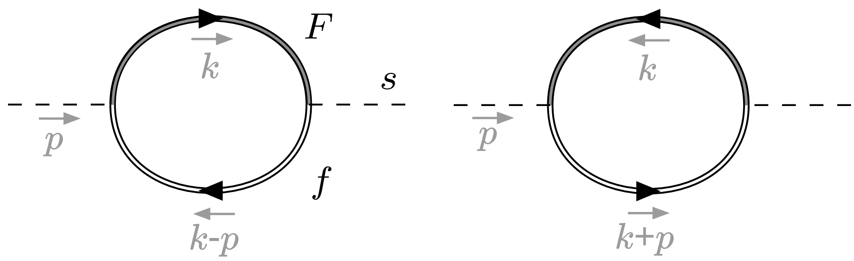

Figure VII.1: The DM self energy diagrams corresponding to Eq. (VII.4). The double lines in the fermion loop indicate a full propagator, and we account for contributions coming from both fermion flow orientations. *Figure created by CT and included in [5].*

fermion loop, corresponding to particle and antiparticle contributions to DM production.

On the CTP contour, the 1-loop DM self-energy can be expressed using the standard QFT Feynman rules, with particular attention to the CTP indices. The self-energy can be directly obtained by functional differentiation of the 2PI effective action. Functional derivatives of the generating functional also reveal the Feynman rules of the theory, which, on the CTP contour, are the same as those in in-vacuum QFT, with the added complexity of doubled degrees of freedom. The following box provides a scheme to account for the CTP indices and propagators correctly.

CTP Feynman Rules

1. Define an arbitrary *fermion flow*.
2. The CTP vertices are assigned against the fermion flow. The propagators have the indices in the order in which the vertices are encountered.
3. For Majorana fermions we always use $S\!\!\!/^{ab}(p)$.
4. For chiral fermions we use the ordinary propagator $S\!\!\!/^{ab}$ if the *charge* flow is parallel to the *fermion* flow. We use the charge-conjugated propagator if the flows are anti-parallel.
5. If the direction of the momentum p is parallel (anti-parallel) to the fermion flow, the sign of the momentum in the propagator is positive (negative).
6. Scalar propagators: the CTP indices are always assigned against the charge flow of the scalar, and the sign of the momentum is $+$ $(-)$ if charge and momentum flows are parallel (antiparallel).
7. Vector bosons function as scalar bosons.

With these rules at our disposal, the diagram in Fig. VII.1 corresponds to the following

DM self-energy on the CTP

$$-i\Pi_s^{ab}(p) = y_{\rm DM}^2 \int \frac{\mathrm{d}^4 k}{(2\pi)^4}\, \mathrm{tr}\Big\{P_L\, i\, \slashed{S}_F^{ab}(k)\, P_R\, i\, \slashed{S}_f^{ba}(k-p) + P_L\, i\, \slashed{S}_F^{ba}(k)\, P_R\, i\, \slashed{S}_f^{ab}(k+p)\Big\}\,, \tag{VII.4}$$

where a, b are the CTP indices, $y_{\rm DM}$ is the DM coupling, k is the loop momentum, and where the trace is performed over the Clifford algebra. Using the KMS relation for the DM self-energy (equivalent to the one for the propagator as in Eq. (VI.93)), Eq. (VII.4) leads to the anti-Hermitian self-energy as follows

$$\begin{aligned}\Pi_s^{\mathcal{A}}(p) = -\frac{y_{\rm DM}^2}{2} f_-^{-1}(p_0) \int \frac{\mathrm{d}^4 k}{(2\pi)^4} \mathrm{tr}\,\Big\{&P_L\, i\, \slashed{S}_F^{<}(k)\, P_R\, i\, \slashed{S}_f^{>}(k-p) \\ &+P_L\, i\, \slashed{S}_F^{>}(k)\, P_R\, i\, \slashed{S}_f^{<}(k+p)\Big\}\,,\end{aligned} \tag{VII.5}$$

Using the fermionic KMS relations in Eq. (VI.93) brings us to

$$\begin{aligned}\Pi_s^{\mathcal{A}}(p) = -2 y_{\rm DM}^2 f_-^{-1}(p_0) \int \frac{\mathrm{d}^4 k}{(2\pi)^4} \Big[&\mathrm{tr}\Big\{P_L \slashed{S}_F^{\mathcal{A}}(k) P_R \slashed{S}_f^{\mathcal{A}}(k-p)\Big\} f_+(k_0)\,(1 - f_+(k_0 - p_0)) \\ &+ \mathrm{tr}\Big\{P_L \slashed{S}_F^{\mathcal{A}}(k) P_R \slashed{S}_f^{\mathcal{A}}(k+p)\Big\} f_+(k_0+p_0)\,(1 - f_+(k_0))\Big]\,,\end{aligned} \tag{VII.6}$$

which yields

$$\begin{aligned}\Pi_s^{\mathcal{A}}(p) =& -2\, y_{\rm DM}^2 \int \frac{\mathrm{d}^4 k}{(2\pi)^4}\, \mathrm{tr}\Big\{P_L \slashed{S}_F^{\mathcal{A}}(k) P_R \slashed{S}_f^{\mathcal{A}}(k-p)\Big\}\, [1 - f_+(k_0) - f_+(p_0 - k_0)] \\ &- (p \leftrightarrow -p)\,.\end{aligned} \tag{VII.7}$$

Here, we used the identities

$$\begin{aligned} f_-^{-1}(p_0) f_+(k_0)(1 - f_+(k_0 - p_0)) &= 1 - f_+(k_0) - f_+(p_0 - k_0), \\ f_-^{-1}(p_0) f_+(k_0 + p_0)(1 - f_+(k_0)) &= -\,(1 - f_+(k_0) - f_+(-p_0 - k_0)). \end{aligned} \tag{VII.8}$$

Eq. (VII.7) is the key expression required to compute and subsequently integrate over the DM momentum, ultimately yielding the DM interaction rate density $\gamma_{\rm DM}$ in Eq. (VI.99). This can be directly evaluated by performing the integrals over the loop momentum $\mathrm{d}^4 k$ and the external DM three-momentum $\mathrm{d}|\vec{p}|$ (the azimuthal integration is trivially performed), yielding:

$$\begin{aligned}\gamma_{\rm DM} = \frac{y_{\rm DM}^2}{4\pi^5} \int \mathrm{d}|\vec{p}|\, \mathrm{d}k^0\, \mathrm{d}|\vec{k}|\, \mathrm{d}\cos\theta\, \frac{|\vec{k}|^2 |\vec{p}|^2}{\omega_p}\, &\mathrm{tr}\Big\{P_L \slashed{S}_F^{\mathcal{A}}(k) P_R \slashed{S}_f^{\mathcal{A}}(q)\Big\} \\ &\times f_-(\omega_p)\, \big[1 - f_+(k^0) - f_+(\omega_p - k^0)\big]\,,\end{aligned} \tag{VII.9}$$

where θ refers to the spatial angle between $\vec{p}$ and $\vec{k}$ and where ω_p is the energy component of the DM momentum. The remaining four-dimensional integral has to be done numerically.

Numerical Implementation

The numerical implementation of the multi-dimensional integration is performed using a custom `C++` routine that employs the VEGAS Monte Carlo algorithm [506] as provided by the GNU Scientific Library (GSL) [507]. The technical details of the code are deferred to Section VIII.1.1. In the following sections, we present a detailed analytical derivation of the various contributions entering Eq. (VII.9), which are required for its numerical evaluation. Each of these contributions is implemented as a dedicated object function in the numerical routine and is shown explicitly after its corresponding mathematical derivation. These components are then assembled and employed in the full numerical evaluation described in Section VIII.1.1. A list of all the functions and routines is presented in Section VII.A (see in particular Table VII.2).

VII.3 1PI-resummed Spectral Densities

Declaration: This section presents both original results and material from the literature, rederived and elaborated by the thesis author, MB, and CT in [5]. The work was developed through close collaboration among all authors, with continuous discussions throughout. The text here is based on the publication but has been extensively revised and supplemented with additional details on analytical derivations and numerical implementations. In the original paper, all authors contributed to structuring, reviewing, and refining the manuscript.

To compute the 1PI-resummed spectral densities entering Eq. (VII.7), we need the anti-Hermitian part of the 1PI-resummed retarded propagators, given by Eq. (VI.89). For the fermion fields F and f these read as

$$\not{S}^{\mathcal{A}}_F(k) = \left(\not{k} - \not{\Sigma}^{\mathcal{H}}_F(k) + m_F\right) \frac{\Gamma_F(k)}{\Omega_F^2(k) + \Gamma_F^2(k)} - \not{\Sigma}^{\mathcal{A}}_F(k) \frac{\Omega_F(k)}{\Omega_F^2(k) + \Gamma_F^2(k)}\,, \tag{VII.10}$$

$$\not{S}^{\mathcal{A}}_f(q) = \left(\not{q} - \not{\Sigma}^{\mathcal{H}}_f(q)\right) \frac{\Gamma_f(q)}{\Omega_f^2(q) + \Gamma_f^2(q)} - \not{\Sigma}^{\mathcal{A}}_f(q) \frac{\Omega_f(q)}{\Omega_f^2(q) + \Gamma_f^2(q)}\,, \tag{VII.11}$$

with

$$\Omega_F(k) \equiv \left(k_\mu - \Sigma^{\mathcal{H}}_{F,\mu}(k)\right)^2 - \left(\Sigma^{\mathcal{A}}_{F,\mu}(k)\right)^2 - m_F^2\,, \tag{VII.12}$$

$$\Omega_f(q) \equiv \left(q_\mu - \Sigma^{\mathcal{H}}_{f,\mu}(q)\right)^2 - \left(\Sigma^{\mathcal{A}}_{f,\mu}(q)\right)^2\,, \tag{VII.13}$$

$$\Gamma_F(k) \equiv 2\left(k_\mu - \Sigma^{\mathcal{H}}_{F,\mu}(k)\right) \Sigma^{\mathcal{A},\mu}_F(k)\,, \tag{VII.14}$$

$$\Gamma_f(q) \equiv 2\left(q_\mu - \Sigma^{\mathcal{H}}_{f,\mu}(q)\right) \Sigma^{\mathcal{A},\mu}_f(q)\,, \tag{VII.15}$$

and $q = k - p$. When $\Gamma(k) \ll \Omega(k)$, the spectral densities exhibit sharp peaks around $\Omega(k)$, indicating that these peaks correspond to propagating degrees of freedom with well-defined dispersion relations. Consequently, the functions $\Gamma_{F,f}$ can be interpreted as thermal widths, which contribute to broadening the density of states.

As shown by Eqs. (VII.12)-(VII.15), the resummed spectral propagators demand to know the form of the anti-Hermitian and Hermitian parts of the self-energy, given by $\not{\Sigma}^{\mathcal{A}}(p)$ and $\not{\Sigma}^{\mathcal{H}}(p)$, respectively. We compute the one-loop fermion self-energy by considering only the gauge corrections shown in the sunset diagram of Fig. VII.2. While additional loop diagrams involving Higgs boson exchanges and Yukawa interactions for SM fermions could be included, such contributions are generally negligible in models where the Yukawa

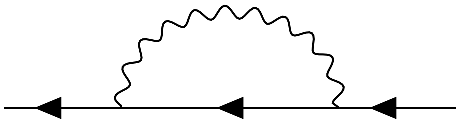

Figure VII.2: One-loop gauge contribution to the fermion self-energy. For right-handed SM fermions and the vectorlike dark fermion F in Eq. (VII.1), the wavy line represents $U(1)$ gauge bosons or gluons (if color-charged). For left-handed fermions, it can also denote $SU(2)$ gauge bosons.

couplings of SM fermions to the vectorlike fermion F are very small. It is essential to note that, in models with top quarks, Yukawa interactions can be substantial, influencing the thermal mass in the dispersion relation. In the ultrarelativistic regime, top quark decays are energetically favorable and kinematically allowed, unlike scenarios where Yukawa couplings are suppressed or absent. At lower temperatures, decays might be kinematically forbidden until the mass of the vectorlike fermion becomes dominant. These effects are beyond the scope of this study.

On the CTP contour, the sunset diagram gives the following self-energy contribution (cf. CTP Feynman Rules)

$$-i\not{\Sigma}^{ab}(k)_{L/R} = -G_{L/R} \int \frac{\mathrm{d}^4\ell}{(2\pi)^4} \gamma^\mu P_{L/R} i\not{S}^{ab}_{L/R}(k-\ell) P_{L/R} \gamma^\nu i\Delta^{ab}_{\mu\nu}(\ell)\,. \tag{VII.16}$$

Here, the factor $G_{L/R}$ summarizes the gauge interactions of the chiral fermion considered. In the SM case, it is given by Eq. (VII.2). $\Delta^{ab}_{\mu\nu}(\ell)$ is the gauge boson propagator. In the Feynman gauge, it is obtained from a scalar propagator by $\Delta^{ab}_{\mu\nu}(\ell) = -g_{\mu\nu}\Delta^{ab}(\ell)$.

Thus, the Hermitian and anti-Hermitian self-energies needed in the resummed fermion propagators can be simply determined by

$$\not{\Sigma}^{\mathcal{H}}(k) = \frac{1}{2}\left[\not{\Sigma}^{++}(k) - \not{\Sigma}^{--}(k)\right]\,, \quad \not{\Sigma}^{\mathcal{A}}(k) = \frac{1}{2}\left[\not{\Sigma}^{-+}(k) - \not{\Sigma}^{+-}(k)\right]\,. \tag{VII.17}$$

VII.3.1 Products of Self-energies

To compute Eqs. (VII.12)-(VII.15), we need to determine the Lorentz-vector $\Sigma^\mu_{L/R}$ (the CTP indices are suppressed). This is defined via $\not{\Sigma}_{L/R} = P_{R/L}\gamma_\mu\Sigma^\mu_{L/R}$ and can be expressed in terms of the Lorentz vectors it depends on, namely p^μ, the momentum of the particle, and u^μ, the plasma reference vector with $u^2 = 1$ and $u^0 > 0$. In what follows, we choose to work in the rest frame of the plasma, implying $u^\mu = (1, \vec{0})$. The self-energy can be decomposed as

$$\Sigma^\mu(k) = \frac{1}{|\vec{k}|^2}[(k^0u^\mu - k^\mu)\mathcal{K} + (k^0k^\mu - k^2u^\mu)\mathcal{U}]\,, \tag{VII.18}$$

$$\mathcal{K} \equiv (k\cdot\Sigma)\,, \qquad \mathcal{U} \equiv (u\cdot\Sigma)\,, \tag{VII.19}$$

as can be shown by contracting the same expression once with k^μ and once with u^μ. These quantities have to be determined for both the Hermitian and anti-Hermitian self-energies. Moreover, they can be decomposed into a vacuum ($T = 0$) and a thermal part ($T \neq 0$). The first is given by the full self-energy evaluated in the $T \to 0$ limit of all distribution functions involved in the calculation, while the latter contains the rest. [1]

When evaluating the product of the resummed fermion propagators in Eq. (VII.9), we need to perform multiplications between Eq. (VII.10) and Eq. (VII.11), which involve Dirac-slashed momenta, self-energies, pole functions Ω and width functions Γ, which are themselves quite convoluted, as shown in Eqs. (VII.12) to (VII.15).

By expanding Eqs. (VII.12) to (VII.15), we find:

$$\Omega_F(k) = k^2 - 2k\cdot\Sigma_F^{\mathcal{H}}(k) + \left(\Sigma_F^{\mathcal{H}}(k)\right)^2 - \left(\Sigma_F^{\mathcal{A}}(k)\right)^2 - m_F^2\,, \tag{VII.20}$$

$$\Omega_f(q) = q^2 - 2q\cdot\Sigma_f^{\mathcal{H}}(q) + \left(\Sigma_f^{\mathcal{H}}(q)\right)^2 - \left(\Sigma_f^{\mathcal{A}}(q)\right)^2\,, \tag{VII.21}$$

$$\Gamma_F(k) = 2k\cdot\Sigma_F^{\mathcal{A}}(k) - \Sigma_F^{\mathcal{H}}(k)\cdot\Sigma_F^{\mathcal{A}}(k)\,, \tag{VII.22}$$

$$\Gamma_f(q) = 2q\cdot\Sigma_f^{\mathcal{A}}(q) - \Sigma_f^{\mathcal{H}}(q)\cdot\Sigma_f^{\mathcal{A}}(q)\,. \tag{VII.23}$$

The trace we have to resolve in Eq. (VII.9) implies the computation of the following four distinct terms:

$$\mathrm{Tr}\Big\{P_L\left(\not{k}-\not{\Sigma}_F^{\mathcal{H}}(k)\right)P_R\left(\not{q}-\not{\Sigma}_f^{\mathcal{H}}(q)\right)\Big\} = 2\,\left(k\cdot q - k\cdot\Sigma_f^{\mathcal{H}}(q) - q\cdot\Sigma_F^{\mathcal{H}}(k) + \Sigma_f^{\mathcal{H}}(q)\cdot\Sigma_F^{\mathcal{H}}(k)\right)\,, \tag{VII.24}$$

$$\mathrm{Tr}\Big\{P_L\left(\not{k}-\not{\Sigma}_F^{\mathcal{H}}(k)\right)P_R\not{\Sigma}_f^{\mathcal{A}}(q)\Big\} = 2\,\left(K\cdot\Sigma_f^{\mathcal{A}}(q) - \Sigma_F^{\mathcal{H}}(k)\cdot\Sigma_f^{\mathcal{A}}(k)\right)\,, \tag{VII.25}$$

$$\mathrm{Tr}\Big\{P_L\not{\Sigma}_F^{\mathcal{A}}(k)P_R\left(\not{q}-\not{\Sigma}_f^{\mathcal{H}}(q)\right)\Big\} = 2\,\left(q\cdot\Sigma_F^{\mathcal{A}}(k) - \Sigma_f^{\mathcal{H}}(q)\cdot\Sigma_F^{\mathcal{A}}(k)\right)\,, \tag{VII.26}$$

$$\mathrm{Tr}\Big\{P_L\not{\Sigma}_F^{\mathcal{A}}(k)P_R\not{\Sigma}_f^{\mathcal{A}}(q)\Big\} = 2\,\Sigma_F^{\mathcal{A}}(k)\cdot\Sigma_f^{\mathcal{A}}(q)\,. \tag{VII.27}$$

This means that we have to compute a total of 20 scalar products:

Same momentum:

$K\cdot\Sigma_F^{\mathcal{A}}(k)$; $k\cdot\Sigma_F^{\mathcal{H}}(k)$; $Q\cdot\Sigma_f^{\mathcal{A}}(q)$; $q\cdot\Sigma_f^{\mathcal{H}}(q)$;
$q\cdot\Sigma_F^{\mathcal{A}}(k)$; $q\cdot\Sigma_F^{\mathcal{H}}(k)$; $k\cdot\Sigma_f^{\mathcal{A}}(q)$; $k\cdot\Sigma_f^{\mathcal{H}}(q)$;

Mixed self-energy products:

$\Sigma_F^{\mathcal{H}}(k)\cdot\Sigma_f^{\mathcal{H}}(q)$; $\Sigma_F^{\mathcal{H}}(k)\cdot\Sigma_f^{\mathcal{A}}(q)$; $\Sigma_F^{\mathcal{H}}(k)\cdot\Sigma_F^{\mathcal{A}}(k)$;
$\Sigma_F^{\mathcal{A}}(k)\cdot\Sigma_f^{\mathcal{A}}(q)$; $\Sigma_F^{\mathcal{A}}(k)\cdot\Sigma_f^{\mathcal{H}}(q)$; $\Sigma_f^{\mathcal{A}}(q)\cdot\Sigma_f^{\mathcal{H}}(q)$;

Square of self-energies:

$\left(\Sigma_F^{\mathcal{H}}(k)\right)^2$; $\left(\Sigma_f^{\mathcal{A}}(q)\right)^2$; $\left(\Sigma_F^{\mathcal{A}}(k)\right)^2$; $\left(\Sigma_f^{\mathcal{H}}(q)\right)^2$.

[1] The vacuum component of the Hermitian self-energy includes both ultraviolet (UV) and infrared (IR) divergences. UV divergences require renormalization, as is standard in zero-temperature QFT. The renormalized observables, such as spectral densities, maintain their analytic form after this process. Importantly, finite-temperature corrections do not alter the renormalization conditions or introduce new UV divergences, due to the natural cutoff provided by the thermal fluctuation correlation length. For IR divergences, the Bloch-Nordsiek [508] and Kinoshita-Lee-Nauenberg [509, 510] theorems ensure that at zero temperature, observables are free from soft and collinear divergences. The thermal components of the Hermitian self-energy, as well as both vacuum and thermal parts of the anti-Hermitian self-energy, are free from divergences.

The tedious task can be simplified by using a series of useful relations, which can be found by combining Eqs. (VII.18) and (VII.19) and that prove to be very useful.

Dirac product of the self-energy:

$$\not{\Sigma}(p) = \gamma^\mu \Sigma_\mu = \frac{1}{2|\vec{p}|^2} \left[\left(p^0 \gamma^0 - \not{p}\right) \mathcal{P} + \left(p^0 \not{p} - p^2 \gamma^0\right) \mathcal{U} \right] . \tag{VII.28}$$

Product of two self-energies:

$$\begin{aligned} \Sigma^{\mathcal{H}}(p) \cdot \Sigma^{\mathcal{A}}(p) &= \frac{1}{4|\vec{p}|^4} \left[(p^0 u^\mu - p^\mu) \mathcal{P}^{\mathcal{H}} + (p^0 p^\mu - p^2 u^\mu) \mathcal{U}^{\mathcal{H}} \right] \left[(p^0 u^\mu - p^\mu) \mathcal{P}^{\mathcal{A}} + (p^0 p^\mu - p^2 u^\mu) \mathcal{U}^{\mathcal{A}} \right] \\ &= -\frac{1}{2|\vec{p}|^2} \left(\mathcal{P}^{\mathcal{H}} \mathcal{P}^{\mathcal{A}} + p^2 \mathcal{U}^{\mathcal{H}} \mathcal{U}^{\mathcal{A}} - p^0 \left(\mathcal{P}^{\mathcal{H}} \mathcal{U}^{\mathcal{A}} - \mathcal{P}^{\mathcal{A}} \mathcal{U}^{\mathcal{H}} \right) \right) , \end{aligned} \tag{VII.29}$$

$$\Sigma^{\mathcal{A}}(p) \cdot \Sigma^{\mathcal{A}}(p) = -\frac{1}{2|\vec{p}|^2} \left(\left(\mathcal{P}^{\mathcal{A}}\right)^2 + p^2 \left(\mathcal{U}^{\mathcal{A}}\right)^2 - 2p^0 \left(\mathcal{P}^{\mathcal{A}} U^{\mathcal{A}} \right) \right) , \tag{VII.30}$$

$$\Sigma^{\mathcal{H}}(p) \cdot \Sigma^{\mathcal{H}}(p) = -\frac{1}{2|\vec{p}|^2} \left(\left(\mathcal{P}^{\mathcal{H}}\right)^2 + p^2 \left(\mathcal{U}^{\mathcal{H}}\right)^2 - 2p^0 \left(\mathcal{P}^{\mathcal{H}} \mathcal{U}^{\mathcal{H}} \right) \right) . \tag{VII.31}$$

Two different momenta (you also pick up a dependence on the angle between them):

$$\begin{aligned} k \cdot \Sigma(p) &= \frac{1}{2|\vec{p}|} \left[\left(p^0 k^0 - p \cdot k\right) \mathcal{P} + \left(p^0 p \cdot k - p^2 k^0\right) \mathcal{U} \right] \\ &= \frac{1}{2|\vec{p}|} \left[|\vec{p}||\vec{k}| \cos\theta_{pk} \mathcal{P} - \left(p^0 |\vec{p}||\vec{k}| \cos\theta_{pk} + |\vec{p}|^2 k^0 \right) \mathcal{U} \right] , \end{aligned} \tag{VII.32}$$

$$\begin{aligned} \Sigma^r(k) \cdot \Sigma^s(p) = \frac{1}{4} \Big[&\cos\theta_{pk} \Big(k_0 \, \mathcal{U}^r(k) \mathcal{P}^s - \mathcal{K}^r \mathcal{P}^s + p_0 \, \mathcal{K}^r \mathcal{U}^s(p) \Big) \\ &- \Big(\cos\theta_{pk} k_0 p_0 - |\vec{k}||\vec{p}| \Big) \, \mathcal{U}^r(k) \, \mathcal{U}^s(p) \Big] , \end{aligned} \tag{VII.33}$$

where, in the last line, the indices r and s refer to either $\mathcal{A}$ or $\mathcal{H}$.

Therefore, what we need to determine are essentially only the functions $\mathcal{P}^{\mathcal{H}}$, $\mathcal{P}^{\mathcal{A}}$, $\mathcal{U}^{\mathcal{H}}$, and $\mathcal{U}^{\mathcal{A}}$. Moreover, due to the Dirac structure of the self-energy, the scalar products can be related to the following traces:

$$\mathrm{Tr}\big\{\not{p}\not{\Sigma}\big\} = 2\,(p \cdot \Sigma) = 2\mathcal{P}, \quad \mathrm{Tr}\big\{\not{u}\not{\Sigma}\big\} = 2\,(u \cdot \Sigma) = 2\mathcal{U} \, , \tag{VII.34}$$

which simplifies the computation process. In particular, we need to calculate only the following four traces:

$$\mathrm{Tr}\Big\{\not{p}\not{\Sigma}^{\mathcal{H}}(p)\Big\}^{(T\neq 0)}, \quad \mathrm{Tr}\Big\{\not{u}\not{\Sigma}^{\mathcal{H}}(p)\Big\}^{(T\neq 0)}, \quad \mathrm{Tr}\Big\{\not{p}\not{\Sigma}^{\mathcal{A}}(p)\Big\}^{(T\neq 0)}, \quad \mathrm{Tr}\Big\{\not{u}\not{\Sigma}^{\mathcal{A}}(p)\Big\}^{(T\neq 0)}. \tag{VII.35}$$

In what follows, we dedicate ample space to illustrating how to calculate such quantities, determining the potential limiting behaviors that simplify the analysis in certain kinematical regimes, and showing how everything is implemented in the numerical code.

VII.3.2 Generic structure of the traces

We show here the generic structure of the CTP contour of the traces we need to calculate. In what follows, the notation $\tilde{\Delta}$ means that we take the scalar propagator but substituting

$f_- \to -f_+$. This happens as soon as we factor out the Clifford algebra structure from the fermion propagators, which simplifies the calculation.

$$\begin{aligned}
\mathrm{Tr}\Big\{\not{p}\Sigma^{ab}(p)\Big\} &= -iG\int\frac{\mathrm{d}^4k}{(2\pi)^4}\,\mathrm{Tr}\Big\{p_\alpha\gamma^\alpha\gamma^\mu P_L i\mathcal{S}^{ab}_{\ell,R}(p-k)P_R\gamma^\nu i\Delta^{ab}_{\mu\nu}(k)\Big\}\\
&= -iGp_\alpha\int\frac{\mathrm{d}^4k}{(2\pi)^4}i\Delta^{ab}_{\mu\nu}(k)\,\mathrm{Tr}\{\gamma^\alpha\gamma^\mu(\not{p}-\not{k})P_R\gamma^\nu\}i\Delta^{ab}_{\ell,R}(p-k)\Big|_{f_-\to-f_+}\\
&\underbrace{=}_{\text{cyclicity}} -iGp_\alpha\int\frac{\mathrm{d}^4k}{(2\pi)^4}i\Delta^{ab}_{\mu\nu}(k)i\Delta^{ab}_{\ell,R}(p-k)\Big|_{f_-\to-f_+}(p_\beta-k_\beta)\\
&\qquad\qquad\qquad\qquad\times\mathrm{Tr}\left\{\gamma^\nu\gamma^\alpha\gamma^\mu\gamma^\beta\frac{1+\gamma^5}{2}\right\}\\
&= -i\frac{G}{2}p_\alpha\int\frac{\mathrm{d}^4k}{(2\pi)^4}(-g_{\mu\nu})i\Delta^{ab}_\gamma(k)\,i\Delta^{ab}_{\ell,R}(p-k)(p_\beta-k_\beta)\\
&\qquad\qquad\qquad\qquad\times 4\left[g^{\nu\alpha}g^{\mu\beta}-g^{\nu\mu}g^{\alpha\beta}+g^{\nu\beta}g^{\alpha\mu}+i\epsilon^{\nu\alpha\mu\beta}\right]\\
&= -4iG\int\frac{\mathrm{d}^4k}{(2\pi)^4}i\Delta^{ab}_\gamma(k)\,i\Delta^{ab}_{\ell,R}(p-k)\Big|_{f_-\to-f_+}p\cdot(p-k)
\end{aligned}\tag{VII.36}$$

Even if the fermion is massive, like the dark sector vectorlike heavy fermion, the mass term in the numerator of the propagator does not contribute, because it would just be $P_L m_F P_R = m_F P_L P_R = 0$. That is why we have not considered it. Here, we used the property $P_L\gamma^\beta = \gamma^\beta P_R$, and the fact that the contraction of the totally antisymmetric pseudo-tensor $\epsilon^{\nu\alpha\mu\beta}$ with a symmetric tensor like the metric $g_{\mu\nu}$ is zero. Analogously, the contraction with the plasma vector u, leads to a similar result, just with $u\cdot(p-k) = p_0 - k_0$ instead of $p\cdot(p-k)$[2]:

$$\mathrm{Tr}\Big\{\not{u}\Sigma^{ab}(p)\Big\} = -4iG\int\frac{\mathrm{d}^4k}{(2\pi)^4}i\Delta^{ab}_\gamma(k)\,i\Delta^{ab}_{\ell,R}(p-k)\;\cdot(p_0-k_0)\,. \tag{VII.37}$$

We proceed with evaluating first the Hermitian and then the anti-Hermitian contractions.

VII.3.3 Hermitian contractions

VII.3.3.1 Contraction with p

The starting point is the expression given by Eq. (VI.26):

$$\mathrm{Tr}\Big\{\not{p}\Sigma^{\mathcal{H}}(p)\Big\} = \frac{1}{2}\left(\mathrm{Tr}\Big\{\not{p}\Sigma^{++}(p)\Big\} - \mathrm{Tr}\Big\{\not{p}\Sigma^{--}(p)\Big\}\right)\,. \tag{VII.38}$$

We proceed with calculating it.

$$\begin{aligned}
\mathrm{Tr}\Big\{\not{p}\Sigma^{\mathcal{H}}(p)\Big\} &= -2iG\int\frac{\mathrm{d}^4k}{(2\pi)^4}p\cdot(p-k)\left[i\Delta^{++}_\gamma(k)\,i\tilde{\Delta}^{++}_{\ell,R}(p-k) - i\Delta^{--}_\gamma(k)\,i\tilde{\Delta}^{--}_{\ell,R}(p-k)\right]\\
= -2iG\int\frac{\mathrm{d}^4k}{(2\pi)^4}(p^2-p\cdot k)&\Big[i\left(\Delta^F_\gamma(k)+\Delta^{\mathcal{H}}_\gamma(k)\right)i\left(\tilde{\Delta}^F_{\ell,R}(p-k)+\tilde{\Delta}^{\mathcal{H}}_{\ell,R}(p-k)\right)\\
&- i\left(\Delta^F_\gamma(k)+\Delta^{\mathcal{H}}_\gamma(k)\right)i\left(\tilde{\Delta}^F_{\ell,R}(p-k)+\tilde{\Delta}^{\mathcal{H}}_{\ell,R}(p-k)\right)\Big]
\end{aligned}$$

[2]Notice that, since u is a dimensionless vector, the contraction with u has energy dimension 1, while the contraction with the momentum p has energy dimension 2.

$$
\begin{aligned}
&= 4G \int \frac{\mathrm{d}^4 k}{(2\pi)^4}(p^2 - p\cdot k)\left[i\Delta_\gamma^F(k)\tilde{\Delta}^{\mathcal{H}}_{\ell,R}(p-k) + \Delta_\gamma^{\mathcal{H}}(k) i\tilde{\Delta}^F_{\ell,R}(p-k)\right] \\
&\underbrace{=}_{(*)} 4G \int \frac{\mathrm{d}^4 k}{(2\pi)^4}(p^2 - p\cdot k)\Big\{[1+2f_-(k_0)]\,\delta(k^2)\,\pi\,\mathrm{sign}(k_0)\mathrm{PV}\frac{1}{(p-k)^2 - m_F^2} \\
&\qquad\qquad + [1-2f_+(p_0-k_0)]\,\delta((p-k)^2)\,\pi\,\mathrm{sign}(p_0-k_0)\mathrm{PV}\frac{1}{k^2}\Big\}
\end{aligned}
$$

$$
\underbrace{=}_{(\dagger)} \underbrace{4\pi G \int \frac{\mathrm{d}^4 k}{(2\pi)^4}[1+2f_-(|k_0|)]\,\mathrm{PV}\frac{\delta(k^2)}{(p-k)^2 - m_F^2}(p^2 - p\cdot k)}_{(I)} \tag{VII.39}
$$

$$
+ \underbrace{4\pi G \int \frac{\mathrm{d}^4 k}{(2\pi)^4}[1-2f_+(|p_0-k_0|)]\,\mathrm{PV}\frac{\delta((p-k)^2 - m_F^2)}{k^2 - m_F^2}(p^2 - p\cdot k)}_{(II)} \tag{VII.40}
$$

Here, PV is Cauchy's principal value. We have used in $(*)$ the properties of the CTP propagators as illustrated in Section VI.3.2.2, while in $(\dagger)$, we used the fact that

$$
\mathrm{sign}(x)(1 \pm 2f_\mp(x)) = 1 \pm 2f_\mp(|x|)
$$

We start with part (I) above:

$$
\begin{aligned}
(I) &= 4\pi G \int \frac{\mathrm{d}^3|\vec{k}|}{(2\pi)^4}[1+2f_-(|k_0|)] \int \mathrm{d}k_0 \frac{\delta(k_0 - |\vec{k}|) + \delta(k_0 + |\vec{k}|)}{2|\vec{k}|}\mathrm{PV}\frac{1}{(p-k)^2 - m_F^2}(p^2 - p\cdot k) \\
&= \frac{G}{4\pi^2}\int_0^\infty \mathrm{d}|\vec{k}|\,|\vec{k}| \sum_{k_0 = \pm|\vec{k}|}[1+2f_-(|k_0|)] \int_{-1}^{1} \mathrm{d}\cos\theta\, \frac{p^2 - p_0 k_0 + |\vec{p}||\vec{k}|\cos\theta}{p^2 - m_F^2 - 2p_0 k_0 + 2|\vec{p}||\vec{k}|\cos\theta} \\
&= \frac{G}{8\pi^2}\int_0^\infty \mathrm{d}|\vec{k}||\vec{k}| \sum_{\pm}[1+2f_-(|k_0|)]\left(4 + \frac{p^2 + m_F^2}{2|\vec{p}||\vec{k}|}\sum_\pm \ln\left|\frac{p^2 - m_F^2 \mp 2p_0|\vec{k}| + 2|\vec{p}||\vec{k}|}{p^2 - m_F^2 \mp 2p_0|\vec{k}| - 2|\vec{p}||\vec{k}|}\right|\right) \\
&= \underbrace{\frac{G}{2\pi^2}\int \mathrm{d}|\vec{k}||\vec{k}|^2 + \frac{G}{16\pi^2}\frac{p^2 + m_F^2}{|\vec{p}|}\int \mathrm{d}|\vec{k}| \sum_\pm \ln\left|\frac{p^2 - m_F^2 \mp 2p_0|\vec{k}| + 2|\vec{p}||\vec{k}|}{p^2 - m_F^2 \mp 2p_0|\vec{k}| - 2|\vec{p}||\vec{k}|}\right|}_{Vacuum} \qquad \text{(VII.41)} \\
&\quad \underbrace{+\frac{GT^2}{6} + \frac{G}{16\pi^2}\frac{p^2 + m_F^2}{|\vec{p}|}\int \mathrm{d}|\vec{k}| f_-(|\vec{k}|) \sum_\pm \ln\left|\frac{p^2 - m_F^2 \mp 2p_0|\vec{k}| + 2|\vec{p}||\vec{k}|}{p^2 - m_F^2 \mp 2p_0|\vec{k}| - 2|\vec{p}||\vec{k}|}\right|}_{Thermal}. \qquad \text{(VII.42)}
\end{aligned}
$$

In the first step, we utilized the known properties of the delta function and integrated over $\mathrm{d}k_0$ to eliminate them. In the second step, we integrated over $\mathrm{d}\cos\theta$, while in the last step we arranged the expression into a *Vacuum* part without the Bose-Einstein distribution, and a *Thermal* part including it. The vacuum part is UV divergent, and it is dealt with through standard renormalization techniques. We thus only retain the pure thermal part.

The second part, (II), is derived in the following:

$$
\begin{aligned}
(II) &= 4\pi G \int \frac{\mathrm{d}^4 k}{(2\pi)^4}[1-2f_+(|k_0|)]\,\frac{\delta(k_0 - \omega_k) + \delta(k_0 + \omega_k)}{2\omega_k} \\
&\qquad\qquad \times \mathrm{PV}\frac{1}{p^2 + k^2 - 2p_0 k_0 + 2|\vec{p}||\vec{k}|\cos\theta}\left(p_0 k_0 - |\vec{p}||\vec{k}|\cos\theta\right) \\
&= 2\pi G \int \frac{\mathrm{d}^3|\vec{k}|}{(2\pi)^4}\sum_{k_0 = \pm\omega_k}\frac{1}{\omega_k}[1-2f_+(\omega_k)]\,\frac{p_0 k_0 - |\vec{p}||\vec{k}|\cos\theta}{p^2 + m_F^2 - 2p_0 k_0\cos\theta}
\end{aligned}
$$

$$= \frac{G}{8\pi^2}\int_0^\infty \mathrm{d}|\vec{k}|\frac{|\vec{k}|^2}{\sqrt{|\vec{k}|^2+m_F^2}}\left[1-2f_+(\omega_k)\right]$$
$$\times \sum_{k_0=\pm\omega_k}\int_{-1}^{1}\mathrm{d}\cos\theta\left(-1+(p^2+m_F^2)\frac{1}{p^2+\omega_k^2-2p_0k_0+2|\vec{p}||\vec{k}|\cos\theta}\right)$$

$$= \underbrace{\frac{G}{2\pi^2}\int_0^\infty \mathrm{d}|\vec{k}|\frac{|\vec{k}|^2}{\omega_k} + \frac{G}{16\pi^2|\vec{p}|}(p^2+m_F^2)\int_0^\infty \mathrm{d}|\vec{k}|\frac{|\vec{k}|}{\omega_k}\sum_{\pm}\ln\left|\frac{p^2+m_F^2\mp 2p_0\omega_k+2|\vec{p}||\vec{k}|}{p^2+m_F^2\mp 2p_0\omega_k-2|\vec{p}||\vec{k}|}\right|}_{Vacuum} \tag{VII.43}$$

$$\underbrace{+\frac{G}{\pi^2}\int_0^\infty \mathrm{d}|\vec{k}|\frac{|\vec{k}|^2}{\omega_k}f_+(\omega_k) - \frac{G(p^2+m_F^2)}{8\pi^2|\vec{p}|}\int_0^\infty \mathrm{d}|\vec{k}|\frac{|\vec{k}|}{\omega_k}f_+(\omega_k)\sum_{\pm}\ln\left|\frac{p^2+m_F^2\mp 2p_0\omega_k+2|\vec{p}||\vec{k}|}{p^2+m_F^2\mp 2p_0\omega_k-2|\vec{p}||\vec{k}|}\right|}_{Thermal}. \tag{VII.44}$$

We followed the same steps and performed the same integrations as for part (I), with the complication that the delta function evaluates at the poles $k_0 = \pm\omega_k = \pm\sqrt{|\vec{k}|^2+m_F^2}$ Again, the vacuum part is reabsorbed by standard renormalization techniques, whereas the thermal part is the one that influences the dynamics at finite temperatures.

Collecting the pieces together, we obtain the Hermitian contraction of the fermionic self-energy with the momentum p as

$$\underbrace{\mathrm{Tr}\left\{\not{p}\Sigma^{\mathcal{H}}(p)\right\}^{(T\neq 0)}}_{\texttt{kSigmaH\_M}} = \frac{GT^2}{6} + \frac{G}{\pi^2}\underbrace{\int_0^\infty \mathrm{d}k\frac{k^2}{\omega_{F,k}}f_+(\omega_{F,k})}_{\texttt{C++: k2omegafp}}$$
$$+\frac{G}{8\pi^2}\frac{p^2+m_F^2}{|\vec{p}|}\underbrace{\int_0^\infty \mathrm{d}k\, f_-(k)\sum_{\pm}\ln\left|\frac{p^2-m_F^2+2k(|\vec{p}|\mp p_0)}{p^2-m_F^2-2k(|\vec{p}|\pm p_0)}\right|}_{I_{2-}^{(M)},\ \texttt{C++: I2mM}}$$
$$-\frac{G}{8\pi^2}\frac{p^2+m_F^2}{|\vec{p}|}\underbrace{\int_0^\infty \mathrm{d}k\, f_+(\omega_{F,k})\sum_{\pm}\ln\left|\frac{p^2+m_F^2\mp 2p_0\omega_{F,k}+2|\vec{p}|k}{p^2+m_F^2\mp 2p_0\omega_{F,k}-2|\vec{p}|k}\right|}_{J_{2+}^{(M)},\ \texttt{C++: J2pM}}. \tag{VII.45}$$

As anticipated right before the start of this section, each of the derived components has been implemented in the `C++` numerical code used to calculate the multi-dimensional integration in Eq. (VII.9) (cf. Chapter VIII for details on the integration method). For instance, the quantity just calculated has been implemented in a corresponding `kSigmaH_M` function as follows:

```
double kSigmaH_M (double xk0, double xk, double mF){
    if(HTL_ON == true) return G/pow(2.*M_PI,2) * M_PI*M_PI / 2.;
    return G / (M_PI * M_PI) / 2.
           * ( M_PI*M_PI / 6. + k2omegafp(mF)
             + (xk0*xk0 - xk*xk + mF*mF )/8./xk
             * ( I2mM(xk0,xk,mF) - J2pM(xk0,xk,mF) )
           );
}
```

Notice that all quantities are expressed in natural units, i.e., we rescale all dimensionful quantities by powers of the plasma temperature. At the same time, the integrals $I_2^{(M)}$ and $J_{2+}^{(M)}$ have been implemented in the functions `I2mM` and `J2pM` that we are going to illustrate in the following paragraphs.

$I_{2-}^{(M)}$ Integral

To implement the various components, we use the fact that the integral $I_{2-}^{(M)}$ can be expressed as (cf. [479] for the massless version)

$$p_{m_F}^- := \frac{k^2 - m_F^2}{p_0 - |\vec{p}|} \tag{VII.46}$$

$$p_{m_F}^+ := \frac{k^2 - m_F^2}{p_0 + |\vec{p}|} \tag{VII.47}$$

$$\boxed{I_{2\pm}^{(M)} \equiv -\frac{p_{m_F}^+}{|p_{m_F}^+|}\mathfrak{a}_\pm(|k_{m_F}^+|) + \frac{p_{m_F}^-}{|p_{m_F}^-|}\mathfrak{a}_\pm(|p_{m_F}^-|)} \tag{VII.48}$$

where

$$\boxed{\mathfrak{a}_\pm(y) \equiv \int_0^\infty \mathrm{d}x f_\pm(x) \ln\left|\frac{2x+y}{2x-y}\right|.} \tag{VII.49}$$

Notice that this integral function is uneven in the argument, $\mathfrak{a}_\pm(-y) = -\mathfrak{a}_\pm(y)$ and thus $\mathfrak{a}_\pm(0) = 0$. Moreover, the following limiting value holds that can help achieve a more performative numerical implementation (cf. also [479]):

$$\underbrace{\mathfrak{a}_+(y)}_{\texttt{C++: ap}} \to \begin{cases} \frac{|y|}{2}(\underbrace{C}_{\approx 1.72645} - \ln|y|) & \text{if} \quad |y| \to 0 \\ \frac{\pi^2}{3y} & \text{if} \quad |y| \to \infty \end{cases}, \qquad \underbrace{\mathfrak{a}_-(y)}_{\texttt{C++ am}} \to \begin{cases} 0 & \text{if} \quad |y| \to 0 \\ \frac{2\pi^2}{3y} & \text{if} \quad |y| \to \infty \end{cases} \tag{VII.50}$$

These functions are implemented in the numerical code as follows:

```
// First integral
double k2omegafp (double mF) {
    // Small masses: analytic result
    if(mF<pow(10.,-2))
        return M_PI *M_PI / 12.;
    // Use pre-computed tabulated result
    if(mF>pow(10.,-2) && mF<10.)
         return( pow(10., Tabulated_Integral_1d( log10(fabs(mF)), -2., 1., 0.01,
    table_dint )));
    // Large masses: non-relativistic Bessel K
    return( gsl_sf_bessel_Kn(1,mF));

// Helper function to calculate I2mM integral
double am (double y){
    if (fabs(y)< pow(10,-4))
        return 0;
    if (fabs(y)> pow(10,4))
        return 2. * M_PI*M_PI / 3. / fabs(y);
    // Otherwise return pre-computed tabulated result
    return pow(10.,Tabulated_Integral_1d( log10(fabs(y)), -4., 4., 0.01, table_am ));
```

```
}

double I2mM (double xk0, double xk, double mF){

    double kmp = ((xk0+xk)*(xk0-xk)-mF*mF) / ((xk0-xk));
    double kmm = ((xk0+xk)*(xk0-xk)-mF*mF) / ((xk0+xk));
    return - kmp/fabs(kmp) * am(fabs( kmp ))
           + kmm/fabs(kmm) * am(fabs( kmm ));
}

}
```

$J^{(M)}_{2+}$ Integral

The integral $J^{(M)}_{2+}$ can also be decomposed into a sum of integrals in one variable. The decomposition was not in the code that led to [5] and was found only later for this thesis. It proceeds as follows. First, we make a change of variable using

$$\omega = \sqrt{k^2 + m_F^2} \implies \mathrm{d}k = \frac{\omega}{\omega^2 - m_F^2}\mathrm{d}\omega\,. \tag{VII.51}$$

This renders the Fermi-Dirac function linear in the variable of integration ω:

$$J^{(M)}_{2\pm} = \int_{m_F}^{\infty} \mathrm{d}\omega \frac{\omega f_\pm(\omega)}{\sqrt{\omega^2 - m_F^2}} \sum_{\pm'} \ln \left| \frac{p^2 + m_F^2 \mp' 2p_0\omega + 2|\vec{p}|\sqrt{\omega^2 - m_F^2}}{p^2 + m_F^2 \mp' 2p_0\omega - 2|\vec{p}|\sqrt{\omega^2 - m_F^2}} \right| . \tag{VII.52}$$

If we define

$$Y_\pm(\omega) := p^2 + m_F^2 \mp 2p_0\omega\,, \tag{VII.53}$$

and the generalized integral function

$$\boxed{\mathfrak{b}_\pm(y) \equiv \int_{m_F}^{\infty} \mathrm{d}\omega \frac{\omega f_\pm(\omega)}{\sqrt{\omega^2 - m_F^2}} \ln \left| \frac{2|\vec{p}|\sqrt{\omega^2 - m_F^2} + y}{2|\vec{p}|\sqrt{\omega^2 - m_F^2} - y} \right| ,} \tag{VII.54}$$

we can express $J^{(M)}_{2\pm}$ as

$$\boxed{J^{(M)}_{2\pm} = \mathfrak{b}_\pm(Y_+(m_F)) + \mathfrak{b}_\pm(Y_-(m_F))\,.} \tag{VII.55}$$

Small-y behavior ($|y| \ll 2|\vec{p}|\sqrt{\omega^2 - m_F^2}$) For small $|y|$, the logarithm can be expanded as

$$\ln\left(\frac{1 + y/(2|\vec{p}|\sqrt{\omega^2 - m_F^2})}{1 - y/(2|\vec{p}|\sqrt{\omega^2 - m_F^2})}\right) \simeq \frac{y}{|\vec{p}|(\omega^2 - m_F^2)^{1/2}} + \frac{y^3}{12|\vec{p}|^3(\omega^2 - m_F^2)^{3/2}} + \dots , \tag{VII.56}$$

which, when inserted into Eq. (VII.54), yields

$$\mathfrak{b}_\pm(y) \simeq \frac{y}{|\vec{p}|} \int_{m_F}^{\infty} \mathrm{d}\omega \frac{\omega f_+(\omega)}{\omega^2 - m_F^2} + (O)(y^3)\,. \tag{VII.57}$$

The leading term behaves linearly in y for vanishing y. Thus, we have

$$\boxed{\mathfrak{b}_+(y) \simeq C_1 y, \quad C_1 = \frac{1}{|\vec{p}|}\int_{m_F}^{\infty} \mathrm{d}\omega \frac{\omega f_+(\omega)}{\omega^2 - m_F^2}\,.} \tag{VII.58}$$

The constant C_1 depends on the value of m_F. However, in the ultrarelativistic regime (UR), where $m_F \ll T$, we have

$$\mathfrak{b}_+(y) \simeq \frac{y}{|\vec{p}|}\int_0^{\infty} \frac{f_+(\omega)}{\omega}\,d\omega + \mathcal{O}(y^3). \tag{VII.59}$$

At finite temperature, the infrared behavior of the integral is regulated by m_F, leading to

$$\boxed{\mathfrak{b}_+^{\mathrm{UR}}(y) \simeq \frac{y}{2|\vec{p}|}\left[\ln\left(\frac{T}{m_F}\right) + C_s\right], \qquad |y| \ll 2|\vec{p}|T,} \tag{VII.60}$$

where C_s is a numerical constant of order unity that has to be found by fitting the regulated result with various values of m_F/T.

Large-y behavior ($|y| \gg 2|\vec{p}|\sqrt{\omega^2 - m_F^2}$) For large $|y|$, the logarithm can be expanded as

$$\ln\left|\frac{2|\vec{p}|\sqrt{\omega^2 - m_F^2} + y}{2|\vec{p}|\sqrt{\omega^2 - m_F^2} - y}\right| \simeq \frac{4|\vec{p}|\sqrt{\omega^2 - m_F^2}}{y} + \mathcal{O}(1/y^3)\,, \tag{VII.61}$$

yielding

$$\mathfrak{b}_+(y) \simeq \frac{4|\vec{p}|}{y}\int_{m_F}^{\infty} \mathrm{d}\omega \frac{\omega f_+(\omega)}{\sqrt{\omega^2 - m_F^2}}\sqrt{\omega^2 - m_F^2} \simeq \frac{4|\vec{p}|}{y}\int_{m_F}^{\infty} \mathrm{d}\omega \omega f_+(\omega) \tag{VII.62}$$

which implies

$$\boxed{\mathfrak{b}_+(y) \simeq \frac{|\vec{p}|\pi^2 T^2}{3y}} \tag{VII.63}$$

which is also the result for the UR-approximated result ($m_F \ll T$).

As already said, the decomposition explained above was not used in the code that led to [5] and was found only later for this thesis. Clearly, its integration in the numerical routine is straightforward. The code as implemented for [5] follows from:

```
double J2pM (double xk0, double xk, double mF){

    double r = log10(sqrt(xk0*xk0 + xk*xk));
    double theta = atan(fabs(xk0)/xk);
    // Use pre-computed tabulated result when possible
    if(r>-3. && r < 5.){
        return Tabulated_Integral_3d(log10(mF),-2.,1.,97./3232.,r,-3.,5.,8./399.,theta,0.,
    M_PI/2.,M_PI/2./399.,table_pSigmaH);
    }
    // Otherwise integrate
    return pSigmaH_int(xk0,xk,mF);
}

// pSigma contraction
```

```
// Use numerical integration method from GSL
// QAGI adaptive integration
// gsl_integration_qagiu
double pSigmaH_int(double xk0, double xk, double z){

  struct fparams2 pars= {xk0 ,xk, z};

  double res, err;

  gsl_set_error_handler_off();
  gsl_integration_workspace * w = gsl_integration_workspace_alloc(4000);

  gsl_function F;
  // Integrand function
  F.function = &fpSigma;
  F.params = &pars;

  int status = gsl_integration_qagiu(&F, 0., 1.e-6, 1.e-6, 4000, w, &res, &err);

  if(status == GSL_EDIVERGE){
      status = gsl_integration_qagiu(&F, 0., 1.e-9, 1.e-9, 4000, w, &res, &err);
      if (status == GSL_EDIVERGE){ status = gsl_integration_qagiu(&F, 0., 1.e-12, 1.e-12,
    4000, w, &res, &err);}
  }
  gsl_integration_workspace_free(w);

  return res;

}

// Integrand function
double fpSigma (double y, void * p){

  struct fparams2 * fp = (struct fparams2 *)p;

  double xk0 =  fp->a;
  double xk =  fp->b;
  double z =  fp->c;
  double y0 = sqrt(y*y+z*z);

  double a1 = xk0*xk0-xk*xk + z*z - 2.*xk0*y0 + 2.*y*xk;
  double a2 = xk0*xk0-xk*xk + z*z - 2.*xk0*y0 - 2.*y*xk;
  double b1 = xk0*xk0-xk*xk + z*z + 2.*xk0*y0 + 2.*y*xk;
  double b2 = xk0*xk0-xk*xk + z*z + 2.*xk0*y0 - 2.*y*xk;
  double x = nF(y0)*log(fabs(a1/a2*b1/b2));

  return x;
}
```

Massless fermion

For a massless fermion, Eq. (VII.45) simplifies to

$$\mathrm{Tr}\Big\{\not{p}\Sigma^{\mathcal{H}}(p)\Big\}^{(T\neq 0)}_{m_F=0} = \frac{GT^2}{4} + \frac{G}{8\pi^2}\frac{p^2}{|\vec{p}|}\int_0^\infty \mathrm{d}k\,(f_-(k)-f_+(k))\sum_\pm \ln\left|\frac{p^2+2k(|\vec{p}|\mp p_0)}{p^2-2k(|\vec{p}|\pm p_0)}\right| \tag{VII.64}$$

$$= \frac{GT^2}{4} + \frac{G}{8\pi^2}\frac{p^2}{|\vec{p}|}\left(I_{2-}-I_{2+}\right)\,, \tag{VII.65}$$

where

$$I_{2\pm} \equiv \frac{p_0 - |\vec{p}|}{|p_0 + |\vec{p}||}\mathfrak{a}_\pm(|p_0 - |\vec{p}||) - \frac{p_0 + |\vec{p}|}{|p_0 + |\vec{p}||}\mathfrak{a}_\pm(|p_0 + |\vec{p}||)\,. \tag{VII.66}$$

The trace and the integral functions I_{2-} and I_{2+} are implemented as

```
double kSigmaH(double xk0, double xk) {
    if(HTL_ON == true) return G/pow(2.*M_PI,2) * M_PI * M_PI / 2.;
    else {
        return G/pow(2.*M_PI,2) *
            ((xk0*xk0 - xk*xk)/4./xk * (I2m(xk0,xk) - I2p(xk0,xk)) + M_PI * M_PI / 2.);
    }
}

double I2m (double xk0, double xk){
    return - (xk0+xk)/fabs(xk0+xk) * am(fabs(xk0+xk))
            + (xk0 - xk)/fabs(xk0 - xk) * am(fabs(xk0-xk));
}

double I2p (double xk0, double xk){
    return - (xk0+xk)/fabs(xk0+xk) * ap(fabs(xk0+xk))
            + (xk0 - xk)/fabs(xk0 - xk) * ap(fabs(xk0-xk));
}
```

VII.3.3.2 Contraction with u

For the contraction with u^μ, $\mathrm{Tr}\left\{\not{u}\Sigma^{\mathcal{H}}(p)\right\}$, the calculation proceeds in a very similar way, with the only difference of substituting $p^2 - p\cdot k$ with $p_0 - k_0$. Starting directly after having integrated over $\mathrm{d}k_0$ and the azimuthal angle $\mathrm{d}\phi$, we have

$$\begin{aligned}(I)_u &= \frac{G}{4\pi^2}\int_0^\infty \mathrm{d}|\vec{k}||\vec{k}| \sum_{k_0=\pm|\vec{k}|}[1+2f_-(|k_0|)]\int_{-1}^1 \mathrm{d}\cos\theta \frac{p_0 - k_0}{p^2 - m_F^2 \mp 2|\vec{p}||\vec{k}| + 2|\vec{p}||\vec{k}|\cos\theta} \\ &= \frac{G}{8\pi^2|\vec{p}|}\int_0^\infty \mathrm{d}|\vec{k}|\,[1+2f_-(|k_0|)]\sum_\pm (p_0 \mp |\vec{k}|)\ln\left|\frac{p^2 - m_F^2 \mp 2p_0|\vec{k}| + 2|\vec{p}||\vec{k}|}{p^2 - m_F^2 \mp 2p_0|\vec{k}| - 2|\vec{p}||\vec{k}|}\right| \end{aligned} \tag{VII.67}$$

$$\tag{VII.68}$$

and

$$\begin{aligned}(II)_u &= \frac{G}{4\pi^2}\int_0^\infty \mathrm{d}|\vec{k}|\frac{|\vec{k}|^2}{\omega_k}[1+2f_+(|k_0|)]\sum_\pm(\pm\omega_k)\int_{-1}^1 \mathrm{d}\cos\theta\frac{1}{p^2 + m_F^2 \mp 2p_0\omega_k + 2|\vec{p}||\vec{k}|\cos\theta} \\ &= \frac{G}{8\pi^2|\vec{p}|}\int_0^\infty \mathrm{d}|\vec{k}||\vec{k}|\,[1+2f_+(|k_0|)]\sum_\pm(\pm)\ln\left|\frac{p^2 + m_F^2 \mp 2p_0\omega_k + 2|\vec{p}||\vec{k}|}{p^2 + m_F^2 \mp 2p_0\omega_k - 2|\vec{p}||\vec{k}|}\right| \end{aligned} \tag{VII.69}$$

Adding the $(I)_u$ and $(II)_u$ parts together, we obtain

$$\begin{aligned}\mathrm{Tr}\left\{\not{u}\Sigma^{\mathcal{H}}(p)\right\}^{(T\neq 0)} &= \frac{G}{4\pi^2}\frac{1}{|\vec{p}|}\int_0^\infty \mathrm{d}k\, f_-(k)\sum_{\pm'}(p_0 \mp' k)\ln\left|\frac{p^2 - m_F^2 + 2k(|\vec{p}|\mp' p^0)}{p^2 - m_F^2 - 2k(|\vec{p}|\pm' p^0)}\right| \\ &+ \frac{G}{4\pi^2}\frac{1}{|\vec{p}|}\int_0^\infty \mathrm{d}k\,k\, f_+(\omega_{F,k})\sum_{\pm'}(\mp')\ln\left|\frac{p^2 + m_F^2 \mp' 2p_0\,\omega_{F,k} + 2|\vec{p}|k}{p^2 + m_F^2 \mp' 2p_0\,\omega_{F,k} - 2|\vec{p}|k}\right| \\ &= \frac{G}{8\pi^2|\vec{p}|}\left(p_0 I_{2-} + I_{3-}^{(M)} - J_{3+}^{(M)} + 3\pi^2 T^2 \ln\left|\frac{p_0 + |\vec{p}|}{p_0 - |\vec{p}|}\right|\right), \end{aligned} \tag{VII.70}$$

where I_{2-} was already given in Eq. (VII.48), and where we have defined

$$I_{3\pm}^{(M)} \equiv \int_0^\infty \mathrm{d}k\, k\, f_\pm(k) \sum_{\pm'} (\mp') \ln \left| \frac{p^2 - m_F^2 + 2k(|\vec{p}|\mp' p^0)}{p^2 - m_F^2 - 2k(|\vec{p}|\pm' p^0)} \right| , \tag{VII.71}$$

$$J_{3\pm}^{(M)} \equiv \int_0^\infty \mathrm{d}k\, k\, f_\pm(\omega_{F,k}) \sum_{\pm'} (\mp') \ln \left| \frac{p^2 + m_F^2 \mp' 2p_0\, \omega_{F,k} + 2|\vec{p}|k}{p^2 + m_F^2 \mp' 2p_0\, \omega_{F,k} - 2|\vec{p}|k} \right| . \tag{VII.72}$$

$I_{3\pm}$ Integral

The $I_{3\pm}^{(M)}$ can be simplified as

$$\boxed{I_{3\pm}^{(M)} = \mathfrak{c}_\pm(|p_{m_F}^-|) - \mathfrak{c}_\pm(|p_{m_F}^+|)\,,} \tag{VII.73}$$

where

$$\boxed{\mathfrak{c}_\pm(y) \equiv \int_0^\infty \mathrm{d}k\, k f_\pm(k) \ln \left| \frac{2k+y}{2k-y} \right| .} \tag{VII.74}$$

Small-y regime. Expanding $\ln|y^2 - 4x^2| \simeq \ln\big(4x^2\big)$,

$$\mathfrak{c}_-(y \to 0) = 2\int_0^\infty \frac{x\ln(2x)}{e^x - 1}\, dx \simeq 1.79617.$$

Large-y regime. For $y \gg 1$,

$$\mathfrak{c}_-(y) \simeq 2\ln y \int_0^\infty \frac{x}{e^x-1}\, dx = \frac{\pi^2}{3} \ln y.$$

These limits are implemented in the `cmMint` function outside of the tabulated region.

$J_{3\pm}$ Integral

Regarding the $J_{3\pm}$ integral, a decomposition was not found during the preparation of [5] and was not implemented in the numerical code. However, we can also show that $J_{3\pm}$ can be decomposed similarly as for $J_{2\pm}$ in Eq. (VII.52). First, change the integration variable to $\mathrm{d}\omega$ using that $k\mathrm{d}k = \omega_{m_F,k}\mathrm{d}\omega_{F,k} \equiv \omega\mathrm{d}\omega$, obtaining:

$$J_{3\pm} = \int_{m_F}^\infty \mathrm{d}\omega\, \omega f_\pm(\omega) \sum_{\pm'} (\mp') \ln \left| \frac{p^2 + m_F^2 \mp' 2p_0\omega + 2|\vec{p}|\sqrt{\omega^2 - m_F^2}}{p^2 + m_F^2 \mp' 2p_0\omega - 2|\vec{p}|\sqrt{\omega^2 - m_F^2}} \right| . \tag{VII.75}$$

Then we define the following auxiliary single-variable function,

$$\mathfrak{d}_\pm^{(m_F)}(y) \equiv \int_{m_F}^\infty \mathrm{d}\omega\, \omega f_\pm(\omega) \ln \left| \frac{2\sqrt{\omega^2 - m_F^2} + y}{2\sqrt{\omega^2 - m_F^2} - y} \right| , \tag{VII.76}$$

which allows to express Eq. (VII.75) as

$$\boxed{J_{3\pm} = \mathfrak{d}_\pm^{(m_F)}(|P_{m_F}^-|) - \mathfrak{d}_\pm^{(m_F)}(|P_{m_F}^+|)\,,} \tag{VII.77}$$

where

$$P^{\pm}_{m_F} = \frac{p^2 + m_F^2 \mp 2p_0 m_F}{p_0 \pm |\vec{p}|}\,. \tag{VII.78}$$

For small and large y, one finds the asymptotic behaviors

$$\boxed{\begin{aligned} \mathfrak{d}_{\pm}^{(m_F)}(y) &\simeq y\, A_{\pm}(m_F), \quad y \ll 2\sqrt{\omega^2 - m_F^2},\\ \mathfrak{d}_{\pm}^{(m_F)}(y) &\simeq \frac{4\,B_{\pm}(m_F)}{y}, \quad y \gg 2\sqrt{\omega^2 - m_F^2}, \end{aligned}}$$

where

$$A_{\pm}(m_F) = \int_{m_F}^{\infty} d\omega\, \frac{\omega\, f_{\pm}(\omega)}{\sqrt{\omega^2 - m_F^2}}, \qquad B_{\pm}(m_F) = \int_{m_F}^{\infty} d\omega\, \omega\, \sqrt{\omega^2 - m_F^2}\, f_{\pm}(\omega).$$

The interpolating functions $A(m_F)$ and $B(m_F)$ can be numerically determined by interpolating over several values of m_F.

All the functions above are implemented in the code as:

```
double uSigmaH_M (double xk0, double xk, double mF){
    // HTL result
    if(HTL_ON == true) return G/16.xk *
                            log( fabs((xk0+xk) / (xk0-xk)) );
    // Full result
    return G/8./M_PI/M_PI/xk * ( xk0*I2mM(xk0,xk,mF)
                            - I3TpM(xk0,xk,mF)
                            + I3TmM(xk0,xk,mF)
                            + log( fabs((xk0+xk) / (xk0-xk)) )
                            * M_PI * M_PI * 3. );
}
```

```
double I3TmM (double xk0, double xk, double mF){

    double kmp = ((xk0+xk)*(xk0-xk)-mF*mF) / ((xk0-xk));
    double kmm = ((xk0+xk)*(xk0-xk)-mF*mF) / ((xk0+xk));
    return( cmMint(fabs(kmm)) - cmMint(fabs(kmp)) );
}

double cmMint (double y) {
    if (y < pow(10., -2))
        return 1.79617;
    if (y > pow(10., 3))
        return 1. / 3. * M_PI * M_PI * log(y);
    return pow(10., Tabulated_Integral_1d(log10(fabs(y)), -2., 3., 0.01, table_cMmint));
}


double I3TpM (double xk0, double xk, double mF){

    double r = log10(sqrt(xk0*xk0 + xk*xk));
    double theta = atan(fabs(xk0)/xk);
    n_funcalls=n_funcalls+1;

    if(r>-3 && r<5.){
```

```
        n_TabInt=n_TabInt+1;
        return xk0/fabs(xk0)*Tabulated_Integral_3d(log10(mF),-2.,1.,97./3232.,r
    ,-3.,5.,8./399.,theta,0.,M_PI/2.,M_PI/2./399.,table_uSigmaH);
    }
    return xk0/fabs(xk0)*uSigmaH_int(xk0,xk,mF);
}

// uSigma contraction
// Use numerical integration method from GSL
// QAGI adaptive integration
// gsl_integration_qagiu
double uSigmaH_int(double xk0, double xk, double z){

  struct fparams2 pars= {xk0 ,xk, z};

  double res, err;

  gsl_set_error_handler_off();
  gsl_integration_workspace * w = gsl_integration_workspace_alloc(4000);

  gsl_function F;
  F.function = &fuSigma; // Integrand
  F.params = &pars;

  int status = gsl_integration_qagiu(&F, 0., 1.e-6, 1.e-6, 4000, w, &res, &err);

  if(status == GSL_EDIVERGE){
      status = gsl_integration_qagiu(&F, 0., 1.e-9, 1.e-9, 4000, w, &res, &err);
      if (status == GSL_EDIVERGE){ status = gsl_integration_qagiu(&F, 0., 1.e-12, 1.e-12,
    4000, w, &res, &err);}
  }
  gsl_integration_workspace_free(w);

  return res;

}

// Integrand
double fuSigma (double y, void * p){

  struct fparams2 * fp = (struct fparams2 *)p;

  double xk0 =  fp->a;
  double xk =  fp->b;
  double z =  fp->c;
  double y0 = sqrt(y*y+z*z);

  double a1 = xk0*xk0-xk*xk + z*z - 2.*xk0*y0 + 2.*y*xk;
  double a2 = xk0*xk0-xk*xk + z*z - 2.*xk0*y0 - 2.*y*xk;
  double b1 = xk0*xk0-xk*xk + z*z + 2.*xk0*y0 - 2.*y*xk;
  double b2 = xk0*xk0-xk*xk + z*z + 2.*xk0*y0 + 2.*y*xk;
  double x = y * nF(y0)*log(fabs(a1/a2*b1/b2));

  return x;
}
```

For a massless fermion, one obtains

$$\mathrm{Tr}\Big\{\not{u}\Sigma^{\mathcal{H}}(p)\Big\}^{(T\neq 0)}_{m_F=0} = \frac{G}{4\pi^2}\frac{1}{|\vec{p}|}\int_0^\infty \mathrm{d}k\, k\,\left(f_-(k)+f_+(k)\right)\sum_{\pm}(\mp)\ln\left|\frac{p^2+2k(|\vec{p}|\mp p^0)}{p^2-2k(|\vec{p}|\pm p^0)}\right|$$

$$+\frac{G}{4\pi^2}\frac{p_0}{|\vec{p}|}\int_0^\infty \mathrm{d}k\, f_-(k)\sum_\pm \ln\left|\frac{p^2+2k(|\vec{p}|\mp p^0)}{p^2-2k(|\vec{p}|\pm p^0)}\right|\,. \tag{VII.79}$$

Here, we define

$$\boxed{\underbrace{\mathfrak{c}(y)}_{\texttt{C++: cint}} \equiv \mathfrak{c}_+(y)+\mathfrak{c}_-(y) = \int_0^\infty \mathrm{d}k\, k\,[f_+(k)+f_-(k)]\ln\left|\frac{2k+y}{2k-y}\right|} \tag{VII.80}$$

to simplify the first integral in Eq. (VII.79), namely

$$I^{(0)}_{3\pm} = \mathfrak{c}_\pm(|p_0-|\vec{p}||) - \mathfrak{c}^{(0)}_\pm(|p_0+|\vec{p}||) \tag{VII.81}$$

If we expand the integrand function for large y, we find (cf. also [479])

$$\begin{aligned}\mathfrak{c}(y) &\simeq \frac{\pi^2}{2}\ln y - \frac{\pi^2}{6}(3+7\ln 2.36\ln A + 3\ln\pi) && \text{(VII.82)}\\ &\simeq \frac{\pi^2}{2}\ln y - \frac{\pi^2}{6}2.33106\,, && \text{(VII.83)}\end{aligned}$$

where $A \simeq 1.282427$ is the Glaisher-Kinkelin constant,[3] whereas for small-y values, we find

$$\mathfrak{c}(y) \simeq 0.1733\, y^2\,. \tag{VII.84}$$

The expressions for the contraction with u for a massless fermion are implemented in the following code:

```
double uSigmaH (double xk0, double xk){

    if(HTL_ON == true) return G/16./xk * log( fabs((xk0+xk) / (xk0-xk)) );
    return G/8./M_PI/M_PI/xk * ( I3T(xk0,xk)
                                 + xk0 * I2m(xk0,xk)
                                 + log( fabs((xk0+xk) / (xk0-xk)) )
                                 * M_PI*M_PI/2. );
}

double I3T (double xk0, double xk){
    return cint(fabs(xk0-xk)) - cint(fabs(xk0+xk));
}

double cint (double y) {
    if (y < pow(10., -5))
        return 0.17328679619 * y * y;
    if (y > pow(10., 3))
        return M_PI * M_PI / 2. * log(y) - M_PI * M_PI / 6. * (2.33106);
    return pow(10., Tabulated_Integral_1d(log10(fabs(y)), -5., 3., 0.01, table_cint));
}
```

VII.3.4 Anti-Hermitian Contractions

VII.3.4.1 Contraction with p, Anti-Hermitian

For the anti-Hermitian parts, we use the properties described in Sections VI.2.2 and VI.3.2.2, in particular that

$$\mathrm{Tr}\Big\{\not{p}\Sigma^{\mathcal{A}}\Big\} = \frac{1}{2}f_+^{-1}(p_0)\,\mathrm{Tr}\Big\{\not{p}\, i\Sigma^{>}(p)\Big\}\,.$$

[3] https://mathworld.wolfram.com/Glaisher-KinkelinConstant.html

Thus,

$$\mathrm{Tr}\Big\{\not p\, i\not\Sigma^{>}(p)\Big\} = 4G\int \frac{\mathrm{d}^4k}{(2\pi)^4}\, i\Delta_{\gamma}^{>}(k)\, i\tilde{\Delta}_{\ell,R}^{>}(p-k)\, p\cdot(p-k)$$

$$= 4G\int \frac{\mathrm{d}^4k}{4\pi^2}\delta(k^2)\delta\Big((p-k)^2-m_F^2\Big)\Big[\Big(1-f_+(p_0-k_0)\Big)\Big(1+f_-(k_0)\Big)\Big]$$
$$\times\,\mathrm{sign}(k_0)\mathrm{sign}(p_0-k_0)(p^2-p\cdot k)$$

$$\underbrace{=}_{k\to p-k} \frac{G}{\pi^2}e^{p_0}f_+(p_0)\,\mathrm{sign}(p^2-m_F^2)\frac{p^2+m_F^2}{2} \tag{VII.85}$$

$$\times\int \mathrm{d}^4k\,\delta(k^2-m_F^2)\delta((p-k)^2)\Big[1-f_+(k_0)+f_-(p_0-k_0)\Big] \tag{VII.86}$$

In the first step, we used the formulae shown in Section VI.3.2.2. In the second step, we shifted the integration variable $k\to p-k$ to ease the integration over the delta function with the fermion mass m_F. In particular, we also have $p^2-p\cdot k\to p\cdot k$. Moreover, we used the on-shellness property (under integration condition), which implies

$$\mathrm{sign}(k_0)\mathrm{sign}(p_0-k_0) = \mathrm{sign}(p^2-m_F^2)\,, \tag{VII.87}$$

and

$$0=(p-k)^2=p^2+k^2-2p\cdot k = p^2+m_F^2-2p\cdot k \implies p\cdot k = \frac{p^2+m_F^2}{2}\,. \tag{VII.88}$$

Finally, we made use of the following identity:

$$e^{p_0}f_+(p_0) = [1-f_+(p_0-k_0)+f_+(k_0)] = 1-f_+(p_0-k_0)+f_-(k_0)-f_+(p_0-k_0)f_-(k_0)$$

Therefore, we obtain

$$= \frac{G}{4\pi}e^{p_0}f_+(p_0)\mathrm{sign}(p^2-m_F^2)\frac{p^2+m_F^2}{|\vec{p}|}\underbrace{\int_{\mathcal{B}}\mathrm{d}k_0\,\Big[1-f_+(k_0)+f_-(p_0-k_0)\Big]}_{\mathcal{I}(k_0)|_{\mathcal{B}}}$$

which can be integrated using

$$\mathcal{I}(k_0)\Big|_{\mathcal{B}} = \mathcal{I}(k_0)\Big|_{k_-^0}^{k_+^0} + \theta(-p^2)\,\mathcal{I}(k_0)\Big|_{-\infty}^{+\infty}\,,$$

with

$$k_\pm^0 = \frac{p_0}{2p^2}(p^2+m_F^2)\pm\frac{|\vec{p}|}{2p^2}\left|p^2-m_F^2\right|\,.$$

The result is

$$\mathrm{Tr}\Big\{\not p\not\Sigma^{\mathcal{A}}(p)\Big\} = \frac{G}{8\pi}\mathrm{sign}(p^2-m_F^2)\frac{p^2+m_F^2}{|\vec{p}|}\left[\theta(-p^2)p^0+T\ln\left|\frac{\sinh\Big(\frac{k_+^0-p^0}{2T}\Big)\cosh\Big(\frac{k_-^0}{2T}\Big)}{\sinh\Big(\frac{k_-^0-p^0}{2T}\Big)\cosh\Big(\frac{k_+^0}{2T}\Big)}\right|\right]\,. \tag{VII.89}$$

```
double kSigmaA_M (double xk0, double xk, double mF){
// We add: 1. vacuum contribution 2. Thermal Part - HTL 3. HTL (HTL part is identical 0
    here). This is for the m=0 case
// We have a expression not split into vacuum and T neq 0 part for the massive case
    if(HTL_ON == true) return 0;
    double xk2 = xk0*xk0 -xk*xk;
    double logshch = log(
                    fabs(
                         cosh(xp0p/2.) / cosh(xp0m/2.)
                         * sinh((xp0m-xk0)/2.) / sinh((xp0p-xk0)/2.)
                        )
                       );
    double xp0p = 1./2./(xk2) *
                 (xk0 * (xk2 + mF*mF)
                   + xk*fabs(xk2 - mF*mF) );
    double xp0m = 1./2./(xk2) *
                 (xk0 * (xk2 + mF*mF)
                   - xk*fabs(xk2 - mF*mF) );
    return G/16./M_PI * (xk2 - mF*mF)
                    / fabs(xk2 - mF*mF)
                    * (xk2 + mF*mF) / xk
                    * ( Theta(-xk2) * xk0
                    + logshch );
}
```

The massless variant of the anti-Hermitian contraction with k follows straightforwardly from the expressions above by setting $m_F = 0$.

VII.3.4.2 Contraction with u, Anti-Hermitian

To calculate $\mathrm{Tr}\left\{\not{u}\Sigma^{\mathcal{A}}(p)\right\}$ follow the same steps as for the computation of $\mathrm{Tr}\left\{\not{p}\Sigma^{\mathcal{A}}(p)\right\}$, with the only difference that $p^2 - p\cdot k \to p_0 - k_0$, which becomes simply k_0 after shifting integration variable with $k \to p - k$. Therefore:

$$\mathrm{Tr}\left\{\not{u}\Sigma^{>}(p)\right\} = \frac{G}{2\pi} e^{p_0} f_+(p_0) \mathrm{sign}(p^2 - m_F^2) \frac{1}{|\vec{p}|} \int_{\mathcal{B}} \mathrm{d}k_0\, k_0 \left[1 - f_+(k_0) + f_-(p_0 - k_0)\right]. \tag{VII.90}$$

This integration involves the first moment of the Bose-Einstein and Fermi-Dirac distribution functions, namely[4]

$$\int_0^\infty \mathrm{d}x\, x^n f_\pm(x-\mu) = \mp\Gamma(n+1)\,\mathrm{Li}_{n+1}(\mp e^{\mu}). \tag{VII.91}$$

Here, $\mathrm{Li}_s(x)$ is the **polylogarithm** of order s. If the chemical potential μ is zero, or, equivalently, if the argument of the distribution function is exactly the integration variable, the relation in Eq. (VII.91) simplifies to

$$\int_0^\infty \mathrm{d}x\, x^n f_\pm(x) = \mp\Gamma(n+1)\,\mathrm{Li}_{n+1}(\mp 1) = \begin{cases} \Gamma(n+1)\zeta(n+1) & \text{Bose-Einstein,} \\ (1-2^{-n})\Gamma(n+1)\zeta(n+1) & \text{Fermi-Dirac.} \end{cases} \tag{VII.92}$$

[4] https://mathworld.wolfram.com/Polylogarithm.html

Exploiting these mathematical relations, the integral in Eq. (VII.90) becomes

$$\text{(VII.90)} = \frac{G}{2\pi|\vec{p}|} e^{p_0} f_+(p_0)\mathrm{sign}(p^2 - m_F^2) \tag{VII.93}$$

$$\mathfrak{Re}\left\{ Tk_0 \ln\left|\frac{f_-(k_0 - p_0)}{f_+(k_0)}\right| + T^2\mathrm{Li}_2\left(-e^{k_0}\right) - T^2\mathrm{Li}_2\left(e^{k_0 - p_0}\right)\right\}_{\mathcal{B}}, \tag{VII.94}$$

where $\mathrm{Li}_2(x)$ is the **dilogarithm** function, the polylogarithm of order 2, also known as Spence's function. The real part $\mathfrak{Re}$ is taken to ensure the reality of the expression. In fact, the dilogarithm can become complex when the arguments of the exponentials cross branch cuts. Relating the Wightmann Eq. (VII.94) with its spectral counterpart and integrating over the domain $\mathcal{B}$, we obtain

$$\begin{aligned}\mathrm{Tr}\Big\{\not{u}\Sigma^{\mathcal{A}}(p)\Big\} = \frac{G}{4\pi}\frac{\mathrm{sign}(p^2 - m_F^2)}{|\vec{p}|}\Bigg[\theta(-p^2)\left(-\frac{\pi^2T^2}{2} + \frac{(p^0)^2}{2}\right) \\ + T\,\mathfrak{Re}\Big\{k^0 \ln\left|\frac{f_-(k^0 - p^0)}{f_+(k^0)}\right| + T\mathrm{Li}_2\left(-e^{k^0/T}\right) - T\mathrm{Li}_2\left(e^{(k^0 - p^0)/T}\right)\Big\}\Big|_{k_-^0}^{k_+^0}\Bigg].\end{aligned} \tag{VII.95}$$

This function is implemented in the numerical code as follows:

```
double uSigmaA_M(double xk0, double xk, double mF) {
    double xk2 = xk0 * xk0 - xk * xk;
    if (HTL_ON == true) return G / 8. / M_PI / xk * I1HTL(xk0, xk);
    double xp0p = 1. / 2. / xk2 * (xk0 * (xk2 + mF * mF) + xk
                            * fabs(xk2 - mF * mF));
    double xp0m = 1. / 2. / xk2 * (xk0 * (xk2 + mF * mF) - xk
                            * fabs(xk2 - mF * mF));
    return G / 8. / M_PI * GSL_SIGN(xk2 - mF * mF) / xk
           * (Theta(-xk0 * xk0 + xk * xk)
           * (-M_PI * M_PI / 2. + xk0 * xk0 / 2.)
            + f1TM(xp0p, xk0) - f1TM(xp0m, xk0));
}

double f1TM(double xp0, double xk0) {
    return xp0 * log(fabs((1 + exp(xp0)) / (1 - exp(xp0 - xk0))))
             + gsl_sf_dilog(-exp(xp0)) - gsl_sf_dilog(exp(x - xk0));
}
```

The massless variant of the anti-Hermitian contraction with u follows straightforwardly from the expressions above by setting $m_F = 0$.

VII.4 DM Self-energy with HTL Propagators

Declaration: this section presents results from the literature and new results developed by the thesis author and MB for [5]. All authors discussed the results and their interpretation. The text follows what is presented in the paper, but has been largely reworked and integrated with information regarding analytical derivations and numerical implementations. In the paper, all authors contributed to structuring, reviewing, and refining the manuscript.

VII.4.1 Resummed Propagators in the HTL Approximation

In the previous section, we derived spectral densities that can be simplified under the assumption that the loop momenta ℓ in the fermion self-energies are much larger than the other relevant mass scales $(k, m_F, m_{\rm DM})$. This simplification involves treating the problem as if there were a clear separation between hard scales ($\mathcal{O}(\pi T)$) and soft scales ($\mathcal{O}(gT)$). This approach is known as Hard Thermal Loop (HTL) effective perturbation theory, where the self-energies are resummed to capture the leading contributions from thermal fluctuations with hard virtual momenta [435, 436, 511–515].

In a small coupling expansion, this resummation is crucial whenever the external momentum is soft. Contributions that would appear as higher-order in g in vacuum become as significant as the tree-level term in a hot plasma, necessitating resummation to maintain perturbative accuracy. Practically, the HTL approximation involves expanding in $k/\ell \sim g/\pi$ and retaining only the leading terms. This approximation is expected to be valid if $g \ll 1$.

We must now evaluate whether this simplified HTL scheme, commonly used in leptogenesis scenarios, is appropriate for describing freeze-in DM production. Given that freeze-in dynamics occur at temperatures $T \sim m_F$, the momentum of the heavy fermion F in the DM self-energy is of order $k \sim m_F \sim T$. Consequently, the expansion parameter k/ℓ is of order one, indicating that the HTL approximation may not be well-justified for the bulk of DM production.

To highlight the differences from the 1PI-resummed case, we collect now the HTL self-energy, spectral densities, and production rates. The impact on freeze-in production will be discussed in Section VIII.2.

Hermitian contractions

In the HTL limit, where all masses are negligible, and the loop momentum is the dominating scale ($k \gg m_F, p, p_0$), the whole expression in Eq. (VII.45) simplifies to:

$$\mathrm{Tr}\Big\{\not{p}\not{\Sigma}^{\mathcal{H}}(p)\Big\}^{\rm HTL} = \frac{GT^2}{4} + \frac{G}{\pi^2}\int_0^\infty \mathrm{d}k k f_+(k) = \frac{GT^2}{8}\,. \tag{VII.96}$$

Clearly, given that in-vacuum masses play no role within the HTL limit, the same result holds for a massless fermion (cf. Eq. (VII.65)).

In the HTL limit, the contraction with the plasma vector u in Eq. (VII.70) simplifies to

$$\mathrm{Tr}\Big\{\not{u}\not{\Sigma}^{\mathcal{H}}(p)\Big\}^{\rm HTL} = \frac{GT^2}{16|\vec{p}|}\ln\left|\frac{p_0+|\vec{p}|}{p_0-|\vec{p}|}\right| \tag{VII.97}$$

Anti-Hermitian contractions

For the anti-Hermitian parts, the contraction with the fermion momentum results in a vanishing trace:

$$\mathrm{Tr}\Big\{\not{p}\not{\Sigma}^{\mathcal{A}}(p)\Big\}^{\rm HTL} = 0\,, \tag{VII.98}$$

To demonstrate this, we start from the full expression before integration:

$$\mathrm{Tr}\Big\{\not{p}\not{\Sigma}^{\mathcal{A}}(p)\Big\} \propto \int \frac{\mathrm{d}^4k}{(2\pi)^4}\,\mathrm{Tr}\Big\{p_\alpha\gamma^\alpha\gamma^\mu P_{L,R}\, i\not{S}^{>}_{\ell,R}(k)P_{R/L}\gamma^\nu i\Delta^{>}_{\mu\nu}(p-k)\Big\} \tag{VII.99}$$

$$\propto \int d^4k\,\delta(k^2-m_F^2)\,\delta((p-k)^2)\,\mathrm{Tr}\{\not{p}\not{k}\}\,. \tag{VII.100}$$

The HTL limit corresponds to the situation where the loop momentum is hard ($k \sim T$) and the external momentum is soft ($p_0, |\vec{p}|, m_F \ll T$). The two delta functions enforce the on-shell conditions

$$k^2 = m_F^2, \qquad (p-k)^2 = 0.$$

from which one obtains

$$p\cdot k = p_0 k_0 - \vec{p}\cdot\vec{k} = \frac{p^2 + m_F^2}{2}.$$

This fixes k_0 for each direction of $\vec{k}$ as

$$k_0 = \frac{p_0(p^2+m_F^2)/2 + |\vec{p}|\,|\vec{k}|\cos\theta}{p_0} \simeq |\vec{k}|\Big(1+\mathcal{O}\Big(\frac{p}{T}\Big)\Big)\,,$$

so that the integral effectively samples momenta $|\vec{k}|\sim T$ with angles satisfying

$$p_0 = \hat{k}\cdot\vec{p} + \mathcal{O}\left(\frac{p^2}{T}\right), \tag{VII.101}$$

where $\hat{k} = \vec{k}/|\vec{k}|$. Using this approximation, the two delta functions reduce to

$$\delta(k^2 - m_F^2)\,\delta((p-k)^2) \;\longrightarrow\; \frac{1}{4|\vec{k}|^2}\,\delta(p_0 - \hat{k}\cdot\vec{p})\,\Big[1+\mathcal{O}\Big(\frac{p}{T}\Big)\Big].$$

At the same time, the Dirac trace appearing in the contraction $\mathrm{Tr}\Big\{\not{p}\Sigma^{\mathcal{A}}\Big\}$ is proportional to

$$\mathrm{Tr}\big\{\not{p}\not{k}\big\} = 4p\cdot k = 4(p_0k_0 - \vec{p}\cdot\vec{k}) \simeq 4k_0\,(p_0 - \vec{p}\cdot\hat{k}). \tag{VII.102}$$

Combining Eqs. (VII.101) and (VII.102), we see that the integrand of the loop integral is multiplied by the factor $(p_0 - \hat{k}\cdot\vec{p})$ and simultaneously by $\delta(p_0 - \hat{k}\cdot\vec{p})$. Hence,

$$(p_0 - \hat{k}\cdot\vec{p})\,\delta(p_0 - \hat{k}\cdot\vec{p}) = 0, \tag{VII.103}$$

and the entire integrand vanishes pointwise. This demonstrates that

$$\boxed{\mathrm{Tr}\Big[\not{p}\Sigma^{\mathcal{A}}(p)\Big]_{\mathrm{HTL}} = 0,} \tag{VII.104}$$

independently of the details of the statistical factors. The vanishing occurs because, in the HTL regime, both internal lines are placed on shell, and the delta-function constraint forces $p_0 = \hat{k}\cdot\vec{p}$, so that the kinematic contraction $p\cdot(\gamma^0 - \hat{k}\cdot\vec{\gamma})$ identically cancels.

The contraction with the plasma four-vector is instead non-vanishing only for spacelike external momenta, yielding

$$\mathrm{Tr}\Big\{\not{u}\Sigma^{\mathcal{A}}(p)\Big\}^{\mathrm{HTL}} = \theta(-k^2)\frac{4G}{\pi}|\vec{k}|T^2\,. \tag{VII.105}$$

VII.4.2 Dispersion Relations

In summary, using $\mathcal{K} = 2\,\mathrm{Tr}\{\not{k}\not{\Sigma}\}$, we have:

$$\mathcal{K}^{\mathcal{H}}_{\mathrm{HTL}} = \frac{1}{4}GT^2, \qquad \mathcal{U}^{\mathcal{H}}_{\mathrm{HTL}} = \frac{G}{8|\vec{k}|}T^2 \log\left|\frac{k^0 + |\vec{k}|}{k^0 - |\vec{k}|}\right|, \tag{VII.106}$$

$$\mathcal{K}^{\mathcal{A}}_{\mathrm{HTL}} = 0, \qquad \mathcal{U}^{\mathcal{A}}_{\mathrm{HTL}} = \theta\left(-k^2\right)\frac{G}{\pi}8|\vec{k}|T^2\,. \tag{VII.107}$$

The numerical code implements the HTL-approximated contractions when the global flag variable `HTL_ON` is set to `TRUE` (cf. the numerical implementation in the previous sections).

Note that the functions in Eqs. (VII.106) and (VII.107) depend only on the temperature T and the external momentum k, with all vacuum mass scales neglected in accordance with the high-temperature expansion. Substituting these expressions into Eq. (VII.18), and subsequently into the definitions of $\Omega_{F/f}$ and $\Gamma_{F/f}$ in Eqs. (VII.12)–(VII.15), and finally into Eqs. (VII.10) and (VII.11), yields the HTL limit of the corresponding spectral densities.

Furthermore, the thermal widths $\Gamma^{\mathrm{HTL}}_{F/f}$, which are directly proportional to $\mathcal{U}^{\mathcal{A}}_{\mathrm{HTL}}$, are nonzero only for space-like momenta ($k^2 < 0$). This kinematic domain corresponds to the so-called *continuum* region, whose properties will be discussed in detail in Section VII.5.

For timelike momenta $k^2 > 0$, the HTL widths vanish, $\Gamma^{\mathrm{HTL}}_{F/f} = 0$, and the HTL spectral densities in Eq. (VI.79) simplify to delta functions [5]

[5] The Dirac delta distribution can be obtained as the limit of a normalized Lorentzian function. Define

$$L_\epsilon(x) \;=\; \frac{1}{\pi}\frac{\epsilon}{x^2+\epsilon^2}, \qquad \epsilon > 0. \tag{VII.108}$$

It is straightforward to verify that

$$\int_{-\infty}^{+\infty} L_\epsilon(x)\,\mathrm{d}x \;=\; \frac{1}{\pi}\int_{-\infty}^{+\infty}\frac{\epsilon\,\mathrm{d}x}{x^2+\epsilon^2} \;=\; 1, \tag{VII.109}$$

so $L_\epsilon(x)$ is normalized for all ϵ. In the limit $\epsilon \to 0^+$, the function becomes infinitely peaked at $x = 0$ while preserving unit area, and we define

$$\boxed{\delta(x) \;=\; \lim_{\epsilon\to 0^+}\frac{1}{\pi}\frac{\epsilon}{x^2+\epsilon^2}}\,. \tag{VII.110}$$

For any smooth test function $f(x)$,

$$\int_{-\infty}^{+\infty} f(x)\,\delta(x)\,\mathrm{d}x \;=\; \lim_{\epsilon\to 0^+}\int_{-\infty}^{+\infty} f(x)\,L_\epsilon(x)\,\mathrm{d}x \;=\; f(0), \tag{VII.111}$$

confirming the defining property of the Dirac delta. This representation also implies the useful identity

$$\frac{1}{x \pm i\epsilon} \;=\; \mathrm{PV}\left(\frac{1}{x}\right) \mp i\pi\,\delta(x), \tag{VII.112}$$

with PV the Cauchy's principal value, which connects the Lorentzian regularization to the spectral representation of propagators. This is also known as the Sokhotski–Plemelj theorem.

$$\not{S}^{\mathcal{A},\mathrm{HTL}}_{F/f}(k) = \pi\,\mathrm{sign}(k^0)\left(\not{k} - \not{\Sigma}^{\mathcal{H},\mathrm{HTL}}_{F/f}(k) - m_{F/f}\right)\delta\left(\left[k - \Sigma^{\mathcal{H},\mathrm{HTL}}_{F/f}(k)\right]^2 - m^2_{F/f}\right)\,, \quad k^2 > 0 \tag{VII.113}$$

where $m_{F/f}$ is the in-vacuum mass.

Here, we encounter a scenario analogous to the tree-level in-vacuum spectral densities, where the system exhibits particle-like behavior with a well-defined dispersion relation described by the zeros of the delta function's argument:

$$g_{F/f}(k) \equiv \left[k - \Sigma^{\mathcal{H},\mathrm{HTL}}_{F/f}(k)\right]^2 - m^2_{F/f} \overset{!}{=} 0\,. \tag{VII.114}$$

Here, we have defined the **dispersion relation functions** $g_{F/f}$. Let us explicitly write the function $g_F(k_0)$ to make the dependence on k_0 and $|\vec{k}|$ manifest. We first expand the square of the Hermitian self-energy using Eq. (VII.31),

$$g_F(k_0) = k_0^2 - |\vec{k}|^2 - 2(k\cdot\Sigma^{\mathcal{H}}) - \frac{2}{k^2}\left[(k\Sigma^{\mathcal{H}})^2 + k^2(u\Sigma^{\mathcal{H}})^2 - 2k_0(k\Sigma^{\mathcal{H}})(u\Sigma^{\mathcal{H}})\right] - m_F^2\,,$$

and then we make use of Eqs. (VII.106) and (VII.107), to get:

$$\begin{aligned} g_F(k_0) &= k^2 - \frac{GT^2}{4} - \frac{2T^2}{k^2}\left[\frac{G^2}{64} + k^2\frac{G^2}{256|\vec{k}|^2}\ln^2\left|\frac{k_0+|\vec{k}|}{k_0-|\vec{k}|}\right| - 2k_0\frac{G^2}{128|\vec{k}|}\ln\left|\frac{k_0+|\vec{k}|}{k_0-|\vec{k}|}\right|\right] - m_F^2 \\ &= k_0^2 - |\vec{k}|^2 - \frac{GT^2}{4} - \frac{G^2T^2}{32\,(k_0^2-|\vec{k}|^2)}\left[1 + \frac{k_0^2-|\vec{k}|^2}{4|\vec{k}|^2}\ln^2\left|\frac{k_0+|\vec{k}|}{k_0-|\vec{k}|}\right| - 2\,\frac{k_0}{|\vec{k}|}\ln\left|\frac{k_0+|\vec{k}|}{k_0-|\vec{k}|}\right|\right] - m_F^2\,. \end{aligned} \tag{VII.115}$$

For vanishing in-vacuum masses, $m_{F/f} = 0$, Eq. (VII.115) can be analytically solved for the zero component of the four-momentum, yielding the following solutions [516]

$$\left(k^0_+\right)^2 = \omega_+^2(|\vec{k}|) = |\vec{k}|^2\left[\frac{W_{-1}\left(-\exp\left(-\alpha|\vec{k}|^2-1\right)\right)-1}{W_{-1}\left(-\exp\left(-\alpha|\vec{k}|^2-1\right)\right)+1}\right]^2\,, \tag{VII.116}$$

$$\left(k^0_-\right)^2 = \omega_-^2(|\vec{k}|) = |\vec{k}|^2\left[\frac{W_0\left(-\exp\left(-\alpha|\vec{k}|^2-1\right)\right)-1}{W_0\left(-\exp\left(-\alpha|\vec{k}|^2-1\right)\right)+1}\right]^2\,, \tag{VII.117}$$

where $\alpha = 16/(GT^2)$ and where W_0 and W_{-1} are Lambert-W functions. These solutions correspond physically to *quasi-particle* and *hole* poles. For fermions with non-zero in-vacuum mass, an analytic solution is not available, and thus Eq. (VII.114) must be solved numerically. It is important to note, however, that massive fermions also exhibit two-pole branches with similar characteristics. Notably, in the large momentum limit, $|\vec{k}| \gg T$, the quasi-particles have a dispersion relation of the form

$$\left(k^0\right)^2 = |\vec{k}|^2 + \frac{G}{4}T^2 \equiv |\vec{k}|^2 + m^2_{\mathrm{th}}\,, \tag{VII.118}$$

where m_{th} is the *thermal mass* of the field, and it corresponds to the momentum-independent part of the thermal Hermitian self-energy. For fermions solely interacting with gauge bosons in the plasma, the thermal mass is thus simply given by

$$m^2_{\mathrm{th}} = \frac{G}{4}T^2\,. \tag{VII.119}$$

VII.4.3 Kinematic Regimes for the HTL integration

We now evaluate the DM self-energy in the HTL approximation. Our starting point is the general expression

$$\Pi_s^{\mathcal{A}}(p) = -2\, y_{\rm DM}^2 \int \frac{d^4k}{(2\pi)^4}\, \mathrm{Tr}\Big[P_L\, \rho\!\!\!/_F^{\mathcal{A}}(k)\, P_R\, \rho\!\!\!/_f^{\mathcal{A}}(k-p)\Big]\, [1 - f_+(k_0) - f_+(p_0-k_0)] \\ -(p \leftrightarrow -p), \tag{VII.120}$$

In the HTL limit, we replace both fermionic spectral functions in Eqs. (VII.10) and (VII.11) with their resummed expressions. After the trivial integration over the azimuthal angle ϕ, the remaining integrations in Eq. (VII.120) (over k_0, $|\vec{k}|$, and $\cos\theta_{kq}$) naturally separate into four distinct kinematic regions. These regions are determined by whether k^2 (the heavy-fermion momentum) and q^2 (the light-fermion momentum) are timelike or spacelike:

$$\Pi_{s,\mathrm{HTL}}^{\mathcal{A}}(p) = \Pi_{s,\mathrm{TT}}^{\mathcal{A}}(p) + \Pi_{s,\mathrm{TS}}^{\mathcal{A}}(p) + \Pi_{s,\mathrm{ST}}^{\mathcal{A}}(p) + \Pi_{s,\mathrm{SS}}^{\mathcal{A}}(p). \tag{VII.121}$$

where:

TT : both momenta k and q are timelike ($k^2 > 0$ and $q^2 > 0$);
TS : k is timelike ($k^2 > 0$) and q is spacelike ($q^2 < 0$);
ST : k is spacelike ($k^2 < 0$) and q is timelike ($q^2 > 0$);
SS : both momenta k and q are spacelike ($k^2 < 0$ and $q^2 < 0$).

Each contribution corresponds to a specific combination of the supports of the two spectral functions and thus has a clear physical interpretation. Whenever one of the momenta is timelike, Eq. (VII.107) shows that the corresponding fermion is placed on its mass shell, so its spectral density reduces to a delta-function structure.

Our strategy is therefore straightforward: whenever delta functions are present, we determine their zeros, allowing us to integrate over k_0 using $\delta(g_F(k))$ and over $\cos\theta_{kq}$ using $\delta(g_f(q))$. After fixing k_0 and $\cos\theta_{kq}$ in this way, we perform the remaining radial integral over $|\vec{k}|$. We now examine each kinematic regime in turn.

VII.4.3.1 Double timelike momenta ($k^2 > 0$ and $q^2 > 0$)

When both internal momenta are timelike, the spectral self-energies reduce to delta functions. Inserting these into Eq. (VII.120) gives

$$\Pi_s^{\mathcal{A}}(p) = -\frac{y_{\rm DM}^2}{2\pi^2} \int d^4k\, \mathrm{sgn}(k^0)\,\mathrm{sgn}(p_0-k_0)\ \mathrm{Tr}\big\{P_L(\not{k} - \Sigma_F^{\mathcal{H}}(k))P_R(\not{q} - \Sigma_f^{\mathcal{H}}(q))\big\} \\ \times \delta_F(g_F(k_0))\, \delta_f(g_f(q_0))\, [1 - f_+(k_0) - f_+(p_0-k_0)], \tag{VII.122}$$

where the trace over Dirac indices yields scalar combinations of the form

$$\mathrm{Tr}\big[P_L(\not{k} - \Sigma_F^{\mathcal{H}}(k))P_R(\not{q} - \Sigma_f^{\mathcal{H}}(q))\big] = 2[k\cdot q - k\cdot\Sigma_f^{\mathcal{H}}(q) - q\cdot\Sigma_F^{\mathcal{H}}(k) + \Sigma_F^{\mathcal{H}}(k)\cdot\Sigma_f^{\mathcal{H}}(q)]. \tag{VII.123}$$

To evaluate this contribution, we employ the results in Eqs. (VII.32), (VII.33), (VII.106) and (VII.107). The remaining task is to treat the delta functions, identify their solutions, and understand the integration domain. The delta functions in Eq. (VII.122) place the fermions on their HTL quasiparticle mass shells, whose zeros define the four branches $k^0 = \pm\omega_{+,m_F}, \pm\omega_{-,m_F}$. Thus, this kinematic regime corresponds to processes in which both internal lines describe thermal quasiparticle modes, i.e., decays or inverse decays in the medium.

For the massless SM fermion ($m_f = 0$), the dispersion relations are known analytically and given in Eqs. (VII.116) and (VII.117). For the massive heavy fermion F, they must be obtained numerically.

Using the standard identity for delta functions yields

$$\int dk^0\, \delta\left(g_F(k_0)\right) = \sum_i \frac{1}{|g'_F(k_i^0)|}, \quad g'_F(k_i^0) = \frac{\mathrm{d}}{\mathrm{d}k^0}\Big(\left[k - \Sigma_F^{\mathcal{H},\mathrm{HTL}}(k)\right]^2 - m_F^2\Big)\Big|_{k^0=k_i^0}. \tag{VII.124}$$

Here, we evaluate the derivative from Eq. (VII.115), yielding

$$\begin{aligned} g'_F(k^0) = \frac{1}{128\,|\vec{k}|^4\,(k_0^2 - |\vec{k}|^2)} \Big[&4k_0|\vec{k}|^3\Big(-G^2T^2 + 64\,|\vec{k}|^2(k_0^2 - |\vec{k}|^2)\Big) \\ &+4G^2|\vec{k}|(k_0^2 - |\vec{k}|^2)\ln\left|\frac{k_0 + |\vec{k}|}{k_0 - |\vec{k}|}\right| - G^2k_0(k_0^2 - |\vec{k}|^2)\ln^2\left|\frac{k_0 + |\vec{k}|}{k_0 - |\vec{k}|}\right|\Big]. \end{aligned} \tag{VII.125}$$

Similarly, for the light fermion f, exploiting the integral over the cosine of the radial angle, one obtains

$$\int \mathrm{d}\cos\theta_{kq}\, \delta(g_f(q_0)) = \sum_j \frac{1}{\left|g'_f(q_j^0)\right|}, \quad g'_f(q_j^0) = \frac{\mathrm{d}}{\mathrm{d}\cos\theta_{kq}}\left(q - \Sigma_f^{\mathcal{H},HTL}(q)\right)^2\Big|_{\cos\theta_{kq}=\cos\theta_{kq}^j}. \tag{VII.126}$$

Here, the derivative $g'_f = \mathrm{d}g_f/\mathrm{d}\cos\theta_{kq}$ is given by:

$$g'_f(q) = \frac{p\,|\vec{k}|}{128}\Big[256 - \frac{4G^2}{|\vec{q}|^6 - q_0^2|\vec{q}|^4}\left(|\vec{q}|^2 - 2q_0^2\right) + \frac{8G^2q_0}{|\vec{q}|^5}\ln\left|\frac{q_0 + |\vec{q}|}{q_0 - |\vec{q}|}\right| \tag{VII.127}$$

$$+\frac{G^2}{|\vec{q}|^6}\left(|\vec{q}|^2 - 2q_0^2\right)\ln^2\left|\frac{q_0 + |\vec{q}|}{q_0 - |\vec{q}|}\right|\Big]. \tag{VII.128}$$

where $|\vec{q}|$ is fixed by the loop momentum $|\vec{k}|$, the external momentum $|\vec{p}|$ and $\cos\theta_j$. Using Eqs. (VII.123), (VII.125) and (VII.128) into Eq. (VII.123) gives the following TT contribution to the DM self-energy in the HTL limit:

$$\begin{aligned} \Pi^{\mathcal{A}}_{s,TT}(p) = \frac{y_{DM}^2}{2\pi}\int \mathrm{d}|\vec{k}| \sum_i\sum_j &\left[k_iq_j - q_j\Sigma_F^{\mathcal{H}}(k_i) - k_i\Sigma_f^{\mathcal{H}}(q_j) + \Sigma_f^{\mathcal{H}}(q_j)\,\Sigma_F^{\mathcal{H}}(k_i)\right] \\ &\times\left[1 - f_+(k_i^0) - f_+(-q_j^0)\right]\frac{\mathrm{sign}\left(k_i^0q_j^0\right)|\vec{k}|^2}{|g'_F\left(k_i^0\right)||g'_f\left(\cos\theta_j\right)|} \\ &\times\Theta\left(|\vec{q}|_j - \Big||\vec{p}| - |\vec{k}|\Big|\right)\Theta\left(-|\vec{q}|_j + \Big||\vec{p}| + |\vec{k}|\Big|\right), \end{aligned} \tag{VII.129}$$

where the step functions encode the kinematic constraints implied by $q = k - p$. The Heaviside functions in Eq. (VII.129) are required for the numerical implementation: As we search for the $|\vec{q}|_j$ solving Eq. (VII.128), we have to verify if each $|\vec{q}|_j$ can be generated from an angle θ_j satisfying $-1 \le \cos\theta_j \le 1$, which is the case as long as $\Big||\vec{p}| - |\vec{k}|\Big| \le |\vec{q}| \le \Big||\vec{p}| + |\vec{k}|\Big|$.

VII.4.3.2 Timelike–spacelike momenta ($k^2 > 0$, $q^2 < 0$)

When k is timelike and q spacelike, only the F propagator is on shell and given by Eq. (VII.113), whereas the f propagator corresponds to its HTL spectral function in the continuum region, i.e., it has a finite width $\Gamma_f(q) \neq 0$. Thus, only one delta function has to be considered. Inserting these forms into Eq. (VII.120) and integrating over k^0 with the on-shell delta function of $S_F^{\mathcal{A}}(k)$ fixes $k^0 = k_i^0(|\vec{k}|)$ and hence $q^0 = k_i^0 - p^0$.

The resulting expression reads

$$\Pi^{\mathcal{A}}_{s,TS}(p) = 2\,\frac{y_{\mathrm{DM}}^2}{(2\pi)^2}\int d|\vec{k}|\, d\cos\theta \sum_i \frac{|\vec{k}|^2}{|g_F'(k_i^0)|}\,\mathrm{sgn}(k_i^0)\left[1 - f_+(k_i^0) - f_+(p^0 - k_i^0)\right](A - B), \tag{VII.130}$$

with

$$\Pi^{\mathcal{A}}_{s,TS}(p) = 2\frac{y_{DM}^2}{(2\pi)^2}\int \mathrm{d}\cos\theta\,\mathrm{d}|\vec{k}|\sum_i \frac{|\vec{k}|^2}{|g_F'\left(k_i^0\right)|}\,(A - B)\ \mathrm{sign}\left(k_i^0\right)\left[1 - f_+(k_i^0) - f_+(p^0 - k_i^0)\right], \tag{VII.131}$$

$$A = \frac{\Gamma_f\left(q\right)\left(k_i q - k_i \Sigma_f^{\mathcal{H}}\left(q\right) - q\Sigma_F^{\mathcal{H}}\left(k_i\right) + \Sigma_F^{\mathcal{H}}\left(k_i\right)\Sigma_f^{\mathcal{H}}\left(q\right)\right)}{\Omega_f^2(q) + \Gamma_f^2(q)}, \tag{VII.132}$$

$$B = \frac{\Omega_f\left(q\right)\left(k_i \Sigma_f^{\mathcal{A}}\left(q\right) - \Sigma_F^{\mathcal{H}}\left(k_i\right)\Sigma_f^{\mathcal{A}}\left(q\right)\right)}{\Omega_f^2(q) + \Gamma_f^2(q)}, \tag{VII.133}$$

Here, Ω_f and Γ_f are the Hermitian and anti-Hermitian components of the light-fermion self-energy. The first term, A, represents the absorptive contribution due to the nonzero width of the spacelike f mode, while B arises from interference between the Hermitian and anti-Hermitian parts. The angular and radial integrations are performed numerically, using $q^0 = k_i^0 - p^0$ and $|\vec{q}| = \sqrt{|\vec{p}|^2 + |\vec{k}|^2 - 2|\vec{p}||\vec{k}|\cos\theta}$.

The configuration with $k^2 < 0$ and $q^2 > 0$ (**ST**) is completely analogous and is obtained by interchanging $k \leftrightarrow q$ and $f \leftrightarrow F$.

VII.4.3.3 Double spacelike momenta ($k^2 < 0$ and $q^2 < 0$)

When both internal momenta are spacelike, the delta functions in Eq. (VII.113) have no support, and both fermionic spectral densities are given by their HTL continuum expressions. In this case, both propagators carry finite widths, and the self-energy must be evaluated numerically over the Landau-damping region ($k^2 < 0$, $q^2 < 0$), yielding

$$\Pi^{\mathcal{A}}_{s,SS}(p) = -2\,y_{\mathrm{DM}}^2\int \frac{d^4k}{(2\pi)^4}\ \mathrm{Tr}\Big[P_L\, \$^{\mathcal{A}}_{F,\mathrm{HTL}}(k)\, P_R\, \$^{\mathcal{A}}_{f,\mathrm{HTL}}(q)\Big]\left[1 - f_+(k_0) - f_+(p_0 - k_0)\right], \tag{VII.134}$$

The integrand receives contributions only from the spacelike region enforced by the $\theta(-k^2)$ and $\theta(-q^2)$ factors. Physically, this configuration corresponds to processes in which both internal lines are off-shell and interact through Landau damping in the medium. As in the resummed one-particle-irreducible (1PI) propagator, this part of the self-energy describes the *continuum* contribution and does not correspond to isolated quasiparticle poles.

VII.5 Pole structure

Declaration: this section presents results from the literature, re-elaborated by the thesis author and MB for [5]. The interpretation of the results was carried out in close collaboration with all authors, with primary responsibility taken by the thesis author and MB. The text is taken from the paper with small stylistic modifications. In the original paper, all authors contributed to structuring, reviewing, and refining the manuscript.

After this long derivation, we understand that the spectral self-energies in the 1PI case as well as in the HTL approximation have a complex structure and that this crucially influences the DM self-energy and, thus, it interaction rate density. In particular, the pole structure of Eqs. (VII.10) and (VII.11) can be quite complex. To accurately determine this structure without resorting to a high-temperature (HTL) expansion (see Section VII.4.1), numerical methods are required. At finite temperatures, several poles may correspond to propagating modes and collective excitations with well-defined quantum numbers [412]. In a hot plasma, these poles are typically classified as *quasi-particles* if they exhibit a positive helicity-to-chirality ratio, or *hole* modes if this ratio is negative.

In the low-momentum region, these modes are clearly distinguishable, with spectral densities sharply peaking at the poles. This is illustrated by the brighter contours in the left panel of Fig. VII.3, where each mode roughly contributes half of the density of states.

At higher momenta, hole excitations become massless and effectively decouple from the plasma, while the screened quasi-particle modes asymptotically approach the in-vacuum fermionic state. In the "off-shell" regime, there are additional contributions from "virtual" modes, which involve energy exchanges between fermion quanta and the thermal bath, even though such exchanges would be forbidden in vacuum.

These contributions are proportional to the thermal width Γ and, while suppressed, account for the irreducible *Landau damping* by the medium through the exchange of "off-shell" states with the plasma. Compared to the HTL-approximated version (see Section VII.4.1), the spectral densities below the lightcone are more damped, as shown in the right panel of Fig. VII.3. The plot shows that the ratio of $(u \cdot S^{\mathcal{A}})_{\mathrm{HTL}}$ to $(u \cdot S^{\mathcal{A}})_{\mathrm{1PI}}$ gets larger with increasing values of $|\vec{k}|/T$. This is because the 1PI contribution includes an exponential suppression that occurs once $k \gtrsim T$. For a thorough discussion on collective excitations in the plasma, refer to early works [517–519] and more recent studies on early Universe particle production [489, 493].

VII.5.1 Kinematic regions

Here, we want to give a physical interpretation to the four kinematic regimes in which we have divided the computation.

$\mathbf{k^2 > 0}$, $\mathbf{q^2 > 0}$: Both fermions exhibit timelike momenta, with their spectral densities peaking at the poles where a particle-like interpretation of the interacting fermionic states is applicable, provided the thermal width is sufficiently narrow. The contributions from hole peaks are negligible for DM production compared to those from quasi-particle peaks, and hole excitations effectively decouple at high momenta. Consequently, the DM interaction rate given by Eq. (VII.9) is primarily influenced by kinematics that enable the quasi-particle peaks of the spectral distributions to overlap. From a particle-like perspective, these contributions can be interpreted as *decay processes* of the form $F \to f + s$, where the approximate masses are $M_i^2 = m_i^2 + m_{\mathrm{th},i}^2$, with m_i representing the in-vacuum masses and $m_{\mathrm{th},i} = \sqrt{G}T/2$ the thermal masses of the fermions[6]. At high temperatures, since both fermions receive identical gauge thermal corrections, their dispersion relations converge. Consequently, decays are not kinematically allowed at early "times" $z = m_F/T$. In other words, the contribution to DM production from the 1PI-resummed spectral densities is suppressed.

The kinematic window opens as soon as the in-vacuum mass m_F becomes comparable to the plasma temperature, specifically when

$$z > \sqrt{G}\frac{m_{\mathrm{DM}} m_F}{m_F^2 - m_{\mathrm{DM}}^2}\,. \tag{VII.135}$$

$\mathbf{k^2 > 0}$ **and** $\mathbf{q^2 < 0}$, $\mathbf{k^2 < 0}$ **and** $\mathbf{q^2 > 0}$ **:** This regime provides the predominant contribution to the DM interaction rate when the kinematics prevent both fields from aligning with the timelike peaks of their spectral densities. In this scenario, the spacelike fermion can be interpreted as mediating interactions with the thermal plasma off-shell. Thus, these regimes can be understood as *scattering processes* that produce DM quanta.

$\mathbf{k^2 < 0}$, $\mathbf{q^2 < 0}$ **:** When both momenta are spacelike, the spectral densities reside in the continuum, and neither is enhanced by being nearly on the mass-shell. Consequently, this regime contributes minimally to the DM interaction rate. From a particle interpretation perspective, the convolution of these spectral densities can be physically interpreted as two exchanges of "off-shell" virtual fermion quanta with the thermal environment.

VII.6 Tree-level Propagators

Declaration: this section presents known results from the literature, re-elaborated by the thesis author and MB for [5]. The work was developed through close collaboration among all authors, with continuous discussions throughout. The text is a reworked and extended version of what was presented in the paper. In the original paper, all authors contributed to structuring, reviewing, and refining the manuscript.

We now consider the tree-level limit of the HTL-resummed fermionic spectral densities, focusing only on the leading-order correction in gT to the HTL fermionic self-energies. This approximation implies that thermal widths are set to zero, and only the momentum-independent thermal masses, as given in Eq. (VII.119), are retained in the dispersion relations. Consequently, the spectral densities in the DM self-energy loop simplify to delta functions above the light cone, yielding:

$$\not{\rho}_F^{\mathcal{A}}(k) = \pi\delta(k^2 - m_F^2)(\not{k} + m_F)\,\mathrm{sign}(k^0)\,, \tag{VII.136}$$

$$\not{\rho}_f^{\mathcal{A}}(k-p) = \pi\delta\left((k-p)^2 - m_f^2\right)\left(\not{k} - \not{p} + m_f\right)\,\mathrm{sign}(k^0 - p^0)\,, \tag{VII.137}$$

where the masses are determined solely by the in-vacuum masses and the momentum-independent thermal masses. This configuration accounts only for DM production from decays of on-shell fermionic states with in-vacuum and thermal masses as specified in Eq. (VII.118).

[6] Decays of the type $f \to F + s$ and inverse decays $F + f \to s$ are kinematically forbidden since Yukawa interactions and in-vacuum masses for the SM fermions are neglected.

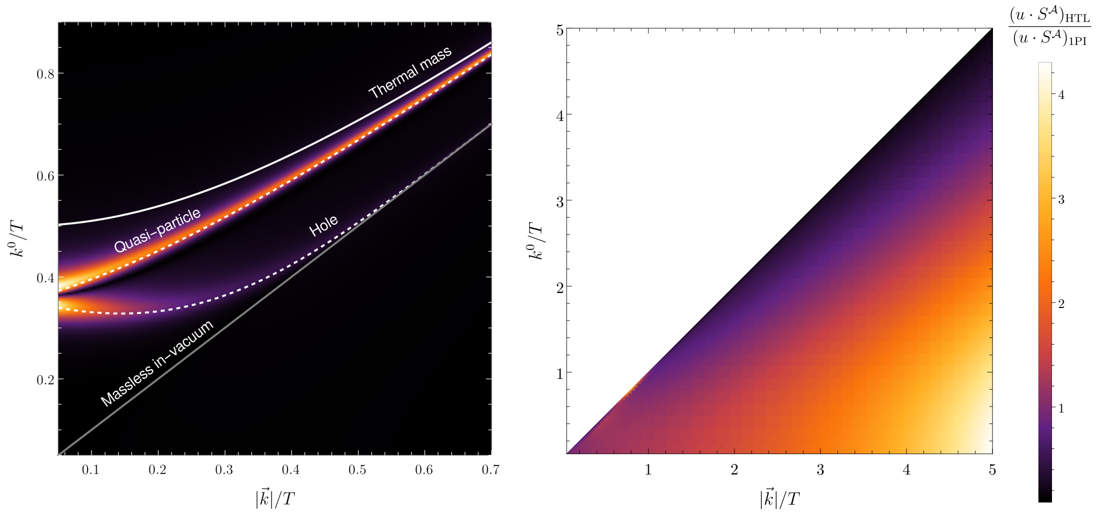

Figure VII.3: *Left panel:* the spectral density $(u \cdot S^{\mathcal{A}})_{\rm 1PI}$ in linear scale for a massless fermion as a function of the energy k^0/T and spatial $|\vec{k}|/T$ components of its momentum, normalized to the plasma temperature. Brighter colors signal larger values and they are in correspondence of the quasi-particle and hole peaks. Notice how the latter fades away at large momenta as holes decouple from the plasma. The white dashed lines mark the quasi-particle and hole branches in the HTL approximation (cf. Eqs. (VII.116) and (VII.117)), while the white solid line corresponds to the dispersion relation with momentum-independent thermal mass in Eq. (VII.118). Notice also that, in the dark regions, $(u \cdot S^{\mathcal{A}})_{\rm 1PI}$ is small but not zero. *Right panel:* ratio of $u \cdot S^{\mathcal{A}}$ in the HTL approximation to the 1PI one for a broader kinematic range. Below the light cone, the HTL spectral density becomes larger than the 1PI one for hard momenta, which instead captures an exponential suppression as soon as $k \gtrsim T$. *Figure created by the thesis author and included in [5].*

To obtain the tree-level limit of the DM self-energy, we substitute these expressions into Eq. (VII.7), resulting in:

$$\Pi_s^{\mathcal{A}}(p) = 4\pi^2 y_{\rm DM}^2 \int \frac{{\rm d}^4k}{(2\pi)^4}\delta(k^2 - m_F^2)\delta((k-p)^2 - m_f^2)\left[k^2 - k\cdot p\right] \\ \times \left[1 - f_+(k_0) - f_+(p_0 - k_0)\right] {\rm sign}(k_0)\,{\rm sign}(k_0 - p_0)\,. \tag{VII.138}$$

This integral can be analytically evaluated. It is convenient to transform the integration measure as follows:

$$ {\rm d}^4k \longrightarrow \frac{1}{2|\vec{p}|}{\rm d}\phi\,{\rm d}k_0\;{\rm d}(p\cdot k)\;{\rm d}\big(k^2\big)\;, \tag{VII.139}$$

which simplifies the integration over the delta functions. Furthermore, since the particles in the loop are on-shell, we have:

$$ {\rm sign}(k_0)\,{\rm sign}(k_0 - p_0) = -{\rm sign}(p^2 - m_F^2 - m_f^2)\,. \tag{VII.140}$$

Incorporating these observations, Eq. (VII.138) simplifies to:

$$\Pi_s^{\mathcal{A}}(p) = \frac{y_{\rm DM}^2}{16\pi\,|\vec{p}|}\left|p^2 - m_F^2 - m_f^2\right| \int_{\mathcal{B}} {\rm d}k_0\;\left[1 - f_+(k_0) - f_+(p_0 - k_0)\right]\,, \tag{VII.141}$$

where the integration boundaries of $\mathcal{I}$ are defined as:

$$\mathcal{I}\Big|_{\mathcal{B}} = \mathcal{I}\Big|_{k_-^0}^{k_+^0}\theta(p^2) + \mathcal{I}\Big|_{-\infty}^{+\infty}\theta(-p^2)\,, \tag{VII.142}$$

with:

$$k^0_\pm = \frac{p_0}{2p^2}\left(p^2 + m_F^2 - m_f^2\right) \pm \frac{|\vec{p}|}{2p^2}\sqrt{\lambda\left(p^2, m_F^2, m_f^2\right)}, \tag{VII.143}$$

$$\lambda\left(p^2, m_F^2, m_f^2\right) = \left(p^2 - (m_F + m_f)^2\right)\left(p^2 - (m_F - m_f)^2\right). \tag{VII.144}$$

Evaluating the integral in Eq. (VII.141) with the full distribution functions at finite temperature yields:

$$\Pi_s^{\mathcal{A}}(p) = \frac{y_{\rm DM}^2}{16\pi\,|\vec{p}|}\left|p^2 - m_F^2 - m_f^2\right|\left(p_0\,\theta(-p^2) + T\ln\left|\frac{\cosh\left((p_0 - k^0_-)/2T\right)}{\cosh\left((p_0 - k^0_+)/2T\right)}\frac{\cosh\left(k^0_+/2T\right)}{\cosh\left(k^0_-/2T\right)}\right|\right). \tag{VII.145}$$

Finally, the differential interaction rate of DM, which implies the on-shellness conditions $p^2 = m_{\rm DM}^2 > 0$ and $p_0 = \omega_p = \sqrt{m_{\rm DM}^2 + |\vec{p}|^2}$, is given by:

$$\frac{\Pi_s^{\mathcal{A}}(p)}{\omega_p} = \frac{y_{\rm DM}^2\,T}{16\pi\,\omega_p\,|\vec{p}|}\left|m_{\rm DM}^2 - m_F^2 - m_f^2\right|\ln\left|\frac{\cosh\left((\omega_p - k^0_-)/2T\right)}{\cosh\left((\omega_p - k^0_+)/2T\right)}\frac{\cosh\left(k^0_+/2T\right)}{\cosh\left(k^0_-/2T\right)}\right|. \tag{VII.146}$$

It is important to note that the differential rate can describe both decays and inverse decays depending on the kinematic regions. However, in our setup, the hierarchy $M_F > M_f + m_{\rm DM}$ (cf. Eq. (VII.135)) ensures that only the decay process $F \to f + s$ is kinematically allowed. The same differential rate can be derived using a Boltzmann equation approach without approximating the equilibrium distribution functions to Maxwell-Boltzmann distributions [382,404,406]. The CTP formalism, however, allows for a direct treatment of the quantum relativistic nature of the interacting particles from a first-principles perspective.

To obtain the total DM production rate $\gamma_{\rm DM}$ from decays (accounting for relativistic quantum statistics), we integrate the expression in Eq. (VII.146) over $\mathrm{d}|\vec{p}|$. As with the HTL case, we expect the tree-level approximation to yield significant discrepancies in the DM relic abundance compared to 1PI-resummed spectral densities, especially when decay processes are suppressed (small mass splitting between F and DM) and the high-temperature expansion becomes unreliable. Moreover, tree-level propagators neglect scattering contributions, leading to a significantly lower DM production rate compared to 1PI-resummed spectral densities when scattering processes are relevant, particularly for small mass splittings and large gauge couplings, as will be discussed in the next chapter.

VII.6.1 Semi-classical Boltzmann Approach

In this section, we summarize the standard semi-classical treatment of dark matter (DM) freeze-in based on the Boltzmann equation (cf. Section III.5.2). This will serve as a reference for comparison with the fully quantum-field-theoretical CTP approach developed later. The comoving number density of DM is defined as

$$Y_{\rm DM} \equiv \frac{n_{\rm DM}}{s}, \tag{VII.147}$$

and its evolution is governed by the Boltzmann equation (cf. Eq. (III.45)),

$$z\,H(z)\,s(z)\,\frac{\mathrm{d}Y_{\rm DM}}{\mathrm{d}z} = \gamma_{\rm DM}(T), \qquad z \equiv \frac{m_F}{T}, \tag{VII.148}$$

where s is the entropy density, H the Hubble rate, and $\gamma_{\rm DM}$ the total DM production rate density. In the parameter region relevant for freeze-in, the dominant contribution arises from the decay of the heavy vectorlike fermion mediator F into a Standard Model fermion f and the scalar DM particle s.

General structure of decay production

All decay contributions to $\gamma_{\rm DM}$ follow the same master expression,

$$\gamma_{\rm DM}^{(\rm dec)}(T) = \int \frac{\mathrm{d}^3 p_F}{(2\pi)^3}\, f_F^{\rm eq}(E_F)\, \frac{M_F(T)}{E_F}\, \Gamma_{F\to fs}(T)\,, \tag{VII.149}$$

where $f_F^{\rm eq}$ is the equilibrium distribution of the decaying particle and $\Gamma_{F\to fs}(T)$ is the temperature-dependent decay width. For Maxwell–Boltzmann statistics, one obtains the standard integral,

$$\int \frac{\mathrm{d}^3 p}{(2\pi)^3}\, \frac{M_F}{E}\, e^{-E/T} = \frac{M_F^2\, T}{2\pi^2}\, K_1\!\left(\frac{M_F}{T}\right), \tag{VII.150}$$

with K_1 being a modified Bessel function of the second kind, leading to the compact result

$$\gamma_{\rm DM}^{(\rm dec)}(T) = \frac{M_F^2(T)\, T}{2\pi^2}\, K_1\!\left(\frac{M_F(T)}{T}\right)\, \Gamma_{F\to fs}(T)\,. \tag{VII.151}$$

Decay width from the matrix element

The relevant interaction is described by the Yukawa term

$$\mathcal{L}_{\rm int} = y_{\rm DM}\, \bar{f}\, F\, s + \text{h.c.} \tag{VII.152}$$

for the decay

$$F(p) \;\to\; f(k) + s(q)\,. \tag{VII.153}$$

The squared, spin-summed matrix element is

$$\begin{aligned} \overline{|\mathcal{M}|^2} &= y_{\rm DM}^2\, \mathrm{Tr}\big[(\not{k} + m_f)(\not{p} + m_F)\big] \\ &= y_{\rm DM}^2\, (m_F^2 + m_f^2 - m_{\rm DM}^2)\,. \end{aligned} \tag{VII.154}$$

Using the standard two-body phase-space integral,

$$\int \mathrm{d}\Phi_2 = \frac{1}{16\pi\, m_F^2}\, \sqrt{\lambda(m_F^2, m_f^2, m_{\rm DM}^2)}\,, \tag{VII.155}$$

the vacuum decay width becomes

$$\begin{aligned} \Gamma_{F\to fs} &= \frac{1}{2m_F} \int \mathrm{d}\Phi_2\, \overline{|\mathcal{M}|^2} \\ &= \frac{y_{\rm DM}^2\, m_F}{16\pi} \left(1 + \frac{m_f^2}{m_F^2} - \frac{m_{\rm DM}^2}{m_F^2}\right) \sqrt{\lambda(m_F^2, m_f^2, m_{\rm DM}^2)}\,. \end{aligned} \tag{VII.156}$$

In-vacuum decay rate density

Inserting Eq. (VII.156) into Eq. (VII.151) with $M_F \to m_F$, we obtain

$$(\gamma_{\rm DM})_{\rm dec} = \frac{y_{\rm DM}^2\, m_F}{16\pi^3} \left(1 + \frac{m_f^2}{m_F^2} - \frac{m_{\rm DM}^2}{m_F^2}\right) \sqrt{\lambda(m_F^2, m_f^2, m_{\rm DM}^2)}\, T\, K_1\!\left(\frac{m_F}{T}\right). \tag{VII.157}$$

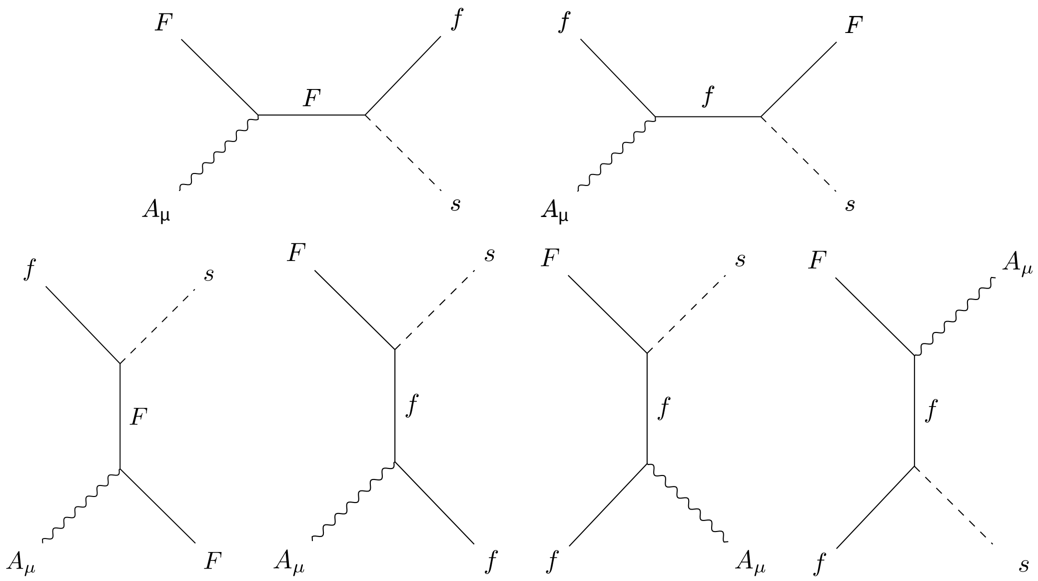

Figure VII.4: The scattering diagrams for the s- and t-channel processes illustrating the single-particle production of the scalar singlet DM candidate s. The diagram for double production is neglected due to suppression by a factor of $y_{\rm DM}^2/G$. Fermion flow directions are not explicitly shown; both possible orientations for each diagram should be considered. *Figure created by CT and included in [5].*

Thermal corrections

Thermal effects can be included at leading order by promoting vacuum masses to thermal masses,

$$m_i^2 \;\to\; M_i^2(T) = m_i^2 + m_{i,\rm th}^2(T)\,. \tag{VII.158}$$

In our model, the fermionic thermal masses satisfy

$$m_{i,\rm th}^2 = \frac{G\,T^2}{4}\,, \tag{VII.159}$$

while the DM thermal mass is negligible due to its feeble coupling. The thermal decay width is then obtained by the replacement $m_i \to M_i(T)$ in Eq. (VII.156),

$$\Gamma_{F\to fs}(T) = \Gamma_{F\to fs}\Big|_{m_i\to M_i(T)}\,. \tag{VII.160}$$

Inserting into Eq. (VII.151) and using $M \equiv M(T)$ to ease the notation, we find the thermally corrected decay rate density

$$(\gamma_{\rm DM})_{\rm dec,th} = \frac{y_{\rm DM}^2\,M_F}{16\pi^3}\left(1+\frac{M_f^2}{M_F^2}-\frac{m_{\rm DM}^2}{M_F^2}\right)\sqrt{\lambda\Big(M_F^2, M_f^2, m_{\rm DM}^2\Big)}\,T\,K_1\!\left(\frac{M_F}{T}\right). \tag{VII.161}$$

VII.6.2 Scatterings and the interaction rate

At sufficiently high temperatures, $2 \leftrightarrow 2$ scattering processes may provide an important contribution to freeze-in production because the collision operator (cf. Eq. (III.56)) is proportional to the equilibrium number densities, which scale in the high-temperatures regime as $n^{\rm eq} \sim T^3$. Scatterings become particularly relevant when the dominant decay channel is suppressed, e.g. in the presence of a small mass splitting $\delta = (m_F - m_{\rm DM})/m_F$ which shrinks the available phase space. In the simplified t-channel model here considered, we restrict the Boltzmann treatment of scatterings to the processes displayed in Fig. VII.4, which correspond to the following processes,

$$\begin{aligned} F + f &\to s + A, \\ F + A &\to s + f, \\ f + A &\to s + F, \end{aligned} \qquad \text{(VII.162)}$$

where A denotes a gauge boson. All potential t-channel infrared (IR) divergences in these channels are regulated by including appropriate thermal masses in the gauge-boson (and other light) propagators, as discussed below.

IR regulation and thermal masses

When nearly massless particles (with $m \ll T$) are exchanged in the t-channel, the scattering amplitude can produce logarithmic IR enhancements. A physically motivated regularization is obtained by replacing the vacuum propagator denominators by their HTL–resummed counterparts; at leading order this is equivalent to endowing the exchanged gauge boson (or light fermion) with a thermal mass

$$m_{\rm th}^2 \propto G^2 T^2\,,$$

which removes the IR singularity because $m_{\rm th} \sim \mathcal{O}(T)$. In the Boltzmann treatment, we implement this regularization by using thermal masses inside the propagators that appear in the tree-level matrix elements used to compute the scattering cross sections. This prescription is standard in the literature (see e.g. Refs. [408, 520]) and is sufficient for our leading-order comparison with the CTP calculation.

Omission of interference terms

When squaring the matrix elements, we keep only the squared s- and t-channel contributions and systematically omit interference terms. This choice is motivated by two observations: (i) within the 2PI/CTP expansion squared amplitudes appear already at leading order (LO) while interference terms generally arise at next-to-leading order (NLO) and would require a two-loop calculation of the DM self-energy to be captured; and (ii) we explicitly verified (analytically and numerically) that the interference between s- and t-channel amplitudes alters the total squared matrix element only at the $\mathcal{O}(10\%)$ level for the parameter space of interest. Consequently, neglecting interference terms provides a consistent LO comparison between the Boltzmann and CTP formalisms.

VII.6.2.1 Total scattering contribution

With the above prescriptions, the total DM production rate density from scatterings is

$$(\gamma_{\rm DM})_{\rm scat} = \gamma_{Ff\to sA} + \gamma_{FA\to sf} + \gamma_{fA\to sF}\,, \qquad \text{(VII.163)}$$

where each individual contribution is evaluated using the $2 \to 2$ interaction rate given in Eq. (III.59), which reads as

$$\gamma_{ij\to sk}(T) = \frac{T}{64\pi^4}\int_{\mathfrak{s}_{\rm min}}^{\infty} {\rm d}\mathfrak{s}\; \hat\sigma_{ij\to sk}(\mathfrak{s})\,\sqrt{\mathfrak{s}}\; K_1(\sqrt{\mathfrak{s}}/T), \qquad \text{(VII.164)}$$

with $\mathfrak{s}_{\min} = \max\{(m_i + m_j)^2, (m_{\rm DM} + m_k)^2\}$ and $\hat{\sigma}_{ij\to sk}$. We have chosen to represent the Mandelstam variable in a gothic font, $\mathfrak{s}$, to avoid confusion with the dark matter (DM) particle, which is denoted by an italicized. The reduced cross-section is (cf. also Eq. (III.60))

$$\hat{\sigma}_{ij\to sk}(\mathfrak{s}) \equiv 2s\,\lambda\Big(1, \frac{m_i^2}{\mathfrak{s}}, \frac{m_j^2}{\mathfrak{s}}\Big)\,\sigma_{ij\to sk}(\mathfrak{s}). \tag{VII.165}$$

We recall the relation between the differential cross section and the squared matrix element for $2 \to 2$ processes in the centre-of-mass frame [483]:

$$\frac{\mathrm{d}\sigma}{\mathrm{d}\Omega} = \frac{1}{64\pi^2\mathfrak{s}}\,\frac{|\vec{p}_3|}{|\vec{p}_1|}\,\overline{|\mathcal{M}|^2}, \tag{VII.166}$$

where $|\vec{p}_1| = \frac{\sqrt{\mathfrak{s}}}{2}\lambda^{1/2}(1, m_i^2/s, m_j^2/\mathfrak{s})$ and $|\vec{p}_3| = \frac{\sqrt{\mathfrak{s}}}{2}\lambda^{1/2}(1, m_{\rm DM}^2/s, m_k^2/\mathfrak{s})$. Integrating over the solid angle gives the total $\sigma(\mathfrak{s})$ which then enters $\hat{\sigma}(\mathfrak{s})$ through Eq. (VII.165).

In practice, to compute $\gamma_{ij\to sk}$ we:

1. Compute the tree-level squared amplitude $\overline{|\mathcal{M}|^2}$ for the channel, keeping only the squared s- and t-channel contributions (no interference). To do this, we use `FeynCalc` [521, 522].
2. From $\overline{|\mathcal{M}|^2}$ obtain $\sigma_{ij\to sk}(\mathfrak{s})$ by performing the angular integral (the cross-sections can be found in Section VII.B.);
3. Build the reduced cross section $\hat{\sigma}(\mathfrak{s})$ via (VII.165);
4. Integrate $\hat{\sigma}(\mathfrak{s})$ in (VII.164) numerically, using thermal masses $m_{\rm th}(T)$ in the propagators to regulate any t-channel singularity.

We stress that using thermal masses in the propagator denominators is essential to avoid unphysical logarithmic divergences of the form $\log(m/T)$. The thermal mass provides the physical IR cutoff $m \to m_{\rm th} \sim gT$, so that the logarithm becomes $\log(g)$ and remains finite for weak coupling g.

VII.6.2.2 Final Interaction Rate

The total DM production rate density which enters the Boltzmann equation is obtained by adding the thermally corrected decay and scattering contributions,

$$\gamma_{\rm DM}(T) \;=\; (\gamma_{\rm DM})_{\rm dec,th}(T) + (\gamma_{\rm DM})_{\rm scat}(T)\,, \tag{VII.167}$$

with $(\gamma_{\rm DM})_{\rm scat}$ given by (VII.163) and each γ_{ijk} computed through (VII.164).

Concluding Remarks

In this chapter, we have presented a comprehensive and detailed application of the CTP formalism combined with the 2PI effective action approach to compute DM production rates in the freeze-in mechanism. Starting from the vectorlike portal FIMP model, we systematically derived the DM production rate from the self-energy obtained through the 2PI effective action, explicitly showing how thermal effects enter through resummed propagators in the self-energy loop.

The technical core of our analysis has been the computation of 1PI-resummed spectral densities, which required a careful treatment of fermion self-energies at finite temperature.

We provided full analytical derivations of the Hermitian and anti-Hermitian components, analyzed the pole structure of the fermionic spectral density, and presented both the HTL approximation and tree-level results for comparison. Each analytical component has been implemented in dedicated numerical routines, demonstrating the modularity and efficiency of our computational framework.

Furthermore, we established a connection to the conventional Boltzmann approach by deriving the corresponding cross-sections and interaction rates, thereby bridging the first-principles CTP formalism and the more traditional semi-classical treatment. This comparison is essential for validating our results and understanding the validity regime of different approximations.

The detailed derivations, analytical results, and numerical implementations presented here constitute original contributions to the field and represent, to our knowledge, the first comprehensive study of DM freeze-in production based on the CTP and 2PI formalisms. These results provide the foundation for the phenomenological analysis and numerical applications that will be presented in the following chapter.

VII.A Functions and Routines for Spectral Densities

Table VII.2: Detailed overview of all fermionic self-energy contraction functions used in the code.

Function	**Description**
`kSigmaH` Eq. (VII.65)	Hermitian part of the massless fermion self-energy contracted with external momentum k. It contains either the pure HTL expression or the full one-loop thermal and vacuum contributions depending on `HTL_ON`. This function enters the helicity structure of the propagator and contributes to the modification of the dispersion relation.
`uSigmaH` Eq. (VII.79)	Hermitian massless self-energy contracted with the heat-bath four-vector $u^\mu = (1, \mathbf{0})$. It contains logarithmic contributions arising from angular integrals and controls how the medium modifies the temporal part of the fermion self-energy. It contributes to determining the thermal mass and collective mode structure.
`kSigmaA`	Anti-hermitian part of the massless self-energy contracted with k^μ. Represents absorptive (damping) processes through the imaginary part of the self-energy. Includes vacuum and thermal finite-width contributions, vanishing in pure HTL.
`uSigmaA`	Anti-hermitian part contracted with u^μ. Contains the thermal scattering rate contributions, including imaginary terms from logarithmic singularities. Contributes directly to fermion damping in the medium.
`SigmaH2`	Scalar combination built from via Lorentz-contraction with $(\Sigma^{\mathcal{H}})^2$ Constructed from $k\Sigma^{\mathcal{H}}$ and $u\Sigma^{\mathcal{H}}$, it enters the denominator of the resummed propagator. Encodes the effective "mass-squared" correction from hermitian parts.

Continued on next page

Function	**Description**
`SigmaA2`	Analogous to `SigmaH2` but built from the anti-hermitian parts. Encodes the square of the damping contributions and appears in the imaginary part of the propagator denominator. Important for determining widths of quasiparticles.
`SigmaHA`	Mixed hermitian–antihermitian Lorentz-scalar contraction. Appears in the imaginary/real mixing structure in the fermion propagator. Relevant when considering interference between dispersive and absorptive effects.
`kSigmaH_M` Eq. (VII.45)	Hermitian massive fermion self-energy contracted with k^μ. Generalizes the massless expression by replacing integrals with mass-dependent versions (`I2mM`, `J2pM`, etc.). Contains new massive thermal and vacuum structures, modifying the dispersion relation for $m_F \neq 0$.
`uSigmaH_M` Eq. (VII.70)	Massive version of the hermitian contraction with u^μ. Includes new mass-dependent terms reflecting the threshold structure and non-relativistic corrections. Important for heavy-fermion thermal propagation.
`kSigmaA_M` Eq. (VII.89)	Anti-hermitian massive self-energy contracted with k^μ. Encodes the damping behavior of massive fermions in the medium.
`uSigmaA_M` Eq. (VII.95)	Anti-hermitian massive contraction with u^μ. Contains mass-dependent absorptive thermal terms and vacuum terms. Determines the width and non-relativistic damping of heavy fermions.
`SigmaH2_M`	Massive analogue of `SigmaH2`. Constructed from `kSigmaH_M` and `uSigmaH_M` and includes new mass-dependent interference terms. Enters the denominator of the massive resummed propagator.
`SigmaA2_M`	Massive analogue of `SigmaA2`. Encodes the squared damping contributions for massive fermions. Relevant for decay widths and spectral-function calculations.
`SigmaHA_M`	Massive analogue of `SigmaHA_M`. Important for the interplay of dispersion and damping in massive fermion propagation.
`DenpSA_M`	Complete denominator of the massive fermion propagator, including hermitian, antihermitian, and mass terms. Built from the combinations "H^2", "A^2", and "HA", it determines the location and width of quasiparticle poles.
`kSigmaHq`	Massless hermitian self-energy contracted with the momentum of another fermion with momentum q^μ. Used in mixed-momentum processes and in constructing scattering kernels involving two fermion lines.

Continued on next page

Function	**Description**
`kSigmaAq`	Anti-hermitian analogue of `kSigmaHq`. Contains finite-width contributions when the self-energy is evaluated at a different momentum.
`qSigmaH_Mk`	Hermitian massive self-energy contracted with a massless momentum q^μ. Appears in mixed massive–massless processes, such as DM–fermion interactions.
`qSigmaA_Mk`	Anti-hermitian analogue of `qSigmaH_Mk`. Contributes to massless–massive interference damping rates.
`SigmaH2_Mk_q`	Scalar hermitian–hermitian mixed product of massive and massless self-energies. Important for interference terms in mixed-species scattering amplitudes and resummed vertices.
`SigmaA2_Mk_q`	Anti-hermitian analogue of `SigmaH2_Mk_q`. Contributes to imaginary parts of mixed propagators.
`Sigma_HMk_Aq`	Mixed hermitian–antihermitian scalar built from massive (H) and massless (A) contributions. Encodes interference between dispersive massive effects and absorptive massless effects.
`Sigma_AMk_Hq`	Opposite interference combination (massive A with massless H).

VII.A.1 Massless Fermion Self-Energy

```
// ============================================================
// MASSLESS FERMION SELF-ENERGY
// Hermitian (H) and anti-hermitian (A) parts contracted with
// external momentum k and plasma vector u.
// Used to construct quantities SigmaH2, SigmaA2, SigmaHA.
// ============================================================

double kSigmaH(double xk0, double xk) {
    if(HTL_ON == true) return G/pow(2.*M_PI,2) * M_PI * M_PI / 2.;
    else {
        return G/pow(2.*M_PI,2) *
           ((xk0*xk0 - xk*xk)/4./xk * (I2m(xk0,xk) - I2p(xk0,xk)) + M_PI * M_PI / 2.);
    }
}

double uSigmaH(double xk0, double xk) {
    if(HTL_ON == true)
        return G/8./M_PI/M_PI/xk * log(fabs((xk0+xk)/(xk0-xk))) * M_PI * M_PI / 2.;
    else {
        return G/8./M_PI/M_PI/xk *
            ( I3T(xk0,xk) + xk0*I2m(xk0,xk)
              + log(fabs((xk0+xk)/(xk0-xk)))*M_PI * M_PI / 2. );
    }
}

double kSigmaA(double xk0, double xk) {
    if(HTL_ON == true) return 0;
    return G/16./M_PI * (xk0*xk0 - xk*xk) / fabs(xk) * I0vac(xk0,xk)
          + G/16./M_PI * (xk0*xk0 - xk*xk) / fabs(xk) * I0T(xk0,xk);
```

```
}

double uSigmaA(double xk0, double xk) {
    if(HTL_ON == true) return G/8./M_PI/xk * I1HTL(xk0,xk);
    return G/8./M_PI/xk * (I1vac(xk0,xk) + I1T(xk0,xk) + I1HTL(xk0,xk));
}

// Scalar combinations H^2, A^2, and mixed HA
double SigmaH2(double xk0, double xk) {
    return 1./(xk*xk) *
       ( -pow(kSigmaH(xk0,xk),2)
         -(xk0*xk0-xk*xk)*pow(uSigmaH(xk0,xk),2)
         +2.*xk0*kSigmaH(xk0,xk)*uSigmaH(xk0,xk) );
}

double SigmaA2(double xk0, double xk) {
    return 1./(xk*xk) *
       ( -pow(kSigmaA(xk0,xk),2)
         -(xk0*xk0-xk*xk)*pow(uSigmaA(xk0,xk),2)
         +2.*xk0*kSigmaA(xk0,xk)*uSigmaA(xk0,xk) );
}

double SigmaHA(double xk0, double xk) {
    return 1./(xk*xk) *
       ( -kSigmaH(xk0,xk)*kSigmaA(xk0,xk)
         -(xk0*xk0-xk*xk)*uSigmaH(xk0,xk)*uSigmaA(xk0,xk)
         +xk0*(kSigmaH(xk0,xk)*uSigmaA(xk0,xk)
               +uSigmaH(xk0,xk)*kSigmaA(xk0,xk)) );
}
```

VII.A.2 Massive Fermion Self-Energy

```
// ==============================================================
// MASSIVE FERMION SELF-ENERGY
// Mass-dependent generalizations of H, A, H^2, A^2, and HA.
// ==============================================================

double kSigmaH_M (double xk0, double xk, double mF){
    if(HTL_ON == true) return G/pow(2.*M_PI,2) * M_PI*M_PI / 2.;
    return G / (M_PI * M_PI) / 2.
            * ( M_PI*M_PI / 6. + k2omegafp(mF)
              + (xk0*xk0 - xk*xk + mF*mF )/8./xk
              * ( I2mM(xk0,xk,mF) - J2pM(xk0,xk,mF) )
            );
}

double uSigmaH_M (double xk0, double xk, double mF){
    if(HTL_ON == true) return G/16.xk *
                            log( fabs((xk0+xk) / (xk0-xk)) );
    // Full result
    return G/8./M_PI/M_PI/xk * ( xk0*I2mM(xk0,xk,mF)
                            - I3TpM(xk0,xk,mF)
                            + I3TmM(xk0,xk,mF)
                            + log( fabs((xk0+xk) / (xk0-xk)) )
                            * M_PI * M_PI * 3. );

double kSigmaA_M (double xk0, double xk, double mF){
// We add: 1. vacuum contribution 2. Thermal Part - HTL 3. HTL (HTL part is identical 0
    here). This is for the m=0 case
// We have a expression not split into vacuum and T neq 0 part for the massive case
```

```
    if(HTL_ON == true) return 0;
    double xk2 = xk0*xk0 -xk*xk;
    double logshch = log(
                    fabs(
                         cosh(xp0p/2.) / cosh(xp0m/2.)
                         * sinh((xp0m-xk0)/2.) / sinh((xp0p-xk0)/2.)
                        )
                       );
    double xp0p = 1./2./(xk2) *
                 (xk0 * (xk2 + mF*mF)
                   + xk*fabs(xk2 - mF*mF) );
    double xp0m = 1./2./(xk2) *
                 (xk0 * (xk2 + mF*mF)
                   - xk*fabs(xk2 - mF*mF) );
    return G/16./M_PI * (xk2 - mF*mF)
                     / fabs(xk2 - mF*mF)
                     * (xk2 + mF*mF) / xk
                     * ( Theta(-xk2) * xk0
                     + logshch );
}

double uSigmaA_M(double xk0, double xk, double mF) {
    double xk2 = xk0 * xk0 - xk * xk;
    if (HTL_ON == true) return G / 8. / M_PI / xk * I1HTL(xk0, xk);
    double xp0p = 1. / 2. / xk2 * (xk0 * (xk2 + mF * mF) + xk
                                 * fabs(xk2 - mF * mF));
    double xp0m = 1. / 2. / xk2 * (xk0 * (xk2 + mF * mF) - xk
                                 * fabs(xk2 - mF * mF));
    return G / 8. / M_PI * GSL_SIGN(xk2 - mF * mF) / xk
           * (Theta(-xk0 * xk0 + xk * xk)
           * (-M_PI * M_PI / 2. + xk0 * xk0 / 2.)
            + f1TM(xp0p, xk0) - f1TM(xp0m, xk0));
}

double SigmaH2_M(double xk0, double xk, double mF) {
    return 1./(xk*xk) *
       ( -pow(kSigmaH_M(xk0,xk,mF),2)
         -(xk0*xk0-xk*xk)*pow(uSigmaH_M(xk0,xk,mF),2)
         +2.*xk0*kSigmaH_M(xk0,xk,mF)*uSigmaH_M(xk0,xk,mF) );
}

double SigmaA2_M(double xk0, double xk, double mF) {
    return 1./(xk*xk) *
       ( -pow(kSigmaA_M(xk0,xk,mF),2)
         -(xk0*xk0-xk*xk)*pow(uSigmaA_M(xk0,xk,mF),2)
         +2.*xk0*kSigmaA_M(xk0,xk,mF)*uSigmaA_M(xk0,xk,mF) );
}

double SigmaHA_M(double xk0, double xk, double mF) {
    return 1./(xk*xk) *
       ( -kSigmaH_M(xk0,xk,mF)*kSigmaA_M(xk0,xk,mF)
         -(xk0*xk0-xk*xk)*uSigmaH_M(xk0,xk,mF)*uSigmaA_M(xk0,xk,mF)
         +xk0*(kSigmaH_M(xk0,xk,mF)*uSigmaA_M(xk0,xk,mF)
               +uSigmaH_M(xk0,xk,mF)*kSigmaA_M(xk0,xk,mF)) );
}
```

VII.A.3 Mixed-Momentum Contractions

```
// ==============================================================
// MIXED-MOMENTUM SELF-ENERGY CONTRACTIONS
```

```
// Combines massive and massless self-energies, evaluated at
// different momenta k and q.
// ============================================================

// Massless Sigma_H contracted with k
double kSigmaHq(double xk0, double xk, double xq0, double xq, double xqk) {
    return 1./(xq*xq) *
       ( xqk*kSigmaH(xq0,xq)
         + (xq*xq*xk0 - xq0*xqk)*uSigmaH(xq0,xq) );
}

// Massless Sigma_A contracted with k
double kSigmaAq(double xk0, double xk, double xq0, double xq, double xqk) {
    return 1./(xq*xq) *
       ( xqk*kSigmaA(xq0,xq)
         + (xq*xq*xk0 - xq0*xqk)*uSigmaA(xq0,xq) );
}

// Massive Sigma_H contracted with q
double qSigmaH_Mk(double xk0, double xk, double xq0, double xq, double xqk, double mF) {
    return 1./(xk*xk) *
       ( xqk*kSigmaH_M(xk0,xk,mF)
         + (xk*xk*xq0 - xk0*xqk)*uSigmaH_M(xk0,xk,mF) );
}

// Massive Sigma_A contracted with q
double qSigmaA_Mk(double xk0, double xk, double xq0, double xq, double xqk, double mF) {
    return 1./(xk*xk) *
       ( xqk*kSigmaA_M(xk0,xk,mF)
         + (xk*xk*xq0 - xk0*xqk)*uSigmaA_M(xk0,xk,mF) );
}

// Scalar products of massive and massless Hermitian self-energies
double SigmaH2_Mk_q(double xk0, double xk, double xq0, double xq, double xqk, double mF) {
    return 1./(xk*xk*xq*xq) *
        ( -xqk*kSigmaH_M(xk0,xk,mF)*kSigmaH(xq0,xq)
          + (xq*xq*xk*xk - xq0*xk0*xqk)*uSigmaH_M(xk0,xk,mF)*uSigmaH(xq0,xq)
          + xq0*xqk*kSigmaH_M(xk0,xk,mF)*uSigmaH(xq0,xq)
          + xk0*xqk*uSigmaH_M(xk0,xk,mF)*kSigmaH(xq0,xq) );
}

// Scalar products of massive and massless anti-Hermitian self-energies
double SigmaA2_Mk_q(double xk0, double xk, double xq0, double xq, double xqk, double mF) {
    return 1./(xk*xk*xq*xq) *
        ( -xqk*kSigmaA_M(xk0,xk,mF)*kSigmaA(xq0,xq)
          + (xq*xq*xk*xk - xq0*xk0*xqk)*uSigmaA_M(xk0,xk,mF)*uSigmaA(xq0,xq)
          + xq0*xqk*kSigmaA_M(xk0,xk,mF)*uSigmaA(xq0,xq)
          + xk0*xqk*uSigmaA_M(xk0,xk,mF)*kSigmaA(xq0,xq) );
}

// Scalar products of massive Hermitian and massless anti-Hermitian self-energies
double Sigma_HMk_Aq(double xk0, double xk, double xq0, double xq, double xqk, double mF) {
    return 1./(xk*xk*xq*xq) *
        ( -xqk*kSigmaH_M(xk0,xk,mF)*kSigmaA(xq0,xq)
          + (xq*xq*xk*xk - xq0*xk0*xqk)*uSigmaH_M(xk0,xk,mF)*uSigmaA(xq0,xq)
          + xq0*xqk*kSigmaH_M(xk0,xk,mF)*uSigmaA(xq0,xq)
          + xk0*xqk*uSigmaH_M(xk0,xk,mF)*kSigmaA(xq0,xq) );
}

// Scalar products of massive anti-Hermitian and massless Hermitian self-energies
double Sigma_AMk_Hq(double xk0, double xk, double xq0, double xq, double xqk, double mF) {
```

```
    return 1./(xk*xk*xq*xq) *
        ( -xqk*kSigmaA_M(xk0,xk,mF)*kSigmaH(xq0,xq)
          + (xq*xq*xk*xk - xq0*xk0*xqk)*uSigmaA_M(xk0,xk,mF)*uSigmaH(xq0,xq)
          + xq0*xqk*kSigmaA_M(xk0,xk,mF)*uSigmaH(xq0,xq)
          + xk0*xqk*uSigmaA_M(xk0,xk,mF)*kSigmaH(xq0,xq) );
}
```

VII.B Cross Sections for the Boltzmann Approach

In this appendix, we collect the results for the scattering cross-sections necessary to compute the DM interaction rate in Eq. (III.59), and Eq. (VII.165). The matrix elements have been computed using `FeynCalc` [521, 522], while we have integrated them using standard integration techniques in `Mathematica`. Only the propagators receive a thermal mass correction, which is indicated with a capital letter $M = \sqrt{m_{\rm vac}^2 + m_{\rm th}^2}$. For in-vacuum masses, we use lowercase m letters. Consider SM leptons and gauge bosons to be massless.

VII.B.1 $f(k_1) + A_\mu(k_2) \to F(p_1) + s(p_2)$

N.B. the same cross-sections are obtained for the process $F(k_1) + A_\mu(k_2) \to f(p_1) + s(p_2)$ by simply exchanging the fermion masses.

We first write the matrix elements (amplitude) for the scattering processes.

t-channel amplitude

$$\mathcal{M}_t = \frac{1}{t - M_F^2}\, \bar{u}(p_1, m_F)\, \gamma^\mu \left(\not{k}_1 - \not{p}_2 + m_F\right) \gamma^5\, u(k_1, m_f)\, \varepsilon_\mu^*(k_2)\,. \tag{VII.B.1}$$

s-channel amplitude

$$\mathcal{M}_s = \frac{1}{s - M_f^2}\, \bar{u}(p_1, m_F)\, \gamma^5 \left(\not{k}_1 + \not{k}_2 + m_f\right) \gamma^\mu\, u(k_1, m_f)\, \varepsilon_\mu^*(k_2)\,. \tag{VII.B.2}$$

By squaring the total amplitude, we obtain three contributions:

$$|\mathcal{M}|^2 = |\mathcal{M}_s|^2 + |\mathcal{M}_t|^2 + 2\Re\left(\mathcal{M}_u\, \mathcal{M}_t^*\right). \tag{VII.B.3}$$

Employing Eq. (VII.166), we obtain the following pure channel and interference cross-section terms.

Pure s-channel production $\sigma_{fA}^{(s)}$

$$\sigma_{fA}^{(s)} = -\frac{(m_{\rm DM}^2 - m_F^2 - s)(M_F^2 + s)\sqrt{\lambda(s, m_F^2, m_{\rm DM}^2)}}{16\pi (M_f^2 - s)^2\, s^2} \tag{VII.B.4}$$

Pure t-channel production $\sigma_{fA}^{(t)}$

$$\sigma_{fA}^{(t)}(s) = -\frac{1}{8\pi}\,\frac{1}{s^4}\Bigg[s\sqrt{\lambda(s, m_F^2, m_{\rm DM}^2)}\, \mathcal{N}_t^{(fA)}(s) \Big/ \mathcal{D}_t^{(fA)}(s)$$

$$+ s\,\mathcal{Q}_t^{(fA)}(s)\Bigg(\ln\Big[-m_{\rm DM}^2 s + s(-m_F^2+2M_F^2+s-\sqrt{\lambda(s,m_F^2,m_{\rm DM}^2)})\Big]$$
$$-\ln\Big[-m_{\rm DM}^2 s + s(-m_F^2+2M_F^2+s+\sqrt{\lambda(s,m_F^2,m_{\rm DM}^2)})\Big]\Bigg)\Bigg]. \qquad \text{(VII.B.5)}$$

Here, we have introduced the following polynomial functions:

$$\begin{aligned}\mathcal{N}_t^{(fA)}(s) &= (m_{\rm DM}^2-M_F^2)(M_F^2-m_F^2)(5m_{\rm DM}^2+m_F^2-6M_F^2)\\ &+ m_{\rm DM}^2\left(2m_F^2-2m_FM_F-5M_F^2\right)s\\ &+ M_F^2\left(-3m_F^2+2m_FM_F+6M_F^2\right)s+M_F^2s^2;\end{aligned} \qquad \text{(VII.B.6)}$$

$$\mathcal{D}_t^{(fA)}(s) = (m_{\rm DM}^2-M_F^2)(m_F^2-M_F^2)+M_F^2 s; \qquad \text{(VII.B.7)}$$

$$\begin{aligned}\mathcal{Q}_t^{(fA)}(s) &= 2(m_{\rm DM}^2-M_F^2)\left(m_{\rm DM}^2+2m_F^2-3M_F^2\right)\\ &-\left(2m_{\rm DM}^2+(m_F-3M_F)(m_F+M_F)\right)s+s^2.\end{aligned} \qquad \text{(VII.B.8)}$$

Interference between s- and t-channel $\sigma_{fA}^{(st)}$

$$\sigma_{fA}^{(st)}(s) = \frac{1}{4\pi\, s^4\,(M_f^2-s)}\Bigg\{\frac{1}{2}s^2\left(m_{\rm DM}^2+m_F^2-2M_f^2+s\right)\sqrt{\lambda(s,m_F^2,m_{\rm DM}^2)}$$
$$+ s^2\Big[(m_F-M_f)(-m_{\rm DM}+M_f)(m_{\rm DM}+M_f)(m_F+M_f)-m_FM_fs\Big]$$
$$\times\Bigg[\ln\Big(-m_{\rm DM}^2 s+s(-m_F^2+2M_f^2+s-\sqrt{\lambda(s,m_F^2,m_{\rm DM}^2)})\Big)$$
$$-\ln\Big(-m_{\rm DM}^2 s+s(-m_F^2+2M_f^2+s+\sqrt{\lambda(s,m_F^2,m_{\rm DM}^2)})\Big)\Bigg]\Bigg\}. \qquad \text{(VII.B.9)}$$

VII.B.2 $f(k_1)+F(k_2)\to A_\mu(p_1)+s(p_2)$

The same procedure applies to this scattering process.

u-channel

$$\mathcal{M}_u = \frac{1}{u-m_F^2}\,\bar{v}(k_2,m_F)\,\gamma^\mu\left(\not{k}_1-\not{p}_2+m_F\right)\gamma^5\,u(k_1,m_f)\,\varepsilon_\mu^*(p_1)\,. \qquad \text{(VII.B.10)}$$

t-channel

$$\mathcal{M}_t = \frac{1}{t-m_F^2}\,\bar{v}(k_2,m_F)\,\gamma^5\left(\not{k}_1-\not{p}_1+m_F\right)\gamma^\mu\,u(k_1,m_f)\,\varepsilon_\mu^*(p_1)\,. \qquad \text{(VII.B.11)}$$

Pure u-channel production $\sigma_{fF}^{(u)}$

$$\sigma_{fF}^{u}(s) = \frac{1}{8\pi}\,\frac{1}{(m_{\rm DM}^2-s)^2}\Bigg[(m_{\rm DM}^2-s)\sqrt{\lambda(s,m_F^2,M_f^2)}\,\mathcal{N}_u(s)\Big/\Big(s\,\mathcal{D}_u(s)\Big)$$
$$+\mathcal{Q}_u(s)\Big/(m_F^2-s)^2$$

$$
\begin{aligned}
&\times \Bigg(\ln\left[-m_F^2 + 2M_f^2 - \sqrt{\lambda(s, m_F^2, M_f^2)} + \frac{m_{\rm DM}^2(-m_F^2 + \sqrt{\lambda(s, m_F^2, M_f^2)} - s)}{s} + s \right] \\
&\quad - \ln\left[-m_F^2 + 2M_f^2 + \sqrt{\lambda(s, m_F^2, M_f^2)} + s - \frac{m_{\rm DM}^2(m_F^2 + \sqrt{\lambda(s, m_F^2, M_f^2)} + s)}{s} \right] \Bigg) \Bigg].
\end{aligned} \tag{VII.B.12}
$$

Here, we have introduced the following polynomial functions:

$$
\begin{aligned}
\mathcal{N}_u(s) &= m_{\rm DM}^8 m_F^2 + m_{\rm DM}^6 (m_F - M_f)(m_F^2(m_F + M_f) + 2M_f s) \\
&\quad + m_{\rm DM}^4 s \Big(2(m_F + M_f)(m_F^3 - m_F^2 M_f - 2m_F M_f^2 + M_f^3) + (m_F^2 - 4m_F M_f + M_f^2)s \Big) \\
&\quad + s^2 \Big(4(m_F - M_f) M_f^4 (m_F + M_f) - 2M_f^3(m_F + M_f)s + M_f^2 s^2 \Big) \\
&\quad + m_{\rm DM}^2 s \Big(-4m_F^2(m_F - M_f)M_f^2(m_F + M_f) + (m_F + M_f)(m_F^3 - m_F^2 M_f + 4M_f^3)s \\
&\qquad\qquad + 2m_F(-m_F + M_f)s^2 \Big).
\end{aligned} \tag{VII.B.13}
$$

$$
\begin{aligned}
\mathcal{D}_u(s) &= m_{\rm DM}^4 m_F^2 + s(-(m_F - M_f)M_f^2(m_F + M_f) + M_f^2 s) \\
&\quad + m_{\rm DM}^2 (m_F^2(m_F - M_f)(m_F + M_f) - (m_F^2 + M_f^2)s).
\end{aligned} \tag{VII.B.14}
$$

$$
\begin{aligned}
\mathcal{Q}_u(s) &= m_{\rm DM}^6 - m_{\rm DM}^4(2(-m_F^2 - m_F M_f + M_f^2) + s) \\
&\quad + s(-2M_f^2(m_F^2 - 2M_f^2) + 2m_F M_f s - s^2) \\
&\quad + m_{\rm DM}^2(-2m_F^2 M_f^2 + 2(m_F^2 - 2m_F M_f - M_f^2)s + s^2).
\end{aligned} \tag{VII.B.15}
$$

Pure t-channel production $\sigma_{fF}^{(t)}$

$$
\begin{aligned}
\sigma_{fF}^t(s) &= \frac{1}{8\pi} \frac{1}{(m_{\rm DM}^2 - s)^2} \Bigg[(m_{\rm DM}^2 - s) \sqrt{\lambda(s, m_F^2, M_f^2)}\, \mathcal{N}_t(s) \Big/ \Big(s\, \mathcal{D}_t(s) \Big) \\
&\quad + \mathcal{Q}_t(s) \Big/ (m_F^2 - s)^2 \\
&\quad \times \Bigg(\ln\left[m_F^2 - 2M_f^2 + \sqrt{\lambda(s, m_F^2, M_f^2)} - s + \frac{m_{\rm DM}^2(-m_F^2 - \sqrt{\lambda(s, m_F^2, M_f^2)} + s)}{s} \right] \\
&\quad - \ln\left[m_F^2 - 2M_f^2 - \sqrt{\lambda(s, m_F^2, M_f^2)} - s + \frac{m_{\rm DM}^2(-m_F^2 + \sqrt{\lambda(s, m_F^2, M_f^2)} + s)}{s} \right] \Bigg) \Bigg].
\end{aligned} \tag{VII.B.16}
$$

Here, we have introduced the following polynomial functions:

$$
\begin{aligned}
\mathcal{N}_t(s) &= -m_{\rm DM}^6 M_f(-m_F^2 M_f + 2M_f s) + m_{\rm DM}^4 s(2M_f^2(m_F^2 + M_f^2) + M_f^2 s) \\
&\quad + m_{\rm DM}^2 s(-4m_F^2 M_f^2(m_F^2 + M_f^2) + M_f(m_F^2 M_f + 4M_f^3)s) \\
&\quad + s^2(-4M_f^2(-m_F^4 + M_f^4) - 2M_f^2(2m_F^2 + M_f^2)s + M_f^2 s^2).
\end{aligned} \tag{VII.B.17}
$$

$$
\mathcal{D}_t(s) = m_{\rm DM}^2 M_f^2 (m_F^2 - s) + s(-(m_F - M_f)M_f^2(m_F + M_f) + M_f^2 s). \tag{VII.B.18}
$$

$$
\begin{aligned}
\mathcal{Q}_t(s) &= m_{\rm DM}^6 + m_{\rm DM}^4(-2(m_F^2 + M_f^2) - s) \\
&\quad + s(-2(m_F^2 - 2M_f^2)(m_F^2 + M_f^2) + 2m_F^2 s - s^2)
\end{aligned}
$$

$$+ m_{\rm DM}^2(2m_F^2(m_F^2+M_f^2) - 2M_f^2 s + s^2). \tag{VII.B.19}$$

Interference between u- and t-channel $\sigma_{fF}^{(ut)}$

$$\begin{aligned}
\sigma(s) = \frac{1}{4\pi}\,&\frac{1}{(m_{\rm DM}^2-s)^2(m_F^2-s)^2(m_{\rm DM}^2+m_F^2-M_f^2-s)s}\\
\times\Bigg[&-(m_{\rm DM}^2-s)\sqrt{(m_F^2-s)^2}\,(m_{\rm DM}^2+m_F^2-M_f^2-M_f^2-s)(m_{\rm DM}^4+s(-2m_FM_f+s))\\
&+s\,\mathcal{P}_1(s)\,\ln\!\left(-m_F^2+2M_f^2-\sqrt{(m_F^2-s)^2}+\frac{m_{\rm DM}^2(-m_F^2+\sqrt{(m_F^2-s)^2}-s)}{s}+s\right)\\
&+s\,\mathcal{P}_2(s)\,\ln\!\left(m_F^2-2M_f^2+\sqrt{(m_F^2-s)^2}-s+\frac{m_{\rm DM}^2(-m_F^2-\sqrt{(m_F^2-s)^2}+s)}{s}\right)\\
&+s\,\mathcal{P}_3(s)\,\ln\!\left(m_F^2-2M_f^2-\sqrt{(m_F^2-s)^2}-s+\frac{m_{\rm DM}^2(-m_F^2+\sqrt{(m_F^2-s)^2}+s)}{s}\right)\\
&+\mathcal{P}_4(s)\,\ln\!\left(-m_F^2+2M_f^2+\sqrt{(m_F^2-s)^2}+s-\frac{m_{\rm DM}^2(m_F^2+\sqrt{(m_F^2-s)^2}+s)}{s}\right)\Bigg].
\end{aligned} \tag{VII.B.20}$$

Here, we have introduced the following polynomial functions:

$$\begin{aligned}
\mathcal{P}_1(s) = &-m_{\rm DM}^6(2m_F-M_f)(m_F+M_f)+m_{\rm DM}^4\Big(-2m_F^4+m_F^3M_f-M_f^2(M_f^2+s)\\
&+m_F^2(3M_f^2+2s)+m_F(M_f^3+3M_fs)\Big)\\
&+m_{\rm DM}^2\Big(2m_F^3(m_F-M_f)M_f(m_F+M_f)-4m_FM_f^3s+M_f(-3m_F+M_f)s^2\Big)\\
&+s\Big(2m_FM_f^3(-m_F+M_f)(m_F+M_f)-M_f(m_F^3-m_F^2M_f-3m_FM_f^2+M_f^3)s\\
&\quad+(m_F-M_f)M_fs^2\Big),
\end{aligned} \tag{VII.B.21}$$

$$\begin{aligned}
\mathcal{P}_2(s) = &\,m_{\rm DM}^6M_f^2-m_{\rm DM}^4M_f^2(M_f^2+m_F(m_F+M_f)+s)\\
&+m_{\rm DM}^2(2m_F^3M_f^2M_f+M_f^2s^2)\\
&+s\Big(2m_FM_f^2(-m_F+M_f)(m_F+M_f)M_f-M_f^2s^2\\
&\quad+(-M_f^4+m_FM_f^2(m_F+M_f))s\Big),
\end{aligned} \tag{VII.B.22}$$

$$\begin{aligned}
\mathcal{P}_3(s) = &-m_{\rm DM}^6M_f^2+m_{\rm DM}^4M_f^2(M_f^2+m_F(m_F+M_f)+s)\\
&+m_{\rm DM}^2(-2m_F^3M_f^2M_f-M_f^2s^2)\\
&+s\Big(-2m_FM_f^2(-m_F+M_f)(m_F+M_f)M_f+M_f^2s^2\\
&+(M_f^4-m_FM_f^2(m_F+M_f))s\Big),
\end{aligned} \tag{VII.B.23}$$

$$\begin{aligned}
\mathcal{P}_4(s) = &\,m_{\rm DM}^6(2m_F-M_f)(m_F+M_f)+m_{\rm DM}^4\Big(2m_F^4-m_F^3M_f+M_f^2(M_f^2+s)\\
&-m_F^2(3M_f^2+2s)-m_F(M_f^3+3M_fs)\Big)\\
&+m_{\rm DM}^2\Big(-2m_F^3(m_F-M_f)M_f(m_F+M_f)+4m_FM_f^3s+(3m_F-M_f)M_fs^2\Big)\\
&+s\Big(2m_F(m_F-M_f)M_f^3(m_F+M_f)+M_f(m_F^3-m_F^2M_f-3m_FM_f^2+M_f^3)s
\end{aligned}$$

$$+ M_f(-m_F + M_f)s^2\Big). \tag{VII.B.24}$$

CHAPTER VIII

Scalar DM from Non-Equilibrium QFT: Numerical Analysis and Results

In the preceding two chapters, we established the theoretical framework for describing dark matter production in a thermal plasma using the closed-time-path (CTP) formalism within a two-particle-irreducible (2PI) approach. We demonstrated how the spectral properties of plasma excitations interacting with dark matter influence the corresponding interaction rates, and provided a detailed discussion of the key ingredients necessary for their computation.

In this chapter, we complete the analysis by numerically evaluating the interaction rate and integrating it over time to track its evolution, along with that of the dark matter relic abundance, throughout the Universe's expansion history. By systematically comparing the CTP-based treatment with the hard-thermal-loop (HTL) approximation and the semi-classical Boltzmann approach, we quantify the differences between these methods across a broad region of parameter space. The numerical strategy and implementation of the time integration are also described in detail.

Statement of Personal Contribution for this Chapter This chapter presents

results published in [5] from the numerical analysis conducted by the thesis author and MB, with support from CT for the numerical implementation. The thesis author was particularly involved in:

- The development of the `C++` numerical code together with MB, substantially expanding and reworking a first version of CT developed for [468]. An overview of the code is provided in this chapter and in the previous one.
- The deployment on High-Performance Computers together with MB.
- The development of the `Mathematica` notebooks together with MB for analytics and numerical analysis, including the creation of plots.
- The creation of Figs. VIII.2, VIII.4, VIII.3, VIII.5, VIII.6, VIII.7, VIII.8, VIII.9, VIII.10 using the data generated by simulations run by the thesis author, MB, and CT.

VIII.1 Numerical Procedure

Declaration: this section presents results published in [5] from the numerical analysis conducted by the thesis author and MB, with support from CT for the numerical implementation. The thesis author was particularly involved in:

- *Translating the analytical findings presented in the previous chapter into* `C++` *code, starting from an existing code base written by CT for [468]. This effort was conducted together with MB. Part of the code has already been presented in the previous chapter. Here, we focus on the integration routine.*
- *Optimizing the numerical code and implementing its parallel submission on multiple nodes of a high-performance computing resource to generate the simulation data. This effort was conducted together with MB.*
- *Using* `Mathematica` *to analyze the simulation data and generate the plots for their visualization and interpretation. This effort was conducted together with MB.*

The running effect estimate was estimated by MB and the thesis author. The following text is a substantially reworked and expanded version of what was presented in Section 4.1 of [5]. The text in the paper has been written by the thesis author and by MB and was reviewed and corrected by all authors.

In this section, we examine the DM interaction rate densities γ_{DM} and the resulting relic abundance of DM, as defined by Eq. (VIII.23), using the approaches we detailed in Chapter VII. These are shown in Table VIII.1, where we subdivide the approaches into two *Method Classes*: Boltzmann-approach and CTP-approach. Within the Boltzmann method, we calculate the DM relic abundance using decays with in-vacuum masses only (item 1, Eq. (VII.157)), with the addition of thermal masses (item 2, Eq. (VII.161)), and then by further adding scatterings with thermal mass-regulated propagators (item 3, Eq. (VII.167)). Within the CTP method, we use the Full 1PI-resummed propagators (item 4, Eq. (VII.9)), HTL-approximated 1PI-resummed propagators (item 5, use Eq. (VI.99) with Eq. (VII.121)), and tree-level propagators (item 6, use Eq. (VI.99) with Eq. (VII.146)). More specifically, we are interested in comparing the DM interaction rates

No.	**Name**	**Method**	$M_{\mathrm{vac.}}$	$M_{\mathrm{th.}}$	**Scatt.?**	γ_{DM}
1	Decays with $M_{\mathrm{vac.}}$	Boltzmann	✓	✗	✗	(VII.157)
2	Decays with $M_{\mathrm{vac.}}$ and $M_{\mathrm{th.}}$	Boltzmann	✓	✓	✗	(VII.161)
3	Decays + scatterings with $M_{\mathrm{th.}}$-regulated propagators	Boltzmann	✓	✓	✓	(VII.167)
4	Full 1PI-resummed	CTP	✓	✓	✓	(VI.99), (VII.9)
5	HTL 1PI-resummed	CTP	✓	✓	✓	(VI.99), (VII.121)
6	Tree-Level	CTP	✓	✓	✗	(VII.146)

Table VIII.1: Comparison of the different methods used to compute the DM interaction rate density γ_{DM}. We compare the three Boltzmann-based approaches (items 1, 2, and 3) and the two approximated CTP approaches (items 5 and 6) with the full 1PI-resummed approach on the CTP (item 4). The fourth, fifth, and sixth columns indicate whether vacuum masses, thermal masses, and scattering contributions are included. The last column refers to the DM interaction rate densities utilized in each computation method.

and the relic density obtained using 1PI-resummed propagators within the CTP formalism (see item 6 in Table VIII.1) with those computed using the other methods (items 1 to 5 in Table VIII.1). It is important to note that for CTP-based methods, we account for full relativistic quantum statistics, whereas in the Boltzmann equation approaches, we use non-relativistic Maxwell-Boltzmann distribution functions.

To compute the interaction rate densities derived in the previous chapter, we employ a dedicated numerical integration framework developed in `C++`. The resulting rates are then imported into `Mathematica`, where they are interpolated and used to solve the Boltzmann equation governing the time evolution of the comoving yield and the relic abundance. In the following section, we outline the key components of this numerical routine and discuss its implementation. This setup allows a direct comparison between the results obtained from different analytical approximations and the fully 1PI-resummed interaction rates derived within the Closed-Time-Path (CTP) formalism, which represents the central outcome of this work.

VIII.1.1 Overview of C++ numerical code

The goal of the numerical code is essentially to calculate a 4-dimensional phase-space integral (cf. (VII.9)):

$$\gamma_{\rm DM} = \frac{y_{\rm DM}^2}{4\pi^5} \int \mathrm{d}|\vec{p}|\, \mathrm{d}k^0\, \mathrm{d}|\vec{k}|\, \mathrm{d}\cos\theta\, \frac{|\vec{k}|^2|\vec{p}|^2}{\omega_p}\, \mathrm{tr}\Big\{P_L \$_F^{\mathcal{A}}(k) P_R \$_f^{\mathcal{A}}(q)\Big\} \\ \times f_-(\omega_p)\left[1 - f_+(k^0) - f_+(\omega_p - k^0)\right] , \qquad \text{(VIII.1)}$$

The code integrates over the free kinematical variables of the interaction process involving DM and the particles it interacts with. Specifically,

$$|\vec{k}|, \quad |\vec{p}|, \quad k^0, \quad \cos\theta,$$

where $\cos\theta$ is the angle between $\vec{k}$ and $\vec{p}$

The integrand is first expressed in terms of physical dimensionless variables, where each dimensionful quantity is normalized by the temperature. For example:

$$\begin{aligned}
&|\vec{k}| \to x_k = |\vec{k}|/T \to \texttt{xk},\\
&k^0 \to x_{k^0} = k^0/T \to \texttt{xk0},\\
&|\vec{p}| \to x_p = |\vec{p}|/T \to \texttt{xp},\\
&\cos\theta \to \texttt{costh}\,.
\end{aligned}$$

By also defining the transferred momentum as $q = k - p$, from which we have

$$\begin{aligned}
|\vec{q}| &= \sqrt{|\vec{k}|^2 + |\vec{p}|^2 + 2|\vec{k}||\vec{p}|\cos\theta},\\
\vec{q}\cdot\vec{k} &= |\vec{k}|^2 - 2|\vec{k}||\vec{p}|\cos\theta,
\end{aligned}$$

the integrand can thus be expressed as:

```
double Integrand(
                double xk0,
                double xk,
                double xp,
                double costh,
```

```
                double z
                )
{

    double mDM = z/(1.+delDM);
    double xp0 = sqrt(xp*xp + mDM*mDM);
    double xq0 = xk0 - xp0;
    double xq = sqrt(xk*xk + xp*xp - 2. * xk*xp * costh);
    double xqk = xk*xk - xp*xk*costh;//xq*xk*costh;
    double numerator = Numerator_Fk_fq(xk0, xk, xq0, xq, xqk, z);
    double denominator = Denominator_Fk_fq(xk0, xk, xq0, xq, xqk, z);

    return(
        2.*ydm*ydm*xk*xk/(pow(2.*M_PI,3)) *
        (numerator/denominator) *
        (1. - nF(xk0) - nF(-xq0))
    );
}
```

Here, the `Numerator_Fk_fq` and `Denominator_Fk_fq` functions, which are the numerator and the denominator obtained by manipulating the trace $\mathrm{tr}\left\{P_L \slashed{S}_F^{\mathcal{A}}(k) P_R \slashed{S}_f^{\mathcal{A}}(q)\right\}$ using Eqs. (VII.10), (VII.11) and (VII.20) to (VII.23).

Numerator

The numerator is defined in the following numerical function:

```
double Numerator_Fk_fq(
    double xk0, double xk, double xq0, double xq, double xqk, double mF)
{
    double abF = 2. * ( kSigmaA_M(xk0,xk,mF) - SigmaHA_M(xk0,xk,mF) );
    double abf = 2. * ( kSigmaA(xq0,xq) - SigmaHA(xq0,xq) );
    double a2mb2F = xk0*xk0 - xk*xk
        + SigmaH2_M(xk0,xk,mF)
        - 2. * kSigmaH_M(xk0,xk,mF)
        - SigmaA2_M(xk0,xk,mF)
        - mF*mF;
    double a2mb2f = xq0*xq0-xq*xq
        + SigmaH2(xq0,xq)
        - 2. * kSigmaH(xq0,xq)
        - SigmaA2(xq0,xq);

    double numerator = 2. *
        ( abF * abf * (xk0*xq0 - xqk - kSigmaHq(xk0,xk,xq0,xq,xqk)
        - qSigmaH_Mk(xk0,xk,xq0,xq,xqk,mF)
        + SigmaH2_Mk_q(xk0,xk,xq0,xq,xqk,mF))
        + a2mb2F * a2mb2f * SigmaA2_Mk_q(xk0,xk,xq0,xq,xqk,mF)
        - abF * a2mb2f * ( kSigmaAq(xk0,xk,xq0,xq,xqk)
        - Sigma_HMk_Aq(xk0,xk,xq0,xq,xqk,mF) )
        - a2mb2F * abf
        * ( qSigmaA_Mk(xk0,xk,xq0,xq,xqk,mF)
        - Sigma_AMk_Hq(xk0,xk,xq0,xq,xqk,mF)
        )
    );

    return numerator;
 }
```

Denominator

The denominator is defined in the following code snippet:

```
double Denominator_Fk_fq(
    double xk0, double xk, double xq0, double xq, double xqk, double mF
    ){
    return DenpSA (xq0, xq) * DenpSA_M (xk0, xk, mF);
}

double DenpSA (double xk0, double xk){
    return(
        pow(xk0*xk0 - xk*xk
        - 2. * kSigmaH(xk0,xk)
        + SigmaH2(xk0,xk)
        - SigmaA2(xk0,xk),2)
        + 4. * pow(kSigmaA(xk0,xk)
        - SigmaHA(xk0,xk),2)
    );
}

double DenpSA_M (double xk0, double xk, double mF){
    return(
        pow(xk0*xk0 - xk*xk
        - 2. * kSigmaH_M(xk0,xk,mF)
        + SigmaH2_M(xk0,xk,mF)
        - SigmaA2_M(xk0,xk,mF)
        - mF*mF, 2)
        + 4. * pow( kSigmaA_M(xk0,xk,mF)
        - SigmaHA_M(xk0,xk,mF), 2)
    );
}
```

Change of Integration Variable

The functions necessary to calculate the self-energy contribution of the fermionic loop are contained in a separate library `Functions.h` that is used by the main integration routine. The details of such functions are found in Chapter VII, in particular in Section VII.3.3, Section VII.3.4, and Section VII.A.

The integral is then transformed into a 4-hypercube space $[0,1]^4$, which is better suited for the Monte Carlo integration using the following transformations:

$$
\begin{aligned}
x_k &= \frac{t_1}{1-t_1},\\
x_p &= \frac{t_2}{1-t_2},\\
x_{k^0} &= \frac{t_3}{1-|t_3|},\\
\cos\theta &= t_4,
\end{aligned}
$$

where $t_i \in [0,1]$ for $i = 1,2,3,4$. The Jacobian J of the transformation is the determinant of the Jacobian matrix, which follows from:

$$J = \begin{vmatrix} \frac{\partial x_k}{\partial t} & \frac{\partial x_k}{\partial t_2} & \frac{\partial x_k}{\partial t_3} & \frac{\partial x_k}{\partial t_4} \\ \frac{\partial x_p}{\partial t} & \frac{\partial x_p}{\partial t_2} & \frac{\partial x_p}{\partial t_3} & \frac{\partial x_p}{\partial t_4} \\ \frac{\partial x_{k_0}}{\partial t} & \frac{\partial x_{k_0}}{\partial t_2} & \frac{\partial x_{k_0}}{\partial t_3} & \frac{\partial x_{k_0}}{\partial t_4} \\ \frac{\partial \cos\theta}{\partial t} & \frac{\partial \cos\theta}{\partial t_2} & \frac{\partial \cos\theta}{\partial t_3} & \frac{\partial \cos\theta}{\partial t_4} \end{vmatrix}$$

$$= \begin{vmatrix} \frac{1}{(1-t_1)^2} & 0 & 0 & 0 \\ 0 & \frac{1}{(1-t_2)^2} & 0 & 0 \\ 0 & 0 & \frac{1}{(1-|t_3|)^2} & 0 \\ 0 & 0 & 0 & 1 \end{vmatrix}$$

$$= \frac{1}{(1-t_1)^2(1-t_2)^2(1-|t_3|)^2}, \tag{VIII.2}$$

and the transformed integrand is now expressed as

```
double Integrandfull_Transformed(
          double t1, double t2, double t3, double t4, double z)
{

    double xk = t1/(1.-t1);
    double xp = t2/(1.-t2);
    double xk0 = t3/(1.-fabs(t3));
    double costh = t4;

    double mdm = z/(1.+delDM);
    double xp0 = sqrt(xp*xp + mdm*mdm);

    double jacobian = 1. / (
        pow(1.-t1,2) * pow(1.-t2,2) * pow(1. - fabs(t3),2) );

 return( fabs(jacobian)* xp*xp / xp0 * 4. * M_PI/(pow(2.*M_PI,3)) *
        Integrand_NEW(xk0,xk,xp,costh,z) * nB(xp0)
 );

}
```

The only universal constants are the parameters as in Eq. (VIII.3):

$$G \to \mathtt{G}$$
$$\delta = \frac{m_F - m_{\rm DM}}{m_{\rm DM}} \to \mathtt{delDM},$$
$$z \equiv \frac{m_F}{T} \to \mathtt{z}.$$

The integration can be set up by defining a function that will feed the integration routine:

```
struct fparams {double zz;};
```

```
double myf (double x[], size_t dim, void * p){

    struct fparams * fp = (struct fparams *)p;

    double aux = Integrandfull_Transformed (
                        x[0], x[1], x[2], x[3], fp->zz
                    );
    if (!isnan(aux)) return  aux;
    else return 0.;

}
```

Here, the parameter zz is just the time variable $z = m_F/T$. In the main function, the integration is done with the following code

```
int main(){

// Some preparatory code for the multi-parameter scan
// ....
//
double zz = 0.1 // Some number you assign

fparams params = {zz};

// Result and error variable for the integration
double res, err;

// Integration boundaries
double xl[4] = { 0., 0., -1., -1.};
double xu[4] = { 1., 1., 1., 1.};

// Random number generator
// GSL's Taus generator:
gsl_rng *rng = gsl_rng_alloc(gsl_rng_taus2);
// Initialize the GSL generator with time:
gsl_rng_set(rng, time(NULL));

//Monte-Carlo function defined in "gsl_monte.h"
// double (* f) (double * x, size_t dim, void * params)
gsl_monte_function F;

F.f = &myf;   // Which function it has to point to -> myf defined above
F.dim = 4;    // Number of dimensions to integrate over.
F.params = &params; // Pointer to parameters of the function (zz)

size_t calls = 1e5; // Number of evaluations to estimate integral

// Allocate and initialize a workspace for Monte Carlo integration
in *dim* dimensions.
gsl_monte_vegas_state *s = gsl_monte_vegas_alloc (4);
// The workspace is used to maintain the state of the integration.
gsl_monte_vegas_params params;
gsl_monte_vegas_params_get(s, &params);

// Warm-up pre-integration
gsl_monte_vegas_integrate (&F, xl, xu, 4, calls, rng, s, &res, &err);

gsl_monte_vegas_params_get(s, &params);
printf(" stage = %i \n",(params).stage);
```

```
// additions change stage
params.stage = 2;
gsl_monte_vegas_params_set(s, &params);
size_t accumulated_calls;
accumulated_calls = calls;

double resolution = 1.;
if(zz>7) resolution = 2.;

// We check when the relative error (err/res) falls below 1%
while ( (fabs(err/res)*100>resolution))
{
    count = count +1;
    params.stage = 2;
    gsl_monte_vegas_params_set(s, &params);
    accumulated_calls = accumulated_calls + calls;
    gsl_monte_vegas_integrate (&F, xl, xu, 4, calls, rng, s, &res, &err);
    // Write result on file
    if (mytestfile.is_open()){
        mytestfile << zz<<"    "<<res<<"    "<<err
        <<"    "<<err/res<<"
        "<<gsl_monte_vegas_chisq (s)
        <<"    "<< accumulated_calls <<endl;
    }
}

// Close file
    mytestfile.close();

// Free memory
    gsl_monte_vegas_free (s);
    gsl_rng_free(rng);

    return 0;

}
```

VIII.1.2 Summary of the GSL VEGAS Monte Carlo Algorithm

We provide a summary of the key features of the VEGAS Monte Carlo algorithm method here. For more information on the routine implemented in the GNU Scientific Library, we refer to the official documentation in [507] and `https://www.gnu.org/software/gsl/doc/html/montecarlo.html`.

The VEGAS algorithm is an adaptive Monte Carlo integration method based on importance sampling. Its central idea is to approximate the optimal sampling density $g(\mathbf{x}) \propto |f(\mathbf{x})|$ by constructing a separable probability distribution

$$g(\mathbf{x}) = g_1(x_1)\, g_2(x_2) \cdots g_d(x_d),$$

which reduces the number of required histogram bins from K^d to Kd in d dimensions. Each g_i is estimated from histograms of the integrand collected during sampling, and the domain is divided into typically 50–100 bins per dimension. However, the exact number is chosen adaptively based on the number of requested function calls.

VEGAS proceeds in multiple passes (iterations). In each iteration, it draws N sample points using the current approximation of $g(\mathbf{x})$, computes an estimate of the integral and its variance, and then rebins the grid according to the variance-weighted histogram data. The rebinning aggressiveness is controlled by the parameter `alpha` (default 1.5), with smaller values producing slower adaptation and larger values producing more rapid grid changes. One typically performs an initial "warm-up" iteration with relatively few calls (e.g. 10^3–10^4) to obtain a rough grid, followed by several main iterations with larger sample sizes (e.g. 10^5–10^6 calls per iteration).

Each iteration yields an independent value I_k with error estimate σ_k, and the final result is a weighted average,

$$I = \frac{\sum_k I_k/\sigma_k^2}{\sum_k 1/\sigma_k^2}, \qquad \sigma^2 = \left(\sum_k 1/\sigma_k^2\right)^{-1}.$$

The GSL algorithm also calculates the reduced chi-squared of the distribution

$$\chi^2/\nu = \frac{1}{\nu}\sum_k \frac{(I_k - I)^2}{\sigma_k^2},$$

which is expected to be near unity when the importance-sampling grid is well adapted and the variance estimates are reliable. A significantly larger value indicates that more iterations or a larger number of samples per iteration may be required.

The GSL interface provides functions to allocate a VEGAS state, initialize or reset the sampling grid, adjust parameters such as `alpha`, the number of iterations, and the sampling mode (importance, stratified, or combined), and to retrieve both iteration-level and averaged results. Some of these have been displayed in the code presented above.

VEGAS is most effective when the integrand displays high variance, where simple sampling would not capture sharp peaks sufficiently. Importance sampling is thus particularly suited for the case treated in this chapter, where the integrand displays very large and narrow peaks from the fermionic self-energies, which are essentially broadened delta functions.

VIII.1.3 Parameter definition, scan strategy, and numerical implementation

All dimensionful quantities entering the DM interaction rate density $\gamma_{\rm DM}$ are normalized to the plasma temperature T. The computation is therefore carried out entirely in terms of dimensionless variables. The set of free input parameters is defined as

$$G, \qquad \delta \equiv \frac{m_F - m_{\rm DM}}{m_{\rm DM}}, \qquad z \equiv \frac{m_F}{T}, \tag{VIII.3}$$

where G denotes the effective gauge coupling defined in Eq. (VII.2), δ parametrizes the relative mass splitting between the heavy fermion mediator and the DM particle, and z controls the temperature dependence of the production process.

The numerical scan is performed over a discrete grid in the three-dimensional parameter space (G, δ, z). The corresponding scan ranges and discretization choices are summarized in Table VIII.2.

In total, this results in $13 \times 10 \times 32 = 4160$ parameter points, each evaluated independently by the numerical code.

Parameter	Definition	Range	Sampling
G	Effective gauge coupling	$0.4 \leq G \leq 1.6$	Linear, step size 0.1
$\log_{10}\delta$	Relative mass splitting	$[-1, 1]$	Linear, 10 points
z	Inverse temperature	$[0.01, 10]$	32 logarithmic points

Table VIII.2: Definition and discretization of the free input parameters used in the numerical scan.

Validity regime and electroweak symmetry.

The computation is performed assuming the unbroken electroweak phase. This assumption is valid provided that the freeze-in DM production occurs at temperatures

$$T_{\text{fi}} \simeq \frac{m_F}{5} \gtrsim T_{\text{EW}}, \tag{VIII.4}$$

where $T_{\text{EW}} \simeq 160$ GeV is the electroweak crossover temperature [523]. Consequently, for mediator masses $m_F \gtrsim \mathcal{O}(\text{TeV})$, the freeze-in process takes place entirely in the symmetric phase, and electroweak symmetry breaking effects can be consistently neglected.

Numerical implementation.

The numerical configuration of the integration procedure is summarized in Table VIII.3.

Setting	Value
Integration method	VEGAS (adaptive Monte Carlo)
Library	GNU Scientific Library (GSL)
Target relative error	$\leq 1\%$
Parameter points	4160
Programming language	`C++`

Table VIII.3: Numerical setup used for the evaluation of the rate density integrals.

VIII.1.3.1 Running of the effective gauge coupling

To assess the impact of renormalization-group running on the effective gauge coupling G, we estimate running effects at one-loop order under the assumption that the heavy fermion mediator is charged only under $SU(3)_c$ and transforms in the fundamental representation. This is expected to be the dominant gauge contribution. Effectively, this corresponds to adding a single color-charged fermion species, analogous to a fourth fermion generation.

At one-loop order, the QCD gauge coupling g_3 evolves according to [105, 432]

$$\frac{\mathrm{d}g_3}{\mathrm{d}\ln\mu} = -c\,\frac{g_3^3}{16\pi^2}\,, \tag{VIII.5}$$

with

$$c = \frac{11}{3}N_c - \frac{1}{6}n_S - \frac{4}{3}n_G = \frac{33}{6}\,, \tag{VIII.6}$$

where $N_c = 3$, $n_S = 0$, and $n_G = 4$. The solution of Eq. (VIII.5) is

$$g_3^2(\mu) = \left[g_3^{-2}(\mu_0) + \frac{c}{16\pi^2}\ln\left(\frac{\mu}{\mu_0}\right)\right]^{-1}. \tag{VIII.7}$$

We choose the reference scale $\mu_0 = m_F$ and define

$$g_3(m_F) \equiv g_3^M, \qquad G^M \equiv \frac{4}{3}\left(g_3^M\right)^2, \tag{VIII.8}$$

which coincides with the effective gauge coupling used throughout the numerical analysis.

Choice of renormalization scale.

We consider the following assignments for the running scale:

$$\mu = \max(m_F, T)$$

. While alternative choices such as $\mu = \pi T$ or $\mu = T$ are commonly adopted in thermal field theory, we find that they do not qualitatively affect the results. In practice, we adopt $\mu = \max(m_F, T)$, which avoids the appearance of a Landau pole associated with confinement in the $T \ll m_F$ regime.

Analytical estimate of running effects.

To obtain a semi-analytical estimate of running-coupling corrections, we focus on scattering processes, which dominate the DM production rate for small mass splittings ($\delta \ll 1$) and $z < 1$. In this regime, the scattering contribution to the interaction rate density can be schematically modeled as

$$\gamma_{\rm scatt}(z) \;\sim\; G(\mu)\, e^{-z}, \tag{VIII.9}$$

up to logarithmic corrections in G. Replacing $G^M \to G(\mu)$ with $\mu = \max(m_F, T)$, the relative change induced by running effects may be approximated as

$$\frac{\dfrac{G^M}{e(z=1)} + \displaystyle\int_0^1 \mathrm{d}z \left[(G^M)^{-1} + \frac{3c}{64\pi^2}\ln\left(z^{-1}\right)\right]^{-1} e^{-z}}{G^M}. \tag{VIII.10}$$

This expression cannot be evaluated in closed form. However, further insight can be gained by considering limiting cases.

In the regime where the logarithmic term is subdominant,

$$\frac{c}{16\pi^2}\ln\left(z^{-1}\right) \ll (g_3^M)^{-2}, \tag{VIII.11}$$

which corresponds numerically to $0.12\, G^M \ll 1$ for $\mu/\mu_0 \sim 100$, Eq. (VIII.10) simplifies to

$$\frac{G^M - \int_0^1 \mathrm{d}z\, \frac{3c(G^M)^2}{64\pi^2}\ln\left(z^{-1}\right)e^{-z}}{G^M} \;\simeq\; 1 - 0.8\,\frac{3c}{64\pi^2}G^M \;\simeq\; 1 - 0.02\, G^M. \tag{VIII.12}$$

For the parameter range considered in this work, $G^M \lesssim 1.2$, the above approximation remains valid. We therefore expect running-coupling effects to induce at most a relative suppression of scattering rates at the level of 2%–3%.

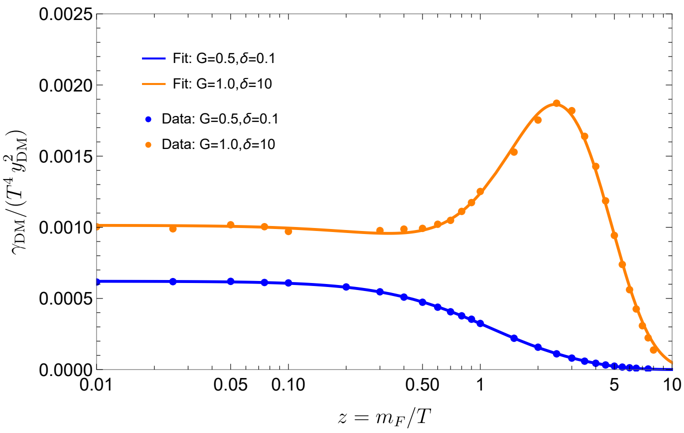

Figure VIII.1: We display the numerically obtained data points for the DM interaction rate density using 1PI-resummed propagators, as well as our fit to the data for two choices of (G, δ). *Figure created by MB and included in [5].*

Comparison with numerical results.

This analytical estimate is in excellent agreement with numerical checks. As a matter of fact, explicit integrations of the full thermal-mass–regulated scattering rates, including the running of $G(\mu)$, yield deviations in the relic abundance of at most 1.5%. Given the numerical cost of evaluating fully resummed rates, we thus conclude that neglecting running effects introduces an uncertainty well below other theoretical systematics (around $\mathcal{O}(1\%)$).

Finally, we emphasize that this estimate applies primarily to the small–δ regime, where scattering processes dominate DM production. For larger mass splittings, decays become the leading contribution. However, since decay-driven freeze-in occurs over a narrower temperature interval, running effects are expected to be even less significant in that regime.

VIII.2 Comparison of the Interaction Rates

Declaration: In this section, the numerical results, including the comparison of interaction rates, were produced by the thesis author and MB. The interpretation of these results was performed in close collaboration with all authors, with primary responsibility taken by the thesis author and MB. The fitting procedure was conceived and carried out by MB. The text closely follows the presentation in [5], with minor stylistic and content adjustments. The manuscript was written by the thesis author and MB, while all authors contributed to its organization, review, and refinement.

In this section, we compare the interaction rate densities $\gamma_{\rm DM}$ obtained using the different computational frameworks introduced in the previous sections.

VIII.2.1 Parametric fit of the interaction rate

To facilitate a systematic comparison between methods and to enable efficient integration of the rate densities, we fit the numerically evaluated interaction rates obtained with HTL- and 1PI-resummed propagators using the *ansatz*

$$\frac{\gamma_{\rm DM}(z)}{y_{\rm DM}^2 T^4} = A\, z^3 K_1(az) + B\, z K_1(bz)\,, \tag{VIII.13}$$

where A, a, B, and b are fit parameters that depend on (G, δ), and K_1 denotes the modified Bessel function of the second kind. The two terms are designed to separately capture the decay-dominated (low-temperature) and scattering-dominated (high-temperature) regimes.

In Fig. VIII.1, we show representative examples of the fitted curves alongside the raw numerical data obtained with 1PI-resummed propagators, demonstrating excellent agreement across the full temperature range.

VIII.2.2 Asymptotic behavior and physical interpretation

The functional form in Eq. (VIII.13) is motivated by the distinct physical mechanisms governing DM production in the ultraviolet ($z \ll 1$) and infrared ($z \gtrsim 1$) regimes.

High-temperature regime ($z \ll 1$)

At high temperatures, the mass splitting between the parent particle F and the DM candidate is negligible, rendering decays phase-space suppressed and eventually kinematically forbidden (cf. Eq. (VII.135)). In this regime, DM production is dominated by scatterings, enhanced by the large number density of relativistic plasma constituents, $n^{\rm eq} \sim T^3$.

In vacuum, scattering-induced interaction rates scale parametrically as

$$\gamma_{\rm scatt} \propto zK_1(z), \tag{VIII.14}$$

which motivates the second term in Eq. (VIII.13). For $z \ll 1$, this contribution approaches a constant, giving rise to the plateau observed in Fig. VIII.2. Since the dominant scattering amplitudes involve gauge interactions, the height of this plateau increases with the effective gauge coupling G.

Taking the $z \to 0$ limit of the fit function yields

$$Az^3 K_1(az) + BzK_1(bz) \xrightarrow{z\to 0} \frac{B}{b}, \tag{VIII.15}$$

which depends only on G. Assuming that the leading scattering processes involve a single gauge vertex ($\propto G$) together with t-channel fermion exchange ($\propto G \ln G$) [462], we find that the fitted parameters are well described by

$$\frac{B}{b} = 1.0 \times 10^{-3}\, G - 3.32 \times 10^{-4}\, G \ln G\,. \tag{VIII.16}$$

Low-temperature regime ($z \gtrsim 1$)

At low temperatures, DM production is dominated by decays of the parent particle F, provided that the mass splitting δ is sufficiently large to allow kinematically accessible decays and that F remains thermally populated. In this regime, the interaction rate scales as

$$\gamma_{\rm dec} \propto z^3 K_1(z), \tag{VIII.17}$$

which motivates the first term in Eq. (VIII.13). This behavior explains the pronounced peaks observed in Fig. VIII.2 for benchmarks with $\delta = 10$.

For $z \to \infty$, the fit function asymptotes to

$$Az^3 K_1(az) + BzK_1(bz) \xrightarrow{z\to\infty} \frac{A}{\sqrt{a}} \exp(-az) z^{5/2}. \tag{VIII.18}$$

In decay-dominated freeze-in scenarios, this combination can be identified with the dimensionless decay rate,

$$\frac{A}{\sqrt{a}} = \frac{\Gamma_F}{m_F^2}, \tag{VIII.19}$$

where Γ_F is the in-vacuum decay width of the parent particle. Evaluating Γ_F using in-vacuum masses and expanding in the non-relativistic limit yields the parametric dependence

$$\frac{A}{\sqrt{a}} = 0.067\, \frac{\delta^2(\delta+2)^2}{16\pi(1+\delta)^4}\,, \tag{VIII.20}$$

which accurately reproduces the fitted normalization in the large-z regime. As δ decreases, the available phase space for decays rapidly shrinks, causing the decay contribution to become negligible and leaving scatterings as the dominant production channel.

VIII.2.3 Interpretation of Results

In Fig. VIII.2, we show the evolution of $\gamma_{\rm DM}$ as a function of the dimensionless inverse temperature $z \equiv m_F/T$ for four representative benchmark points,

$$(G, \delta) \in \{(1.2, 10), (1.2, 0.1), (0.5, 10), (0.5, 0.1)\}\,. \tag{VIII.21}$$

These benchmarks are chosen to probe both weak and strong effective couplings, as well as regimes where DM production is dominated either by decays ($\delta \gtrsim 1$) or by scatterings ($\delta \ll 1$).

CTP with HTL-resummed propagators

The HTL-resummed solution generally predicts a larger contribution from scatterings, while the decay-dominated regime (large z) shows similar rates. However, around the transition region near $z \sim 1$, the HTL solution tends to underestimate the interaction rate density. This occurs because, for small z, where scatterings are dominant, the primary contribution comes from momentum configurations where one of the fermionic propagators carries spacelike momentum. The HTL approximation, which neglects the in-vacuum mass of the parent particle, does not account for the exponential suppression at large spacelike momenta present in the 1PI-resummed propagator (cf. Fig. VII.3), leading to a larger rate in this regime.

As decays become relevant, HTL-resummed propagators, which behave like delta functions for timelike momenta, exhibit a sharp transition. In contrast, 1PI-resummed propagators have finite widths even for timelike momenta, with "smeared" spectral densities capturing decay contributions over a broader momentum range, including smaller z values (explaining why the solid red lines in Fig. VIII.2 rise earlier). This effect is more pronounced for larger values of G. Once decays are fully accessible, HTL rates tend to overestimate the decay contribution because the finite width of 1PI-resummed propagators smooths the quasi-particle peak, resulting in a slight reduction in the rate when quasi-particle solutions are kinematically accessible.

CTP with tree-level propagators

Here, the rate is computed using Eq. (VII.146), which includes only decays with thermal masses and quantum relativistic statistics, excluding scattering contributions. This rate

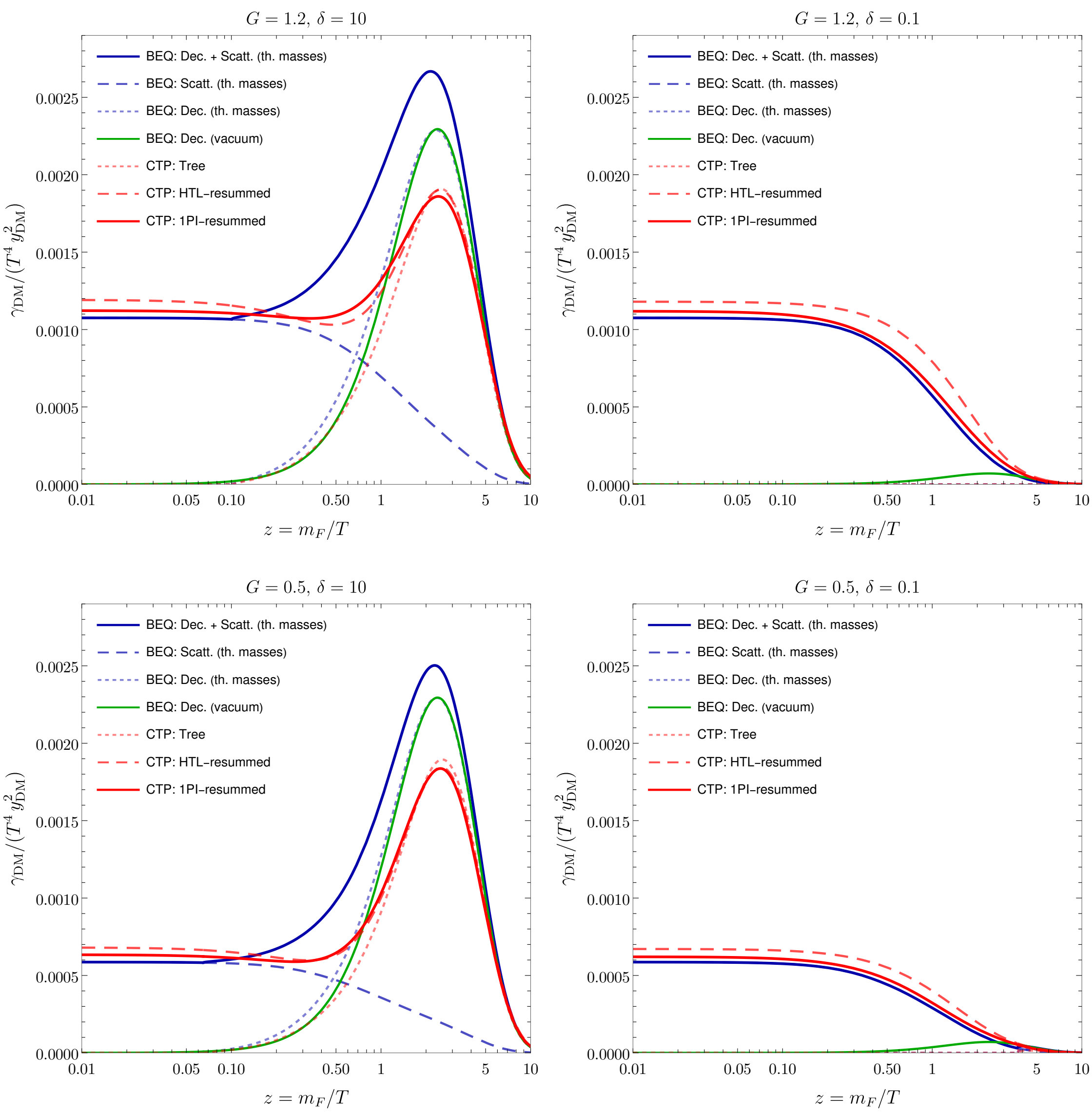

Figure VIII.2: Evolution of the interaction rate density in terms of the time variable $z = m_F/T$ for a calculation using: the Boltzmann equation (BEQ) including decays only (blue and short dashing), scatterings (blue and long dashing) with thermal masses and their sum (solid blue). The rate from decays with in-vacuum masses is shown with solid green lines. In the CTP formalism, the rates are derived with 1PI-resummed propagators (red, solid), using HTL propagators (red, long dashing), and tree-level propagators (red, short dashing). The latter also corresponds to decays with thermal masses and full quantum relativistic statistics. *Figure created by the thesis author with notebooks co-developed by the thesis author and MB using simulation data generated by the thesis author and MB and included in [5].*

is equivalent to the one obtained with HTL timelike propagators when approximating $(\Sigma^{\mathcal{H}}_{F/f})^2 = m^2_{\text{th}}$. Consequently, the interpretation closely aligns with the discussion of decays within the HTL approximation.

Boltzmann equation with decays and scatterings using thermal masses:

Using thermal masses leads to an underestimation of scattering contributions and an overestimation of decay contributions. The underestimation arises because Boltzmann statistics are used instead of quantum statistics in the collision term calculation. The overestimation at larger z may result from several factors. First, using Boltzmann statistics (blue short-dashed lines) instead of the appropriate Bose-Einstein and Fermi-Dirac distributions (red short-dashed lines) results in an overestimation of decay contributions due to reduced Pauli blocking for final-state fermions. Additionally, as shown in Fig. VII.3, approximating fermion dispersion relations solely with in-vacuum and thermal masses tends to overestimate the total mass, thereby increasing the decay contribution when decays are efficient. A larger thermal mass also reduces the kinematically allowed window for decays earlier. Moreover, thermal mass-regulated scatterings contribute non-negligibly for a significantly longer period compared to the scattering processes captured by 1PI-resummed propagators. These differences account for the discrepancy in the height of the decay peaks between the solid blue and red curves.

Boltzmann equation with vacuum decays

This approach disregards scattering contributions and thus significantly underestimates the production rate at small z. For larger z, where decays dominate the interaction rate, the resulting rate falls between those obtained from decays with thermal masses and the CTP rates. The lower rate compared to the one including scattering contributions (solid blue) is mainly due to the omission of scatterings and thermal masses.

VIII.3 Comparison of the Relic Densities

Declaration: In this section, the numerical results, including the comparison of interaction rates, were generated by the thesis author and MB. The interpretation of these results was carried out in close collaboration with all authors, with primary responsibility taken by the thesis author and MB. The text largely follows the presentation in [5], with minor stylistic and content adjustments. The manuscript was written by the thesis author and MB, while all authors contributed to its organization, review, and refinement.

To place the approaches of Table VIII.1 on equal footing, we compare their predictions for the relic abundance by integrating the rate equation in the regime where backreactions are negligible. This yields

$$Y_{\mathrm{DM}}(z) = \int_0^z \frac{\mathrm{d}z'}{z'} \frac{\gamma_{\mathrm{DM}}(G,\delta;z')}{s(z')H(z')} = \frac{y_{\mathrm{DM}}^2 M_{\mathrm{Pl}}}{m_F} \frac{135\sqrt{10}}{2\pi^3 g_{\star s}(m_F) g_\star(m_F)} \mathcal{I}(G,\delta;z), \tag{VIII.22}$$

where $\mathcal{I}(G,\delta;z) = \int_0^z \mathrm{d}z'\, \gamma_{\mathrm{DM}}/(T^4 y_{\mathrm{DM}}^2)$. Here, M_{Pl} is the reduced Planck mass and $g_{\star s}, g_\star$ are the effective relativistic degrees of freedom (cf. Section III.1.2). Using Eq. (III.46) and $m_F = (1+\delta)\, m_{\mathrm{DM}}$, the abundance at time z reads

$$\Omega_{\mathrm{DM}} h^2(z) = 0.12 \left(\frac{y_{\mathrm{DM}}}{2.46\times 10^{-13}}\right)^2 \frac{\mathcal{I}(G,\delta;z)}{1+\delta}\,. \tag{VIII.23}$$

Figure VIII.3 tracks the time evolution of Ω_{DM} obtained from the different rate inputs summarized in Fig. VIII.2. Solid red lines correspond to the CTP calculation with fully 1PI-resummed propagators; dashed red to the HTL approximation; short-dashed red to the CTP result with tree-level propagators and thermal masses. In the Boltzmann class, the green solid curve shows decays with vacuum masses (Eq. (VII.157)); blue dot-dashed

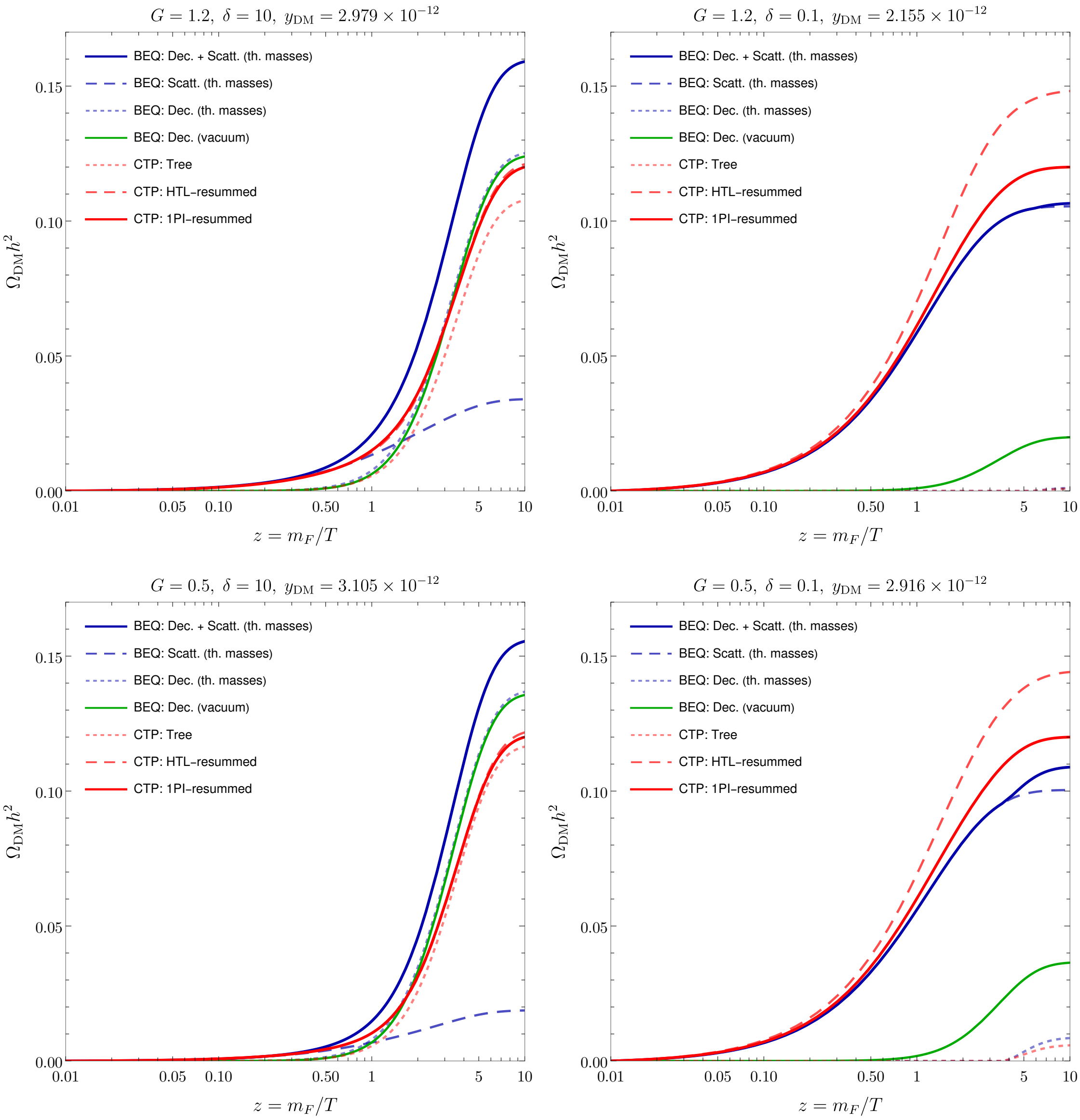

Figure VIII.3: Evolution of the DM relic abundance. The color scheme of the plotted lines and the values of G and δ chosen in each panel are the same as in Fig. VIII.2. *Figure created by the thesis author with notebooks co-developed by the thesis author and MB using simulation data generated by the thesis author and MB and included in [5].*

includes thermal masses in decays (Eq. (VII.161)); blue dashed adds thermally regulated scatterings (Eq. (VII.167)); their combination appears as a solid blue curve. The benchmarks $(G, \delta) \in \{(1.2, 10), (1.2, 0.1), (0.5, 10), (0.5, 0.1)\}$ expose decay- versus scattering-dominated regimes. The same information normalized to the fully resummed CTP prediction is shown in Fig. VIII.4.

The deviation maps in Figures VIII.5 and VIII.9 summarize, across (G, δ), the fractional shift of $\Omega_{\rm DM}$ predicted by each approximation relative to the fully 1PI-resummed result. Warm tones indicate an overestimate; cool tones, an underestimate.

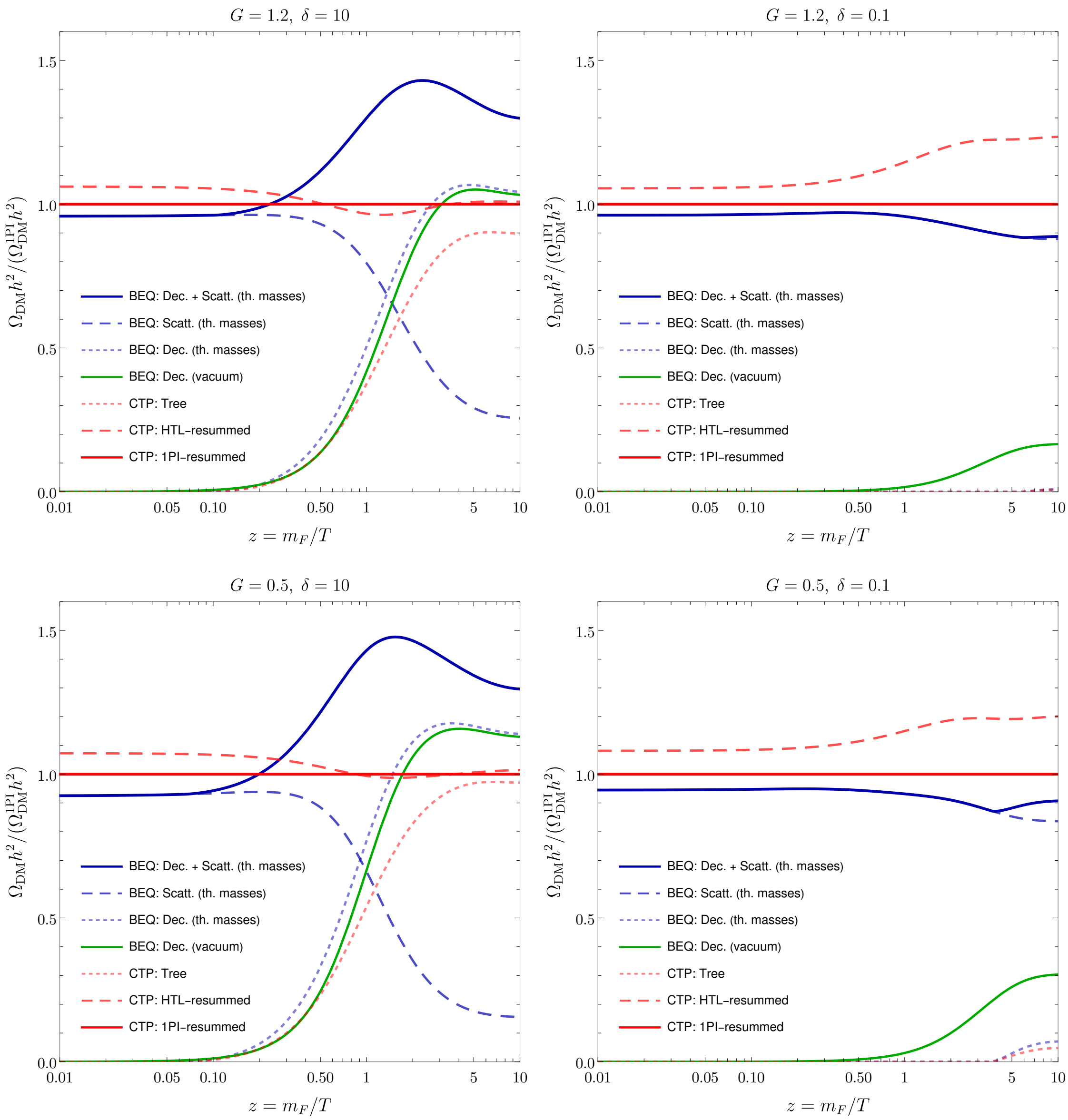

Figure VIII.4: Evolution of the DM relic abundance normalized to the values obtained with 1PI-resummed propagators. The color scheme of the plotted lines and the values of G and δ chosen in each panel are the same as in Fig. VIII.2. *Figure created by the thesis author with notebooks co-developed by the thesis author and MB using simulation data generated by the thesis author and MB and included in [5].*

VIII.3.1 Interpretation of Results

Boltzmann approach with decays (vacuum masses)

This baseline excludes scatterings and uses Maxwell–Boltzmann statistics, thereby both missing the dominant production at small δ and inflating the decay contribution at late times. Consequently, $\Omega_{\rm DM}$ is moderately high at large δ (up to 14%) and severely low at small δ (down to -86%). A diagonal band where these biases compensate is visible in Fig. VIII.5; the residual G-dependence follows from the scaling of scattering contributions with gauge couplings.

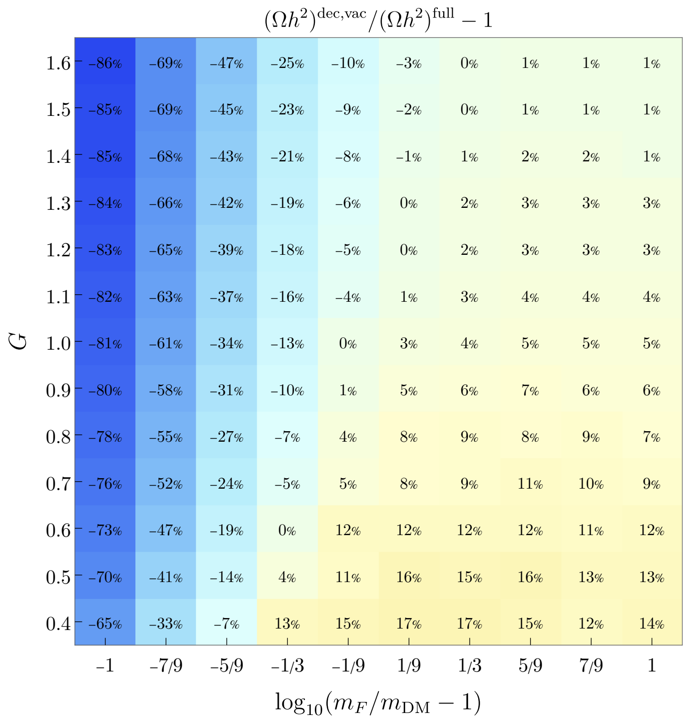

Figure VIII.5: Relative correction on the relic abundance calculated by taking into account one-loop fully-resummed propagators with respect to the one calculated within the Boltzmann approach, only considering vacuum decays. The percentage deviation is also shown in warm colors when positive, and with cold colors when negative. *Figure by the thesis author with and included in [5].*

Boltzmann approach with decays (thermal masses)

Thermal masses shut off decays at high temperatures and enhance the late-time overestimate in the non-relativistic regime. As seen in Fig. VIII.6, the deviation reaches $\sim +15\%$ at large δ but becomes even more negative at small δ (down to -100%) where decays are suppressed. Including quantum statistics (captured by the CTP tree-level result, Fig. VIII.7) strengthens this trend via Pauli blocking. Among decay-only treatments, this option yields the largest overall error; a compensation band persists.

Boltzmann approach considering decays and scatterings with thermal masses

Adding thermally regulated t-channel scatterings (Fig. VIII.8) cures the small-δ deficit: for $\delta \lesssim 25\%$ the deviation is negative but limited to $\sim -10\%$. At large δ, the decay overestimate persists (up to $\sim +35\%$). The two trends cancel for intermediate δ and moderate G, leaving $\mathcal{O}(1\%)$ differences. Once the explicit G-dependence of scatterings is included, the residual deviation is governed primarily by δ. Incorporating the correct bath statistics for decays (approximated by the CTP tree-level result) reduces the large-δ overshoot to $\sim +15\%$.

HTL propagators

HTL propagators reproduce the decay-dominated regime to within a few percent, but they overestimate the scattering contribution (Fig. VIII.9). As a result, the small-δ region exhibits a positive bias (up to $+27\%$) that grows with G, consistent with the HTL expansion

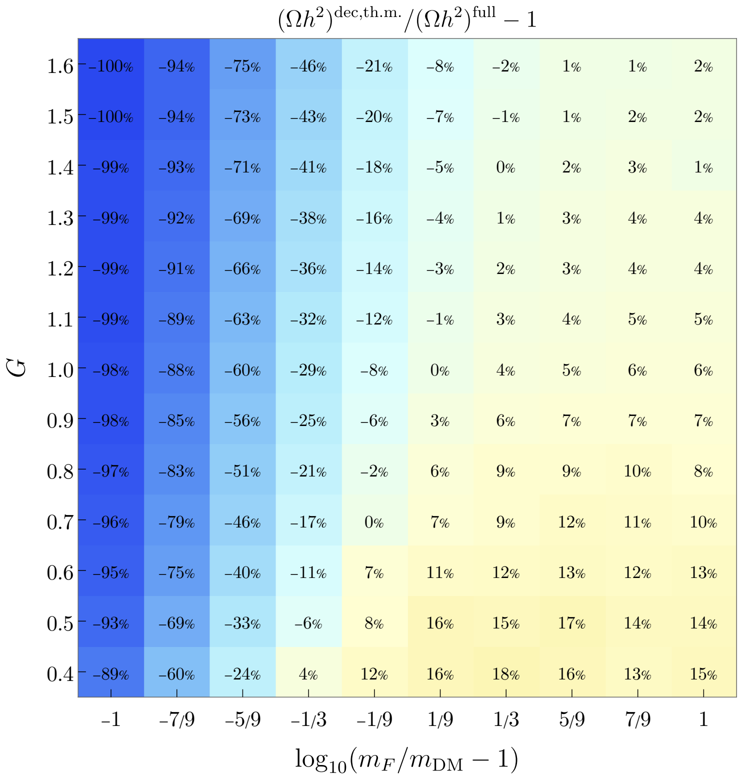

Figure VIII.6: Same caption as Fig. VIII.5 but considering vacuum and thermal masses instead of only vacuum masses. *Figure by the thesis author with and included in [5].*

being organized in powers of G/π. We now quantify the contributions to the relic density that were omitted in this work. As previously discussed, we truncate the expansion of the 2PI effective action at LO, which leads to the omission of two potentially relevant contributions.

First, interference terms between t-channel and s-channel scatterings only emerge at NLO in the 2PI effective action expansion and are therefore not included. However, within the Boltzmann equation framework, these terms are found to be sub-leading (around $\mathcal{O}(10\%)$) relative to the squared s- and t-channel contributions, and we expect a similar level of significance with our method. Second, this truncation excludes contributions to DM production arising from the LPM effect.

In Ref. [432], a similar scenario to ours is analyzed (albeit with different statistics: a scalar mediator and fermionic DM), showing that the LPM effect enhances the scattering contribution to the DM relic abundance by approximately $\mathcal{O}(50\%)$ (10%) for small (large) mass splittings. However, these results are derived in the ultrarelativistic limit and extrapolated to the non-relativistic regime, while the treatment of the LPM effect involving two in-vacuum mass scales, as in our scenario, has not yet been explored in the literature.

To estimate the potential corrections to our results, we proceed as follows: based on Ref. [432], we assume that the LPM effect enhances the DM production rate from scatterings by 50% for $\delta = 0.1$ and by 10% for $\delta = 10$, with a linear interpolation of the enhancement in δ between these points. Practically, we implement this by replacing the coefficient $B \to (1.504 - 0.04\delta)B$ in Eq. (VIII.13). We then compare the resulting DM relic density to the uncorrected density. The results of this comparison are presented in the (G, δ) plane in Fig. VIII.10. We find that by truncating the effective action at LO,

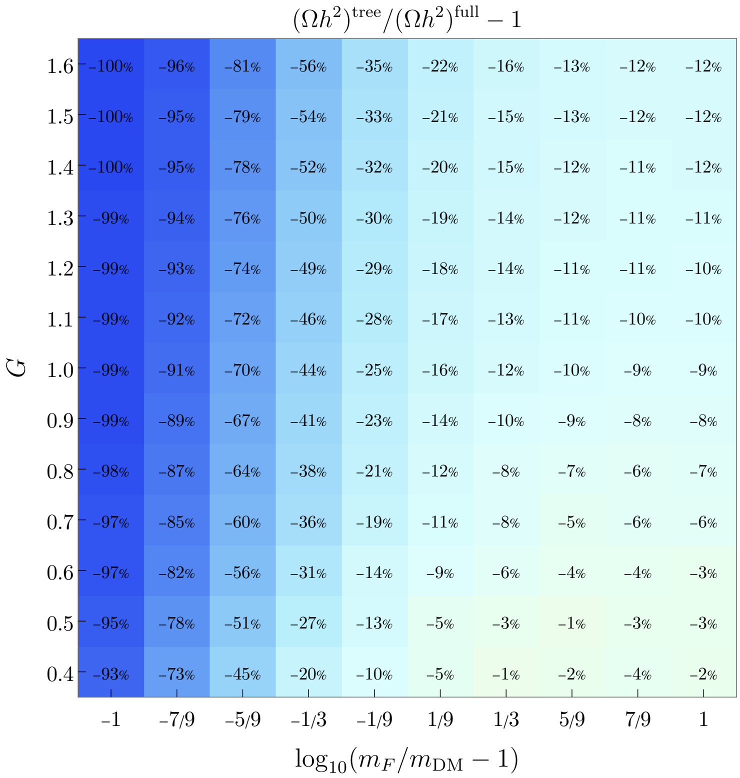

Figure VIII.7: Same caption as Fig. VIII.5 but considering vacuum and thermal masses as well as the correct quantum statistics instead of vacuum masses only and Boltzmann statistics. *Figure by the thesis author with and included in [5].*

the relic density can be underestimated by up to $\sim 30\%$ for the smallest mass splittings, where scatterings dominate the DM interaction rate. For large mass splittings, the relic density is only mildly affected, differing by just a few percent.

Recent work, presented both in a master's thesis [505] and in a subsequent publication [10] that builds upon our analysis, demonstrates that a proper treatment of the LPM effect within the model considered in this chapter leads to significantly milder corrections. In particular, the resulting modifications to the interaction rates range from approximately -10% in the limit of nearly degenerate masses to negligible effects for large mass splittings.

A related source of theoretical uncertainty stems from the non-conservation of local symmetries. Truncating the loop expansion of the 2PI effective action, as done in this work, prevents the cancellation of gauge-dependent parts of diagrams with higher-loop topologies, leading to gauge-dependent observables [465, 476, 524–526].

In practice, however, a truncation and a gauge choice must be made. In our case, this corresponds to considering the LO (two-loop) expansion of the 2PI effective action and adopting the Feynman gauge. We therefore expect any omitted gauge-dependent contributions to the 1PI-resummed propagators and the DM relic abundance to lie within the same uncertainty band as the higher-order corrections that were not included in our calculation.

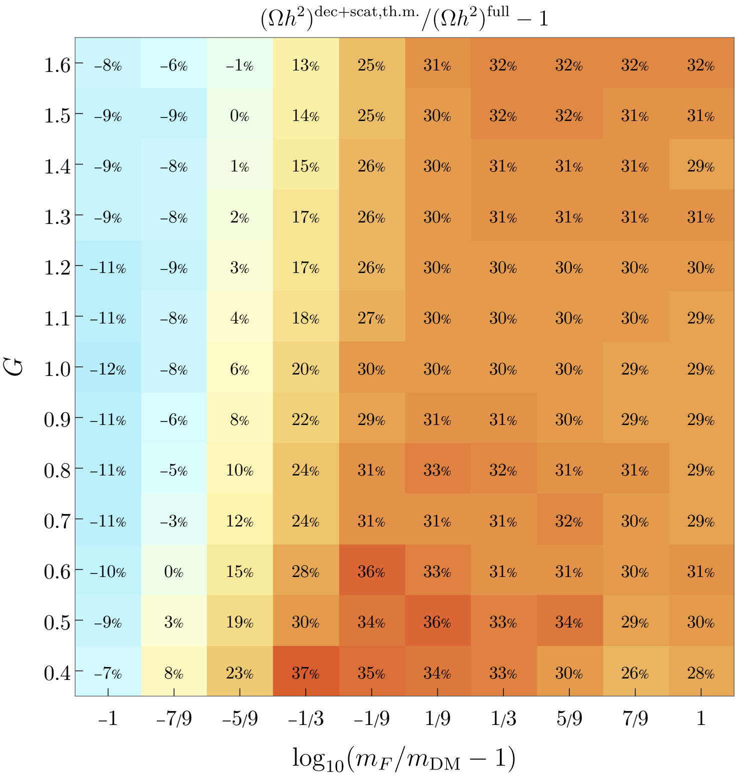

Figure VIII.8: Same caption as in Fig. VIII.5, but including thermal masses for decays as well as thermal mass-regulated scatterings. *Figure by the thesis author with and included in [5].*

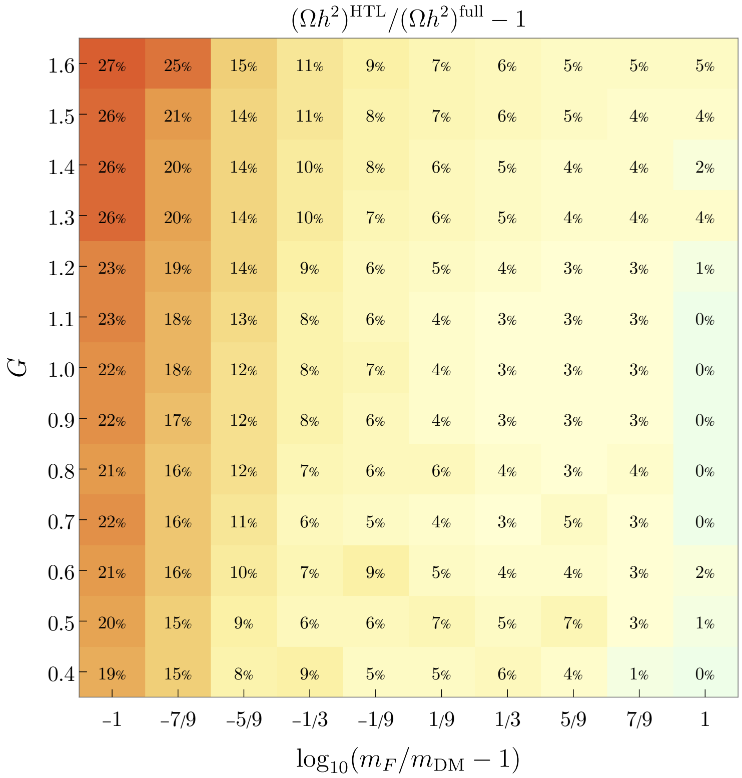

Figure VIII.9: Same caption as in Fig. VIII.5 but comparing the DM abundance using one-loop fully-resummed propagators with the one calculated with HTL-resummed propagators. *Figure by the thesis author with and included in [5].*

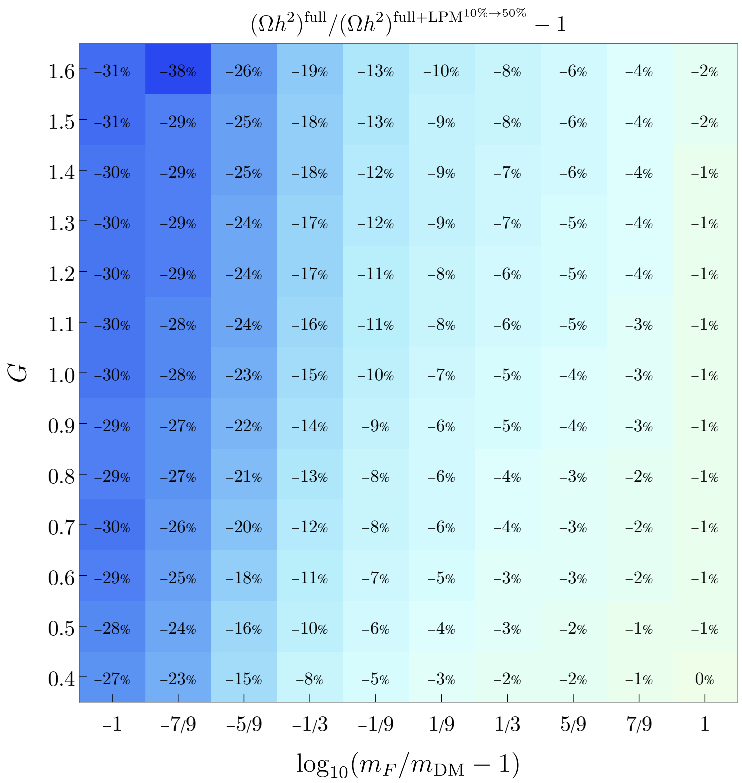

Figure VIII.10: Relative correction to the relic density calculated with 1PI-resummed propagators when further considering a 50% (10%) enhancement of the scattering rate producing DM for $\delta = 0.1$ ($\delta = 10$), the estimated contribution of the LPM effect from Ref. [432]. For mass splittings in between, we linearly interpolated the enhancement in δ. The percentage deviation is shown in colder colours when more negative. *Figure created by the thesis author with simulation data generated by the thesis author and MB and included in [5].*

VIII.4 Conclusions and Outlooks

Throughout this chapter, we carried out an *ab initio* computation of freeze-in on the closed-time path (CTP) with 1PI-resummed fermion propagators and contrasted it with semi-classical Boltzmann descriptions of increasing sophistication. We find that a decays-only Boltzmann treatment is not reliably predictive: depending on whether thermal masses are included, it can misestimate Ω_{DM} by up to $\mathcal{O}(100\%)$ ($\sim 86\%$ without thermal masses). Adding thermally regulated t-channel scatterings restores agreement at small mass splittings, down to deviations of $\mathcal{O}(-10\%)$, but tends to overproduce by $\mathcal{O}(35\%)$ when mediator decays dominate; in this regime, the deviation is largely insensitive to the effective gauge coupling G. Within the CTP framework, HTL-resummed propagators reproduce the large-hierarchy limit at the percent level, while yielding up to $\mathcal{O}(25\%)$ more DM in the compressed region, with the discrepancy increasing toward larger G. By contrast, tree-level propagators entirely miss ultrarelativistic scattering production, leading to $\mathcal{O}(100\%)$ underproduction at small δ, although they track the decay-dominated regime ($\delta \simeq 10$). These conclusions are generic for scalar DM produced through gauge-interacting vertices.

We also assessed systematic uncertainties associated with effects beyond our truncation. A naive estimate based on the LPM enhancement of scatterings could imply an additional underestimation of the relic density by up to $\sim 30\%$ at small δ; however, recent dedicated analyses for this model find that a proper LPM treatment yields substantially milder corrections, from about -10% in the nearly degenerate limit to negligible at large splittings. Gauge dependence induced by working at LO in the 2PI effective action (here in Feynman gauge) is expected to be of comparable size to the omitted higher-order corrections. Finally, in models involving top quarks, Yukawa-induced thermal corrections split the fermionic dispersion relations and can shift the relative importance of decays and scatterings; accounting for these effects will refine the quantitative comparison across methods.

Outlook

Natural extensions of this work include: (i) a first-principles treatment of the LPM effect in the present two-mass-scale setup to replace the extrapolations used in earlier estimates; (ii) going beyond LO in the 2PI truncation or employing improved resummations to reduce gauge artefacts and assess the stability of the predictions; (iii) incorporating Yukawa-induced thermal corrections from the top sector to quantify their impact, especially in the mass-compressed region. Taken together, these steps will turn the comparisons presented here into precision tools for freeze-in calculations in gauge-interacting dark sectors.

CHAPTER IX

Issues with Charged Scalars on the CTP

The scenario analyzed in the previous section relies on a simplified t-channel Dark Matter (DM) model where DM is a singlet scalar field and the mediator is a vector-like fermion, charged under the SM gauge group. Another interesting and relevant situation arises when DM is a Majorana fermion, chargeless under the SM gauge group, while the mediator is a charged complex scalar field. This scenario was examined in [1] and is thoroughly explained in Chapter V. Such a model has been extensively investigated in multiple studies addressing the freeze-out regime, where Majorana DM evades direct detection constraints via loop-suppressed couplings to gauge bosons. Meanwhile, the parent scalar can be produced at colliders and in astrophysical environments [293, 308, 319–323, 346, 347, 385, 527, 528].

Finite-temperature corrections to DM production in this model have been recently studied in [529] for co-annihilations and in [432] for freeze-in and superWIMP production, including the LPM effect, as discussed in the previous chapter. However, an analysis of such models along the lines of what we have presented in Chapter VII and in [5] has not yet been done.

This same model is commonly featured in leptogenesis scenarios where the Majorana fermion is a massive right-handed neutrino (RHN) and the charged scalar companion is the SM Higgs field. In this case, the fermion they interact with is a SM lepton, as the RHN does not couple to quarks. However, there is a small but important difference compared to the simplified DM model above: the RHN is the most massive state and eventually decays to produce the lepton asymmetry necessary for yielding a net baryon abundance via the so-called *sphaleron* non-perturbative processes [127–129, 530–533].

The mechanisms by which the baryon asymmetry of the Universe (BAU) can be created are varied and remain an active area of research. In our context, we focus on the case of a BAU produced via out-of-equilibrium decays of RHNs, resembling freeze-in production. Another difference is that the Higgs can be massless in high-scale leptogenesis scenarios, but its potential and vacuum expectation value (vev) require a TQFT treatment at and below the electroweak crossover. This contrasts with our freeze-in DM scenario where the parent is heavier in-vacuum than the DM, and where the gauge-singlet fermion is stable and does not decay away. As highlighted at the beginning of Chapter VI, leptogenesis studies using TQFT methods have a longer tradition, especially in the CTP formalism.

Understanding the implications of analyzing these models at finite temperatures in the CTP formalism is of utmost interest and remains unexplored for both DM freeze-in and leptogenesis. In fact, as far as we are aware, there are currently no complete calculations of the production rate of DM/RHNs using 1PI-resummed propagators that do not rely on perturbative approximations or HTL-resummed propagators.

In this chapter, we present advancements in this direction that could help address this problem in the future. The calculation of fundamental quantities such as self-energies and resummed propagators closely follows the case already discussed, with minor modifications. However, a major issue arises when considering the spectral properties of the resummed complex scalar propagator at finite temperature. We collect some results and thoughts regarding this issue.

Statement of Personal Contribution for this Chapter
The theoretical ideas and derivations presented in this chapter are novel though based on known results from the literature that have been used as starting point. The analysis here presented has not been published and is the result of an independent research effort conducted by the thesis' author.

IX.1 Model Lagrangian

The Lagrangian of the model reads in a similar way as the Lagrangian employed in the case of long-range effects in colored co-annihilations (cf. Eq. (V.1)). If we call the scalar mediator with the Greek letter Φ and the Majorana fermion with the Greek letter χ, the most generic Lagrangian density reads as

$$\mathcal{L} = \mathcal{L}_{\mathrm{SM}} + \mathcal{L}_{\Phi} + \mathcal{L}_{\chi} + \mathcal{L}_{\Phi\chi} + \mathcal{L}_4 \,, \tag{IX.1}$$

where

$$\mathcal{L}_{\Phi} = |D_\mu\Phi|^2 + m_\Phi^2(\Phi^\dagger\Phi) - \lambda(\Phi^\dagger\Phi)^2 + \text{mixed terms}, \tag{IX.2}$$

$$\mathcal{L}_{\chi} = \frac{1}{2}\bar{\chi}\left(\partial\!\!\!/ - m_\chi\right)\chi \tag{IX.3}$$

$$\mathcal{L}_{\chi\Phi} = -y\,\Phi\,\bar{\chi}P_{L/R}\,f_{\mathrm{SM}} + \text{h.c.}, \tag{IX.4}$$

where the summation over flavour families is implicit. The last term corresponds to scalar four-point interactions. In the leptogenesis case, there are no interactions of this type besides the Higgs quartic, already included in $\mathcal{L}_\Phi$, whereas in the DM context, there could be couplings between the dark scalar and the SM Higgs, if allowed by the symmetries of the model. For instance, these interactions could take the form of

$$\mathcal{L}_4 = -\,\lambda(H^\dagger H)(\Phi^\dagger\Phi) - A(\Phi_L H)\Phi_R + \dots\,, \tag{IX.5}$$

where the first term applies to both $SU(2)$ singlets and doublets, while the latter is analogous to the MSSM couplings which mix right-handed and left-handed sfermions.

IX.2 Rate Equation

To calculate the Majorana fermion production rate, we refer again to the CTP formalism and closely follow the derivations carried out in the previous chapters for scalar DM in the vectorlike model. The Kadanoff-Baym equations for the Majorana fermion propagators $\not{S}$ follow directly from Eq. (VI.43). After re-writing them in Wigner space (cf. Eq. (VI.3.2)), we obtain

$$\left(\not{k} - M_\chi - \not{\Sigma}_\chi^H + i\frac{1}{2}\gamma^0\partial_t\right)\not{S}_\chi^{</>} - \not{\Sigma}_\chi^{</>}\not{S}_\chi^H = \frac{1}{2}\left(\not{\Sigma}_\chi^{>}\not{S}_\chi^{<} - \not{\Sigma}_\chi^{<}\not{S}_\chi^{>}\right) \tag{IX.6}$$

$$\equiv \not{C}_\chi\,, \tag{IX.7}$$

with the r.h.s. being the collision operator. Following the same approximations employed for the case of scalar FIMP DM, we can arrive at the Boltzmann equation for the distribution function of χ, f_χ. We add Eq. (IX.7) to its hermitian conjugate, and, after rearranging the terms into commutators and anticommutators, we obtain

$$\frac{i}{2}\partial_t\left\{\gamma^0, \not{S}_\chi^{</>}\right\} + \left[\not{k} - M_\chi - \not{\Sigma}_\chi^H, \not{S}_\chi^{</>}\right] - \left[\not{\Sigma}_\chi^{</>}, \not{S}_\chi^H\right] = \not{C}_\chi + \not{C}_\chi^\dagger\,. \tag{IX.8}$$

We multiply this equation by

$$-\int\frac{\mathrm{d}p^0}{2\pi}\mathrm{sign}(p^0)\frac{1}{4}\,\mathrm{Tr}\{...\}\,.$$

which leads to

$$-\int\frac{\mathrm{d}p^0}{2\pi}\mathrm{sign}(p^0)\frac{1}{4}\,\mathrm{Tr}\left\{\frac{1}{2}\partial_t\left\{\gamma^0, i\not{S}_\chi^{<}(p)\right\}\right\} = \cdots = \partial_t f_\chi(p)\,, \tag{IX.9}$$

recovering the time derivative of the Majorana fermion distribution function. By equating this to the new r.h.s, we get

$$\partial_t f_\chi(t,p) = \frac{1}{4}\int\frac{\mathrm{d}p^0}{2\pi}\mathrm{sign}(p^0)\,\mathrm{Tr}\left\{\not{C}_\chi(p) + \not{C}_\chi^\dagger(p)\right\}, \tag{IX.10}$$

analog of Eq. (VI.95). Since the Majorana fermion is feebly-interacting, we can neglect the Hermitian self-energies in the evolution equation and simply use the tree-level propagators for $\not{S}_\chi$. Hence, we obtain

$$\begin{aligned}\partial_t f_\chi(t,p) &= \frac{1}{4}\int\frac{\mathrm{d}p^0}{2\pi}\mathrm{sign}(p^0)\,\mathrm{Tr}\left\{i\not{\Sigma}_\chi^{>}(p)i\not{S}_\chi^{<}(p) - i\not{\Sigma}_\chi^{<}(p)i\not{S}_\chi^{>}(p)\right\}.\\ &= \frac{1}{4}\int\frac{\mathrm{d}p^0}{2\pi}\mathrm{sign}(p^0)\,\mathrm{Tr}\left\{i\not{\Sigma}_\chi^{>}(p)2\not{S}_\chi^{\mathcal{A}}(p)(-f(p)) - i\not{\Sigma}_\chi^{<}(p)2\not{S}_\chi^{\mathcal{A}}(p)(1-f(p))\right\}.\end{aligned} \tag{IX.11}$$

where, in the last line, we have employed the *Kadanoff-Baym ansatz* (cf. Eq. (VI.93b)) which allows us to relate the Wightmann functions even in an out-of-equilibrium context.

We can now use the KMS relations for the Majorana fermion self-energies, since the particles involved in the one-loop diagrams up to order y^2 (a SM fermion and a dark scalar) are in thermal equilibrium:

$$i\not{\Sigma}_\chi^{>} = -2\not{\Sigma}_\chi^{\mathcal{A}} f_\chi^{\mathrm{eq}}(p)\,, \tag{IX.12}$$

$$i\not{\Sigma}_\chi^{<} = 2\not{\Sigma}_\chi^{\mathcal{A}}\left(1 - f_\chi^{\mathrm{eq}}(p)\right)\,. \tag{IX.13}$$

Thus, we obtain

$$
\begin{aligned}
\partial_t f_\chi(t,p) &= \frac{1}{4}\int \frac{\mathrm{d}p^0}{2\pi}\mathrm{sign}(p^0)\,\mathrm{Tr}\Big\{\not{\Sigma}_\chi^{\mathcal{A}}(p)\not{S}_\chi^{\mathcal{A}}(p)\Big\} \\
&\qquad\qquad \times\big[(1-f_\chi^{\mathrm{eq}}(p^0))(-f_\chi(t,p)) + f_\chi^{\mathrm{eq}}(p^0)(1-f_\chi(t,p))\big] \\
&= -\int \frac{\mathrm{d}p^0}{2\pi}\,\mathrm{Tr}\Big\{\not{p}\not{\Sigma}_\chi^{\mathcal{A}}(p)\Big\}\pi\delta(p^2-m_\chi^2)\,\big(f_\chi(t,p)-f_\chi^{\mathrm{eq}}(p^0)\big) \\
&= -\sum_{p^0=\pm\sqrt{|\vec{p}|^2+m_\chi^2}} \frac{1}{4|p^0|}\,\mathrm{Tr}\Big\{\not{p}\not{\Sigma}_\chi^{\mathcal{A}}(p)\Big\}\,\big(f_\chi(t,p)-f_\chi^{\mathrm{eq}}(p^0)\big) \\
&= -\frac{1}{2|p^0|}\,\mathrm{Tr}\Big\{\not{p}\not{\Sigma}_\chi^{\mathcal{A}}(p)\Big\}\Big|_{p^0=\sqrt{|\vec{p}|^2+m_\chi^2}}\,\big(f_\chi(t,p)-f_\chi^{\mathrm{eq}}(p^0)\big)\,.
\end{aligned}
\tag{IX.14}
$$

We identify the differential interaction rate $\Gamma_\chi(p)$ with

$$
\Gamma_\chi(|\vec{p}|) \equiv \frac{1}{2|p^0|}\,\mathrm{Tr}\Big\{\not{p}\not{\Sigma}_\chi^{\mathcal{A}}(p)\Big\}\Big|_{p^2=m_\chi^2}
\tag{IX.15}
$$

and we rewrite Eq. (IX.14) as

$$
\partial_t f_\chi(t,p) = -\Gamma_\chi(|\vec{p}|)(f_\chi(t,p)-f_\chi^{\mathrm{eq}}(p^0)) \simeq \Gamma_\chi(|\vec{p}|)\, f_\chi^{\mathrm{eq}}(p^0)|_{p^2=m_\chi^2}\,.
\tag{IX.16}
$$

In the last step, we used one of the freeze-in assumptions, namely that the FIMP particle χ has a negligible initial abundance and that back-reactions are negligible, which means $f_\chi \ll f_\chi^{\mathrm{eq}}$. By integrating over the three-momentum, we obtain the evolution equation for the FIMP number density (in analogy with Eq. (VI.98)):

$$
\frac{\mathrm{d}}{\mathrm{d}t}n_\chi = \gamma_\chi \equiv \int \frac{\mathrm{d}^3\vec{p}}{(2\pi)^3}\frac{\Pi_s^{\mathcal{A}}(\omega_p,|\vec{p}|)}{\omega_p}f_-(\omega_p)\,.
\tag{IX.17}
$$

$$
\dot{n}_\chi = \gamma_\chi \equiv \frac{2}{(2\pi)^2}\int \mathrm{d}|\vec{p}|\frac{|\vec{p}|^2}{p^0}\,\mathrm{tr}\{\not{p}\Sigma_\chi^{\mathcal{A}}(p)\}f_\chi^{\mathrm{eq}}\left(|p^0|\right)\,.
\tag{IX.18}
$$

As a final remark, the l.h.s. as it stands right now does not include the expansion of the universe because the quantities are considered as comoving. The generalization to an expanding background is straightforward and follows what we illustrated in Section VI.4, leading to the usual diffusion term in an FLRW expanding background with quantities expressed in physical coordinates

$$
\partial_t f_\chi(t,p) \longrightarrow \partial_t f_\chi(t,p) + 3Hf_\chi(t,p)\,,
\tag{IX.19}
$$

with $H=\dot{a}/a$ the Hubble rate and $a(t)$ the Universe scale factor.

IX.3 Self-Energy and Production Rate

The fermion self-energy on which the collision operator, also known as the production rate, depends is derived from the 2PI effective action of the model (cf. Section VI.3). In particular, its definition follows from Eq. (VI.35). In analogy with the discussion in Section VII.2 for a scalar DM, the 2PI effective action Γ_2 is given by a fermionic loop with a full scalar propagator inserted in between. As already clarified in the scalar DM scenario (cf. Section VII.2), we shall omit vertex-type contributions resulting from the second (NLO) term in Γ_2, which would include interference of s-channel and t-channel scatterings, as well as the LPM effect in the ultrarelativistic regime. For works addressing such corrections, we refer to [534] for the leptogenesis case and to [432] for the Majorana DM case.

On the CTP contour, the 1-loop self-energy is obtained by functionally differentiating Γ_2 or, alternatively, by following the CTP Feynman rules described in Section VII.2. In momentum space, it reads as

$$\begin{aligned}-i\not{\Sigma}_\chi^{\mathcal{A}}(p) &= ab\,y^2 \int \frac{\mathrm{d}^4k}{(2\pi)^4} \Big(P_L\, i\,\not{S}_f^{ab}(k)\, i\,\Delta_\Phi^{ba}(k-p) + P_R\, i\,\not{S}_f^{ab}(k)\, i\,\Delta_\Phi^{ba}(k-p)\Big) \\ &= -ab\,y^2 \int \frac{\mathrm{d}^4k}{(2\pi)^4}\, i\,\not{S}_f^{ab}(k)\; i\Delta^{ba}(k-p)\,. \qquad \text{(IX.20)}\end{aligned}$$

What we need is the spectral self-energy, i.e. the anti-Hermitian part of the retarded self-energy, which reads as

$$\begin{aligned}\not{\Sigma}_\chi^{\mathcal{A}}(p) &= \frac{i}{2}\left(\not{\Sigma}_\chi^{>} - \not{\Sigma}_\chi^{<}\right) = \frac{1}{2} f_+^{-1}(p^0)\,\not{\Sigma}_\chi^{<}(p) = \frac{1}{2} y^2\, f_+(p^0)^{-1} \int \frac{\mathrm{d}^4k}{(2\pi)^4}\, i\not{S}_f^{<}\, i\Delta_\Phi^{<}(p-k) \\ &= 2\,y^2 \int \frac{\mathrm{d}^4k}{(2\pi)^4}\, \not{S}_f^{\mathcal{A}}(k)\, \Delta_\Phi^{\mathcal{A}}(p-k)\left(1 + f_-(p^0-k^0) - f_+(k^0)\right)\,. \qquad \text{(IX.21)}\end{aligned}$$

To arrive at the last expression we have made use of the KMS relation between Wightmann functions (including the FIMP self-energy) as a consequence of thermal equilibrium for the fields in the self-energy loop, and we converted the same functions by making use of the fermion and scalar spectral representations. Consequently, the production rate follows by tracing over $\not{p}\not{\Sigma}_\chi^{\mathcal{A}}$, as required by Eq. (IX.15), with the trace over the Clifford algebra reducing to computing $\mathrm{Tr}\,\not{p}\not{S}_\chi^{\mathcal{A}}(p)$.

At this point, we need to ask ourselves what is the form of the propagator in the loop integral. The 2PI effective action dictates employing the formally exact (full) propagators of the theory, which are however unknown. As already done for the scalar DM vectorlike model, we shall use 1PI-resummed, HTL-resummed, and tree-level propagators. We do not need to repeat the analysis for the resummed (1PI or HTL) fermion propagator $\not{S}_f^{\mathcal{A}}$ since even in the model here examined, the dominant contribution to the SM fermion self-energy comes from its gauge interactions in the sunset diagram of Fig. VII.2. The spectral properties of a fermion in the thermal plasma were discussed at length in the previous chapters and remain applicable in our context. What remains to be understood are the properties of an in-medium scalar field, specifically by examining the structure of its resummed retarded propagator and its spectrum and damping.

IX.4 Resummed Scalar Propagator

After performing a gradient expansion of the Kadanoff-Baym equations for the two-point Green's functions of scalar fields and after taking their Wigner transform, the resummed retarded and advanced propagators read as in Eq. (VI.84), namely

$$i\Delta_\Phi^{R/A}(k) = \frac{i}{k^2 - m_\Phi^2 - \Pi_\Phi^{R/A}} = \frac{i}{k^2 - m_\Phi^2 - \Pi_\Phi^{\mathcal{H}} \pm i\Pi_\Phi^{\mathcal{A}}}\,, \qquad \text{(IX.22)}$$

where $+$ $(-)$ applies to the retarded (advanced) case and where we have introduced the Hermitian and anti-Hermitian self-energies. In analogy to Eq. (VI.85) and Eq. (VI.86), the anti-Hermitian (spectral density) and Hermitian resummed scalar propagators follow as

$$\Delta_\Phi^{\mathcal{A}} = -\Im \Delta_\Phi^R = \frac{\Pi_\Phi^{\mathcal{A}}}{\left(k^2 - m^2 - \Pi_\Phi^{\mathcal{H}}\right)^2 + \left(\Pi_\Phi^{\mathcal{A}}\right)^2}\,, \tag{IX.23}$$

$$\Delta_\Phi^{\mathcal{H}} = \Re \Delta_\Phi^R = \frac{k^2 - m^2 - \Pi_\Phi^{\mathcal{H}}}{\left(k^2 - m_\Phi^2 - \Pi_\Phi^{\mathcal{H}}\right)^2 + \left(\Pi_\Phi^{\mathcal{A}}\right)^2}\,. \tag{IX.24}$$

The Hermitian self-energy corresponds to a modification of the position of the pole describing the mass-shell and the dispersion relation, while the anti-Hermitian self-energy is interpreted as a thermal width, responsible for the damping of the scalar field correlations and its dissipation into the plasma. This is in complete analogy to and even simpler than the case for fermions, which we have discussed at length in Section VII.3.

The self-energy of the scalar field is diagrammatically given by

$-i\Pi_\Phi^{ab}(p)\ =$ 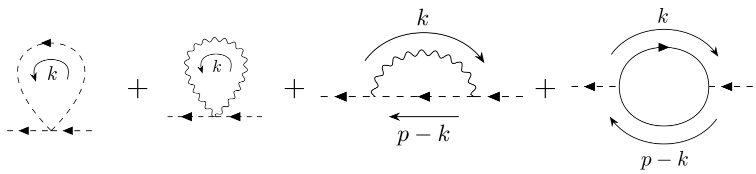 $,\qquad$ (IX.25)

where a sum over oppositely charged flow is assumed, where needed. The last diagram is proportional to the feeble coupling squared and can be safely neglected. We proceed now to calculate the self-energy contribution from the first three diagrams, which we dub as the *four-scalar*, the *seagull* (four-point interaction with gauge bosons), and the *sunset* diagrams.

We will first adopt the same strategy used in the case of resummed fermion propagators, namely, using the CTP Feynman rules and employing the Feynman gauge. This will lead to simple expressions, but to a major issue regarding the spectral sum of the resummed scalar propagator, which will result in being negative, leading to a breakdown of unitarity and causality of the theory. Possible solutions to such a problem will be explored in Section IX.5.

IX.4.1 Four-scalar

On the CTP, the self-energy reads as

$$-i\Pi_{4S}^{ab} = -i\lambda\kappa \int \frac{\mathrm{d}^4 k}{(2\pi)^4}\, i\Delta^{ab}(k)\,, \tag{IX.26}$$

where κ is a combinatorial factor from the Feynman rules related to the interaction vertex (Wick contractions). For instance, $\kappa = 6$ if only fields of the same type are involved, but $\kappa = 3$ if a vertex like $\Phi^\dagger \Phi H^\dagger H$ is involved.

For this first diagram, the anti-Hermitian part of the self-energy is identically zero, because the Wightmann self-energy is not defined. The reason is that at the interaction vertex, we would need fields sitting on both the positive and the negative time branches of the CTP contour, which is not possible. Thus,

$$\Pi_{4S}^{\mathcal{A}} = 0\,. \tag{IX.27}$$

The Hermitian part is non-vanishing and reads as

$$
\begin{aligned}
-i\Pi^{\mathcal{H}}_{4S} &= \frac{1}{2}\left((-i\Pi^{++}_{\Phi}) - (-i\Pi^{--}_{\Phi})\right) = \frac{\kappa}{2}\int \frac{\mathrm{d}^4k}{(2\pi)^4}(-i\lambda)\left(i\Delta^{++}(k) + i\Delta^{--}(k)\right) \\
&= -i\lambda\kappa \int \frac{\mathrm{d}^4k}{(2\pi)^4}\, i\Delta^F(k) = -i\lambda\kappa\int \frac{\mathrm{d}^4k}{(2\pi)^4}\left(1+2f_-(|k^0|)\right)\,\mathrm{sign}(k^0)\,\Delta^{\mathcal{A}}\,, \qquad \text{(IX.28)}
\end{aligned}
$$

where we used the relation between the statistical and the spectral propagators given by $i\Delta^F(k) = (1+2f_-(k^0))\Delta^{\mathcal{A}}(k)$. If the scalar field in the loop has an in-vacuum mass, say m_Φ, the Hermitian self-energy becomes

$$
\Pi^{\mathcal{H}}_{4S} = \kappa\lambda\int\frac{\mathrm{d}^4k}{(2\pi)^4}(1+2f_-(|k^0|))\,\pi\,\delta\Big(k^2 - m_\Phi^2\Big)\,. \qquad \text{(IX.29)}
$$

We can split the *vacuum* and the *thermal* parts, where for the first one we have

$$
\begin{aligned}
\Pi^{\mathcal{H},\mathrm{vac}}_{4S} &= \kappa\lambda\int\frac{\mathrm{d}^4k}{(2\pi)^4}\pi\delta\left(k^2-m_\Phi^2\right) = \frac{\lambda\kappa}{4\pi^2}\int_0^\Lambda \mathrm{d}k\,\frac{k^2}{\sqrt{k^2+m_\Phi^2}} \\
&= \frac{\lambda\kappa}{4\pi^2}\left[\Lambda\sqrt{\Lambda^2+m_\Phi^2} - m_\Phi^2\,\mathrm{arctanh}\left(\frac{\Lambda}{\sqrt{\Lambda^2+m_\Phi^2}}\right)\right]\,, \qquad \text{(IX.30)}
\end{aligned}
$$

where a UV cutoff was introduced. In the massless limit, $m_\Phi = 0$, this term reduces to $\lambda\kappa\Lambda^2/4\pi^2$. The thermal part is instead given by

$$
\Pi^{\mathcal{H},\mathrm{th}}_{4S} = \lambda\kappa\int\frac{\mathrm{d}^4k}{(2\pi)^4}f_-(|k^0|)2\pi\delta(k^2-m_\Phi^2) = \frac{\lambda\kappa}{2\pi^2}\int_0^\infty \mathrm{d}|\vec{k}|\,\frac{|\vec{k}|^2}{\sqrt{|\vec{k}|^2+m_\Phi^2}}f_-\left(\sqrt{|\vec{k}|^2+m_\Phi^2}\right)\,. \qquad \text{(IX.31)}
$$

This integral is finite and convergent thanks to the presence of the Bose-Einstein distribution, but has no analytical form. If we call it $\mathcal{I}(m_\Phi)$, we can find a series expansion and asymptotic behaviours which read as

$$
\begin{aligned}
\mathcal{I}(m_\Phi) &= \int_0^\infty \mathrm{d}|\vec{k}|\,\frac{|\vec{k}|^2}{\sqrt{|\vec{k}|^2+m_\Phi^2}}f_-\left(\sqrt{|\vec{k}|^2+m_\Phi^2}\right) \qquad \text{(IX.32)}\\
&= \int_{m_\Phi}^\infty \mathrm{d}y\,\frac{\sqrt{y^2-m_\Phi^2}}{e^{y/T}-1} = m_\Phi T\sum_{n=1}^\infty\frac{K_1(n\,\frac{m_\Phi}{T})}{n}\,, \qquad \text{(IX.33)}\\
&\simeq \begin{cases} \dfrac{\pi^2}{6} & m_\Phi \ll T \\ \dfrac{m_\Phi}{T}\,K_1(m_\Phi/T) & m_\Phi \gg T \end{cases}\,, \qquad \text{(IX.34)}
\end{aligned}
$$

where in the first step we have performed the change of variable $|\vec{k}| \to \sqrt{y^2-m_\Phi^2}$, while the series expansion follows from the series representation of the Bose-Einstein distribution. Thus, we see that a very massive field will have a suppressed four-scalar loop, while a massless one entails

$$
\Pi^{\mathcal{H},\mathrm{th}}_{4S} = \lambda\kappa\frac{T^2}{12}\,. \qquad \text{(IX.35)}
$$

This corresponds to the thermal mass of a scalar field (without gauge interactions).

IX.4.2 Seagull

The seagull diagram also has a vanishing anti-Hermitian part on the CTP:

$$\Pi^{\mathcal{A}}_{\text{seagull}} = 0\,. \tag{IX.36}$$

For the Hermitian part, we need to compute a similar integral as in Eq. (IX.26), with the only difference that, since we have a gauge boson in the loop, we also have to take into account the gauge couplings, the hypercharge, and the quadratic Casimirs, yielding

$$\Pi_{\Phi}^{\text{seagull},\mathcal{H}} = -\frac{1}{2}\left(2Y_{\Phi}^2 g_1^2 + \frac{3}{2}g_2^2 + \frac{8}{3}g_3^2\right)\int \frac{\mathrm{d}^4k}{(2\pi)^4} g^{\mu\nu}\, i\Delta^F_{\mu\nu}(k)\,, \tag{IX.37}$$

where we defined the effective gauge coupling in the same way as in Eq. (VII.2):

$$G = Y_{\Phi}^2 g_1^2 + \frac{3}{4}g_2^2 + \frac{4}{3}g_3^2\,. \tag{IX.38}$$

By assuming the Feynman gauge, with which we can directly substitute $\Delta_{\mu\nu} = -g_{\mu\nu}\Delta$, we can easily manipulate the expression and arrive at

$$\begin{aligned}\Pi_{\Phi}^{\text{seagull},\mathcal{H}} &= -G\int \frac{\mathrm{d}^4k}{(2\pi)^4} g^{\mu\nu}(-g_{\mu\nu}\Delta^F_{\gamma}) = 4G\int \frac{\mathrm{d}^4k}{(2\pi)^4}(1+2f_-(|k^0|))\pi\delta(k^2)\\ &= \Pi_{\Phi}^{\mathcal{H},\text{seagull,vac}} + 4G\int \frac{\mathrm{d}^4k}{(2\pi)^3}\delta(k^2)f_-(|k^0|)\\ &= \frac{G\Lambda^2}{2\pi^2} + \frac{1}{3}GT^2,\end{aligned} \tag{IX.39}$$

where we recognize the vacuum term and the correction to the scalar field thermal mass. It is independent of whether the external scalar is massive or not.

IX.4.3 Sunset

The sunset diagram is more complicated due to the explicit dependence on the external momentum p, which on the CTP yields the following self-energy

$$-i\Pi_{\Phi}^{ab,\,\text{sunset}}(p) = -G\int \frac{\mathrm{d}^4k}{(2\pi)^4}(p+k)^{\mu}(p+k)^{\nu}\, i\Delta^{ab}_{\gamma,\mu\nu}(p-k)\, i\Delta^{ab}_{\Phi}(k)\,. \tag{IX.40}$$

We consider the case of the Feynman gauge again and substitute $\Delta_{\mu\nu} = -g_{\mu\nu}\Delta$.

Hermitian Part

The Hermitian part follows from its definition in Eq. (VI.26) and, after some manipulation, it reads as

$$\begin{aligned}\Pi_{\Phi}^{\mathcal{H},\,\text{sunset}} = -\frac{G}{2}\int \frac{\mathrm{d}^4k}{(2\pi)^3}(p+k)^2\Bigg[&\mathcal{P}\frac{\delta((p-k)^2)}{k^2-m_{\Phi}^2}(1+2f_-(|p^0-k^0|))\\ &+\mathcal{P}\frac{\delta(k^2-m_{\Phi}^2)}{(p-k)^2}(1+2f_-(|k^0|))\Bigg]\,.\end{aligned} \tag{IX.41}$$

Now, we divide it into *vacuum* (without f_-) and *thermal* contribution. The vacuum one has an intricate expression and is not of interest to our discussion here. Moreover, in the second term, we perform the variable shift $k \to p-k$ and we obtain

$$\Pi_{\Phi}^{\mathcal{H}} = \Pi_{\Phi}^{\mathcal{H},\text{vac.}} - G\int \frac{\mathrm{d}^4k}{(2\pi)^3}\left[(2p-k)^2\mathcal{P}\frac{\delta(k^2)}{(p-k)^2-m_{\Phi}^2} + (p+k)^2\mathcal{P}\frac{\delta(k^2-m_{\Phi}^2)}{(p-k)^2}\right]f_-(|k^0|)\,. \tag{IX.42}$$

We immediately integrate the thermal part over $\mathrm{d}\phi$ and over $\mathrm{d}k^0$ and then over $\mathrm{d}\cos\theta$ to obtain

$$
\begin{aligned}
&-\frac{G}{4\pi^2}\int \mathrm{d}|\vec{k}|\mathrm{d}\cos\theta\,|\vec{k}|^2\sum_{\pm}\Bigg\{\frac{1}{2|\vec{k}|}\frac{4p^2\mp 4p^0|\vec{k}|+4|\vec{p}||\vec{k}|\cos\theta}{p^2-m_\Phi^2\mp 2p^0|\vec{k}|+2|\vec{p}||\vec{k}|\cos\theta}f_-(|\vec{k}|)\\
&\qquad\qquad+\frac{1}{2\sqrt{|\vec{k}|^2+m_\Phi^2}}\frac{p^2+m_\Phi^2\pm 2p^0\sqrt{|\vec{k}|^2+m_\Phi^2}-2|\vec{p}||\vec{k}|\cos\theta}{p^2+m_\Phi^2\mp 2p^0\sqrt{|\vec{k}|^2+m_\Phi^2}+2|\vec{p}||\vec{k}|\cos\theta}f_-\left(\sqrt{|\vec{k}|^2+m_\Phi^2}\right)\Bigg\}\\
&=(\ldots)\\
&=-\frac{G}{6}T^2-\frac{G}{4\pi^2}\int\mathrm{d}|\vec{k}|\Bigg\{-\frac{2|\vec{k}|^2}{\sqrt{|\vec{k}|^2+m_\Phi^2}}f_-\left(\sqrt{|\vec{k}|^2+m_\Phi^2}\right)\\
&+\frac{p^2+m_\Phi^2}{2|\vec{p}|}\sum_{\pm}\left(\frac{|\vec{k}|}{\sqrt{|\vec{k}|^2+m_\Phi^2}}\ln\left|\frac{p^2+m_\Phi^2\mp 2p^0\sqrt{|\vec{k}|^2+m_\Phi^2}+2|\vec{p}||\vec{k}|}{p^2+m_\Phi^2\mp 2p^0\sqrt{|\vec{k}|^2+m_\Phi^2}-2|\vec{p}||\vec{k}|}\right|f_-\left(\sqrt{|\vec{k}|^2+m_\Phi^2}\right)\right)\\
&+\ln\left|\frac{p^2-m_\Phi^2\mp 2p^0|\vec{k}|+2|\vec{p}||\vec{k}|}{p^2-m_\Phi^2\mp 2p^0|\vec{k}|-2|\vec{p}||\vec{k}|}\right|f_-(|\vec{k}|)\Bigg\}\,. \qquad \text{(IX.43)}
\end{aligned}
$$

In the first step, we left the contribution of the two delta functions from integration over $\mathrm{d}k^0$ implicitly given in the sum, where $\pm$ stems from $k^0=\pm|\vec{k}|$. In the second equality, we integrated over $\cos\theta$, which can be performed analytically but requires some steps. The final expression cannot be further simplified and needs to be computed numerically. Combining Eqs. (IX.31), (IX.39) and (IX.43), we obtain the total Hermitian self-energy, which we could also dub as the momentum-dependent thermal mass correction to the dispersion relation of the scalar field in-medium.

In the limit with massless scalars $m_\Phi\to 0$ (e.g., in leptogenesis scenarios), the integrands of the sunset diagram massively simplify, yielding the following result

$$
\begin{aligned}
\Pi^{\mathcal{H},T\neq 0}|^{\text{sunset}}_{m_\Phi=0}&=\frac{-G}{2\pi^2}\int\mathrm{d}|\vec{k}|\,|\vec{k}|f_-(|\vec{k}|)-\frac{G}{4\pi^2}\frac{p^2}{|\vec{p}|}\int\mathrm{d}|\vec{k}|\sum_{\pm}\ln\left|\frac{p^2\mp 2p^0|\vec{k}|+2|\vec{p}||\vec{k}|}{p^2\mp 2p^0|\vec{k}|-2|\vec{p}||\vec{k}|}\right|f_-(|\vec{k}|)\\
&=-\frac{GT^2}{12}-\frac{G}{4\pi^2}\frac{p^2}{|\vec{p}|}\int\mathrm{d}|\vec{k}|\sum_{\pm}\ln\left|\frac{p^2\mp 2p^0|\vec{k}|+2|\vec{p}||\vec{k}|}{p^2\mp 2p^0|\vec{k}|-2|\vec{p}||\vec{k}|}\right|f_-(|\vec{k}|)\,. \qquad \text{(IX.44)}
\end{aligned}
$$

The total temperature-dependent Hermitian self-energy for a massless scalar field is thus given by

$$
\Pi^{\mathcal{H},T\neq 0}|_{m_\Phi=0}=\frac{\lambda\kappa T^2}{12}+\frac{GT^2}{4}-\frac{G}{4\pi^2}\frac{p^2}{|\vec{p}|}\int\mathrm{d}|\vec{k}|\sum_{\pm}\ln\left|\frac{p^2\mp 2p^0|\vec{k}|+2|\vec{p}||\vec{k}|}{p^2\mp 2p^0|\vec{k}|-2|\vec{p}||\vec{k}|}\right|f_-(|\vec{k}|)\,. \qquad \text{(IX.45)}
$$

Notice that the second term vanishes if we take the HTL limit, namely if we assume that the loop momentum is much larger than the external one, $k\gg p$, so that we recover the well-known HTL thermal mass for a complex gauge-charged scalar, which is

$$
m_\Phi^{\text{th}}=\frac{\lambda\kappa T^2}{12}+\frac{GT^2}{4}\,. \qquad \text{(IX.46)}
$$

With the external momentum dependence, the integral has to be computed numerically.

Anti-Hermitian Part

The sunset diagram also contains an anti-Hermitian part, which is the spectral self-energy of the scalar field. This reads as

$$\begin{aligned}i\Pi^{\mathcal{A}}(p) &= \frac{1}{2}\left(i\Pi^{>}(p) - i\Pi^{<}(p)\right)\\ &= G\int\frac{\mathrm{d}^4k}{(2\pi)^4}\,(p+k)^\mu(p+k)^\nu\,\frac{1}{2}\left(i\Delta^{>}_{\Phi}(k)\,i\Delta^{>}_{\gamma,\mu\nu}(p-k) - i\Delta^{<}_{\Phi}(k)\,i\Delta^{<}_{\gamma,\mu\nu}(p-k)\right)\,.\end{aligned} \tag{IX.47}$$

By employing the Feynman gauge ($\Delta_{\mu\nu} = -g_{\mu\nu}\Delta$) and the KMS relations for both the vector and the scalar propagators (cf. Eq. (VI.58)), we end up with

$$\begin{aligned}\Pi^{\mathcal{A}}(p) = -2\pi^2 G\int\frac{\mathrm{d}^4k}{(2\pi)^4}\,(p+k)^2\,\delta(k^2-m_\Phi^2)\,\delta((p-k)^2)\\ \times\,\mathrm{sign}(k^0)\mathrm{sign}(p^0-k^0)\left[1+f_-(k^0)+f_-(p^0-k^0)\right],\end{aligned} \tag{IX.48}$$

where the delta functions come from the tree-level propagators, i.e., considering the fields in the loop as *on-shell*. We change integration variables as in Eq. (VII.139) to

$$\mathrm{d}^4k = \frac{1}{2|\vec{p}|}\mathrm{d}\phi\,\mathrm{d}k^0\;\mathrm{d}(p\cdot k)\;\mathrm{d}(k^2)\,, \tag{IX.49}$$

so that we can easily exploit the two delta functions to carry out the $\mathrm{d}k^2$ and the $\mathrm{d}(p\cdot k)$ integrations, while the azimuthal integration over $\mathrm{d}\phi$ is trivially realized. We obtain

$$\begin{aligned}\Pi^{\mathcal{A}}(p) &= -\frac{G}{8\pi}\frac{p^2+m_\Phi^2}{|\vec{p}|}\int_{\mathcal{B}}\mathrm{d}k^0\,\mathrm{sign}(k^0)\mathrm{sign}(p^0-k^0)\left[1+f_-(k^0)+f_-(p^0-k^0)\right]\\ &= -\frac{G}{8\pi}\frac{p^2+m_\Phi^2}{|\vec{p}|}\mathrm{sign}(p^2-m_\Phi^2)\int_{\mathcal{B}}\mathrm{d}k^0\,\left[1+f_- - (k^0)+f_-(p^0-k^0)\right]\,.\end{aligned} \tag{IX.50}$$

In the second line, we have used the property that, since the particles are on-shell, the following equality holds

$$\mathrm{sign}(p^2-m_\Phi^2) = \mathrm{sign}(k^0)\,\mathrm{sign}(p^0-k^0)\,. \tag{IX.51}$$

This is easy to show via a particle kinematics argument. Consider an initial-state momentum p and two final-state momenta k and q, for which $k^2 = m_1^2$ and $q^2 = m_2^2$. Energy-momentum conservation dictates that $p^\mu = q^\mu + k^\mu$. By squaring this relation and by using the on-shell conditions, one obtains

$$\begin{aligned}p^2 - m_1^2 - m_2^2 &= 2q^0k^0 - 2|\vec{q}||\vec{k}|\cos\theta\\ &= 2q^0k^0\left(1 - \frac{|\vec{q}||\vec{k}|}{|q^0||k^0|}\frac{\cos\theta}{\mathrm{sign}(q^0k^0)}\right)\,.\end{aligned}$$

Since $|q^0|\geq|\vec{q}|$ and $|k^0|\geq|\vec{k}|$, the term in the parentheses is always greater than or equal to zero. Hence,

$$\mathrm{sign}(p^2-m_1^2-m_2^2) = \mathrm{sign}(q^0)\mathrm{sign}(k^0).$$

By substituting q with $p-k$, we get the result in Eq. (IX.51).

The integral is evaluated as

$$\int_{\mathcal{B}} \mathrm{d}k^0 \, \left[1 + f_- - (k^0) + f_-(p^0 - k^0)\right] = \left[-k^0 - T \ln \left| \frac{f_-(k^0)}{f_-(p^0 - k^0)} \right| \right]_{\mathcal{B}} \tag{IX.52}$$

where the integration boundaries are such that

$$\mathcal{I}(k^0)\Big|_{\mathcal{B}} = \mathcal{I}(k^0) \left[\theta(p^2)\Big|_{k_-^0}^{k_+^0} + \theta(-p^2) \left(\Big|_{-\infty}^{k_+^0} + \Big|_{k_-^0}^{+\infty} \right)\right] \tag{IX.53}$$

$$= \mathcal{I}(k^0) \left(\Big|_{k_-^0}^{k_+^0} + \theta(-p^2) \Big|_{-\infty}^{+\infty} \right) , \tag{IX.54}$$

with

$$k_\pm^0 = \frac{p^0}{2p^2}(p^2 + m_\Phi^2 - m_\gamma^2) \pm \frac{|\vec{p}|}{2p^2} \sqrt{\lambda(p^2, m_\Phi^2, m_\gamma^2)} \underset{m_\gamma = 0}{\longrightarrow} \frac{p^0}{2p^2}(p^2 + m_\Phi^2) \pm \frac{|\vec{p}|}{2p^2} \left|p^2 - m_\Phi^2\right| . \tag{IX.55}$$

One can check that the integration in $\theta(-p^2)\mathcal{I}|_{-\infty}^{+\infty}$ does not vanish, for example by using a UV regulator in this way:

$$\lim_{\Lambda\to\infty} \int_{-\Lambda}^{\Lambda} \mathrm{d}k^0 (1 + f_-(k^0) + f_-(p^0 - k^0)) = \lim_{\Lambda\to\infty} -2\Lambda - T \ln \left| \frac{f_-(\Lambda)}{f_-(p^0 - \Lambda)} \frac{f_-(p^0 + \Lambda)}{f_-(-\Lambda)} \right| = p^0, \tag{IX.56}$$

where we used the fact that $f_-(\Lambda) \simeq e^{-\Lambda}$, $f_-(-\Lambda) \simeq -1$, $f_-(p^0 - \Lambda) \simeq -1$, and $f_-(p^0 + \Lambda) \simeq e^{-(p^0 + \Lambda)}$. We therefore remain with

$$\mathcal{I}(k^0)\Big|_{\mathcal{B}} = \theta(-p^2)p^0 + k_-^0 - k_+^0 + T \ln \left| \frac{f_-(k_-^0) f_-(p^0 - k_+^0)}{f_-(p^0 - k_-^0) f_-(k_+^0)} \right|, \tag{IX.57}$$

and the spectral self-energy results in

$$\Pi^{\mathcal{A}}(p) = -\frac{G}{8\pi} \frac{p^2 + m_\Phi^2}{|\vec{p}|} \mathrm{sign}(p^2 - m_\Phi^2) \left[\theta(-p^2)p^0 + k_-^0 - k_+^0 + \ln \left| \frac{f_-(k_-^0) f_-(p^0 - k_+^0)}{f_-(k_+^0) f_-(p^0 - k_-^0)} \right| \right] . \tag{IX.58}$$

In the massless limit, $m_\Phi = 0$, this simplifies to

$$\begin{aligned}
\Pi^{\mathcal{A}}(p) &= -\frac{G}{8\pi} \frac{p^2}{|\vec{p}|} \mathrm{sign}(p^2) \left[\theta(-p^2)p^0 - |\vec{p}| \, \mathrm{sign}(p^2) + 2T \ln \left| \frac{1 - e^{\frac{p^0 + |\vec{p}| \mathrm{sign}(p^2)}{2T}}}{1 - e^{\frac{p^0 - |\vec{p}| \, \mathrm{sign}(p^2)}{2T}}} \right| \right] \\
&= \frac{G}{8\pi} \frac{p^2}{|\vec{p}|} \left[p^0 \theta(-p^2) + |\vec{p}| - 2T \mathrm{sign}(p^2) \ln \left| \frac{1 - e^{\frac{p^0 + |\vec{p}| \mathrm{sign}(p^2)}{2T}}}{1 - e^{\frac{p^0 - |\vec{p}| \, \mathrm{sign}(p^2)}{2T}}} \right| \right] .
\end{aligned} \tag{IX.59}$$

Now, this self-energy contains both the "vacuum" and the "thermal" parts

$$\Pi^{\mathcal{A}} = \Pi^{\mathcal{A},\mathrm{vac.}} + \Pi^{\mathcal{A},T\neq 0}. \tag{IX.60}$$

The vacuum term is easy to derive and is simply

$$\begin{aligned}
\Pi^{\mathcal{A},\mathrm{vac.}} &= -\frac{G}{16\pi} \frac{p^2}{|\vec{p}|} \int_{\mathcal{B}} \left(\mathrm{sign}(k^0) + \mathrm{sign}(p^0 - k^0)\right) \\
&= -\frac{G}{8\pi} \frac{p^2}{|\vec{p}|} (k_+^0 - k_-^0) \theta(p^2) \mathrm{sign}(p^0)
\end{aligned}$$

$$= -\frac{G}{8\pi} p^2 \theta(p^2) \mathrm{sign}(p^0) \,, \tag{IX.61}$$

where we used the fact that, since $\mathrm{sign}(k^0)\mathrm{sign}(p^0 - k^0) = \mathrm{sign}(p^2)$, the integrand does not vanish only if $p^2 > 0$. This also implies that the vacuum spectral self-energy for lightlike and spacelike external momenta is zero (in the massless scenario considered here). In addition, the total sign of the sum inside the integral depends on the sign of p^0, as can be explicitly checked. We can subtract this term from the total spectral self-energy in Eq. (IX.59) to obtain the temperature-dependent part

$$\begin{aligned}\Pi^{\mathcal{A},T\neq 0} &= \Pi^{\mathcal{A}} - \Pi^{\mathcal{A},\mathrm{vac.}} \\ &= \frac{G}{8\pi}\frac{p^2}{|\vec{p}|}\left[\theta(-p^2)p^0 + |\vec{p}|(1+\theta(p^2)\mathrm{sign}(p^0)) - 2T\mathrm{sign}(p^2)\ln\left|\frac{1-e^{\frac{p^0+|\vec{p}|\mathrm{sign}(p^2)}{2T}}}{1-e^{\frac{p^0-|\vec{p}|\mathrm{sign}(p^2)}{2T}}}\right|\right]\end{aligned} \tag{IX.62}$$

$$= \frac{G}{8\pi}\frac{p^2}{|\vec{p}|} \times \begin{cases} 2|\vec{p}|\theta(p^0) - 2\ln\left|\dfrac{1-e^{\frac{p^0+|\vec{p}|}{2}}}{1-e^{\frac{p^0-|\vec{p}|}{2}}}\right| & \text{if} \quad p^2 > 0 \\ p^0 + |\vec{p}| - 2\ln\left|\dfrac{1-e^{\frac{p^0+|\vec{p}|}{2}}}{1-e^{\frac{p^0-|\vec{p}|}{2}}}\right| & \text{if} \quad p^2 < 0 \end{cases} \,, \tag{IX.63}$$

where in the first line with $p^2 > 0$ we used $1 + \mathrm{sign}(p^0) = 2\theta(p^0)$. We will now focus on the massless case, because of its more manageable expressions, while the same conclusions hold for a massive scalar. The anti-Hermitian part of the retarded self-energy for a massless charged scalar is plotted against p^0/T with solid lines in the upper panel of Fig. IX.1 together with its Hermitian part in opaque dashed lines for four different values of $|\vec{p}|/T$ corresponding to $|\vec{p}|/T = 0.1, 0.5, 1.0, 1.5$ and for $G = 1$. Notice how the first is odd in p^0, while the second is even, as expected. Combining these two functions into Eq. (IX.23) yields the resummed scalar propagator in the lower panel for the same choice of momenta. Notice the on-shell resonances about the quasi-particle poles.

However, the spectral density is found to be *negative* for positive p^0. This is a consequence of $\Pi^{\mathcal{A}}$ turning negative when going from spacelike momenta (inner part of the plot) to timelike momenta (outer part). This is a problem for two reasons. First, $\Pi^{\mathcal{A}}$ is associated with the width of the scalar and it is proportional to its decay (damping) rate in-vacuum (in-medium). Therefore, a negative self-energy for timelike momenta implies a negative rate, which is obviously nonsense. Second, because the sign of the resummed spectral density (the resummed anti-Hermitian propagator $\Delta^{\mathcal{A}}$ in Eq. (IX.23)) is the sign of $\Pi^{\mathcal{A}}$, we need to check if the *spectral sum* of the scalar propagator, which comes from requiring that the theory is canonically quantized (cf. Eq. (VI.13)) and is unitary and causal, is correct, namely that

$$\int \frac{\mathrm{d}k^0}{\pi}\, k^0\, \Delta^{\mathcal{A}}(k) = 1 \,. \tag{IX.64}$$

For a tree-level propagator, where the spectral self-energy is zero and spectral densities are delta functions, this is trivially realized, also in the massive case. For a 1PI-resummed propagator, we have instead

$$\int \frac{\mathrm{d}k^0}{\pi}\, k^0\, \Delta^{\mathcal{A}}(k) = \int \frac{\mathrm{d}k^0}{\pi}\, k^0\, \frac{\Pi^{\mathcal{A}}_{\Phi}}{\left(k^2 - \Pi^{\mathcal{H}}_{\Phi}\right)^2 + \left(\Pi^{\mathcal{A}}_{\Phi}\right)^2} \,, \tag{IX.65}$$

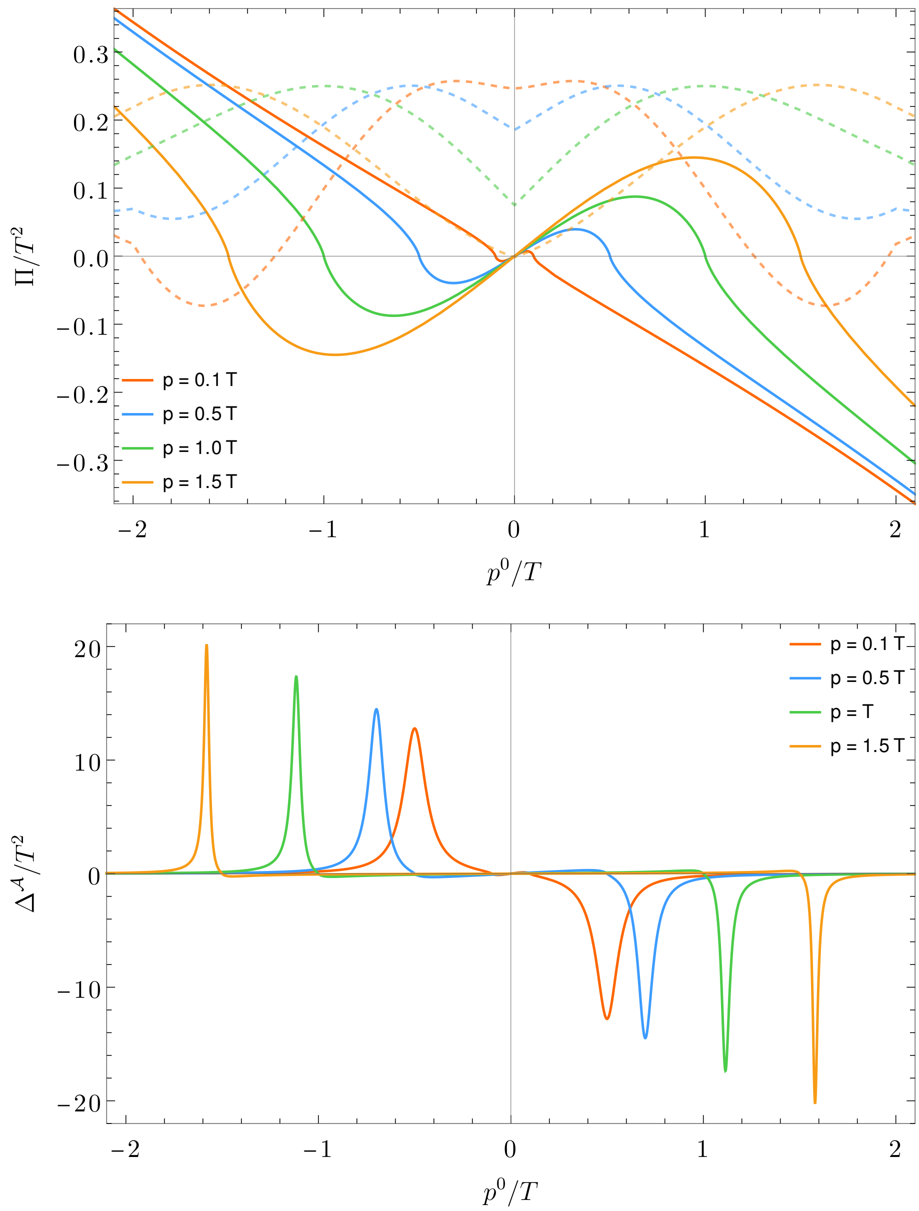

Figure IX.1: *Upper panel:* shown is the anti-Hermitian $\Pi^{\mathcal{A}}$ (Hermitian $\Pi^{\mathcal{H}}$) self-energy in solid (dashed faded) lines of a massless charged scalar as a function of p^0/T for four fixed values of the three-momentum magnitude p/T. Notice the anti-symmetrical (symmetrical) behavior in p^0. *Lower panel:* Spectral density $\Delta^{\mathcal{A}}$ from Eq. (IX.23). Notice the resonances close to the quasi-particle poles and the ill-behaved opposite sign. For these plots, we set $G = 1$.

If we define $\mu^2 \equiv \Pi^{\mathcal{H}}$ and if we assume the narrow-width-approximation (NWA) for which $\Pi^{\mathcal{A}}(k) \equiv k_0\,\Gamma$, we can rewrite the integrand as [479]

$$\frac{\Pi^{\mathcal{A}}_{\Phi}}{\left(k^2 - \Pi^{\mathcal{H}}_{\Phi}\right)^2 + \left(\Pi^{\mathcal{A}}_{\Phi}\right)^2} \longrightarrow \frac{k_0\,\Gamma}{\left(k_0^2 - \left(|\vec{k}|^2 + \mu^2\right)\right)^2 + k_0^2\Gamma^2}\,. \tag{IX.66}$$

The denominator has poles whenever the quartic equation for k_0 is satisfied,

$$k_0^4 - +k_0^2\left[\Gamma^2 - 2(|\vec{k}|^2 + \mu^2)\right] + \left(|\vec{k}|^2 + \mu^2\right)^2 = 0 \tag{IX.67}$$

$$\implies k_0 = \sqrt{\mu^2 + |\vec{k}|^2 - \frac{\Gamma}{2}\left(\Gamma \mp \sqrt{\Gamma^2 - 4\left(|\vec{k}|^2 + \mu^2\right)}\right)} \equiv \omega^\pm\,, \tag{IX.68}$$

so that the integral becomes

$$\int \frac{\mathrm{d}k^0}{\pi} \frac{k_0^2\Gamma}{(k_0-\omega^+)(k_0+\omega^+)(k_0-\omega^-)(k_0+\omega^-)} \simeq \mathrm{sign}(\Gamma)\,. \tag{IX.69}$$

Here, we used the Cauchy integration formula over a closed contour in the upper k_0 complex plane. This result qualitatively shows that the positivity of the spectral sum depends on the sign of the width in the NWA. An analogous result is found for a massive scalar field; only the definition of μ changes.

To have a more quantitative understanding, we directly compute the spectral sum for a massless scalar field by using the full expressions in Eqs. (IX.45) and (IX.59).

The spectral density is plotted in Fig. IX.1 as a function of the zeroth component of the scalar 4-momentum.

IX.5 Restoring the Spectral Sum

To the best of our knowledge, the issue of restoring the spectral sum of the 1PI-resummed gauge-charged scalar propagator has not been thoroughly addressed in the literature, with the notable exception of the attempt and indications provided in [479]. In that work, it is suggested that the negativity of the spectral function might be related to the non-self-consistent calculation of the resummed Higgs propagator due to the truncation of the Schwinger-Dyson equations. The author speculates that a self-consistent solution could resolve this issue, which we will briefly revisit in Section IX.5.3.

The most straightforward solution involves using an HTL-approximated form of the propagator. In this approximation, the thermal width, i.e., the anti-Hermitian part of the self-energy, is identically zero, and the resummed spectral density takes the form of a Dirac delta function centered at the mass-shell of the in-medium quasi-particle. The dispersion relation of this quasi-particle is modified by the Hermitian part of the retarded self-energy, resulting in a momentum-independent thermal mass:

$$\Pi^{\mathcal{A}} = 0, \qquad \Pi^{\mathcal{H}} = m_{\mathrm{th}}^2 = \left(\frac{\lambda\kappa}{12} + \frac{G}{4}\right) T^2, \tag{IX.70}$$

$$\Delta^{\mathcal{A}} = \pi\delta(p^2 - m_{\mathrm{th}}^2), \qquad \Delta^{\mathcal{H}} = \mathrm{PV}\frac{1}{p^2 - m_{\mathrm{th}}^2}. \tag{IX.71}$$

In this way, the resummed spectral density has the same form as the tree-level one, so that the spectral sum is automatically satisfied and the interaction rate has no pathology. In particular, the HTL interaction rate for the Majorana fermion FIMP follows from taking the trace $\mathrm{tr}\left\{\not{p}\Sigma_\chi^{\mathcal{A}}\right\}$ with the spectral self-energy given in Eq. (IX.21) with an HTL scalar spectral density as in Eq. (IX.71) and an HTL fermion spectral density as in Eq. (VII.113). In the high-temperature limit, we can instead use the tree-level propagators for both scalars and fermions (delta functions) with in-vacuum and thermal masses in their dispersion relations.

Why this is the case could be related to issues with gauge invariance. As mentioned in VIII.2, the truncation of the 2PI effective action inevitably introduces gauge dependencies due to the omission of higher-order diagrams whose gauge-dependent part would lead to an overall satisfaction of the Nielsen identities of the theory. The fact that the formally exact 2PI effective action is gauge-independent has been demonstrated in [476, 524, 525], where it has also been shown that gauge-dependencies come at higher orders in the truncation. As shown in [535], the spectral densities for gauge-charged vectorlike fermions have a subleading dependence on the gauge fixing parameter and are not expected to change the DM rate sensitively. However, the fact that the HTL resummation leads to gauge-independent quantities [436] could be the reason why the HTL scalar spectral density has a regular spectral sum.

IX.5.1 Gauge Dependencies

To further investigate this possibility, we need to better understand how gauge interactions work at finite temperatures. So far, we have always carried out our calculations in the Feynman gauge, which is a particular gauge fixing choice among the infinitely many in the class of covariant gauges given by the Lagrangian term

$$\mathcal{L}_{\rm gf} = \frac{1}{2\xi}(\partial_\mu A^\mu)^2. \tag{IX.72}$$

The Feynman gauge corresponds to setting $\xi = 1$. In vacuum QFT, assuming a generic value of ξ leads to the following gauge boson retarded propagator [483]

$$\Delta_{\mu\nu}(k) = \left(-g_{\mu\nu} + (1-\xi)\frac{k_\mu k_\nu}{k^2}\right)\frac{1}{k^2}\,, \tag{IX.73}$$

and the Feynman gauge simply corresponds to having $\Delta_{\mu\nu}(k) = -g_{\mu\nu}/k^2 = -g_{\mu\nu}\Delta(k)$, where $\Delta(k)$ is the retarded propagator of a scalar field. The last relation is exactly what was assumed in the previous sections, extending its validity to *all* CTP propagators at finite temperatures, in particular to the gauge boson spectral density. Is this, in general, a correct assumption? Can it be extended to a generic gauge?

A naive computation gives us a practical answer. Let us consider the case of the Hermitian self-energy from the sunset diagram as in Section IX.4.3. By inserting the expression in Eq. (IX.73) in Eq. (IX.40) and by manipulating the expression similarly to how we arrived at Eq. (IX.42), one realizes that the integrand has a term that goes like

$$\int \frac{\mathrm{d}^4k}{(2\pi)^4}(2p-k)^\mu(2p-k)^\nu\left(-g_{\mu\nu} + (1-\xi)\frac{k_\mu k_\nu}{k^2}\right)2\pi\delta(k^2)\frac{1}{(p-k)^2 - m_\Phi^2}f_-(|k^0|) + \dots\,. \tag{IX.74}$$

The expression above cannot be integrated because it is singular in k. The on-shellness condition imposed by the delta function makes it impossible to perform the integration for the term proportional to $(1-\xi)/k^2$, which is divergent. Indeed, it can be verified that no cancellation occurs and that this expression is ill-defined. Notice that the Feynman gauge circumvents this issue by setting such a term to zero from the beginning,

It looks like a direct extension of Eq. (IX.73) to the CTP contour is simply wrong. Indeed, this was acknowledged in the mid-80s [422, 426, 536–539], where it was shown that a path-integral quantization at thermal equilibrium with a covariant gauge fixing Lagrangian leads to the following gauge boson propagator

$$iD^{ab}_{\mu\nu}(k) = \left(-g_{\mu\nu} + (1-\xi)k_\mu k_\nu\frac{\partial}{\partial k^2}\right)iD^{ab}(k)\,, \tag{IX.75}$$

where $i\Delta^{ab}(p)$ is the usual CTP scalar propagator. The novelty here is encoded in the derivative wrt. k^2 instead of a multiplying factor $1/k^2$, an expedient that can make the integral in Eq. (IX.74) non singular.

However, it was later noticed by Landshoff and Rebhan in 1992 [540] that this trick does not solve the issue of thermalizing unphysical degrees of freedom, i.e., the ghost fields introduced via the Faddeev-Popov trick [541]. A correct treatment would give a thermal part only to the two physical vector boson states and leave unphysical states and ghosts to the vacuum part for the right quantization of the theory. This is exactly what the Landshoff and Rebhan prescription (from now on *LR*) in [540] does and we briefly repeat their argument (cf. also [542–544]). In thermal field theory, the partition function and thermal averages are defined as

$$Z = \sum_i \langle i|e^{-\beta\hat{H}}|i\rangle \ , \tag{IX.76}$$

$$\left\langle \hat{O} \right\rangle = \sum_i \langle i|e^{-\beta\hat{H}}\hat{O}|i\rangle \ . \tag{IX.77}$$

In both cases, the sum is over a complete orthonormal set of physical states $|i, \mathrm{phys}\rangle$, which, in the case of scalar field theories, span the entire Hilbert space, so one may replace the sums with traces of the operators:

$$Z = \sum_i \langle i|e^{-\beta\hat{H}}|i\rangle \longrightarrow \mathrm{tr}\left\{e^{-\beta\hat{H}}\right\}, \tag{IX.78}$$

$$\left\langle \hat{O} \right\rangle = \sum_i \langle i|e^{-\beta\hat{H}}\hat{O}|i\rangle \longrightarrow \mathrm{tr}\left\{e^{-\beta\hat{H}}\hat{O}\right\}. \tag{IX.79}$$

However, in the case of a gauge theory, the Hilbert space also contains unphysical states and one needs a gauge fixing procedure to get rid of them when computing physical observables. As well known, the traditional way is to cancel the contribution from these redundant states by introducing ghost fields [545, 546]. The point of [540] is to directly perform the sum with only physical states from the beginning so that only these acquire a thermal part and can be put on-shell. The derivation follows the Gupta-Bleuler procedure [547, 548] and will not be repeated here. The results are given as follows.

The sum over the polarization tensors $\epsilon^\mu_\lambda(k)$ in a covariant gauge as imposed by Eq. (IX.72) takes the general form

$$\sum_{\lambda=1}^{2} \epsilon^\mu_\lambda(k)\epsilon^\nu_\lambda(k) \equiv T^{\mu\nu} = -G^{\mu\nu} + \frac{u^\mu k^\nu + u^\nu k^\mu}{u\cdot k} - u^2\frac{k^\mu k^\nu}{(u\cdot k)^2}\,, \tag{IX.80}$$

where we took polarization vectors orthogonal to u^μ, the plasma 4-velocity, and to k^μ, and where the modified metric $G^{\mu\nu}(k)$ corresponds to the tensor structure

$$G^{\mu\nu}(k) = -g^{\mu\nu} + \frac{k^\mu f^\nu + k^\nu f^\mu}{f\cdot k} - (f^2 - \xi k^2)\frac{k^\mu k^\nu}{(f\cdot k)^2} \tag{IX.81}$$

and only modifies the *vacuum* part of the propagator. This structure comes from considering a more general linear gauge with a quadratic gauge-breaking term given by

$$\mathcal{L}_{\mathrm{lin.\,gf}} = \frac{1}{2\xi}\left(A^\mu f_\mu f_\nu A^\nu\right) \ , \tag{IX.82}$$

with f^μ the gauge breaking term. If $f^\mu = ik^\mu$, we recover the covariant gauge as in Eq. (IX.73), while for $f^\mu = (0, i\mathbf{k})$ we recover the Coulomb gauge. Notice also that in the frame where the plasma is at rest, $u^\mu = (1, \mathbf{0})$, the polarization tensor for covariant gauges reads as

$$T^{\mu\nu}(k) \longrightarrow T^{ij}(k) = \delta^{ij} - \frac{k^i k^j}{\mathbf{k}^2}\,, \tag{IX.83}$$

and it is zero whenever μ or ν equal 0. The same holds in the Coulomb gauge. The resulting gauge boson propagator on the CTP is given by [540]

$$D^{\mu\nu}(k) = -\,G^{\mu\nu}\begin{pmatrix} \dfrac{1}{k^2+i\epsilon} & -2\pi i\delta(k^2)\,\theta(-k\cdot u) \\ -2\pi i\delta(k^2)\,\theta(+k\cdot u) & \dfrac{-1}{k^2-i\epsilon} \end{pmatrix} \tag{IX.84}$$

$$-\,iT^{\mu\nu}(k)\,2\pi\delta(k^2)\,f_-(|k^0|)\begin{pmatrix} 1 & 1 \\ 1 & 1 \end{pmatrix}\,, \tag{IX.85}$$

while the ghost propagator is exactly equal to the vacuum part of the gauge boson one in Eq. (IX.84).

While keeping a covariant formulation of the gauge theory can be viewed as desirable in the real-time formalism, where quantities are calculated as in zero-temperature QFT with modified Feynman rules, we want to highlight how most of the calculations for hot gauge theories are done in the non-covariant Coulomb gauge [412, 543]. As also nicely stressed in [549, 550], sticking to covariant formulations of gauge-breaking terms at finite-T is not very practical, since Lorentz invariance is broken by the existence of a preferred reference frame, the plasma frame. Moreover, in the Coulomb gauge, only the physical vector boson degrees of freedom play a role and acquire a thermal part. Also, resummed gauge boson propagators are better expressed in the Coulomb gauge, where the separation into longitudinal and transverse degrees of freedom is manifest. A way to keep the covariant formulation of the CTP propagators that holds in the Coulomb gauge is

$$\Delta^{\mu\nu}_{ab}(k) = -R^{\mu\nu}\Delta_{ab}(k)\,, \tag{IX.86}$$

where

$$R^{\mu\nu} = g^{\mu\nu} + \frac{k^\mu k^\nu}{\kappa^2} - \frac{k\cdot u}{\kappa^2}(u^\mu k^\nu + u^\nu k^\mu) + \frac{k^2}{\kappa^2}u^\mu u^\nu\,, \tag{IX.87}$$

and where $k\cdot u \equiv \omega$ and $\kappa = \sqrt{\omega^2 - k^2} = \mathbf{k}^2$ are the energy and the magnitude of the 3-momentum of the gauge boson. We notice that this formulation resembles the LR prescription. Indeed, the thermal part arising from the two formulations is the same, while the zero-temperature part in the LR prescription is given by Eq. (IX.81). Thus, the thermal part of both formulations agrees when calculated in the Coulomb gauge. In particular, in the plasma frame with $u^\mu = (1, \mathbf{0})$, we have

$$R_{\mu\nu} = \begin{cases} -\delta_{ij} + \dfrac{k_i k_j}{\mathbf{k}^2} & \text{if } i, j \neq 0, \\ 0 & \text{otherwise} \end{cases}\,. \tag{IX.88}$$

IX.5.2 Coulomb Gauge

We revisit the calculation of the seagull (cf. Section IX.4.2) and sunset (cf. Section IX.4.3) diagrams involving a tree-level gauge boson propagator, this time in the Coulomb gauge.

Instead of employing $\Delta^{ab}_{\mu\nu} = -g_{\mu\nu}\Delta^{ab}$, we use

$$\Delta^{ab}_{\mu\nu}(k) = \begin{cases} \left(\delta_{ij} - \frac{k_i k_j}{\mathbf{k}^2}\right) \Delta^{ab}(k) & \text{if } i,j \neq 0, \\ 0 & \text{otherwise} \end{cases} . \tag{IX.89}$$

The gauge boson spectral density reads as

$$\Delta^{\mathcal{A}}_{\mu\nu}(k) = \frac{i}{2}\left(\Delta^{>}_{\mu\nu}(k) - \Delta^{<}_{\mu\nu}(k)\right) = \frac{i}{2}\left(\delta_{ij} - \frac{k_i k_j}{\mathbf{k}^2}\right)\left(\Delta^{>}(k) - \Delta^{<}(k)\right) \tag{IX.90}$$

$$= -\frac{1}{2}\left(\delta_{ij} - \frac{k_i k_j}{\mathbf{k}^2}\right)\left[2\pi\delta(k^2)\left(f_-(|k_0|) + \theta(-k_0)\right) - 2\pi\delta(k^2)\left(f_-(|k_0|) + \theta(+k_0)\right)\right] \tag{IX.91}$$

$$= \left(\delta_{ij} - \frac{k_i k_j}{\mathbf{k}^2}\right) \pi\, \delta(k^2)\mathrm{sign}(k_0)\,. \tag{IX.92}$$

We start with the anti-Hermitian one, which gives rise to our sign problem. Modifying the expression in Eq. (IX.48) in the Coulomb gauge, we arrive at

$$\begin{aligned}
\Pi^{\mathcal{A},\mathrm{sun}}(p) = G\int \frac{\mathrm{d}^4k}{(2\pi)^4}\,(2p-k)^\mu(2p-k)^\nu\, 2\pi\delta(k^2)\, 2\pi\delta((p-k)^2) \\
\times\, \mathrm{sign}(k^0)\mathrm{sign}(p^0-k^0)\left[1 + f_-(k^0) + f_-(p^0-k^0)\right](-R_{\mu\nu}(p-k))\,, \\
= \frac{G}{2\pi^2}\mathrm{sign}(p^2)|\vec{p}|\int \mathrm{d}k^0\; \mathrm{d}(p\cdot k)\left(1 - \frac{\left(p^0k^0 - p\cdot k\right)^2}{|\vec{p}|^2 k_0^2}\right)\times \\
\times\, \delta(p\cdot k - p^2)\left[1 + f_-(k^0) + f_-(p^0-k^0)\right] \\
= \frac{G}{4\pi}\mathrm{sign}(p^2)|\vec{p}|\int_{\mathcal{B}} \mathrm{d}k^0\left[1 + f_-(k^0) + f_-(p^0-k^0)\right] + \\
- \frac{G}{4\pi}\frac{\mathrm{sign}(p^2)}{|\vec{p}|}\int_{\mathcal{B}} \mathrm{d}k^0\left[p_0^2 + \frac{p^4}{k_0^2} - 2\frac{p_0p^2}{k_0}\right]\left[1 + f_-(k^0) + f_-(p^0-k^0)\right] \\
= \Pi^{\mathcal{A}}_{\xi=1}(p) + \Pi^{\mathcal{A}}_{\mathrm{new}}(p)\,,
\end{aligned} \tag{IX.93}$$

where we used

$$(2p-k)^\mu(2p-k)^\nu\left(-R_{\mu\nu}(p-k)\right) = 4|\vec{p}|^2(1-\cos^2\theta_{pk})\,. \tag{IX.94}$$

The first term is equivalent to the sunset self-energy in the Feynman gauge, $\Pi^{\mathcal{A}}_{\xi=1}$, while the second term is new and needs to be analyzed. Despite the presence of terms with inverse powers of k^0, the integral is finite because the integration never crosses the zero within the integration boundaries. In fact, we can write them as in Eq. (IX.53) with $k^0_\pm = (p_0 - |\vec{p}|\mathrm{sign}(p^2))/2$, yielding

$$\begin{aligned}
\Big|_{\mathcal{B}} &= \Big|_{\frac{p_0-|\vec{p}|}{2}}^{\frac{p_0+|\vec{p}|}{2}}\theta(p^2) + \left(\Big|_{-\infty}^{\frac{p_0-|\vec{p}|}{2}} + \Big|_{\frac{p_0+|\vec{p}|}{2}}^{+\infty}\right)\theta(-p^2) \\
&\equiv \Big|_{\mathrm{sign}(p_0)\frac{|p_0-|\vec{p}||}{2}}^{\mathrm{sign}(p_0)\frac{|p_0+|\vec{p}||}{2}}\theta(p^2) + \left(\Big|_{-\infty}^{\frac{-|p_0-|\vec{p}||}{2}} + \Big|_{\frac{|p_0+|\vec{p}||}{2}}^{+\infty}\right)\theta(-p^2)\,,
\end{aligned} \tag{IX.95}$$

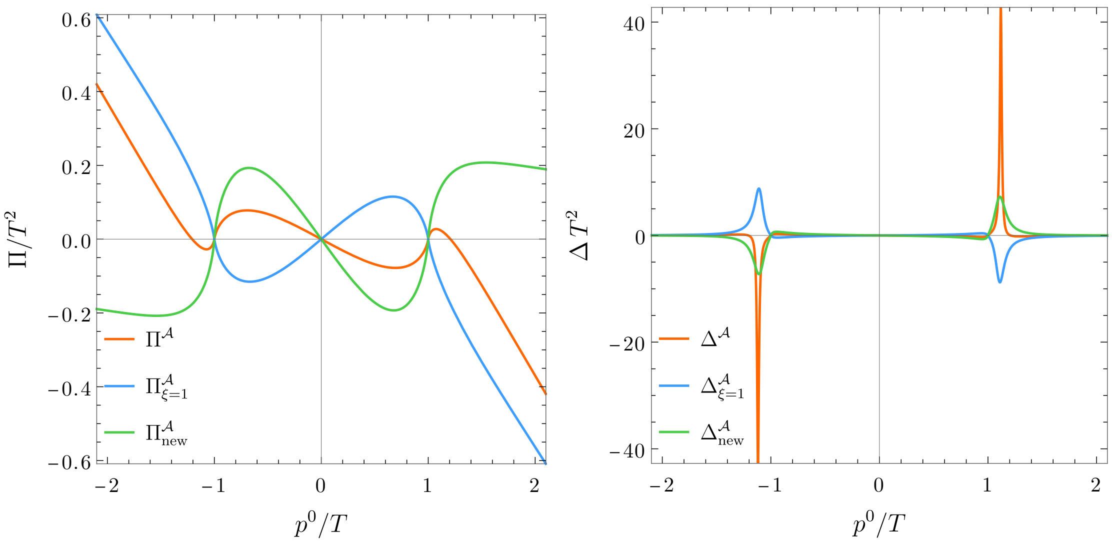

Figure IX.2: *Left panel:* spectral self-energy in the Coulomb gauge against p^0/T for $G = 1$ and $|\vec{p}|/T = 1$. The orange line shows the result of Eq. (IX.93), while the blue and green lines correspond respectively to $\Pi^{\mathcal{A}}_{\xi=1}$ and $\Pi^{\mathcal{A}}_{\rm new}$. *Right panel:* the corresponding spectral density Eq. (IX.96) in the Coulomb gauge with the same color scheme. The spectral sums for the total, '$\xi = 1$', and 'new' densities are 0.15, −1.03, and 0.75, respectively.

which demonstrates our claim for both the timelike and the spacelike case. The anti-Hermitian self-energy in Coulomb gauge is plotted in the left panel of Fig. IX.2 against p^0/T for fixed $|\vec{p}|/T = 1$ and $G = 1$. The orange blue and green lines correspond to the $\Pi^{\mathcal{A}}_{\xi=1}$ and $\Pi^{\mathcal{A}}_{\rm new}$ of Eq. (IX.93), while the orange line is their sum. Notice how the '$\xi = 1$' part has the opposite sign of the 'new' part, but both functions are antisymmetric in p^0 and have the same zeros. By inserting these three types of $\Pi^{\mathcal{A}}$ in the resummed spectral density $\Delta^{\mathcal{A}}$, we can check whether it behaves correctly and the spectral sum issue is cured. First, we use a simple thermal mass $m^2_\Phi = GT^2/4$ in the pole of the propagator, namely

$$\Delta^{\mathcal{A},{\rm Cou}}_\Phi = \frac{\Pi^{\mathcal{A},{\rm Cou}}_\Phi}{\left(p^2 - m^2_\Phi\right)^2 + \left(\Pi^{\mathcal{A},{\rm Cou}}_\Phi\right)^2}\,, \tag{IX.96}$$

which is plotted in the right panel of Fig. IX.2, where we use the same color scheme of the left panel. We note that the spectral density now has the correct behavior, displaying a positive resonance for positive p^0 and a negative one otherwise. When computing the spectral sum for this choice of parameters ($G = 1$ and $|\vec{p}|/T = 1$), we find

$$\int \frac{{\rm d}k^0}{\pi}\, k^0 \Delta^{\mathcal{A}} = 0.15\,, \quad \int \frac{{\rm d}k^0}{\pi}\, k^0 \Delta^{\mathcal{A}}_{\xi=1} = -1.03\,, \quad \int \frac{{\rm d}k^0}{\pi}\, k^0 \Delta^{\mathcal{A}}_{\rm New} = 0.74\,, \tag{IX.97}$$

showing a marked improvement with respect to the Feynman gauge result. For other choices of $|\vec{p}|/T$ and G, the spectral sum does not show a stable behavior, yielding both negative and positive values.

We now turn to compute the Hermitian part of the retarded self-energy in the Coulomb gauge. For the 'seagull' diagram, we just need the statistical propagator, which is given by

$$i\Delta^F_{\mu\nu}(k) = (1 + 2f_-(|k_0|))\,{\rm sign}(k_0)\,\Delta^{\mathcal{A}}_{\mu\nu}(k) = (1 + 2f_-(|k_0|))\,\pi\delta(k^2)\left(\delta_{ij} - \frac{k_i k_j}{\mathbf{k}^2}\right)\,. \tag{IX.98}$$

Thus, the 'seagull' contribution is

$$\begin{aligned}\Pi^{\mathcal{H},\,\mathrm{sea}}(p) &= -G\int \frac{\mathrm{d}^4k}{(2\pi)^4} g^{\mu\nu}\, i\Delta^F_{\mu\nu}(k) = \int \frac{\mathrm{d}^4k}{(2\pi)^4} g^{\mu\nu}\left(1+2f_-(|k_0|)\right)\pi\delta(k^2)\left(\delta_{ij}-\frac{k_ik_j}{\mathbf{k}^2}\right)\\ &= \frac{G}{2\pi^2}\int_0^\Lambda \mathrm{d}|\vec{k}|\,|\vec{k}| + \frac{G}{\pi^2}\int_0^\infty \mathrm{d}|\vec{k}|\,|\vec{k}| f_-(|\vec{k}|)\\ &= \frac{G\Lambda^2}{4\pi^2}+\frac{GT^2}{6}\,. \end{aligned} \tag{IX.99}$$

Notice that the Coulomb gauge provides a seagull self-energy whose temperature-dependent part is *half* the result obtained in the Feynman gauge as a result of having only two physical degrees of freedom put on-shell and thermalized instead of four.

The 'sunset' contribution is much more involved and it reads as

$$\begin{aligned}\Pi^{\mathcal{H},\,\mathrm{sun}}(p) &= -i\frac{G}{2}\int \frac{\mathrm{d}^4k}{(2\pi)^4}(p+k)^\mu(p+k)^\nu\left(i\Delta^{++}_\Phi(k)i\Delta^{++}_{\mu\nu}(p-k) - i\Delta^{--}_\Phi(k)i\Delta^{--}_{\mu\nu}(p-k)\right)\\ &= G\int \frac{\mathrm{d}^4k}{(2\pi)^3}\left(\delta_{ij}-\frac{(p_i-k_i)(p_j-k_j)}{(\vec{p}-\vec{k})^2}\right)\left(\frac{\delta(k^2)}{(p-k)^2}f_-(|k_0|)+\frac{\delta((p-k)^2)}{k^2}f_-(|p_0-k_0|)\right)\,. \end{aligned} \tag{IX.100}$$

In the second line, we used Eq. (IX.89) and we only kept the thermal part. The contraction of the four-momenta with the Coulomb term from the gauge boson propagator gives

$$(p+k)^\mu(p+k)^n u\left(\delta_{ij}-\frac{(p_i-k_i)(p_j-k_j)}{(\vec{p}-\vec{k})^2}\right) = 4|\vec{p}|^2|\vec{k}|^2\frac{1-\cos^2\theta_{pk}}{|\vec{p}|^2+|\vec{k}|^2-2|\vec{p}||\vec{k}|\cos\theta_{pk}}\,. \tag{IX.101}$$

We integrate the first term in Eq. (IX.100) proportional to $\delta(k^2)$, which we name $\Pi^{\mathcal{H},\,\mathrm{sun}}_A(p)$, over $\mathrm{d}k^0$ and then over $\mathrm{d}\cos\theta$ to obtain

$$\begin{aligned}\Pi^{\mathcal{H},\,\mathrm{sun}}_A(p) &= \frac{G}{(2\pi)^3}\int_0^\infty \mathrm{d}|\vec{k}| f_-(|\vec{k}|)\frac{\pi}{2|\vec{p}|}\Bigg\{4|\vec{k}||\vec{p}| + \frac{1}{|\vec{k}|^2\mp 2|\vec{k}|p_0+p_0^2}\times\\ &\times\sum_\pm\Bigg[2(|\vec{k}|^2-|\vec{p}|^2)^2\ln\frac{||\vec{k}|-|\vec{p}||}{|\vec{k}|+|\vec{p}|} + \left(p^2+2|\vec{k}|(|\vec{p}|\mp p_0)\right)\left(-p^2+2|\vec{k}|(|\vec{p}|\pm p_0)\right)\times\\ &\qquad\times\ln\left|\frac{-p^2\pm 2|\vec{k}|p_0}{p^2\mp 2|\vec{k}|p_0}\frac{p^2\mp 2|\vec{k}|p_0+2|\vec{k}||\vec{p}|}{-p^2\pm 2|\vec{k}|p_0+2|\vec{k}||\vec{p}|}\right|\Bigg]\Bigg\}\,. \end{aligned} \tag{IX.102}$$

The second term, which we call $\Pi^{\mathcal{H},\,\mathrm{sun}}_B(p)$, is proportional to $\delta((p-k)^2)$ is more involved but the two integrations can still be performed. It reads as follows,

$$\Pi^{\mathcal{H},\,\mathrm{sun}}_B(p) = \frac{GT^2}{6}+ \tag{IX.103}$$

$$\begin{aligned}&+\frac{G}{(2\pi)^2}\int_0^\infty \mathrm{d}|\vec{k}| f_-(|\vec{k}|)\sum_\pm\Bigg\{\ln\left|\frac{p^2\mp 2p_0|\vec{k}|+2|\vec{p}||\vec{k}|}{p^2\mp 2p_0|\vec{k}|-2|\vec{p}||\vec{k}|}\right|\left(|\vec{p}|+\frac{|\vec{k}|^2}{2|\vec{p}|}-\frac{p^2\mp 2p_0|\vec{k}|}{2|\vec{p}|}\right)\\ &+\frac{1}{4|\vec{k}|^2|\vec{p}|}\left[|\vec{p}|^2+(\pm 2|\vec{k}|-p_0)p_0\right]\left[4|\vec{k}||\vec{p}|+\left(|\vec{p}|^2+(\pm 2|\vec{k}|-p_0)p_0\right)\ln\left|\frac{-p^2\pm 2|\vec{k}|p_0-2|\vec{p}||\vec{k}|}{-p^2\pm 2|\vec{k}|p_0+2|\vec{p}||\vec{k}|}\right|\right]\Bigg\}. \end{aligned} \tag{IX.104}$$

The total Hermitian self-energy reads as (only the temperature-dependent parts)

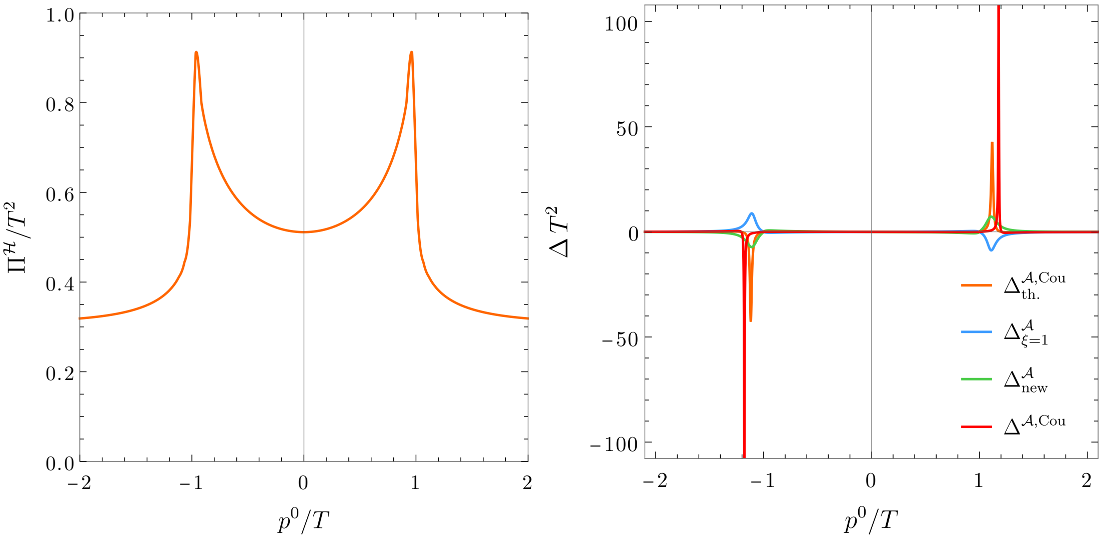

Figure IX.3: The Hermitian self-energy of Eq. (IX.105) (left panel) and the resummed spectral density (right panel) in the Coulomb gauge for $G = 1$ and $|\vec{p}|/T = 1$. The spectral densities are the same of Fig. IX.2 with the addition of the red line corresponding to Eq. (IX.23) where Eq. (IX.105) is used in the denominator.

$$\Pi^{\mathcal{H}} = \Pi^{\mathcal{H},\mathrm{sea}} + \Pi^{\mathcal{H},\mathrm{sun}}_{A} + \Pi^{\mathcal{H},\mathrm{sun}}_{B} \tag{IX.105}$$

and is shown in the left panel of Fig. IX.3 with $G = 1$ and $|\vec{p}|/T = 1$. The right panel illustrates with a red line the spectral density for the same choice of parameters obtained with Eq. (IX.23) and using Eq. (IX.105) in the denominator instead of a simple thermal mass as in Eq. (IX.96). We also display the same lines as in Fig. IX.2 for comparison. The obtained delta-function-like shapes display the right behavior and are centered at a slightly shifted pole with respect to the lines in Fig. IX.2. This is to be expected since the Hermitian self-energy is a much more complex function than a bare thermal mass. Nevertheless, the fact that the pole is close to its high-temperature limit is another encouraging sign that the calculation goes in the right direction. Moreover, the spectral sum for this parameter point amounts to ≈ 0.74, improving the previous result shown in Eq. (IX.97) of ≈ 0.15. However, when tested for other parameter points (e.g., other values of $|\vec{p}|/T$ or G) the spectral density behavior was found to be unstable, sometimes giving positive spectral sums and sometimes negative ones. This signals that resorting to the Coulomb gauge cannot be the definitive solution to ensure the theoretical consistency of 1PI-resummed propagators of a SM-charged complex scalar field.

IX.5.3 Other Possibilities

Even if the Coulomb gauge appears to correct the ill-defined 1PI-resummed spectral density of a gauge-charged complex scalar field in the Feynman gauge, one can object that this is still a particular, although motivated, choice of gauge. Therefore, a gauge-independent analysis is desired. The HTL scheme offers a framework where resummed Green's functions are gauge-independent so that one could check if the calculation with HTL-resummed gauge boson propagators also yields a spectral sum close to 1. In Section IX.B, we lay the foundations for a calculation in this direction, where we give an analytical expression for the anti-Hermitian self-energy with HTL gauge boson propagators.

Another solution might be the one proposed in [479], where the author speculates about the possibility that a self-consistent solution of the Schwinger-Dyson equations for the spectral propagator could yield the correct result even in Feynman gauge and without resorting to the HTL-approximation. The idea is to solve for the one-loop propagator *and* for the one-loop self-energies at the same time, by solving the following system of equations

$$\Delta_\Phi^{\mathcal{A}}(p) = \frac{\Pi^{\mathcal{A}}[\Delta_\Phi, \Delta_\gamma](p)}{\left(p^2 - \Pi^{\mathcal{A}}[\Delta_\Phi, \Delta_\gamma](p)\right)^2 + \left(\Pi^{\mathcal{A}}[\Delta_\Phi, \Delta_\gamma](p)\right)^2}\,, \tag{IX.106}$$

$$\Pi_\Phi^{\mathcal{A}}[\Delta_\Phi, \Delta_\gamma](p) = -2G\int \frac{\mathrm{d}^4k}{(2\pi)^4}(p+k)^2\Delta_\Phi^{\mathcal{A}}(k)\Delta_\gamma^{\mathcal{A}}(p-k)\left(1 + f_-(u\cdot k) + f_-(u\cdot(p-k))\right)\,. \tag{IX.107}$$

This is a complicated non-linear integro-differential system, which needs dedicated methods. A possibility is offered by *wavelet analysis* [551], or by various types of *spectral methods*, notably by using Chebyshev series [552], Legendre series [553], or collocation methods [554], which have also been employed for such types of systems. Eventually, it can also be that one has to resort to more efficient computational methods relying on solutions of the Schwinger-Dyson system on the lattice.

Concluding Remarks

The study of particle production at finite temperatures for Majorana FIMPs is highly relevant in the context of both simplified models and leptogenesis. In this work, we reviewed the calculation of the FIMP interaction rate using the CTP formalism, following the same strategy employed in Chapter VII. We encountered a fundamental issue with 1PI-resummed propagators of gauge-charged scalar fields. Specifically, the spectral density yielded negative spectral sums when corrections from gauge interactions in the Feynman gauge were included. This anomaly suggests a potential conceptual or operational issue with the computation of this crucial quantity.

To address this, we explored the possibility that gauge dependencies could be influencing the results. Such dependencies are expected due to the systematic truncation of the coupled Schwinger-Dyson equations. We explicitly analyzed the case of the Coulomb gauge, the most commonly used choice in finite-temperature quantum field theory. While the spectral sum was positive for some parameter choices in this gauge, it remained negative for others, indicating the relevance of gauge choice and underscoring the need for a gauge-independent calculation.

We finally proposed that using Hard Thermal Loop (HTL) resummed gauge boson propagators in the scalar self-energy calculation might resolve the issue, as detailed in Section IX.B. Additionally, a systematic solution of the Schwinger-Dyson equations using different calculation methods might ultimately provide a definitive answer.

IX.A Tree-level Interaction Rate

Using tree-level propagators, the interaction rate for the Majorana fermion is well-behaved and reads from

$$\begin{aligned}\gamma^{\mathrm{tree}}(p) = \mathrm{Tr}\Big\{\not{p}\Sigma_\chi^{\mathrm{LO},\mathcal{A}}(p)\Big\} = \\ 2g_{\mathrm{DM}}^2\int \frac{\mathrm{d}^4k}{(2\pi)^2}(p\cdot k)\,\delta(k^2-m_f^2)\,\delta\left((p-k)^2-m_\Phi^2\right)\times \\ \times\,\mathrm{sign}(k^0)\mathrm{sign}(p^0-k^0)\left(1+f_-(p^0-k^0)-f_+(k^0)\right)\,.\end{aligned} \tag{IX.A.1}$$

The first assumption we make is to put the SM fermion in-vacuum mass to zero, $m_f = 0$, as we do expect to describe the evolution of the DM density at temperatures $T \gtrsim \Lambda_{\rm EW}$. By performing the integration over the delta function and over the azimuthal angle, we remain with

$$\begin{aligned}\gamma^{\rm tree}(p) &= \frac{g_{\rm DM}^2}{2\pi}\frac{\mathrm{sign}(p^2-m_\Phi^2)}{|\vec{p}|}\frac{p^2-m_\Phi^2}{4}\int_{k_-^0}^{k_+^0}\mathrm{d}k^0(1+f_-(p^0-k^0)-f_+(k^0)) \\ &= \frac{g_{\rm DM}^2}{8\pi}\frac{p^2-m_\Phi^2}{|\vec{p}|}\,\mathrm{sign}(p^2-m_\Phi^2)\left[k_-^0-k_+^0-T\ln\left|\frac{f_+(k_+^0)f_-(p^0-k^0)}{f_+(k_-^0)f_-(p^0-k_+^0)}\right|\right]\,,\end{aligned} \tag{IX.A.2}$$

where, if $p^2 \neq 0$,

$$k_\pm^0 = \frac{p^0}{2p^2}(p^2+m_1^2-m_2^2) \pm \frac{|\vec{p}|}{2p^2}\lambda^{1/2}(p^2,m_1^2,m_2^2)\,, \tag{IX.A.3}$$

which, with $m_1^2 = m_f^2 = 0$ and $m_2^2 = m_\Phi^2$, becomes

$$k_\pm^0 = \frac{1}{2p^2}\left[p^0(p^2-m_\Phi^2) \pm |\vec{p}||p^2-m_\Phi^2|\right]\,. \tag{IX.A.4}$$

Now, since we want to calculate the differential production rate on-shell, we put $p^2 = m_\chi^2$ and we obtain

$$\Gamma_\chi^{\rm LO} = g_\Phi\frac{1}{2|p^0|}\mathcal{H}\Big|_{p^2=m_\chi^2} = g_\Phi\frac{g_{\rm DM}^2}{16\pi}\frac{m_\chi^2-m_\Phi^2}{|p^0||\vec{p}|}\left[k^0+T\ln\left|\frac{f_+(k^0)}{f_-(p^0-k^0)}\right|\right]_{k_-^0}^{k_+^0}\,, \tag{IX.A.5}$$

where we introduced the number of degrees of freedom g_Φ of the dark scalar accounting for colour and weak isospin. By rearranging the terms, we arrive at the final result

$$\Gamma_\chi^{\rm LO} = g_\Phi\frac{g_{\rm DM}^2}{16\pi}\frac{m_\chi^2-m_\Phi^2}{|p^0||\vec{p}|}T\left(\ln\left|\frac{\sinh\big(\beta(p^0-k_+^0)/2\big)}{\cosh\big(\beta(p^0-k_-^0)/2\big)}\right|-\ln\left|\frac{\sinh\big(\beta k_-^0/2\big)}{\cosh\big(\beta k_+^0/2\big)}\right|\right)\,. \tag{IX.A.6}$$

The $T \to 0$ limit is obtained by using the vacuum limit of the distribution functions

$$f_\pm(p^0) \to \pm\theta(-p^0)\,, \tag{IX.A.7}$$

yielding

$$\begin{aligned}\Gamma_\chi^{\rm LO,vac} &= g_\Phi\frac{g_{\rm DM}^2}{16\pi\,|p^0|}\frac{m_\chi^2-m_\Phi^2}{|\vec{p}|}\mathrm{sign}(m_\chi^2-m_\Phi^2)\mathrm{sign}(p^0)(k_+^0-k_-^0)\theta(m_\chi^2-m_\Phi^2) \\ &= \frac{g_{\rm DM}^2}{16\pi\,|p^0|}\frac{(m_\chi^2-m_\Phi^2)^2}{m_\chi^2}\,\mathrm{sign}(p^0)\theta(m_\chi-m_\Phi)\,.\end{aligned} \tag{IX.A.8}$$

The Heaviside theta function tells us that in the scenario with χ heavier than Φ, $m_\chi > m_\Phi$, the vacuum rate vanishes. This is physically consistent with having assumed that DM production proceeds via the decays of Φ particles, which are in equilibrium with the SM bath, and, therefore, their number density in-vacuum is zero. In other words, the "vanilla" freeze-in scenario cannot be reproduced in the zero temperature limit. Typically, the standard freeze-in calculation assumes Boltzmann distributions for the equilibrium distribution functions and neglects the effects of Pauli-blocking and Bose-enhancement, which is a good approximation if the energies of the particles involved are large compared to the temperature, in our case $\left|p^0\right|, \left|k^0\right|, \left|p^0 - k^0\right| \gg T$. To reproduce the results of the standard freeze-in calculation in the CTP context, we need to include NLO order contributions in the expansion of the distribution functions

$$f_\pm\left(p^0\right) \approx \pm\Theta\left(-p^0\right)\left[1 \mp \exp\left(\frac{p^0}{T}\right)\right] + \Theta\left(p^0\right)\exp\left(-\frac{p^0}{T}\right). \tag{IX.A.9}$$

For the integral in Eq. (IX.A.2), we use this approximation and $\mathrm{sign}(p^0 - k^0) = \mathrm{sign}(p^0)$ and $\mathrm{sign}(k^0) = \mathrm{sign}(p^0)\mathrm{sign}(m_\chi^2 - m_\Phi^2)$, obtaining

$$\begin{aligned}\Gamma_\chi\left(|\vec{p}|\right) &= -\frac{g_{\mathrm{DM}}^2 g_\Phi}{8\pi|p^0|}\frac{\Theta\left(\left[m_\Phi^2 - p^2\right]^2\right)}{|\vec{p}|}\frac{p^2 - m_\Phi^2}{2}\times \\ &\times\int_{k_-^0}^{k_+^0}\mathrm{d}k^0\left[\exp\left(-\mathrm{sign}(p^0)\frac{p^0-k^0}{T}\right) + \exp\left(\mathrm{sign}(p^0)\frac{k^0}{T}\right)\right] \\ &\overset{p^0\geq 0}{=} -\frac{g_{\mathrm{DM}}^2}{16\pi p^0\,|\vec{p}|}\left(p^2 - m_\Phi^2\right)T\left[\exp\left(-\frac{p^0-k^0}{T}\right) + \exp\left(\frac{k^0}{T}\right)\right]\Bigg|_{k_-^0}^{k_+^0}.\end{aligned} \tag{IX.A.10}$$

In the last step, we used the anti-symmetrical property of the interaction rate under the shift $p^0 \to -p^0$. In the literature, the freeze-in interaction rate is typically given on the level of the number density and results:

$$\partial_t n_\chi = \frac{g_\Phi}{2\pi^2}m_\Phi^2\Gamma_\Phi T K_1\left(\frac{m_\Phi}{T}\right) = \Gamma_{\chi,n}n_\chi\,, \tag{IX.A.11}$$

where Γ_Φ is the decay rate of the mother particle at rest. Thus, via Eq. (IX.14) we can identify

$$\begin{aligned}\Gamma_{\chi,n}n_\chi &= \int g_\chi\frac{d^3p}{(2\pi)^3}\Gamma_\chi\left(|\vec{p}|\right)f_\chi^{\mathrm{eq}}\left(p^0\right) \\ &= \frac{g_\chi g_\Phi g_{\mathrm{DM}}^2}{16\pi}\frac{m_\Phi^2 - m_\chi^2}{2\pi^2}T\int\mathrm{d}|\vec{p}|\frac{|\vec{p}|}{p^0}\left[\exp\left(-\frac{2p^0-k^0}{T}\right) + \exp\left(\frac{k^0-p^0}{T}\right)\right]\Bigg|_{k_-^0}^{k_+^0}.\end{aligned} \tag{IX.A.12}$$

In the second step, we have approximated $f_\chi^{\mathrm{eq}}\left(p^0\right) = \exp\left(-\frac{p^0}{T}\right)$. In the spirit of our previous approximation, we only keep the leading order term in the integral. Since $k_+^0 - p_0 > 0$ and since $k_+^0 - p^0 > k_+^0 - 2p^0 > k_-^0 - p^0 > k_-^0 - 2p^0$ for $p^0 > 0$, we can approximate the integral further as

$$\begin{aligned}\Gamma_{\chi,n}n_\chi &\approx \frac{g_\chi g_\Phi g_{\mathrm{DM}}^2}{16\pi}\frac{m_\Phi^2 - m_\chi^2}{2\pi^2}T\int\mathrm{d}|\vec{p}|\frac{|\vec{p}|}{p^0}\exp\left(\frac{k_+^0 - p^0}{T}\right) \\ &= \frac{g_\chi g_\Phi g_{\mathrm{DM}}^2}{16\pi}\frac{m_\Phi^2 - m_\chi^2}{2\pi^2}T\int\mathrm{d}p^0\exp\left(\frac{|\vec{p}|\left(m_\Phi^2 - m_\chi^2\right) + p^0\left(m_\Phi^2 + m_\chi^2\right)}{2m_\chi^2 T}\right).\end{aligned} \tag{IX.A.13}$$

In the limit $m_\chi \to 0$, an analytical solution is found as

$$\begin{aligned}\Gamma_{\chi,n} n_\chi &\overset{m_\chi\to 0}{=} \frac{g_\chi g_\Phi g_{\rm DM}^2}{16\pi}\frac{m_\Phi^2}{2\pi^2} T m_\Phi K_1\left(\frac{m_\Phi}{T}\right) \\ &= \frac{g_\Phi}{2\pi^2}\Gamma_\Phi m_\Phi^2 T K_1\left(\frac{m_\Phi}{T}\right)\,, \end{aligned} \tag{IX.A.14}$$

where we identified $\Gamma_\Phi = \frac{g_\chi g_{\rm DM}^2}{16\pi} m_\Phi$ as the decay rate at rest for $m_\chi = 0$. Hence, we recover the freeze-in rate that is commonly employed within the Boltzmann formalism if we approximate the distribution functions as in Eq. (IX.16) and only consider the leading order contribution in the resulting integrated sum of the distribution functions appearing in the self-energy. Finally, if we were to retain the asymptotic (high-temperature) thermal masses of the BSM scalar and of the SM quark, we could write the interaction rate as

$$\begin{aligned}\gamma^{\rm tree}_{{\rm high}-T} = \frac{g_{\rm DM}^2}{8\pi}\frac{m_\chi^2+m_f^2-m_\Phi^2}{|\vec p|}\,&{\rm sign}(m_\chi^2-m_f^2-m_\Phi^2) \\ &\times\left[-\frac{|\vec p|}{2m_\chi^2}\lambda^{1/2}(m_\chi^2,m_f^2,m_\Phi^2) + T\ln\left|\frac{f_+(k_+^0)f_-(p^0-k_-^0)}{f_-(p^0-k_+^0)f_+(k_-^0)}\right|\right]\,, \end{aligned} \tag{IX.A.15}$$

with $k_\pm^0$ given by Eq. (IX.A.3) with m_1^2 and m_2^2 given by the sum of the squared in-vacuum and thermal masses of Φ and f.

IX.B HTL-resummed Propagators

Hot gauge theories usually require resumming gauge boson propagators when soft momenta are hit, as we have described at length in Section VII.4.1, talking about the HTL approximation scheme. This scheme has the advantage of being gauge independent and, therefore, we may investigate what happens to the scalar field self-energies when we use HTL-resummed gauge boson propagators in the sunset and seagull diagrams of Section IX.4.2. This section collects some steps in this direction. They are not complete and have not been tested, but serve as a basis to address the problem of the negative spectral sum from another (in principle gauge-independent) perspective than the Coulomb gauge solution we provided.

The finite-temperature propagator for a massless gauge boson is split into longitudinal and transverse contributions, plus a term from assuming a covariant gauge fixing; it reads

$$\begin{aligned} i\Delta_{\mu\nu}(Q) &= P^T_{\mu\nu}\Delta_T(Q) + P^L_{\mu\nu}\Delta_L(Q) - \xi\frac{Q_\mu Q_\nu}{Q^2}\Delta(Q) \\ &= P^T_{\mu\nu}\frac{i}{Q^2-\Pi_T(Q)} + P^L_{\mu\nu}\frac{i}{Q^2-\Pi_L(Q)} - \xi\frac{Q_\mu Q_\nu}{Q^2}\frac{i}{Q^2}. \end{aligned} \tag{IX.B.1}$$

In the following, we will assume the Feynman gauge, $\xi = 1$, since HTL propagators are gauge-independent. The transverse and longitudinal projectors are defined as

$$P^T_{\mu\nu} = -g_{\mu\nu} + \frac{Q_\mu Q_\nu}{Q^2} + \frac{N_\mu N_\nu}{N^2} \tag{IX.B.2}$$

$$P^L_{\mu\nu} = -\frac{N_\mu N_\nu}{N^2}, \tag{IX.B.3}$$

where N_μ is the projection of the four-velocity of the medium U_μ onto the direction orthogonal to the external momentum Q_μ:

$$N^\mu = U^\mu - \frac{Q\cdot U}{Q^2}Q^\mu, \quad Q\cdot N = 0\,. \tag{IX.B.4}$$

A common convention considers $U_\mu = (1,\vec{0})$ in the medium rest frame. The terms Π_T and Π_L are the transverse and longitudinal components of the polarization tensor, which in the Feynman gauge is defined via

$$\Pi_{\mu\nu}(Q) = \Pi^T(Q)P^T_{\mu\nu} + \Pi^L(Q)P^L_{\mu\nu}, \quad (\xi = 1)\,. \tag{IX.B.5}$$

This is the only form it can have by the Ward identity, which states that the one-loop self-energy needs to be transverse, $Q^\mu\Pi_{\mu\nu}(Q) = 0$. This also justifies why the gauge-dependent part of the propagator does not receive any self-energy correction.

In what follows, we will explicitly calculate all the contributions to the self-energy tensor $\Pi_{\mu\nu}$ and then we will extract its longitudinal and transverse parts via the following relations:

$$\Pi_L = P_{L,\mu\nu}\Pi^{\mu\nu} = -\frac{U_\mu U_\nu}{U^2}\Pi^{\mu\nu} = \frac{Q^2}{q^2}\Pi^{00}\,, \tag{IX.B.6}$$

$$\Pi_T = \frac{1}{2}P_{T,\mu\nu}\Pi^{\mu\nu} = -\frac{1}{2}[\Pi + \Pi_L], \quad \Pi \equiv g_{\mu\nu}\Pi^{\mu\nu}\,. \tag{IX.B.7}$$

Notice that, at this stage, we have never assumed anything about the Keldysh-Schwinger structure of the polarization tensor. These relations hold generically, for each of the four Keldysh-Schwinger polarization tensors. We now introduce the dispersion relations for transverse modes ω_T and for longitudinal modes ω_L, defined by

$$\omega_T^2(k) = |\vec{k}|^2 + \Pi_T^{\mathcal{H}}(k_0 = \omega_T(|\vec{k}|), |\vec{k}|)\,, \tag{IX.B.8}$$

$$\omega_L^2(k) = |\vec{k}|^2 + \Pi_L^{\mathcal{H}}(k_0 = \omega_T(|\vec{k}|), |\vec{k}|)\,, \tag{IX.B.9}$$

$$\tag{IX.B.10}$$

In the zero momentum limit, $|\vec{k}| \to 0$, both frequencies reduce to the plasma frequency

$$\omega_P = \frac{eT}{3}\,. \tag{IX.B.11}$$

Using $|\vec{k}| = k$, $x = k_0/k$, $m^2 = e^2T^2/6$, the transverse and longitudinal spectral densities read as [412]

$$\rho_{T,L}(k) = 2\pi Z_{T,L}(k)\left[\delta(k_0 - \omega_{T,L}(k)) - \delta(k_0 + \omega_{T,L}(k))\right] + \beta_{T,L}(k_0,k)\,, \tag{IX.B.12}$$

$$Z_L(k) = \frac{\omega_L(k)\left(\omega_L^2(k) - k^2\right)}{k^2\left(k^2 + 2m^2 - \omega_L(k)\right)}, \qquad Z_T(k) = \frac{\omega_T(k)\left(\omega_T^2(k) - k^2\right)}{3\omega_P\omega_T^2(k) - \left(\omega_T^2(k) - k^2\right)^2}\,, \tag{IX.B.13}$$

$$\beta_L(k_0,k) = \frac{m^2 x\,\theta(1-x^2)}{\left[k^2 + 2m^2\left(1 - \frac{x}{2}\ln\left|\frac{x+1}{x-1}\right|\right)\right]^2 + \pi^2 m^4 x^2}\,, \tag{IX.B.14}$$

$$\beta_T(k_0,k) = \frac{2m^2 x(1-x^2)\theta(1-x^2)}{4\left(k^2(x^2-1) - m^2\left[x^2 + \frac{x(1-x^2)}{2}\ln\left|\frac{x+1}{x-1}\right|\right]\right)^2 + \pi^2 m^4 x^2(1-x^2)^2}\,. \tag{IX.B.15}$$

We can now use all these formulae for the HTL-resummed gauge boson propagators to derive an expression for the anti-Hermitian self-energy of the charged scalar $\Pi_\Phi^{\mathcal{A}}$. Since this only depends on the sunset diagram Eq. (IX.40), we can directly determine its expression as follows

$$\begin{aligned} i\Pi_\Phi^{\mathcal{A}} &= G f_-^{-1}(p_0) \int \frac{\mathrm{d}^4k}{(2\pi)^4} (2p-k)^\mu (2p-k)^\nu \frac{1}{2} i\Delta_\Phi^<(p-k)\, i\Delta_{\mu\nu}^<(k) = \\ &= \frac{G}{2} f_-^{-1}(p_0) \int \frac{\mathrm{d}^4k}{(2\pi)^4} 2\pi\delta\left((p-k)^2 - m_\Phi^2\right) \mathrm{sign}(p^0-k^0) f_-(p_0-k_0) f_-(k_0) \\ &\qquad \times (2p-k)^\mu (2p-k)^\nu \left[P_{\mu\nu}^T\, \rho_T(k) + P_{\mu\nu}^L \frac{|\vec{k}|^2}{k^2}\, \rho_L(k) + \xi \frac{k_\mu k_\nu}{k^4} \right] . \end{aligned} \tag{IX.B.16}$$

We now use the following properties:

① $(2p-k)^\mu (2p-k)^\nu\, k_\mu k_\nu = \left((p-k)^2 - p^2\right)^2 \underbrace{\longrightarrow}_{(p-k)^2=0,\, m_\Phi^2} p^4,\ \left(m_\Phi^2 - p^2\right)^2 \equiv \tilde{p}^4\,;$

② $(2p-k)^\mu (2p-k)^\nu\, P_{\mu\nu}^T(k) = (2p-k)^\mu (2p-k)^\nu \left(-R_{\mu\nu}(k)\right) \underbrace{=}_{\text{(IX.94)}} 4|\vec{p}|^2 (1-\cos^2\theta_{pk})\,;$

③ $(2p-k)^\mu (2p-k)^\nu\, P_{\mu\nu}^L(k) = -(2p-k)^2 + \dfrac{\left(k^2 - 2p\cdot k\right)^2}{k^2} - (2p-k)^\mu (2p-k)^\nu\, P_{\mu\nu}^T(k)\,.$

These allow us to rewrite Eq. (IX.B.16) in the following way

$$\begin{aligned} i\Pi_\Phi^{\mathcal{A}} &= \frac{G}{16\pi^3} \int \mathrm{d}^4k \left(1 + f_-(k_0) + f_-(p_0-k_0)\right) \mathrm{sign}(p^0-k^0) \delta\left((p-k)^2 - m_\Phi^2\right) \\ &\times \left\{ \xi \frac{\tilde{p}^4}{k^4} - \left[3p^2 + 2p\cdot k + m_\Phi^2\right] \frac{|\vec{k}|^2}{k^2} \rho_L(k) + \frac{\tilde{p}^4}{k^4} |\vec{k}|^2 \rho_L(k) \right. \\ &\qquad \left. + (2p-k)^\mu (2p-k)^\nu P_{\mu\nu}^T \left[\rho_T(k) - \frac{|\vec{k}|^2}{k^2} \rho_L(k) \right] \right\} \\ &= \frac{G}{8\pi^2} \int \mathrm{d}|\vec{k}| |\vec{k}|^2 \mathrm{d}k^0 \mathrm{d}\cos\theta \left(1 + f_-(k_0) + f_-(p_0-k_0)\right) \mathrm{sign}(p^0-k^0)\, \delta\left((p-k)^2 - m_\Phi^2\right) \\ &\times \left\{ \underbrace{\frac{\tilde{p}^4}{k^4} \left(\xi + |\vec{k}|^2 \rho_L(k)\right)}_{(a)} - \underbrace{\left(3p^2 + 2p_0k_0 - 2|\vec{p}||\vec{k}|\cos\theta + m_\Phi^2\right) \frac{|\vec{k}|^2}{k^2} \rho_L(k)}_{(b)} \right. \\ &\qquad \left. + \underbrace{4|\vec{p}|^2 \left(1 - \cos^2\theta\right) \left(\rho_T(k) - \frac{|\vec{k}|^2}{k^2} \rho_L(k) \right)}_{(c)} \right\} . \end{aligned} \tag{IX.B.17}$$

The integral over $\cos\theta$ sets the boundary conditions via the delta function:

$$0 = (p-k)^2 - m_\Phi^2 = p^2 + k^2 - 2p\cdot k - m_\Phi^2 = p^2 + k_0^2 - |\vec{k}|^2 - 2p_0k_0 + 2|\vec{p}||\vec{k}|\cos\theta - m_\Phi^2\,.$$

Whenever no extra delta function is involved, i.e., for the gauge-fixing-dependent term and the spacelike terms of the spectral functions, we remain with two integrations

$$\mathcal{B} = \left\{ p_0 - |\vec{p}| - |\vec{k}| \le k_0 \le p_0 - \left| |\vec{p}| - |\vec{k}| \right| \cup p_0 + \left| |\vec{p}| - |\vec{k}| \right| \le k_0 \le p_0 + |\vec{p}| + |\vec{k}| \right\}, \tag{IX.B.18}$$

when $m_\Phi^2 = 0$, the massless case, or

$$\mathcal{B} = \Bigg\{ p^0 - \sqrt{\left(|\vec{p}| + |\vec{k}|\right)^2 + m_\phi^2} \le k^0 \le p^0 - \sqrt{\left(|\vec{p}| - |\vec{k}|\right)^2 + m_\phi^2} \quad \cup \tag{IX.B.19}$$

$$p^0 + \sqrt{\left(|\vec{p}| - |\vec{k}|\right)^2 + m_\phi^2} \le k^0 \le p^0 + \sqrt{\left(|\vec{p}| + |\vec{k}|\right)^2 + m_\phi^2} \Bigg\}\,, \tag{IX.B.20}$$

for the massive case. If, however, we hit the plasmon quasi-particle poles for timelike momenta, the delta functions bring away the integral over $\mathrm{d}k_0$, which implies that the integration boundaries are transferred onto the integral over the spatial momentum by requiring that

$$\left\{ \begin{array}{l} 0 = (p-k)^2 = p^2 + k^2 - 2p\cdot k = p^2 + k_0^2 - |\vec{k}|^2 - 2p_0 k_0 + 2|\vec{p}||\vec{k}|\cos\theta\,, \\ 0 = k_0 = \pm\omega_{L,T}(|\vec{k}|) \end{array} \right.$$

giving rise to the following system of inequalities for $|\vec{k}|$ which constitute the new integration boundaries

$$\mathcal{B}_k = \left\{ \begin{array}{l} |\vec{k}|^2 - \omega_{L,T}^2(|\vec{k}|) + 2p_0\omega_{L,T}(|\vec{k}|) - p^2 + 2|\vec{p}||\vec{k}| \ge 0 \\ |\vec{k}|^2 - \omega_{L,T}^2(|\vec{k}|) + 2p_0\omega_{L,T}(|\vec{k}|) - p^2 - 2|\vec{p}||\vec{k}| \le 0 \end{array} \right. . \tag{IX.B.21}$$

In the limit where the external scalar field is at rest $\vec{p} \to 0$, where the limit is understood in comparison to the soft scale gT or the scalar (thermal) mass m_Φ, the last term in Eq. (IX.B.17), including the transverse component of the gauge boson, disappears, as well as terms proportional to $\cos\theta$.

CHAPTER X

Dark Matter Freeze-In during Inflationary Reheating

In this final chapter, we explore an alternative approach to understanding freeze-in DM production by examining how the cosmological expansion history itself influences DM abundance, rather than focusing solely on the collisional dynamics within the Boltzmann equation. Specifically, we investigate how different reheating scenarios following inflation affect the DM relic density and consequently shape the parameter space of simplified t-channel DM models. This analysis enables us to demonstrate that i) the cosmological background during DM production fundamentally alters model predictions, and ii) novel connections emerge between collider phenomenology and early Universe physics.

This chapter synthesizes research published in [4], to which the thesis author contributed substantially. The work builds upon foundational analysis from the master's thesis [555], co-supervised by the thesis author. Results not directly derived by the thesis author are appropriately attributed to their original sources.

Statement of Personal Contribution for this Chapter The research presented in this chapter is derived from a collaborative project that resulted in Ref. [4], from which this chapter takes the conducted analysis, presented results, and derived conclusions. The principal contributions to this publication of the thesis author include:

- Formulating the initial research concept with JH.
- Conducting the literature research regarding reheating models and applications to DM production.
- Deriving the equations and cross-checking with the results derived by JL (who contributed during the first stages of the project).
- Writing the largest part of the manuscript.

X.1 Motivations

Throughout the preceding chapters of this thesis, we have extensively examined various approaches to enhancing the collisional component of the DM rate equation, either through long-range non-perturbative phenomena (Chapters IV and V) or by incorporating thermal corrections from non-equilibrium quantum field theory (Chapters VI to IX). However, the left-hand side of the Boltzmann equation—commonly referred to as the Liouville or diffusion term—has remained unchanged, with the implicit assumption that the system evolves within a Friedmann-Lemaître-Robertson-Walker (FLRW) background dominated by radiation energy density.

This assumption is well-founded given that we know the Universe must have been radiation-dominated at least by the time of Big Bang Nucleosynthesis (BBN), approximately one second after the Big Bang when the temperature was around 1 MeV [556].

Nevertheless, multiple theoretical frameworks suggest that *prior* to BBN, the cosmic evolution could have been considerably more complex, involving several *non-standard* cosmological epochs where radiation did not constitute the dominant cosmic fluid. The primary example emerges from inflation, the leading theory that resolves some of the most significant challenges facing the standard ΛCDM cosmological model (cf. Section X.2) [274,281]. Inflation also provides mechanisms to generate all particle content in the Universe through a process known as *reheating*. As we will demonstrate in Section X.3, an extended reheating phase following inflation—where the inflaton dominates the cosmic energy budget before decaying and producing the radiation bath—results in substantial modifications to the expansion rate.

Additional reheating phases could also arise from the decay of massive fields such as string theory moduli [168, 290, 557–565]. Moreover, exotic new fields could have influenced the earliest cosmic epochs, including non-relativistic species [566], quintessential fluids [567, 568], Early Dark Energy [569], among many others comprehensively reviewed in Ref. [570]. Finally, additional degrees of freedom beyond the Standard Model could have enabled intricate dynamics that made the early Universe a substantially more complex environment, including first-order phase transitions, cosmic defect formation and evolution, non-equilibrium conditions, and non-perturbative particle production [274, 430, 571–573].

While we currently lack definitive evidence supporting any particular theory, we also have no cosmological observations that can probe epochs before BBN, which remains the earliest period directly accessible to experimental investigation. However, this situation may soon change if a positive signal from a stochastic gravitational wave background compatible with early Universe physics is detected [173]. Combined with improved observations of the Cosmic Microwave Background (CMB) [574] and Large-Scale Structure [575] from future experiments, this could enable us to access this largely unexplored cosmic epoch. Furthermore, as current and future collider searches probe the Standard Model at and beyond the TeV scale [224, 576], understanding the interplay between possible early Universe scenarios and the Standard Model becomes crucial for interpreting potential signals of New Physics or exclusion limits for theories beyond the Standard Model. This includes, for example, baryogenesis and leptogenesis mechanisms, neutrino mass generation, and naturally, dark matter production.

If DM production occurred during a non-standard cosmological epoch, it could have profound implications for model parameters. In the freeze-in mechanism (cf. Section III.5.2), the DM comoving number density typically reaches its maximum at temperatures corresponding to the highest mass scale involved in the production process, such as the mass of a decaying heavy mediator. If this freeze-in temperature occurs within a faster-than-radiation expansion era, it results in a reduced DM yield, necessitating stronger interactions—either through larger couplings or more massive particles—with dramatic consequences for detection strategies.

Previous investigations (see, e.g., [168, 560, 565, 577–580]) have explored deviations from standard expansion histories and their effects on DM production. Specifically, Ref. [411] examined the impact of a prolonged reheating phase on simplified t-channel DM models and found that larger couplings are generally required, resulting in shorter-lived signatures at colliders compared to standard freeze-in scenarios during radiation domination. This work improved upon Ref. [382], which assumed instantaneous reheating, even when considering reheating temperatures lower than the mass of the decaying mediator. Such an assumption leads to inaccurate results because it neglects the bulk of freeze-in production, thereby underestimating the DM yield.

However, what remains unexplored is the interplay between different reheating scenarios derived from well-motivated inflaton potentials and their combined impact on DM phenomenology—particularly regarding collider signatures—and cosmological observations, such as CMB measurements.

In this chapter, we address these issues by examining the effects of various inflationary reheating scenarios on freeze-in DM production within a simplified t-channel model (cf. Section II.2.4). We begin by reviewing the motivations and key aspects of cosmic inflation in Section X.2, followed by a discussion of post-inflation reheating dynamics in Section X.3, where we clarify the essential factors governing cosmic expansion. In Section X.4, we integrate the freeze-in mechanism described in Section III.5.2 into this cosmological framework, while Section X.5 illustrates how these factors influence potential collider signals. By combining these findings with CMB constraints discussed in Section X.2.5, we demonstrate how reheating scenarios and their parameters critically affect predictions of collider observables and the interpretation of potential detections (cf. Section X.6).

X.2 Inflation

Declaration: this section is a review of major literature results about inflation and inflaton models.

X.2.1 Shortcomings of the Hot Big Bang Model

Cosmic inflation is a theoretical framework in cosmology that proposes a rapid and exponential expansion of space in the very early Universe, occurring within the first fractions of a second in the Universe's life. This paradigm is desired for several reasons:

1. **Solving the Horizon Problem:** The horizon problem arises from the observation that regions of the Universe separated by vast distances appear to have nearly identical properties, such as the CMB temperature. However, according to the standard Big Bang model, there hasn't been enough time since the Big Bang for light to have traveled between these regions and equalized their temperatures. Inflation provides a solution by positing that regions originally in causal contact became causally disconnected during inflation, but preserved similar statistical properties which later translate into a uniform CMB temperature distribution.
2. **Addressing the Flatness Problem:** The Universe appears to be extremely close to flat on large scales even though the energy density of spatial curvature is expected to grow with time. Thus, the flatness problem arises from the question of why the Universe's density parameter, which determines its curvature, is so close to the critical value that would make it still flat today. Inflation naturally leads to a Universe that is very close to flat without the need for finely tuned initial conditions, as the rapid expansion dilutes any initial curvature to an exponentially small value.
3. **Absence of Cosmic Relics:** In the early Universe, phase transitions from symmetry-breaking processes of fundamental forces (e.g., the electroweak phase tran-

sition) could have produced topological defects such as monopoles, cosmic strings, domain walls, and textures. These defects are relics that occurred during these phase transitions. However, their presence in the Universe is not observed, which would pose a challenge to the standard Big Bang model. Inflation provides a resolution to this problem through a mechanism known as "cosmic supercooling". During inflation, the rapid expansion of space effectively "irons out" any pre-existing defects by exponentially diluting their densities.

4. **Formation of Large-Scale Structure:** Inflation provides a physical mechanism for the origin of the primordial density fluctuations that seeded the formation of large-scale structures like galaxies and galaxy clusters. Quantum fluctuations during inflation get imprinted on the fabric of spacetime, leading to variations in the density of matter. Over time, gravitational instability amplifies these density fluctuations, eventually giving rise to the rich cosmic web of structures observed in the Universe today. This also explains why the Cosmic Microwave Background (CMB) radiation, which is the remnant heat from the Big Bang, exhibits tiny temperature fluctuations on large scales.

X.2.2 Slow-roll Inflation

For Inflation to solve the aforementioned problems, the comoving Hubble radius $(aH)^{-1}$, within which causal connections between different patches happen within a Hubble time H^{-1}, had to be very large right at the start of inflation. In this way, all portions of the Universe were in causal contact. During inflation, the Hubble sphere shrank exponentially, and particles initially in causal contact with one another could no longer communicate: their modes *exited* the (Hubble) horizon. If the entire observable Universe was within the comoving Hubble radius, then the horizon problem is technically solved.

For the Hubble radius to decrease, we need [283]

$$\frac{\mathrm{d}}{\mathrm{d}t}(aH)^{-1} = -\frac{\ddot{a}}{(\dot{a})^2} < 0 \implies \ddot{a} > 0\,, \tag{X.1}$$

hence an *accelerated* expansion of the Universe. In particular, one finds that, for the horizon problem to be solved, the scale factor at the end of inflation had to be *at least* around $50 - 60$ e-folds larger than that at the beginning. Remarkably, the same order of e-folds is necessary to solve the flatness fine-tuning problem and can also get rid of topological relics. From Eq. (X.1), one can also write

$$0 > \frac{\mathrm{d}}{\mathrm{d}t}(aH)^{-1} = -\frac{1}{a}\left(1 + \frac{\dot{H}}{H^2}\right) \equiv -\frac{1}{a}(1-\varepsilon), \tag{X.2}$$

where

$$\varepsilon \equiv -\frac{\dot{H}}{H^2} < 1 \tag{X.3}$$

is the first slow-roll parameter and the condition it must satisfy for inflation to happen (being smaller than 1) is called the *first slow-roll condition.* In combination with the first Friedmann equation, $H^2 = \rho/(3M_{\mathrm{Pl}}^2)$, and the continuity equation $\dot{\rho} = -3H(\rho + P)$, it also implies that

$$\varepsilon = -\frac{\dot{H}}{H} = \frac{3}{2}\left(1 + \frac{P}{\rho}\right) < 1 \implies \frac{P}{\rho} < -\frac{1}{3}\,, \tag{X.4}$$

which means that something with *negative* pressure (and nearly constant energy density) is necessary for inflation, similar to a cosmological constant.

Since we want inflation to last at least 50−60 *e*-folds, we also require that ε remains small for the entire duration. This condition is controlled by the *second slow-roll parameter*

$$\eta \equiv \frac{\dot{\varepsilon}}{H\varepsilon}\,, \tag{X.5}$$

which measures the fractional change of ε per Hubble time. Thus, the Universe keeps inflating as long as $|\eta| < 1$, the *second slow-roll condition*.

X.2.3 Scalar Field Inflation

The simplest way to describe the dynamics of inflation is with a real scalar field ϕ, the *inflaton*, minimally coupled to gravity, whose Lagrangian density reads as [483]

$$\mathcal{L}_\phi = -\frac{1}{2} g^{\mu\nu}\partial_\mu\phi\partial_\nu\phi - V(\phi)\,, \tag{X.6}$$

where $g^{\mu\nu}$ is the metric (the FLRW in our case) and $V(\phi)$ is the field's potential. We consider ϕ to be spatially homogeneous and isotropic; its energy density and pressure can be derived from its energy-momentum tensor, reading as [283]

$$\rho_\phi = \frac{\dot{\phi}^2}{2} + V(\phi), \qquad P_\phi = \frac{\dot{\phi}^2}{2} - V(\phi)\,, \qquad w_\Phi = \frac{P_\Phi}{\rho_\Phi} = \frac{\frac{\dot{\phi}^2}{2} - V(\phi)}{\frac{\dot{\phi}^2}{2} + V(\phi)}. \tag{X.7}$$

Thus, the first slow-roll condition is satisfied if the inflaton energy density and pressure dominate the Hubble rate, and if $P_\phi < 0$, implying $V(\phi) > \dot{\phi}^2/2$. This is why these scenarios are called *slow-roll*: the inflaton needs to have a small kinetic energy density to slowly roll down its (very flat) potential during inflation towards its vacuum expectation value (which signals the end of the inflationary expansion). This also implies that during inflation, the Hubble rate can be approximated as

$$H^2 \approx \frac{\rho_\phi}{3M_{\rm Pl}^2} \approx \frac{V(\phi)}{3M_{\rm Pl}^2}\,. \tag{X.8}$$

Let us now consider the Klein-Gordon equation of motion of the inflaton ϕ [274],

$$\ddot{\phi} + 3H\dot{\phi} = V'(\phi)\,, \tag{X.9}$$

where $'$ denotes a derivative with respect to ϕ. The slow-roll condition allows to neglect the double time derivative, so that

$$\dot{\phi} \approx -\frac{V'(\phi)}{3H}\,. \tag{X.10}$$

With these approximations, from the above definitions of ε and η we can define the *potential slow-roll parameters* as [283]

$$\varepsilon_V \equiv \frac{M_{\rm Pl}^2}{2}\left(\frac{V'}{V}\right)^2\,, \quad \eta_V \equiv M_{\rm Pl}^2\left(\frac{V''}{V}\right)\,. \tag{X.11}$$

which are useful quantities assessing whether a given scalar field potential can lead to slow-roll inflation. Clearly, during inflation, the potential slow-roll parameters need to remain small: $\varepsilon_V \ll 1$, $|\eta_V| \ll 1$.

The end of inflation is defined by requiring that the slow-roll parameters are not small anymore. As soon as one becomes of order 1, inflation stops. Parametrically, this is obtained with $\max\{\varepsilon_V(\phi_{\rm end}), \eta_V(\phi_{\rm end})\} \equiv 1$. We can find the energy density of the inflaton field at this moment by imposing the equation-of-state parameter to be $w_\phi = -1/3$. This implies $\dot{\phi}^2_{\rm end} = V(\phi_{\rm end})$, which also yields

$$\rho_{\phi_{\rm end}} = \frac{3}{2} V(\phi_{\rm end})\,. \tag{X.12}$$

X.2.4 Power Spectrum

One of the most striking predictions of inflation is that the quantum fluctuations of the inflaton field get imprinted on the Universe as quasi-Gaussian oscillations in the local energy density profile. These tiny discrepancies grow over time as gravitational instabilities, leading to the formation of the first structures once gravity pulls matter inwards in over-dense regions. These inhomogeneities in the expectation values of correlations between the inflaton field value at different points in space can be described in momentum space by their *power spectrum* $\Delta(k)$, where k is the wavenumber associated with a correlation length $\lambda = 2\pi/k$.

The power spectrum can be described by a power law as [283]

$$\Delta(k) = A_{s,\star} \left(\frac{k}{k_\star}\right)^{n_s - 1}\,, \tag{X.13}$$

where $A_{s,\star}$ is the amplitude at a given *pivot* scale $k_\star$. The spectral index n_s measures how distant the power spectrum is from being scale-invariant, where $n_s = 1$, and $\Delta(k)$ is constant in k. A scale-invariant (or Harrison-Zeldovich) spectrum means that no quantum effect was imprinted on the fabric of spacetime at the beginning of time and, hence, that some fundamental symmetry was responsible for the initial conditions that led to a homogeneous and flat Universe. On the contrary, any deviation from scale-invariance is a sign that correlations were impressed with a dynamic process such as slow-roll inflation. In addition to these parameters, inflation also predicts an unavoidable production of a stochastic background of gravitational waves (GW) as a result of the tensor perturbations on the metric induced by the inflaton quantum fluctuations. Also, the power spectrum of GWs can be represented by a power law and, to compare with observations of the CMB, we use the *tensor-to-scalar ratio* r parameter, measuring the ratio between the tensor and scalar power spectrum amplitudes at a given pivot scale:

$$r_\star = \frac{A_{t,\star}}{A_{s,\star}}\,. \tag{X.14}$$

The most up-to-date measurements by the Planck collaboration [581] give us

$$n_s = 0.9659 \pm 0.0040\,, \qquad A_{s,\star} = (2.1 \pm 0.1) \times 10^{-9}\,, \tag{X.15}$$

whereas the most stringent upper bound on r comes from the recent 2021 analysis by BICEP/Keck (BK) [582],

$$r_{0.05} < 0.035, \qquad 95\%\,\text{C.L.}\,, \tag{X.16}$$

where $r_{0.05}$ means that the chosen pivot scale is $k_\star = 0.05\,\mathrm{Mpc}^{-1}$. These findings are in favor of, but still do not prove an inflationary explanation.

These observables can be related to the form of the potential V in a scalar field theory of inflation. For instance, the amplitude of the Gaussian curvature perturbation is [281]

$$A_{s,\star} = \frac{V}{24\pi^2 \varepsilon_V M_{\rm Pl}^4}\,. \tag{X.17}$$

while, the tensor-to-scalar ratio and spectral index are given by [281]

$$r = 16\varepsilon_V\,; \quad n_s = 1 - 6\varepsilon_V + 2\eta_V\,. \tag{X.18}$$

Therefore, we can constrain the parameters of a chosen inflaton model by directly comparing the predictions on n_s,, r, and $A_{s,\star}$ with experimental observations.

Another useful quantity is the total number $N_\star$ of e–folds that occurred *after* the modes at the CMB pivot scale $k_\star = 0.05\,\mathrm{Mpc}^{-1}$ first crossed the horizon until the end of inflation, defined as [283, 583]

$$N_\star = \int_{\phi_{\rm end}}^{\phi_\star} \frac{1}{\sqrt{2\varepsilon_V}} \frac{d\phi}{M_{\rm Pl}}\,. \tag{X.19}$$

This is determined by the model parameters, which are directly constrained by demanding $N_\star$ to be around 60 (the number of e-folds required for a complete inflation scenario). In Fig. X.1, we show the results obtained by the Planck collaboration in the final release of 2018 [581], and their combination with constraints from BICEP/Keck and WMAP observations conducted by the BICEP/Keck collaboration in 2021 [582]. The theoretical predictions from some inflationary models are displayed with different colors and are required to reproduce a number of e-folds $N_\star$ between 50 and 60. In particular, so-called R^2 and α-attractor inflation models are currently favored and will be the topic of the next section. A last remark is, however, necessary. While we have cited the constraints on $r_{0.05}$ in Eq. (X.16), we have displayed the experimental results for $r_{0.002}$. We can easily map one observable to the other by writing the spectrum of tensor perturbations [584]

$$\Delta_t(k) = A_{t,\,0.05}\left(\frac{k}{0.05\,\mathrm{Mpc}^{-1}}\right)^{n_t} = r_{0.05}\,A_{s,\,0.05}\left(\frac{k}{0.05\,\mathrm{Mpc}^{-1}}\right)^{-r_{0.05}/8}\,, \tag{X.20}$$

where we have used Eq. (X.14) and the consistency relation $n_t = -r/8$ for single field slow-roll models. We can use the same definition of r at the pivot scale $0.002\,\mathrm{Mpc}^{-1}$, from which we obtain the following relation with $r_{0.05}$

$$r_{0.002} = r_{0.05}\left(\frac{0.002}{0.05}\right)^{-r_{0.05}/8-n_s+1}\,. \tag{X.21}$$

X.2.5 Universal Attractor Models

As Fig. X.1 shows, the simplest single-field inflationary models with a monomial potential are being excluded by current observations. On the contrary, more convoluted possibilities, such as α-attractors, are consistent with the experimental constraints. The prime type of model in this category is Starobinsky inflation, dating back to ideas of the early 80's [585–587]. It consists of a modification of the Einstein-Hilbert action by adding a curvature term proportional to the Ricci scalar R squared, hence it is also called a $R+R^2$ or simply

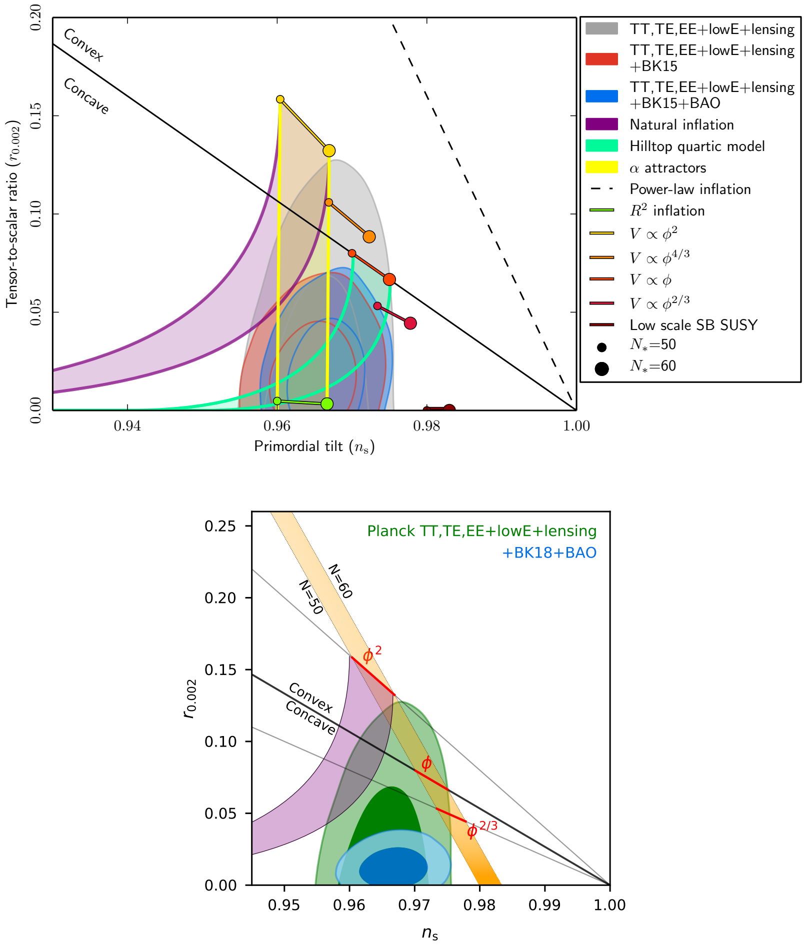

Figure X.1: Constraints on n_s and r at 68% and 95% CL at the pivot scale $k = 0.002\,\mathrm{Mpc}^{-1}$. The upper panel shows the result by Planck 2018 (figure from [581]), while the lower panel come from the BICEP/Keck 2021 analysis (figure from [582]). The theoretical predictions from some inflationary models are displayed.

R^2 model[1]. It falls in the broader category of $f(R)$ theories of modified gravity [588]. As it was shown in [589], this formulation is equivalent to General Relativity with the addition of a massive scalar field Φ with the following (Starobinsky) potential [585]

$$V(\phi) = \Lambda^4 \left(1 - e^{-\sqrt{\frac{2}{3}}\frac{\Phi}{M_{\mathrm{Pl}}}}\right)^2 . \tag{X.22}$$

Here, Λ represents a normalization scale, which dominate the dynamics during inflation, when ϕ takes large values and behaves as a cosmological constant, leading to a quasi-de Sitter expansion. The field rolls down the flat potential, as displayed in Fig. X.2, and eventually falls into its true vacuum, ending inflation and reheating the Universe. At this point, the inflaton potential can be approximated for small field values as

$$V(\Phi) \simeq \frac{2\,\Lambda^4}{3}\frac{\Phi^2}{M_{\mathrm{Pl}}^2}, \quad \text{or, equivalently, as} \quad V(\Phi) \simeq \lambda M_{\mathrm{Pl}}^2 \Phi^2, \tag{X.23}$$

[1]The Ricci scalar is given by the trace $R = g^{\mu\nu}R_{\mu\nu}$, where $R_{\mu\nu}$ is the Ricci curvature tensor that represents the degree to which the geometry determined by a metric tensor $g_{\mu\nu}$ deviates from that of flat space

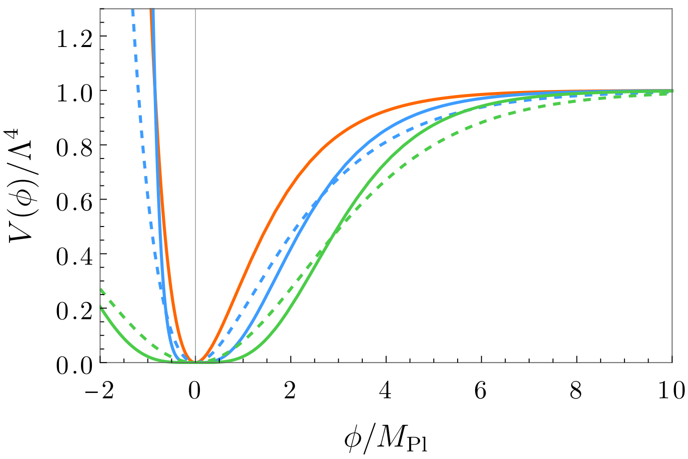

Figure X.2: The orange line is the Starobinsky potential from Eq. (X.22). The blue (green) line corresponds to an E-model (T-model) potential with $\alpha = 1$ and $n = 2$, or, equivalently $k = 4$ (cf. Eqs. (X.24) and (X.25)). Dashed lines indicate the potentials with $\alpha = 2$ and $n = 1$.

where we have defined the dimensionless parameter $\lambda = (\Lambda/M_{\rm Pl})^4$. Notice that Starobinsky inflation is similar to Higgs inflation [590], where the SM Higgs couples non-minimally to gravity and plays the role of the inflaton.

This equivalence is not a coincidence, but rather stems from the fact that a more general class of non-minimally coupled theories, known as *universal attractors* [591, 592], encompasses Higgs and Starobinsky inflation as special cases. In particular, it is found that an entire class of no-scale supergravity theories [593–598] leads to inflationary scenarios that exhibit Starobinsky-like flat potentials at large field values and are currently in agreement with observations. The term "no-scale" comes from the fact that the scale at which supersymmetry is broken is initially undetermined in these models. They have the attractive property of being able to maintain a hierarchy of energy scales without requiring fine-tuning. In particular, the exact energy scale at which inflation occurs does not depend on the supersymmetry-breaking scale, which could be anywhere between the TeV scale of the LHC up to 10^{10} TeV, the upper limit imposed by CMB constraints on the tensor-to-scalar ratio r. Notice that this upper bound is much smaller than $M_{\rm Pl} \sim 10^{15}$ TeV. Moreover, they provide scalar potentials that are flat enough to drive the slow-roll inflationary expansion for the right amount of time.

In this analysis, we focus on the so-called E and T α-attractors, provided by the following inflaton potentials [591, 592]:

$$V(\Phi) = \Lambda^4 \left(1 - e^{-\sqrt{\frac{2}{3\alpha}}\frac{\Phi}{M_{\rm Pl}}}\right)^{2n}, \qquad \text{E-model}, \tag{X.24}$$

$$V(\Phi) = \Lambda^4 \left[\tanh\left(\frac{\Phi}{\sqrt{6\alpha}M_{\rm Pl}}\right)\right]^{2n}, \qquad \text{T-model}. \tag{X.25}$$

Here, n is a positive integer, while $\alpha > 0$ is a parameter that classifies various possible realizations of the potential from supergravity. Notice that for $n = 1$ and $\alpha = 1$ the E-model recovers the Starobinsky potential [585].

Notice that, within the current experimental sensitivity, all these models lead essentially to similar behavior *during* inflation. What makes them distinguishable is the dynamics *at the end* of inflation, or in other words, how the inflaton oscillates around the minimum of its potential in the post-inflationary reheating phase. This is a crucial observation, especially when considering the potential creation of DM particles during this epoch.

The interplay between CMB constraints on the non-standard expansion, primarily governed by the reheating potential, and experimental investigations of DM—such as those conducted at colliders—presents an opportunity to simultaneously glean insights into both phenomena (cf. Section X.6).

X.3 Reheating Dynamics and Beyond

Declaration: The results presented in this section are mainly based on existing literature and have been reformulated by the thesis author, YX, JL, and MB, for [4]. The text presented in this section is based on what was presented in the publication, but reworked in style and expanded in content. In the paper, the text was written by the thesis author and YX, while all authors reviewed and corrected the text. Additional material has been incorporated based on recent theoretical developments in the field.

X.3.1 Connection between α-Attractors and the Monomial Potential

Following the end of inflation, the inflaton field undergoes oscillations around the minimum of its potential, initiating the *reheating* process of the Universe by decaying into highly energetic particles. These particles gradually come to dominate the Universe's energy density as the inflaton condensate depletes its energy. The E- and T-type α-attractor potentials in Eqs. (X.24) and (X.25) have a plateau for large field values ($\Phi \gg M_{\rm Pl}$) driving inflation, and a minimum at $\Phi = 0$ where reheating occurs. To study the post-inflationary dynamics, we expand each potential around this minimum.

E-model:

In the vicinity of $\Phi = 0$, the exponential term can be expanded via Taylor series:

$$e^{-\sqrt{\frac{2}{3\alpha}}\frac{\Phi}{M_{\rm Pl}}} = 1 - \sqrt{\frac{2}{3\alpha}}\frac{\Phi}{M_{\rm Pl}} + \frac{1}{2}\frac{2}{3\alpha}\frac{\Phi^2}{M_{\rm Pl}^2} - \frac{1}{6}\left(\frac{2}{3\alpha}\right)^{\frac{3}{2}}\frac{\Phi^3}{M_{\rm Pl}^3} + \cdots .$$

Substituting this expansion into Eq. (X.24) yields, at leading order,

$$\begin{aligned} V_E(\Phi) &\simeq \Lambda^4\left[\sqrt{\frac{2}{3\alpha}}\frac{\Phi}{M_{\rm Pl}} - \frac{1}{2}\left(\frac{2}{3\alpha}\right)\frac{\Phi^2}{M_{\rm Pl}^2} + \mathcal{O}(\Phi^3/M_{\rm Pl}^3)\right]^{2n} \\ &\simeq \Lambda^4\left(\frac{2}{3\alpha}\right)^n\left(\frac{\Phi}{M_{\rm Pl}}\right)^{2n}\left[1 + \mathcal{O}\left(\frac{\Phi}{M_{\rm Pl}}\right)\right]. \end{aligned} \tag{X.26}$$

Thus, in the neighborhood of its minimum, the potential exhibits the behavior

$$V_E(\Phi) \propto \Phi^{2n},$$

corresponding to a polynomial potential with parameters

$$k_E = 2n, \qquad \lambda_E = \Lambda^4\left(\frac{2}{3\alpha}\right)^n, \qquad M = M_{\rm Pl}. \tag{X.27}$$

T-model:

Similarly, expanding the hyperbolic tangent near the origin,

$$\tanh\left(\frac{\Phi}{\sqrt{6\alpha}M_{\rm Pl}}\right) = \frac{\Phi}{\sqrt{6\alpha}M_{\rm Pl}} - \frac{1}{3}\left(\frac{\Phi}{\sqrt{6\alpha}M_{\rm Pl}}\right)^3 + \mathcal{O}(\Phi^5)\,,$$

and substituting into Eq. (X.25) yields

$$V_T(\Phi) \simeq \Lambda^4 \left(\frac{\Phi}{\sqrt{6\alpha}M_{\rm Pl}}\right)^{2n}\left[1+\mathcal{O}\left(\frac{\Phi^2}{M_{\rm Pl}^2}\right)\right], \tag{X.28}$$

which again has the leading power $V_T(\Phi) \propto \Phi^{2n}$ and the corresponding parameters

$$k_T = 2n, \qquad \lambda_T = \Lambda^4\,(6\alpha)^{-n}, \qquad M = M_{\rm Pl}. \tag{X.29}$$

Unified monomial form.

Both expansions reduce to an effective low-energy potential of the form

$$V(\Phi) = \lambda\,\frac{\Phi^k}{M^{k-4}}, \qquad k = 2n, \tag{X.30}$$

where the dimensionless coupling λ encodes the dependence on the microscopic parameters (Λ, α, n):

$$\lambda \simeq \begin{cases} \Lambda^4\left(\dfrac{2}{3\alpha}\right)^{k/2} & \text{(E-model)},\\ \Lambda^4\,(6\alpha)^{-k/2} & \text{(T-model)}. \end{cases}$$

The effective scale M can, without loss of generality, be identified with the reduced Planck mass $M_{\rm Pl}$, which sets the natural cutoff of the inflaton sector.

Physical interpretation.

During inflation, the field probes the plateau region of Eqs. (X.24) and (X.25), but following the conclusion of inflation, it oscillates around the minimum $\Phi \simeq 0$, where the potential is accurately described by the monomial form (X.30). Consequently, throughout the reheating phase, the inflaton behaves as if it had a potential $V \propto \Phi^k$, with $k = 2n$ determining its effective equation of state $w_\Phi = (k-2)/(k+2)$ and thereby governing the scaling behavior of ρ_Φ and ρ_R discussed in the subsequent analysis.

The specific form of the inflaton potential is not essential for our analysis, as our primary focus concerns how the reheating phase affects DM production. The potential presented in Eq. (X.30) is adequate for this purpose. However, we will subsequently utilize CMB constraints on E- and T-models to investigate the interconnections between cosmological and collider data regarding both reheating dynamics and DM model parameters (see Section X.5 and Section X.2.5).

X.3.2 Coupled evolution of inflaton and radiation bath

The temporal evolution of the homogeneous inflaton field following inflation is governed by the Klein-Gordon equation introduced in Section X.2.3, now augmented with a decay term $\Gamma_\phi\dot{\phi}$, where Γ_Φ represents the inflaton decay width:

$$\ddot{\Phi} + (3H+\Gamma_\Phi)\,\dot{\Phi} + V'(\Phi) = 0\,, \tag{X.31}$$

where dots denote time derivatives, $H = \dot{a}/a$ is the Hubble expansion rate, and $V'(\Phi) = \partial_\Phi V(\Phi)$. This equation can be rewritten in terms of the energy density and pressure of the inflaton condensate by using Eq. (X.7). Due to the oscillatory behavior, it is more useful to average these quantities over several periods of oscillation. Taking the average of Eq. (X.31), we can neglect the term proportional to $\langle \Gamma_\Phi \rangle$ and $\langle H \rangle$. This is a good approximation as long as the decay width and the Hubble rate do not vary significantly within a few oscillations, which is a reasonable assumption considering that reheating occurs when the inflaton potential is very flat. This implies that [599],

$$\langle \dot{\Phi} \rangle \simeq \langle \Phi V'(\Phi) \rangle \,. \tag{X.32}$$

Making use of the Virial theorem for the potential $V(\Phi) \propto \Phi^k$, namely,

$$\left\langle \frac{\dot{\Phi}^2}{2} \right\rangle = \frac{k}{2} \langle V(\Phi) \rangle \,, \tag{X.33}$$

and substituting Eq. (X.33) into Eq. (X.7), we obtain the density, isotropic pressure, and the equation of state for the inflaton [599, 600]:

$$\langle \rho_\Phi \rangle = \frac{\dot{\Phi}}{2} + V(\Phi) = \left(\frac{k}{2} + 1 \right) \lambda \frac{\langle \Phi^k \rangle}{M_{\rm Pl}^{k-4}} \,, \tag{X.34}$$

$$\langle P_\Phi \rangle = \frac{\dot{\Phi}}{2} - V(\Phi) = \left(\frac{k}{2} - 1 \right) \lambda \frac{\langle \Phi^k \rangle}{M_{\rm Pl}^{k-4}} \,, \tag{X.35}$$

$$\langle w_\Phi \rangle = \frac{\langle \rho_\Phi \rangle}{\langle P_\phi \rangle} = \frac{k-2}{k+2} \,. \tag{X.36}$$

Note that the $k = 2$ case corresponds to the inflaton oscillating with a quadratic potential and behaving like pressureless matter, while for $k = 4$, its equation of state describes a radiation-like condensate with $P = \rho/3$.

By combining Eqs. (X.34)-(X.36) with Eq. (X.31), we obtain the equation for the time evolution of the inflaton energy density

$$\dot{\rho}_\Phi + \frac{6k}{k+2} H \, \rho_\Phi = -\frac{2k}{k+2} \Gamma_\Phi \, \rho_\Phi \,. \tag{X.37}$$

The factor $\frac{2k}{k+2} = 1 + w_\Phi$ accounts for the specific equation of state of the decaying inflaton fluid. The decay of the inflaton produces highly energetic particles behaving like a relativistic fluid, whose energy density $\rho_{\rm R}$ evolves according to

$$\dot{\rho}_R + 4H\rho_R = \frac{2k}{k+2} \Gamma_\Phi \, \rho_\Phi \,. \tag{X.38}$$

The system of equations for $\rho_\Phi(t)$, $\rho_R(t)$ and $a(t)$ is closed by the first Friedmann equation

$$H^2 = \frac{\rho_\Phi + \rho_R}{3 M_{\rm Pl}^2} \,, \tag{X.39}$$

yielding a solution for the energy densities as functions of the scale factor a.

An analytic solution can be derived by first solving Eq. (X.37) for ρ_Φ by assuming $\Gamma_\Phi \ll H$ when $a_{\rm end} \ll a \ll a_{\rm rh}$, where $a_{\rm end}$ and $a_{\rm rh}$ are the scale factors at the beginning and the end of the reheating phase, respectively. This is a well-motivated approximation since the inflaton decay width is negligible compared to the Hubble rate at the beginning of the reheating phase. We thus obtain

$$\rho_\Phi(a) \simeq \rho_\Phi(a_{\rm rh}) \left(\frac{a_{\rm rh}}{a}\right)^{\frac{6k}{k+2}} \quad \text{if} \quad a_{\rm end} \ll a \ll a_{\rm rh}\,. \tag{X.40}$$

At later times, $a > a_{\rm rh}$, the inflaton will decay away with $e^{-\Gamma_\phi t}$, assuming that Γ_Φ is constant in time, as is the case for $k = 2$. In contrast, for $k > 2$, the decay width can acquire a dependence on time (cf. Eqs. (X.50) and (X.58)) and the scaling of $\rho_\Phi(t)$ will be model-dependent in general but close-to-exponential.

Solving for $\rho_{\rm R}(a)$

Using $\dot{\rho}_R = aH\,\frac{d\rho_R}{da}$ and substituting Eq. (X.40) into Eq. (X.38), we obtain

$$aH\,\frac{d\rho_R}{da} + 4H\rho_R = \frac{2k}{k+2}\Gamma_\Phi(a)\,\rho_\Phi(a). \tag{X.41}$$

Dividing both sides by aH yields a first-order inhomogeneous differential equation:

$$\frac{d\rho_R}{da} + \frac{4\rho_R}{a} = \frac{2k}{k+2}\frac{\Gamma_\Phi(a)\,\rho_\Phi(a)}{aH(a)}. \tag{X.42}$$

Multiply Eq. (X.42) by a^4 to obtain

$$\frac{d}{da}\big[a^4\rho_R(a)\big] = \frac{2k}{k+2}a^3\,\frac{\Gamma_\Phi(a)\,\rho_\Phi(a)}{H(a)}\,. \tag{X.43}$$

Integrating from $a_{\rm end}$ (the onset of reheating) to a general scale factor a gives

$$a^4\rho_R(a) - a_{\rm end}^4\rho_R(a_{\rm end}) = \frac{2k}{k+2}\int_{a_{\rm end}}^{a} d(a')\,(a')^3\,\frac{\Gamma_\Phi(a')\,\rho_\Phi(a')}{H(a')}. \tag{X.44}$$

Since the initial radiation density is negligible, $\rho_R(a_{\rm end}) \simeq 0$, the solution becomes

$$\rho_R(a) = \frac{2k}{k+2}\frac{1}{a^4}\int_{a_{\rm end}}^{a} da'\,(a')^3\,\frac{\Gamma_\Phi(a')\,\rho_\Phi(a')}{H(a')}\,. \tag{X.45}$$

Using $H(a') \simeq \sqrt{\rho_\Phi(a')/(3M_{\rm Pl}^2)}$, Eq. (X.45) becomes

$$\rho_R(a) \simeq \frac{2k}{k+2}\frac{\sqrt{3}\,M_{\rm Pl}}{a^4}\int_{a_{\rm end}}^{a} da'\,(a')^3\,\Gamma_\Phi(a')\,\rho_\Phi^{1/2}(a')\,, \tag{X.46}$$

in agreement with [4, 601].

Equation (X.46) explicitly shows how radiation is continuously sourced by the decay of the inflaton condensate. At early times ($a \simeq a_{\rm end}$), ρ_R is tiny because the integrand is suppressed by $\Gamma_\Phi \ll H$; as the Universe expands, ρ_Φ decreases and Γ_Φ/H grows, causing ρ_R to build up until it eventually equals ρ_Φ at reheating completion ($a = a_{\rm RH}$). The integrand also reveals that the time dependence of $\Gamma_\Phi(a')$ controls whether the functional dependence of the energy transfer on the scale factor (and thus on time). This dependence is determined by the prevalent decay channel of the inflaton, which is the subject of the next sections.

Temperature of the thermal bath

The temperature of the radiation thermal bath is then determined by inverting Eq. (III.22), yielding

$$T(a) = \left(\frac{30\, \rho_R(a)}{\pi^2 g_\star} \right)^{1/4} , \tag{X.47}$$

where $g_\star \sim \mathcal{O}(100)$ denotes the effective number of relativistic degrees of freedom that we assume to be constant throughout the reheating process, which is a good assumption for the considered temperatures of $T > 1$ GeV. We define the scale factor $a_{\rm rh}$ and the reheating temperature $T_{\rm rh} = T(a_{\rm rh})$ as the point in time when the energy density of radiation becomes equal to that of the inflaton,

$$\rho_\Phi(a_{\rm rh}) = \rho_R(a_{\rm rh}) , \tag{X.48}$$

and starts to dominate. We should note that this definition of the reheating temperature is not equivalent to the definition used in the instantaneous reheating approximation, which is based on the relations $\Gamma_\Phi = H$ in the context of matter-dominated (MD) reheating [274]. Note that $T_{\rm rh}$ marks the onset of the radiation phase, and in this sense, the definition in Eq. (X.48) is more accurate.

In section Section X.5, we show that the definition of the reheating temperature, as well as the properties of the inflaton decay products, can have a substantial impact on the interpretation of experimental constraints.

X.3.3 Beyond Perturbative Reheating: Preheating and Non-linear Dynamics

While the preceding analysis treats inflaton decay perturbatively through effective decay widths Γ_Φ, the early stages of reheating can involve highly non-perturbative processes that dramatically alter the energy transfer dynamics. This initial non-perturbative phase, termed *preheating*, has been extensively studied in the literature and can significantly impact the efficiency of reheating.

Parametric Resonance.

The mechanism underlying preheating is parametric resonance: as the inflaton oscillates coherently around the minimum of its potential, it induces time-dependent effective masses for coupled fields [572, 602]. Consider a scalar field χ coupled to the inflaton through an interaction $\frac{1}{2}g^2\Phi^2\chi^2$. The equation of motion for Fourier modes χ_k in an expanding universe takes the form

$$\ddot{\chi}_k + 3H\dot{\chi}_k + \left[k^2/a^2 + g^2\Phi^2(t)\right] \chi_k = 0 , \tag{X.49}$$

which describes a parametric oscillator with time-dependent frequency modulated by $\Phi(t)$. When the inflaton oscillates as $\Phi(t) \simeq \Phi_0(t)\cos(mt)$, this leads to explosive particle production in certain momentum bands, with occupation numbers growing exponentially as $n_k \sim e^{2\mu_k t}$, where μ_k is the Floquet exponent characterizing the instability [603].

Narrow vs. Broad Resonance.

As described in [604], the efficiency of preheating depends critically on the dimensionless parameter $q \equiv g^2\Phi_0^2/(4m^2)$, where m is the inflaton mass. For $q \ll 1$ (*narrow resonance*), particle production is moderate and occurs in discrete momentum bands. However, for $q \gg 1$ (*broad resonance*), the instability bands merge and particle production becomes extremely efficient, with characteristic Floquet exponents $\mu_k \sim 0.1 - 0.3\, m$ [603]. In this regime, a significant fraction of the inflaton energy can be transferred to daughter particles within just a few inflaton oscillations—far more efficiently than perturbative decay would suggest. For potentials with $V(\Phi) \propto \Phi^k$ with $k > 2$, the resonance structure becomes more complex. The anharmonicity of inflaton oscillations leads to different resonance patterns described by generalized Floquet equations (Mathieu or Lamé equations) [605].

Stochastic Resonance.

In expanding universes, the growth of fluctuations is counteracted by Hubble damping. Moreover, the changing amplitude $\Phi_0(t) \propto a^{-3k/(k+2)}$ due to cosmic expansion means that the effective coupling evolves in time. This can lead to *stochastic resonance* [603], where the phases of successive parametric kicks become uncorrelated, resulting in a random-walk-like growth of occupation numbers rather than purely exponential amplification. Nevertheless, even in the stochastic regime, preheating can be highly efficient if $\mu_k \gg H$.

Backreaction and Fragmentation.

Parametric resonance does not continue indefinitely. Eventually, the large occupation numbers of produced particles lead to backreaction effects that modify the inflaton dynamics [605, 606]. There are two primary mechanisms:

- *Rescattering*: Interactions among the highly populated daughter modes become important, leading to redistribution of energy across different momenta and potential thermalization.
- *Self-interaction*: For potentials with significant self-coupling, the inflaton field can fragment into spatially localized configurations such as oscillons—long-lived, quasi-stable solitonic objects that decay much more slowly than the homogeneous condensate.

Lattice simulations have revealed that following preheating, the system enters a turbulent regime characterized by self-similar evolution and energy cascades across different momentum scales [607, 608]. This turbulent phase is crucial for understanding how the non-thermal spectrum produced during preheating eventually thermalizes.

Fermion and Gauge Boson Production.

While parametric resonance is most efficient for bosonic fields, fermions can also be produced through analogous mechanisms, albeit with important differences [573]. Pauli blocking prevents unbounded occupation numbers, making fermionic preheating less explosive than the bosonic case. Nevertheless, coherent oscillations of the inflaton can still lead to significant fermion production through parametric excitation, particularly for Yukawa couplings $y\Phi\bar{\psi}\psi$.

For gauge fields, tachyonic instabilities can arise if the inflaton carries appropriate quantum numbers. In models with pseudo-scalar inflatons coupled to gauge fields through $\Phi F\tilde{F}$ interactions, explosive production of gauge quanta can occur, leading to nearly instantaneous energy transfer [609, 610].

Thermalization.

Neither perturbative decay nor preheating directly produce thermal spectra. The highly non-thermal distributions resulting from parametric resonance must undergo further evolution to reach local thermal equilibrium required for Big Bang nucleosynthesis [443,608,611]. The thermalization timescale depends on the interaction rates among decay products:

- *Kinetic equilibrium*: Redistribution of energy through elastic scatterings, establishing a thermal momentum distribution.
- *Chemical equilibrium*: Adjustment of particle abundances through number-changing processes to match thermal values.

Studies using quantum kinetic theory and classical-statistical lattice simulations suggest that for typical couplings, thermalization can occur within a few Hubble times after preheating ends [611]. However, the detailed thermalization dynamics remain an active area of research, particularly regarding the role of turbulent cascades in achieving full equilibrium (see, e.g., the recent [612, 613]).

Observational Implications.

The distinction between perturbative and non-perturbative reheating has important phenomenological consequences. Non-perturbative processes can:

- Significantly enhance gravitational wave production through collision of particles, bubble walls, or oscillons.
- Modify predictions for dark matter abundance if dark matter particles are produced during or after preheating.
- Impact baryogenesis scenarios that rely on out-of-equilibrium dynamics.
- Alter the effective number of e-folds between horizon crossing and reheating completion, affecting CMB predictions.

For the purposes of our analysis, we adopt the perturbative framework detailed in the following sections, which remains valid provided that: (i) coupling constants are sufficiently small to avoid broad resonance ($q \ll 1$), (ii) the inflaton decay completes before significant backreaction effects emerge, and (iii) thermalization occurs rapidly compared to the Hubble expansion rate after preheating. These conditions are generally satisfied for the low reheating temperature scenarios ($T_{\rm rh} < 10$ TeV) considered in this work, where small couplings are required to achieve gradual inflaton decay.

X.3.4 Bosonic Reheating

Inflationary reheating may proceed through inflaton decays into scalar particle pairs via a trilinear interaction of the form $\mu\Phi|X|^2$. This mechanism can be naturally realized through the coupling $\mu_H\Phi|H|^2$, enabling the inflaton to reheat the Universe by decaying into Higgs bosons. Additional bosonic decay channels become possible if further scalar fields are introduced beyond the Standard Model. In the context of this chapter, we investigate FIMP models featuring Majorana DM generated from the decay of heavier charged scalar parent particles P, as detailed in Section X.4 and Section II.2.4. Within this framework, the inflaton could decay into parent particle pairs P through the interaction $\mu_P\Phi|P|^2$. We assume that the produced scalars achieve rapid thermalization via their gauge interactions, allowing us to incorporate them into the radiation bath described by Eq. (X.38).

We consider the scenario where the intrinsic masses of the decay products are negligible relative to the inflaton mass. Under this assumption, the inflaton decay width can be expressed as follows [599, 601, 614]

$$\Gamma_{\Phi\to XX^\dagger}(t) = \frac{\mu_{\rm eff}^2(k)}{8\pi m_\Phi(t)}\,, \tag{X.50}$$

where

$$\mu_{\rm eff}^2(k) = \mu^2\,\alpha_\mu(k,\mathcal{R})\,\frac{(k+2)(k-1)}{4}\sqrt{\frac{\pi\,k}{2(k-1)}}\frac{\Gamma(\frac{k+2}{2k})}{\Gamma(\frac{1}{k})} \tag{X.51}$$

represents an effective coupling derived from proper averaging over inflaton oscillations. In this context, μ may correspond to either μ_H or μ_P; provided that the scalar daughter particles contribute to the radiation bath, the specific microphysical details become irrelevant to our analysis. The function $\alpha_\mu(k,\mathcal{R})$ depends on a kinematic factor $\mathcal{R}$ that essentially characterizes whether the inflaton-induced P mass $m_{\rm eff}^2(t) = 2\mu\Phi$ is comparable to the inflaton mass m_Φ ($\mathcal{R} \gtrsim 1$) or not ($\mathcal{R} < 1$). Our analysis primarily focuses on low-reheating temperature scenarios, achieved through gradual inflaton decay, which implies that μ is assumed to be very small (for instance, relative to $M_{\rm Pl}$) and consequently $\mathcal{R} \ll 1$. Under these conditions, α_μ exhibits only weak dependence on increasing k, with $\alpha_\mu \simeq 1$ for $k = 2$ and $\alpha_\mu \simeq 0.9$ for $k = 4$ [599].

The inflaton mass can be extracted from its potential (cf. Eq. (X.30)), giving

$$m_\Phi^2(t) = V''(\Phi) = k(k-1)\lambda\frac{\Phi^{k-2}(t)}{M_{\rm Pl}^{k-4}} \simeq k(k-1)\lambda^{\frac{2}{k}}M_{\rm Pl}^{\frac{2(4-k)}{k}}\,\rho_\Phi^{\frac{k-2}{k}}(t)\,, \tag{X.52}$$

where we employed the so-called "envelope approximation" for ρ_Φ, defined by $\rho_\Phi(t) = 3V(\Phi_0(t))/2$, with $\Phi_0(t)$ capturing the redshift and decay effects of the condensate $\Phi(t) \simeq \Phi_0(t)P(t)$ at large scales, while $P(t)$ describes its short-scale anharmonicity [599, 600]. It is important to note that for the standard $k = 2$ case, $m_\Phi = \sqrt{2\lambda}\,M_{\rm Pl}$ remains constant over time, whereas for $k > 2$ it diminishes with ρ_Φ throughout reheating.

This behavior leads to two important implications: first, the bosonic decay width experiences kinematic enhancement at later times, resulting in an accelerated reheating phase; second, the inflaton mass may potentially approach or fall below the mass of the decay products, thereby violating the perturbative reheating assumption and necessitating consideration of additional phenomena such as back-reaction effects. This situation is prevented provided that $\mathcal{R} \ll 1$ throughout the entire reheating phase. Nevertheless, Ref. [599] demonstrated that for $k = 4$ within an α-attractor T-model, $\mathcal{R} \gtrsim 1$ occurs when $10^{-19} \lesssim \mu/M_{\rm Pl} \lesssim 10^{-9}$.

However, given our focus on low reheating temperature scenarios (i.e., $T_{\rm rh} < 10\,\text{TeV}$), we have verified that typical values of $\mu/M_{\rm Pl}$ fall below 10^{-19} (cf. Eq. (X.57)), suggesting that any kinematic enhancement of the decay rate or non-perturbative particle production would likely manifest only during the final stages of reheating. Furthermore, Ref. [599] also identified non-perturbative effects at temperatures reaching $T_{\rm max}$ in scenarios where reheating is mediated by inflaton scattering. This particular case is not addressed in our analysis and would be irrelevant given the hierarchy $T_{\rm max} \gg m_P$ under consideration. With these assumptions at hand, by inserting Eq. (X.50) into Eq. (X.46), one obtains after integration [599]

$$\rho_R(a) \simeq \frac{\sqrt{3}}{8\pi}\frac{1}{1+2k}\sqrt{\frac{k}{k-1}}\frac{\mu_{\rm eff}^2}{\lambda^{\frac{1}{k}}}M_{\rm Pl}^{\frac{2k-4}{k}}\,\rho_\Phi^{\frac{1}{k}}(a_{\rm rh})\left(\frac{a_{\rm rh}}{a}\right)^{\frac{6}{2+k}}\left[1-\left(\frac{a_{\rm end}}{a}\right)^{\frac{2(1+2k)}{2+k}}\right]. \tag{X.53}$$

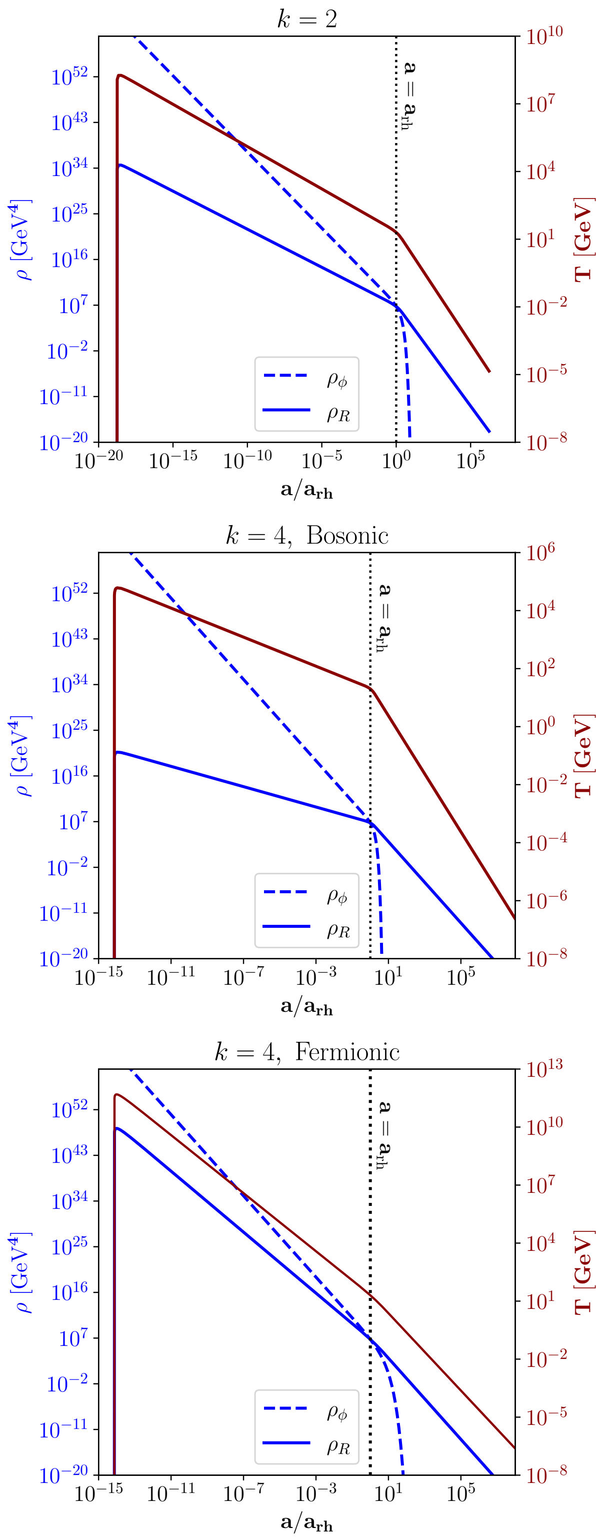

Figure X.3: Time evolution of energy densities for $T_{\rm rh} = 20$ GeV: the inflaton (blue dashed lines), radiation (blue solid lines), and the radiation temperature (red solid lines). The panels correspond to reheating potentials with $k = 2$ (top), bosonic $k = 4$ (middle), and fermionic $k = 4$ (bottom). *Figures created by YX and included in [4].*

This expression reveals that the radiation energy density and bath temperature vanish at the conclusion of inflation, $\rho_R(a_{\rm end}) = 0$ and $T(a_{\rm end}) = 0$, but rapidly attain a maximum at $a_{\rm max} \simeq a_{\rm end}(\frac{2k+4}{3})^{\frac{k+2}{4k+2}}$.

Furthermore, throughout the reheating epoch ($a \gg a_{\rm end}$), the radiation energy density exhibits redshifting behavior $\rho_R(a) \propto a^{-\frac{6}{2+k}}$, leading to

$$T(a) \simeq T_{\rm rh} \left(\frac{a_{\rm rh}}{a}\right)^{\frac{3}{4+2k}} . \tag{X.54}$$

Specifically, this indicates that for $k = 2$ (matter-like reheating) we observe $\rho_R \propto a^{-3/2}$ and $T \propto a^{-3/8}$, whereas for $k = 4$ (radiation-like reheating) we find $\rho_R \propto a^{-1}$ and $T \propto a^{-1/4}$. Tab. X.1 summarizes the various scaling behaviors relevant to our analysis. It is worth noting that these patterns differ from the redshifting characteristics during adiabatic cosmic expansion with entropy conservation, where $\rho_R \propto a^{-4}$ and $T \propto a^{-1}$.

Utilizing this solution and combining Eq. (X.54) with Eq. (X.40) and Eq. (X.39) provides the Hubble expansion rate during bosonic reheating when Φ dominates,

$$H(T) \simeq \frac{\sqrt{\rho_\Phi(T_{\rm rh})}}{\sqrt{3} M_{\rm Pl}} \left(\frac{T}{T_{\rm rh}}\right)^{2k} . \tag{X.55}$$

The maximum and reheating temperatures can be determined from Eq. (X.47) by applying the corresponding $a_{\rm max}$ and enforcing $\rho_\Phi = \rho_{\rm R}$ at $a_{\rm rh}$, respectively. Consequently, we obtain [599]

$$T^4_{{\rm max},b} = \frac{15}{4\pi^3 g_\star} \frac{k}{\sqrt{3k(k-1)}} \frac{M_{\rm Pl}^{\frac{2k-4}{k}}}{\lambda^{\frac{1}{k}}} \mu^2_{\rm eff} \rho^{\frac{1}{k}}_{\rm end} \left(\frac{3}{2k+4}\right)^{\frac{2k+4}{2k+1}} \tag{X.56}$$

and [599]

$$T^4_{{\rm rh},b} = \frac{30}{\pi^2 g_\star} \left[\frac{\sqrt{3}}{8\pi\,(1+2k)} \sqrt{\frac{k}{k-1}} \lambda^{-\frac{1}{k}} \frac{\mu^2_{\rm eff}}{M^2_{\rm Pl}}\right]^{\frac{k}{k-1}} M^4_{\rm Pl}\,. \tag{X.57}$$

The evolution of $\rho_\Phi(a)$, $\rho_R(a)$, and $T(a)$ in BR, obtained by numerically solving the Eqs. (X.37)-(X.39), as explained in the previous section, are shown in the left panel ($k = 2$) and the central panel ($k = 4$) of Fig. X.3.

X.3.5 Fermionic Reheating

The inflaton may alternatively reheat the Universe through decays into fermion pairs via a trilinear coupling of the form $y\Phi\bar{F}F$, a mechanism referred to as "fermionic reheating" (FR). This scenario presents additional complexity, as scalar inflaton fields cannot directly decay into Standard Model fermion pairs due to their chiral nature. Consequently, the introduction of additional Majorana or vector-like fermion species becomes necessary. In the context of this chapter, we investigate FIMP models that could involve a scalar singlet DM candidate generated through the decay of heavier vector-like parent particles carrying Standard Model gauge charges (cf. Sections II.2.4 and X.4). Such particles could serve as inflaton decay products and, upon rapid thermalization via gauge interactions, be incorporated into the radiation bath. Since we do not consider direct inflaton couplings to DM particles, models featuring only Majorana DM with charged scalar parents cannot accommodate this scenario unless an additional vector-like fermion is introduced. The decay width for final-state fermions with negligible masses is given by

$$\Gamma_{\Phi\to F\bar{F}}(t) = \frac{y_{\rm eff}^2(k)}{8\pi} m_\Phi(t)\,, \tag{X.58}$$

where [599]

$$y_{\rm eff}^2(k) = y^2 \alpha_y(k,\mathcal{R}) \sqrt{\frac{\pi k}{2(k-1)}} \frac{\Gamma(\frac{k+2}{2k})}{\Gamma(\frac{1}{k})} \tag{X.59}$$

represents the effective coupling obtained through averaging over inflaton oscillations, with the inflaton mass specified by Eq. (X.52). For the function $\alpha_y(k,\mathcal{R})$, a similar argument as for $\alpha_\mu(k,\mathcal{R})$ can be applied: the inflaton-induced fermion mass squared $y^2\Phi^2$ is negligible ($\mathcal{R} \ll 1$) if y is tiny enough, $y < \mathcal{O}(10^{-6})$, so that α_y is approximately constant in $\mathcal{R}$, while it only varies between $\alpha_y = 1$ at $k = 2$ and $\alpha_y \simeq 1.05$ at $k = 4$ [599]. [2]

Inserting Eq. (X.58) into Eq. (X.46) yields [599]

$$\rho_R(a) \simeq \frac{\sqrt{3}}{8\pi} \frac{k\sqrt{k(k-1)}}{7-k} y_{\rm eff}^2 \lambda^{\frac{1}{k}} M_{\rm Pl}^{\frac{4}{k}} \rho_\Phi^{\frac{k-1}{k}}(a_{\rm rh}) \left(\frac{a_{\rm rh}}{a}\right)^{\frac{6(k-1)}{2+k}} \left[1 - \left(\frac{a_{\rm end}}{a}\right)^{\frac{2(7-k)}{2+k}}\right], \tag{X.60}$$

with $\rho_R(a_{\rm end}) = 0$, but the maximum occurs at $a_{\rm max} \simeq a_{\rm end}(\frac{2k+4}{3k-3})^{\frac{k+2}{14-2k}}$, which differs from the bosonic scenario. For the relevant values of k in our analysis ($k < 7$), during the reheating phase we find $\rho_R(a) \propto a^{-\frac{6(k-1)}{2+k}}$, with the Standard Model temperature evolving according to

$$T(a) \simeq T_{\rm rh} \left(\frac{a_{\rm rh}}{a}\right)^{\frac{3k-3}{4+2k}}. \tag{X.61}$$

Consequently, for quadratic potentials ($k = 2$), we observe $\rho_R \propto a^{-3/2}$ and $T \propto a^{-3/8}$, similar to bosonic reheating, but for quartic potentials ($k = 4$) radiation redshifts as $\rho_R \propto a^{-3}$ and the temperature-scale factor relationship becomes $T \propto a^{-3/4}$, indicating more rapid cooling of the radiation bath compared to bosonic reheating. Tab. X.1 provides a comprehensive summary of the various behaviors relevant to our investigation. Combining Eq. (X.61) with Eq. (X.40) and Eq. (X.39) yields the Hubble expansion rate during fermionic reheating when Φ dominates,

$$H(T) \simeq \frac{\sqrt{\rho_\Phi(T_{\rm rh})}}{\sqrt{3}M_{\rm Pl}} \left(\frac{T}{T_{\rm rh}}\right)^{\frac{2k}{k-1}}. \tag{X.62}$$

The maximum and reheating temperatures in this case are given by [599]

$$T_{{\rm max},f}^4 = \frac{15}{4\pi^3 g_\star} \frac{k^2}{\sqrt{3k(k-1)}} \lambda^{\frac{1}{k}} M_{\rm Pl}^{\frac{4}{k}} y_{\rm eff}^2\, \rho_{\rm end}^{\frac{k-1}{k}} \left(\frac{3k-3}{2k+4}\right)^{\frac{2k+4}{7-k}} \tag{X.63}$$

[2] Notice that, differently from the bosonic case, the broad resonance regime ($\mathcal{R} \gg 1$) would be less impactful as effects from non-perturbative backreaction would be damped by Pauli blocking [573, 615]. Nonetheless, the inflaton decay rate would also be reduced by a factor $\mathcal{R}^{-1/2}$, leading to a more prolonged reheating phase. These effects are, however, not of relevance as long as $y < 10^{-5}$ [616], a necessary condition to be in a low reheating temperature scenario.

and [599]

$$T_{\mathrm{rh},f}^4 = \frac{30}{\pi^2 g_\star} \left[\frac{k\sqrt{3k(k-1)}}{7-k} \lambda^{\frac{1}{k}} \frac{y_{\mathrm{eff}}^2}{8\pi} \right]^k M_{\mathrm{Pl}}^4 \,. \tag{X.64}$$

The temporal evolution of $\rho_\Phi(a)$, $\rho_R(a)$, and $T(a)$ during fermionic reheating is illustrated in the left panel ($k = 2$) and right panel ($k = 4$) of Fig. X.3. For $k = 2$, the scaling behavior of $\rho_R(a)$ in the bosonic scenario matches that of fermionic reheating, as depicted by the blue solid line in the left panel of Fig. X.3. However, as the parameter k increases, the distinction between the two scenarios becomes more evident. Specifically, in the bosonic scenario, ρ_R is suppressed relative to the fermionic case, owing to the characteristic temporal dependence of the decay rate. It is crucial to recognize that in bosonic reheating, the decay rate scales as $1/m_\Phi(t)$ (cf. Eq. (X.50)) whereas in the fermionic case it scales as $m_\Phi(t)$ (cf. Eq. (X.58)). This fundamental difference in decay rate behavior explains the less steep slope observed in the solid blue line of the bosonic case compared to the fermionic scenario in Fig. X.3, particularly for $k > 2$.

X.4 Freeze-In Production during Reheating

Declaration: The results presented in this section have been mainly developed by the thesis author, MB, and JL for [4]. A preliminary raw version of such results also appeared in [555]. The thesis author contributed to the analytical study, the discussions, and the interpretation of results. The text presented in this section is based on what was presented in the publication, but reworked in style. The original text was written by the thesis author and by MB. In the paper, all authors participated in the discussions, the interpretation of results, and reviewed and corrected the text.

We are now positioned to analyze the impact of an inflationary reheating period on the production of DM particles.

We focus on DM freeze-in production via the the process $P \to \chi\, f_{\mathrm{SM}}$, where a SM-charged parent mediator P, assumed to be in thermal equilibrium with the SM bath, decays into a DM candidate χ and a SM fermion f_{SM}. This DM model lies within the simplified t-channel models discussed throughout this thesis work.

While thermal equilibrium is typically assumed, it is important to note the potential limitations of this assumption and what applies in this scenario:

1. **Pre-Thermalization:** Immediately after inflation, the particle bath is populated by non-thermalized decay products of the inflaton, in a phase known as *pre-thermalization*. In principle, particle production of non-thermalized particles is more complex and could, in principle, yield results that differ from those assuming thermalized states. However, in Appendix D of [4], we estimated the maximum effects of pre-thermalization on the DM relic abundance for $k = 2$ and found them negligible whenever $m_P/T_{\mathrm{rh}} \lesssim 10^3$, a condition that encompasses the scenarios analyzed here. Thus, we disregard pre-thermalization effects and assume the parent particles remain in equilibrium with the SM at all times.
2. **Finite-temperature effects:** Notice also that, as discussed at length in Chapters VII to IX, scattering processes and finite-temperature effects can significantly correct the relic abundance from freeze-in when the mass difference between DM and the parent particle is small. However, if $m_P \gg m_\chi$, such corrections are expected to

Table X.1: Detailed analytical results for Bosonic (BR) and Fermionic (FR) reheating scenarios with $V(\Phi) = \lambda\,\Phi^k/M_{\rm Pl}^{k-4}$. Formulas include full prefactors and apply for $\Gamma_\Phi \ll H$.

Quantity	**Bosonic Reheating (BR)**		**Fermionic Reheating (FR)**	
	$k=2$	$k=4$	$k=2$	$k=4$
Inflaton decay width $\Gamma_\Phi(t)$	$\dfrac{\mu_{\rm eff}^2}{8\pi\, m_\Phi}, \quad m_\Phi = \sqrt{2\lambda}\, M_{\rm Pl}$	$\dfrac{\mu_{\rm eff}^2}{8\pi\, m_\Phi(t)}, \quad m_\Phi \propto \rho_\Phi^{1/2}$	$\dfrac{y_{\rm eff}^2}{8\pi}\, m_\Phi, \quad m_\Phi = \sqrt{2\lambda}\, M_{\rm Pl}$	$\dfrac{y_{\rm eff}^2}{8\pi}\, m_\Phi(t), \quad m_\Phi \propto \rho_\Phi^{1/2}$
Inflaton energy density	$\rho_\Phi \propto a^{-3}$	$\rho_\Phi \propto a^{-4}$	same as BR	same as BR
Radiation energy density $\rho_R(a)$	$\rho_R \propto a^{-3/2}$	$\rho_R \propto a^{-1}$	$\rho_R \propto a^{-3/2}$	$\rho_R \propto a^{-3}$
Temperature scaling $T(a)$	$T \propto a^{-3/8}$	$T \propto a^{-1/4}$	$T \propto a^{-3/8}$	$T \propto a^{-3/4}$
Hubble rate $H(T)$	$\dfrac{\sqrt{\rho_\Phi(T_{\rm RH})}}{\sqrt{3}M_{\rm Pl}}\left(\dfrac{T}{T_{\rm RH}}\right)^4$	$\dfrac{\sqrt{\rho_\Phi(T_{\rm RH})}}{\sqrt{3}M_{\rm Pl}}\left(\dfrac{T}{T_{\rm RH}}\right)^8$	$\dfrac{\sqrt{\rho_\Phi(T_{\rm RH})}}{\sqrt{3}M_{\rm Pl}}\left(\dfrac{T}{T_{\rm RH}}\right)^4$	$\dfrac{\sqrt{\rho_\Phi(T_{\rm RH})}}{\sqrt{3}M_{\rm Pl}}\left(\dfrac{T}{T_{\rm RH}}\right)^{8/3}$
Maximum temperature $T_{\rm max}^4$	$\dfrac{15}{4\pi^3 g_\star}\dfrac{2}{\sqrt{6}}\dfrac{\mu_{\rm eff}^2\, M_{\rm Pl}}{\sqrt{\lambda}}\,\rho_{\rm end}^{1/2}\left(\dfrac{3}{8}\right)^{8/5}$	$\dfrac{15}{4\pi^3 g_\star}\dfrac{4}{\sqrt{12}}\dfrac{M_{\rm Pl}^{2/3}}{\lambda^{1/4}}\,\mu_{\rm eff}^2\,\rho_{\rm end}^{1/4}\left(\dfrac{3}{12}\right)^{4/3}$	$\dfrac{15}{4\pi^3 g_\star}\dfrac{4}{\sqrt{6}}\,\lambda^{1/2} M_{\rm Pl}^2\, y_{\rm eff}^2\,\rho_{\rm end}^{1/2}\left(\dfrac{3}{8}\right)^{8/5}$	$\dfrac{15}{4\pi^3 g_\star}\dfrac{16}{\sqrt{12}}\,\lambda^{1/4} M_{\rm Pl}\, y_{\rm eff}^2\,\rho_{\rm end}^{3/4}\left(\dfrac{9}{12}\right)^{4/3}$
Reheating temperature $T_{\rm RH}^4$	$\dfrac{30}{\pi^2 g_\star}\left[\dfrac{\sqrt{3}}{8\pi(5)}\sqrt{\dfrac{2}{1}}\dfrac{\mu_{\rm eff}^2}{M_{\rm Pl}^2\,\lambda^{1/2}}\right]^2 M_{\rm Pl}^4$	$\dfrac{30}{\pi^2 g_\star}\left[\dfrac{\sqrt{3}}{8\pi(9)}\sqrt{\dfrac{4}{3}}\dfrac{\mu_{\rm eff}^2}{M_{\rm Pl}^2\,\lambda^{1/4}}\right]^{4/3} M_{\rm Pl}^4$	$\dfrac{30}{\pi^2 g_\star}\left[\dfrac{2\sqrt{6}}{5}\dfrac{y_{\rm eff}^2\,\lambda^{1/2}}{8\pi}\right]^2 M_{\rm Pl}^4$	$\dfrac{30}{\pi^2 g_\star}\left[\dfrac{4\sqrt{12}}{3}\dfrac{y_{\rm eff}^2\,\lambda^{1/4}}{8\pi}\right]^4 M_{\rm Pl}^4$
Equation of state w_Φ	0 (matter-like)	1/3 (radiation-like)	0 (matter-like)	1/3 (radiation-like)

be less than $\mathcal{O}(10\%)$. This is indeed the case in the scenario here considered, where we only focus on production from parent particle decay with a clearly separate mass hierarchy between the parent particle and DM.

3. **Gravitational Production:** Additionally, we acknowledge that the gravitational production of DM via graviton-mediated scatterings—an irreducible contribution to the DM abundance—is Planck-suppressed (cf. Refs. [617–619]) and, therefore, irrelevant in low-reheating temperature scenarios like those considered in this study.

Dark Matter Production during Reheating

As discussed in Chapter III, the temporal evolution of the DM number density $n_{\rm DM}$ follows the Boltzmann equation

$$\dot{n}_{\rm DM} + 3Hn_{\rm DM} = \gamma_{\rm dec}\,, \tag{X.65}$$

where $\gamma_{\rm dec}$ represents the collision term associated with the decays of a heavy parent particle P into DM pairs. Neglecting back-reaction effects and assuming negligible intrinsic masses for the decay products, the collision term takes the form

$$\gamma_{\rm dec} = \frac{g_P}{2\pi^2}\,\Gamma_P\, m_P^2\, T\, K_1\!\left(\frac{m_P}{T}\right), \tag{X.66}$$

where g_P counts the internal degrees of freedom of the parent particle and Γ_P denotes its total decay width into DM states. In our framework, we do not specify a particular particle-physics model for Γ_P, as it will subsequently be constrained directly through the LLP decay length $c\tau = \Gamma_P^{-1}$ (cf. Section X.5).

Solving the Boltzmann Equation during Reheating

Throughout the reheating phase, cosmic expansion proceeds non-adiabatically, with entropy being continuously generated through inflaton decays. Consequently, it becomes advantageous to monitor DM production using the *comoving number density*

$$\mathcal{X}(a) \equiv n_{\rm DM}(a)\left(\frac{a}{a_{\rm end}}\right)^3, \tag{X.67}$$

which evolves according to

$$\frac{d\mathcal{X}(a)}{d\ln a} = \left(\frac{a}{a_{\rm end}}\right)^3 \frac{\gamma_{\rm dec}(a)}{H(a)}. \tag{X.68}$$

Here, $H(a)$ represents the total Hubble expansion rate, encompassing both inflaton and radiation contributions:

$$H(a) = \frac{\sqrt{\rho_\Phi(a) + \rho_{\rm R}(a)}}{\sqrt{3}\,M_{\rm Pl}}, \tag{X.69}$$

and $\gamma_{\rm dec}(a) \equiv \gamma_{\rm dec}(T(a))$ as specified in Eq. (X.66). This equation can be integrated numerically once the temporal evolution of $\rho_\Phi(a)$ and $\rho_{\rm R}(a)$ is established (cf. Section X.3).

The function $\mathcal{X}(a)$ encapsulates the total number of DM particles per comoving volume generated up to scale factor a, incorporating the non-adiabatic effects of entropy injection during reheating. It therefore represents the most natural variable for describing DM genesis within a general cosmological background.

Connecting to the Entropy-Normalized Yield

Following the completion of reheating when the Universe transitions to radiation domination, entropy generation terminates and the comoving entropy $S(T) = s(T)\, a^3(T)$ achieves conservation. Within this regime, the standard *comoving yield* can be defined as

$$Y_{\rm DM}(T) \equiv \frac{n_{\rm DM}}{s(T)} = \frac{\mathcal{X}(a(T))}{S(T)}\,, \tag{X.70}$$

where $s(T)$ represents the entropy density of the thermal bath. The present-day DM relic abundance is then expressed as

$$\Omega_{\rm DM} h^2 = \frac{\rho_{\rm DM}}{\rho_c/h^2} = \frac{m_{\rm DM}\, \mathcal{X}_{\rm DM}(a_0)}{\rho_c/h^2} \left(\frac{a_{\rm end}}{a_0}\right)^3, \tag{X.71}$$

which can alternatively be formulated in terms of $Y_{\rm DM}$ at late times when Y becomes constant.

Analytical approximations can be derived by inserting Eq. (X.66) and the appropriate temperature–scale factor relationship during reheating (cf. Eqs. (X.54), (X.61)). This yields a relic abundance of the form [4]

$$\frac{\Omega_{\rm DM}}{0.12} \simeq \left(\frac{1.5\ {\rm m}}{c\tau}\right) \left(\frac{106.75}{g_*}\right)^{3/2} \left(\frac{m_{\rm DM}}{100\ {\rm keV}}\right) \left(\frac{200\ {\rm GeV}}{m_P}\right)^2 \tag{X.72}$$

$$\times \begin{cases} \dfrac{2k+4}{3} \left(\dfrac{T_{\rm RH}}{m_P}\right)^{4k-1} \mathcal{I}_{\rm rh,b} + \mathcal{I}^0_{\rm RD}, & {\rm BR}, \\[2ex] \dfrac{2k+4}{3k-3} \left(\dfrac{T_{\rm RH}}{m_P}\right)^{\frac{9-k}{k-1}} \mathcal{I}_{\rm rh,f} + \mathcal{I}^0_{\rm RD}, & {\rm FR}, \end{cases} \tag{X.73}$$

with the integrals over the Bessel functions encoding the freeze-in history:

$$\mathcal{I}_{\rm rh,b} = \int_{z_{\rm end}}^{z_{\rm RH}} dz'\, z'^{2+4k} K_1(z')\,, \tag{X.74}$$

$$\mathcal{I}_{\rm rh,f} = \int_{z_{\rm end}}^{z_{\rm RH}} dz'\, z'^{\frac{2k+6}{k-1}} K_1(z')\,, \tag{X.75}$$

$$\mathcal{I}^0_{\rm RD} = \int_{z_{\rm RH}}^{\infty} dz'\, z'^3 K_1(z')\,. \tag{X.76}$$

The first two integrals describe DM production during the reheating phase in bosonic and fermionic scenarios, respectively, while $\mathcal{I}^0_{\rm RD}$ captures the contribution from the subsequent radiation-dominated epoch.

Relation to the Standard Freeze-In Picture and Dilution Factor

In the conventional radiation-dominated freeze-in scenario ($T_{\rm RH} > m_P$), entropy is conserved and Eq. (X.65) can be rewritten directly in terms of the comoving yield $Y_{\rm DM} = n_{\rm DM}/s$:

$$Y^{\rm RD}_{\rm DM}(T) \sim \frac{\Gamma_P}{H(T)} \sim \Gamma_P \frac{m_P M_{\rm Pl}}{T^3} \implies Y^{\rm RD}_{\rm DM}(z_{\rm fi}) \sim z^3_{\rm fi} \frac{\Gamma_P M_{\rm Pl}}{m_P^2}. \tag{X.77}$$

However, when $T_{\rm fi} > T_{\rm RH}$, the expansion rate and entropy production during reheating modify the DM yield significantly. Entropy injection leads to a *dilution factor*

$$D(T) = \frac{S(T)}{S(T_{\rm RH})} = \frac{s(T)\, a^3(T)}{s(T_{\rm RH})\, a^3(T_{\rm RH})} \simeq \begin{cases} \left(\dfrac{T_{\rm RH}}{T}\right)^{1+2k}, & \text{BR}, \\ \left(\dfrac{T_{\rm RH}}{T}\right)^{\frac{7-k}{k-1}}, & \text{FR}, \end{cases} \tag{X.78}$$

which accounts for the continuous entropy production before full radiation domination.

This dilution effect lowers the final DM yield relative to the standard RD estimate, with the correction scaling as

$$Y_{\rm DM}^{\rm RH}(T) \sim \frac{\Gamma_P m_P M_{\rm Pl}}{T^3} \times \begin{cases} \left(\dfrac{T_{\rm RH}}{T}\right)^{4k-1}, & \text{BR}, \\ \left(\dfrac{T_{\rm RH}}{T}\right)^{\frac{9-k}{k-1}}, & \text{FR}. \end{cases} \tag{X.79}$$

Evaluating this at the typical freeze-in temperature $T_{\rm fi} \simeq m_P/z_{\rm fi}$ (with $z_{\rm fi} \simeq 4{-}10$) yields

$$Y_{\rm DM}^{\rm RH}\left(\frac{m_P}{z_{\rm fi}}\right) \sim z_{\rm fi}^3 \frac{\Gamma_P M_{\rm Pl}}{m_P^2} \times \begin{cases} \left(\dfrac{z_{\rm fi} T_{\rm RH}}{m_P}\right)^{4k-1}, & \text{BR}, \\ \left(\dfrac{z_{\rm fi} T_{\rm RH}}{m_P}\right)^{\frac{9-k}{k-1}}, & \text{FR}. \end{cases} \tag{X.80}$$

Figure X.4 illustrates the evolution of the DM yield as a function of the time variable $z = m_P/T$, derived from a numerical solution of the differential equations system, including Eq. (X.37), Eq. (X.38) (which determine the Hubble rate in Eq. (X.69)), and the Boltzmann equation in Eq. (X.68).

Dilution Effects

In Fig. X.4, we observe an extended period of pure DM dilution for large $m_P/T_{\rm rh}$ ratios. Additionally, as soon as $m_P/T_{\rm rh} \gtrsim 1$, the genesis of DM primarily occurs at larger z in the $k = 4$ BR scenario compared to $k = 2$ and $k = 4$ in FR. The DM production rate exhibits the scaling behavior

$$\frac{d\mathcal{X}_{\rm DM}}{dz} = \begin{cases} z^{2+4k} K_1(z) & \text{BR} \\ z^{\frac{2k+6}{k-1}} K_1(z) & \text{FR} \end{cases}. \tag{X.81}$$

Consequently, we anticipate the peak of DM production occurring at later times in BR scenarios, specifically $(z_{\rm fi})_{{\rm BR},\,k=4} > (z_{\rm fi})_{k=2} \gtrsim (z_{\rm fi})_{{\rm FR},\,k=4}$.

When combined with the dilution factor presented in Eq. (X.78), we can comprehend the relative peak heights for the different reheating scenarios illustrated in Fig. X.4. The dilution factor expressed as

$$D(z_{\rm fi}) = \begin{cases} z_{\rm fi}^{1+2k} \left(\dfrac{T_{\rm rh}}{m_P}\right)^{1+2k} & \text{BR} \\ z_{\rm fi}^{\frac{7-k}{k-1}} \left(\dfrac{T_{\rm rh}}{m_P}\right)^{\frac{7-k}{k-1}} & \text{FR} \end{cases}, \tag{X.82}$$

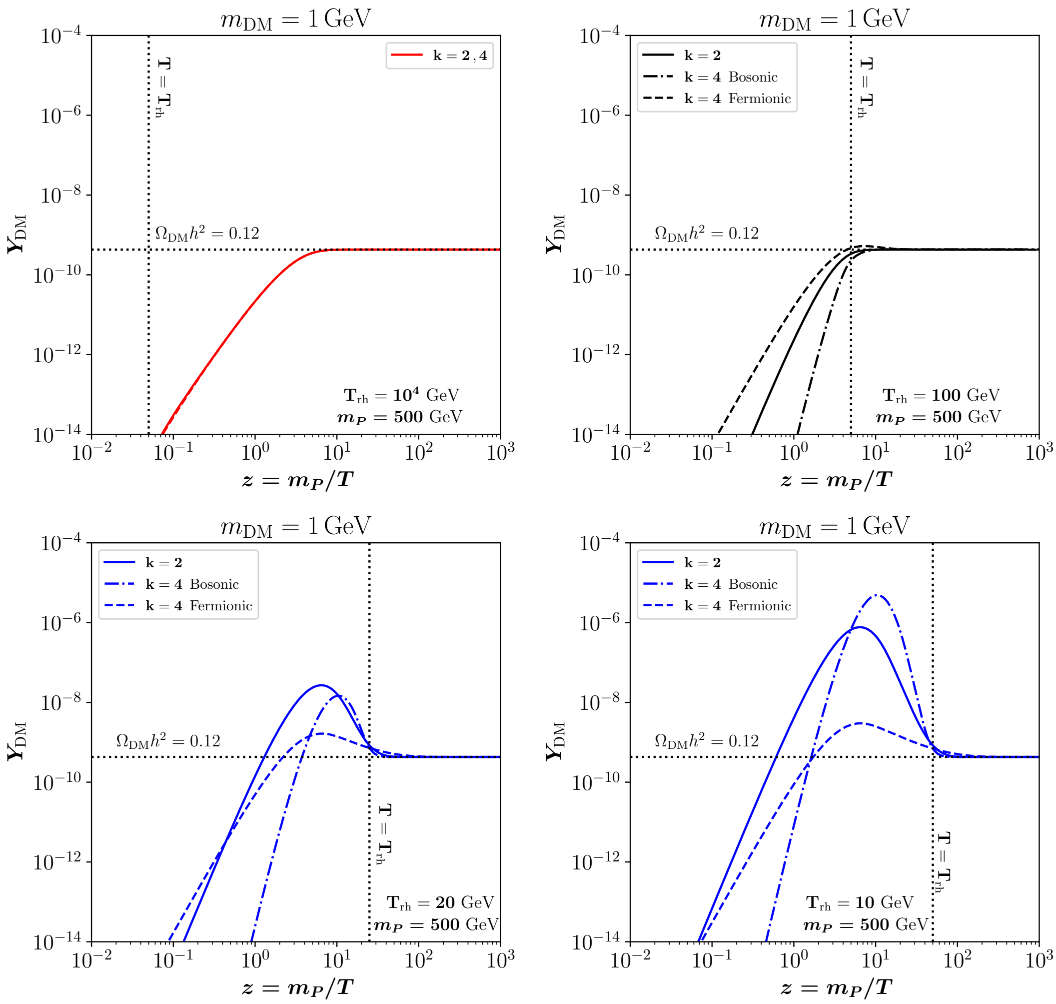

Figure X.4: Evolution of the DM comoving number density $Y_{\rm DM}$ for $m_{\rm DM} = 1\,\rm GeV$, and $m_P = 500\,\rm GeV$. From upper-left to bottom-right, we fix the reheating temperature at the values 10^4, 100, 20, and 10 GeV. The $k = 2$ scenario is depicted with solid lines, while dashed and dot-dashed lines portray the FR and BR scenarios with $k = 4$ potentials. The measured relic abundance, $\Omega_{\rm DM}h^2 = 0.12$, corresponds to the decay length values in Tab. X.2. *Figures created by YX and included in [4].*

diminishes (or grows) with the highest power in $m_P/T_{\rm rh}$ (or $z_{\rm fi}$) for the BR scenario with $k = 4$, followed by the reheating scenario with $k = 2$, and subsequently the FR scenario with $k = 4$. As a consequence, the hierarchy for $m_P/T_{\rm rh} \gtrsim 1$,

$$D^{\mathrm{BR},k=4}\left(T_{\rm fi}\right) > D^{\mathrm{FR,k=2,k=4}}\left(T_{\rm fi}\right) \,, \tag{X.83}$$

eventually reverses for $m_P/T_{\rm rh} \gg 1$.

Validity of Freeze-in Assumptions

We verify whether the DM evolution consistently remains within the freeze-in regime until production cessation. This condition is satisfied when the interaction rate stays below the expansion rate, $\Gamma(T) < H(T)$, enabling us to neglect back-reaction effects. Equivalently, this requires that the DM yield remains smaller than its equilibrium value,

Type	$T_{\rm rh}$ [GeV]	$c\tau$ [m]
$k=2$	10	1.8×10^{-2}
$k=4$ BR	10	1.8×10^{-6}
$k=4$ FR	10	1.7×10^{2}
$k=2$	20	2.2×10^{0}
$k=4$ BR	20	3.6×10^{-2}
$k=4$ FR	20	4.7×10^{2}
$k=2$	100	3.3×10^{3}
$k=4$ BR	100	3.4×10^{3}
$k=4$ FR	100	4.1×10^{3}
$k=2$	10^4	1.3×10^{4}
$k=4$ BR	10^4	1.3×10^{4}
$k=4$ FR	10^4	1.3×10^{4}

Table X.2: Values of $c\tau$ that account for the observed DM relic abundance for $m_{\rm DM}=1\,$GeV and $m_P=500\,$GeV. We show the results for BR and FR with $k=2$ and $k=4$, and $T_{\rm rh}=10,\,20,\,100,\,10^4\,$GeV. *Table created by YX and the thesis author and included in [4].*

which is expressed as (using Eq. (III.18))

$$Y_{\rm DM}^{\rm eq}=\frac{n_{\rm DM}^{\rm eq}}{s}=\frac{2T^3}{\pi^2}\frac{45}{2\pi^2 g_{\star s}T^3}=45/(\pi^4 g_{\star s})\,.$$

To determine which parameter combinations fulfill this requirement, we first fix the DM yield to the observed value,

$$Y_{\rm DM}^0\,m_{\rm DM}=4.3\cdot10^{-10}\,{\rm GeV}\,,$$

via Eq. (X.80), which consequently determines the value of Γ_P. We then substitute it into $Y_{\rm DM}(z_{\rm fi})\simeq\Gamma(z_{\rm fi})/H(z_{\rm fi})$ and compare with the equilibrium value. This implies that the following relations must be satisfied:

$$\frac{m_P}{T_{\rm rh}}<\begin{cases}160\left(\dfrac{m_{\rm DM}}{\rm GeV}\right)^{1/5}\dfrac{z_{\rm fi}}{5} & k=2\\[2mm] 70\left(\dfrac{m_{\rm DM}}{\rm GeV}\right)^{1/9}\dfrac{z_{\rm fi}}{10} & k=4\ {\rm BR}\\[2mm] 10^8\left(\dfrac{m_{\rm DM}}{\rm GeV}\right)\dfrac{z_{\rm fi}}{5} & k=4\ {\rm FR}\end{cases}\,. \tag{X.84}$$

This is satisfied for the choice of parameters illustrated in Fig. X.4. However, it becomes easier to violate the freeze-in assumptions at low reheating temperatures because, as we lower the DM mass, the interaction rate has to increase to compensate for the smaller DM energy density. For instance, choosing $m_{\rm DM}=12\,$keV the lower bound on FIMP masses from the Lyman-α according to [184, 620] implies that DM equilibrates if $m_P=500\,$GeV and $T_{\rm rh}=10\,$GeV. In what follows, the freeze-in conditions are always fulfilled.

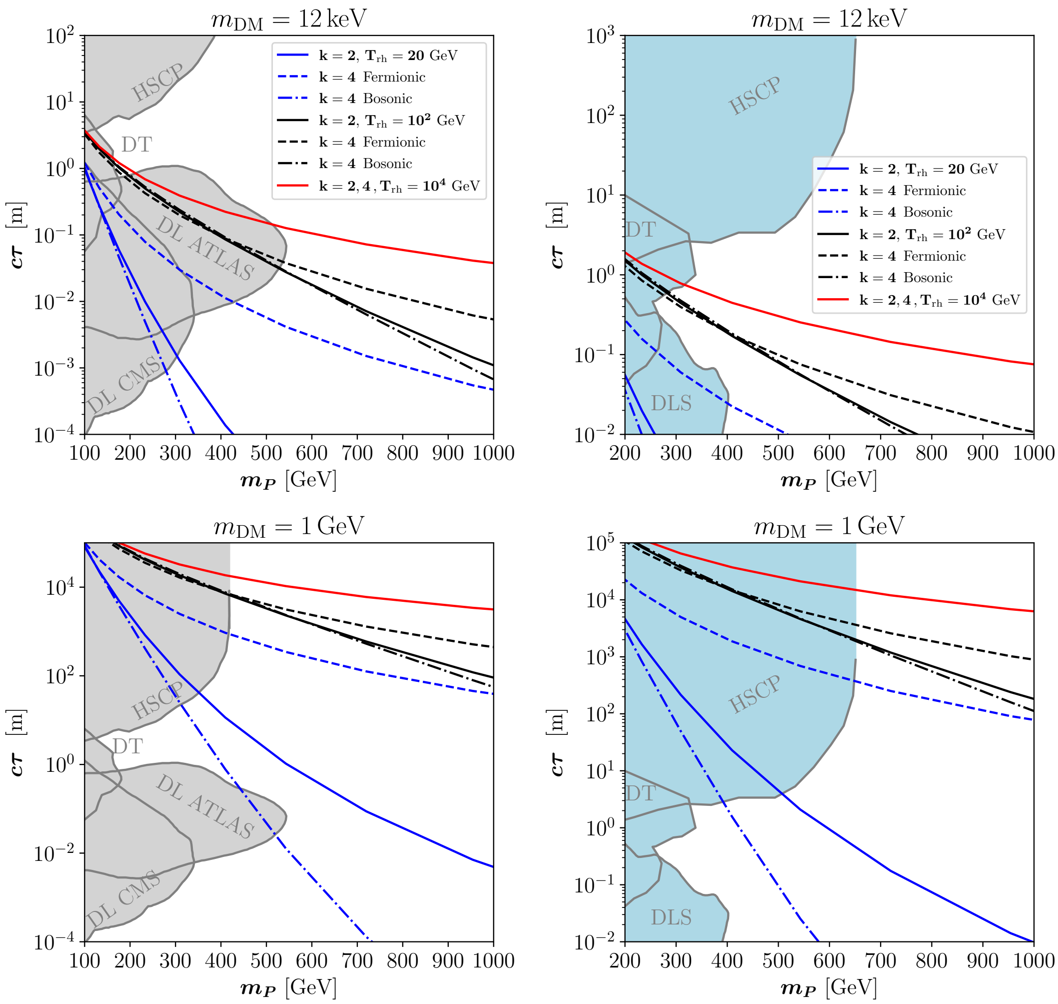

Figure X.5: Mapping the parent lifetime $c\tau$ versus mass m_P that reproduces the observed relic density. Top panels: $m_{\rm DM} = 12\,$keV; bottom: $1\,$GeV. Color code: $T_{\rm rh} = 20\,$GeV (blue), $100\,$GeV (black), $10^4\,$GeV (red). Line styles: solid ($k = 2$); dashed (FR, $k = 4$); dot-dashed (BR, $k = 4$). For $T_{\rm rh} = 10^4\,$GeV, the reheating history is immaterial over the mass range displayed, hence the red curves overlap. Shaded regions summarize current LLP constraints: gray (muonphilic Majorana DM) from Ref. [411] and light blue (leptophilic scalar singlet) from Ref. [184]. *Figures created by YX and included in [4].*

X.5 Interplay with Long-Lived-Particle Searches

Declaration: The results presented in this section have been developed by the thesis author, MB, JL, and YX for [4]. The thesis author contributed to the discussions and interpretation of results. The text presented here is based on what was presented in [4] but reworked in the presentation style and has been written by the thesis author and by MB. In particular, the thesis author wrote Section X.5.2. In the paper, all authors participated in the discussions, the interpretation of results, and reviewed and corrected the text.

X.5.1 Lifetime Inference from the Relic Density

We survey how the parent lifetime $c\tau = \Gamma^{-1}$ scales with the mediator mass m_P across four benchmark cosmologies consistent with the relic density. Two realizations are considered:

(i) Majorana DM with a scalar parent, and (ii) scalar–singlet DM with a vectorlike fermion parent. For each model we show $m_{\rm DM} = 12\,\text{keV}$ (upper panels) and $m_{\rm DM} = 1\,\text{GeV}$ (lower panels). The DM couples to a right-handed lepton; the collider overlays in Fig. X.5 correspond to the muonphilic configuration for the Majorana case.

Line styles encode the expansion history: solid ($k = 2$), dashed (FR, $k = 4$), and dot–dashed (BR, $k = 4$). For $k = 2$, FR and BR coincide and therefore both appear as solid curves. Colors indicate the reheating temperature: $T_{\rm rh} = 10^4\,\text{GeV}$ (red), $10^2\,\text{GeV}$ (black), and $20\,\text{GeV}$ (blue). In the high–$T_{\rm rh}$ regime ($T_{\rm rh} \gg m_P$), freeze-in proceeds after reheating and becomes insensitive to the details of the reheating dynamics, explaining the overlap of the red families. At lower $T_{\rm rh}$, the black/blue families converge as m_P decreases.

For $k > 2$, the inflaton mass and decay width track the condensate energy density, modifying the expansion rate in bosonic reheating (BR) versus fermionic reheating (FR) and feeding back into DM production during reheating. In practice, dilution during BR is typically stronger than in FR, which pushes toward shorter $c\tau$ in BR at fixed $(m_P, T_{\rm rh})$ (cf. Tab. X.2).

Since $\Omega_{\rm DM}h^2 \propto m_{\rm DM}/(c\tau)$, increasing $m_{\rm DM}$ requires longer lifetimes to keep $\Omega_{\rm DM}h^2$ fixed—hence the upward shift of the curves in Fig. X.5 when moving from 12 keV to 1 GeV.

Relative to Refs. [184, 411], our calculation adopts the thermodynamically consistent definition of reheating (Eq. (X.48)) and follows the full non-adiabatic evolution. These differences matter when inferring CMB bounds on $T_{\rm rh}$ and generally lead those earlier approximations to underestimate $\Omega_{\rm DM}$ (see Appendix C of [4]).

X.5.2 LLP Search Landscape and Implications

The shaded regions in Fig. X.5 summarize the current LHC reach for long-lived charged parents: gray for the muonphilic Majorana setup [411] and light blue for the leptophilic scalar–singlet case [184] (cf. also Section II.3.3). Below we sketch the salient features of the searches used in those recasts; for technical details of recasting and reinterpretation, see the cited works.

HSCP searches (slepton-like, ionizing tracks) probe the longest lifetimes. In the scalar–singlet scenario [184], CMS excludes vectorlike fermion parents with $c\tau \gtrsim 0.1\,(100)$ m at $m_P \simeq 200\,(600)$ GeV [229]. For the muonphilic Majorana setup, the reinterpretation in Ref. [411] yields slightly stronger bounds for scalar parents, excluding $c\tau \gtrsim 0.3\,(100)$ m at $m_P \sim 100\,(400)$ GeV using CMS [229] and ATLAS [235].

Displaced-lepton (DL) searches constrain intermediate lifetimes. ATLAS [231] is most sensitive near $c\tau \sim 10^{-2}$ m and analyzes both displaced $e\mu$ and same-flavor pairs, while CMS [232, 237] targets $c\tau \sim 10^{-3}$ m focusing on $e\mu$. Ref. [411] reinterprets both ATLAS and CMS DL results for a scalar parent, whereas Ref. [184] employs the CMS analyses available at the time.

Disappearing-track (DT) searches target lifetimes between the DL and HSCP regimes [230, 233, 234, 236, 621]. In the recasts of Refs. [184, 411], DT sensitivity extends only up to $m_P \sim 180\,(350)$ GeV, respectively. For the muonphilic scalar parent in Ref. [411], CMS DT results [233] were also interpreted as kinked-track signatures; the gray DT region in Fig. X.5 should therefore be seen as a forecast.

The interplay with Fig. X.5 highlights that a faithful treatment of reheating is essential to identify which LLP channels dominate. As an example, for a 1 GeV Majorana DM candidate (left, bottom), large $T_{\rm rh}$ (red) leaves HSCP as the primary handle, whereas at

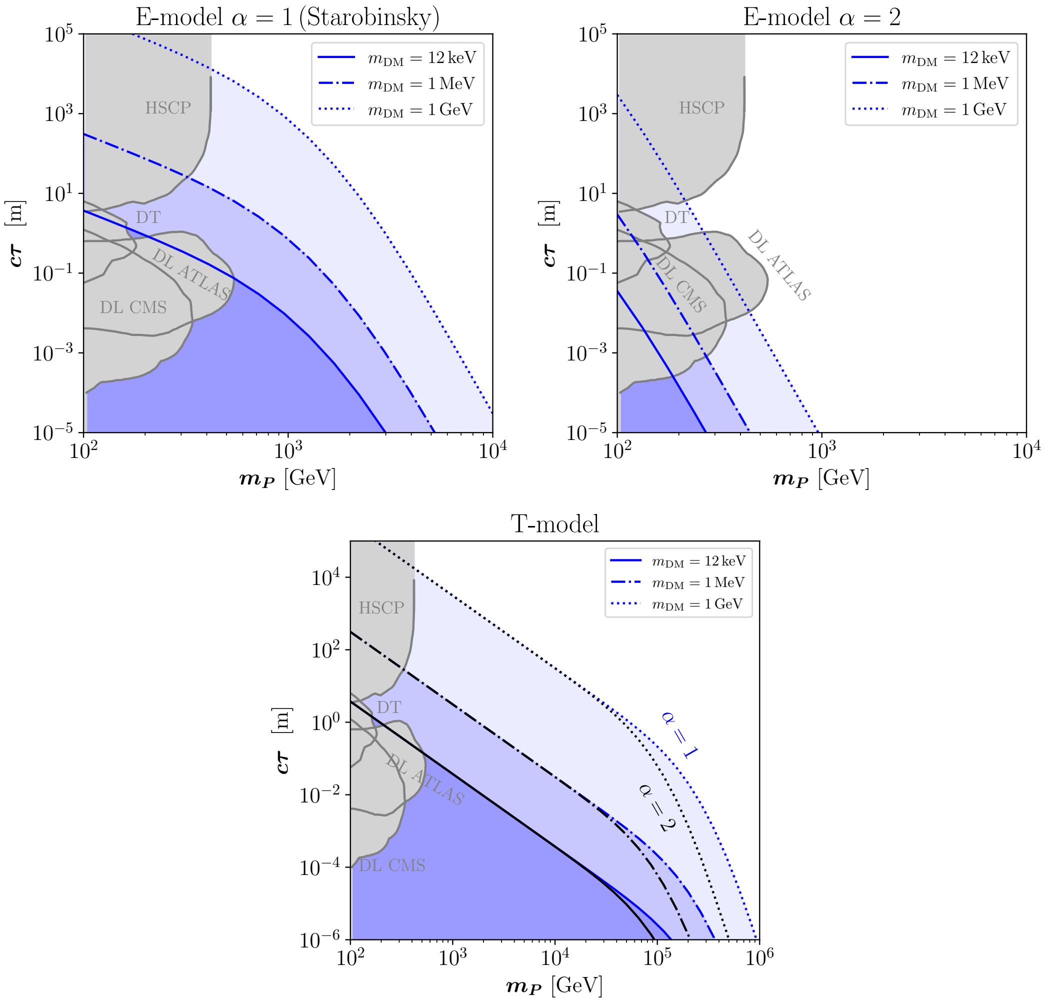

Figure X.6: Joint cosmology–collider constraints for the leptophilic Majorana DM model (scalar parent) assuming $k = 2$ reheating. Left: Starobinsky ($\alpha = 1$) E-model; center: E-model with $\alpha = 2$; right: T-model ($\alpha = 1$ in blue, $\alpha = 2$ in black). Blue shaded regions indicate where reproducing $\Omega_{\rm DM}$ conflicts with the CMB-driven lower bound on $T_{\rm rh}$ for $m_{\rm DM} = 12\,\rm keV$ (solid), $1\,\rm MeV$ (dot–dashed), and $1\,\rm GeV$ (dotted). Gray areas denote LLP exclusions (see Ref. [411] and text). *Figures created by YX and included in [4].*

low $T_{\rm rh}$ (blue) DL searches gain traction.

A future LLP signal could even differentiate BR from FR and infer the power k of the reheating potential when $T_{\rm rh} \lesssim m_P$. This is reflected in the distinct $c\tau$ predictions: solid ($k = 2$), dashed ($k = 4$, FR), dot–dashed ($k = 4$, BR). Disentangling these requires combining the LLP information (parent quantum numbers and lifetime) and $m_{\rm DM}$ with cosmological inference of $T_{\rm rh}$, which depends on the inflationary model class discussed next.

X.6 Interplay with CMB Observations

Declaration: The results presented in this section have been developed by the thesis author, MB, and YX for [4]. In particular, YX led the analysis on the cosmological constraints (also discussed in Appendix X.A), while the thesis author contributed to the interpreta-

tion and discussion of the results. The text presented in this section is based on what was presented in Section IV.C in [4], but restructured in style and content. In the paper, all authors participated in the discussions, the interpretation of results, and reviewed and corrected the text. The phase of inflationary reheating can leave a measurable imprint

on both dark matter (DM) production and collider observables. Understanding this connection requires combining the predictions of inflationary models with the limits derived from cosmological data—particularly the Cosmic Microwave Background (CMB). In this section, we explore this interplay, focusing on the α–attractor E- and T-models, whose effective reheating potentials take the form

$$V(\Phi) \propto \Phi^k, \tag{X.85}$$

as discussed in Sections X.2.3 and X.2.4.

This section aims to investigate how inflationary constraints on the reheating temperature $T_{\rm rh}$, derived from CMB observables such as n_s and r, translate into limits on the parent particle decay length $c\tau$ in DM models constrained by collider searches. These complementary bounds allow one to connect early-Universe cosmology with laboratory-based searches for long-lived particles (LLPs).

Inflationary Observables and Reheating Connection

Inflationary α–attractor models predict precise relations among the scalar spectral index n_s, the tensor-to-scalar ratio r, the amplitude A_s of primordial perturbations, and the number of e-folds $N_\star$ between horizon exit and the end of inflation (cf. Eqs. (X.A.5)–(X.A.18)). Current observations from Planck [581] and BICEP/Keck [582] strongly constrain these quantities (cf. Section X.2.4):

- $A_{s,\star} = (2.1 \pm 0.1) \times 10^{-9}$;
- $n_s = 0.9659 \pm 0.0040$ (68% C.L.);
- $r_{0.05} < 0.035, \qquad 95\%\,\text{C.L.}$.

Reheating affects when the CMB pivot scale $k_\star$ re-enters the horizon, linking $T_{\rm rh}$ to the inflationary parameters through the relation (see Section X.A.3 or [4, 622] for the derivation)

$$T_{\rm rh} = \left[\left(\frac{43}{11 g_{*s,\rm rh}} \right)^{\frac{1}{3}} \frac{a_0 T_0}{k_\star} H_\star e^{-N_\star} \left(\frac{45 V_{\rm end}}{\pi^2 g_{*\rm rh}} \right)^{-\frac{1}{3(1+w_{\rm rh})}} \right]^{\frac{3(1+w_{\rm rh})}{3w_{\rm rh}-1}} . \tag{X.86}$$

Thus, by fixing A_s and n_s, one can infer the allowed range for $T_{\rm rh}$ in each inflationary model.

For the α–attractor E and T models:

- Increasing n_s corresponds to a higher number of e-folds $N_\star$;
- The smallest allowed value of n_s sets the *minimum* reheating temperature $T_{\rm rh}^{\rm min}$;
- For $k = 4$ ($w_{\rm rh} = 1/3$), reheating behaves like radiation domination, and $T_{\rm rh}$ becomes unconstrained [622].

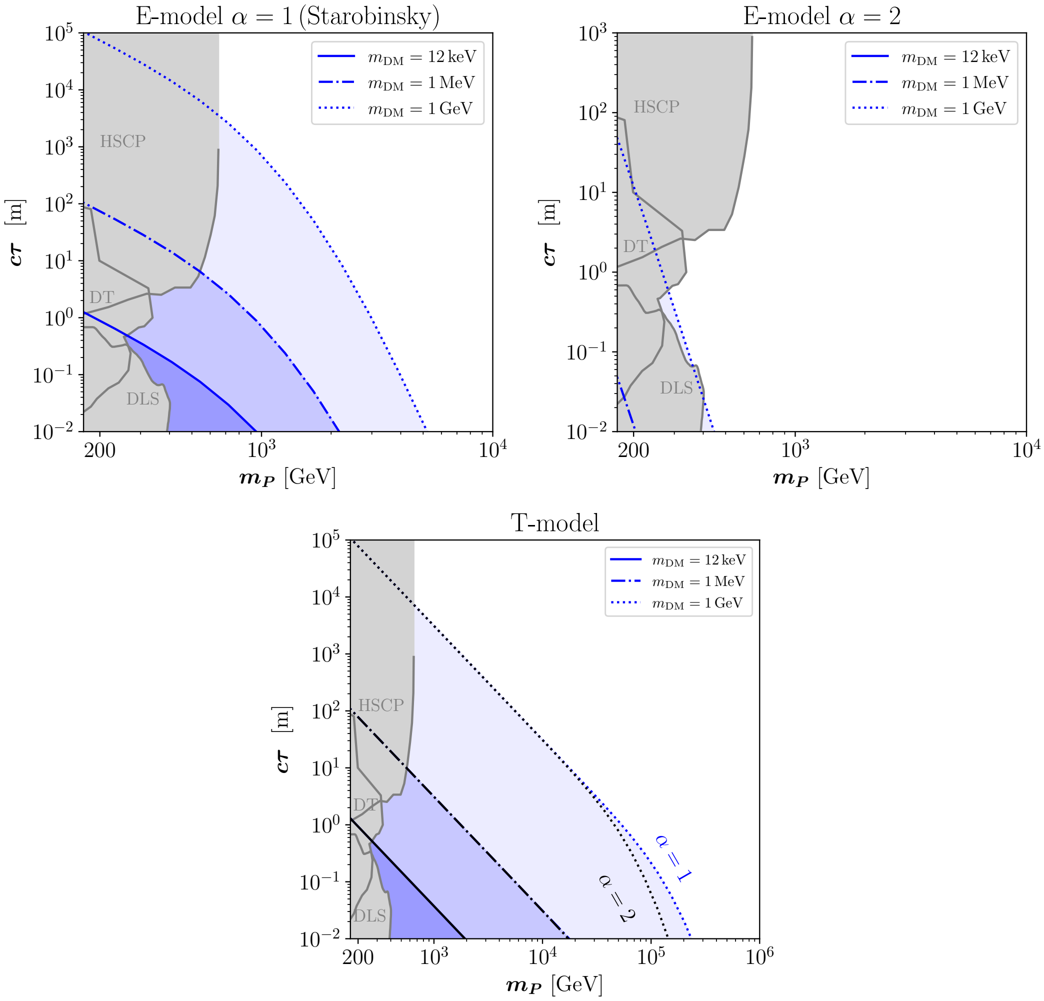

Figure X.7: Combined LLP and inflationary constraints for Majorana (left) and scalar singlet (right) DM models in cosmologies with $k = 2$. The panels correspond to α–attractor E- and T-models, with blue regions excluded by $n_s < 0.9579$ (2σ) [582]. LLP exclusions follow [184]. *Figures created by YX and included in [4].*

Results: CMB Bounds on the Reheating Temperature

Figure X.6 and Fig. X.7 illustrate the interplay between LLP searches and inflationary bounds for both Majorana and scalar singlet DM scenarios, assuming a reheating potential with $k = 2$. The three panels correspond to:

- **E-models:** $\alpha = 1$ (Starobinsky inflation) and $\alpha = 2$;
- **T-models:** $\alpha = 1, 2$ (blue and black curves, respectively).

Solid, dot-dashed, and dotted lines correspond to $m_{\rm DM} = 12\,$keV, $1\,$MeV, and $1\,$GeV. The blue-shaded regions mark the parameter space excluded by the 2σ bound $n_s < 0.9579$ from [582]. The resulting minimum reheating temperatures are summarized in Table X.3.

Interpretation:

- T-models impose more stringent reheating temperature bounds than E-models.
- Smaller α values correspond to tighter inflationary constraints.

Model Type	α	**Lower Bound on $T_{\rm rh}$ [GeV]**
E-model	1	1.8×10^2
E-model	2	7.8
T-model	1	4.0×10^4
T-model	2	1.8×10^4

Table X.3: Lower bounds on the reheating temperature $T_{\rm rh}$ inferred from CMB constraints for α–attractor inflationary models. T-models generally yield tighter constraints than E-models, with smaller α leading to higher $T_{\rm rh}$.

Linking $T_{\rm rh}$ to Collider Observables

Lower bounds on $T_{\rm rh}$ imply corresponding lower bounds on the parent lifetime. Because $\Omega_{\rm DM}$ grows with $T_{\rm rh}$ at fixed $(m_P, c\tau)$, achieving $\Omega_{\rm DM} \simeq 0.12$ at larger $T_{\rm rh}$ demands longer $c\tau$:

$$\Omega_{\rm DM} \propto m_{\rm DM}/(c\tau) \quad \Rightarrow \quad T_{\rm rh}^{\rm min} \Rightarrow c\tau^{\rm min}. \tag{X.87}$$

Hence, higher reheating temperatures translate into stronger lower limits on the parent decay length. For $m_{\rm DM} \approx 12$ keV, this floor is unavoidable due to the Lyman-α bound on the minimal DM mass.

At the qualitative level:

- For $k = 2$ and $T_{\rm rh} \gg m_P$: $c\tau \propto m_P^{-2}$;
- For $k = 2$ and $T_{\rm rh} \ll m_P$: $c\tau \propto m_P^{-9}$.

This scaling reproduces the asymptotic regimes identified in Eqs. (X.77) and (X.80). Importantly, unlike collider limits, inflationary constraints are not bounded by kinematics and extend naturally to $m_P \gtrsim 1$ TeV.

Future Sensitivity: Prospects from CMB-S4

Next-generation CMB experiments such as CMB-S4 [623] will significantly improve the precision on n_s and r. [3] Figure X.8 shows projected exclusion regions (magenta) for an E-model with $k = 2$ and $\alpha = 1$ (Starobinsky inflation, fiducial $r = 0.003$). Similar results hold for the T-model.

Stronger projected n_s constraints at 2σ will push the lower bound on $T_{\rm rh}$ upward, thereby shifting the "kink" in the $c\tau$–m_P relation to larger mediator masses. This will tighten the combined cosmological–collider limits on long-lived mediators, extending sensitivity to heavier m_P regimes inaccessible to current LHC searches.

X.7 Conclusions and Outlooks

Throughout this chapter we developed a concrete bridge between inflationary reheating and freeze-in dark matter (FIMP) production, and connected it to collider observables. We

[3] At the time the research underlying [4] and this chapter of the thesis was conducted, the CMB-S4 project was supported by major funding agencies. In 2025, this support was withdrawn, and the project is consequently expected to be discontinued. Nevertheless, the broader legacy of successive CMB experiments in progressively tightening constraints on inflationary parameters is expected to persist. The conclusions and implications discussed here, therefore, remain relevant.

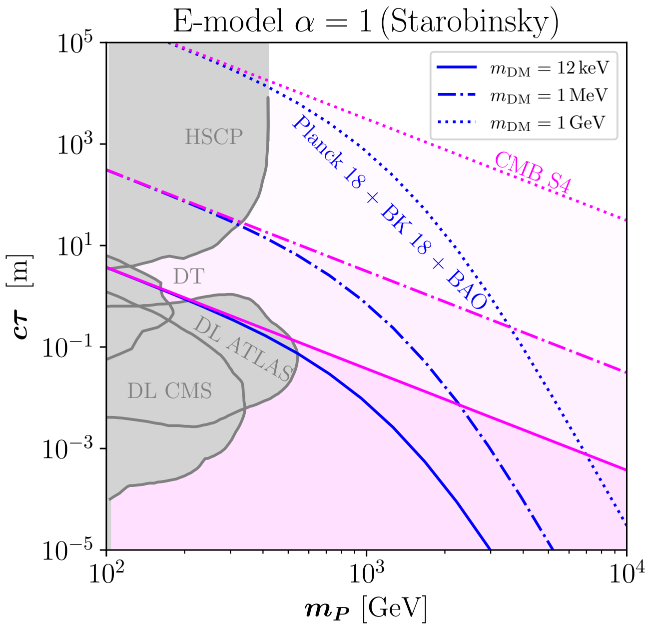

Figure X.8: Projected CMB-S4 exclusion limits (magenta) overlaid on the current inflationary and collider constraints for Starobinsky inflation ($\alpha = 1$, $k = 2$). Improved sensitivity to n_s and r leads to higher inferred reheating temperatures and stronger lower bounds on $c\tau$. *Figure created by YX and included in [4].*

modelled the post-inflation dynamics with monomial reheating potentials $V \propto \Phi^k$ and two decay patterns of the inflaton (bosonic versus fermionic). We solved the Boltzmann system across the reheating and radiation-dominated epochs, expressed the result in terms of an entropy-normalised yield, and identified the dilution associated with the non-adiabatic expansion. We also stated and verified the conditions under which the freeze-in assumption remains valid in this background.

From a phenomenological perspective, the mapping of the relic-density condition onto the parent lifetime–mass plane, $c\tau$ versus m_P (Fig. X.5), yields several robust messages. When $T_{\rm rh} \gg m_P$, production occurs after reheating and becomes insensitive to the details of the reheating history; the different k and BR/FR choices collapse to the same prediction. For $k = 2$, BR and FR are indistinguishable, while for $k > 2$ the stronger dilution in bosonic reheating typically requires shorter lifetimes than in the fermionic case at fixed $(m_P, T_{\rm rh})$. he relative importance of LLP search channels (HSCP, displaced leptons, disappearing/kinked tracks) then depends on $T_{\rm rh}$ and on where a given model sits on the $c\tau$–m_P plane. Importantly, adopting the thermodynamically consistent definition of the reheating temperature in Eq. (X.48) and following the full non-adiabatic evolution leads to quantitative differences with earlier approximations used in the literature.

We further embedded this analysis in inflationary α–attractor E- and T-models. Because $N_\star$ depends on $T_{\rm rh}$, CMB measurements of n_s and r imply model-dependent lower bounds on the reheating temperature (Table X.3) that are stringent for T-models and become weaker as α increases. For $k = 4$ ($w_{\rm rh} = 1/3$), $T_{\rm rh}$ is not constrained by CMB data. Translating $T_{\rm rh}^{\rm min}$ into a minimum lifetime, we obtained combined cosmology–collider exclusions (Figs. X.6 and X.7) that extend beyond kinematic limitations of LHC searches and remain effective even for very heavy parents. Future improvements in n_s and r (e.g. CMB-S4) will raise $T_{\rm rh}^{\rm min}$ and strengthen the lower limits on $c\tau$, shifting the sensitivity to higher m_P.

Taken together, these results show that the microphysics of reheating leaves testable imprints in long-lived particle signatures, and that cosmological data provide orthogonal leverage on the same model space. A potential LLP signal, combined with an inference of $T_{\rm rh}$ from inflation, could discriminate bosonic from fermionic reheating and even point to the effective power k of the reheating potential. The framework developed here thus offers a coherent strategy to interrogate the thermal history of the Universe with both telescopes and colliders.

Outlook

Apart from improving the complementary analysis of CMB data and LLP searches in probing the parameter space, the theoretical uncertainty associated with the production of FIMP DM in non-standard cosmologies can be improved in multiple ways.

Firstly, refining the calculation of the relic abundance by including additional channels, such as inflaton scatterings [599], and non-perturbative particle production during preheating [572, 573, 603, 615], is essential. This can be achieved by utilizing lattice simulations, which have become more accessible thanks to recently published computational packages [610, 624].

Moreover, a thorough analysis of particle production and thermalization processes in the early Universe is needed for collider-friendly models such as the simplified t-channel ones. This analysis should build upon existing work in the field [324, 612, 613, 625–629] but specifically tailored to these models.

Finally, it would be intriguing to connect the phenomenology associated with low-reheating (collider-friendly) and high-reheating temperature (gravitational wave-friendly) scenarios. Performing a global analysis of the entire parameter space and production possibilities would provide valuable insights into the interplay between these regimes.

X.A Inflation Models and Constraints

Declaration: This appendix re-proposes the results presented in Appendix B of [4], mainly written by YX. It serves here to complete the picture on the inflation models and the cosmological constraints that are used within the chapter. In the paper, all authors participated in the discussions, the interpretation of results, and reviewed and corrected the text.

X.A.1 E-model

We first consider the α-attractor inflation scenario described by a potential with an exponential dependence on Φ (E-model) given by [591, 592]

$$V(\Phi) = \Lambda^4 \left(1 - e^{-\sqrt{\frac{2}{3\alpha}}\frac{\Phi}{M_{\rm Pl}}}\right)^{2n} . \tag{X.A.1}$$

Here, n is a positive integer, while $\alpha > 0$ is a parameter that classifies various possible realizations of the potential from supergravity. Notice that for $n = 1$ and $\alpha = 1$, one recovers the Starobinsky model [585]. We can use Eqs. (X.11) and (X.18) to calculate the tensor-to-scalar ratio and spectral index for this class of potentials, which will depend on the model parameters α and n. The quantities, as shown in Appendix B of [4], read in

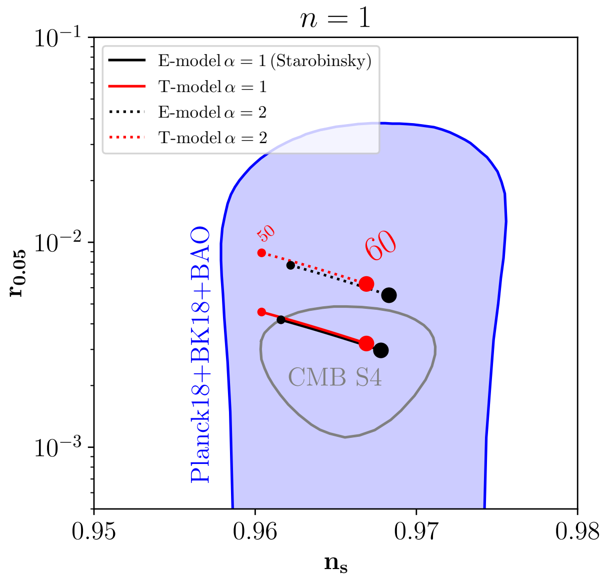

Figure X.9: The $r - n_s$ plane with the predictions for the $n = 1$ T- (red lines) and E-models (black lines), for $\alpha = 1$ (solid lines) and $\alpha = 2$ (dotted lines). The curves lie within 50 (small circles) and 60 (big circles) numbers of e-folds. The blue-shaded region indicates the allowed parameter space at the 95% C.L. at the pivot scale $k_\star = 0.05\text{Mpc}^{-1}$ [582]. Future CMB-S4 projections with fiducial $r = 0.003$ are indicated with a gray contour [623]. *Figures created by YX and included in [4].*

the E-model as

$$r = \frac{64n^2}{3\alpha\left(e^{\sqrt{\frac{2}{3\alpha}}\frac{\Phi_k}{M_{\rm Pl}}} - 1\right)^2}, \tag{X.A.2}$$

$$n_s = 1 - \frac{8n\left(e^{\sqrt{\frac{2}{3\alpha}}\frac{\Phi_k}{M_{\rm Pl}}} + n\right)}{3\alpha\left(e^{\sqrt{\frac{2}{3\alpha}}\frac{\Phi_k}{M_{\rm Pl}}} - 1\right)}. \tag{X.A.3}$$

From the last equation, one can solve for Φ_k to find its parametric dependence, yielding

$$\Phi_k = M_{\rm Pl}\sqrt{\frac{3\alpha}{2}}\ln\left[1 + \frac{4n + 2\sqrt{4n^2 + 6n\,\alpha(1+n)(1-n_s)}}{3\alpha(1-n_s)}\right]. \tag{X.A.4}$$

Inserting this relation back into Eq. (X.A.2), relation between r and n_s is established:

$$r = 48\alpha\left[\frac{n(1-n_s)}{2n + \sqrt{4n^2 + 6n(1+n)(1-n_s)}}\right]^2. \tag{X.A.5}$$

This also depends on the inflaton potential parameters. The total number of e-folds $N_\star$ after inflation that occurred after the CMB pivot scale $k_\star$ has crossed the horizon for the first time follows from Eq. (X.19) as

$$N_\star = \int_{\Phi_{\rm end}}^{\Phi_\star} \frac{1}{\sqrt{2\varepsilon_V}}\frac{d\Phi}{M_{\rm Pl}} = \frac{3\alpha}{4n}\left[e^{\sqrt{\frac{2}{3\alpha}}\frac{\Phi_\star}{M_{\rm Pl}}} - e^{\sqrt{\frac{2}{3\alpha}}\frac{\Phi_{\rm end}}{M_{\rm Pl}}} - \sqrt{\frac{2}{3\alpha}}\frac{(\Phi_\star - \Phi_{\rm end})}{M_{\rm Pl}}\right], \tag{X.A.6}$$

where $\Phi_{\rm end}$ denotes the field value at the end of inflation and is defined via $\max\{\varepsilon_V(\Phi_{\rm end}), \eta_V(\Phi_{\rm end})\} \equiv 1$, such that

$$\Phi_{\rm end} = M_{\rm Pl}\sqrt{\frac{3\alpha}{2}}\ln\left(1+\frac{2n}{\sqrt{3\alpha}}\right)\,. \tag{X.A.7}$$

With Eq. (X.A.4) and Eq. (X.A.7), we can further rewrite Eq. (X.A.6) as

$$N_\star = \frac{3\alpha}{4n}\left[\frac{2\left(n\left(2-\sqrt{3}(1-n_s)\sqrt{\alpha}\right)+\sqrt{4n^2+6n(1+n)(1-n_s)\alpha}\right)}{3(1-n_s)\alpha}\right. \tag{X.A.8}$$

$$\left. -\ln\left(\frac{4n+3(1-n_s)\alpha+2\sqrt{4n^2+6n(1+n)(1-n_s)\alpha}}{(1-n_s)(2\sqrt{3}n+3\sqrt{\alpha})\sqrt{\alpha}}\right)\right], \tag{X.A.9}$$

which establishes a direct relationship with the inflationary parameters and observables. We show in Fig. X.9 the $(r, n_s)-$plane in the case with $n = 1$ ($k = 2$ during reheating) with some benchmark lines from Eq. (X.A.2) and Eq. (X.A.6) with $50 \leq N_\star \leq 60$, together with the current 95 % C.L. limits from [582]. The gray contour displays the projected limits of the future experiment CMB-S4 with a fiducial value $r = 0.003$ [574]. Note that the E-model with $\alpha = 1$ reproduces Starobinsky inflation [585], with its famous predictions

$$n_s = 1-\frac{2}{N_\star},\qquad r=\frac{12}{N_\star^2} \tag{X.A.10}$$

well within the CMB constraints.

Finally, the overall normalization of the potential and hence Λ can be fixed by the amplitude of the scalar perturbations in Eq. (X.17) as follows [599, 630]:

$$\Lambda = M_{\rm Pl}\left(\frac{3}{2}\pi^2 r A_{s,\star}\right)^{1/4}\left[\frac{4n+2\sqrt{4n^2+6n\alpha(1+n)(1-n_s)}}{4n+2\sqrt{4n^2+6n\alpha(1+n)(1-n_s)}+3\alpha(1-n_s)}\right]^{-n/2}. \tag{X.A.11}$$

X.A.2 T-model

The second type of α-attractor models we consider comprises a class of potentials with the following form [591, 592]

$$V(\Phi) = \Lambda^4\left[\tanh\left(\frac{\Phi}{\sqrt{6\alpha}M_{\rm Pl}}\right)\right]^{2n}, \tag{X.A.12}$$

where α, n, and Λ are understood as before. Following the same arguments as just explained for the E-model, the derivation of all the relevant quantities in the T-model can be straightforwardly computed. This was done in Appendix B of [4], resulting in:

$$n_s = 1-\frac{8n}{3\alpha}\left[n+\mathrm{Cosh}\left(\sqrt{\frac{2}{3\alpha}}\frac{\Phi_k}{M_{\rm Pl}}\right)\right]\left[\mathrm{Csch}\left(\sqrt{\frac{2}{3\alpha}}\frac{\Phi_k}{M_{\rm Pl}}\right)\right]^2, \tag{X.A.13}$$

$$\Phi_k = M_{\rm Pl}\sqrt{\frac{3\alpha}{2}}\times\mathrm{arcosh}\left(\frac{4n+\sqrt{9\alpha^2(1-n_s)^2+8n^2(2+3\alpha-3\alpha n_s)}}{3\alpha(1-n_s)}\right), \tag{X.A.14}$$

$$r = \frac{24n\alpha\,(1-n_s)^2}{n\,[4+3\alpha(1-n_s)] + \sqrt{9\alpha^2(1-n_s)^2 + 8n^2(2+3\alpha-3\alpha n_s)}}\,, \tag{X.A.15}$$

$$\Phi_{\rm end} = M_{\rm Pl}\sqrt{\frac{3\alpha}{2}} \times \text{arcosh}\left(1+\frac{4n^2}{3\alpha}\right)\,, \tag{X.A.16}$$

$$N_\star = \frac{3\alpha}{4n^2}\left[\frac{4n+\sqrt{9\alpha^2(1-n_s)^2+8n^2(2+3\alpha-3\alpha n_s)}}{3\alpha(1-n_s)} - \sqrt{1+\frac{4n^2}{3\alpha}}\right]\,, \tag{X.A.17}$$

$$\Lambda = M_{\rm Pl}\left(\frac{3}{2}\pi r A_{s,\star}\right)^{1/4}\left[\frac{4n+\sqrt{9\alpha^2(1-n_s)^2+8n^2(2+3\alpha-3\alpha n_s)}-3\alpha(1-n_s)}{4n+\sqrt{9\alpha^2(1-n_s)^2+8n^2(2+3\alpha-3\alpha n_s)}+3\alpha(1-n_s)}\right]^{-n/4}. \tag{X.A.18}$$

We show in Fig. X.9 the $(r, n_s)-$plane in the $n = 1$ case ($k = 2$ during reheating) with some benchmark scenarios for the E-model (red line) using Eq. (X.A.2) and the T-model (black line) using Eq. (X.A.15) with $50 \leq N_\star \leq 60$, together with the current 95 % C.L. limits from [582].

X.A.3 Matching Reheating to Inflationary Parameters

The period of reheating affects the moment at which the CMB pivot scale re-enters the horizon, allowing to relate CMB predictions with the reheating parameters, e.g. the equation of state $w_{\rm rh} \equiv w_\Phi(a < a_{\rm rh})$, the duration of reheating, as well as the reheating temperature [584, 622, 631]. To show the correlation between inflationary predictions and reheating parameters, we consider the horizon crossing for a given mode, e.g. the pivot scale $k \equiv k_\star = a_\star H_\star$, so that we can write

$$\frac{k_\star}{a_0 H_0} = \frac{a_\star}{a_{\rm end}}\frac{a_{\rm end}}{a_{\rm rh}}\frac{a_{\rm rh}}{a_{\rm eq}}\frac{a_{\rm eq}}{a_0}\frac{H_\star}{H_0}\,, \tag{X.A.19}$$

where a subscript '0' stems from "present day" values. This implies

$$\frac{a_0}{a_{\rm eq}} = \frac{a_\star}{a_{\rm end}}\frac{a_{\rm end}}{a_{\rm rh}}\frac{a_{\rm rh}}{a_{\rm eq}}\frac{a_0 H_\star}{k_\star}\,. \tag{X.A.20}$$

Using $\rho = \rho_{\rm end}\left(\frac{a}{a_{\rm end}}\right)^{-3(1+w_{\rm rh})}$ during reheating (cf. Eq. (X.40)), one has

$$N_{\rm rh} \equiv \ln\left(\frac{a_{\rm rh}}{a_{\rm end}}\right) = \frac{1}{3(1+w_{\rm rh})}\ln\left(\frac{\rho_{\rm end}}{\rho_{\rm rh}}\right)\,, \tag{X.A.21}$$

where $\rho_{\rm rh} = \frac{g_{*,\rm rh}\pi^2}{30}T_{\rm rh}^4$ and $\rho_{\rm end} = \frac{3}{2}V_{\rm end}$ with $V_{\rm end}$ denoting the inflaton potential energy at the end of inflation. After reheating, entropy is conserved, which implies

$$g_{*s,\rm rh}\,T_{\rm rh}^3 = \left(\frac{a_0}{a_{\rm rh}}\right)^3\left(2\,T_0^3 + 6\cdot\frac{7}{8}T_{\nu 0}^3\right)\,, \tag{X.A.22}$$

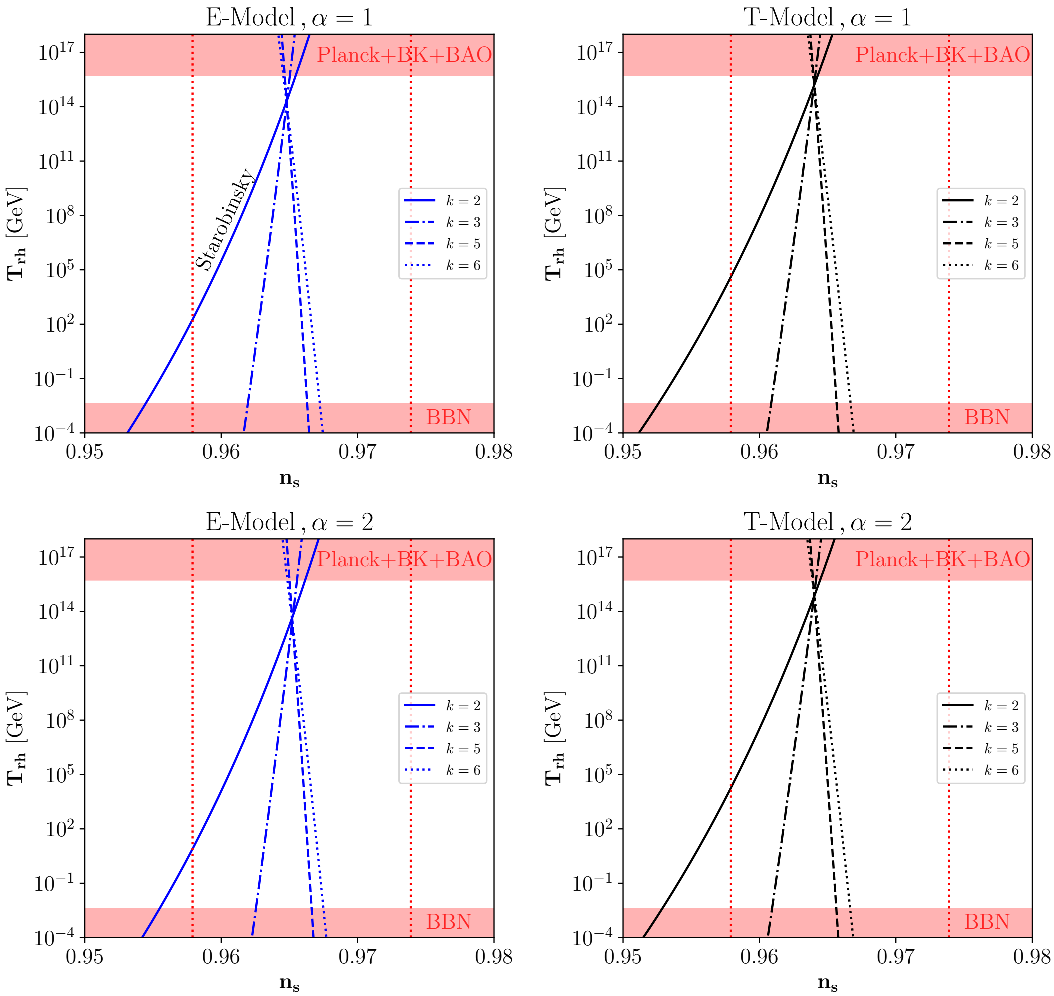

Figure X.10: Reheating temperature values as functions of n_s for α-attractor E- (left column, blue curves) and T-models (right column, black curves) with $\alpha = 1$ (upper row) and $\alpha = 2$ (lower row). We show with solid, dot-dashed, dashed, and dotted lines the predictions for reheating scenarios with $k = 2$, 3, 5, and 6, respectively. Values of $T_{\rm rh}$ within the 2σ constraints from Ref. [582] are allowed. The upper red-shaded area is excluded by limits on r from Ref [582], while the lower one is excluded by BBN [105, 632]. *Figures created by YX and included in [4].*

where $T_{\nu 0} = \left(\frac{4}{11}\right)^{1/3} T_0$ denotes the neutrino decoupling temperature. Thereafter, we find

$$\frac{T_{\rm rh}}{T_0} = \left(\frac{43}{11 g_{*s,\rm rh}}\right)^{1/3} \frac{a_0}{a_{\rm eq}} \frac{a_{\rm eq}}{a_{\rm rh}} = \left(\frac{43}{11 g_{*s,\rm rh}}\right)^{1/3} e^{-N_{\rm rh}} e^{-N_\star} \frac{a_0 H_\star}{k_\star}\,, \tag{X.A.23}$$

where we have used Eq. (X.A.19) in the second step. Using Eq. (X.A.23) and Eq. (X.A.21), one finds [622]

$$N_{\rm rh} = \frac{4}{3(1+w_{\rm rh})}\left[\frac{1}{4}\ln\left(\frac{45}{\pi^2 g_{*,\rm rh}}\right) + \ln\left(\frac{V_{\rm end}^{1/4}}{H_\star}\right) \frac{1}{3}\ln\left(\frac{11\, g_{*s,\rm rh}}{43}\right) + \ln\frac{k_\star}{a_0 T_0} + N_\star + N_{\rm rh}\right]. \tag{X.A.24}$$

If $w_{\rm rh} \neq 1/3$, we have

$$N_{\rm rh} = \frac{4}{1-3w_{\rm rh}}\left[-N_\star - \ln\left(\frac{k_\star}{a_0 T_0}\right) - \frac{1}{4}\ln\left(\frac{45}{g_{*\rm rh}\pi^2}\right) - \frac{1}{3}\ln\left(\frac{11 g_{*s,\rm rh}}{43}\right) + \ln\left(\frac{V_{\rm end}^{1/4}}{H_\star}\right)\right], \tag{X.A.25}$$

where $H_\star = \pi M_{\rm Pl}\sqrt{\frac{rA_{s,\star}}{2}}$. Finally, by using Eq. (X.A.24) and Eq. (X.A.23), we obtain [622]

$$T_{\rm rh} = \left[\left(\frac{43}{11 g_{*s,\rm rh}}\right)^{\frac{1}{3}} \frac{a_0 T_0}{k_\star} H_\star e^{-N_\star} \left(\frac{45 V_{\rm end}}{\pi^2 g_{*\rm rh}}\right)^{-\frac{1}{3(1+w_{\rm rh})}}\right]^{\frac{3(1+w_{\rm rh})}{3w_{\rm rh}-1}}, \tag{X.A.26}$$

where $H_\star$, $N_\star$ and $V_{\rm end}$ depend on the inflation model. Notice that, when $w_{\rm rh} = 1/3$, one cannot solve Eq. (X.A.24) and hence cannot predict $N_{\rm rh}$, since this quantity cancels on each side of the equation. Note that one defines the RD phase when $\rho_{\rm R} \geq \rho_\Phi$, i.e., when the EoS of the Universe approaches 1/3; however, if it is already 1/3 during reheating, then one cannot discriminate between the two regimes, and hence the value of $N_{\rm rh}$ is left undefined (see also [622]).

Reheating constraints are shown in Fig. X.10, where the two vertical red dotted lines correspond to the 2σ range of n_s (cf. Fig. X.1). For the E-model with $\alpha = 1$ and $k = 2n = 2$ (Starobinsky inflation), the minimum reheating temperature allowed is $T_{\rm rh}^{\rm min} \simeq 180.7$ GeV. With larger α, the lower bound on $T_{\rm rh}$ decreases, e.g. $T_{\rm rh}^{\rm min} \simeq 7.8$ GeV with $\alpha = 2$. For T-models, the minimum reheating temperature allowed is $T_{\rm rh}^{\rm min} \simeq 4.0 \times 10^4$ GeV for $\alpha = 1$ and $T_{\rm rh}^{\rm min} \simeq 1.8 \times 10^4$ GeV $\alpha = 2$. For larger values of k, the equation of state $w_{\rm rh}$ increases, implying a change of slope of $T_{\rm rh}$ as a function of n_s.

Epilogue

CHAPTER XI

Summary and Conclusion

In this thesis, we have explored complementary approaches to addressing the Dark Matter (DM) problem within the framework of simplified t-channel DM models by demonstrating how the calculation of the DM relic abundance is affected when accounting for several non-standard effects, such as non-perturbative phenomena from long-range forces, finite-temperature corrections, or low reheating temperature scenarios after inflation. Our findings highlight the importance of these improved calculations for evaluating theoretical uncertainties, determining whether a model is ruled out, and accurately interpreting potential signals of new physics.

Following a comprehensive introduction to the broad topic of DM in Chapter II and a review of the key ingredients for describing its particle production in the early Universe in Chapter III, the first part of this thesis, "WIMPs", focused on understanding the impact of long-range forces within colored co-annihilation scenarios of thermal DM. In Chapter IV, we reviewed how the freeze-out of DM in the co-annihilating regime is mainly driven by the annihilation processes of the co-annihilating partners, the mediators. If gauge-charged, the mediators generate a long-range potential in the non-relativistic regime, distorting their wavefunctions and leading to the Sommerfeld effect (SE) and Bound State Formation (BSF), which we incorporated in the Boltzmann equation of the DM number density.

In Chapter V, we showed that these non-perturbative phenomena significantly impact the phenomenology of t-channel models featuring Majorana DM, especially in the co-annihilating regime. The Sommerfeld-enhanced particle-antiparticle annihilations of the color-charged mediators reduce their number density more efficiently, while the formation and subsequent decay of mediators' bound states act as an additional depletion channel. After incorporating these effects in computational routines for the calculation of the DM relic abundance, we performed a parameter space scan and found that including these effects requires DM couplings up to a factor 10 smaller (5% larger) than if they were neglected when the mediators annihilate dominantly via QCD-dominated (Yukawa-dominated) processes.

We combined our cosmological predictions with constraints from ATLAS mono- and multi-jet searches, as well as from the PICO and XENON1T direct detection (DD) experiments. This demonstrates that including SE and BSF opens up the allowed parameter space, permitting larger DM masses and mass splittings than previously believed. Among various possibilities, we highlighted that searching for high-mass resonances and long-lived particle (LLP) signatures at the LHC complements collider and DD searches, probing parameter regions otherwise unconstrained. Projections from future experimental projects, such as DARWIN and HL-LHC, indicate that simplified t-channel models are highly testable, and our work demonstrates the importance of accurate theoretical predictions for correct interpretations.

The second part of this thesis, "FIMPs", addressed the possibility that DM is a Feebly Interacting Massive Particle (FIMP) and the 'freeze-in' of its relic abundance follows from decays of heavier mediators as well as scattering processes. In Chapter VI, we motivated the need for a 'first-principle approach' to particle production that incorporates finite-temperature corrections from the finite-density medium in which the early Universe dynamics occur. We reviewed the CTP formalism and the 2PI effective action approach, which allow for a derivation of the DM rate equations from methods of non-equilibrium QFT and the incorporation of thermal effects in a self-consistent and controlled way.

Having established the theoretical basis, we calculated the relic abundance in Chapter VII by assuming a scalar DM interacting with a vectorlike gauge-charged fermion and a SM fermion. This involved determining the DM interaction rate by calculating the 1PI-resummed fermion propagators in the DM self-energy, including all in-vacuum mass scales. This required the treatment of highly non-trivial analytical expressions and the numerical evaluation of multidimensional integrals. To this end, we developed original `C++` code enabling efficient and stable computations over a broad region of parameter space. Representative code snippets were presented for each key physical quantity entering the self-energy calculation, together with a detailed analytical discussion of their derivation and asymptotic behaviour in selected kinematic regimes. We showed that the spectral and dissipative properties of 1PI-resummed propagators are similar to those of the simpler, HTL-approximated counterparts, but richer in probing all the kinematic regimes.

In Chapter VIII, we compared the time evolution of the DM interaction rate and number density obtained with 1PI-resummed, HTL-resummed, and tree-level propagators, as well as using the semi-classical Boltzmann-equation approach with and without thermal masses in the S-matrix amplitudes. The evaluation of the dark matter self-energy and the resulting relic abundance relied on multidimensional Monte Carlo integration performed on high-performance computing facilities, with the numerical setup described in a dedicated section of the chapter. We demonstrated how various methods have quantitative differences depending on the strength of the gauge coupling, controlling the dominant finite-temperature corrections to the vectorlike and SM fermions, and the mass-splitting between DM and the vectorlike mediator. We also highlighted how this work aids phenomenological studies by indicating the amount of deviation between more conventional approaches to DM freeze-in from our calculation. We stress that this work is the first combining an established theoretical framework, such as the 2PI effective action approach to the CTP formalism, to compute phenomenologically-relevant quantities in the DM context, and that it can be extended to different contexts such as baryo- and leptogenesis scenarios, gravitational wave production, and non-perturbative particle production.

In Chapter IX, we collected some results analogous to Chapter VII but with a Majorana FIMP and a gauge-charged scalar mediator field, relevant for simplified t-channel DM models and also leptogenesis scenarios. We computed the 1PI-resummed scalar propagator in the Feynman gauge, highlighting how this choice leads to negative spectral sums and a breakdown of the consistency of the theory. We proposed different ways to address this issue, starting from reviewing how gauge dependencies can be treated in a thermal QFT. We then chose to redo the calculation in the Coulomb gauge, the most "natural" choice in hot gauge theories, and we showed that, for some parameter points, the spectral sum turned positive, but, for different choices, it did not. Although we were hitherto unable to find a conclusive solution to the problem, we proposed alternative possibilities such as using HTL-resummed gauge boson propagators or self-consistent solutions to the Schwinger-Dyson equations.

Finally, in Chapter X, we motivated the study of DM freeze-in during a cosmological era not dominated by radiation, such as a prolonged reheating phase after cosmic inflation. After reviewing the basic ideas of slow-roll scalar-field inflation and its observational predictions, we provided a detailed description of reheating dynamics from universal attractor models with inflaton decays into either fermions or bosons, and we showed how to use CMB observables to constrain inflationary parameters. We analyzed DM production from decays of a heavy gauge-charged mediator, demonstrating that different reheating scenarios lead to vastly different predictions for the relic abundance as soon as the reheating temperature is smaller than the mediator's mass. This has striking consequences on the DM coupling and, hence, on the lifetime of the mediator. We showed that the predictions on the lifetime can change by several orders of magnitude within the different expansion histories and that the interpretation of current LLP constraints is reheating-dependent. Moreover, we demonstrated how the interplay between CMB and collider observables implies the possibility of using inflationary observables to probe portions of the parameter space, especially in light of future experiments such as CMB-S4.

In this thesis, we have made significant steps in understanding theoretical uncertainties in DM phenomenology. To achieve this, we have advanced state-of-the-art methods to calculate DM production in the early Universe, which have broader implications beyond DM physics. Although our focus has been on a specific particle DM framework, our analyses can be applied to other DM models that involve long-range effects, finite-temperature corrections, or low-reheating temperature scenarios. Consequently, this work represents an important contribution to the wider effort of enhancing our understanding of the nature and origin of DM and how to interpret potential experimental signatures.

CHAPTER A

Appendix: Notations and Conventions

In this thesis, we have largely made use of the notation that is typically operated in the high-energy physics literature and we have employed some conventions that are of common practice.

Unless specified, all the quantities are expressed in natural units, i.e., we use

$$\hbar = c = k_B = 1\,, \tag{A.1}$$

where $\hbar$ is the reduced Planck constant, c the speed of light in vacuum, and k_B the Boltzmann constant. Natural units allow us to express every dimensional quantity in units of energy expressed in electronvolts and their (sub)multiples.
We adopt the "mostly minuses" convention where the metric signature is $(1,3,0)^+$, or $(+,-,-,-)$. For a flat manifold, the Minkowski metric reads as

$$\eta^{\mu\nu} = \mathrm{diag}\,(1,-1,-1,-1)\ . \tag{A.2}$$

We adopt Einstein's summation convention which implies we sum over repeated (space-time) indices. Thus, the inner product between two four-vectors can be written as $p \cdot k = p_\mu k^\mu = p_0 k_0 - \vec{p}\cdot\vec{k}$. The squared of a four-vector implies the inner product with itself, viz. $p^2 = p_\mu p^\mu$.

The Dirac matrices γ^μ, which are employed in calculations involving spinor vectors and fields, form a basis of the Clifford algebra obeying the anticommuntation relations

$$\{\gamma^\mu, \gamma^\nu\} = \gamma^\mu\gamma^\nu + \gamma^\nu\gamma^\mu = 2\eta^{\mu\nu} I_4\,, \tag{A.3}$$

where I_4 is the 4-dimensional identity matrix. γ^0 is Hermitian, while the other three space-like γ^i are anti-Hermitian. Whenever contracted with a Lorentz vector (p_μ, ∂_μ, etc.), we use the Feynman slashed notation

$$\gamma^\mu p_\mu \equiv \not{p}\,. \tag{A.4}$$

The fifth gamma matrix, γ^5, is defined by $\gamma^5 = i\gamma^0\gamma^1\gamma^2\gamma^3$, from which $(\gamma^5)^2 = I_4$ It is also Hermitian and it anticommutes with all γ^μ. Other properties and identities of the "Dirac gammology" that have been used can be found at this link.

Acknowledgements

I want to thank my colleagues and professors for their continuous support throughout this journey. Your guidance, feedback, and the countless discussions have been essential to my research, and I've learned a ton from all of you.

A special thanks to everyone I've met at conferences, workshops, and schools. You've made this adventure so much more interesting, and I've really appreciated the conversations, the collaborations, and the fresh perspectives you've brought into my work.

Finally, to my friends and family — thank you for sticking with me through the highs and lows. Your encouragement, patience, and belief in me kept me going, even when things got tough. This thesis would not have been possible without you.

List of Figures

Chapter IV

Chapter V

Chapter VI

Chapter VII

Chapter VIII

Chapter IX

Chapter X

List of Tables

Chapter II

Chapter III

Chapter IV

Chapter V

Chapter VI

Chapter VII

Chapter VIII

Chapter IX

Chapter X

Bibliography

[1] M. Becker, E. Copello, J. Harz, K. A. Mohan and D. Sengupta, *Impact of Sommerfeld effect and bound state formation in simplified t-channel dark matter models*, *JHEP* **08** (2022) 145 [2203.04326].

[2] M. Becker, E. Copello, J. Harz, K. A. Mohan and D. Sengupta, *Implications of Nonperturbative Effects for Colored Dark Sectors*, *LHEP* **2023** (2023) 363.

[3] J. L. Feng et al., *The Forward Physics Facility at the High-Luminosity LHC*, *J. Phys. G* **50** (2023) 030501 [2203.05090].

[4] M. Becker, E. Copello, J. Harz, J. Lang and Y. Xu, *Confronting dark matter freeze-in during reheating with constraints from inflation*, *JCAP* **01** (2024) 053 [2306.17238].

[5] M. Becker, E. Copello, J. Harz and C. Tamarit, *Dark matter freeze-in from non-equilibrium QFT: towards a consistent treatment of thermal effects*, *JCAP* **03** (2025) 071 [2312.17246].

[6] C. Arina et al., *t-channel dark matter models – a whitepaper*, *Eur. Phys. J. C* **85** (2025) 975 [2504.10597].

[7] M. Becker, E. Copello, J. Harz and M. Napetschnig, *Manual for SE+BSF4DM – A micrOMEGAs package for Sommerfeld Effect and Bound State Formation in colored Dark Sectors*, 2512.02155.

[8] M. Becker, E. Copello, J. Harz and M. Napetschnig, *Sommerfeld Effect and Bound State Formation for Dark Matter Models with Colored Mediators with SE+BSF4DM*, 2601.03026.

[9] M. Becker, J. Harz, E. Morgante, C. Puchades-Ibáñez and P. Schwaller, *ALP production from abelian gauge bosons: beyond hard thermal loops*, *JHEP* **06** (2025) 160 [2502.01729].

[10] M. Becker, M. J. F. Lozano, J. Harz and C. Tamarit, *Multiple Soft Scatterings in Scalar Dark Matter Freeze-In*, 2506.11185.

[11] G. Bertone and D. Hooper, *History of dark matter*, *Rev. Mod. Phys.* **90** (2018) 045002 [1605.04909].

[12] M. Cirelli, A. Strumia and J. Zupan, *Dark Matter*, 2406.01705.

[13] G. Bertone, D. Hooper and J. Silk, *Particle dark matter: Evidence, candidates and constraints*, *Phys. Rept.* **405** (2005) 279 [hep-ph/0404175].

[14] J. Einasto in *Dark Matter*, 1, 2009, 0901.0632.

[15] K. Garrett and G. Duda, *Dark Matter: A Primer*, *Adv. Astron.* **2011** (2011) 968283 [1006.2483].

[16] R. H. Sanders, *The Dark Matter Problem: A Historical Perspective*. Cambridge University Press, 2010, https://doi.org/10.1017/CBO9781139192309.

[17] S. Profumo, *An Introduction to Particle Dark Matter*. World Scientific, 2017, 10.1142/q0001.
[18] J. Cooley et al., *Report of the Topical Group on Particle Dark Matter for Snowmass 2021*, 2209.07426.
[19] J. C. Kapteyn, *First Attempt at a Theory of the Arrangement and Motion of the Sidereal System*, *Astrophys. J.* **55** (1922) 302.
[20] J. H. Jeans, *The Motions of Stars in a Kapteyn Universe*, *Monthly Notices of the RAS* **82** (1922) 122.
[21] J. H. Oort, *The force exerted by the stellar system in the direction perpendicular to the galactic plane and some related problems*, *Bulletin Astronomical Institute of the Netherlands* **6** (1932) 249.
[22] F. Zwicky, *Die Rotverschiebung von extragalaktischen Nebeln*, *Helv. Phys. Acta* **6** (1933) 110.
[23] F. Zwicky, *On the Masses of Nebulae and of Clusters of Nebulae*, *Astrophys. J.* **86** (1937) 217.
[24] S. Smith, *The Mass of the Virgo Cluster*, *Astrophys. J.* **83** (1936) 23.
[25] V. C. Rubin and J. Ford, W. Kent, *Rotation of the Andromeda Nebula from a Spectroscopic Survey of Emission Regions*, *Astrophys. J.* **159** (1970) 379.
[26] M. S. Roberts, *A High-Resolution 21-CM Hydrogen-Line Survey of the Andromeda Nebula*, *Astrophys. J.* **144** (1966) 639.
[27] K. C. Freeman, *On the Disks of Spiral and S0 Galaxies*, *Astrophys. J.* **160** (1970) 811.
[28] M. S. Roberts and R. N. Whitehurst, *The rotation curve and geometry of M31 at large galactocentric distances.*, *Astrophys. J.* **201** (1975) 327.
[29] V. C. Rubin, W. K. Ford, Jr. and N. Thonnard, *Extended rotation curves of high-luminosity spiral galaxies. IV. Systematic dynamical properties, Sa through Sc*, *Astrophys. J. Lett.* **225** (1978) L107.
[30] V. C. Rubin, N. Thonnard and W. K. Ford, Jr., *Rotational properties of 21 SC galaxies with a large range of luminosities and radii, from NGC 4605 /R = 4kpc/ to UGC 2885 /R = 122 kpc/*, *Astrophys. J.* **238** (1980) 471.
[31] J. Einasto, A. Kaasik and E. Saar, *Dynamic evidence on massive coronas of galaxies*, *Nature* **250** (1974) 309.
[32] S. M. Faber and J. S. Gallagher, *Masses and mass-to-light ratios of galaxies.*, *Annu. Rev. Astron. Astrophys.* **17** (1979) 135.
[33] J. P. Ostriker, P. J. E. Peebles and A. Yahil, *The size and mass of galaxies, and the mass of the universe*, *Astrophys. J. Lett.* **193** (1974) L1.
[34] S. M. Faber and R. E. Jackson, *Velocity dispersions and mass to light ratios for elliptical galaxies*, *Astrophys. J.* **204** (1976) 668.
[35] Y. Jiao, F. Hammer, H. Wang, J. Wang, P. Amram, L. Chemin et al., *Detection of the Keplerian decline in the Milky Way rotation curve*, *Astron. Astrophys.* **678** (2023) A208 [2309.00048].
[36] E. Battaner and E. Florido, "Dark matter in elliptical galaxies." https://ned.ipac.caltech.edu/level5/March01/Battaner/node11.html.
[37] G. Bertin, F. Bertola, L. M. Buson, I. J. Danzinger, H. Dejonghe, E. M. Sadler et al., *A search for dark matter in elliptical galaxies: radially extended spectroscopic observations for six objects.*, *Astron. Astrophys.* **292** (1994) 381.
[38] M. Persic and P. Salucci, *Dark and Visible Matter in Galaxies: Proceedings of a Conference Held in Sesto Pusteria, BZ, Italy, 2-5 July 1996*, ASP Conference Series Proceedings. Astronomical Society of the Pacific, 1997.

[39] M. Loewenstein and R. E. White, III, *Prevalence and properties of dark matter in elliptical galaxies*, *Astrophys. J.* **518** (1999) 50 [astro-ph/9901242].
[40] A. Dekel, F. Stoehr, G. A. Mamon, T. J. Cox and J. R. Primack, *Dark-matter haloes in elliptical galaxies: Lost and found*, *Nature* **437** (2005) 707 [astro-ph/0501622].
[41] J. Wolf, G. D. Martinez, J. S. Bullock, M. Kaplinghat, M. Geha, R. R. Munoz et al., *Accurate Masses for Dispersion-supported Galaxies*, *Mon. Not. Roy. Astron. Soc.* **406** (2010) 1220 [0908.2995].
[42] P. Behroozi, R. H. Wechsler, A. P. Hearin and C. Conroy, *UNIVERSEMACHINE: The correlation between galaxy growth and dark matter halo assembly from z = 0-10*, *MNRAS* **488** (2019) 3143 [1806.07893].
[43] J. N. Bahcall, *Selfconsistent Determinations of the Total Amount of Matter Near the Sun*, *Astrophys. J.* **276** (1984) 169.
[44] K. Kuijken and G. Gilmore, *The mass distribution in the galactic disc -II. Determination of the surface mass density of the galactic disc near the Sun.*, *MNRAS* **239** (1989) 605.
[45] J. I. Read, *The Local Dark Matter Density*, *J. Phys. G* **41** (2014) 063101 [1404.1938].
[46] P. F. de Salas and A. Widmark, *Dark matter local density determination: recent observations and future prospects*, *Rept. Prog. Phys.* **84** (2021) 104901 [2012.11477].
[47] GAIA collaboration, *Gaia Early Data Release 3. Summary of the contents and survey properties*, *Astron. Astrophys.* **649** (2021) A1 [2012.01533].
[48] D. H. Weinberg, J. S. Bullock, F. Governato, R. Kuzio de Naray and A. H. G. Peter, *Cold dark matter: controversies on small scales*, *Proc. Nat. Acad. Sci.* **112** (2015) 12249 [1306.0913].
[49] A. Del Popolo and M. Le Delliou, *Small scale problems of the ΛCDM model: a short review*, *Galaxies* **5** (2017) 17 [1606.07790].
[50] L. Perivolaropoulos and F. Skara, *Challenges for ΛCDM: An update*, *New Astron. Rev.* **95** (2022) 101659 [2105.05208].
[51] J. F. Navarro, C. S. Frenk and S. D. M. White, *The Structure of cold dark matter halos*, *Astrophys. J.* **462** (1996) 563 [astro-ph/9508025].
[52] R. Kuzio de Naray, S. S. McGaugh and W. J. G. de Blok, *Mass Models for Low Surface Brightness Galaxies with High Resolution Optical Velocity Fields*, *Astrophys. J.* **676** (2008) 920 [0712.0860].
[53] S. Y. Kim, A. H. G. Peter and J. R. Hargis, *Missing Satellites Problem: Completeness Corrections to the Number of Satellite Galaxies in the Milky Way are Consistent with Cold Dark Matter Predictions*, *Phys. Rev. Lett.* **121** (2018) 211302 [1711.06267].
[54] D. Clowe, M. Bradac, A. H. Gonzalez, M. Markevitch, S. W. Randall, C. Jones et al., *A direct empirical proof of the existence of dark matter*, *Astrophys. J. Lett.* **648** (2006) L109 [astro-ph/0608407].
[55] M. Bradac, S. W. Allen, T. Treu, H. Ebeling, R. Massey, R. G. Morris et al., *Revealing the properties of dark matter in the merging cluster MACSJ0025.4-1222*, *Astrophys. J.* **687** (2008) 959 [0806.2320].
[56] M. Markevitch, A. H. Gonzalez, D. Clowe, A. Vikhlinin, L. David, W. Forman et al., *Direct constraints on the dark matter self-interaction cross-section from the merging galaxy cluster 1E0657-56*, *Astrophys. J.* **606** (2004) 819 [astro-ph/0309303].

[57] D. Harvey, R. Massey, T. Kitching, A. Taylor and E. Tittley, *The non-gravitational interactions of dark matter in colliding galaxy clusters*, *Science* **347** (2015) 1462 [1503.07675].

[58] E. Hayashi and S. D. M. White, *How Rare is the Bullet Cluster?*, *Mon. Not. Roy. Astron. Soc.* **370** (2006) L38 [astro-ph/0604443].

[59] D. Kraljic and S. Sarkar, *How rare is the Bullet Cluster (in a ΛCDM universe)?*, *JCAP* **04** (2015) 050 [1412.7719].

[60] M. J. Jee, A. Mahdavi, H. Hoekstra, A. Babul, J. J. Dalcanton, P. Carroll et al., *A Study of the Dark Core in A520 with the Hubble Space Telescope: The Mystery Deepens*, *Astrophys. J.* **747** (2012) 96 [1202.6368].

[61] J. M. Diego, A. K. Meena, N. J. Adams, T. Broadhurst, L. Dai, D. Coe et al., *JWST's PEARLS: A new lens model for ACT-CL J0102−4915, "El Gordo," and the first red supergiant star at cosmological distances discovered by JWST*, *Astron. Astrophys.* **672** (2023) A3 [2210.06514].

[62] E. Asencio, I. Banik and P. Kroupa, *A massive blow for ΛCDM − the high redshift, mass, and collision velocity of the interacting galaxy cluster El Gordo contradicts concordance cosmology*, *MNRAS* **500** (2020) 5249 [2012.03950].

[63] E. Asencio, I. Banik and P. Kroupa, *The El Gordo Galaxy Cluster Challenges ΛCDM for Any Plausible Collision Velocity*, *Astrophys. J.* **954** (2023) 162 [2308.00744].

[64] eBOSS collaboration, *The 16th Data Release of the Sloan Digital Sky Surveys: First Release from the APOGEE-2 Southern Survey and Full Release of eBOSS Spectra*, *Astrophys. J. Suppl.* **249** (2020) 3 [1912.02905].

[65] Planck collaboration, *Planck 2018 results. I. Overview and the cosmological legacy of Planck*, *Astron. Astrophys.* **641** (2020) A1 [1807.06205].

[66] M. Vogelsberger, F. Marinacci, P. Torrey and E. Puchwein, *Cosmological Simulations of Galaxy Formation*, *Nature Rev. Phys.* **2** (2020) 42 [1909.07976].

[67] Y. B. Zeldovich, *Gravitational instability: An Approximate theory for large density perturbations*, *Astron. Astrophys.* **5** (1970) 84.

[68] P. J. E. Peebles and J. T. Yu, *Primeval adiabatic perturbation in an expanding universe*, *Astrophys. J.* **162** (1970) 815.

[69] W. H. Press and P. Schechter, *Formation of Galaxies and Clusters of Galaxies by Self-Similar Gravitational Condensation*, *Astrophys. J.* **187** (1974) 425.

[70] P. J. Peebles, *The Large-Scale Structure of the Universe*. Princeton University Press, 11, 1980.

[71] eBOSS collaboration, *Completed SDSS-IV extended Baryon Oscillation Spectroscopic Survey: Cosmological implications from two decades of spectroscopic surveys at the Apache Point Observatory*, *Phys. Rev. D* **103** (2021) 083533 [2007.08991].

[72] G. R. Blumenthal, S. M. Faber, J. R. Primack and M. J. Rees, *Formation of Galaxies and Large Scale Structure with Cold Dark Matter*, *Nature* **311** (1984) 517.

[73] M. Davis, G. Efstathiou, C. S. Frenk and S. D. M. White, *The Evolution of Large Scale Structure in a Universe Dominated by Cold Dark Matter*, *Astrophys. J.* **292** (1985) 371.

[74] J. Wang, S. Bose, C. S. Frenk, L. Gao, A. Jenkins, V. Springel et al., *Universal structure of dark matter haloes over a mass range of 20 orders of magnitude*, *Nature* **585** (2020) 39 [1911.09720].

[75] Planck collaboration, *Planck 2018 results. VI. Cosmological parameters*, *Astron.*

Astrophys. **641** (2020) A6 [1807.06209].
[76] A. A. Penzias and R. W. Wilson, *A Measurement of excess antenna temperature at 4080-Mc/s*, *Astrophys. J.* **142** (1965) 419.
[77] R. H. Dicke, P. J. E. Peebles, P. G. Roll and D. T. Wilkinson, *Cosmic Black-Body Radiation*, *Astrophys. J.* **142** (1965) 414.
[78] J. Silk, *Cosmic black body radiation and galaxy formation*, *Astrophys. J.* **151** (1968) 459.
[79] R. K. Sachs and A. M. Wolfe, *Perturbations of a cosmological model and angular variations of the microwave background*, *Astrophys. J.* **147** (1967) 73.
[80] W. Hu, "Wayne Hu's Tutorials." http://background.uchicago.edu/index.html.
[81] S. Dodelson, *Modern Cosmology*. Academic Press, Amsterdam, 2003.
[82] A. G. Riess et al., *New Parallaxes of Galactic Cepheids from Spatially Scanning the Hubble Space Telescope: Implications for the Hubble Constant*, *Astrophys. J.* **855** (2018) 136 [1801.01120].
[83] A. G. Riess, S. Casertano, W. Yuan, J. B. Bowers, L. Macri, J. C. Zinn et al., *Cosmic Distances Calibrated to 1% Precision with Gaia EDR3 Parallaxes and Hubble Space Telescope Photometry of 75 Milky Way Cepheids Confirm Tension with ΛCDM*, *Astrophys. J. Lett.* **908** (2021) L6 [2012.08534].
[84] W. L. Freedman, *Measurements of the Hubble Constant: Tensions in Perspective*, *Astrophys. J.* **919** (2021) 16 [2106.15656].
[85] W. L. Freedman and B. F. Madore, *Progress in direct measurements of the Hubble constant*, *JCAP* **11** (2023) 050 [2309.05618].
[86] W. Freedman, "New JWST Results: Is the Current Tension in Ho Signaling New Physics." https://meetings.aps.org/Meeting/APR24/Session/S01.2.
[87] DESI collaboration, *DESI 2024 VI: Cosmological Constraints from the Measurements of Baryon Acoustic Oscillations*, 2404.03002.
[88] N. Schöneberg, G. Franco Abellán, A. Pérez Sánchez, S. J. Witte, V. Poulin and J. Lesgourgues, *The H0 Olympics: A fair ranking of proposed models*, *Phys. Rept.* **984** (2022) 1 [2107.10291].
[89] E. Abdalla et al., *Cosmology intertwined: A review of the particle physics, astrophysics, and cosmology associated with the cosmological tensions and anomalies*, *JHEAp* **34** (2022) 49 [2203.06142].
[90] L. Verde, N. Schöneberg and H. Gil-Marín, *A tale of many H_0*, 2311.13305.
[91] V. Poulin, J. L. Bernal, E. D. Kovetz and M. Kamionkowski, *Sigma-8 tension is a drag*, *Phys. Rev. D* **107** (2023) 123538 [2209.06217].
[92] N. J. Secrest, S. von Hausegger, M. Rameez, R. Mohayaee, S. Sarkar and J. Colin, *A Test of the Cosmological Principle with Quasars*, *Astrophys. J. Lett.* **908** (2021) L51 [2009.14826].
[93] J. D. Bowman, A. E. E. Rogers, R. A. Monsalve, T. J. Mozdzen and N. Mahesh, *An absorption profile centred at 78 megahertz in the sky-averaged spectrum*, *Nature* **555** (2018) 67 [1810.05912].
[94] E. Di Valentino, O. Mena, S. Pan, L. Visinelli, W. Yang, A. Melchiorri et al., *In the realm of the Hubble tension—a review of solutions*, *Class. Quant. Grav.* **38** (2021) 153001 [2103.01183].
[95] R. C. Keenan, A. J. Barger and L. L. Cowie, *Evidence for a ˜300 Megaparsec Scale Under-density in the Local Galaxy Distribution*, *Astrophys. J.* **775** (2013) 62 [1304.2884].
[96] M. Haslbauer, I. Banik and P. Kroupa, *The KBC void and Hubble tension contradict ΛCDM on a Gpc scale − Milgromian dynamics as a possible*

solution, *MNRAS* **499** (2020) 2845 [2009.11292].

[97] S. Mazurenko, I. Banik, P. Kroupa and M. Haslbauer, *A simultaneous solution to the Hubble tension and observed bulk flow within 250 h−1 Mpc*, *MNRAS* **527** (2024) 4388 [2311.17988].

[98] M. Taoso, G. Bertone and A. Masiero, *Dark Matter Candidates: A Ten-Point Test*, *JCAP* **03** (2008) 022 [0711.4996].

[99] G. Bertone and T. Tait, M. P., *A new era in the search for dark matter*, *Nature* **562** (2018) 51 [1810.01668].

[100] G. Arcadi, M. Dutra, P. Ghosh, M. Lindner, Y. Mambrini, M. Pierre et al., *The waning of the WIMP? A review of models, searches, and constraints*, *Eur. Phys. J. C* **78** (2018) 203 [1703.07364].

[101] N. Bernal, M. Heikinheimo, T. Tenkanen, K. Tuominen and V. Vaskonen, *The Dawn of FIMP Dark Matter: A Review of Models and Constraints*, *Int. J. Mod. Phys.* **A32** (2017) 1730023 [1706.07442].

[102] G. Arcadi, D. Cabo-Almeida, M. Dutra, P. Ghosh, M. Lindner, Y. Mambrini et al., *The Waning of the WIMP: Endgame?*, 2403.15860.

[103] V. Iršič et al., *Unveiling dark matter free streaming at the smallest scales with the high redshift Lyman-alpha forest*, *Phys. Rev. D* **109** (2024) 043511 [2309.04533].

[104] S. D. McDermott, H.-B. Yu and K. M. Zurek, *Turning off the Lights: How Dark is Dark Matter?*, *Phys. Rev. D* **83** (2011) 063509 [1011.2907].

[105] Particle Data Group collaboration, *Review of Particle Physics*, *PTEP* **2022** (2022) 083C01.

[106] E. Witten, *Cosmic Separation of Phases*, *Phys. Rev. D* **30** (1984) 272.

[107] E. Farhi and R. L. Jaffe, *Strange Matter*, *Phys. Rev. D* **30** (1984) 2379.

[108] R. L. Jaffe, *Perhaps a Stable Dihyperon*, *Phys. Rev. Lett.* **38** (1977) 195.

[109] G. R. Farrar, *Stable Sexaquark*, 1708.08951.

[110] E. W. Kolb and M. S. Turner, *Dibaryons cannot be the dark matter*, *Phys. Rev. D* **99** (2019) 063519 [1809.06003].

[111] Y. B. Zel'dovich and I. D. Novikov, *The Hypothesis of Cores Retarded during Expansion and the Hot Cosmological Model*, *Sov. Astron.* **10** (1967) 602.

[112] S. Hawking, *Gravitationally collapsed objects of very low mass*, *Mon. Not. Roy. Astron. Soc.* **152** (1971) 75.

[113] B. J. Carr, *The Primordial black hole mass spectrum*, *Astrophys. J.* **201** (1975) 1.

[114] G. F. Chapline, *Cosmological effects of primordial black holes*, *Nature* **253** (1975) 251.

[115] S. W. Hawking, *Black hole explosions*, *Nature* **248** (1974) 30.

[116] B. Carr, F. Kuhnel and M. Sandstad, *Primordial Black Holes as Dark Matter*, *Phys. Rev. D* **94** (2016) 083504 [1607.06077].

[117] B. Carr, K. Kohri, Y. Sendouda and J. Yokoyama, *Constraints on primordial black holes*, *Rept. Prog. Phys.* **84** (2021) 116902 [2002.12778].

[118] A. M. Green and B. J. Kavanagh, *Primordial Black Holes as a dark matter candidate*, *J. Phys. G* **48** (2021) 043001 [2007.10722].

[119] M. Sasaki, T. Suyama, T. Tanaka and S. Yokoyama, *Primordial Black Hole Scenario for the Gravitational-Wave Event GW150914*, *Phys. Rev. Lett.* **117** (2016) 061101 [1603.08338].

[120] V. De Luca, G. Franciolini and A. Riotto, *NANOGrav Data Hints at Primordial Black Holes as Dark Matter*, *Phys. Rev. Lett.* **126** (2021) 041303 [2009.08268].

[121] G. Domènech and M. Sasaki, *Gravitational wave hints black hole remnants as dark*

matter, *Class. Quant. Grav.* **40** (2023) 177001 [2303.07661].
[122] K. N. Abazajian et al., *Light Sterile Neutrinos: A White Paper*, 1204.5379.
[123] M. Drewes et al., *A White Paper on keV Sterile Neutrino Dark Matter*, *JCAP* **01** (2017) 025 [1602.04816].
[124] S. Dodelson and L. M. Widrow, *Sterile-neutrinos as dark matter*, *Phys. Rev. Lett.* **72** (1994) 17 [hep-ph/9303287].
[125] X.-D. Shi and G. M. Fuller, *A New dark matter candidate: Nonthermal sterile neutrinos*, *Phys. Rev. Lett.* **82** (1999) 2832 [astro-ph/9810076].
[126] A. D. Sakharov, *Violation of CP Invariance, C asymmetry, and baryon asymmetry of the universe*, *Pisma Zh. Eksp. Teor. Fiz.* **5** (1967) 32.
[127] E. W. Kolb and S. Wolfram, *Baryon Number Generation in the Early Universe*, *Nucl. Phys. B* **172** (1980) 224.
[128] M. A. Luty, *Baryogenesis via leptogenesis*, *Phys. Rev. D* **45** (1992) 455.
[129] W. Buchmuller, P. Di Bari and M. Plumacher, *Leptogenesis for pedestrians*, *Annals Phys.* **315** (2005) 305 [hep-ph/0401240].
[130] F. Wilczek, *Problem of Strong P and T Invariance in the Presence of Instantons*, *Phys. Rev. Lett.* **40** (1978) 279.
[131] S. Weinberg, *A New Light Boson?*, *Phys. Rev. Lett.* **40** (1978) 223.
[132] R. D. Peccei and H. R. Quinn, *CP Conservation in the Presence of Instantons*, *Phys. Rev. Lett.* **38** (1977) 1440.
[133] R. D. Peccei and H. R. Quinn, *Constraints Imposed by CP Conservation in the Presence of Instantons*, *Phys. Rev. D* **16** (1977) 1791.
[134] J. E. Kim, *Weak Interaction Singlet and Strong CP Invariance*, *Phys. Rev. Lett.* **43** (1979) 103.
[135] M. A. Shifman, A. I. Vainshtein and V. I. Zakharov, *Can Confinement Ensure Natural CP Invariance of Strong Interactions?*, *Nucl. Phys. B* **166** (1980) 493.
[136] M. Dine, W. Fischler and M. Srednicki, *A Simple Solution to the Strong CP Problem with a Harmless Axion*, *Phys. Lett. B* **104** (1981) 199.
[137] A. R. Zhitnitsky, *On Possible Suppression of the Axion Hadron Interactions. (In Russian)*, *Sov. J. Nucl. Phys.* **31** (1980) 260.
[138] A. Arvanitaki, S. Dimopoulos, S. Dubovsky, N. Kaloper and J. March-Russell, *String Axiverse*, *Phys. Rev. D* **81** (2010) 123530 [0905.4720].
[139] J. Preskill, M. B. Wise and F. Wilczek, *Cosmology of the Invisible Axion*, *Phys. Lett. B* **120** (1983) 127.
[140] D. J. E. Marsh, *Axion Cosmology*, *Phys. Rept.* **643** (2016) 1 [1510.07633].
[141] W.-Y. Ai, J. S. Cruz, B. Garbrecht and C. Tamarit, *Consequences of the order of the limit of infinite spacetime volume and the sum over topological sectors for CP violation in the strong interactions*, *Phys. Lett. B* **822** (2021) 136616 [2001.07152].
[142] F. Feruglio, A. Strumia and A. Titov, *Modular invariance and the QCD angle*, *JHEP* **07** (2023) 027 [2305.08908].
[143] S. P. Martin, *A Supersymmetry primer*, *Adv. Ser. Direct. High Energy Phys.* **18** (1998) 1 [hep-ph/9709356].
[144] H. Baer and X. Tata, *The Minimal Supersymmetric Standard Model*, p. 127–189. Cambridge University Press, 2023.
[145] J. R. Ellis, J. S. Hagelin, D. V. Nanopoulos, K. A. Olive and M. Srednicki, *Supersymmetric Relics from the Big Bang*, *Nucl. Phys. B* **238** (1984) 453.
[146] G. Jungman, M. Kamionkowski and K. Griest, *Supersymmetric dark matter*, *Phys. Rept.* **267** (1996) 195 [hep-ph/9506380].

[147] H. Pagels and J. R. Primack, *Supersymmetry, Cosmology and New TeV Physics*, *Phys. Rev. Lett.* **48** (1982) 223.

[148] L. Covi, J. E. Kim and L. Roszkowski, *Axinos as cold dark matter*, *Phys. Rev. Lett.* **82** (1999) 4180 [hep-ph/9905212].

[149] C. Arina and N. Fornengo, *Sneutrino cold dark matter, a new analysis: Relic abundance and detection rates*, *JHEP* **11** (2007) 029 [0709.4477].

[150] T. Moroi, H. Murayama and M. Yamaguchi, *Cosmological constraints on the light stable gravitino*, *Phys. Lett.* **B303** (1993) 289.

[151] V. S. Rychkov and A. Strumia, *Thermal production of gravitinos*, *Phys. Rev. D* **75** (2007) 075011 [hep-ph/0701104].

[152] A. Strumia, *Thermal production of axino Dark Matter*, *JHEP* **06** (2010) 036 [1003.5847].

[153] R. T. Co, F. D'Eramo and L. J. Hall, *Gravitino or Axino Dark Matter with Reheat Temperature as high as* 10^{16} *GeV*, *JHEP* **03** (2017) 005 [1611.05028].

[154] R. T. Co, F. D'Eramo, L. J. Hall and K. Harigaya, *Saxion Cosmology for Thermalized Gravitino Dark Matter*, *JHEP* **07** (2017) 125 [1703.09796].

[155] M. Cirelli, N. Fornengo and A. Strumia, *Minimal dark matter*, *Nucl. Phys. B* **753** (2006) 178 [hep-ph/0512090].

[156] M. Cirelli, A. Strumia and M. Tamburini, *Cosmology and Astrophysics of Minimal Dark Matter*, *Nucl. Phys. B* **787** (2007) 152 [0706.4071].

[157] C. Boehm, T. A. Ensslin and J. Silk, *Can Annihilating dark matter be lighter than a few GeVs?*, *J. Phys. G* **30** (2004) 279 [astro-ph/0208458].

[158] J. L. Feng and J. Kumar, *The WIMPless Miracle: Dark-Matter Particles without Weak-Scale Masses or Weak Interactions*, *Phys. Rev. Lett.* **101** (2008) 231301 [0803.4196].

[159] S. Knapen, T. Lin and K. M. Zurek, *Light Dark Matter: Models and Constraints*, *Phys. Rev. D* **96** (2017) 115021 [1709.07882].

[160] P. Arias, D. Cadamuro, M. Goodsell, J. Jaeckel, J. Redondo and A. Ringwald, *WISPy Cold Dark Matter*, *JCAP* **06** (2012) 013 [1201.5902].

[161] W. Hu, R. Barkana and A. Gruzinov, *Cold and fuzzy dark matter*, *Phys. Rev. Lett.* **85** (2000) 1158 [astro-ph/0003365].

[162] L. Hui, J. P. Ostriker, S. Tremaine and E. Witten, *Ultralight scalars as cosmological dark matter*, *Phys. Rev. D* **95** (2017) 043541 [1610.08297].

[163] C. A. J. O'Hare, *Cosmology of axion dark matter*, *PoS* **COSMICWISPers** (2024) 040 [2403.17697].

[164] C. Antel et al., *Feebly-interacting particles: FIPs 2022 Workshop Report*, *Eur. Phys. J. C* **83** (2023) 1122 [2305.01715].

[165] M. J. Strassler and K. M. Zurek, *Echoes of a hidden valley at hadron colliders*, *Phys. Lett. B* **651** (2007) 374 [hep-ph/0604261].

[166] D. J. H. Chung, E. W. Kolb and A. Riotto, *Superheavy dark matter*, *Phys. Rev.* **D59** (1999) 023501 [hep-ph/9802238].

[167] E. W. Kolb, D. J. H. Chung and A. Riotto, *WIMPzillas!*, *AIP Conf. Proc.* **484** (1999) 91 [hep-ph/9810361].

[168] D. J. H. Chung, E. W. Kolb and A. Riotto, *Production of massive particles during reheating*, *Phys. Rev. D* **60** (1999) 063504 [hep-ph/9809453].

[169] E. W. Kolb and A. J. Long, *Cosmological gravitational particle production and its implications for cosmological relics*, 2312.09042.

[170] V. De Luca, A. Mitridate, M. Redi, J. Smirnov and A. Strumia, *Colored Dark Matter*, *Phys. Rev. D* **97** (2018) 115024 [1801.01135].

[171] A. Mitridate, M. Redi, J. Smirnov and A. Strumia, *Dark Matter as a weakly coupled Dark Baryon*, *JHEP* **10** (2017) 210 [1707.05380].
[172] G. D. Kribs and E. T. Neil, *Review of strongly-coupled composite dark matter models and lattice simulations*, *Int. J. Mod. Phys. A* **31** (2016) 1643004 [1604.04627].
[173] NANOGrav collaboration, *The NANOGrav 15 yr Data Set: Evidence for a Gravitational-wave Background*, *Astrophys. J. Lett.* **951** (2023) L8 [2306.16213].
[174] J. Abdallah et al., *Simplified Models for Dark Matter Searches at the LHC*, *Phys. Dark Univ.* **9-10** (2015) 8 [1506.03116].
[175] G. Busoni, A. De Simone, E. Morgante and A. Riotto, *On the Validity of the Effective Field Theory for Dark Matter Searches at the LHC*, *Phys. Lett. B* **728** (2014) 412 [1307.2253].
[176] A. L. Fitzpatrick, W. Haxton, E. Katz, N. Lubbers and Y. Xu, *The Effective Field Theory of Dark Matter Direct Detection*, *JCAP* **02** (2013) 004 [1203.3542].
[177] F. Elahi, C. Kolda and J. Unwin, *UltraViolet Freeze-in*, *JHEP* **03** (2015) 048 [1410.6157].
[178] J. Alwall, P. Schuster and N. Toro, *Simplified Models for a First Characterization of New Physics at the LHC*, *Phys. Rev. D* **79** (2009) 075020 [0810.3921].
[179] LHC New Physics Working Group collaboration, *Simplified Models for LHC New Physics Searches*, *J. Phys. G* **39** (2012) 105005 [1105.2838].
[180] A. DiFranzo, K. I. Nagao, A. Rajaraman and T. M. P. Tait, *Simplified Models for Dark Matter Interacting with Quarks*, *JHEP* **11** (2013) 014 [1308.2679].
[181] F. Kahlhoefer, K. Schmidt-Hoberg, T. Schwetz and S. Vogl, *Implications of unitarity and gauge invariance for simplified dark matter models*, *JHEP* **02** (2016) 016 [1510.02110].
[182] P. Ko, A. Natale, M. Park and H. Yokoya, *Simplified DM models with the full SM gauge symmetry : the case of t-channel colored scalar mediators*, *JHEP* **01** (2017) 086 [1605.07058].
[183] S. El Hedri, A. Kaminska, M. de Vries and J. Zurita, *Simplified Phenomenology for Colored Dark Sectors*, *JHEP* **04** (2017) 118 [1703.00452].
[184] G. Bélanger et al., *LHC-friendly minimal freeze-in models*, *JHEP* **02** (2019) 186 [1811.05478].
[185] E. Morgante, *Simplified Dark Matter Models*, *Adv. High Energy Phys.* **2018** (2018) 5012043 [1804.01245].
[186] K. A. Mohan, D. Sengupta, T. M. P. Tait, B. Yan and C.-P. Yuan, *Direct detection and lhc constraints on a t-channel simplified model of majorana dark matter at one loop*, *JHEP* **2019** (2019) .
[187] C. Arina, B. Fuks, L. Mantani, H. Mies, L. Panizzi and J. Salko, *Closing in on t-channel simplified dark matter models*, *Phys. Lett. B* **813** (2021) 136038 [2010.07559].
[188] C. Arina, B. Fuks and L. Mantani, *A universal framework for t-channel dark matter models*, *Eur. Phys. J. C* **80** (2020) 409 [2001.05024].
[189] C. Arina, B. Fuks, J. Heisig, M. Krämer, L. Mantani and L. Panizzi, *Comprehensive exploration of t-channel simplified models of dark matter*, *Phys. Rev. D* **108** (2023) 115007 [2307.10367].
[190] S. Matsumoto, S. Mukhopadhyay and Y.-L. S. Tsai, *Effective Theory of WIMP Dark Matter supplemented by Simplified Models: Singlet-like Majorana fermion case*, *Phys. Rev. D* **94** (2016) 065034 [1604.02230].

[191] A. De Simone and T. Jacques, *Simplified models vs. effective field theory approaches in dark matter searches*, *Eur. Phys. J. C* **76** (2016) 367 [1603.08002].
[192] C. Degrande, C. Duhr, B. Fuks, D. Grellscheid, O. Mattelaer and T. Reiter, *UFO - The Universal FeynRules Output*, *Comput. Phys. Commun.* **183** (2012) 1201 [1108.2040].
[193] A. Alloul, N. D. Christensen, C. Degrande, C. Duhr and B. Fuks, *FeynRules 2.0 - A complete toolbox for tree-level phenomenology*, *Comput. Phys. Commun.* **185** (2014) 2250 [1310.1921].
[194] G. Belanger, F. Boudjema, A. Pukhov and A. Semenov, *MicrOMEGAs 2.0: A Program to calculate the relic density of dark matter in a generic model*, *Comput. Phys. Commun.* **176** (2007) 367 [hep-ph/0607059].
[195] S. Giagu, *WIMP Dark Matter Searches With the ATLAS Detector at the LHC*, *Front. in Phys.* **7** (2019) 75.
[196] T. Marrodán Undagoitia and L. Rauch, *Dark matter direct-detection experiments*, *J. Phys. G* **43** (2016) 013001 [1509.08767].
[197] E. Aprile et al., *The XENON1T dark matter experiment*, *The European Physical Journal C* **77** (2017) .
[198] D. Akerib et al., *The LUX-ZEPLIN (LZ) experiment*, *Nuclear Instruments and Methods in Physics Research Section A: Accelerators, Spectrometers, Detectors and Associated Equipment* **953** (2020) 163047.
[199] DarkSide-20k collaboration, *DarkSide-20k: A 20 tonne two-phase LAr TPC for direct dark matter detection at LNGS*, *Eur. Phys. J. Plus* **133** (2018) 131 [1707.08145].
[200] PandaX-4T collaboration, *Dark Matter Search Results from the PandaX-4T Commissioning Run*, *Phys. Rev. Lett.* **127** (2021) 261802 [2107.13438].
[201] DAMA collaboration, *The DAMA/LIBRA apparatus*, *Nucl. Instrum. Meth. A* **592** (2008) 297 [0804.2738].
[202] SABRE collaboration, *The SABRE project and the SABRE Proof-of-Principle*, *Eur. Phys. J. C* **79** (2019) 363 [1806.09340].
[203] COSINE-100 collaboration, *Search for a Dark Matter-Induced Annual Modulation Signal in NaI(Tl) with the COSINE-100 Experiment*, *Phys. Rev. Lett.* **123** (2019) 031302 [1903.10098].
[204] CDMS-II collaboration, *Dark Matter Search Results from the CDMS II Experiment*, *Science* **327** (2010) 1619 [0912.3592].
[205] V. Sanglard, *EDELWEISS-II Dark Matter search: Status and first results*, *Journal of Physics: Conference Series* **203** (2010) 012037.
[206] CRESST collaboration, *The CRESST dark matter search*, *Astropart. Phys.* **12** (1999) 107 [hep-ex/9904005].
[207] PICO collaboration, *Dark Matter Search Results from the PICO-60 C_3F_8 Bubble Chamber*, *Phys. Rev. Lett.* **118** (2017) 251301 [1702.07666].
[208] J. M. Gaskins, *A review of indirect searches for particle dark matter*, *Contemp. Phys.* **57** (2016) 496 [1604.00014].
[209] W. B. Atwood et al., *The Large Area Telescope on the Fermi Gamma-Ray Space Telescope Mission*, *The Astrophysical Journal* **697** (2009) 1071–1102.
[210] R. Battiston, *The antimatter spectrometer (AMS-02): A particle physics detector in space*, *Nuclear Instruments and Methods in Physics Research Section A: Accelerators, Spectrometers, Detectors and Associated Equipment* **588** (2008) 227.
[211] K. Bernlöhr et al., *The optical system of the HESS imaging atmospheric Cherenkov*

telescopes, Part 1: Layout and components of the system, *Astropart. Phys.* **20** (2003) 111 [astro-ph/0308246].

[212] T. C. Weekes et al., *VERITAS: The Very energetic radiation imaging telescope array system*, *Astropart. Phys.* **17** (2002) 221 [astro-ph/0108478].

[213] MAGIC collaboration, *The MAGIC telescope*, *Nucl. Phys. B Proc. Suppl.* **114** (2003) 247.

[214] D. A. Schwartz, *Invited Review Article: The Chandra X-ray Observatory*, *Review of Scientific Instruments* **85** (2014) 061101.

[215] C. Winkler et al., *The INTEGRAL mission*, *Astronomy and Astrophysics* **411** (2003) L1.

[216] O. Adriani et al., *The PAMELA Mission: Heralding a new era in precision cosmic ray physics*, *Phys. Rept.* **544** (2014) 323.

[217] Pierre Auger collaboration, *The Pierre Auger Cosmic Ray Observatory*, *Nucl. Instrum. Meth. A* **798** (2015) 172 [1502.01323].

[218] M. Actis et al., *Design concepts for the Cherenkov Telescope Array CTA: an advanced facility for ground-based high-energy gamma-ray astronomy*, *Experimental Astronomy* **32** (2011) 193–316.

[219] F. Halzen and S. R. Klein, *IceCube: An Instrument for Neutrino Astronomy*, *Rev. Sci. Instrum.* **81** (2010) 081101 [1007.1247].

[220] M. Ageron et al., *ANTARES: The first undersea neutrino telescope*, *Nuclear Instruments and Methods in Physics Research A* **656** (2011) 11 [1104.1607].

[221] S. Fukuda et al., *The Super-Kamiokande detector*, *Nuclear Instruments and Methods in Physics Research Section A: Accelerators, Spectrometers, Detectors and Associated Equipment* **501** (2003) 418.

[222] F. Kahlhoefer, *Review of LHC Dark Matter Searches*, *Int. J. Mod. Phys. A* **32** (2017) 1730006 [1702.02430].

[223] LHC Study Group collaboration, *The Large Hadron Collider: Conceptual design*, .

[224] I. Zurbano Fernandez et al., *High-Luminosity Large Hadron Collider (HL-LHC): Technical design report*, .

[225] S. Myers, *The LEP collider, from design to approval and commissioning*, .

[226] ATLAS collaboration, *The ATLAS Experiment at the CERN Large Hadron Collider*, *JINST* **3** (2008) S08003.

[227] CMS collaboration, *The CMS Experiment at the CERN LHC*, *JINST* **3** (2008) S08004.

[228] ATLAS collaboration, *Dark matter summary plots for s-channel, 2HDM+a, Higgs portal and Dark Higgs models*, tech. rep., CERN, Geneva, 2023.

[229] CMS collaboration, *Search for heavy stable charged particles with* 12.9 fb^{-1} *of 2016 data*, tech. rep., 2016.

[230] ATLAS collaboration, *Search for charginos nearly mass degenerate with the lightest neutralino based on a disappearing-track signature in pp collisions at* $\sqrt{s}$*=8 TeV with the ATLAS detector*, *Phys. Rev. D* **88** (2013) 112006 [1310.3675].

[231] ATLAS collaboration, *Search for Displaced Leptons in* $\sqrt{s} = 13$ *TeV pp Collisions with the ATLAS Detector*, *Phys. Rev. Lett.* **127** (2021) 051802 [2011.07812].

[232] CMS collaboration, *Search for Displaced Supersymmetry in events with an electron and a muon with large impact parameters*, *Phys. Rev. Lett.* **114** (2015) 061801 [1409.4789].

[233] CMS collaboration, *Search for disappearing tracks in proton-proton collisions at*

$\sqrt{s} = 13$ *TeV*, *Phys. Lett. B* **806** (2020) 135502 [2004.05153].
[234] ATLAS collaboration, *Search for long-lived charginos based on a disappearing-track signature in pp collisions at $\sqrt{s} = 13$ TeV with the ATLAS detector*, *JHEP* **06** (2018) 022 [1712.02118].
[235] ATLAS collaboration, *Search for heavy charged long-lived particles in the ATLAS detector in 36.1 fb^{-1} of proton-proton collision data at $\sqrt{s} = 13$ TeV*, *Phys. Rev. D* **99** (2019) 092007 [1902.01636].
[236] CMS collaboration, *Search for disappearing tracks as a signature of new long-lived particles in proton-proton collisions at $\sqrt{s} = 13$ TeV*, *JHEP* **08** (2018) 016 [1804.07321].
[237] CMS collaboration, *Search for displaced leptons in the e-mu channel*, tech. rep., 2016.
[238] M. Milgrom, *A Modification of the Newtonian dynamics as a possible alternative to the hidden mass hypothesis*, *Astrophys. J.* **270** (1983) 365.
[239] M. Milgrom, *A Modification of the Newtonian dynamics: Implications for galaxies*, *Astrophys. J.* **270** (1983) 371.
[240] M. Milgrom, *A modification of the Newtonian dynamics: implications for galaxy systems*, *Astrophys. J.* **270** (1983) 384.
[241] J. Bekenstein and M. Milgrom, *Does the missing mass problem signal the breakdown of Newtonian gravity?*, *Astrophys. J.* **286** (1984) 7.
[242] R. H. Sanders and S. S. McGaugh, *Modified Newtonian dynamics as an alternative to dark matter*, *Ann. Rev. Astron. Astrophys.* **40** (2002) 263 [astro-ph/0204521].
[243] B. Famaey and S. McGaugh, *Modified Newtonian Dynamics (MOND): Observational Phenomenology and Relativistic Extensions*, *Living Rev. Rel.* **15** (2012) 10 [1112.3960].
[244] I. Banik and H. Zhao, *From Galactic Bars to the Hubble Tension: Weighing Up the Astrophysical Evidence for Milgromian Gravity*, *Symmetry* **14** (2022) 1331 [2110.06936].
[245] S. S. McGaugh, J. M. Schombert, G. D. Bothun and W. J. G. de Blok, *The Baryonic Tully-Fisher relation*, *Astrophys. J. Lett.* **533** (2000) L99 [astro-ph/0003001].
[246] D. C. Rodrigues, V. Marra, A. del Popolo and Z. Davari, *Absence of a fundamental acceleration scale in galaxies*, *Nature Astron.* **2** (2018) 668 [1806.06803].
[247] S. S. McGaugh, P. Li, F. Lelli and J. M. Schombert, *Presence of a fundamental acceleration scale in galaxies*, *Nature Astronomy* **2** (2018) 924.
[248] D. C. Rodrigues, V. Marra, A. Del Popolo and Z. Davari, *Reply to 'Presence of a fundamental acceleration scale in galaxies' and 'A common Milgromian acceleration scale in nature'*, *Nature Astron.* **2** (2018) 927 [1811.05882].
[249] P. Li, F. Lelli, S. McGaugh, J. Schombert and K.-H. Chae, *A cautionary tale in fitting galaxy rotation curves with Bayesian techniques - Does Newton's constant vary from galaxy to galaxy?*, *Astron. Astrophys.* **646** (2021) L13 [2101.11644].
[250] R. Sancisi, *The Visible matter - Dark matter coupling*, *IAU Symp.* **220** (2004) 233 [astro-ph/0311348].
[251] S. Dodelson, *The Real Problem with MOND*, *Int. J. Mod. Phys. D* **20** (2011) 2749 [1112.1320].
[252] P. Kroupa, E. Gjergo, E. Asencio, M. Haslbauer, J. Pflamm-Altenburg, N. Wittenburg et al., *The many tensions with dark-matter based models and implications on the nature of the Universe*, *PoS* **CORFU2022** (2023) 231

[2309.11552].
[253] R. Ibata, A. Sollima, C. Nipoti, M. Bellazzini, S. C. Chapman and E. Dalessandro, *The globular cluster NGC 2419: a crucible for theories of gravity*, *Astrophys. J.* **738** (2011) 186 [1106.4909].
[254] R. H. Sanders, *NGC 2419 does not challenge MOND, Part 2*, *MNRAS* **422** (2012) L21 [1111.4334].
[255] S. S. McGaugh, *A tale of two paradigms: the mutual incommensurability of ΛCDM and MOND*, *Can. J. Phys.* **93** (2015) 250 [1404.7525].
[256] M. Milgrom, *Quasi-linear formulation of MOND*, *Mon. Not. Roy. Astron. Soc.* **403** (2010) 886 [0911.5464].
[257] M. Milgrom, *MOND theory*, *Can. J. Phys.* **93** (2015) 107 [1404.7661].
[258] J. D. Bekenstein, *Relativistic gravitation theory for the MOND paradigm*, *Phys. Rev. D* **70** (2004) 083509 [astro-ph/0403694].
[259] J. Sakstein and B. Jain, *Implications of the Neutron Star Merger GW170817 for Cosmological Scalar-Tensor Theories*, *Phys. Rev. Lett.* **119** (2017) 251303 [1710.05893].
[260] S. Boran, S. Desai, E. O. Kahya and R. P. Woodard, *GW170817 Falsifies Dark Matter Emulators*, *Phys. Rev. D* **97** (2018) 041501 [1710.06168].
[261] T. Jacobson and D. Mattingly, *Gravity with a dynamical preferred frame*, *Phys. Rev. D* **64** (2001) 024028 [gr-qc/0007031].
[262] T. G. Zlosnik, P. G. Ferreira and G. D. Starkman, *Modifying gravity with the Aether: An alternative to Dark Matter*, *Phys. Rev. D* **75** (2007) 044017 [astro-ph/0607411].
[263] M. Milgrom, *Bimetric MOND gravity*, *Phys. Rev. D* **80** (2009) 123536 [0912.0790].
[264] E. P. Verlinde, *Emergent Gravity and the Dark Universe*, *SciPost Phys.* **2** (2017) 016 [1611.02269].
[265] S. Hossenfelder, *Covariant version of Verlinde's emergent gravity*, *Phys. Rev. D* **95** (2017) 124018 [1703.01415].
[266] C. Skordis and T. Zlosnik, *New Relativistic Theory for Modified Newtonian Dynamics*, *Phys. Rev. Lett.* **127** (2021) 161302 [2007.00082].
[267] T. Mistele, S. McGaugh and S. Hossenfelder, *Aether scalar tensor theory confronted with weak lensing data at small accelerations*, *Astron. Astrophys.* **676** (2023) A100 [2301.03499].
[268] Q. Guo et al., *Further evidence for a population of dark-matter-deficient dwarf galaxies*, *Nature Astron.* **4** (2019) 246 [1908.00046].
[269] P. van Dokkum et al., *A trail of dark-matter-free galaxies from a bullet-dwarf collision*, *Nature* **605** (2022) 435 [2205.08552].
[270] S. Comerón, I. Trujillo, M. Cappellari, F. Buitrago, L. E. Garduño, J. Zaragoza-Cardiel et al., *The massive relic galaxy NGC 1277 is dark matter deficient. From dynamical models of integral-field stellar kinematics out to five effective radii*, *Astron. Astrophys.* **675** (2023) A143 [2303.11360].
[271] E. Asencio, I. Banik, S. Mieske, A. Venhola, P. Kroupa and H. Zhao, *The distribution and morphologies of Fornax Cluster dwarf galaxies suggest they lack dark matter*, *MNRAS* **515** (2022) 2981 [2208.02265].
[272] I. Banik, C. Pittordis, W. Sutherland, B. Famaey, R. Ibata, S. Mieske et al., *Strong constraints on the gravitational law from Gaia DR3 wide binaries*, *MNRAS* **527** (2024) 4573 [2311.03436].
[273] K.-H. Chae, *Breakdown of the Newton–Einstein Standard Gravity at Low Acceleration in Internal Dynamics of Wide Binary Stars*, *Astrophys. J.* **952**

(2023) 128 [2305.04613].
[274] E. W. Kolb and M. S. Turner, *The Early Universe*, vol. 69. Front.Phys., 1990, 10.1201/9780429492860.
[275] J. K. Yadav, J. S. Bagla and N. Khandai, *Fractal Dimension as a measure of the scale of Homogeneity*, *MNRAS* **405** (2010) 2009 [1001.0617].
[276] A. Friedmann, *Über die krümmung des raumes*, *Zeitschrift fur Physik* **10** (1922) 377.
[277] G. Lemaître, *Expansion of the universe, a homogeneous universe of constant mass and increasing radius accounting for the radial velocity of extra-galactic nebulae*, *MNRAS* **91** (1931) 483.
[278] H. P. Robertson, *Kinematics and world-structure iii.*, *The Astrophys. J.* **83** (1936) 257.
[279] A. G. Walker, *On milne's theory of world-structure*, *Proceedings of the London Mathematical Society* **2** (1937) 90.
[280] A. Einstein, *Die Grundlage der allgemeinen Relativitätstheorie*, *Annalen der Physik* **354** (1916) 769.
[281] D. Baumann, *Inflation*, in *Theoretical Advanced Study Institute in Elementary Particle Physics: Physics of the Large and the Small*, pp. 523–686, 2011, 0907.5424, DOI.
[282] S. Weinberg, *Gravitation and Cosmology*. John Wiley and Sons, New York, 1972.
[283] D. Baumann, "Cosmology: Part III Mathematical Tripos." https://homes.psd.uchicago.edu/~liantaow/my-teaching/dark-matter-472/lectures.pdf, 2015.
[284] R. C. Tolman, *On the Weight of Heat and Thermal Equilibrium in General Relativity*, *Phys. Rev.* **35** (1930) 904.
[285] J. Liouville, *Note sur la théorie de la variation des constantes arbitraires*, *Journal de Mathématiques Pures et Appliquées* (1838) 342.
[286] K. Huang, *Statistical Mechanics*. John Wiley and Sons, New York, 2000.
[287] E. Christoffel, *Ueber die Transformation der homogenen Differentialausdrücke zweiten Grades*, *Journal für die reine und angewandte Mathematik* **70** (1869) 46.
[288] G. Källén, *Elementary particle physics*. Addison-Wesley, Reading, MA, 1964.
[289] M. Abramowitz and I. A. Stegun, *Handbook of mathematical functions: with formulas, graphs, and mathematical tables*, vol. 55. Courier Corporation, 1965.
[290] R. J. Scherrer and M. S. Turner, *On the Relic, Cosmic Abundance of Stable Weakly Interacting Massive Particles*, *Phys. Rev.* **D33** (1986) 1585.
[291] L. J. Hall, K. Jedamzik, J. March-Russell and S. M. West, *Freeze-In Production of FIMP Dark Matter*, *JHEP* **03** (2010) 080 [0911.1120].
[292] K. Griest and D. Seckel, *Three exceptions in the calculation of relic abundances*, *Phys. Rev. D* **43** (1991) 3191.
[293] M. Garny, J. Heisig, B. Lülf and S. Vogl, *Coannihilation without chemical equilibrium*, *Phys. Rev. D* **96** (2017) .
[294] R. T. D'Agnolo, D. Pappadopulo and J. T. Ruderman, *Fourth exception in the calculation of relic abundances*, *Phys. Rev. Lett.* **119** (2017) .
[295] J. L. Feng, A. Rajaraman and F. Takayama, *SuperWIMP dark matter signals from the early universe*, *Phys. Rev. D* **68** (2003) 063504 [hep-ph/0306024].
[296] T. Bringmann, *Particle Models and the Small-Scale Structure of Dark Matter*, *New J. Phys.* **11** (2009) 105027 [0903.0189].
[297] T. Binder, T. Bringmann, M. Gustafsson and A. Hryczuk, *Early kinetic decoupling*

of dark matter: when the standard way of calculating the thermal relic density fails, *Phys. Rev. D* **96** (2017) 115010 [1706.07433].

[298] E. D. Carlson, M. E. Machacek and L. J. Hall, *Self-interacting Dark Matter*, *Astrophys. J.* **398** (1992) 43.

[299] D. N. Spergel and P. J. Steinhardt, *Observational Evidence for Self-Interacting Cold Dark Matter*, *Phys. Rev. Lett.* **84** (2000) 3760 [astro-ph/9909386].

[300] Y. Hochberg, E. Kuflik, T. Volansky and J. G. Wacker, *Mechanism for Thermal Relic Dark Matter of Strongly Interacting Massive Particles*, *Phys. Rev. Lett.* **113** (2014) 171301 [1402.5143].

[301] E. Kuflik, M. Perelstein, N. R.-L. Lorier and Y.-D. Tsai, *Elastically Decoupling Dark Matter*, *Phys. Rev. Lett.* **116** (2016) 221302 [1512.04545].

[302] F. D'Eramo and J. Thaler, *Semi-annihilation of Dark Matter*, *JHEP* **06** (2010) 109 [1003.5912].

[303] D. E. Kaplan, M. A. Luty and K. M. Zurek, *Asymmetric Dark Matter*, *Phys. Rev.* **D79** (2009) 115016 [0901.4117].

[304] K. M. Zurek, *Asymmetric Dark Matter: Theories, Signatures, and Constraints*, *Phys. Rept.* **537** (2014) 91 [1308.0338].

[305] P. Asadi, E. D. Kramer, E. Kuflik, G. W. Ridgway, T. R. Slatyer and J. Smirnov, *Accidentally Asymmetric Dark Matter*, *Phys. Rev. Lett.* **127** (2021) 211101 [2103.09822].

[306] P. Asadi, E. D. Kramer, E. Kuflik, G. W. Ridgway, T. R. Slatyer and J. Smirnov, *Thermal squeezeout of dark matter*, *Phys. Rev. D* **104** (2021) 095013 [2103.09827].

[307] J. Edsjö and P. Gondolo, *Neutralino relic density including coannihilations*, *Phys. Rev. D* **56** (1997) 1879–1894.

[308] M. Garny, J. Heisig, M. Hufnagel and B. Lülf, *Top-philic dark matter within and beyond the wimp paradigm*, *Phys. Rev. D* **97** (2018) .

[309] S. Mizuta and M. Yamaguchi, *Coannihilation effects and relic abundance of Higgsino dominant LSP(s)*, *Phys. Lett. B* **298** (1993) 120 [hep-ph/9208251].

[310] J. R. Ellis, T. Falk, K. A. Olive and M. Srednicki, *Calculations of neutralino-stau coannihilation channels and the cosmologically relevant region of MSSM parameter space*, *Astropart. Phys.* **13** (2000) 181 [hep-ph/9905481].

[311] C. Boehm, A. Djouadi and M. Drees, *Light scalar top quarks and supersymmetric dark matter*, *Phys. Rev. D* **62** (2000) 035012 [hep-ph/9911496].

[312] J. R. Ellis, K. A. Olive and Y. Santoso, *Calculations of neutralino stop coannihilation in the CMSSM*, *Astropart. Phys.* **18** (2003) 395 [hep-ph/0112113].

[313] J. Hisano, S. Matsumoto and M. M. Nojiri, *Unitarity and higher order corrections in neutralino dark matter annihilation into two photons*, *Phys. Rev. D* **67** (2003) 075014 [hep-ph/0212022].

[314] J. Edsjo, M. Schelke, P. Ullio and P. Gondolo, *Accurate relic densities with neutralino, chargino and sfermion coannihilations in mSUGRA*, *JCAP* **04** (2003) 001 [hep-ph/0301106].

[315] G. Belanger, F. Boudjema, C. Hugonie, A. Pukhov and A. Semenov, *Relic density of dark matter in the NMSSM*, *JCAP* **09** (2005) 001 [hep-ph/0505142].

[316] H. Baer, T. Krupovnickas, A. Mustafayev, E.-K. Park, S. Profumo and X. Tata, *Exploring the BWCA (bino-wino co-annihilation) scenario for neutralino dark matter*, *JHEP* **12** (2005) 011 [hep-ph/0511034].

[317] S. Profumo and C. E. Yaguna, *Gluino coannihilations and heavy bino dark matter*,

Phys. Rev. D **69** (2004) 115009 [hep-ph/0402208].
[318] N. Arkani-Hamed, A. Delgado and G. F. Giudice, *The Well-tempered neutralino*, *Nucl. Phys. B* **741** (2006) 108 [hep-ph/0601041].
[319] J. Harz, B. Herrmann, M. Klasen, K. Kovarik and Q. L. Boulc'h, *Neutralino-stop coannihilation into electroweak gauge and Higgs bosons at one loop*, *Phys. Rev. D* **87** (2013) 054031 [1212.5241].
[320] J. Harz, B. Herrmann, M. Klasen, K. Kovařík and M. Meinecke, *SUSY-QCD corrections to stop annihilation into electroweak final states including Coulomb enhancement effects*, *Phys. Rev. D* **91** (2015) 034012 [1410.8063].
[321] J. Harz, B. Herrmann, M. Klasen and K. Kovarik, *One-loop corrections to neutralino-stop coannihilation revisited*, *Phys. Rev. D* **91** (2015) 034028 [1409.2898].
[322] J. Harz, B. Herrmann, M. Klasen, K. Kovarik and P. Steppeler, *Theoretical uncertainty of the supersymmetric dark matter relic density from scheme and scale variations*, *Phys. Rev. D* **93** (2016) 114023 [1602.08103].
[323] S. Schmiemann, J. Harz, B. Herrmann, M. Klasen and K. Kovařík, *Squark-pair annihilation into quarks at next-to-leading order*, *Phys. Rev. D* **99** (2019) 095015 [1903.10998].
[324] K. Harigaya, M. Kawasaki, K. Mukaida and M. Yamada, *Dark Matter Production in Late Time Reheating*, *Phys. Rev. D* **89** (2014) 083532 [1402.2846].
[325] A. Hryczuk, R. Iengo and P. Ullio, *Relic densities including Sommerfeld enhancements in the MSSM*, *JHEP* **03** (2011) 069 [1010.2172].
[326] A. Hryczuk and R. Iengo, *The one-loop and Sommerfeld electroweak corrections to the Wino dark matter annihilation*, *JHEP* **01** (2012) 163 [1111.2916].
[327] M. Beneke, C. Hellmann and P. Ruiz-Femenia, *Non-relativistic pair annihilation of nearly mass degenerate neutralinos and charginos I. General framework and S-wave annihilation*, *JHEP* **03** (2013) 148 [1210.7928].
[328] C. Hellmann and P. Ruiz-Femenía, *Non-relativistic pair annihilation of nearly mass degenerate neutralinos and charginos II. P-wave and next-to-next-to-leading order S-wave coefficients*, *JHEP* **08** (2013) 084 [1303.0200].
[329] M. Beneke, C. Hellmann and P. Ruiz-Femenia, *Non-relativistic pair annihilation of nearly mass degenerate neutralinos and charginos III. Computation of the Sommerfeld enhancements*, *JHEP* **05** (2015) 115 [1411.6924].
[330] M. Beneke, C. Hellmann and P. Ruiz-Femenia, *Heavy neutralino relic abundance with Sommerfeld enhancements - a study of pMSSM scenarios*, *JHEP* **03** (2015) 162 [1411.6930].
[331] A. Birkedal, A. Noble, M. Perelstein and A. Spray, *Little Higgs dark matter*, *Phys. Rev. D* **74** (2006) 035002 [hep-ph/0603077].
[332] L. Lopez Honorez, E. Nezri, J. F. Oliver and M. H. G. Tytgat, *The Inert Doublet Model: An Archetype for Dark Matter*, *JCAP* **02** (2007) 028 [hep-ph/0612275].
[333] M. J. Baker et al., *The Coannihilation Codex*, *JHEP* **12** (2015) 120 [1510.03434].
[334] L. D. Landau and E. M. Lifshits, *Quantum Mechanics: Non-Relativistic Theory*, vol. v.3 of *Course of Theoretical Physics*. Butterworth-Heinemann, Oxford, 1991.
[335] A. Sommerfeld, *About the diffraction and braking of electrons*, *annals of physics* **403** (1931) 257.
[336] N. Arkani-Hamed, D. P. Finkbeiner, T. R. Slatyer and N. Weiner, *A Theory of Dark Matter*, *Phys. Rev. D* **79** (2009) 015014 [0810.0713].
[337] R. Iengo, *Sommerfeld enhancement: general results from field theory diagrams*,

JHEP **2009** (2009) 024–024.
[338] S. Hannestad and T. Tram, *Sommerfeld Enhancement of DM Annihilation: Resonance Structure, Freeze-Out and CMB Spectral Bound*, *JCAP* **01** (2011) 016 [1008.1511].
[339] K. Blum, R. Sato and T. R. Slatyer, *Self-consistent Calculation of the Sommerfeld Enhancement*, *JCAP* **06** (2016) 021 [1603.01383].
[340] S. Cassel, *Sommerfeld factor for arbitrary partial wave processes*, *Journal of Physics G: Nuclear and Particle Physics* **37** (2010) 105009.
[341] E. E. Salpeter and H. A. Bethe, *A Relativistic equation for bound state problems*, *Phys. Rev.* **84** (1951) 1232.
[342] S. El Hedri, A. Kaminska and M. de Vries, *A sommerfeld toolbox for colored dark sectors*, *The European Physical Journal C* **77** (2017) .
[343] A. Messiah, *Quantum Mechanics Volume I*. North-Holland Publishing Company, 1970.
[344] H. A. Bethe and E. E. Salpeter, *Quantum Mechanics of One- and Two-Electron Atoms*. Springer Berlin, Heidelberg, 1957.
[345] K. Petraki, M. Postma and M. Wiechers, *Dark-matter bound states from feynman diagrams*, *JHEP* **2015** (2015) .
[346] M. Garny and J. Heisig, *Bound state effects on dark matter coannihilation: pushing the boundaries of conversion-driven freeze-out*, 2112.01499.
[347] T. Binder, M. Garny, J. Heisig, S. Lederer and K. Urban, *Excited bound states and their role in dark matter production*, *Phys. Rev. D* **108** (2023) 095030 [2308.01336].
[348] V. B. Berestetskii, E. M. Lifshitz and V. B. Pitaevskii, *Relativistic quantum theory. Pt.1*. Pergamon Press, 1971.
[349] B. v. Harling and K. Petraki, *Bound-state formation for thermal relic dark matter and unitarity*, *JCAP* **2014** (2014) 033–033.
[350] K. Petraki, M. Postma and J. de Vries, *Radiative bound-state-formation cross-sections for dark matter interacting via a Yukawa potential*, *JHEP* **04** (2017) 077 [1611.01394].
[351] J. Harz and K. Petraki, *Radiative bound-state formation in unbroken perturbative non-Abelian theories and implications for dark matter*, *JHEP* **07** (2018) 096 [1805.01200].
[352] J. Harz and K. Petraki, *Higgs-mediated bound states in dark-matter models*, *JHEP* **2019** (2019) .
[353] P. Ko, T. Matsui and Y.-L. Tang, *Dark matter bound state formation in fermionic Z_2 DM model with light dark photon and dark Higgs boson*, *JHEP* **10** (2020) 082 [1910.04311].
[354] R. Oncala and K. Petraki, *Bound states of wimp dark matter in higgs-portal models. part ii. thermal decoupling*, *JHEP* **2021** (2021) .
[355] R. Oncala and K. Petraki, *Bound states of WIMP dark matter in Higgs-portal models. Part I. Cross-sections and transition rates*, *JHEP* **06** (2021) 124 [2101.08666].
[356] W. E. Caswell and G. P. Lepage, *Effective Lagrangians for Bound State Problems in QED, QCD, and Other Field Theories*, *Phys. Lett. B* **167** (1986) 437.
[357] G. T. Bodwin, E. Braaten and G. P. Lepage, *Rigorous QCD analysis of inclusive annihilation and production of heavy quarkonium*, *Phys. Rev. D* **51** (1995) 1125 [hep-ph/9407339].
[358] A. Pineda and J. Soto, *Effective field theory for ultrasoft momenta in NRQCD and*

NRQED, *Nucl. Phys. B Proc. Suppl.* **64** (1998) 428 [hep-ph/9707481].
[359] A. Pineda and J. Soto, *Potential NRQED: The Positronium case*, *Phys. Rev. D* **59** (1999) 016005 [hep-ph/9805424].
[360] N. Brambilla, A. Pineda, J. Soto and A. Vairo, *Potential NRQCD: An Effective theory for heavy quarkonium*, *Nucl. Phys. B* **566** (2000) 275 [hep-ph/9907240].
[361] N. Brambilla, A. Pineda, J. Soto and A. Vairo, *Effective Field Theories for Heavy Quarkonium*, *Rev. Mod. Phys.* **77** (2005) 1423 [hep-ph/0410047].
[362] G. Paz, *An Introduction to NRQED*, *Mod. Phys. Lett. A* **30** (2015) 1550128 [1503.07216].
[363] P. Asadi, M. Baumgart, P. J. Fitzpatrick, E. Krupczak and T. R. Slatyer, *Capture and Decay of Electroweak WIMPonium*, *JCAP* **02** (2017) 005 [1610.07617].
[364] S. Biondini and S. Vogl, *Coloured coannihilations: Dark matter phenomenology meets non-relativistic EFTs*, *JHEP* **02** (2019) 016 [1811.02581].
[365] S. Biondini and V. Shtabovenko, *Non-relativistic and potential non-relativistic effective field theories for scalar mediators*, *JHEP* **08** (2021) 114 [2106.06472].
[366] S. Biondini and V. Shtabovenko, *Bound-state formation, dissociation and decays of darkonium with potential non-relativistic Yukawa theory for scalar and pseudoscalar mediators*, *JHEP* **03** (2022) 172 [2112.10145].
[367] S. Biondini, N. Brambilla, G. Qerimi and A. Vairo, *Effective field theories for dark matter pairs in the early universe: cross sections and widths*, *JHEP* **07** (2023) 006 [2304.00113].
[368] R. H. Cyburt, J. R. Ellis, B. D. Fields, K. A. Olive and V. C. Spanos, *Bound-State Effects on Light-Element Abundances in Gravitino Dark Matter Scenarios*, *JCAP* **11** (2006) 014 [astro-ph/0608562].
[369] J. D. March-Russell and S. M. West, *WIMPonium and Boost Factors for Indirect Dark Matter Detection*, *Phys. Lett. B* **676** (2009) 133 [0812.0559].
[370] W. Shepherd, T. M. P. Tait and G. Zaharijas, *Bound states of weakly interacting dark matter*, *Phys. Rev. D* **79** (2009) 055022 [0901.2125].
[371] M. B. Wise and Y. Zhang, *Stable Bound States of Asymmetric Dark Matter*, *Phys. Rev. D* **90** (2014) 055030 [1407.4121].
[372] J. Ellis, F. Luo and K. A. Olive, *Gluino coannihilation revisited*, *JHEP* **2015** (2015) .
[373] A. Mitridate, M. Redi, J. Smirnov and A. Strumia, *Cosmological Implications of Dark Matter Bound States*, *JCAP* **05** (2017) 006 [1702.01141].
[374] E. A. Milne, *The Effect of Collisions on Monochromatic Radiative Equilibrium*, *MNRAS* **88** (1928) 493.
[375] T. Binder, A. Filimonova, K. Petraki and G. White, *Saha equilibrium for metastable bound states and dark matter freeze-out*, 2112.00042.
[376] J. Harz and K. Petraki, *Higgs enhancement for the dark matter relic density*, *Phys. Rev. D* **97** (2018) .
[377] A. DiFranzo, K. I. Nagao, A. Rajaraman and T. M. Tait, *Simplified models for dark matter interacting with quarks*, *JHEP* **2013** (2013) .
[378] J. Hisano, S. Matsumoto, M. Nagai, O. Saito and M. Senami, *Non-perturbative effect on thermal relic abundance of dark matter*, *Phys. Lett. B* **646** (2007) 34 [hep-ph/0610249].
[379] M. Beneke, P. Falgari and C. Schwinn, *Soft radiation in heavy-particle pair production: All-order colour structure and two-loop anomalous dimension*, *Nucl. Phys. B* **828** (2010) 69 [0907.1443].
[380] M. Beneke, R. Szafron and K. Urban, *Wino potential and Sommerfeld effect at*

NLO, *Phys. Lett. B* **800** (2020) 135112 [1909.04584].
[381] D. Buttazzo, G. Degrassi, P. P. Giardino, G. F. Giudice, F. Sala, A. Salvio et al., *Investigating the near-criticality of the Higgs boson*, *JHEP* **12** (2013) 089 [1307.3536].
[382] G. Bélanger, F. Boudjema, A. Goudelis, A. Pukhov and B. Zaldivar, *micrOMEGAs5.0 : Freeze-in*, *Comput. Phys. Commun.* **231** (2018) 173 [1801.03509].
[383] G. Alguero, G. Belanger, F. Boudjema, S. Chakraborti, A. Goudelis, S. Kraml et al., *micrOMEGAs 6.0: N-component dark matter*, 2312.14894.
[384] A. Belyaev, N. D. Christensen and A. Pukhov, *Calchep 3.4 for collider physics within and beyond the standard model*, *Computer Physics Communications* **184** (2013) 1729–1769.
[385] M. Garny and J. Heisig, *Interplay of super-WIMP and freeze-in production of dark matter*, *Phys. Rev. D* **98** (2018) 095031 [1809.10135].
[386] XENON collaboration, *First Dark Matter Search Results from the XENON1T Experiment*, *Phys. Rev. Lett.* **119** (2017) 181301 [1705.06655].
[387] DARWIN collaboration, *DARWIN: towards the ultimate dark matter detector*, *JCAP* **11** (2016) 017 [1606.07001].
[388] ATLAS collaboration, *Search for squarks and gluinos in final states with jets and missing transverse momentum using 139 fb^{-1} of $\sqrt{s}$ =13 TeV pp collision data with the ATLAS detector*, *JHEP* **02** (2021) 143 [2010.14293].
[389] ATLAS collaboration, *Search for new phenomena in high-mass diphoton final states using 37 fb^{-1} of proton–proton collisions collected at $\sqrt{s} = 13$ TeV with the ATLAS detector*, *Phys. Lett. B* **775** (2017) 105 [1707.04147].
[390] CMS collaboration, *Searches for Long-Lived Charged Particles in pp Collisions at $\sqrt{s}$=7 and 8 TeV*, *JHEP* **07** (2013) 122 [1305.0491].
[391] CMS Collaboration collaboration, *Search for heavy stable charged particles with* 12.9 fb^{-1} *of 2016 data*, tech. rep., CERN, Geneva, 2016.
[392] M. Cahill-Rowley, S. El Hedri, W. Shepherd and D. G. E. Walker, *Perturbative Unitarity Constraints on Charged/Colored Portals*, *Phys. Dark Univ.* **22** (2018) 48 [1501.03153].
[393] A. Schuessler and D. Zeppenfeld, *Unitarity constraints on MSSM trilinear couplings*, in *15th International Conference on Supersymmetry and the Unification of Fundamental Interactions (SUSY07)*, pp. 236–239, 10, 2007, 0710.5175.
[394] Y. Kats and M. D. Schwartz, *Annihilation decays of bound states at the lhc*, *JHEP* **2010** (2010) .
[395] J. Alwall, R. Frederix, S. Frixione, V. Hirschi, F. Maltoni, O. Mattelaer et al., *The automated computation of tree-level and next-to-leading order differential cross sections, and their matching to parton shower simulations*, *JHEP* **07** (2014) 079 [1405.0301].
[396] S. Dulat, T.-J. Hou, J. Gao, M. Guzzi, J. Huston, P. Nadolsky et al., *New parton distribution functions from a global analysis of quantum chromodynamics*, *Phys. Rev. D* **93** (2016) 033006 [1506.07443].
[397] B. Dumont, B. Fuks, S. Kraml, S. Bein, G. Chalons, E. Conte et al., *Toward a public analysis database for LHC new physics searches using MADANALYSIS 5*, *Eur. Phys. J. C* **75** (2015) 56 [1407.3278].
[398] ATLAS collaboration, *Search for new phenomena in events with an energetic jet and missing transverse momentum in pp collisions at $\sqrt{s}$ =13 TeV with the*

ATLAS detector, *Phys. Rev. D* **103** (2021) 112006 [2102.10874].

[399] T. Sjöstrand, S. Ask, J. R. Christiansen, R. Corke, N. Desai, P. Ilten et al., *An introduction to PYTHIA 8.2*, *Comput. Phys. Commun.* **191** (2015) 159 [1410.3012].

[400] S. Hoeche, F. Krauss, N. Lavesson, L. Lonnblad, M. Mangano, A. Schalicke et al., *Matching parton showers and matrix elements*, in *HERA and the LHC: A Workshop on the Implications of HERA for LHC Physics: CERN - DESY Workshop 2004/2005 (Midterm Meeting, CERN, 11-13 October 2004; Final Meeting, DESY, 17-21 January 2005)*, pp. 288–289, 2005, hep-ph/0602031, DOI.

[401] ATLAS collaboration, *Search for resonances in diphoton events at* $\sqrt{s}$*=13 TeV with the ATLAS detector*, *JHEP* **09** (2016) 001 [1606.03833].

[402] S. P. Martin, *Diphoton decays of stoponium at the Large Hadron Collider*, *Phys. Rev. D* **77** (2008) 075002 [0801.0237].

[403] B. Batell and S. Jung, *Probing Light Stops with Stoponium*, *JHEP* **07** (2015) 061 [1504.01740].

[404] O. Lebedev and T. Toma, *Relativistic Freeze-in*, *Phys. Lett. B* **798** (2019) 134961 [1908.05491].

[405] G. Bélanger, C. Delaunay, A. Pukhov and B. Zaldivar, *Dark matter abundance from the sequential freeze-in mechanism*, *Phys. Rev. D* **102** (2020) 035017 [2005.06294].

[406] T. Bringmann, S. Heeba, F. Kahlhoefer and K. Vangsnes, *Freezing-in a hot bath: resonances, medium effects and phase transitions*, *JHEP* **02** (2022) 110 [2111.14871].

[407] M. Garny, J. Heisig, B. Lülf and S. Vogl, *Coannihilation without chemical equilibrium*, *Phys. Rev. D* **96** (2017) 103521 [1705.09292].

[408] M. J. Baker, M. Breitbach, J. Kopp and L. Mittnacht, *Dynamic Freeze-In: Impact of Thermal Masses and Cosmological Phase Transitions on Dark Matter Production*, *JHEP* **03** (2018) 114 [1712.03962].

[409] J. M. No, P. Tunney and B. Zaldivar, *Probing Dark Matter freeze-in with long-lived particle signatures: MATHUSLA, HL-LHC and FCC-hh*, *JHEP* **03** (2020) 022 [1908.11387].

[410] Q. Decant, J. Heisig, D. C. Hooper and L. Lopez-Honorez, *Lyman-*α *constraints on freeze-in and superWIMPs*, *JCAP* **03** (2022) 041 [2111.09321].

[411] L. Calibbi, F. D'Eramo, S. Junius, L. Lopez-Honorez and A. Mariotti, *Displaced new physics at colliders and the early universe before its first second*, *JHEP* **05** (2021) 234 [2102.06221].

[412] M. Le Bellac, *Thermal Field Theory*, Cambridge Monographs on Mathematical Physics. Cambridge University Press, 1996, 10.1017/CBO9780511721700.

[413] J. I. Kapusta and C. Gale, *Finite-temperature field theory: Principles and applications*, Cambridge Monographs on Mathematical Physics. Cambridge University Press, 2011, 10.1017/CBO9780511535130.

[414] M. G. Mustafa, *An introduction to thermal field theory and some of its application*, *Eur. Phys. J. ST* **232** (2023) 1369 [2207.00534].

[415] T. Matsubara, *A New approach to quantum statistical mechanics*, *Prog. Theor. Phys.* **14** (1955) 351.

[416] M. Laine and A. Vuorinen, *Basics of Thermal Field Theory*, vol. 925. Springer, 2016, 10.1007/978-3-319-31933-9, [1701.01554].

[417] L. V. Keldysh, *Diagram technique for nonequilibrium processes*, *Zh. Eksp. Teor.*

Fiz. **47** (1964) 1515.
[418] J. S. Schwinger, *Brownian motion of a quantum oscillator*, *J. Math. Phys.* **2** (1961) 407.
[419] J. M. Cornwall, R. Jackiw and E. Tomboulis, *Effective Action for Composite Operators*, *Phys. Rev. D* **10** (1974) 2428.
[420] K.-c. Chou, Z.-b. Su, B.-l. Hao and L. Yu, *Equilibrium and Nonequilibrium Formalisms Made Unified*, *Phys. Rept.* **118** (1985) 1.
[421] R. E. Cutkosky, *Singularities and discontinuities of Feynman amplitudes*, *J. Math. Phys.* **1** (1960) 429.
[422] R. L. Kobes, G. W. Semenoff and N. Weiss, *Real Time Feynman Rules for Gauge Theories With Fermions at Finite Temperature and Density*, *Z. Phys. C* **29** (1985) 371.
[423] R. L. Kobes and G. W. Semenoff, *Discontinuities of Green Functions in Field Theory at Finite Temperature and Density*, *Nucl. Phys. B* **260** (1985) 714.
[424] R. L. Kobes and G. W. Semenoff, *Discontinuities of Green Functions in Field Theory at Finite Temperature and Density. 2*, *Nucl. Phys. B* **272** (1986) 329.
[425] R. Kobes and G. Semenoff, *Cutkosky rules for condensed-matter systems*, *Phys. Rev. B* **34** (1986) 4338.
[426] N. P. Landsman and C. G. van Weert, *Real and Imaginary Time Field Theory at Finite Temperature and Density*, *Phys. Rept.* **145** (1987) 141.
[427] P. F. Bedaque, A. K. Das and S. Naik, *Cutting rules at finite temperature*, *Mod. Phys. Lett. A* **12** (1997) 2481 [`hep-ph/9603325`].
[428] P. V. Landshoff, *Simple physical approach to thermal cutting rules*, *Phys. Lett. B* **386** (1996) 291 [`hep-ph/9606426`].
[429] T. Lundberg and R. Pasechnik, *Thermal Field Theory in real-time formalism: concepts and applications for particle decays*, *Eur. Phys. J. A* **57** (2021) 71 [`2007.01224`].
[430] E. Calzetta and B. L. Hu, *Nonequilibrium Quantum Fields: Closed Time Path Effective Action, Wigner Function and Boltzmann Equation*, *Phys. Rev. D* **37** (1988) 2878.
[431] E. A. Calzetta and B.-L. B. Hu, *Nonequilibrium Quantum Field Theory*. Oxford University Press, 2009, 10.1017/9781009290036.
[432] S. Biondini and J. Ghiglieri, *Freeze-in produced dark matter in the ultra-relativistic regime*, *JCAP* **03** (2021) 075 [`2012.09083`].
[433] S. Biondini and M. Laine, *Re-derived overclosure bound for the inert doublet model*, *JHEP* **08** (2017) 047 [`1706.01894`].
[434] S. Biondini and M. Laine, *Thermal dark matter co-annihilating with a strongly interacting scalar*, *JHEP* **04** (2018) 072 [`1801.05821`].
[435] R. D. Pisarski, *Scattering Amplitudes in Hot Gauge Theories*, *Phys. Rev. Lett.* **63** (1989) 1129.
[436] E. Braaten and R. D. Pisarski, *Soft Amplitudes in Hot Gauge Theories: A General Analysis*, *Nucl. Phys. B* **337** (1990) 569.
[437] U. Kraemmer and A. Rebhan, *Advances in perturbative thermal field theory*, *Rept. Prog. Phys.* **67** (2004) 351 [`hep-ph/0310337`].
[438] L. D. Landau and I. Pomeranchuk, *Limits of applicability of the theory of bremsstrahlung electrons and pair production at high-energies*, *Dokl. Akad. Nauk Ser. Fiz.* **92** (1953) 535.
[439] A. B. Migdal, *Bremsstrahlung and pair production in condensed media at high-energies*, *Phys. Rev.* **103** (1956) 1811.

[440] J. Ghiglieri and M. Laine, *Smooth interpolation between thermal Born and LPM rates*, *JHEP* **01** (2022) 173 [2110.07149].

[441] L. P. Kadanoff and G. Baym, *Quantum statistical mechanics*. CRC Press, 2018.

[442] J. Berges, *N-particle irreducible effective action techniques for gauge theories*, *Phys. Rev. D* **70** (2004) 105010 [hep-ph/0401172].

[443] J. Berges, *Introduction to nonequilibrium quantum field theory*, *AIP Conf. Proc.* **739** (2004) 3 [hep-ph/0409233].

[444] A. Riotto, *Towards a nonequilibrium quantum field theory approach to electroweak baryogenesis*, *Phys. Rev. D* **53** (1996) 5834 [hep-ph/9510271].

[445] W. Buchmuller and S. Fredenhagen, *Quantum mechanics of baryogenesis*, *Phys. Lett. B* **483** (2000) 217 [hep-ph/0004145].

[446] G. F. Giudice, A. Notari, M. Raidal, A. Riotto and A. Strumia, *Towards a complete theory of thermal leptogenesis in the SM and MSSM*, *Nucl. Phys. B* **685** (2004) 89 [hep-ph/0310123].

[447] V. Cirigliano, C. Lee, M. J. Ramsey-Musolf and S. Tulin, *Flavored Quantum Boltzmann Equations*, *Phys. Rev. D* **81** (2010) 103503 [0912.3523].

[448] A. Salvio, P. Lodone and A. Strumia, *Towards leptogenesis at NLO: the right-handed neutrino interaction rate*, *JHEP* **08** (2011) 116 [1106.2814].

[449] T. Prokopec, M. G. Schmidt and S. Weinstock, *Transport equations for chiral fermions to order h bar and electroweak baryogenesis. Part 1*, *Annals Phys.* **314** (2004) 208 [hep-ph/0312110].

[450] T. Prokopec, M. G. Schmidt and S. Weinstock, *Transport equations for chiral fermions to order h-bar and electroweak baryogenesis. Part II*, *Annals Phys.* **314** (2004) 267 [hep-ph/0406140].

[451] B. Garbrecht and T. Konstandin, *Separation of Equilibration Time-Scales in the Gradient Expansion*, *Phys. Rev. D* **79** (2009) 085003 [0810.4016].

[452] M. Garny, A. Hohenegger, A. Kartavtsev and M. Lindner, *Systematic approach to leptogenesis in nonequilibrium QFT: Self-energy contribution to the CP-violating parameter*, *Phys. Rev. D* **81** (2010) 085027 [0911.4122].

[453] M. Garny, A. Hohenegger, A. Kartavtsev and M. Lindner, *Systematic approach to leptogenesis in nonequilibrium QFT: Vertex contribution to the CP-violating parameter*, *Phys. Rev. D* **80** (2009) 125027 [0909.1559].

[454] M. Garny, A. Hohenegger and A. Kartavtsev, *Medium corrections to the CP-violating parameter in leptogenesis*, *Phys. Rev. D* **81** (2010) 085028 [1002.0331].

[455] M. Garny, A. Kartavtsev and A. Hohenegger, *Leptogenesis from first principles in the resonant regime*, *Annals Phys.* **328** (2013) 26 [1112.6428].

[456] M. Beneke, B. Garbrecht, C. Fidler, M. Herranen and P. Schwaller, *Flavoured Leptogenesis in the CTP Formalism*, *Nucl. Phys. B* **843** (2011) 177 [1007.4783].

[457] M. Beneke, B. Garbrecht, M. Herranen and P. Schwaller, *Finite Number Density Corrections to Leptogenesis*, *Nucl. Phys. B* **838** (2010) 1 [1002.1326].

[458] C. Fidler, M. Herranen, K. Kainulainen and P. M. Rahkila, *Flavoured quantum Boltzmann equations from cQPA*, *JHEP* **02** (2012) 065 [1108.2309].

[459] T. Frossard, M. Garny, A. Hohenegger, A. Kartavtsev and D. Mitrouskas, *Systematic approach to thermal leptogenesis*, *Phys. Rev. D* **87** (2013) 085009 [1211.2140].

[460] B. Garbrecht and M. Garny, *Finite Width in out-of-Equilibrium Propagators and Kinetic Theory*, *Annals Phys.* **327** (2012) 914 [1108.3688].

[461] B. Garbrecht, F. Glowna and M. Herranen, *Right-Handed Neutrino Production at Finite Temperature: Radiative Corrections, Soft and Collinear Divergences*, *JHEP* **04** (2013) 099 [1302.0743].
[462] B. Garbrecht, F. Glowna and P. Schwaller, *Scattering Rates For Leptogenesis: Damping of Lepton Flavour Coherence and Production of Singlet Neutrinos*, *Nucl. Phys. B* **877** (2013) 1 [1303.5498].
[463] B. Garbrecht, F. Gautier and J. Klaric, *Strong Washout Approximation to Resonant Leptogenesis*, *JCAP* **09** (2014) 033 [1406.4190].
[464] B. Garbrecht and P. Schwaller, *Spectator Effects during Leptogenesis in the Strong Washout Regime*, *JCAP* **10** (2014) 012 [1404.2915].
[465] B. Garbrecht and P. Millington, *Constraining the effective action by a method of external sources*, *Nucl. Phys. B* **906** (2016) 105 [1509.07847].
[466] M. Drewes, B. Garbrecht, D. Gueter and J. Klaric, *Leptogenesis from Oscillations of Heavy Neutrinos with Large Mixing Angles*, *JHEP* **12** (2016) 150 [1606.06690].
[467] B. Garbrecht, *Why is there more matter than antimatter? Calculational methods for leptogenesis and electroweak baryogenesis*, *Prog. Part. Nucl. Phys.* **110** (2020) 103727 [1812.02651].
[468] B. Garbrecht, P. Klose and C. Tamarit, *Relativistic and spectator effects in leptogenesis with heavy sterile neutrinos*, *JHEP* **02** (2020) 117 [1904.09956].
[469] P. F. Depta, A. Halsch, J. Hütig, S. Mendizabal and O. Philipsen, *Complete leading-order standard model corrections to quantum leptogenesis*, *JHEP* **09** (2020) 036 [2005.01728].
[470] K. Kainulainen, *CP-violating transport theory for electroweak baryogenesis with thermal corrections*, *JCAP* **11** (2021) 042 [2108.08336].
[471] M. Beneke, F. Dighera and A. Hryczuk, *Relic density computations at NLO: infrared finiteness and thermal correction*, *JHEP* **10** (2014) 045 [1409.3049].
[472] T. Binder, L. Covi and K. Mukaida, *Dark Matter Sommerfeld-enhanced annihilation and Bound-state decay at finite temperature*, *Phys. Rev. D* **98** (2018) 115023 [1808.06472].
[473] T. Binder, B. Blobel, J. Harz and K. Mukaida, *Dark matter bound-state formation at higher order: a non-equilibrium quantum field theory approach*, *JHEP* **09** (2020) 086 [2002.07145].
[474] T. Binder, K. Mukaida, B. Scheihing-Hitschfeld and X. Yao, *Non-Abelian electric field correlator at NLO for dark matter relic abundance and quarkonium transport*, *JHEP* **01** (2022) 137 [2107.03945].
[475] W.-Y. Ai, A. Beniwal, A. Maggi and D. J. E. Marsh, *From QFT to Boltzmann: Freeze-in in the presence of oscillating condensates*, 2310.08272.
[476] M. E. Carrington, G. Kunstatter and H. Zaraket, *2PI effective action and gauge invariance problems*, *Eur. Phys. J. C* **42** (2005) 253 [hep-ph/0309084].
[477] P. Millington and A. Pilaftsis, *Perturbative nonequilibrium thermal field theory*, *Phys. Rev. D* **88** (2013) 085009 [1211.3152].
[478] P. Millington and A. Pilaftsis, *Perturbative Non-Equilibrium Thermal Field Theory to all Orders in Gradient Expansion*, *Phys. Lett. B* **724** (2013) 56 [1304.7249].
[479] F. Glowna, *Right-handed Neutrino Production at Finite Temperatures: Radiative Corrections, Soft and Collinear Divergences*, Ph.D. thesis, Munich, Tech. U., 2015.
[480] P. M. Bakshi and K. T. Mahanthappa, *Expectation value formalism in quantum field theory. 1.*, *J. Math. Phys.* **4** (1963) 1.

[481] P. M. Bakshi and K. T. Mahanthappa, *Expectation value formalism in quantum field theory. 2.*, *J. Math. Phys.* **4** (1963) 12.

[482] M. Garny and M. M. Muller, *Kadanoff-Baym Equations with Non-Gaussian Initial Conditions: The Equilibrium Limit*, *Phys. Rev. D* **80** (2009) 085011 [0904.3600].

[483] M. E. Peskin and D. V. Schroeder, *An Introduction to quantum field theory.* Addison-Wesley, Reading, USA, 1995.

[484] C. Greiner and S. Leupold, *Stochastic interpretation of Kadanoff-Baym equations and their relation to Langevin processes*, *Annals Phys.* **270** (1998) 328 [hep-ph/9802312].

[485] D. Boyanovsky, H. J. de Vega, R. Holman, D. S. Lee and A. Singh, *Dissipation via particle production in scalar field theories*, *Phys. Rev. D* **51** (1995) 4419 [hep-ph/9408214].

[486] D. Boyanovsky, H. J. de Vega, R. Holman, S. P. Kumar and R. D. Pisarski, *Real time relaxation of condensates and kinetics in hot scalar QED: Landau damping*, *Phys. Rev. D* **58** (1998) 125009 [hep-ph/9802370].

[487] D. Boyanovsky, H. J. de Vega and S.-Y. Wang, *Dynamical renormalization group approach to quantum kinetics in scalar and gauge theories*, *Phys. Rev. D* **61** (2000) 065006 [hep-ph/9909369].

[488] D. Boyanovsky, K. Davey and C. M. Ho, *Particle abundance in a thermal plasma: Quantum kinetics vs. Boltzmann equation*, *Phys. Rev. D* **71** (2005) 023523 [hep-ph/0411042].

[489] M. Drewes, *On the Role of Quasiparticles and thermal Masses in Nonequilibrium Processes in a Plasma*, 1012.5380.

[490] K. Hamaguchi, T. Moroi and K. Mukaida, *Boltzmann equation for non-equilibrium particles and its application to non-thermal dark matter production*, *JHEP* **01** (2012) 083 [1111.4594].

[491] M. Drewes, S. Mendizabal and C. Weniger, *The Boltzmann Equation from Quantum Field Theory*, *Phys. Lett. B* **718** (2013) 1119 [1202.1301].

[492] M. Drewes, *Novel collective excitations in a hot scalar field theory*, *Phys. Lett. B* **732** (2014) 127 [1311.6641].

[493] M. Drewes and J. U. Kang, *The Kinematics of Cosmic Reheating*, *Nucl. Phys. B* **875** (2013) 315 [1305.0267].

[494] M. Drewes and J. U. Kang, *Sterile neutrino Dark Matter production from scalar decay in a thermal bath*, *JHEP* **05** (2016) 051 [1510.05646].

[495] K. Kainulainen and O. Koskivaara, *Non-equilibrium dynamics of a scalar field with quantum backreaction*, *JHEP* **12** (2021) 190 [2105.09598].

[496] F. Giacchino, L. Lopez-Honorez and M. H. G. Tytgat, *Scalar Dark Matter Models with Significant Internal Bremsstrahlung*, *JCAP* **10** (2013) 025 [1307.6480].

[497] F. Giacchino, A. Ibarra, L. Lopez Honorez, M. H. G. Tytgat and S. Wild, *Signatures from Scalar Dark Matter with a Vector-like Quark Mediator*, *JCAP* **02** (2016) 002 [1511.04452].

[498] S. Colucci, B. Fuks, F. Giacchino, L. Lopez Honorez, M. H. G. Tytgat and J. Vandecasteele, *Top-philic Vector-Like Portal to Scalar Dark Matter*, *Phys. Rev. D* **98** (2018) 035002 [1804.05068].

[499] C. E. Yaguna, *The Singlet Scalar as FIMP Dark Matter*, *JHEP* **08** (2011) 060 [1105.1654].

[500] N. Bernal, X. Chu, C. Garcia-Cely, T. Hambye and B. Zaldivar, *Production Regimes for Self-Interacting Dark Matter*, *JCAP* **03** (2016) 018 [1510.08063].

[501] P. Aurenche, F. Gelis and H. Zaraket, *Landau-Pomeranchuk-Migdal effect in thermal field theory*, *Phys. Rev. D* **62** (2000) 096012 [hep-ph/0003326].

[502] P. B. Arnold, G. D. Moore and L. G. Yaffe, *Photon emission from quark gluon plasma: Complete leading order results*, *JHEP* **12** (2001) 009 [hep-ph/0111107].

[503] A. Anisimov, D. Besak and D. Bodeker, *Thermal production of relativistic Majorana neutrinos: Strong enhancement by multiple soft scattering*, *JCAP* **03** (2011) 042 [1012.3784].

[504] J. Ghiglieri and M. Laine, *Neutrino dynamics below the electroweak crossover*, *JCAP* **07** (2016) 015 [1605.07720].

[505] M. J. Fernandez Lozano, *Freeze-In Dark Matter Production at Finite Temperature*, 2024.

[506] G. P. Lepage, *A New Algorithm for Adaptive Multidimensional Integration*, *J. Comput. Phys.* **27** (1978) 192.

[507] M. Galassi et al., *GNU Scientific Library Reference Manual (3rd Ed.)*. Network Theory Ltd, 2009.

[508] F. Bloch and A. Nordsieck, *Note on the Radiation Field of the electron*, *Phys. Rev.* **52** (1937) 54.

[509] T. Kinoshita, *Mass singularities of Feynman amplitudes*, *J. Math. Phys.* **3** (1962) 650.

[510] T. D. Lee and M. Nauenberg, *Degenerate Systems and Mass Singularities*, *Phys. Rev.* **133** (1964) B1549.

[511] J. Frenkel and J. C. Taylor, *High Temperature Limit of Thermal QCD*, *Nucl. Phys. B* **334** (1990) 199.

[512] J. C. Taylor and S. M. H. Wong, *The Effective Action of Hard Thermal Loops in QCD*, *Nucl. Phys. B* **346** (1990) 115.

[513] E. Braaten and R. D. Pisarski, *Simple effective Lagrangian for hard thermal loops*, *Phys. Rev. D* **45** (1992) R1827.

[514] E. Braaten and R. D. Pisarski, *Calculation of the quark damping rate in hot QCD*, *Phys. Rev. D* **46** (1992) 1829.

[515] R. D. Pisarski, *Damping rates for moving particles in hot QCD*, *Phys. Rev. D* **47** (1993) 5589.

[516] C. P. Kiessig, M. Plumacher and M. H. Thoma, *Decay of a Yukawa fermion at finite temperature and applications to leptogenesis*, *Phys. Rev. D* **82** (2010) 036007 [1003.3016].

[517] V. V. Klimov, *Spectrum of Elementary Fermi Excitations in Quark Gluon Plasma. (In Russian)*, *Sov. J. Nucl. Phys.* **33** (1981) 934.

[518] H. A. Weldon, *Effective Fermion Masses of Order gT in High Temperature Gauge Theories with Exact Chiral Invariance*, *Phys. Rev. D* **26** (1982) 2789.

[519] H. A. Weldon, *Covariant Calculations at Finite Temperature: The Relativistic Plasma*, *Phys. Rev. D* **26** (1982) 1394.

[520] A. Goudelis, P. Papachristou and V. C. Spanos, *Mechanism for baryogenesis via feebly interacting massive particles*, *Phys. Rev. D* **105** (2022) 043521 [2111.05740].

[521] R. Mertig, M. Bohm and A. Denner, *FEYN CALC: Computer algebraic calculation of Feynman amplitudes*, *Comput. Phys. Commun.* **64** (1991) 345.

[522] V. Shtabovenko, R. Mertig and F. Orellana, *FeynCalc 9.3: New features and improvements*, *Comput. Phys. Commun.* **256** (2020) 107478 [2001.04407].

[523] M. D'Onofrio and K. Rummukainen, *Standard model cross-over on the lattice*,

Phys. Rev. D **93** (2016) 025003 [1508.07161].
[524] A. Arrizabalaga and J. Smit, *Gauge fixing dependence of Phi derivable approximations*, *Phys. Rev. D* **66** (2002) 065014 [hep-ph/0207044].
[525] E. Mottola, *Gauge invariance in 2pi effective actions*, in *5th Internationa Conference on Strong and Electroweak Matter*, pp. 432–436, 2003, hep-ph/0304279, DOI.
[526] U. Reinosa and J. Serreau, *2PI functional techniques for gauge theories: QED*, *Annals Phys.* **325** (2010) 969 [0906.2881].
[527] A. Ibarra, A. Pierce, N. R. Shah and S. Vogl, *Anatomy of Coannihilation with a Scalar Top Partner*, *Phys. Rev. D* **91** (2015) 095018 [1501.03164].
[528] J. Bollig and S. Vogl, *Impact of bound states on non-thermal dark matter production*, 2112.01491.
[529] S. Biondini, *Bound-state effects for dark matter with Higgs-like mediators*, *JHEP* **06** (2018) 104 [1805.00353].
[530] M. Fukugita and T. Yanagida, *Baryogenesis Without Grand Unification*, *Phys. Lett. B* **174** (1986) 45.
[531] A. Riotto and M. Trodden, *Recent progress in baryogenesis*, *Ann. Rev. Nucl. Part. Sci.* **49** (1999) 35 [hep-ph/9901362].
[532] R. Barbieri, P. Creminelli, A. Strumia and N. Tetradis, *Baryogenesis through leptogenesis*, *Nucl. Phys.* **B575** (2000) 61 [hep-ph/9911315].
[533] W. Buchmuller, R. D. Peccei and T. Yanagida, *Leptogenesis as the origin of matter*, *Ann. Rev. Nucl. Part. Sci.* **55** (2005) 311 [hep-ph/0502169].
[534] D. Besak and D. Bodeker, *Thermal production of ultrarelativistic right-handed neutrinos: Complete leading-order results*, *JCAP* **03** (2012) 029 [1202.1288].
[535] S.-Y. Wang, *Gauge dependence of the fermion quasiparticle poles in hot gauge theories*, *Phys. Rev. D* **70** (2004) 065011 [hep-ph/0406002].
[536] A. J. Niemi and G. W. Semenoff, *Thermodynamic Calculations in Relativistic Finite Temperature Quantum Field Theories*, *Nucl. Phys. B* **230** (1984) 181.
[537] A. J. Niemi and G. W. Semenoff, *Finite Temperature Quantum Field Theory in Minkowski Space*, *Annals Phys.* **152** (1984) 105.
[538] R. L. Kobes and K. L. Kowalski, *Path Integral Formulation of Real Time Finite Temperature Field Theory*, *Phys. Rev. D* **34** (1986) 513.
[539] K. L. Kowalski, *Comment on Real Time Finite Temperature Gauge Field Propagators*, *Z. Phys. C* **36** (1987) 665.
[540] P. V. Landshoff and A. Rebhan, *Covariant gauges at finite temperature*, *Nucl. Phys. B* **383** (1992) 607 [hep-ph/9205235].
[541] L. D. Faddeev and V. N. Popov, *Feynman Diagrams for the Yang-Mills Field*, *Phys. Lett. B* **25** (1967) 29.
[542] P. V. Landshoff and A. Rebhan, *Thermalization of longitudinal gluons*, *Nucl. Phys. B* **410** (1993) 23 [hep-ph/9303276].
[543] A. Rebhan, *Thermal gauge field theories*, *Lect. Notes Phys.* **583** (2002) 161 [hep-ph/0105183].
[544] P. V. Landshoff and A. Rebhan, *Frozen ghosts in thermal gauge field theory*, 0903.1865.
[545] C. W. Bernard, *Feynman Rules for Gauge Theories at Finite Temperature*, *Phys. Rev. D* **9** (1974) 3312.
[546] H. Hata and T. Kugo, *An Operator Formalism of Statistical Mechanics of Gauge Theory in Covariant Gauges*, *Phys. Rev. D* **21** (1980) 3333.
[547] S. N. Gupta, *Theory of longitudinal photons in quantum electrodynamics*, *Proc.*

Phys. Soc. A **63** (1950) 681.
[548] K. Bleuler, *A New method of treatment of the longitudinal and scalar photons*, *Helv. Phys. Acta* **23** (1950) 567.
[549] J. C. D'Olivo, J. F. Nieves, M. Torres and E. Tututi, *QED at finite temperature in the Coulomb gauge*, `hep-ph/9402222`.
[550] J. C. D'Olivo and J. F. Nieves, *Remarks on the Coulomb and covariant gauges in finite temperature QED*, *Phys. Lett. B* **359** (1995) 148 [`hep-ph/9508394`].
[551] Y. Wang and L. Zhu, *Solving nonlinear Volterra integro-differential equations of fractional order by using Euler wavelet method*, *Advances in Difference Equations* **2017** (2017) .
[552] A. Daşcıoğlu and H. Yaslan, *Chebyshev Polynomial Solution of Nonlinear Fredholm-Volterra Integro-Differential Equations*, *Çankaya University, Journal of Arts and Sciences* **5** (2006) 89.
[553] N. Hale, *An ultraspherical spectral method for linear Fredholm and Volterra integro-differential equations of convolution type*, *IMA Journal of Numerical Analysis* **39** (2018) 1727.
[554] M. R. Eslahchi, M. Dehghan and M. Parvizi, *Application of the collocation method for solving nonlinear fractional integro-differential equations*, *Journal of Computational and Applied Mathematics* **257** (2014) 105.
[555] J. Lang, *Phenomenology of Freeze-in Dark Matter Production*, 2023.
[556] R. H. Cyburt, B. D. Fields, K. A. Olive and T.-H. Yeh, *Big Bang Nucleosynthesis: 2015*, *Rev. Mod. Phys.* **88** (2016) 015004 [`1505.01076`].
[557] M. S. Turner, *Coherent Scalar Field Oscillations in an Expanding Universe*, *Phys. Rev.* **D28** (1983) 1243.
[558] R. J. Scherrer and M. S. Turner, *Decaying Particles Do Not Heat Up the Universe*, *Phys. Rev.* **D31** (1985) 681.
[559] D. H. Lyth and E. D. Stewart, *Thermal inflation and the moduli problem*, *Phys. Rev.* **D53** (1996) 1784 [`hep-ph/9510204`].
[560] G. F. Giudice, E. W. Kolb and A. Riotto, *Largest temperature of the radiation era and its cosmological implications*, *Phys. Rev. D* **64** (2001) 023508 [`hep-ph/0005123`].
[561] B. S. Acharya, G. Kane, S. Watson and P. Kumar, *A Non-thermal WIMP Miracle*, *Phys. Rev.* **D80** (2009) 083529 [`0908.2430`].
[562] G. L. Kane, P. Kumar, B. D. Nelson and B. Zheng, *Dark matter production mechanisms with a nonthermal cosmological history: A classification*, *Phys. Rev.* **D93** (2016) 063527 [`1502.05406`].
[563] G. Kane, K. Sinha and S. Watson, *Cosmological Moduli and the Post-Inflationary Universe: A Critical Review*, *Int. J. Mod. Phys. D* **24** (2015) 1530022 [`1502.07746`].
[564] A. L. Erickcek, *The Dark Matter Annihilation Boost from Low-Temperature Reheating*, *Phys. Rev.* **D92** (2015) 103505 [`1504.03335`].
[565] R. T. Co, F. D'Eramo, L. J. Hall and D. Pappadopulo, *Freeze-In Dark Matter with Displaced Signatures at Colliders*, *JCAP* **12** (2015) 024 [`1506.07532`].
[566] M. Kamionkowski and M. S. Turner, *Thermal relics: Do we know their abundances?*, *Phys. Rev. D* **42** (1990) 3310.
[567] P. J. E. Peebles and B. Ratra, *Cosmology with a Time Variable Cosmological Constant*, *Astrophys. J.* **325** (1988) L17.
[568] B. Ratra and P. J. E. Peebles, *Cosmological Consequences of a Rolling Homogeneous Scalar Field*, *Phys. Rev.* **D37** (1988) 3406.

[569] T. Karwal and M. Kamionkowski, *Dark energy at early times, the Hubble parameter, and the string axiverse*, *Phys. Rev. D* **94** (2016) 103523 [1608.01309].
[570] R. Allahverdi et al., *The First Three Seconds: a Review of Possible Expansion Histories of the Early Universe*, *Open J.Astrophys.* **4** (2020) [2006.16182].
[571] A. H. Guth, *The Inflationary Universe: A Possible Solution to the Horizon and Flatness Problems*, *Phys. Rev. D* **23** (1981) 347.
[572] L. Kofman, A. D. Linde and A. A. Starobinsky, *Reheating after inflation*, *Phys. Rev. Lett.* **73** (1994) 3195 [hep-th/9405187].
[573] P. B. Greene and L. Kofman, *Preheating of fermions*, *Phys. Lett. B* **448** (1999) 6 [hep-ph/9807339].
[574] CMB-S4 collaboration, *CMB-S4 Science Book, First Edition*, 1610.02743.
[575] L. Amendola et al., *Cosmology and fundamental physics with the Euclid satellite*, *Living Rev. Rel.* **21** (2018) 2 [1606.00180].
[576] FCC collaboration, *FCC-hh: The Hadron Collider: Future Circular Collider Conceptual Design Report Volume 3*, *Eur. Phys. J. ST* **228** (2019) 755.
[577] F. D'Eramo, N. Fernandez and S. Profumo, *Dark Matter Freeze-in Production in Fast-Expanding Universes*, *JCAP* **1802** (2018) 046 [1712.07453].
[578] F. D'Eramo, N. Fernandez and S. Profumo, *When the Universe Expands Too Fast: Relentless Dark Matter*, *JCAP* **1705** (2017) 012 [1703.04793].
[579] N. Bernal, F. Elahi, C. Maldonado and J. Unwin, *Ultraviolet Freeze-in and Non-Standard Cosmologies*, *JCAP* **11** (2019) 026 [1909.07992].
[580] J. Silva-Malpartida, N. Bernal, J. Jones-Pérez and R. A. Lineros, *From WIMPs to FIMPs with Low Reheating Temperatures*, 2306.14943.
[581] Planck collaboration, *Planck 2018 results. X. Constraints on inflation*, *Astron. Astrophys.* **641** (2020) A10 [1807.06211].
[582] BICEP, Keck collaboration, *Improved Constraints on Primordial Gravitational Waves using Planck, WMAP, and BICEP/Keck Observations through the 2018 Observing Season*, *Phys. Rev. Lett.* **127** (2021) 151301 [2110.00483].
[583] A. D. Linde, *Inflationary Cosmology*, *Lect. Notes Phys.* **738** (2008) 1 [0705.0164].
[584] M. Drewes, L. Ming and I. Oldengott, *LiteBIRD and CMB-S4 sensitivities to reheating in plateau models of inflation*, *JCAP* **05** (2024) 081 [2303.13503].
[585] A. A. Starobinsky, *A New Type of Isotropic Cosmological Models Without Singularity*, *Phys. Lett. B* **91** (1980) 99.
[586] V. F. Mukhanov and G. V. Chibisov, *Quantum Fluctuations and a Nonsingular Universe*, *JETP Lett.* **33** (1981) 532.
[587] A. A. Starobinsky, *The Perturbation Spectrum Evolving from a Nonsingular Initially De-Sitter Cosmology and the Microwave Background Anisotropy*, *Sov. Astron. Lett.* **9** (1983) 302.
[588] T. P. Sotiriou and V. Faraoni, *f(R) Theories Of Gravity*, *Rev. Mod. Phys.* **82** (2010) 451 [0805.1726].
[589] B. Whitt, *Fourth Order Gravity as General Relativity Plus Matter*, *Phys. Lett. B* **145** (1984) 176.
[590] F. L. Bezrukov and M. Shaposhnikov, *The Standard Model Higgs boson as the inflaton*, *Phys. Lett. B* **659** (2008) 703 [0710.3755].
[591] R. Kallosh and A. Linde, *Universality Class in Conformal Inflation*, *JCAP* **07** (2013) 002 [1306.5220].
[592] R. Kallosh and A. Linde, *Non-minimal Inflationary Attractors*, *JCAP* **10** (2013) 033 [1307.7938].

[593] J. R. Ellis, A. B. Lahanas, D. V. Nanopoulos and K. Tamvakis, *No-Scale Supersymmetric Standard Model*, *Phys. Lett.* **134B** (1984) 429.
[594] J. R. Ellis, C. Kounnas and D. V. Nanopoulos, *No Scale Supersymmetric Guts*, *Nucl. Phys. B* **247** (1984) 373.
[595] A. B. Lahanas and D. V. Nanopoulos, *The Road to No Scale Supergravity*, *Phys. Rept.* **145** (1987) 1.
[596] J. Ellis, D. V. Nanopoulos and K. A. Olive, *No-Scale Supergravity Realization of the Starobinsky Model of Inflation*, *Phys. Rev. Lett.* **111** (2013) 111301 [1305.1247].
[597] J. Ellis, D. V. Nanopoulos and K. A. Olive, *Starobinsky-like Inflationary Models as Avatars of No-Scale Supergravity*, *JCAP* **10** (2013) 009 [1307.3537].
[598] E. Witten, *Dimensional Reduction of Superstring Models*, *Phys. Lett.* **155B** (1985) 151.
[599] M. A. G. Garcia, K. Kaneta, Y. Mambrini and K. A. Olive, *Inflaton Oscillations and Post-Inflationary Reheating*, *JCAP* **04** (2021) 012 [2012.10756].
[600] M. A. G. Garcia, K. Kaneta, Y. Mambrini and K. A. Olive, *Reheating and Post-inflationary Production of Dark Matter*, *Phys. Rev. D* **101** (2020) 123507 [2004.08404].
[601] N. Bernal and Y. Xu, *WIMPs during reheating*, *JCAP* **12** (2022) 017 [2209.07546].
[602] J. H. Traschen and R. H. Brandenberger, *Particle Production During Out-of-equilibrium Phase Transitions*, *Phys. Rev. D* **42** (1990) 2491.
[603] L. Kofman, A. D. Linde and A. A. Starobinsky, *Towards the theory of reheating after inflation*, *Phys. Rev. D* **56** (1997) 3258 [hep-ph/9704452].
[604] D. Baumann, *The Physics of Inflation.* CreateSpace Independent Publishing Platform, 2015.
[605] P. B. Greene, L. Kofman, A. D. Linde and A. A. Starobinsky, *Structure of resonance in preheating after inflation*, *Phys. Rev. D* **56** (1997) 6175 [hep-ph/9705347].
[606] M. A. Amin, M. P. Hertzberg, D. I. Kaiser and J. Karouby, *Nonperturbative Dynamics Of Reheating After Inflation: A Review*, *Int. J. Mod. Phys. D* **24** (2014) 1530003 [1410.3808].
[607] R. Micha and I. I. Tkachev, *Relativistic turbulence: A Long way from preheating to equilibrium*, *Phys. Rev. Lett.* **90** (2003) 121301 [hep-ph/0301101].
[608] R. Micha and I. I. Tkachev, *Turbulent thermalization*, *Phys. Rev. D* **70** (2004) 043538 [hep-ph/0403101].
[609] P. Adshead, J. T. Giblin, T. R. Scully and E. I. Sfakianakis, *Gauge-preheating and the end of axion inflation*, *JCAP* **12** (2015) 034 [1502.06506].
[610] D. G. Figueroa, A. Florio, F. Torrenti and W. Valkenburg, *CosmoLattice: A modern code for lattice simulations of scalar and gauge field dynamics in an expanding universe*, *Comput. Phys. Commun.* **283** (2023) 108586 [2102.01031].
[611] J. Berges, K. Boguslavski, S. Schlichting and R. Venugopalan, *Basin of attraction for turbulent thermalization and the range of validity of classical-statistical simulations*, *JHEP* **05** (2014) 054 [1312.5216].
[612] K. Mukaida and M. Yamada, *Cascades of high-energy SM particles in the primordial thermal plasma*, *JHEP* **10** (2022) 116 [2208.11708].
[613] M. Drees and B. Najjari, *Multi-species thermalization cascade of energetic particles in the early universe*, *JCAP* **08** (2023) 037 [2205.07741].
[614] K. Ichikawa, T. Suyama, T. Takahashi and M. Yamaguchi, *Primordial Curvature Fluctuation and Its Non-Gaussianity in Models with Modulated Reheating*,

Phys. Rev. D **78** (2008) 063545 [0807.3988].
[615] M. A. G. Garcia, K. Kaneta, Y. Mambrini, K. A. Olive and S. Verner, *Freeze-in from preheating*, *JCAP* **03** (2022) 016 [2109.13280].
[616] M. Drewes, J. U. Kang and U. R. Mun, *CMB constraints on the inflaton couplings and reheating temperature in α-attractor inflation*, *JHEP* **11** (2017) 072 [1708.01197].
[617] N. Bernal, M. Dutra, Y. Mambrini, K. Olive, M. Peloso and M. Pierre, *Spin-2 Portal Dark Matter*, *Phys. Rev. D* **97** (2018) 115020 [1803.01866].
[618] Y. Mambrini and K. A. Olive, *Gravitational Production of Dark Matter during Reheating*, *Phys. Rev. D* **103** (2021) 115009 [2102.06214].
[619] N. Bernal, J. Harz, M. A. Mojahed and Y. Xu, *Graviton- and Inflaton-mediated Dark Matter Production after Large Field Polynomial Inflation*, 2406.19447.
[620] J. Heeck and D. Teresi, *Cold keV dark matter from decays and scatterings*, *Phys. Rev. D* **96** (2017) 035018 [1706.09909].
[621] CMS collaboration, *Search for disappearing tracks in proton-proton collisions at $\sqrt{s} = 8$ TeV*, *JHEP* **01** (2015) 096 [1411.6006].
[622] J. L. Cook, E. Dimastrogiovanni, D. A. Easson and L. M. Krauss, *Reheating predictions in single field inflation*, *JCAP* **04** (2015) 047 [1502.04673].
[623] K. Abazajian et al., *CMB-S4 Science Case, Reference Design, and Project Plan*, 1907.04473.
[624] D. G. Figueroa, A. Florio, F. Torrenti and W. Valkenburg, *The art of simulating the early Universe – Part I*, *JCAP* **04** (2021) 035 [2006.15122].
[625] A. Kurkela and G. D. Moore, *Thermalization in Weakly Coupled Nonabelian Plasmas*, *JHEP* **12** (2011) 044 [1107.5050].
[626] K. Harigaya and K. Mukaida, *Thermalization after/during Reheating*, *JHEP* **05** (2014) 006 [1312.3097].
[627] K. Mukaida and M. Yamada, *Thermalization Process after Inflation and Effective Potential of Scalar Field*, *JCAP* **02** (2016) 003 [1506.07661].
[628] M. A. G. Garcia and M. A. Amin, *Prethermalization production of dark matter*, *Phys. Rev. D* **98** (2018) 103504 [1806.01865].
[629] M. Drees and B. Najjari, *Energy spectrum of thermalizing high energy decay products in the early universe*, *JCAP* **10** (2021) 009 [2105.01935].
[630] J. Ellis, M. A. G. Garcia, D. V. Nanopoulos and K. A. Olive, *Calculations of Inflaton Decays and Reheating: with Applications to No-Scale Inflation Models*, *JCAP* **07** (2015) 050 [1505.06986].
[631] L. Dai, M. Kamionkowski and J. Wang, *Reheating constraints to inflationary models*, *Phys. Rev. Lett.* **113** (2014) 041302 [1404.6704].
[632] M. Kawasaki, K. Kohri and N. Sugiyama, *MeV scale reheating temperature and thermalization of neutrino background*, *Phys. Rev. D* **62** (2000) 023506 [astro-ph/0002127].

This document has been written using the ShareLaTeX/Overleaf server provided by the Zentrum für Datenvereinbarung[1] of the Johannes Gutenberg University Mainz and typeset based on a modified version of the La Trobe PhD Thesis Template[2], which itself is a customization of the classicthesis[3] LaTeX template. Feynman diagrams were drawn with TikZ-Feynman[4]. Some intermediate computations and checks, as well as generation of plots, were performed using Wolfram Mathematica[5], where key packages and tools employed are MaTeX[6], FeynCalc[7], FeynRules[8]. Numerical calculations have been performed using Wolfram Mathematica, `C++`, and `Python` libraries and packages.

[1] https://www.zdv.uni-mainz.de/sharelatex-overleaf-latex-zdv-uni-mainz-de/
[2] https://github.com/bashimao/ltu-thesis
[3] https://bitbucket.org/amiede/classicthesis
[4] https://ctan.org/pkg/tikz-feynman?lang=de
[5] https://www.wolfram.com/mathematica/
[6] http://szhorvat.net/pelican/latex-typesetting-in-mathematica.html
[7] https://feyncalc.github.io/
[8] https://feynrules.irmp.ucl.ac.be/